



*The 2018-2019  
Cornell NanoScale Facility  
Research  
Accomplishments*



250 Duffield Hall • 343 Campus Road • Ithaca NY 14853-2700  
Phone: 607.255.2329 • Fax: 607.255.8601 •  
Email: [information@cnf.cornell.edu](mailto:information@cnf.cornell.edu) • Website: [www.cnf.cornell.edu](http://www.cnf.cornell.edu)

# **Cornell NanoScale Facility**

## **2018-2019**

# **Research Accomplishments**

**CNF Lester B. Knight Director:  
Christopher Kemper Ober**

**Director of Operations:  
Ronald Olson**

Cornell NanoScale Facility (CNF) is a member of the  
National Nanotechnology Coordinated Infrastructure (*[www.nnci.net](http://www.nnci.net)*)  
and is supported by the National Science Foundation under Grant No. NNCI-1542081,  
the New York State Office of Science, Technology and Academic Research,  
Cornell University, Industry, and our Users.

**The 2018-2019 CNF Research Accomplishments are also available on the web:  
[http://cnf.cornell.edu/publications/research\\_accomplishments](http://cnf.cornell.edu/publications/research_accomplishments)**

© 2019







Shear-Rate Controlled Microfluidic Devices to Examine von Willebrand Factor-Mediated Platelet Deposition. .... 32

Handheld Chem/Biosensor Combining Metasurfaces and Engineered Sensor Proteins to Enhance Surface Plasmon Resonance (SPR) ... 34

Metasurface Enhanced Infrared Spectroscopy for Live Cells .... 36

Retinal Implant Project . .... 38

Characterizing the Role of Tumor-Derived Extracellular Vesicles in Breast Cancer .. .... 40

Circulating Extracellular Vesicles and Physical Stress in ME/CF ... .... 42

Development of Microfluidic Device for Protein Synthesis and Modification.. .... 44

Development of a Heparin-Based Coacervate Loaded Liposomes as Non-Invasive Therapy for Myocardial Infarction... .... 46

Phytophthora Zoospore Chemotaxis .... 48

Characterization of Cancer Microvesicles ... .... 50

**Chemistry, 52-61**

Sample Preparation for Single-Electron Spin Detection . .... 52

Investigation of Area Selective Atomic Layer Deposition with Microreactor and in situ Surface Analysis .... 54

Thin Film, Laser-Etched Sorbent Sheets for Spatially Resolved and High Throughput Analysis of Volatiles .... 56

Fabrication of Graphene Microelectrodes ... .... 58

Small Molecule Photoresists for EUV Lithography .... 60

**Electronics, 62-75**

Power Electronic Devices Based on Ga<sub>2</sub>O<sub>3</sub>... .... 62

WSe<sub>2</sub> RF MOSFETs and CMOS Integration .. .... 64

Fully Transparent Oxide Thin-Film Transistor with Record Current and On/Off Ratio.. .... 66

Injectable Micro-Scale Opto-Electrically Transduced Electrodes ... .... 68

Trench Formation and Filling in Silicon Carbide... .... 70

Emerging III-Nitride Devices for Terahertz Electronics... .... 72

Fully Passivated InAlN/GaN HEMTs on Silicon with  $f_T/f_{MAX}$  of 144/141 GHz .. .... 74

**Materials, 76-109**

Area-Selective Deposition to Enable Single-digit nm Fabrication .. ....76

Metal-Organic Hybrid Photoresists ... ..78

Transient Laser Heating Derived Mesoporous Materials Directed  
by Gyroidal Templates from Block Copolymer Self-Assembly... ..80

Three-Dimensional Printing with Silica Cages . ....82

Fabricating Advanced Characterization  
Platforms for Polyelectrolyte Brushes..... ..84

Nanometer-Scale Area-Selective Formation of Polymer Brushes ... ..86

Engineering Transport in Confined  
Environments of Stable Radical Polymers .. ....88

Production of Beta-Tungsten as a Function of Sputtering Pressure .... ..90

Nanotube Transistor Arrays on a TEM Substrate .. ....92

Inertial Spreading and Imbibition  
of a Liquid Drop Through a Porous Surface .... ..94

Fabrication of Graphene-Encapsulated Photocathodes... ..96

Al<sub>2</sub>O<sub>3</sub> Deposition and Characterization on III-Nitride Surfaces for  
Improvement of Dielectric/Semiconductor  
Interface Properties and Device Reliability. .... ..98

Thermal and Electrical Properties  
of Quasi-1D van der Waals Nanowires... ..100

Fabricating Lithographically Designed Cylindrical Colloidal Particles .... ..102

Development of Microsensors for Air Quality Monitoring... ..104

Scissionable Polymer Photoresist for Extreme Ultraviolet Lithography... ..106

Quantum Materials for Communication, Computing, and Storage .... ..108

**Mechanical Devices, 110-135**

Responsive Liquid Crystal Micro Actuators  
for Microrobotic Applications . ....110

ALD for Membranes, Metamaterials, and Mechanisms... ..112

Localized Microfluidic Actuation and Mixing  
Using Planar Fresnel Type Gigahertz Ultrasonic Transducer .... ..114

N-Z Power NEMS Electrostatic RF Wakeup Receiver with Pt Contact . ....116

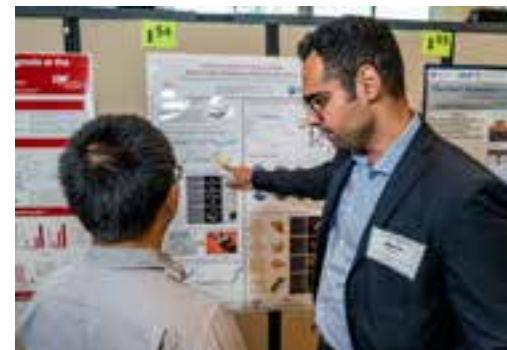
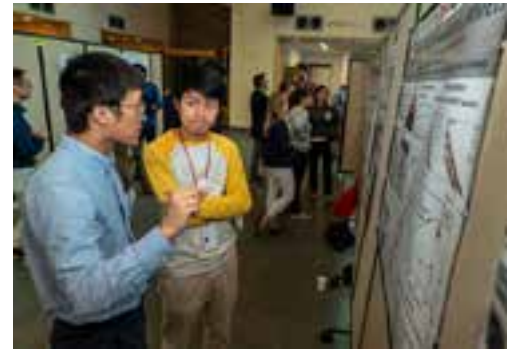
Boiling Heat Transfer Enhancement by  
Coupling Nanoscale Evaporation in Buried Nanochannels.. ....118

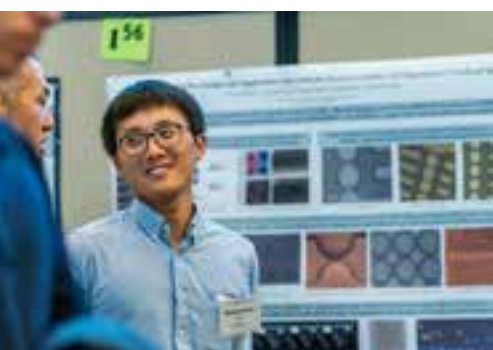
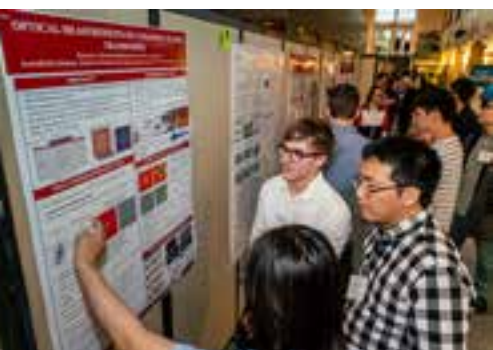
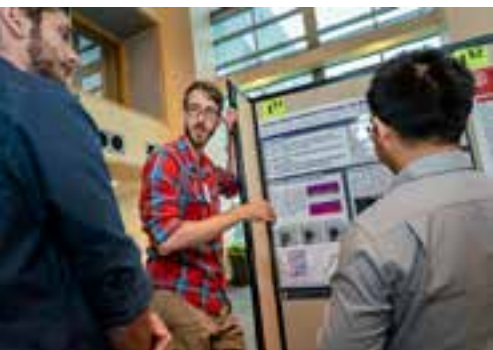
Fabrication of AlN HBAR Devices  
for Spin Manipulation of Diamond NV Centers .... ..120

NanoThermoMechanical Logic Thermal Gates. .... ..122

Making a Microfluidic Device to Mimic Flow Through Porous Medium .. ..124

Atomically Thin Metamaterial  
Robots, Origami, and Artificial Flagella . ....126





A MEMS Microphone Using Levitation Force ... .. 128

Carbon Dioxide as Thermal Fluid in Micro Systems . .... 130

Fabricating Vitreous Silica Micropillars  
for Uniaxial Compression with *in situ* Raman Spectroscopy .... .. 132

Construction of Microplasma Test Array .... .. 134

**Optics & Opto-Electronics, 136-157**

Self-Starting Lithium Niobate Soliton Microcombs..... .. 136

High-Q Two-Dimensional Lithium Niobate  
Photonic Crystal Slab Nanoresonators... .. 138

Fabrication of Anti-Resonant Reflecting  
Optical Waveguides for On-Chip Raman Spectroscopy... .. 140

High Quality Factor PECVD Si<sub>3</sub>N<sub>4</sub>  
Ring Resonators Compatible with CMOS Process. .... .. 142

III-N UV Photonic Devices .. .... 144

Development of Single and Double Layer  
Anti-Reflective Coatings for Astronomical Instruments.. .... 146

Fabricating All-Glass, 1 cm Diameter Metalens  
Working at Visible Wavelength .... .. 148

Metasurface-Based Infrared Optical Devices ... .. 150

Exploratory Etching and Electrodeposition Project ... .. 152

Metamaterial Spectrometer: A Low SWaP, Robust, High Performance  
Hyperspectral Sensor for Land and Atmospheric Remote Sensing .... .. 154

Ion Mill X-Ray Reflection Gratings .... .. 156

**Physics & Nanostructure Physics, 158-199**

Spin-Orbit Torque Switching of Magnetic  
Tunnel Junctions by Oxide Material.. .... 158

Reducing Write Current of Three Terminal Magnetic Tunnel Junctions by  
Engineering the Spin Hall Channel Structures .... .. 160

Spin Currents and Spin Fluctuations  
in Fe<sub>x</sub>Pt<sub>1-x</sub> Alloys and Heterostructures .... .. 162

Non-Local Spin Transport in Complex Oxide Thin Films .... .. 164

Photodiode Devices for Stimulation,  
Electrolysis, and Bubble Production . .... 166

Nanofabricated Superconducting Devices  
for Vortex Dynamics and Qubits .. .... 168

Fabrication of Nanofluidic Cavities for Superfluid 3He Studies .... .. 170

Fabrication of Nanoscale Josephson Junctions  
for Quantum Coherent Superconducting Circuits. .... .. 172

Spin Seebeck Imaging of Spin-Torque Switching  
in Antiferromagnetic Pt/NiO Heterostructures .... .. 174

**Physics & Nanostructure Physics, continued**

Fabrication and Measurements of Arrays  
of Constriction-Based Spin-Hall Nano-Oscillators .....176

Diamond and SiC Semi-Confocal Acoustic Resonator .....178

Coherent Spin-Magnon Coupling for Quantum-to-Quantum Transduction 180

Optical Properties of Locally Strained WSe<sub>2</sub> Monolayers .....182

μm-Scale Graphene-Based Hall Sensors with Tunable Sensitivity . ....184

Gigahertz Surface Acoustic Waves  
on Periodically Patterned Layered Nanostructures.....186

Ultrafast Energy-Efficient Spin-Torque MRA Memories... .....188

Low Loss Photonic Packaging Using Fusion Splicing . ....190

Spin Tunnel Field-Effect Transistors  
Based on Two-Dimensional van der Waals Heterostructures.....192

Non-Linear Anomalous Hall Effect in Few-Layer WTe<sub>2</sub>.....194

Mass Transport on Graphene .. .....196

Superconducting Thin Film Growth and Post Laser Annealing. ....198

**Process & Characterization, 200-207**

Directed Self Assembly of a Stable Radical Polymer.. .....200

Nanoscale Periodic Pillar Feature Process Survival.....202

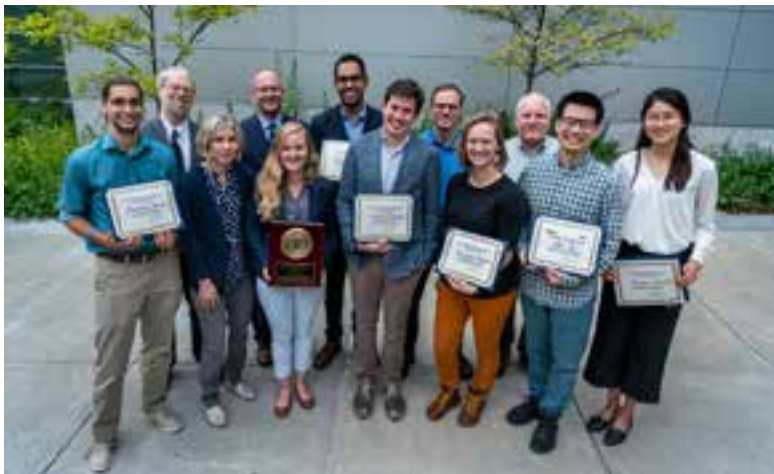
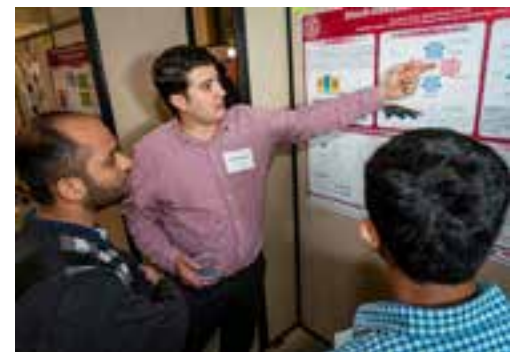
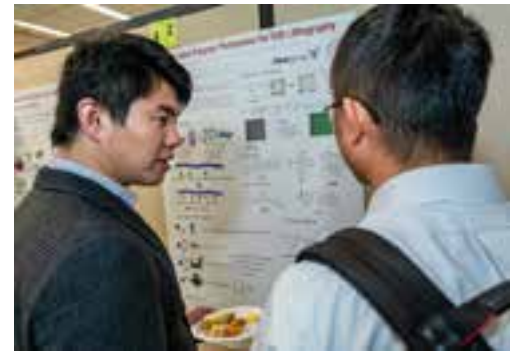
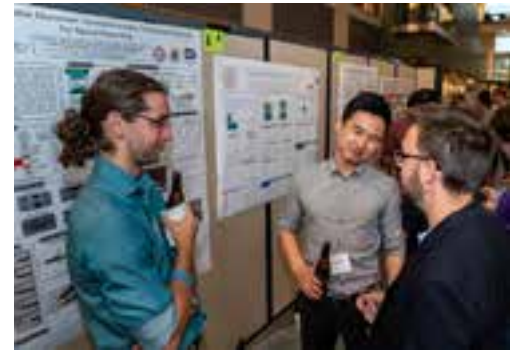
Size Characterization of Plasma Membrane  
Vesicles, Virus Particles, and Synthetic Vesicles .....204

Nanoslit Silicon Nitride Fabrication for Virus Filtration . ....206

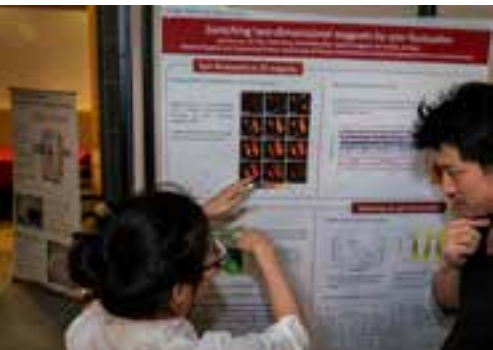
**Index, 208-212**

Reports by CNF Project Number... .....208

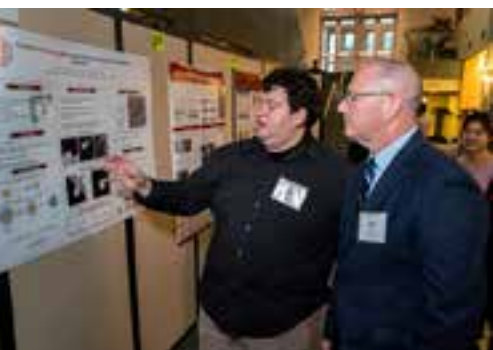
CNF Principal Investigators & Users.. .....209



# Directors' Introduction, 2019



It is a pleasure to write to you as we report exciting research in which the use of the **Cornell NanoScale Facility** played a pivotal role. We have also had a very good year in which we hired a new Director of Operations, Ron Olson, we have implemented some new process capabilities, and we have installed or will be buying and installing a range of new equipment, aligned with our strategic direction. Cornell is one of the sites that make up the National Nanotechnology Coordinated Infrastructure, NNCI. We hosted the NNCI network-wide convocation for many dozens of REU students who spent the summer at many sites in the network. More about these events are described below.



We would also like to take this opportunity to remind you that CNF serves as an open resource for scientists and engineers covering a broad range of nanotechnology areas, with emphasis on providing complex integration capabilities focused on the nanofabrication needs of the research community. We aid the research goals of CNF users through our staff of experts dedicated to providing rapid, affordable, hands-on, 24/7, open access to an integrated set of advanced nanofabrication tools. The CNF offers a flexible, uniquely sophisticated toolset (i.e., over 150 available lab instruments) along with a superior track record of enabling successful research projects. The user program has generated both regional and national interest drawing researchers from throughout the United States especially for projects requiring particularly challenging multi-step micro- and nanofabrication processes, or access to unique instruments.

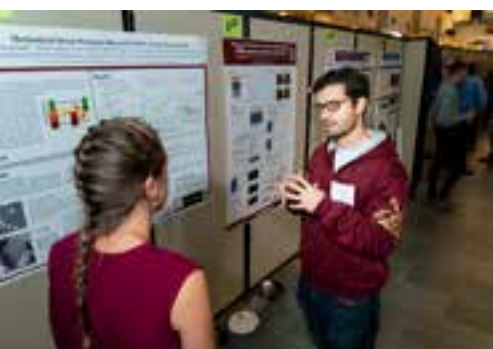


To meet our varied demands, CNF employs a technical staff of 23 (21 FTE) who maintain the equipment and baseline processes while assisting users at all levels — specifically focusing on the needs of the external user community. CNF maintains a full complement of processing and characterization equipment, with emphasis on electron beam lithography at the smallest dimensions, advanced stepper-based photolithography, as well as a wide array of deposition and etching resources necessary to meet the needs of a wide spectrum of materials. The CNF continues to be an interdisciplinary facility with activities spread across the physical sciences, engineering, and life sciences. Actively seeking to stay at the technology forefront CNF is responsive to new user requests and research trends.



## NNCI

Cornell is one of 16 sites that make up the National Nanotechnology Coordinated Infrastructure, NNCI, which is approaching its five-year mark. All 16 sites will take part in the renewal process for the next five years. This will involve writing a new proposal outlining plans for the CNF going forward. The support from the National Science Foundation that comes from our membership in NNCI is pivotal in keeping CNF at the forefront of nanofabrication and enables us to provide a knowledgeable staff to serve the user community.



## CNF USER PROGRAM

The CNF user program remains very strong. CNF welcomes over 500 users per year totaling more than 50,000 total hours of time in the Fab. In 2018, CNF users published at least 178 publications, 87 presentations, and 79 patents/applications/disclosures. Highlights of this research are presented in the CNF Research Accomplishments.

In order to continually improve our operation, CNF has long had a User Committee to provide constructive feedback to management. In Summer 2019, the user committee was reconstituted, with the appointment of eleven experienced CNF users.

This committee will meet periodically and provide advice to CNF management on operation procedures, existing and newly desired capabilities aimed towards the goal of continually improving the CNF user experience.

## CNF STRATEGIC DIRECTIONS

Considering a wide-range of input from recent workshops, the External Advisory Board, and discussions with faculty groups, five focus areas have been identified to help guide our future efforts and investments. These include heterointegration, 2-D materials, biotechnology, quantum materials and devices and Artificial Intelligence (AI) in the cleanroom. We believe these are the areas where CNF can have the most impact.

### 1. Heterointegration

The demand for connecting and packaging wafers, chips, stacks of chips, electronics/photonics and other discrete devices of different materials and functionality is growing. Wafer bonding and flip chip bonding are but two of the technologies that support this genre of fabrication. In addition to electrical connectivity, mechanical, fluidic, and photonic connections can be important for future applications. CNF intends to be at the forefront in providing this technology to its users.

### 2. 2-D Materials

Cornell is rapidly becoming a national center for activities involving 2D materials. Four recent faculty hires in this area add to Cornell's already strong position. Additionally, the PARADIM Materials Innovation Platform will bring a major influx of materials-by-design users to campus. Processing these novel materials will present equipment and contamination issues for fabrication facilities such as CNF.

### 3. Biotechnology

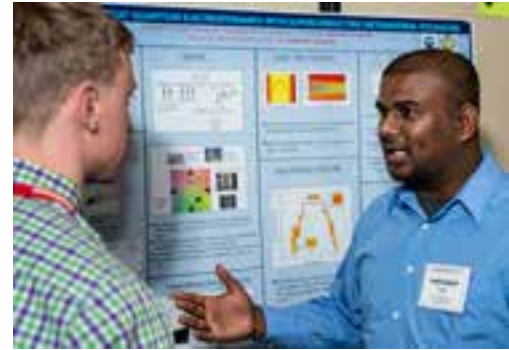
CNF has long been active in this area; life science projects, in fact, comprise the largest concentration of users in CNF. This includes a variety of sensor and microfluidic projects, to name two areas. While building on the traditional nanofabrication technologies, many of these projects present challenges in new materials. CNF will continue to actively support and encourage research in this area.

### 4. Quantum Materials and Devices

Quantum computing and the materials that enable it are a rapidly growing technology area. CNF provides nanofabrication support to the new quantum materials and devices being designed and investigated nationally. One of the CNF highlights includes a science paper highlighting work by researchers in Wisconsin and Syracuse who utilized CNF in the creation of new quantum devices. CNF is constantly working to improve the tools and knowledge base needed to facilitate the development of this important field.

### 5. Artificial Intelligence in the Cleanroom

SEMI announced they will be teaming with Cornell University to accelerate technology development using machine learning and artificial intelligence. CNF will take part in a pilot study to connect several tools and apply AI methods to analyze production of prototype MEMS structures. The motivation for this study is twofold. It will help CNF improve its process and increase the implementation speed of reliable new methods developed by students in the cleanroom. It will also aid the semiconductor industry in the application of these methods across toolsets; providing production companies and tool manufacturers with a means to share data while minimizing the worry of proprietary information leaks.





## NEW EQUIPMENT AND CAPABILITIES

CNF continues to upgrade its processing capabilities within our limited capital equipment budget. New processes have been developed by the CNF staff over the past year to meet the user demands for new materials and improved process control.

### LITHOGRAPHY

CNF's ASML deep UV stepper is one of the most advanced photolithography instruments in any academic laboratory. It is heavily used by both academic and industrial users. In 2019, we upgraded the ASML operator workstation to a Linux based system improving reliability, speed, and ease of operation.

CNF is replacing resist spinners with new CEE (Cost Effective Equipment) spin coat systems for improved reliability and process stability.

CNF staff have developed advanced software (JETStream) for solving difficult lithography problems such as writing on non-planar substrates or resolving exposure of geometric shapes below 40 nm on the JEOL JBX-9500FS and the JBX-6300FS electron beam lithography systems. These tools have been released to users. These software solutions were highlighted in a recent article by CNF staff Don Tennant, Amrita Banerjee, John Treichler, and Alan Bleier in JEOL News, 54, 28-34, (2019) (<https://www.jeolusa.com/NEWS-EVENTS/JEOL-NEWS-Magazine>).



To simplify e-beam lithography job setup, a CompileSDF application icon has been added to the JEOL JBX-6300FS to allow users to compile schedule files graphically instead of typing the "sched" command in a terminal window. After compiling, the user can click the ACHK button to view the layout of the job. Additional scripts are being added to center the objective aperture automatically instead of manually adjusting it.

CNF recently received an award for almost \$400,000 from the National Science Foundation under the Major Research Instrumentation (MRI) program for a Nanoscribe Photonic Professional GT 2 3D Laser Lithography System, a sub-micron scale 3D micro and nanofabrication tool based on precise implementation of 2-photon processes. This system will enable the fabrication of nano-, micro- and mesostructures with feature sizes down to 160 nm up to several millimeters. A team of Cornell faculty have committed to development of devices and processes with this new technology. Having this capability available will lead to increased capabilities for research topics ranging from biology and biomedical studies to photonics and material science. This system will be available in January 2020.



### ETCH

In the etch area, the staff and CNF Fellows developed new innovative processes for:

- Etching of TaN, TiN, Nb, Mo, MoSi<sub>2</sub> utilizing chlorine-based chemistries in the Plasma-Therm 770-ICP system
- Deep etching of GaN with 5:1 aspect ratio and smooth near vertical sidewalls for GaN HEMTS
- Low frequency bias and pulsed ICP Si etch with no microtrenching and inverse RIE-lag effect employing HBr/Ar utilizing the Oxford Cobra ICP etch system
- Artifact free SiC etch developed in the Oxford Cobra ICP system
- Utilization of Block Co-Polymer to fabricate high aspect ratio Si Nano wires

New capabilities have been developed using thermal nano imprint with a hybrid lithographic scheme to fabricate a template and then pattern transfer into Si and Si based dielectrics using advanced ICP based reactive ion etching.

CNF has entered into a joint development agreement with Plasma-Therm for atomic layer etching. Plasma-Therm will be providing an advanced Atomic Layer Etch (ALE)



system and CNF will be providing process development support. ALE allows precise (atomic layer by layer) etching and is critical to fabrication of devices with novel 2D materials ( $\text{MoS}_2$ , graphene,  $\text{WS}_2$ ,  $\text{WSe}_2$ ) as well as traditional metal oxide gate dielectrics.

## WET CHEMISTRY

CNF's advanced lithography capability has brought increased demand for processing of 200 mm wafers with the AMSL stepper. The CNF will be adding a heated quartz tank in the KOH hood capable of accommodating 200 mm wafers for ammonium hydroxide/hydrogen peroxide/RC1 cleaning. This tank will be paired with a 200 mm DI water dump rinser and 200 mm spin rinse dryer (SRD) unit. The hood modification will allow for cleaning of 200 mm wafers prior to critical lithography or deposition steps and/or cleaning after lithography re-work.

Lift-off remains a staple of many process sequences; at CNF it has always been a manual process. To improve reproducibility, CNF is acquiring a stand-alone liftoff tool from C&D Semiconductor. This system was custom designed for lift off processing utilizing spray DI and solvents. The system is capable of processing 100 mm and 150 mm wafers with the ability to upgrade to 200 mm and is equipped with filtration for precious metal reclaim.

## DEPOSITION

This year, 2019, brought some new additions to the thin film department. Last fall marked the introduction of the OEM Endeavor M1 system for deposition of piezoelectric materials. This tool utilizes a unique sputter gun design to deposit highly crystalline aluminum nitride at a substantially higher rate than standard sputtering techniques. Some very exciting research has been generated using this tool to investigate film morphology and etch rates. Also in 2019, CNF replaced its 30 year old CVC 601 sputtering system with a second AJA Orion sputter deposition system. This new AJA adds several capabilities such as DC co-sputtering and sputtering of magnetic films.

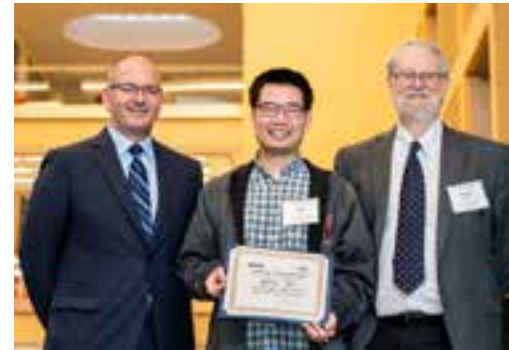
The Arradiance ALD system was upgraded with the addition of an ozone generator to provide increased capability for low temperature processing. New ozone-based processes have also been established for Pt,  $\text{Al}_2\text{O}_3$  and  $\text{TiO}_2$ .

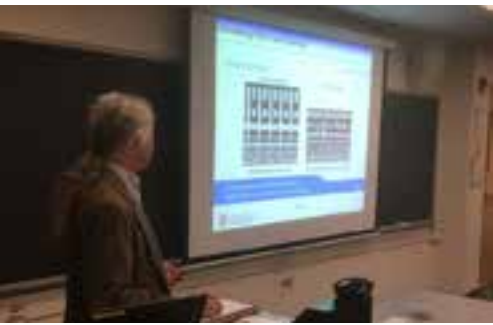
In an effort to expand deposition capabilities, CNF purchased an eight-inch wafer lift-off dome for CHA Mark 50 electron-beam evaporator. The platen will be able to hold seven, eight-inch wafers for thin film deposition.

## TEST AND ADVANCED PACKAGING

Supporting our strategic focus in heterointegration, a Finetech Fineplacer pico ma flip chip bonder is being installed for a wide range of micro assembly applications. These applications include flip chip bonding, die attach, and other novel bonding advanced packaging applications. This system has a 5  $\mu\text{m}$  placement accuracy, 450°C maximum heating temperature and variable bonding force range. Component size can vary from 0.125 mm  $\times$  0.125 mm to 100 mm  $\times$  100 mm with the ability to customize for other component sizes.

The CNF upgraded its 12+ year old Keithley 4200 Parameter Analyzer with a current state-of-the-art 4200A-SCS Analyzer. The new unit is configured with four source measure units (with pre-amps) providing output ranges of +/- 100 mA and +/- 210 V with a measurement resolution to 0.2  $\mu\text{V}$  and 10  $\mu\text{A}$ . The unit is also configured with a capacitance-voltage unit and an I-V/C-V multi switch module. The machine mounted on a rolling cart can be relocated to the SEM room for test measurements on the SEM-





mounted Zyvex or Xallant nano-probers when needed. It will replace the 25+ year old Keithley test instruments currently used on the Everbeing probe station.

In order to provide fast and reliable characterization in many thin film and device test applications, CNF acquired a Xallent nanoprobe for use with the next generation thin film and semiconductor test applications. The Xallent nanoprobe technology, featuring nanofabricated probes, was largely developed within CNF and is now commercialized by Xallent. The DARIUS (SEM and ambient air based) and SAKYIWA (ambient air based) nanoprobers enable capacitance-voltage and sheet resistance measurements in thin films and semiconductor production applications in ambient or vacuum. This system was purchased with the support of the Kavli Institute at Cornell for Nanoscale Science.



## LIFE SCIENCES

Several years ago, CNF assumed responsibility for additional equipment and space when the former NBTC was dissolved. CNF continues to expand its support of those life science users with the addition of a Biosafety Level 2 work space in Duffield 201.



## COMPUTATION

Through the efforts of David Freed, VP, Software Products at Lam Research and former CNF user, CNF acquired academic user licenses for Coventor SEMulator3D software for utilization on CNF's workstations, AWS cloud, and conversion computers. This software enables 3D simulation/modeling of complex process sequences for semiconductor and MEMS devices and provides the ability to predict downstream consequences of process changes otherwise requiring build-and-test cycles in the fab. This tool will be accessible to academic users only. CNF installation is in beta-release to staff and selected users. It will be available to the larger user database after extensive training sessions later this fall. We encourage users to take advantage of this powerful new capability



CNF updated the operating system across all general use Windows PCs. New Windows workstations were installed in the CAD Room, User Lounge, and Clean Room. The CNF Simulation Cluster was brought back online with a new head node, two new computational nodes and two new network switches enabling simulation of devices and processes. Additionally, new server hardware was purchased for the CNF THIN backend servers enabling user access to CORAL. A new backend database running directly on the user website was released for the reformatted equipment information sheets.



In 2019, we undertook an effort to completely replace our 20 year old website for increased reliability and functionality. The redesigned website was recently completed and introduced to the public immediately after the CNF Annual Meeting. The new website utilizes responsive design compatible with many devices including phones, tablets and computers. Take a look! <http://cnf.cornell.edu/>

## STAFFING NEWS

**Don Tennant** — Don recently retired as Director of Operations, a position he served in since 2006. Don is one of the pioneers of nanofabrication, known for his work on e-beam lithography and EUV patterning. CNF is fortunate to have had him at the helm for the last 13 years, including the critical transition from NNIN to NNCI. During this time, CNF replaced a majority of its processing facilities, including two new electron beam lithography systems. Don will stay connected to CNF as a Senior Strategic Advisor.

**Introduction from Ron Olson** — I am honored and excited to begin my service as the next Director of Operations. After benefiting as a CNF user earlier in my career, the opportunity to return to Cornell at this juncture is a privilege. My goal is to continue to improve upon the great work initiated since CNF's inception in 1977. I strive to build upon the foundation marked by years of success and growth. I am fortunate to follow in the footsteps of Don Tennant who has done such a great job over the past 13 years. Benefiting from the leadership of Chris Ober, Lynn Rathbun, and the accomplished technical staff there is no doubt CNF remains positioned to lead the industry by providing next-generation, state-of-the-art equipment, processes and facilities to the users.

I offer 32+ years of progressive experience as an innovator in fab operations as well as process and device development. Capitalizing on my past experiences while building upon established expertise, I intend to continue and improve advancements in science, engineering and technology at the nanoscale level. The goal of enhancing nanotechnology equipment, materials, processes and expertise available to CNF users remains in the forefront.

My wife, Maria and I are the proud parents of five — Cameron, Olivia, Ellisa, Bryce, and Madelyn. We enjoy visiting our children and supporting them in their various endeavors, cooking and spending time outdoors with Coast, our Golden Retriever.

My full biography can be found on the CNF home page.

**Beth Rhoades** — In the summer of 2019, long time staff member Beth Rhoades left CNF for a teaching position in the Cornell Vet School. Beth, a Ph.D. biologist, had served as CNF Biology Liaison since 2008. At CNF she supported life science users as well as a variety of fabrication tools and processes, many related to microfluidics. In addition to user support, Beth took major initiative in overseeing CNF's K-12 outreach activities including 4H, our TCN short course, and organization of our demonstration resources. We wish Beth the best in her new endeavors. Beth will still help coordinate our activities on a part time basis.

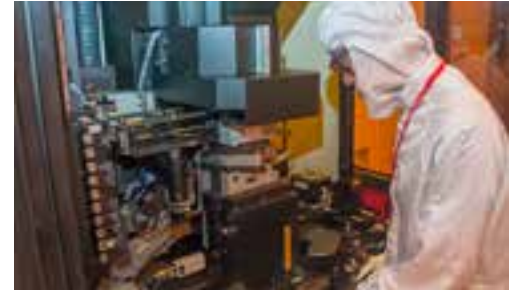
## EDUCATIONAL OUTREACH

CNF continues to actively participate in numerous educational outreach activities, last year hosting over 160 visits, special events, educational tours and workshops at Cornell and in the greater community. We met with over 4,000 people including prospective graduate students, middle schoolers, new faculty, visiting dignitaries, and corporate executives. Major community outreach events included the 4H Career Explorations event in June and the Jr. FIRST LEGO League expo in January.

CNF's renovated "demonstration room" allows us to host small groups of students with live demonstrations of nanotechnology concepts. This, coupled with FaceTime tours of the clean room, provide a great experience for visiting school groups.

For more than 20 years, CNF has hosted a Research Experiences for Undergraduates (REU) Program — an informative research experience for a diverse group of talented undergraduates. The CNF REU Program accepts undergraduate students from across the United States; exposing them to a state-of-the-art facility and world class Cornell staff. In addition to five CNF REU students, we collaborate with the Platform for the Accelerated Realization, Analysis, and Discovery of Interface Materials (PARADIM) REU Program and their interns. Over the course of the 10-week summer program, participants engaged in shared research discussions, presentation and poster training, coupled with a lot of food and fun! Data we have collected over the last 20 years shows that at least 50% of these participants go on to receive a Ph.D. in science/engineering.

This year, CNF was honored to host the network-wide National Nanotechnology Coordinated Infrastructure (NNCI) REU Convocation. Seventy-two REU interns from





across the NNCI sites, joined by dozens of NNCI REU staff, gathered to present their research and to learn about next-step career prospects. Opportunities to engage at Ithaca's famous Sciencenter and take a turn at swing dancing allowed for relaxation and networking with peers. All of the video presentations by this next generation of nanoscale scientists are available at <http://www.cnf.cornell.edu/>

Since 2008, CNF has also supported an International Research Experiences for Undergraduates Program that gives a select group of students an opportunity to conduct research in an international environment. In 2019, six students spent the summer in Japan at the National Institute of Material Science (NIMS). This program has demonstrated significant success in developing "globally aware scientists", i.e. students with the demonstrated ability to successfully work in groups across cultures, a critical skill for 21<sup>st</sup> century research.



CNF is grateful to the NSF for its continued funding of Cornell REU activities. Corporate funding to help augment the program is welcomed. Please contact Dr. Lynn Rathbun, REU Programs Manager, to discuss corporate sponsorship ([rathbun@cnf.cornell.edu](mailto:rathbun@cnf.cornell.edu)).

CNF hosted two short courses during the year — "Technology & Characterization at the Nanoscale" (CNF TCN) — open to participants from academia, industry, and government. The TCN includes lectures, demonstrations and popular hands-on lab activities in the cleanroom. Thanks to funding from the NSF, this course is free for graduate students from U.S.A. institutions outside Cornell, up to five students per external university. Find all the details at <http://www.cnf.cornell.edu/>



For many years, CNF has had an interactive nanotechnology exhibit "Take a Nanooze Break" at Disney Epcot. In 2017, CNF and Prof. Carl Batt, who leads our "Nanooze" effort, received supplemental funding from NSF to upgrade this exhibit. This update has been completed. Through this exhibit, literally 100s of thousands of visitors are exposed to nanotechnology.



CNF continues to print and distribute Nanooze, CNF's educational publication for K-12 students. Content of this popular publication is developed by Prof. Carl Batt. A total of sixteen issues have been produced and each presents a topic of current interest in an 8-page format of short articles and interviews, with accessible text and colorful graphics. The most recent issue highlighted Biomimetics. One hundred thousand copies of each issue are printed; they are distributed free of charge to 1000s of classrooms across the country. If you are interested or know a school that would benefit from this informative nano-news magazine, please visit <http://www.nanooze.org/contact/> to complete the interest form.



Many visitors to Cornell are unfamiliar with nanotechnology and Cornell's commitment and contributions to nanotechnology. In 2019, we developed a new introductory CNF video for use with visiting alumni, parent, and student groups. The video not only presents nanotechnology and CNF's unique facilities, but also features several faculty discussing the promise of nanotechnology and CNF's support of their research. The eight minute video premiered at Cornell Reunion 2019 in June and is available on the new CNF web site.

With your support, we look forward to renewed membership in NNCI, ongoing support by NSF and continuation as one of the major academic nanofabrication facilities in the US.

Comments, feedback and suggestions about CNF are always welcome.

**Chris Ober**

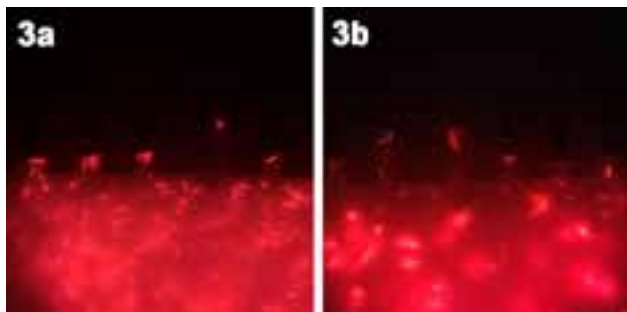
Lester B. Knight Director, CNF • [director@cnf.cornell.edu](mailto:director@cnf.cornell.edu)

**Ron Olson**

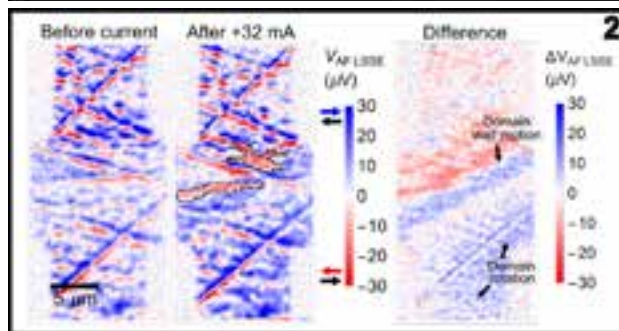
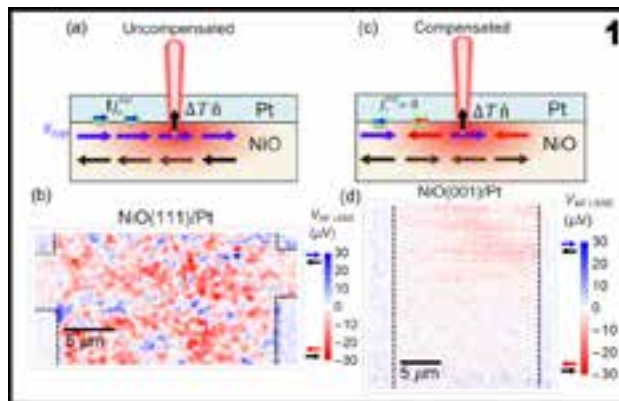
Director of Operations, CNF • [olson@cnf.cornell.edu](mailto:olson@cnf.cornell.edu)



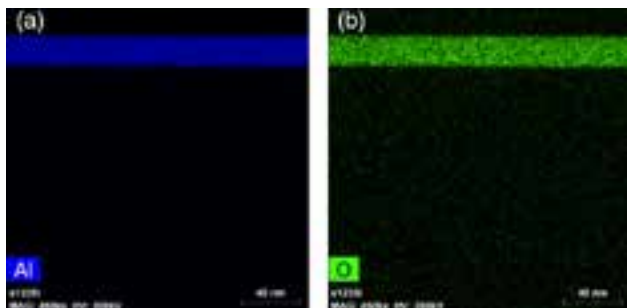
# Full Color Versions of a Few Research Images



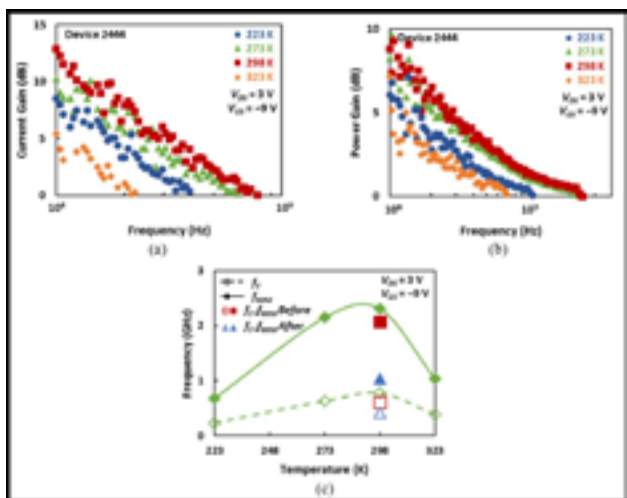
2019 CNF REU Intern: Jacob Baker  
Full report starts on page 2



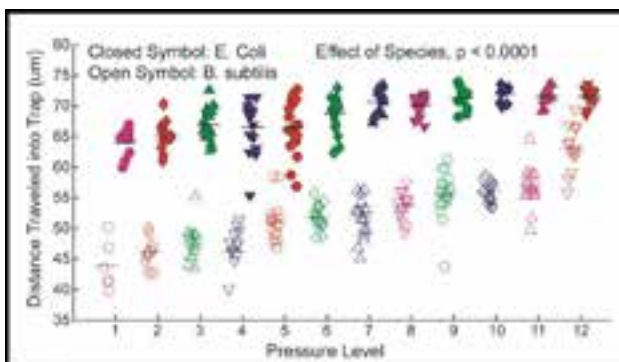
CNF Project Number: 2091-11  
Principal Investigator(s): Gregory D. Fuchs  
User(s): Isaiah Gray, Gregory M. Stiehl  
Full report starts on page 174



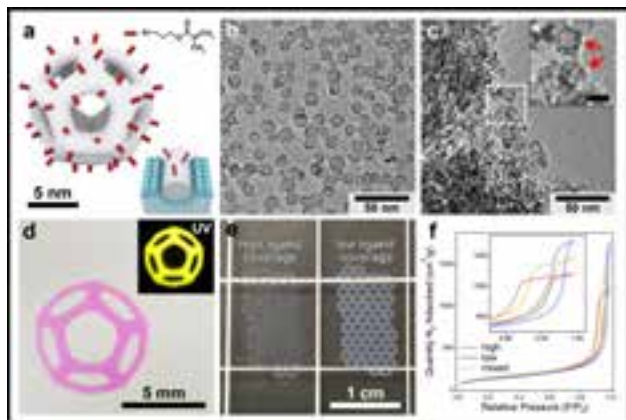
CNF Project Number: 2684-18  
Principal Investigator(s): Fatemeh Shahedipour-Sandvik  
User(s): Benjamin McEwen  
Full report starts on page 98



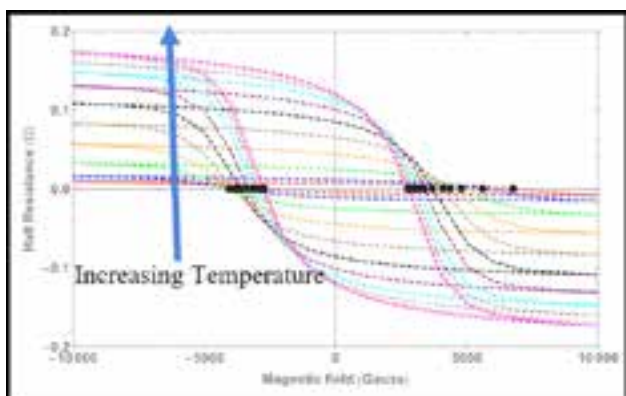
CNF Project Number: 2509-16  
Principal Investigator(s): James C.M. Hwang  
User(s): Kuanchen Xiong, Lei Li  
Full report starts on page 64



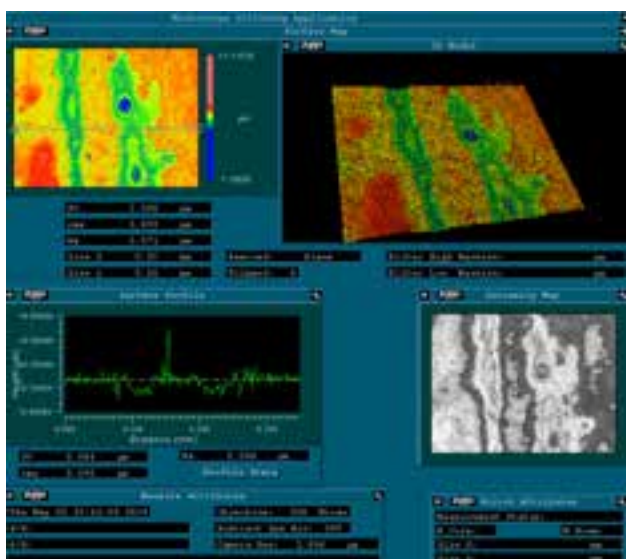
CNF Project Number: 1970-10  
Principal Investigator(s): Christopher J. Hernandez  
User(s): Christine E. Harper, Melanie F. Roberts  
Full report starts on page 22



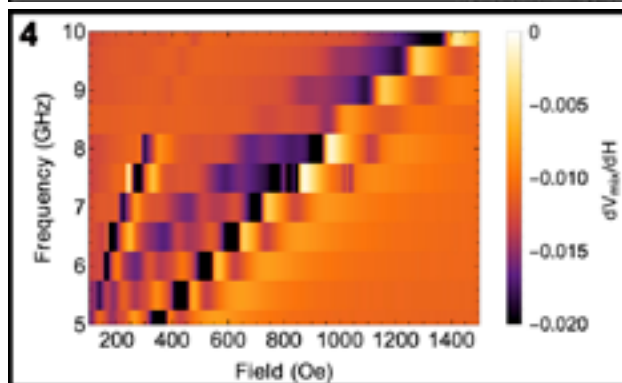
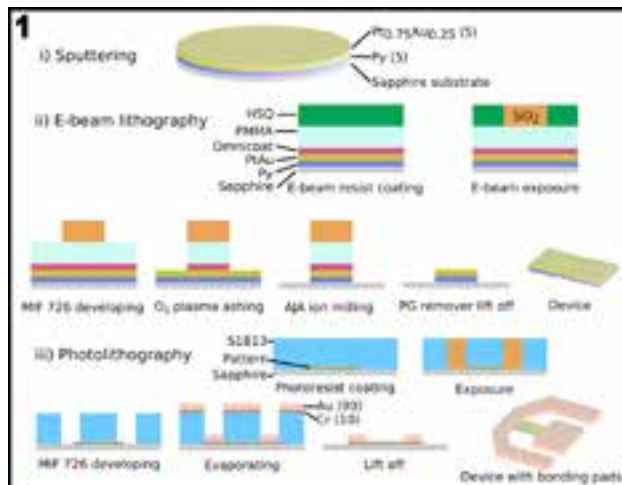
CNF Project Number: 1645-08  
 Principal Investigator(s): Tobias Hanrath  
 User(s): Jen-Yu Huang  
 Full report starts on page 82



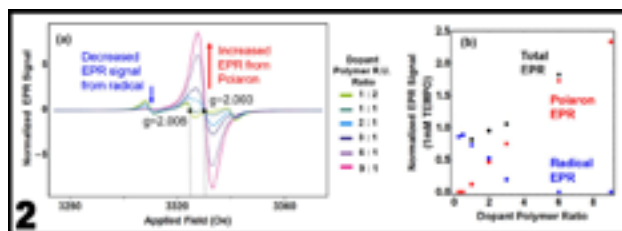
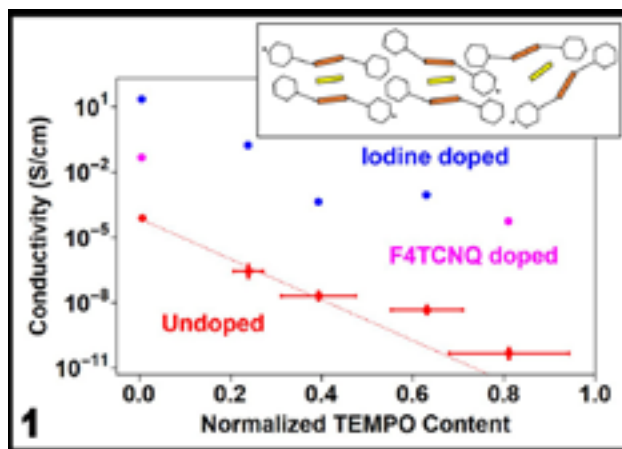
CNF Project Number: 2801-19  
 Principal Investigator(s): Debdeep Jena, Huili Grace Xing  
 User(s): John Wright, Phillip Dang, Zexuan Zang, Jashan Singhal, Hyunjea Lee  
 Full report starts on page 108



CNF Project Number: 2779-19  
 Principal Investigator(s): Matthias Liepe  
 User(s): Zeming Sun  
 Full report starts on page 198



CNF Project Number: 2091-11  
 Principal Investigator(s): Gregory D. Fuchs  
 User(s): Yanyou Xie  
 Full report starts on page 176



CNF Project Number: 2091-11  
 Principal Investigator(s): Gregory D. Fuchs  
 User(s): Albert M. Park  
 Full report starts on page 88

# 2018 CNF-Research-Related Patents, Presentations, and Publications

- "1.5 kV Vertical Ga2O3 Trench-MIS Schottky Barrier Diodes"; Li, W., K.Nomoto, Z.Hu, N.Tanen, K.Sasaki, A.Kuramata, D.Jena and H.G.Xing; IEEE Device Research Conference, University of California, Santa Barbara, June 2018; Li, W., K.Nomoto, Z.Hu, N.Tanen, K.Sasaki, A.Kuramata, D.Jena, and H.G.Xing; Device Research Conference (DRC), 2018, 76th Annual (pp.289-290). IEEE. (2018). [Cornell University]
- "1230 V B-Ga2O3 trench Schottky barrier diodes with an ultra-low leakage current of <1  $\mu$ A/cm<sup>2</sup>"; Li, W., Z.Hu, K.Nomoto, Z.Zhang, J.-Y.Hsu, T.Q.Tu, K.Sasaki, A.Kuramata, D.Jena, and H.G.Xing; Appl.Phys.Lett.113, 202101 (2018); <https://doi.org/10.1063/1.5052368> Editor's Pick Featured by Semiconductor Today (2018). [Cornell University]
- "2.44 kV Ga2O3 vertical trench Schottky barrier diodes with very low reverse leakage current"; Li, W., K.Nomoto, Z.Hu, R.Jinno, Z.Zhang, T.Q.Tu, K.Sasaki, A.Kuramata, D.Jena and H.G.Xing; IEEE International Electron Device Meeting (IEDM) 2018. (2018); Li, W., Z.Hu, K.Nomoto, R.Jinno, Z.Zhang, T.Q.Tu, K.Sasaki, A.Kuramara, D.Jena, and H.G.Xing; 2018 IEEE International Electron Devices Meeting (IEDM), pp.8-5, 2018. (2018). [Cornell University]
- "512-Element Actively Steered Silicon Phased Array for Low-Power LIDAR"; Miller, S.A., C.T.Phare, Y.Chang, X.Ji, O.A.Jimenez Gordillo, A.Mohanty, S.P.Roberts, M.C.Shin, B.Stern, M.Zadka, and M.Lipson; Conference on Lasers and Electro-Optics, OSA Technical Digest (online) (Optical Society of America, 2018), paper JTh5C.2 (2018). [Columbia University]
- "83-ps Timing Jitter With a Red-Enhanced SPAD and a Fully Integrated Front End Circuit"; Ceccarelli, F., G.Acconcia, A.Gulinatti, M.Ghioni, and I.Rech; IEEE Photonics Technology Letters, vol.30, no.19, pp.1727-1730, 2018.doi: 10.1109/LPT.2018.2867805 (2018). [Politecnico di Milano]
- "A 250  $\mu$ m  $\times$  57  $\mu$ m Microscale Opto-electronically Transduced Electrodes (MOTEs) for Neural Recording"; Lee, S.; Cortese, A.J.; Gandhi, A.P.; Agger, E.R.; McEuen, P.L.; Molnar, A.C.; IEEE Transactions on Biomedical Circuits and Systems, Vol.12, Issue 6, p.1256-1266, DOI:10.1109/TBCAS.2018.2876069 (2018). [Cornell University]
- "A comparative study of flow boiling HFE-7100 in silicon nanowire and plainwall microchannels"; Alam, T.; Li, W.; Chang, W.; Yang, F.; Khan, J.; Li, C.; International Journal of Heat and Mass Transfer, Vol.124, p.829-840, DOI:10.1016/j.ijheatmasstransfer.2018.04.010 (2018). [University of SC]
- "A high-energy density antiferroelectric made by interfacial electrostatic engineering"; Mundy, J.A.; Heikes, C.A.; Grosso, B.F.; Segedin, D.F.; Wang, Z.; Goodge, B.H.; Meier, Q.N.; Nelson, C.T.; Prasad, B.; Kourkoutis, L.F.; arXiv preprint arXiv:1812.09615 (2018). [Cornell University]
- "A high-voltage p-channel FET based on III-Nitride heterostructures"; Bader, S., R.Chaudhuri, D.Jena, and H.G.Xing; Docket No.8358-01-US, Country of Filing; United States, App Type; MPR - Manuscript Provisional, App Status; Filed Date; 11/7/18, App#; 62/756,874 (2018). [Cornell University]
- "A Microfluidic-Based Model for Spatially Constrained Culture of Intestinal Microbiota"; Pajoumshariati, S.R.; Azizi, M.; Zhang, S.; Dogan, B.; Simpson, K.W.; Abbaspourrad, A.; Advanced Functional Materials, Vol.28, Issue 48, p.1805568, DOI:10.1002/adfm.201805568 (2018). [Cornell University]
- "A Polarization-induced 2D hole gas in undoped gallium nitride quantum wells"; Chaudhuri, R., S.J.Bader, Z.Chen, D.A.Muller, H.G.Xing and D.Jena; Submitted.<https://arxiv.org/abs/1807.08836> (2018). [Cornell University]
- "A portable device for nucleic acid quantification powered by sunlight, a flame or electricity"; Snodgrass, R.; Gardner, A.; Semeere, A.; Kopparchy, V.L.; Duru, J.; Maurer, T.; Martin, J.; Cesarmam, E.; Erickson, D.; Nature Biomedical Engineering, Vol.2, Issue 9, p.657-665, DOI:10.1038/s41551-018-0286-y (2018). [Cornell University]
- "A pumpless body-on-a-chip model using a primary culture of human intestinal cells and a 3D culture of liver cells"; Chen, H.J., P.Miller, M.L.Shuler; Lab Chip; 18(14):2036-2046.doi: 10.1039/c8lc00111a (2018) (2018). [Cornell University]
- "A system for multiplexed analysis of cells"; Bisogni, A., H.Craighead, D.Lin, H.Tian; Docket #8444, App Status; Filed by Cornell; 11/20/18, App#; Invention (2018); Bisogni, A., H.Craighead, D.Lin, H.Tian; Docket #8444-01-US, Country of Filing; USA, App Type; MPR - Manuscript Provisional, App Status; Filing Date; 11/28/18, App Number; 62/772,620 (2018). [Cornell]
- "Aberration Diverse Optical Coherent Tomography (OCT) Imaging to Suppress Optical Scattering Noise"; Adie, S., M.Lamont, S.Liu; Docket No.8179-01-US, Country of Filing; United States, App Type; MPR - Manuscript Provisional, App Status; Converted, Filing Date; 3/20/18, App#; 62/645,724 (2018). [Cornell University]
- "Abrupt transitions in matrix stiffness create endothelial stress concentrations."; Vanderburgh, J.A., Potharazu, A., Taufalele, P.V.and Reinhart-King, C.A.; Biomedical Engineering Society Annual Meeting, Atlanta, GA.Podium presentation (October, 2018). (2018). [Cornell University]
- "Accessing the Exceptional Points in Coupled Fabry-Perot Resonators through Hybrid Integration"; Zhu, Y.; Zhu, L.; Acs Photonics, Vol.5, Issue 12, p.4920-4927, DOI:10.1021/acsp Photonics.8b01075 (2018). [Clemson University]
- "Accurate Image-based Measurements of Biological Forces in a Dual Optical Trap"; J.Inman, J.Killian, M.Wang; Docket No.8136, App Status; Filed - by Cornell, Filing Date; 2/8/18, App#; Invention (2018). [Cornell University]
- "Acoustic Sensing Systems, Devices and Methods"; A.Lal; Docket No.7683-01-US, Country of Filing; United States, App Type; MPR - Manuscript Provisional, App Status; Converted, Filing Date; 2/2/18, App#; 62/625,887 (2018). [Cornell University]
- "Acoustic-assisted 3D Printing of Tough Silicone Nanocomposite"; Z.Liu, W.an, R.Shepherd, K.Wang; Docket No.8403, App Status; UnFiled Date; 10/8/18, App#; Invention (2018). [Cornell University]
- "Activation of buried p-GaN in MOCVD regrown vertical structures"; W.Li, K.Nomoto, K.Lee, S.M.Islam, Z.Hu, M.Zhu, X.Gao, A.Xie, M.Pilla, D.Jena, H.G.Xing; Appl.Phys.Lett.113, 062105 (2018) DOI: 10.1063/1.5041879 Featured by Semiconductor Today (2018). [Cornell University]
- "Actuation of Higher Harmonics in Large Arrays of Micromechanical Cantilevers for Expanded Resonant Peak Separation"; Dick, N.; Grutzik, S.; Wallin, C.B.; Ilic, B.R.; Krylov, S.; Zehnder, A.T.; Journal of Vibration and Acoustics-Transactions of the Asme, Vol.140, Issue 5, p.51013, DOI:10.1115/1.4039568 (2018). [Cornell University]

- "Adaptive metalenses with simultaneous electrical control of focal length, astigmatism, and shift"; She, A.; Zhang, S.; Shian, S.; Clarke, D.R.; Capasso, F.; *Science Advances*, Vol.4, Issue 2, p.eaap9957, DOI:10.1126/sciadv.aap9957 (2018). [Harvard]
- "All-dry transferred single- and few-layer MoS<sub>2</sub> field effect transistor with enhanced performance by thermal annealing"; Islam, A.; Lee, J.; Feng, P.X.-L.; *Journal of Applied Physics*, Vol.123, Issue 2, p.25701, DOI:10.1063/1.5008846 (2018). [Case Western Reserve University]
- "All-Electrical Transduction of Black Phosphorus Tunable 2d Nanoelectromechanical Resonators"; Islam, A.; Lee, J.; Feng, P.X.-L.; 2018 IEEE Micro Electro Mechanical Systems (MEMS), p.1052-1055 (2018). [Case Western Reserve University]
- "An Active Visible Nanophotonics Platform for Sub-Millisecond Deep Brain Neural Stimulation"; A.Mohanty, Q.Li, M.A.Tadayon, G.R.Bhatt, E.Shim, X.Ji, J.Cardenas, S.A.Miller, A.Kepecs, and M.Lipson; *Conference on Lasers and Electro-Optics, OSA Technical Digest (online) (Optical Society of America, 2018)*, paper ATH3Q.1 (2018). [Columbia University]
- "An Integrated Microfluid Device for Capture and Spectroscopic Characterization of Live Cells"; G.Kelp, G.Shvets; Docket No.8311-01-US, Country of Filing; United States, App Type; MPR - Manuscript Provisional, App Status; Filing Date; 7/25/18, App Number; 62/702,963 (2018). [Cornell]
- "An Integrated Microfluid Device for Simultaneous Capture and Spectroscopic Characterization of Live Cells"; G.Kelp, G.Shvets; Docket No.8311, App Status; Filed - by Cornell, Filing Date; 6/25/18, App Number; Invention (2018). [Cornell]
- "Anisotropic polarization-induced conductance at a ferroelectric-insulator interface"; Zhang, Y.; Lu, H.; Xie, L.; Yan, X.; Paudel, T.; Kim, J.; Cheng, X.; Wang, H.; Heikes, C.; Li, L.; Xu, M.; Schlom, D.; Chen, L.; Wu, R.; Tsybal, E.; Gruverman, A.; Pan, X.; *Nature Nanotechnology*, Vol.13, Issue 12, p.1132-+, DOI:10.1038/s41565-018-0259-z (2018). [Cornell University]
- "Anisotropic Thermal Conductivity of Suspended Black Phosphorus Probed by Opto-Thermomechanical Resonance Spectromicroscopy"; Islam, A.; van den Akker, A.; Feng, P.X.-L.; *Nano Letters*, Vol.18, Issue 12, p.7683-7691, DOI:10.1021/acs.nanolett.8b03333 (2018). [Case Western Reserve University]
- "Apparatus and Method for Point-of-Care Diagnostics and Antibiotic Resistance Identification, and Applications Therof"; D.Erickson, S.Lee, S.Mehta; Docket No.7108-03-US, Country of Filing; United States, App Type; CIP - Continuation in Part, App Status; Prosecution, Filing Date; 1/19/18, App#; 15/875,686 (2018). [Cornell University]
- "Apparatus and Methods for Detecting a Vibratory Signal"; B.Davaji, S.Gupta, A.Lal, S.Nadig; Docket No.7431-03-US, Country of Filing; United States, App Type; US from PCT, App Status; Filed Date; 11/7/18, App#; 16/099,584 (2018). [Cornell University]
- "Apparatus and methods for low temperature small angle X-ray scattering"; S.P.Meisberger, M.A.Warkentin, J.B.Hopkins, A.M.Katz, L. Pollack, R.E.Thorne; Patent number: 9927336 (2018), Filed: June 4, 2013, Date of Patent: March 27, 2018, Assignee: Cornell University (2018). [Cornell University]
- "Apparatus for and Method of Terminating a High Frequency Arrhythmic Electric State of a Biological Tissue"; E.Bodenschatz, F.Fenton, R.Gilmour, V.Krinski, S.Luther; Docket No.5166-19-HK, Country of Filing; Hong Kong, App Status; Issued, Filing Date; 8/6/15, App Number; 15107561.7, Patent Number & Issue Date; 1207017, 3/9/18 (2018). [Cornell]
- "Apparatuses with Atomically-Thin Ohmic Edge Contacts Between Two-Dimensional Materials, Methods of Making Same, and Devices Comprising Same"; H.Gao, M.Guimaraes, K.Kang, J.Park, D.Ralph, S.Xie; Docket No.7404-03-US, Country of Filing; United States, App Type; US from PCT, App Status; Filed Date; 12/13/18, App#; 16/309,637 (2018). [Cornell University]
- "Application of Chemical Reaction Engineering Principles to "Body-on-a-Chip" Systems"; Sung, J.H., Y.Wang, J.M.Lee, and M.Shuler; *AIChE Journal* 64(12): 4351-4360 (2018) (2018). [Cornell]
- "Applying "Body-on-a-Chip" systems to drug development"; Shuler, M.L.; *TERMIS-World Conference*. Kyoto, Japan.Sep.5-8, 2018 (2018). [Cornell University]
- "Atomic Force Microscopy Apparatus, Methods and Applications"; R.Dwyer, J.Marohn, S.Nathan; Docket No.7633-02-PC, Country of Filing; Not Applicable (PCT App), App Type; PCT - Patent Cooperation Treaty, App Status; Filed Date; 5/10/18, App#; PCT/US18/32081 (2018). [Cornell University]
- "Atomic Layer GaSe/MoS<sub>2</sub> van der Waals Heterostructure Photodiodes with Low Noise and Large Dynamic Range"; Islam, A.; Lee, J.; Feng, P.X.-L.; *Acs Photonics*, Vol.5, Issue 7, p.2693-2700, DOI:10.1021/acsp Photonics.8b00318 (2018). [Case Western Reserve University]
- "Atomically Precise Superlattice Membranes"; T.Dunbar, T.Hanrath; Docket No.8099, App Status; UnFiled Date; 1/11/18, App#; Invention (2018). [Cornell University]
- "Automated analysis of cell migration and nuclear envelope rupture in confined environments"; Elacqua, J.J.; McGregor, A.L.; Lammerding, J.; *Plos One*, Vol.13, Issue 4, p.e0195664, DOI:10.1371/journal.pone.0195664 (2018). [Cornell]
- "Band offset and electron affinity of MBE-grown SnSe<sub>2</sub>"; Q.Zhang, M. Li, S.Vishwanath, E.Lochocki, X.Liu, R.Yan, H.Lien, M.Dobrowolska, J.Furdyna, K.hen, G.Cheng, A.Hight Walker, D.J.Gundlach, H.G.Xing and N.V.Nguyen; *Appl.Phys.Letts.*, 112, 042108 (2018) doi.org/10.1063/1.5016183 Editor's Pick (2018). [Cornell University]
- "Band structure engineering of layered WSe<sub>2</sub> via one-step chemical functionalization"; J.Park, A.Rai, J.Hwang, C.Zhang, I.Kawk, S.Wolf, S.Vishwanath, X.Liu, M.Dobrowolska, J.Furdyna, H.G.Xing, N.Bhat, K.Cho, S.K.Banerjee and A.C.Kummel; Submitted, (2018) (2018). [Cornell University]
- "Barrier Tissue mimics for drug development"; Shuler, M.L.; *ACS 255th National Meeting*. New Orleans, LA.March 18-22, 2018 (Gaden Award Lecture) (2018). [Cornell University]
- "Battery-operated integrated frequency comb generator"; Stern, B.; Ji, X.; Okawachi, Y.; Gaeta, A.; Lipson, M.; *Nature*, 556, #7727, p.401, DOI:10.1038/s41586-018-0598-9 (2018). [Columbia]
- "Bidirectional Folding with Nanoscale Sheets for Autonomous Micro-Origami"; Bircan, B.; Miskin, M.; Dorsey, K.; McEuen, P.; Cohen, I.; *Bulletin of the American Physical Society* (2018). [Cornell]
- "Biosensor for use with a surface plasmon resonance (spr) sensor"; Koder R., Schnatz P., Brisendine J., Crouse D., Lepak L., and Bendoyim I.; Patent 2018/ 0003705 A1, PUB JAN 4 2018 (2018). [Phoebus Optoelectronics]
- "Blue (In, Ga) N Light-Emitting Diodes with Buried n+-p+ Tunnel Junctions by Plasma-Assisted Molecular Beam Epitaxy"; Cho, Y.; Bharadwaj, S.; Hu, Z.; Nomoto, K.; Jahn, U.; Xing, H.G.; Jena, D.; arXiv preprint arXiv:1812.07708 (2018). [Cornell University]
- "Body on a chip systems for drug development"; Shuler, M.L.; *National University of Singapore*. Singapore.Feb 9, 2018 (2018). [Cornell University]
- "Body on a Chip systems to improve drug development"; Shuler, M.L.; *IBS 2018: 18th Int'l Biotechnology Symposium*. Montreal, Canada.August 12-17, 2018 (2018). [Cornell University]
- "Body-on-a-Chip systems: drug and diagnostic test development"; Shuler, M.L.; *ACVP & ASVCP 2018 Annual Meeting*. Washington, DC.Nov.3-7, 2018 (2018). [Cornell University]
- "Bowtie Plasmonic Nanoantennas with Nanocrystals: Photon Antibunching, Polarization Selectivity and Tunability"; Lukishova, S.G.; Staffa, J.; Zhu, H.; Kuyk, K.; Liapis, A.; Boyd, R.W.; *Frontiers in Optics, Optical Society of America*, p.JW3A-71 (2018). [University of Rochester]

- "Breakdown mechanism in 1 kA/cm<sup>2</sup> and 960 V E-mode Ga<sub>2</sub>O<sub>3</sub> vertical transistors"; Z.Hu, K.Nomoto, W.Li, Z.Zhang, N.Tanen, K.Sasaki, A.Kurmata, T.Nakamura, D.Jena and H.G.Xing; Appl. Phys.Lett.113, 122103 (2018) doi: 10.1063/1.5038105 Editor's Feature by Semiconductor Today (2018). [Cornell]
- "Capacitively Shunted Flux Qubits and Asymmetric Transmons for Multi-qubit Operations"; J.Ku, Y.Liu, B.Plourde, J.Hertzberg, M. Brink, J.Chow; March Meeting of the American Physical Society Bulletin, 2018, Los Angeles, CA. (2018). [Syracuse University]
- "Carrier envelope offset detection via simultaneous supercontinuum and second-harmonic generation in a silicon nitride waveguide"; Okawachi, Y.; Yu, M.; Cardenas, J.; Ji, X.; Klenner, A.; Lipson, M.; Gaeta, A.L.; Optics Letters, Vol.43, Issue 19, p.4627-4630, DOI:10.1364/OL.43.004627 (2018). [Columbia]
- "Cavitation behind a circular micro pillar"; Nayebzadeh, A.; Wang, Yi.; Tabkhi, H.; Shin, J.; Peles, Y.; International Journal of Multiphase Flow, V.98, p.67-78 (2018). [U. of Central Florida]
- "Characterization of Ultra-High-Q Si<sub>3</sub>N<sub>4</sub> Micro-Ring Resonators with High-Precision Temperature Control"; P.Kaufmann, X.Ji, K.Luke, M.Lipson and S.Ramelow; Conference on Lasers and Electro-Optics, OSA Technical Digest (online) (Optical Society of America, 2018), paper JTua2A.72 (2018). [Columbia University]
- "Charge Transport in Conjugated Polymers with Pendent Stable Radical Groups"; Zhang, Y.; Park, A.M.; McMillan, S.R.; Harmon, N.J.; Flatte, M.E.; Fuchs, G.D.; Ober, C.K.; Chemistry of Materials, Vol.30, Issue 14, p.4799-4807, DOI:10.1021/acs.chemmater.8b02076 (2018). [Cornell University]
- "Chip-Based Frequency Combs for High-Resolution Optical Coherence Tomography"; X.Ji, A.Klenner, X.Yao, Y.Gan, A.L.Gaeta, C.P.Hendon and M.Lipson; Conference on Lasers and Electro-Optics, OSA Technical Digest (online) (Optical Society of America, 2018), paper STh1J.4 (2018). [Columbia University]
- "Circuits and Devices Based on Enhanced Spin Hall Effect for Efficient Spin Transfer Torque"; R.Buhrman, M.-H.Nguyen, C.-F. Pai, D.Ralph; Docket No.6764-08-US, Country of Filing; United States, App Type; CON - Continuation, App Status; Filed Date; 6/25/18, App#; 16/017,565 (2018). [Cornell University]
- "Circuits and Devices Based on Enhanced Spin Hall Effect for Efficient Spin Transfer Torque"; R.Buhrman, M.-H.Nguyen, C.-F.Pai, D.Ralph; Docket No.6764-05-US, Country of Filing; United States, App Status; Issued, Filing Date; 1/17/17, App#; 15/327,017, Patent Number & Issue Date; 10,008,248, Granted June 26, 2018. (2018). [Cornell]
- "Circulating MIR148A associates with sensitivity to adiponectin levels in human metabolic surgery for weight loss"; Ariza-Nieto, M., J.B.Alley, S.Samy, L.Fitzgerald, F.Vermeulen, M.L.Shuler and J.O.Aleman; Endocrine Connections 7: 975-982 (2018) (2018). [Cornell University]
- "CMOS Integration of High Performance Quantum Dot Lasers For Silicon Photonics"; Wang, Z.; PhD Thesis. RIT. (2018). [Rochester Institute of Technology]
- "CMOS-compatible batch processing of monolayer MoS<sub>2</sub> MOSFETs"; K.Xiong, H.Kim, R.J.Marstell, A.Görizt, C.Wipf, L.Li, J.-H.Park, X.Luo, M.Wietstruck, A.Madjar, N.C.Strandwitz, M.Kaynak, Y.H.Lee, and J.C.M.Hwang; J.Phys.D: Appl.Phys., vol.51, pp.15LT02-15LT08, Mar.2018. (2018). [Lehigh University]
- "CNF: A personal perspective"; Ober, C.; Syracuse University, B&CE Seminar, Feb.21, 2018, invited talk. (2018). [Cornell University]
- "CNF: Regional facility for nanofabrication"; Ober, C.; SHyNE Seminar, Northwestern University, Feb.23, 2018. (2018). [Cornell University]
- "Coherent Control of a Superconducting Transmon with Single Flux Quantum Pulses: Part II – Experimental"; JJ Nelson, E.Leonard, M.Beck, K.Dodge, C.Howington, J.Ku, R.McDermott, B.Plourde; March Mtg of the APS Bulletin, 2018, Los Angeles, CA. (2018). [Syracuse University]
- "Coherent quantum dynamics of systems with coupling-induced creation pathways"; Rogers, S.D.; Graf, A.; Javid, U.A.; Lin, Q.; arXiv preprint arXiv:1809.06872 (2018). [U. of Rochester]
- "Collaborative Reader Code Division Multiple Access in the Harmonic RFID System"; X.Hui, E.Kan; Docket No.8145, App Status; Filed - by Cornell, Filing Date; 2/20/18, App#; Invention (2018). [Cornell University]
- "Collaborative Reader Code Divisional Multiple Access (CDMA) and Methods for Same"; X.Hui, E.Kan; Docket No.8145-01-US, Country of Filing; United States, App Type; EPR - Enhanced Provisional, App Status; Filed Date; 5/14/18, App #; 62/671,405 (2018). [Cornell University]
- "Communication is key in nanocatalysts too"; P.Chen; Nanotechweb.org, UK Institute of Physics (2018). [Cornell University]
- "Comparison of unite cell coupling for grating-gate and high electron mobility transistor array THz resonant absorbers"; H.O.Condori Qispes, A.hanana, J.Encomendero, M.Zhu, N.Trometer, A.Nahata, D.Jena, H.G.Xing and B.Sensale-Rodriguez; J.of Appl. Phys.124, 093101 (2018) doi: 10.1063/1.5032102 Editor's Pick Cover Image of JAP (2018). [Cornell University]
- "Control and Readout of Superconducting Qubits with Cryogenic Digital Circuitry"; Plourde, B.; International Workshop on Quantum Control, Coherence, and Computing, October 2018, Stevens Institute of Technology, Hoboken, NJ (2018). [Syracuse]
- "Control of Domain Structures in Multiferroic Thin Films through Defect Engineering"; Li, L.; Jokisaari, J.R.; Zhang, Y.; Cheng, X.; Yan, X.; Heikes, C.; Lin, Q.; Gadre, C.; Schlom, D.; Chen, L.-Q.; Pan, X.; Advanced Materials, Vol.30, Issue 38, p.1802737, DOI:10.1002/adma.201802737 (2018). [Cornell University]
- "Control of spin-orbit torques through crystal symmetry"; G.Stiehl; 2018 March Meeting of the American Physical Society, March 5-9, 2018, Los Angeles, CA (2018). [Cornell University]
- "Controlling surface carrier density by illumination in the transparent conductor La-doped BaSnO<sub>3</sub>"; Lochocki, E.B.; Paik, H.; Uchida, M.; Schlom, D.G.; Shen, K.M.; Applied Physics Letters, Vol.112, Issue 18, p.181603, DOI:10.1063/1.5020716 (2018). [Cornell University]
- "Cooperative communication within and between single nanocatalysts"; Zou, N.; Zhou, X.; Chen, G.; Andoy, N.M.; Jung, W.; Liu, G.; Chen, P.; Nature Chemistry, Vol.10, Issue 6, p.607-614, DOI:10.1038/s41557-018-0022-y (2018). [Cornell University]
- "Correlation between optical fluorescence and microwave transmission during single-cell electroporation"; Li, H.; Xiao, M.; Du, X.; Li, L.; Cheng, X.; Hwang, J.C.M.; IEEE Transactions on Biomedical Engineering, p.DOI: 10.1109/TBME.2018.2885781, DOI: 10.1109/TBME.2018.2885781 (2018). [Lehigh]
- "Counter-rotating cavity solitons in a silicon nitride microresonator"; C.Joshi, A.Klenner, Y.Okawachi, M.Yu, K.Luke, X.Ji, M.Lipson, A.L.Gaeta; Optics Letters 43(3), 547-550 (2018) (2018). [Columbia University]
- "Creation of Localized Skyrmion Bubbles in Co/Pt Bilayers using a Spin Valve Nanopillar"; J.L.Grab, A.E.Rugar, and D.C.Ralph; Phys. Rev.B 97, 184424/1-9 (2018). (2018). [Cornell University]
- "Cryogenic Cooling Apparatus, Methods, and Applications"; B.Aper, D.Closs, S.Hollabaugh, D.Moreau, R.Newman, R.horne, X.Tian; Docket No.8424, App Status; Filed - by Joint Owner, Filing Date; 10/31/18, App#; Invention (2018). [Cornell University]
- "Cryogenic Digital Readout of Superconducting Qubits"; C.Howington, A.Opremcak, I.Pechenezhskiy, M.Vavilov, R.McDermott, B.Plourde; March Meeting of the APS Bulletin, 2018, Los Angeles, CA. (2018). [Syracuse University]
- "Defect-Induced Hedgehog Polarization States in Multiferroics"; Li, L.; Cheng, X.; Jokisaari, J.R.; Gao, P.; Britson, J.; Adamo, C.; Heikes, C.; Schlom, D.G.; Chen, L.-Q.; Pan, X.; Physical Review Letters, Vol.120, Issue 13, p.137602, DOI:10.1103/PhysRevLett.120.137602 (2018). [Cornell University]

- "Degradation of GaN-on-GaN vertical diodes submitted to high current stress"; E.Fabris, M.Meneghini, C.De Santi, Z.Hu, W.Li, K.Nomoto, D.Jena, H.G.Xing, X.Gao, G.Meneghesso and E.Zanoni; ESREF 2018 (2018). [Cornell University]
- "Degradation of GaN-on-GaN vertical diodes submitted to high current stress"; E.Fabris, M.Meneghini, C.De Santi, Z.Hu, W.Li, K.Nomoto, X.Gao, D.Jena, H.G.Xing, E.Zanoni, G.Meneghesso; Microelectronics Reliability 88-90, 568-571 (2018) doi. org/10.1016/j.microrel.2018.06.041 (2018). [Cornell]
- "Demonstration of avalanche capability in polarization-doped vertical GaN pn diodes: studies of walkout due to residue carbon concentration"; C.De Santi, E.Fabris, K.Nomoto, Z.Hu, W.Li, X.Gao, D.Jena, H.G.Xing, G.Meneghesso, M.Meneghini, and E.Zanoni; IEEE International Electron Device Meeting (IEDM) 2018. (2018). [Cornell University]
- "Demystifying the growth of superconducting Sr2RuO4 thin films"; Nair, H.P.; Ruf, J.P.; Schreiber, N.J.; Miao, L.; Grandon, M.L.; Baek, D.J.; Godge, B.H.; Ruff, J.P.C.; Kourkoutis, L.F.; Shen, K.M.; Schlom, D.G.; *Apl Materials*, Vol.6, Issue 10, p.101108, DOI:10.1063/1.5053084 (2018). [Cornell University]
- "Determination of the porosity in a bifacial fabric using micro-computed tomography and three-dimensional reconstruction"; Zhu, L.; Wang, X.; Hinestroza, J.P.; Naebe, M.; *Textile Research Journal*, Vol.88, Issue 11, p.1263-1277, DOI:10.1177/0040517517698987 (2018). [Cornell University]
- "Development of GaN Vertical Trench-MOSFET With MBE Regrown Channel"; W.Li, K.Nomoto, K.Lee, S.M.Islam, Z.Hu, M.Zhu, X.Gao, M.Pilla, D.Jena, and H.G.Xing; *IEEE Transactions on Electron Devices* 65, no.6 (2018): 2558-2564. (2018). [Cornell]
- "Device and Methods for Epigenetic Analysis"; B.Cipriany, H.Craighead, S.Levy, P.Soloway; Docket No.4823-11-US, Country of Filing; United States, App Status; Issued, Filing Date; 8/26/16, App#; 15/249,275, Patent Number & Issue Date; 9,988,667, 6/5/18 (2018). [Cornell University]
- "Device for Recovery and Isolation of Biomolecules"; H.Craighead, C.Tan; Docket No.5088-04-US, Country of Filing; USA, App Status; Issued, Filing Date; 6/10/15, App#; 14/735,874, Patent # & Issue Date; 10/040,047, 8/7/18 (2018). [Cornell]
- "Device, system and methods for efficient fluorescent analysis of DNA from selected cells"; H.Craighead, H.Tian; Docket No.8441, App Status; Filed - by Cornell, Filing Date; 11/19/18, App#; Invention (2018). [Cornell University]
- "Device, system and methods for efficient fluorescent analysis of DNA from selected cells"; H.Craighead, H.Tian; Docket No.8441-01-US, Country of Filing; United States, App Type; MPR - Manuscript Provisional, App Status; Filed Date; 11/28/18, App#; 62/772,618 (2018). [Cornell University]
- "Dielectric properties of amorphous Ta-Ge-O and Ta-Si-O thin films"; Nad, T.A.; van Dover, R.B.; *Journal of Applied Physics*, Vol.123, Issue 24, p.244103, DOI:10.1063/1.5022336 (2018). [Cornell]
- "Digital coherent control of a superconducting qubit"; Leonard Jr, E.; Beck, M.; Nelson, J.J.; Christensen, B.G.; Thorbeck, T.; Howington, C.; Opremcak, A.; Pechenezhskiy, I.V.; Dodge, K.; Dupuis, N.P.; arXiv preprint arXiv:1806.07930 (2018). [Syracuse University]
- "Discerning Black Phosphorus Crystal Orientation and Anisotropy by Polarized Reflectance Measurement"; Islam, A.; Du, W.; Pashaei, V.; Jia, H.; Wang, Z.; Lee, J.; Ye, G.; Chen, X.; Feng, P.; *Acs Applied Materials & Interfaces*, V.10, Issue 30, p.25629-637, DOI:10.1021/acsami.8b05408 (2018). [Case Western Reserve]
- "Discovery of Ordered Vortex Phase in Multiferroic Oxide Superlattices"; Mei, Antonio B.; Ramesh, Ramamoorthy; Schlom, Darrell G.; arXiv preprint arXiv:1810.12895 (2018). [Cornell University]
- "Divided Pulse Lasers"; Erin Lamb, Frank Wise, Logan Wright; Docket No.6582-04-US, Country of Filing; United States, App Type; CON - Continuation, App Status; Filed Date; 10/22/18, App#; 16/167,279 (2018). [Cornell University]
- "Divided Pulse Lasers"; Erin Lamb, Frank Wise, Logan Wright; Docket No.6582-03-US, Country of Filing; United States, App Status; Issued, Filing Date; 7/21/16, App#; 15/113,349, Patent Number & Issue Date; 10/109,976, 10/23/18 (2018). [Cornell]
- "Dual Mode Microendoscope Apparatus, Method and Applications"; Chunhui (Chris) Xu; Docket No.5907-06-CN, Country of Filing; China, App Type; FOR - Foreign DIV, App Status; Filed Date; 5/2/18, App#; 2.0181E+11 (2018). [Cornell University]
- "Dual-Cavity Scanning Comb Spectroscopy"; M.Yu, Y.Okawachi, C.Joshi, X.Ji, M.Lipson, and A.L.Gaeta; Conference on Lasers and Electro-Optics, OSA Technical Digest (online) (Optical Society of America, 2018), paper SW4M.5 (2018). [Columbia]
- "Dynamic metasurface lens based on MEMS technology"; Roy, Tapashree; Zhang, Shuyan; Jung, Il Woong; Troccoli, Mariano; Capasso, Federico; Lopez, Daniel; *Apl Photonics*, Vol.3, Issue 2, p.21302, DOI:10.1063/1.5018865 (2018). [Harvard University]
- "EAGER: Explorations in Long Term Reliable Neural Recordings and Neuro Modulation Using GHz to THz Ultrasonics"; Amit Lal, Ankur Singh, Chunhui (Chris) Xu; Docket No.8282, App Status; Filed - by Cornell, Filing Date; 5/23/18, App#; Invention (2018). [Cornell University]
- "Effect of surface treatment on superconducting qubit coherence"; Bradley Christensen, Pradeep Kumar, JJ Nelson, Yebin Liu, Andrew Ballard, Britton Plourde, Robert McDermott; *March Meeting of the American Physical Society Bulletin*, 2018, Los Angeles, CA. (2018). [Syracuse University]
- "Efficient switching of 3-terminal magnetic tunnel junctions by the giant spin Hall effect of Pt85Hf15 alloy"; Nguyen, Minh-Hai; Shi, Shengjie; Rowlands, Graham E.; Aradhya, Sriharsha V.; Jermain, Colin L.; Ralph, D.C.; Buhrman, R.A.; *Applied Physics Letters*, Vol.112, Issue 6, p.62404, DOI:10.1063/1.5021077 (2018). [Cornell University]
- "Electric field-directed assembly of fullerene crystal rods into hierarchical films"; Stelson, Angela C.; Penterman, Sonny J.; Watson, Chekesha M.Liddell; *Journal of Materials Chemistry C*, Vol.6, Issue 41, p.11118-11127, DOI:10.1039/c8tc02363h (2018). [Cornell University]
- "Electrically Controllable Single-Point Covalent Functionalization of Spin-Cast Carbon-Nanotube Field-Effect Transistor Arrays"; Lee, Yoonhee; Trocchia, Scott M.; Warren, Steven B.; Young, Erik F.; Vernick, Sefi; Shepard, Kenneth L.; *ACS nano*, Vol.12, Issue 10, p.9922-9930 (2018). [Columbia University]
- "Electrically Gated Three-Terminal Circuits and Devices Based on Spin Hall Torque Effects in Magnetic Nanostructures"; R.A.Buhrman, D.C.Ralph, Chi-Feng Pai, and Luqiao Liu; *US Patent* 9,947,382, Granted Apr.17, 2018. (2018). [Cornell]
- "Electrically tunable single-and few-layer MoS2 nanoelectromechanical systems with broad dynamic range"; Lee, Jaesung; Wang, Zenghui; He, Keliang; Yang, Rui; Shan, Jie; Feng, Philip X.-L.; *Science advances*, Vol.4, Issue 3, p.eaa06653 (2018). [Case Western Reserve University]
- "Electroluminescence from Solution-Processed Pinhole-Free Nanometer-Thickness Layers of Conjugated Polymers"; Newby, Carol; Piachaud, Thomas H.; Vaynzof, Yana; Lee, Jin-Kyun; Jung, Seok-Heon; Sadhanala, Aditya; Ober, Christopher K.; Friend, Richard H.; *Nano Letters*, Vol.18, Issue 9, p.5382-5388, DOI:10.1021/acs.nanolett.8b01084 (2018). [Cornell]
- "Electrothermally Tunable Graphene Resonators Operating at Very High Temperature up to 1200 K"; Ye, Fan; Lee, Jaesung; Feng, Philip X.-L.; *Nano Letters*, Vol.18, Issue 3, p.1678-1685, DOI:10.1021/acs.nanolett.7b04685 (2018). [Case Western Reserve University]

- "Enhancement and Depletion Mode Vertical Gallium Oxide (Ga2O3) Power FETs"; Z.Hu, D.Jena, W.Li, K.Nomoto, H.G.Xing; Docket No.8178-01-US, Country of Filing: United States, App Type; MPR - Manuscript Provisional, App Status; Filed Date; 3/28/18, App#: 62/649,281 (2018). [Cornell University]
- "Engineering Carrier Effective Masses in Ultrathin Quantum Wells of IrO2"; Kawasaki, J.K.; Kim, C.H.; Nelson, Jo.N.; Crisp, S.; Zollner, C.J.; Biegenwald, E.; Heron, J.T.; Fennie, C.J.; Schlom, D.G.; Shen, K.M.; Physical Review Letters, Vol.121, Issue 17, p.176802, DOI:10.1103/PhysRevLett.121.176802 (2018). [Cornell]
- "Engineering Dzyaloshinskii-Moriya interaction in B20 thin-film chiral magnets"; Turgut, Emrah; Paik, Hanjong; Nguyen, Kayla; Muller, David A.; Schlom, Darrell G.; Fuchs, Gregory D.; Physical Review Materials, Vol.2, Issue 7, p.74404, DOI:10.1103/PhysRevMaterials.2.074404 (2018). [Cornell University]
- "Engineering the Dzyaloshinskii-Moriya interaction in Mn x Fe 1-x Ge thin films"; Turgut, Emrah; Paik, Hanjong; Nguyen, Kayla; Muller, David; Schlom, Darrell; Fuchs, Gregory; Bulletin of the American Physical Society (2018). [Cornell University]
- "Engineering the Dzyaloshinskii-Moriya interaction in MnxFe1-xGe thin films"; Emrah Turgut, Hanjong Paik, Kayla Nguyen, David Muller, Darrell Schlom, and Gregory D.Fuchs; March Meeting of the APS, Los Angeles, CA 2018 (2018). [Cornell University]
- "Enhanced Oxygen Solubility in Metastable Water under Tension"; Lidon, Pierre; Marker, Sierra C.; Wilson, Justin J.; Williams, Rebecca M.; Zipfel, Warren R.; Stroock, Abraham D.; Langmuir, Vol.34, Issue 40, p.12017-12024, DOI:10.1021/acs.langmuir.8b02408 (2018). [Cornell University]
- "Enhancement and Depletion Mode Vertical Gallium Oxide (Ga2O3) Power FETs"; Z.Hu, D.Jena, W.Li, K.Nomoto, H.G.Xing; Docket No.8178, App Status; Filed - by Cornell, Filing Date; 3/16/18, App#: Invention (2018). [Cornell]
- "Enhancement of punch-through voltage in GaN with buried p-type layer utilizing polarization-induced doping"; W.Li, Mingda Zhu, K.Nomoto, Z.Hu, Xiang Gao, Manyam Pilla, D.Jena and H.G.Xing; IEEE 30th International Symposium on Power Semiconductor Devices and Ics, Chicago, May 2018 (2018); 2018 IEEE 30th International Symposium on Power Semiconductor Devices and ICs (ISPSD), pp.228-231.IEEE, 2018. (2018). [Cornell]
- "Enhancement-mode Ga2O3 vertical transistors with breakdown voltage >1 kV"; Z.Hu, K.Nomoto, W.Li, N.Tanen, K.Sasaki, Akito Kurmata, Tohru Nakamura, D.Jena and H.G.Xing; IEEE Electron Dev.Lett., (2018).DOI: 10.1109/LED.2018.2830184 Featured by Semiconductor Today (2018). [Cornell University]
- "Epigenetic Fingerprinting of DNA using a Solid-State Nanopore"; Alden, Jonathan, A.Cortese, J.Alden, D.Limjoco, M.Pender, P.McEuen; NHGRI Advanced Genome Technology Development Meeting, Boston, MA (May 2018), Poster session (2018). [Cornell University]
- "EUV metal oxide hybrid photoresists: ultra-small structures for high-resolution patterning"; Xu, Hong; Yang, Kou; Sakaia, Kazunori; Kosma, Vasiliki; Kasahara, Kazuki; Giannelis, Emmanuel P.; Ober, Christopher K.; Extreme Ultraviolet (euv) Lithography Ix, International Society for Optics and Photonics, Vol.10583, p.UNSP 105831P (2018). [Cornell University]
- "EUV Photolithography: Resist Progress and Challenges"; Ober, Christopher; SPIE Advanced Lithography, San Jose, CA, Feb.26-March 1, 2018, invited keynote talk. (2018). [Cornell]
- "EUV Photolithography: Resist Progress and Challenges"; Ober, C.; Xu, H.; Kosma, V.; Sakai, K.; Giannelis, E.; Extreme Ultraviolet (euv) Lithography Ix, Spie-Int Soc Optical Engineering, Vol.10583, p.UNSP 1058306 (2018). [Cornell University]
- "EUV photolithography: resist progress in metal-organic complex photoresists"; Xu, Hong; Kosma, Vasiliki; Sakai, Kazunori; Giannelis, Emmanuel P.; Ober, Christopher K.; Journal of Micro/Nanolithography, MEMS, and MOEMS, Vol.18, Issue 1, p.11007 (2018). [Cornell University]
- "Evolution of superconductivity in ultrathin NbS2"; Yan, Rusen; Khalsa, Guru; Schaefer, Brian T.; Jarjour, Alexander; Rouvimov, Sergei; Nowack, Katja C.; King, Huili G.; Jena, Debdeep; arXiv preprint arXiv:1803.06097 (2018). [Cornell University]
- "Experimental and numerical study about local heat transfer in a microchannel with a pin fin"; Wang, Yingying; Shin, Jeong-Heon; Woodcock, Corey; Yu, Xiangfei; Peles, Yoav; International Journal of Heat and Mass Transfer, Vol.121, p.534-546 (2018). [University of Central Florida]
- "Exploration of Alternate Fabrication and Processing Techniques for Superconducting Qubit Junctions"; Yebin Liu, JJ Nelson, Jaseung Ku, Britton Flourde; March Meeting of the American Physical Society Bulletin, 2018, Los Angeles, CA. (2018). [Syracuse]
- "Fast Low-Current Spin-Orbit-Torque Switching of Magnetic Tunnel Junctions through Atomic Modifications of the Free-Layer Interfaces"; Shi, Shengjie; Ou, Yongxi; Aradhya, S.V.; Ralph, D.C.; Buhrman, R.A.; Physical Review Applied, Vol.9, Issue 1, p.11002, DOI:10.1103/PhysRevApplied.9.011002 (2018). [Cornell University]
- "Fast, reliable spin-orbit-torque switching in three terminal magnetic tunnel junctions with Hf dusting layer"; Shi, Shengjie; Ou, Yongxi; Ralph, D.C.; Buhrman, R.A.; Spintronics Xi, International Society for Optics and Photonics, Vol.10732, p.UNSP 107321U (2018). [Cornell University]
- "Fiber to Chip Fusion Splicing for Robust, Low Loss Optical Coupling"; Nauriyal, J., Song, M., Yu, R., and Cardenas, J.; 2018 Conference in Lasers and Electro Optics (CLEO) (2018). [University of Rochester]
- "Fiber to Chip Fusion Splicing for Robust, Low Loss Optical Coupling"; J.Nauriyal, R.Yu, M.Song, and J.Cardenas; arXiv:1810.09531 (Pending, 2018). (2018). [U. of Rochester]
- "First Demonstration of GaN PolarMOS and Its Breakdown Mechanisms"; W.Li, K.Nomoto, Aditya Sundar, Mingda Zhu, Z.Hu, Mingda Zhu, Manyam Pilla, Xiang Gao, D.Jena, and H.G.Xing; International Workshop on Nitride Semiconductors (IWN), 2018. (2018). [Cornell University]
- "First RF Strained AlN/GaN/AlN Quantum Well HEMTs on 6H-SiC"; Austin Hickman, Samuel James Bader, Reet Chaudhuri, K.Nomoto, SM Islam, H.G.Xing, D.Jena; International Workshop on Nitrides, Kanazawa, Japan, Nov.2018 (2018). [Cornell]
- "Free-Standing  $\beta$ -Ga2O3 Thin Diaphragms"; Zheng, Xu-Qian; Lee, Jaesung; Rafique, Subrina; Han, Lu; Zorman, Christian A.; Zhao, Hongping; Feng, Philip X.-L.; Journal of Electronic Materials, Vol.47, Issue 2, p.973-981, DOI:10.1007/s11664-017-5978-7 (2018). [Case Western Reserve University]
- "From Atomic Origami, Towards Cell-Sized Machines"; Miskin, Marc; Dorsey, Kyle; Bircan, Baris; Han, Yimo; Muller, David; McEuen, Paul; Cohen, Itai; Bulletin of the American Physical Society (2018). [Cornell University]
- "Fully Integrated Active Quenching Circuit Driving Custom-Technology SPADs With 6.2 ns Dead Time"; F.Ceccarelli, G.Acconcia, A.Gulinatti, M.Ghioni, and I.Rech; IEEE Photonics Technology Letters, vol.31, no.1, pp.102-105, 2018. doi:10.1109/LPT.2018.2884740 (2018). [Politecnico di Milano]
- "Fully Integrated Chip Platform for Electrically Pumped Frequency Comb Generation"; B.Stern, X.Ji, Y.Okawachi, A.L.Gaeta, M.Lipson; Conference on Lasers and Electro-Optics, OSA Technical Digest (online) (Optical Society of America, 2018), paper SM1D.6 (2018). [Columbia University]
- "Fully integrated ultra-low power Kerr comb generation"; Stern, Brian; Ji, Xingchen; Okawachi, Yoshitomo; Gaeta, Alexander L.; Lipson, Michal; arXiv preprint arXiv:1804.00357 (2018). [Columbia University]

- “Fully Stabilized Optical Frequency Comb from a Semiconductor Disk Laser”; D.Waldburger, A.S.Mayer, C.G.E.Alfieri, J.Nurnberg, A.R.Johnson, X.Ji, A.Klenner, Y.Okawachi, M.Lipson, A.L.Gaeta, and U.Keller; Conference on Lasers and Electro-Optics, OSA Technical Digest (online) (Optical Society of America, 2018), paper SM4L.7 (2018). [Columbia University]
- “GaN/NbN Epitaxial Semiconductor/Superconductor Heterostructures”; B.Downey, D.Jena, D.Katzer, G.Khalsa, D.Meyer, N.Nepal, J.Wright, H.G.Xing, R.Yan; Docket No.8152, App Status; Filed - by Cornell, Filing Date; 2/27/18, App#; Invention (2018). [Cornell University]
- “GaN/NbN epitaxial semiconductor/superconductor heterostructures”; R.Yan, G.Khalsa, S.Vishwanath, Y.Han, J.Wright, S.Katzer, N.Nepal, B.P.Downey, D.A.Muller, H.G.Xing, D.J.Meyer and D.Jena; Nature 555, 183 (2018) doi:10.1038/nature25768.Commentary in Nature “Transistors driven by superconductors” <https://www.nature.com/articles/d41586-018-02717-4> (2018). [Cornell University]
- “GaN/NbN Epitaxial Semiconductor/Superconductor Heterostructures”; B.Downey, D.Jena, D.Katzer, G.Khalsa, D.Meyer, N.Nepal, J.Wright, H.G.Xing, R.Yan; Docket No.8152-01-US, Country of Filing; United States, App Type; MPP - Manuscript Plus Provisional, App Status; Converted, Filing Date; 3/6/18, App#; 62/6239,302 (2018). [Cornell University]
- “Gas-Phase Microresonator-Based Comb Spectroscopy without an External Pump Laser”; Yu, Mengjie; Okawachi, Yoshitomo; Joshi, Chaitanya; Ji, Xingchen; Lipson, Michal; Gaeta, Alexander L.; ACS Photonics, Vol.5, Issue 7, p.2780-2785, DOI:10.1021/acsp Photonics.8b00579 (2018). [Columbia University]
- “Gate-Recessed E-mode p-Channel HFET With High On-Current Based on GaN/AlN 2D Hole Gas”; Bader, S.J.; Chaudhuri, R.; Nomoto, K.; Hickman, A.; Chen, Z.; Then, H.W.; Muller, D.A.; Xing, H.G.; Jena, D.; IEEE Electron Device Letters, Vol.39, Issue 12, p.1848-1851, DOI:10.1109/LED.2018.2874190 (2018). [Cornell University]
- “Generation and Acceleration of Charged Particles Using Compact Devices and Systems”; Serhan Ardanuc, June Ho Hwang, Amit Lal, Farhan Rana, Shi Yue; Docket No.6099-04-US, Country of Filing; United States, App Type; CON - Continuation, App Status; Prosecution, Filing Date; 1/8/18, App#; 15/865,056 (2018). [Cornell University]
- “Generation and Acceleration of Charged Particles Using Compact Devices and Systems”; Serhan Ardanuc, June Ho Hwang, Amit Lal, Farhan Rana, Shi Yue; Docket No.6099-03-US, Country of Filing; United States, App Status; Issued, Filing Date; 4/17/15, App#; 14/436,859, Patent Number & Issue Date; 9,867,272, 1/9/18 (2018). [Cornell University]
- “GHz-THz Ultrasonics and Optics for Neurotechnology Devices, Methods and Applications”; Amit Lal; Docket No.8282-01-US, Country of Filing; United States, App Type; MPR - Manuscript Provisional, App Status; Filed Date; 5/24/18, App#; 62/676,973 (2018). [Cornell]
- “Giant, Temperature-Dependent Spin Hall Torque from Rare-Earth Mixed-Valence YbAl<sub>3</sub>”; N.Reynolds; 2018 March Meeting of the American Physical Society, March 5-9, 2018, Los Angeles, CA (2018). [Cornell University]
- “Graphene Stress Transducer-Based Thermo-Mechanically Fractured Micro Valve”; Ved Gund, Alexander Ruyack, Serhan Ardanuc, Amit Lal; Journal of Microelectromechanical Systems, Vol.27, Issue 3, 2018, pp.555 - 569. (2018). [Cornell University]
- “Graphene-based bimorphs for micron-sized, autonomous origami machines”; Miskin, Marc Z.; Dorsey, Kyle J.; Bircan, Baris; Han, Yimo; Muller, David A.; McEuen, Paul L.; Cohen, Itai; Proceedings of the National Academy of Sciences of the United States of America, Vol.115, Issue 3, p.466-470, DOI:10.1073/pnas.1712889115 (2018). [Cornell University]
- “Growth of LaAlO<sub>3</sub> on silicon via an ultrathin SrTiO<sub>3</sub> buffer layer by molecular-beam epitaxy”; Zhe Wang, Zhen Chen, Antonio B.Mei, Xue Bai, Lena F.Kourkoutis, David A.Muller, and Darrell G.Schlom; Journal of Vacuum Science & Technology A36, 021507 (2018); doi: 10.1116/1.5009185 (2018). [Cornell]
- “High spatial and temporal ranging resolution of passive RFID tags”; Xiaonan Hui, Edwin Kan; Docket No.8372, App Status; Filed - by Cornell, Filing Date; 9/8/18, App #; Invention (2018). [Cornell University]
- “High voltage Gallium oxide (Ga<sub>2</sub>O<sub>3</sub>) trench MOS barrier Schottky and methods of fabricating same”; Z.Hu, D.Jena, W.Li, K.Nomoto, H.G.Xing; Docket No.8418, App Status; Filed - by Cornell, Filing Date; 10/25/18, App#; Invention (2018). [Cornell University]
- “High Voltage Gallium Oxide (Ga<sub>2</sub>O<sub>3</sub>) trench MOS Barrier Schottky and Methods of Fabricating Same”; Z.Hu, D.Jena, W.Li, K.Nomoto, H.G.Xing; Docket No.8418-01-US, Country of Filing; United States, App Type; MPR - Manuscript Provisional, App Status; Filed Date; 11/6/18, App#; 62/756,250 (2018). [Cornell University]
- “High-Overtone Bulk Diffraction Wave Gyroscope”; Benyamin Davaji, Amit Lal, Visarute Pinrod; Docket No.8383, App Status; Filed - by Cornell, Filing Date; 9/18/18, App#; Invention (2018). [Cornell University]
- “High-Overtone Bulk Diffraction Wave Gyroscope”; Benyamin Davaji, Amit Lal, Visarute Pinrod; Docket No.8383-01-US, Country of Filing; United States, App Type; MPR - Manuscript Provisional, App Status; Filed Date; 10/3/18, App#; 62/740,683 (2018). [Cornell University]
- “High-Q integrated photonic microresonators on 3C-SiC-on-insulator (SiCOI) platform”; Fan, Tianren; Moradinejad, Hesam; Wu, Xi; Eftekhar, Ali A.; Adibi, Ali; Optics express, Vol.26, Issue 20, p.25814-25826 (2018). [Georgia Institute of Technology]
- “High-Voltage Properties of Strained GaN Quantum Well HEMTs on AlN”; Austin Hickman, Samuel James Bader, Reet Chaudhuri, K.Nomoto, SM Islam, H.G.Xing, D.Jena; Compound Semiconductor Week, Boston MA, May 2018 (2018). [Cornell]
- “Highly Efficient Spin-Current Generation by the Spin Hall Effect in Au<sub>1-x</sub>Ptx”; Zhu, Lijun; Ralph, Daniel C.; Buhrman, Robert A.; Physical Review Applied, arXiv preprint arXiv:1805.02329, Vol.10, Issue 3, p.31001, DOI:10.1103/PhysRevApplied.10.031001 (2018). [Cornell University]
- “Highly Multiplexed Fluorescence In-Situ Hybridization for Spatial Mapping of Microbial Communities”; Iwijn De Vlaminck, Hao Shi; Docket No.8158, App Status; Filed - by Cornell, Filing Date; 3/5/18, App#; Invention (2018). [Cornell University]
- “Highly Multiplexed Phylogenetic Imaging of Microbial Communities”; Iwijn De Vlaminck, Hao Shi; Docket No.8158-01-US, Country of Filing; United States, App Type; MPR - Manuscript Provisional, App Status; Filed Date; 3/8/18, App#; 62/640,239 (2018). [Cornell]
- “Highly tunable efficient second-harmonic generation in a lithium niobate nanophotonic waveguide”; Luo, Rui; He, Yang; Liang, Hanxiao; Li, Mingxiao; Lin, Qiang; Optica, Vol.5, Issue 8, p.1006-1011, DOI:10.1364/OPTICA.5.001006 (2018). [U. of Rochester]
- “How Biophysical Forces Regulate Human B Cell Lymphomas”; Apoorva, F.; Loiben, A.M.; Shah, S.B.; Purwada, A.; Fontan, L.; Goldstein, R.; Kirby, B.J.; Melnick, A.M.; Cosgrove, B.D.; Singh, A.; Cell Reports, Vol.23, Issue 2, p.499-511, DOI:10.1016/j.celrep.2018.03.069 (2018). [Cornell University]
- “Human “Body-on-a-Chip” systems to test drug efficacy and toxicity”; Shuler, M.L.; SELECTBIO Organ-on-a-Chip and Body-on-a-Chip: in vitro systems mimicking in vivo functions.San Diego, CA.Oct.4-5, 2018 (2018); Select Bio Bioengineering Mtg.Boston, MA.March 26-27, 2018 (2018). [Cornell University]

- “Impact of the synthesis method on the solid-state charge transport of radical polymers”; Zhang, Y.; Park, A.; Cintora, A.; McMillan, S.R.; Harmon, N.J.; Moehle, A.; Flatte, M.E.; Fuchs, G.D.; Ober, C.K.; *Journal of Materials Chemistry C*, Vol.6, Issue 1, p.111-118, DOI:10.1039/c7tc04645f (2018). [Cornell University]
- “Improvement by Channel Recess of Contact Resistance and Gate Control in Large-Scale Spin-Coated MoS<sub>2</sub> MOSFETs”; Xiong, K.; Li, L.; Marstell, R.J.; Madjar, A.; Strandwitz, N.C.; Hwang, J.C.M.; Lin, Z.; Huang, Y.; Duan, X.; Goritz, A.; Wietstruck, M.; Kaynak, M.; *IEEE Electron Device Letters*, Vol.39, Issue 9, p.1453-1456, DOI:10.1109/LED.2018.2854789 (2018). [Lehigh University]
- “Influence of Strain on the Surface-Oxygen Interaction and the Oxygen Evolution Reaction of SrIrO<sub>3</sub>”; Kuo, D.; Eom, C.; Kawasaki, J.; Petretto, G.; Nelson, J.; Hautier, G.; Cruclin, E.; Shen, K.; Schlom, D.; Suntivich, J.; *J. of Physical Chemistry C*, V122, Issue 8, p.4359-64, DOI:10.1021/acs.jpcc.7b12081 (2018). [Cornell University]
- “Integrated Single Frequency, High Power Laser Sources Based on Monolithic and Hybrid Coherent Beam Combining”; Zhu, Yeyu; Zhu, Lin; *IEEE Journal of Selected Topics in Quantum Electronics* (2018). [Clemson University]
- “Integrating is Caring? Or, Caring for Nanotechnology? Being an Integrated Social Scientist”; Viseu, Ana; *Engineering a Better Future*, Springer, p.141-166 (2018). [Cornell University]
- “Interfacing Superconducting Quantum Processors with Cryogenic Digital Circuitry”; Plourde, Britton; *Quantum Information Science Workshop, October 2018*, Michigan State University, East Lansing, MI. (2018). [Syracuse University]
- “Interfacing superconducting qubits with cryogenic digital logic: Control”; Britton Plourde, JJ Nelson, Edward Leonard Jr, Matthew Beck, Kenneth Dodge, Caleb Howington, Jaseung Ku, Oleg Mukhanov, Robert McDermott; *Applied Superconductivity Conference, 2018*, Seattle, WA. (2018). [Syracuse]
- “Interfacing Superconducting Qubits With Cryogenic Digital Logic: Measurement (poster)”; C.Howington, A.Opremcak, R.McDermott, A.Kirichenko, O.A.Mukhanov, B.L.T.Plourde; *Applied Superconductivity Conference, 2018*, Seattle, WA. (2018). [Syracuse University]
- “Intrinsic conductivity mechanisms of radical polymer films with conjugated and non-conjugated backbones”; Albert Park, Yiren Zhang, Alicia Cintora, Stephen McMillan, Nicholas Harmon, Austin Moehle, Michael Flatté, Christopher Ober, and Gregory D.Fuchs; *March Meeting of the APS, Los Angeles, CA 2018* (2018). [Cornell University]
- “Irrelevance of magnetic proximity effect to spin-orbit torques in heavy-metal/ferromagnet bilayers”; Zhu, L.J.; Ralph, D.C.; Buhrman, R.A.; *Physical Review B*, Vol.98, Issue 13, p.134406, DOI:10.1103/PhysRevB.98.134406 (2018). [Cornell]
- “Keck-PAD X-ray Detector”; Sol Gruner, Lucas Koerner, Hugh Philipp, Prafull Purohit, Katherine Shanks, Mark Tate; *Docket No.8319*, App Status; UnFiled Date; 6/28/18, App#; *Invention* (2018). [Cornell University]
- “Large area metalenses: design, characterization, and mass manufacturing”; She, Alan; Zhang, Shuyan; Shian, Samuel; Clarke, David R.; Capasso, Federico; *Optics Express*, Vol.26, Issue 2, p.1573-1585, DOI:10.1364/OE.26.001573 (2018). [Harvard University]
- “Large-scale fabrication of RF MOSFETs on liquid-exfoliated MoS<sub>2</sub>”; K.Xiong, L.Li, A.Madjar, J.C.M.Hwang, Z.Lin, Y.Huang, X.Duan, A.Göriz, M.Wietstruck, and M.Kaynak; *European Microwave Conf.(EuMC)*, Madrid, Spain, Sep.2018 (2018). [Lehigh]
- “Large-scale fabrication of RF MOSFETs on liquid-exfoliated MoS<sub>2</sub>”; K.Xiong, L.Li, A.Madjar, J.C.M.Hwang, Z.Lin, Y.Huang, X.Duan, A.Göriz, M.Wietstruck, and M.Kaynak; *European Microwave Conf.(EuMC)*, Madrid, Spain, Sep.2018, pp.1105-1108 (2018). [Lehigh University]
- “Leveraging Novel Nonlinear Devices for Compact Gigahertz Frequency Combs”; Mayer, Aline S.; *ETH Zurich Research Collection*, PhD Thesis (2018). [ETH, Zurich]
- “Light Confinement and Nonlinear Light-Matter Interaction in Semiconductor Photonic Crystal Cavities”; Mohamed, Mohamed Sabry Abdel-Aliem; *ÉCOLE POLYTECHNIQUE FÉDÉRALE DE LAUSANNE*, PhD Thesis (2018). [Ecole des Mines de Saint Etienne]
- “Light Emitting Diodes Using Ultra-thin Quantum Heterostructures”; SM Islam, D.Jena, Vladimir Protasenko, Jai Verma, H.G.Xing; *Docket No.7925-02-US*, Country of Filing; United States, App Type; US from PRV, App Status; Filed Date; 11/15/18, App#; 16/192,325 (2018). [Cornell University]
- “Light Field Image Sensor, Method and Applications”; Patrick Gill, Alyosha Molnar, Albert Wang; *Docket No.4895-05-KR*, Country of Filing; South Korea, App Status; Issued, Filing Date; 5/22/13, App#; 10-2013-7013124, Patent Number & Issue Date; 10-1904033, 9/27/18 (2018). [Cornell]
- “Localized Microfluidic Mixer Using Planar Fresnel Type GHz Ultrasonic Transducer”; A. Ravi, A. Ruyack, J. Kuo and A. Lal; *2018 IEEE International Ultrasonics Symposium (IUS)*, Kobe, 2018, pp. 1-4. doi: 10.1109/ULTSYM.2018.8579844 (2018). [Cornell University]
- “Low loss fiber to chip packaging”; J.Cardenas; *Integrated Photonics Conference, Alexandria, 1 - 4 Oct. 2018*. Invited talk (2018). [University of Rochester]
- “Low Power Asynchronous GPS Baseband Processor”; Sunil Bhawe, Stephen Longfield, Rajit Manohar, Benjamin Tang; *Docket No.5548-03-US*, Country of Filing; United States, App Status; Issued, Filing Date; 8/22/14, App#; 14/380,700, Patent Number & Issue Date; 10,126,428, 11/13/18 (2018). [Cornell University]
- “Low Power Asynchronous GPS Baseband Processor”; Sunil Bhawe, Stephen Longfield, Rajit Manohar, Benjamin Tang; *Docket No.5548-06-JP*, Country of Filing; Japan, App Status; Issued, Filing Date; 10/15/14, App#; 2014-558924, Patent Number & Issue Date; 6272786, 1/12/18 (2018). [Cornell University]
- “Magnetic imaging of electronic transport in graphene”; Schaefer, Brian; Wang, Lei; Ferguson, George; Watanabe, Kenji; Taniguchi, Takashi; Mueller, Erich; McEuen, Paul; Nowack, Katja; *Bulletin of the American Physical Society* (2018). [Cornell University]
- “Magneto-thermal imaging of exchange bias in Pt/FeRh bilayers”; I.Gray, G.Steihl, J.Heron, D.Ralph, and G.D.Fuchs; *March Meeting of the APS, Los Angeles, CA 2018* (2018). [Cornell University]
- “Materials Overview for 2-Photon 3D Printing Applications”; Ober, C.; *International Conference on Photopolymer Science and Technology, Chiba, Japan, June 2018*, invited talk. (2018). [Cornell University]
- “Measurement of a Superconducting Qubit with a Microwave Photon Counter”; A.Opremcak, I.V.Pechenezhskiy, C.Howington, B.G.Christensen, M.A.Beck, E.Leonard Jr., J.Suttle, C.Wilen, K.N.Nesterov, G.J.Ribeill, T.Thorbeck, F.Schlenker, M.G.Vavilov, B.L.T.Plourde, R.McDermott; *Science* 361, 1239 (2018) (2018). [Syracuse University]
- “Measurements of Oxygen Electroadsorption Energies and Oxygen Evolution Reaction on RuO<sub>2</sub>(110): A Discussion of the Sabatier Principle and Its Role in Electrocatalysis”; Kuo, D.; Paik, H.; Kloppenburg, J.; Faeth, B.; Shen, K.; Schlom, D.; Hautier, G.; Suntivich, J.; *J. of the ACS*, Vol.140, Issue 50, p.17597-17605, DOI:10.1021/jacs.8b09657 (2018). [Cornell University]
- “Measuring and Manipulating the Adhesion of Graphene”; Miskin, Marc Z.; Sun, Chao; Cohen, Itai; Dichtel, William R.; McEuen, Paul L.; *Nano Letters*, Vol.18, Issue 1, p.449-454, DOI:10.1021/acs.nanolett.7b04370 (2018). [Cornell University]

- "Mechanical Stress Regulates Function of Cell Envelope Proteins in Bacteria"; Roberts, M.F., Genova, L.A., Wang, Y-C, Chen, P., Hernandez, C.J.; 8th World Congress of Biomechanics, Dublin, Ireland.Podium (2018) (2018). [Cornell University]
- "MEMS 3-D Scan Mirror With SU-8 Membrane and Flexures for High NA Microscopy"; Liu, Tianbo; Svidunovich, Aaron J.; Wollant, Benjamin C.; Dickensheets, David L.; Journal of Microelectromechanical Systems, Vol.27, Issue 4, p.719-729, DOI:10.1109/JMEMS.2018.2845375 (2018). [Montana State]
- "Metal Nanoparticles and MOF-Inspired Clusters for Microlithography"; Ober, Christopher; Merck Group, Somerville, NJ, April 20, 2018, invited talk. (2018). [Cornell]
- "Metal Oxide Cluster Photoresists: Improved Understanding of EUV Patterning Performance"; Ober, Christopher; International Conference on Photopolymer Science and Technology, Chiba, Japan, June 25 – 28, 2018, invited talk. (2018). [Cornell]
- "Metal-Organic Framework-Inspired Metal-Containing Clusters for High-Resolution Patterning"; Xu, H.; Sakai, K.; Kasahara, K.; Kosma, V.; Yang, K.; Herbol, H.; Odent, J.; Clancy, P.; Giannelis, E.; Ober, C.; Chemistry of Materials, Vol.30, Issue 12, p.4124-4133, DOI:10.1021/acs.chemmater.8b01573 (2018). [Cornell]
- "Method and Apparatus for Minimally-Invasive Implantation of Electrodes and Flexible, Thin-Film Substrates into Cortical or Sub-Cortical Structures of the Brain"; D.Shire, M.Gingerich, P.Wong, L.Ayton and J.Pezaris; U.S.Provisional Application Serial No.62/610,635 and filed on December 27, 2018 (2018). [Harvard University]
- "Methods for Specifying and Fabrication an Object, Associated Apparatus, and Applications"; Jonathan Butcher, Philip Cheung, Laura Hockaday, Kevin Kang, Kevin Yeh; Docket No.4649-04-US, Country of Filing; United States, App Type; CON - Continuation, App Status; Filed Date; 7/23/18, App#; 16/042,461 (2018). [Cornell University]
- "Methods for Specifying and Fabrication an Object, Associated Apparatus, and Applications"; J.Butcher, P.Cheung, L.Hockaday, K.Kang, K.Yeh; Docket No.4649-03-US, Country of Filing; USA, App Status; Issued, Filing Date; 10/28/13, App #; 14/002,190, Patent Number & Issue Date; 10,048,668, 8/14/18 (2018). [Cornell University]
- "Microfluidic-Based Cell-Embedded Microgels Using Nonfluorinated Oil as a Model for the Gastrointestinal Niche"; Pajoumshariati, Seyed Ramin; Azizi, Morteza; Wesner, Daniel; Miller, Paula G.; Shuler, Michael L.; Abbaspourrad, Alireza; Acs Applied Materials & Interfaces, Vol.10, Issue 11, p.9235-9246, DOI:10.1021/acsami.7b16916 (2018). [Cornell University]
- "Micron-scale Confocal X-ray Fluorescence Microscopy Using Collimating Channel Arrays"; Arthur R.Woll, David N.Agyeman-Budu, Zou Finfrock; Synchrotron Radiation Instrumentation(SRI) 2018, Taipei, Taiwan, June 15th, Session H2.2. (2018). [Cornell University]
- "Microphysiological systems with liver module"; Shuler, M.L.; NYAS: translational approaches for human liver disease.New York, NY.Feb 20, 2018 (2018). [Cornell University]
- "Microwave Response of Vortices in Superconducting Resonators with High Kinetic Inductance"; Kenneth Dodge, JJ Nelson, Michael Senatore, Peng Xu, Kevin Osborn, David Pappas, Britton Plourde; March Meeting of the American Physical Society Bulletin, 2018, Los Angeles, CA. (2018). [Syracuse]
- "MM-PAD X-ray Detector"; Sol Gruner, Hugh Philipp, Prafull Purohit, Daniel Schuette, Katherine Shanks, Mark Tate; Docket No.8318, App Status; UnFiled Date; 6/28/18, App#; Invention (2018). [Cornell University]
- "Mode Structure in Superconducting Metamaterial Transmission Line Resonators"; Wang, H.; Zhuravel, A.P.; Indrajeet, S.; Taketani, Bruno G.; Hutchings, M.D.; Hao, Y.; Rouxinol, F.; Wilhelm, F.K.; LaHaye, M.; Ustinov, A.V.; arXiv preprint arXiv:1812.02579 (2018). [Syracuse University]
- "Modular Fabrication Systems and Methods"; L.Bonassar, D.Cohen, H.Lipson, E.Malone; Docket No.3527-10-US, Country of Filing; United States, App Type; CON - Continuation, App Status; Prosecution, Filing Date; 6/29/18, App#; 16/023,153 (2018); Docket No.3527-09-US, Country of Filing; USA, App Status; Issued, Filing Date; 12/10/15, App#; 14/965,317, Patent Number & Issue Date; 10,034,964, 7/31/18 (2018). [Cornell]
- "Monolithic PZT Actuator, Stage, and Method for Making"; S.Ardanuc, A.Lal, S.Nadig; Docket No.6306-04-US, Country of Filing; United States, App Type; CON - Continuation, App Status; Filed Date; 12/17/18, App#; 16/222,243 (2018); Docket No.6306-03-US, Country of Filing; United States, App Status; Issued, Filing Date; 10/19/15, App#; 14/785,442, Patent Number & Issue Date; 10/158,063, 12/18/18 (2018). [Cornell University]
- "Motion Sensor Integrated Nano-Probe N/Mems Apparatus, Method, and Applications"; Kwame Amponsah, Amit Lal; Docket No.5744-04-US, Country of Filing; United States, App Status; Issued, Filing Date; 6/12/14, App#; 14/364,745, Patent Number & Issue Date; 10/048,289, 8/14/18 (2018). [Cornell]
- "Multidimensional Piezoelectric Actuator Having Enhanced Actuation Range"; N.Akbari, C.Xu; Docket No.7841-02-PC, Country of Filing; PCT App, App Type; PCT - Patent Cooperation Treaty, App Status; Filing Date; 5/30/18, App Number; PCT/US18/35150 (2018). [Cornell University]
- "Multi-mode Circuit Quantum Electrodynamics with Superconducting Metamaterial Resonators"; Sagar, I., H. Wang, M. Hutchings, M. LaHaye, B. Plourde, B. Taketani, F. Wilhelm; March Meeting of the American Physical Society Bulletin, 2018, Los Angeles, CA. (2018). [Syracuse University]
- "Multi-Path, Multi-Magnification, Non-Confocal Fluorescence Emission Endoscopy Apparatus and Methods"; Watt Webb, Chunhui (Chris) Xu; Docket No.4080-04-EP, Country of Filing; Europe, App Status; Issued, Filing Date; 11/12/08, App#; 8850990.6, Patent Number & Issue Date; 2209412, 9/10/18 (2018). [Cornell University]
- "Multi-Path, Multi-Magnification, Non-Confocal Fluorescence Emission Endoscopy Apparatus and Methods"; Watt Webb, Chunhui (Chris) Xu; Docket No.4080-07-GB, Country of Filing; United Kingdom, App Status; Issued, Filing Date; 11/12/08, App#; 8805990.6, Patent Number & Issue Date; 2209412, 9/10/18 (2018). [Cornell University]
- "Multi-Path, Multi-Magnification, Non-Confocal Fluorescence Emission Endoscopy Apparatus and Methods"; Watt Webb, Chunhui (Chris) Xu; Docket No.4080-08-DE, Country of Filing; Germany, App Status; Issued, Filing Date; 11/12/08, App#; 6.02008E+11, Patent Number & Issue Date; 2209412, 9/10/18 (2018). [Cornell University]
- "Multi-Photon Wavefront Sensor, Methods and Applications"; David Sinefeld, Fei Xia, Chunhui (Chris) Xu; Docket No.7709-02-PC, Country of Filing; Not Applicable (PCT App), App Type; PCT - Patent Cooperation Treaty, App Status; Filed Date; 2/16/18, App#; PCT/US18/00057 (2018). [Cornell University]
- "Multifunctional Microfluidic Device for Capturing Target Cells and Analyzing Geonomic DNA Isolated from the Target Cells while Under Flow Conditions"; H.Craighead, S.Reinholt; Docket No.7428-03-US, Country of Filing; USA, App Type; US from PCT, App Status; Filed Date; 11/20/18, App#; 16/303,658 (2018). [Cornell University]
- "Multimodal Sensor, Method of Use, and Method of Fabrication"; A.Lakso, V.Pagay, M.Santiago, D.Sessoms, A.Stroock; Docket No.6335-06-AU, Country of Filing; Australia, App Type; FOR - Foreign DIV, App Status; Prosecution, Filing Date; 6/22/18, App#; 2018204539 (2018); Docket No.6335-04-AU, Country of Filing; Australia, App Status; Issued, Filing Date; 12/18/15, App#; 2014277891, Patent Number & Issue Date; 2014277891, 8/2/18 (2018). [Cornell]

- "Nanoliter-Sized Microchamber/Microarray Microfluidic Platform for Antibiotic Susceptibility Testing"; Azizi, M.; Zaferani, M.; Dogan, B.; Zhang, S.; Simpson, K.; Abbaspourrad, A.; Analytical Chemistry, Vol.90, Issue 24, p.14137-14144, DOI:10.1021/acs.analchem.8b03817 (2018). [Cornell University]
- "Nanoparticle catalysts communicate across distances"; P.Chen; Chem.Eng.News 2018, 96, 6 (2018). [Cornell University]
- "Nanopore-Containing Substrates with Aligned Nanoscale Electronic Elements and Methods of Making and Using Same"; J.Alden, A.Barnard, A.Cortese, P.McEuen; Docket No.6798-07-CA, Country of Filing; Canada, App Type; FOR - Foreign, App Status; Filed Date; 5/10/18, App#; 3005143 (2018). [Cornell]
- "NEMS Electrostatic RF Wakeup Switch with Pt FIB Contact"; A.Ruyack, et al.; Electron Device Society (ORAL), 2018. (2018); A.Ruyack, et al.; PowerMEMS (POSTER) 2018 (2018); A.Ruyack, et al.; PowerMEMS (PAPER), 2018. (2018). [Cornell University]
- "New Optical Methods for Characterization of Materials and Biology"; Wojcik, M.; UC Berkeley, PhD Thesis (2018). [Cornell]
- "New tunneling features in polar III-nitride resonant tunneling diodes."; Jimmy Encomendero, Faiza Afroz Faria, S.M.Islam, Vladimir Protasenko, Sergei Rouvimov, Berardi Sensale-Rodriguez, Patrick Fay, D.Jena and H.G.Xing; Semiconductor Today Feature [http://www.semiconductor-today.com/news\\_items/2018/jan/cornell\\_020118.shtml](http://www.semiconductor-today.com/news_items/2018/jan/cornell_020118.shtml) (2018). [Cornell]
- "Non-uniform mechanical stress promotes metal efflux pump disassembly"; Roberts, M.F., Genova, L.Wang, L., Chen, P., Hernandez, C.J.; Biophysical Society Annual Meeting, San Francisco, CA, USA. Podium (2018) (2018). [Cornell University]
- "Nondegenerate Parametric Resonance in Large Ensembles of Coupled Micromechanical Cantilevers with Varying Natural Frequencies"; Wallin, C.; De Alba, R.; Westly, D.; Holland, G.; Grutzik, S.; Rand, R.H.; Zehnder, A.T.; Aksyuk, V.A.; Krylov, S.; Ilic, B.R.; PRL, V.121, Issue 26, p.264301, DOI:10.1103/PhysRevLett.121.264301 (2018). [Tel Aviv University]
- "Nonlinear Optics in III-V Quaternary Semiconductor Waveguides"; Saeidi, Shayan; Université d'Ottawa/University of Ottawa, PhD Thesis (2018). [University of Ottawa]
- "Observation of the nonlinear anomalous Hall effect in 2D WTe<sub>2</sub>"; Kaifei Kang, Tingxin Li, Egon Sohn, Jie Shan, Kin Fai Mak; arXiv:1809.08744 (2018) (2018). [Cornell University]
- "On-chip dual-comb source for spectroscopy"; Dutt, Avik; Joshi, Chaitanya; Ji, Xingchen; Cardenas, Jaime; Okawachi, Yoshitomo; Luke, Kevin; Gaeta, Alexander L.; Lipson, Michal; Science Advances, Vol.4, Issue 3, p.e1701858, DOI:10.1126/sciadv.1701858 (2018). [Columbia University]
- "On-chip Gas Sensors Based on Raman Spectroscopy"; Chengyu Liu, Jin Suntivich; Docket No.8344, App Status; UnFiled Date; 7/27/18, App#; Invention (2018). [Cornell University]
- "Optical Absorption and Emission Mechanisms of Single Defects in Hexagonal Boron Nitride"; Nicholas Jungwirth and Gregory D.Fuchs; March Meeting of the APS, Los Angeles, CA 2018 (2018). [Cornell University]
- "Optical Parametric Chirped-Pulse Amplification"; Walter Fu, Frank Wise; Docket No.7948-01-US, Country of Filing; United States, App Type; MPR - Manuscript Provisional, App Status; Filed Date; 3/30/18, App#; 62/650,984 (2018). [Cornell University]
- "Optimizing the Efficiency of Fabry-Perot Interferometers with Silicon-Substrate Mirrors"; Cothard, N.F.; Abe, M.; Nikola, T.; Stacey, G.J.; Cortes-Medellin, G.; Gallardo, P.A.; Koopman, B.J.; Niemack, M.D.; Parshley, S.C.; Vavagiakis, E.M.; Vetter, K.J.; Advances in Optical and Mechanical Technologies for Telescopes and Instrumentation Iii, Vol.10706, p.107065B (2018). [Cornell University]
- "Optofluidic Photoreactor Apparatus, Method and Applications"; D.Erickson, P.Schein; Docket No.8212, App Status; Filed - by Cornell, Filing Date; 4/9/18, App#; Invention (2018). [Cornell]
- "Orbital state manipulation of a diamond nitrogen-vacancy center using a mechanical resonator"; H.Y.Chen, E.R.MacQuarrie, and G.D.Fuchs; Phys.Rev.Lett.120, 167401 (2018) (2018). [Cornell]
- "Ordered AlxGa1-xAs Nanopillar Arrays via Inverse Metal-Assisted Chemical Etching"; Wilhelm, T.S.; Wang, Z.; Baboli, M.A.; Yan, J.; Preble, S.F.; Mohseni, P.K.; ACS Applied Materials & Interfaces, Vol.10, Issue 32, p.27488-27497, DOI:10.1021/acsami.8b08228 (2018). [Rochester Institute of Technology]
- "Oriented chiral water wires in artificial transmembrane channels"; Kocsis, I.; Sorci, M.; Vanselow, H.; Murail, S.; Sanders, S.E.; Licsandru, E.; Legrand, Y.-M.; van der Lee, A.; Baaden, M.; Petersen, P.B.; Belfort, G.; Barboiu, M.; Science Advances, Vol.4, Issue 3, p.eaao5603, DOI:10.1126/sciadv.aao5603 (2018). [Cornell University]
- "Origin, Evolution, and Movement of Microlayer in Pool Boiling"; Zou, An; Gupta, Manish; Maroo, Shalabh C.; Journal of Physical Chemistry Letters, Vol.9, Issue 14, p.3863-3869, DOI:10.1021/acs.jpcllett.8b01646 (2018). [Syracuse University]
- "Pathways to Mesoporous Resin/Carbon Thin Films with Alternating Gyroid Morphology"; Zhang, Qi; Matsuoka, Fumiaki; Suh, Hyo Seon; Beaucage, Peter A.; Xiong, Shiheng; Smilgies, Detlef-M.; Tan, Kwan Wee; Wemer, Jorg G.; Nealey, Paul F.; Wiesner, Ulrich B.; ACS Nano, Vol.12, Issue 1, p.347-358, DOI:10.1021/acsnano.7b06436 (2018). [Cornell University]
- "Pattern-forming Method and Radiation-sensitive Composition"; Emmanuel Giannelis, Vasiliki Kosma, Christopher Ober, Kazunori Sakai; Docket No.8416-01-US, Country of Filing; United States, App Type; MPR - Manuscript Provisional, App Status; Filed Date; 8/20/18, App#; 62/764,983 (2018). [Cornell University]
- "Pattern-forming Method and Radiation-sensitive Composition"; Emmanuel Giannelis, Vasiliki Kosma, Christopher Ober, Kazunori Sakai; Docket No.8416, App Status; Filed - by Joint Owner, Filing Date; 10/18/18, App#; Invention (2018). [Cornell University]
- "Patterning mechanism of metal based hybrid EUV resists"; Kosma, Vasiliki; Kasahara, Kazuki; Xu, Hong; Sakai, Kazunori; Ober, Christopher K.; Giannelis, Emmanuel P.; Extreme Ultraviolet (euv) Lithography Ix, Spie-Int Soc Optical Engineering, Vol.10583, p.UNSP 105831U (2018). [Cornell University]
- "Picosecond ultrasonic study of surface acoustic waves on periodically patterned layered nanostructures"; Colletta, Michael; Gachuhi, Wanjiru; Gartenstein, Samuel A.; James, Molly M.; Szwed, Erik A.; Daly, Brian C.; Cui, Weili; Antonelli, George A.; Ultrasonics, Vol.87, p.126-132, DOI:10.1016/j.ultras.2018.02.013 (2018). [Vassar College]
- "Platforms Enabled by Buried Tunnel Junction for Integrated Photonic and Electronic Systems"; Shyam Bharadwaj, Alexander Chaney, D.Jena, K.Nomoto, Henryk Turski, H.G.Xing; Docket No.8026-01-US, Country of Filing; United States, App Type; MPR - Manuscript Provisional, App Status; Converted, Filing Date; 2/2/18, App#; 62/625,502 (2018). [Cornell]
- "Polarization control in Nitride Quantum Well Light Emitters Enabled by Bottom Tunnel-junctions"; Turski, H.; Bharadwaj, S.; Jena, D.; arXiv preprint arXiv:1810.01897 (2018). [Cornell]
- "Polarization Field assisted Heterostructure Design for Efficient Deep Ultra-violet Light Emitting Diodes"; SM Islam, D.Jena, Vladimir Protasenko, H.G.Xing; Docket No.7926-02-US, Country of Filing; United States, App Type; US from PRV, App Status; Filed Date; 11/15/18, App#; 16/192,361 (2018). [Cornell]
- "Polarization-induced 2D hole gas enables record GaN/AlN p-channel normally-off FETs"; S.Bader, R.Chaudhuri, K.Nomoto, A.Hickman, Z.Chen, H.Then, D.Muller, H.G.Xing and D.Jena; IEEE Electron Device Letters, 39(12), 1848 (2018) doi:10.1109/LED.2018.2874190 Featured by Semiconductor Today (2018). [Cornell University]

- "Polarization-induced 2d Hole Gases for High-Voltage p-channel Transistors"; Samuel Bader, Reet Chaudhuri, D.Jena, H.G.Xing; Docket No.8340, App Status; Filed - by Cornell, Filing Date; 7/20/18, App Number; Invention (2018). [Cornell]
- "Polarization-induced 2d Hole Gases for High-Voltage p-channel Transistors"; Samuel Bader, Reet Chaudhuri, D.Jena, H.G.Xing; Docket No.8340-01-US, Country of Filing; United States, App Type; MPR - Manuscript Provisional, App Status; Filed Date; 7/20/18, App#; 62/701,219 (2018). [Cornell University]
- "Polarization-induced doping in buried p-type GaN: unique advantage in reverse blocking"; W.Li, Mingda Zhu, K.Nomoto, Z.Hu, Xiang Gao, Manyam Pilla, D.Jena, and H.G.Xing; Electronic Materials Conference (EMC), 2018. (2018). [Cornell University]
- "Polydimethylsiloxane (PDMS) Molds for Creating P-gel Pads and PDMS-coated Glass Microscope Slides"; Dan Luo; Docket No.8184, App Status; Will Not File - Tangible Material, Filing Date; 3/20/18, App#; Shrink Wrap MTA (2018). [Cornell]
- "Porous Zero-Mode Waveguides for Picogram-Level DNA Capture"; Jadhav, V.; Hoogerheide, D.P.; Korlach, J.; Wanunu, M.; Nano letters (2018). [Northeastern University]
- "Potential role of "Body-on-a-Chip" systems in drug development"; Shuler, M.L.; 17th Annual QUAD Symposium.Mashantucket, CT.April 25, 2018 (2018). [Cornell University]
- "Potential Semiconducting and Superconducting Metastable Si<sub>3</sub>C Structures under Pressure"; Gao, Guoying; Liang, Xiaowei; Ashcroft, N.W.; Hoffmann, Roald; Chemistry of Materials, Vol.30, Issue 2, p.421-427, DOI:10.1021/acs.chemmater.7b04243 (2018). [Cornell University]
- "Probing the organization and dynamics of two DNA chains trapped in a nanofluidic cavity"; Capaldi, X.; Liu, Z.; Zhang, Y.; Zeng, L.; Reyes-Lamothe, R.; Reisner, W.; Soft matter, Vol.14, Issue 42, p.8455-8465 (2018). [McGill University]
- "Progress in Metal Organic Cluster EUV Photoresists"; Ober, Christopher; 62nd EIPBN Conference, San Juan, PR, May 29 - June 1, 2018. (2018). [Cornell University]
- "Progress in metal organic cluster EUV photoresists"; Sakai, K.; Xu, H.; Kosma, V.; Giannelis, E.; Ober, C.; Journal of Vacuum Science & Technology B, Vol.36, Issue 6, p.06J504, DOI:10.1116/1.5050942 (2018). [Cornell University]
- "Quantum Control Over Diamond Nitrogen-Vacancy Centers Using a Mechanical Resonator"; Fuchs, Greg (invited); Spin Mechanics and nano MRI, École de Physique des Houches, Chamonix, France, 2018 (2018). [Cornell University]
- "Qubit State Measurement using the Josephson Photomultiplier"; A.Opremcak, I.Pechenezhskiy, C.Howington, B.Christensen, K.Nesterov, M.Vavilov, F.Wilhelm, B.Plourde, R.McDermott; March Meeting of the American Physical Society Bulletin, 2018, Los Angeles, CA. (2018). [Syracuse University]
- "Recessed-channel PtSe<sub>2</sub> MOSFETs with Low Contact Resistance"; L.Li, K.Xiong, R.J.Marstell, A.Madjar, N.C.Strandwitz, J.C.M.Hwang, N.McEvoy, J.B.McManus, G.S.Duesberg, A.Görizt, M.Wietstruck, and M.Kaynak; Graphene and Beyond Workshop, University Park, PA, May 2018. [Lehigh University]
- "Red-Enhanced Photon Detection Module Featuring a 32x1 Single-Photon Avalanche Diode Array"; F.Ceccarelli, A.Gulinatti, I.Labanca, M.Ghioni, and I.Rech; IEEE Photonics Technology Letters, vol.30, no.6, pp.557-560, 2018.doi: 10.1109/LPT.2018.2804909 (2018). [Politecnico di Milano]
- "Reflections on applying engineering to model living systems"; Shuler, M.L.; BIGHEART; National University of Singapore. Singapore, Feb 6, 2018 (2018). [Cornell University]
- "Reflections on applying engineering to the life sciences"; Shuler, M.L.; BMES/CMBE 2018 Cellular and Molecular Bioengineering Conference.Key Largo, FL.Jan.2-6, 2018, Shu Chien Achievement Award Lecture (2018). [Cornell University]
- "Relaxation of asymmetric crystallographic tilt: In situ x-ray diffraction studies of epitaxial electrodeposition of bismuth on GaAs (110)"; Huang, Xin; Plaza, Manuel; Ko, J.Y.Peter; Abruna, Hector D.; Brock, Joel D.; Journal of Applied Physics, Vol.124, Issue 3, p.35301, DOI:10.1063/1.5026630 (2018). [Cornell]
- "Reorientable Spin Direction for Spin Current Produced by the Anomalous Hall Effect"; J.Gibbons; 2018 March Meeting of the American Physical Society, March 5-9, 2018, Los Angeles, CA (2018). [Cornell University]
- "Reorientable Spin Direction for Spin Current Produced by the Anomalous Hall Effect"; Gibbons, J.D.; MacNeill, D.; Buhrman, R.A.; Ralph, D.C.; Physical Review Applied, Vol.9, Issue 6, p.64033, DOI:10.1103/PhysRevApplied.9.064033 (2018). [Cornell University]
- "Revealing the hidden heavy Fermi liquid in CaRuO<sub>3</sub>"; Liu, Yang; Nair, Hari P.; Ruf, Jacob P.; Schlom, Darrell G.; Shen, Kyle M.; Physical Review B, Vol.98, Issue 4, p.41110, DOI:10.1103/PhysRevB.98.041110 (2018). [Cornell University]
- "Rheotaxis-based separation of sperm with progressive motility using a microfluidic corral system"; Zaferani, Meisam; Cheong, Soon Hon; Abbaspourrad, Alireza; Proceedings of the National Academy of Sciences of the United States of America, Vol.115, Issue 33, p.8272-8277, DOI:10.1073/pnas.1800819115 (2018). [Cornell University]
- "Room temperature microwave oscillations in GaN/AlN resonant tunneling diodes with peak current densities up to 220 kA/cm<sup>2</sup>"; J.Encomendero, R.Yan, A.Verma, S.M.Islam, V.Protasenko, S.Rouvimov, P.Fay, D.Jena and H.G.Xing; Appl.Phys.Lett.112, 103101 (2018) DOI: 10.1063/1.5016414 Editor's Pick Cover Image of APL (2018). [Cornell University]
- "Room-temperature graphene-nanoribbon tunneling field effect transistors."; Wan Sik Hwang, Pei Zhao, Sung Geun Kim, Rusen Yan, Gerhard Klimeck, Alan Seabaugh, Susan K.Fullerton-Shirey, H.G.Xing and D.Jena; Nature: 2D Materials and Applications, (Under revision for 2018) (2018). [Cornell University]
- "Rutile IrO<sub>2</sub>/TiO<sub>2</sub> superlattices: A hyperconnected analog to the Ruddelsden-Popper structure"; Kawasaki, J.; Baek, D.; Paik, H.; Nair, H.; Kourkoutis, L.; Schlom, D.; Shen, K.; Physical Review Materials, Vol.2, Issue 5, p.54206, DOI:10.1103/PhysRevMaterials.2.054206 (2018). [Cornell University]
- "S-shaped negative differential resistance in III-nitride blue quantum-well laser diodes grown by plasma-assisted MBE"; H.Turski, R.Yan, A.Chaney, S.Bader, J.Encomendero, Z.Hu, G.Muziol, C.Skierbiszewski, H.G.Xing and D.Jena; IEEE Device Research Conference, UCSB, June 2018. (2018). [Cornell]
- "Scalable and Rechargeable Antimicrobial Coating for Food Safety Applications"; Qiao, Mingyu; Liu, Qingsheng; Yong, You; Pardo, Yudi; Worobo, Randy; Liu, Zheng; Jiang, Shan; Ma, Minglin; Journal of Agricultural and Food Chemistry, Vol.66, Issue 43, p.11441-11450, DOI:10.1021/acs.jafc.8b03864 (2018). [Cornell University]
- "Scanning SQUID microscopy of ion-gel-gated MoS<sub>2</sub>"; Jarjour, A.; Schaefer, B.; Ferguson, G.; Low, D.; Yan, R.; Lee, M.; Jena, D.; Xing, G.; Nowack, K.; Bulletin of the American Physical Society (2018). [Cornell University]
- "Self-starting Fiber Oscillator for Generating Femtosecond Pulses with Megawatt Peak Power"; Walter Fu, Zhanwei Liu, Pavel Sidorenko, Frank Wise; Docket No.7954-01-US, Country of Filing; United States, App Type; MPP - Manuscript Plus Provisional, App Status; Filed Date; 3/27/18, App#; 62/648,876 (2018). [Cornell University]
- "Semiconductor Circuits and Devices Based on Low Energy Consumption Semiconductor Structures Exhibiting Multi-Valued Magnetolectric Spin Hall Effect"; J.Heron, K.Kuhn, M.Rahman, D.Schlom; Docket No.7453-03-US, Country of Filing; United States, App Type; US from PCT, App Status; Filed Date; 12/7/18, App#; 16/308,337 (2018). [Cornell University]

- “Silicon Single Photon Avalanche Diodes (SPAD) for QKD in Space”; Gulinatti, I.Rech, and M.Ghioni; Workshop on QKD for Space Systems, Thales Alenia Space Italia, October 23rd 2018, Rome, Italy (Invited). (2018). [Politecnico di Milano]
- “Silicon-chip-based mid-infrared dual-comb spectroscopy”; Yu, Mengjie; Okawachi, Yoshitomo; Griffith, Austin G.; Picqué, Nathalie; Lipson, Michal; Gaeta, Alexander L.; Nature Communications, Vol.9, Issue 1, p.1869, DOI:10.1038/s41467-018-04350-1 (2018). [Columbia University]
- “Single cell on-chip whole genome amplification via micropillar arrays for reduced amplification bias”; Tian, Harvey C.; Benitez, Jaime J.; Craighead, Harold G.; PLoS one, Vol.13, Issue 2, p.e0191520 (2018). [Cornell University]
- “Solvent-Mediated Self-Assembly in Thin Films of Block Copolymer-Based Supramolecules”; Evans, Katherine, Xu, Ting; American Physical Society March Meeting, Los Angeles, March 5-9, 2018 (2018). [UC Berkeley]
- “Spectral characteristics of single photons emitted from defects in hexagonal boron nitride”; N.Mathur, N.R.Jungwirth, K.Konhasinghe, R.S.Daveau, J.Kuan, N.J.Protic, N.Vamivakas, and G.D.Fuchs; Gordon Research Conference on Defects in Semiconductors (POSTER), Colby-Sawyer College, New London, NH 2018 (2018). [Cornell University]
- “Spin and Orbital Resonance Driven by a Mechanical Resonator”; Fuchs, Greg (invited); 2018 Rocky Mountain Conference on Magnetic Resonance, Snowbird, UT, 2018 (2018). [Cornell]
- “Spin and Orbital Resonance Driven by a Mechanical Resonator”; Fuchs, Greg (invited); Fall Meeting of MRS, Boston, MA 2018 (2018). [Cornell University]
- “Spin Seebeck imaging of spin-torque switching in antiferromagnetic Pt/NiO/Pt”; I.Gray, T.Moriyama, N.Sivadas, B.J.Kirby, R.Need, D.H.Low, G.M.Stiehl, J.T.Heron, D.C.Ralph, K.C.Nowack, T.Ono, and G.D.Fuchs; Spin Caloritronics IX (POSTER), Columbus, OH 2018 (2018). [Cornell University]
- “Spin Seebeck imaging of spin-torque switching in antiferromagnetic Pt/NiO/Pt”; I.Gray, T.Moriyama, N.Sivadas, B.J.Kirby, R.Need, D.H.Low, G.M.Stiehl, J.T.Heron, D.C.Ralph, K.C.Nowack, T.Ono, and G.D.Fuchs; Spin Caloritronics IX, Columbus, OH 2018 (2018). [Cornell University]
- “Spin transistor built on 2D van der Waals heterostructures”; Shengwei Jiang, Lizhong Li, Zefang Wang, Jie Shan, Kin Fai Mak; arXiv:1807.04898 (2018) (2018). [Cornell University]
- “Spin-Orbit Torques in NbSe<sub>2</sub>/Permalloy Bilayers”; Guimaraes, Marcos H.D.; Stiehl, Gregory M.; MacNeill, David; Reynolds, Neal D.; Ralph, Daniel C.; Nano Letters, Vol.18, Issue 2, p.1311-1316, DOI:10.1021/acs.nanolett.7b04993 (2018). [Cornell]
- “Stem cell derived phenotypic human neuromuscular junction model for dose response evaluation of therapeutics”; Santhanam, N., Kumanchik, L., Guo, X., Sommerhage, F., Cai, Y., Jackson, M., Martin, C., Saad, G., McAleer, C., Wang, Y., Lavado, A., Long, C., Hickman, J.J.; Biomaterials, 166, 64–78.http://doi.org/10.1016/j.biomaterials.2018.02.047 (2018) (2018). [Cornell University]
- “Strong confinement of optical fields using localized surface phonon polaritons in cubic boron nitride”; Chatzakis, I.; Krishna, A.; Culbertson, J.; Sharac, N.; Giles, A.; Spencer, M.; Caldwell, J.; Optics Letters, Vol.43, Issue 9, p.2177-2180, DOI:10.1364/OL.43.002177 (2018). [Morgan State University]
- “Strong Enhancement of the Spin Hall Effect by Spin Fluctuations near the Curie Point of FePt<sub>1-x</sub> Alloys”; Ou, Y.; Ralph, D.C.; Buhrman, R.A.; Physical Review Letters, V.120, #9, p.97203, DOI:10.1103/PhysRevLett.120.097203 (2018). [Cornell]
- “Strong Mechanical Modulation of Nitrogen-Vacancy Center Excited States”; Huiyao Chen, Evan MacQuarrie, and Gregory D.Fuchs; March Meeting of the APS, Los Angeles, CA 2018 (2018). [Cornell University]
- “Structural, magnetic, and transport properties of Fe<sub>1-x</sub>Rh<sub>x</sub>/MgO(001) films grown by molecular-beam epitaxy”; Mei, A.; Tang, Y.; Grab, J.; Schubert, J.; Ralph, D.; Schlom, D.; Applied Physics Letters, Vol.113, Issue 8, p.82403, DOI:10.1063/1.5048303 (2018). [Cornell University]
- “Studying Single Defects in New Materials” Defects by Design: Quantum Nanophotonics in Emerging Materials”; Fuchs, Greg (invited); OSA Incubator Meeting, Washington DC 2018 (2018). [Cornell University]
- “Sub-Nanosecond Tuning of Microwave Resonators Fabricated on Ruddlesden-Popper Dielectric Thin Films”; Hagerstrom, A.M.; Lu, X.; Dawley, N.M.; Nair, H.P.; Mateu, J.; Horansky, R.D.; Little, C.A.E.; Booth, J.C.; Long, C.J.; Schlom, D.G.; Orloff, N.D.; Advanced Materials Technologies, Vol.3, Issue 8, p.1800090, DOI:10.1002/admt.201800090 (2018). [Cornell University]
- “Substrate stiffness heterogeneities disrupt endothelial barrier integrity in a micropillar model of heterogeneous vascular stiffening”; VanderBurgh, J.A., Hotchkiss, H., Potharazu, A., Taufalele, P.V.and Reinhart-King, C.A.; Biomedical Engineering Society Annual Meeting, Atlanta, GA.Podium presentation (October, 2018). (2018). [Cornell University]
- “Substrate stiffness heterogeneities disrupt endothelial barrier integrity in a micropillar model of heterogeneous vascular stiffening”; VanderBurgh, J.A., Hotchkiss, H., Potharazu, A., Taufalele, P.V.and Reinhart-King, C.A.; Integrative Biology, 10(12), pp.734-746, featured on the front cover. (2018). [Cornell University]
- “Superconducting Qubit Control with Single Flux Quantum Pulses: Part I - Fabrication”; E.Leonard Jr., JJ Nelson, M.Beck, K.Dodge, C.Howington, J.Ku, A.Kirichenko, D.Yohannes, O.Mukhanov, B.Plourde, R.McDermott; March Meeting of the American Physical Society Bulletin, 2018, Los Angeles, CA. (2018). [Syracuse University]
- “Supported Plant Plasma Lipid Bilayer on-a-Chip”; Susan Daniel; Docket No.8321-01-US, Country of Filing; United States, App Type; MPR - Manuscript Provisional, App Status; Filed Date; 7/11/18, App#; 62/696,424 (2018). [Cornell University]
- “Surface Acoustic Wave (SAW)-based Inertial Sensor Methods and Applications”; S.Ardanuc, A.Lal; Docket No.7370-03-US, Country of Filing; USA, App Type; US from PCT, App Status; Filed Date; 8/31/18, App#; 16/081,559 (2018). [Cornell]
- “Surface-modified CMOS IC electrochemical sensor array targeting single chromaffin cells for highly parallel amperometry measurements”; Huang, Meng; Delacruz, Joannalyn B.; Ruelas, John C.; Rathore, Shailendra S.; Lindau, Manfred; Pflugers Archiv-European Journal of Physiology, Vol.470, Issue 1, p.113-123, DOI:10.1007/s00424-017-2067-y (2018). [Cornell]
- “Synchronization of coupled microresonator frequency combs”; J.K.Jang, A.Klenner, X.Ji, Y.Okawachi, M.Lipson, and A.L.Gaeta; Conference on Lasers and Electro-Optics, OSA Technical Digest (online) (Optical Society of America, 2018), paper SW3A.4 (2018). [Columbia University]
- “Synchronization of coupled optical microresonators”; J.K.Jang, A.Klenner, X, Ji,Y.Okawachi, M.Lipson, and A.L.Gaeta; Nature Photonics 12, 688-693 (2018) (2018). [Columbia University]
- “Synchronization of microresonator optical frequency combs”; J.K.Jang, A.Klenner, X.Ji, Y.Okawachi, M.Lipson, and A.L.Gaeta; Adv Photonics 2018 (BGPP, IPR, NP, NOMA, Sensors, Networks, SPPCom, SOF), OSA Technical Digest (online) (Optical Society of America, 2018), paper JW2I.1 (2018). [Columbia University]
- “Synthesis and Formation Mechanism of All-Organic Block Copolymer-Directed Templating of Laser-Induced Crystalline Silicon Nanostructures”; Tan, Kwan Wee; Werner, Jorg G.; Goodman, Matthew D.; Kim, Ha Seong; Jung, Byungki; Sai, Hiroaki; Braun, Paul V.; Thompson, Michael O.; Wiesner, Ulrich; Acs Applied Materials & Interfaces, Vol.10, Issue 49, p.42777-42785, DOI:10.1021/acsami.8b12706 (2018). [Cornell]

- “Synthesis science of SrRuO<sub>3</sub> and CaRuO<sub>3</sub> epitaxial films with high residual resistivity ratios”; H.P.Nair, Y.Liu, J.P.Ruf, N.J.Schreiber, S.-L.Shang, D.J.Baek, B.H.Goodge, L.F.Kourkoutis, Z.-K.Liu, K.M.Shen, and D.G.Schlom; *APL Materials*, Volume 6, Issue 4, 10.1063/1.5023477 *APL Materials* 6, 046101 (2018); <https://doi.org/10.1063/1.5023477> (2018). [Cornell University]
- “System and Method for Attaching Optical Fibers to Chips”; J.Nauriyal, J.Carden; Patent application filed, pending (2018). [University of Rochester]
- “System And Method For Characterizing Particulates in a Fluid Sample”; David Erickson; Docket No.8405, App Status; Closed - Ownership Disclaimer; Filing Date; 10/9/18, App#; Invention (2018). [Cornell University]
- “System and Method for Isothermal Nucleic Acid Amplification”; Ethel Cesarman, David Erickson, Ryan Snodgrass; Docket No.7674-02-PC, Country of Filing; Not Applicable (PCT App), App Type; PCT - Patent Cooperation Treaty, App Status; Filed Date; 4/10/18, App#; PCT/US18/26865 (2018). [Cornell]
- “System and Method for Reflective Spectroscopy of a Cell Membrane Using a Fiber with a Plasmonic Metasurface”; S.Gupta, G.Shvets; Docket No.7743-02-PC, (PCT App), App Type; PCT - Patent Cooperation Treaty, App Status; Filed Date; 5/8/18, App#; PCT/US18/31599 (2018). [Cornell University]
- “System and Method for Ultra-High Resolution Ranging Using RFID”; X.Hui, E.Kan; Docket No.8372-01-US, Country of Filing; USA, App Type; MPR - Manuscript Provisional, App Status; Filed Date; 10/31/18, App#; 62/753,845 (2018). [Cornell]
- “Temperature-dependence of stress and elasticity in wet-transferred graphene membranes”; De Alba, Roberto; Abhilash, T.S.; Hui, Aaron; Storch, Isaac R.; Craighead, Harold G.; Parpia, Jeevak M.; *Journal of Applied Physics*, Vol.123, Issue 9, p.95109, DOI:10.1063/1.5006332 (2018). [Cornell University]
- “The Challenges of Highly Sensitive EUV Photoresists”; Ober, Christopher K.; Kosma, Vasiliki; Xu, Hong; Sakai, Kazunori; Giannelis, Emmanuel P.; *Journal of Photopolymer Science and Technology*, Vol.31, Issue 2, p.261-265, DOI:10.2494/photopolymer.31.261 (2018). [Cornell University]
- “The chemistry of electronic materials: small and perfect”; Ober, Christopher; 256th ACS National Meeting, Boston, MA, Aug.19-23, 2018, invited talk. (2018). [Cornell University]
- “The chemistry of electronic materials: small and perfect”; Ober, Christopher; CCMR Teacher Seminar, New York, NY, Oct.20, 2018, invited talk. (2018). [Cornell University]
- “The Electronic and Vibronic Properties of Single Photon Emitters in Hexagonal Boron Nitride”; Fuchs, Greg (invited); Boron Nitride Workshop, 3rd International Conference on Physics of 2D Crystals, La Valletta, Malta, 2018 (2018). [Cornell University]
- “The Electronic and Vibronic Properties of Single Photon Emitters in Hexagonal Boron Nitride”; Fuchs, Greg (invited); Physics of Quantum Electronics (PQE), Snowbird, UT 2018 (2018). [Cornell University]
- “Theory and Practice of Electron Diffraction from Single Atoms and Extended Objects using an Electron Microscope Pixel Array Detector”; Michael C.Cao, Yimo Han, Zhen Chen, Yi Jiang, Kayla X.Nguyen, Emrah Turgut, Gregory D.Fuchs, David A.Muller; *Microscopy* 67, i150-i161 (2018). [Cornell University]
- “Thin Film Compositions and Methods”; Lola Brown, Cheol-Joo Kim, Mark Levendorf, Jiwoong Park; Docket No.5970-03-US, Country of Filing; United States, App Status; Issued, Filing Date; 11/13/14, App#; 14/540,423, Patent Number & Issue Date; 9,947,749, 4/17/18 (2018). [Cornell University]
- “Three-dimensional atomic scale electron density reconstruction of octahedral tilt epitaxy in functional perovskites”; Yuan, Y.; Lu, Y.; Stone, G.; Wang, K.; Brooks, C.; Schlom, D.; Sinnott, S.; Zhou, H.; Gopalan, V.; *Nature Communications*, Vol.9, p.5220, DOI:10.1038/s41467-018-07665-1 (2018). [Cornell]
- “Threshold Voltage Engineering in E-mode Ga<sub>2</sub>O<sub>3</sub> Fin-channel Transistors”; W.Li, Z.Hu, Z.Zhang, K.Nomoto, N.Tanen, K.Sasaki, A.Kuramata, Tohru Nakamura, D.Jena and H.G.Xing; *Compound Semiconductor Week (CSW)*, 2018. (2018). [Cornell University]
- “Time multiplexed deep reactive ion etching of germanium and silicon--A comparison of mechanisms and application to x-ray optics”; V.Genova, D.Agyeman-Budu, A.Woll; *Journal of Vacuum Science & Technology B: Mic* (Vol.36, Issue 1) 04 January 2018, DOI: 10.1116/1.4991875 (2018). [Cornell University]
- “Time-Resolved Magnetic Microscopy Using Near-And Far-Field Picosecond Heating”; Bartell, Jason Matthew, PhD Thesis (2018). [Cornell University]
- “Time-resolved magneto-thermal microscopy: high-resolution dynamic imaging of magnetic materials ranging from ferromagnetic metals to antiferromagnetic insulators”; Fuchs, Greg (invited); *Spin Caloritronics IX*, Columbus, OH 2018 (2018). [Cornell University]
- “Transient Local Resolution of Flow Boiling in a Microchannel With a Streamlined Pin Fin”; A.Parahovnik, Y.Wang and Y.Peles; *ASME 2018 16th International Conference on Nanochannels, Microchannels, and Minichannels*, Dubrovnik, Croatia, June 10–13, 2018 (2018). [University of Central Florida]
- “Transmit-Receive Delay Element, Apparatus, Method and Applications”; M.Abdelmejeed, J.Kuo, A.Lal; Docket No.7369-03-US, Country of Filing; United States, App Type; US from PCT, App Status; Filed Date; 9/17/18, App#; 16/085,699 (2018). [Cornell University]
- “Tunable Dissipator for High-fidelity Cavity and Qubit Initialization”; Naveen, A.Opremcak, B.Christensen, C.Wilen, I.Pechenezhskiy, JJ Nelson, C.Wong, M.Vavilov, B.Plourde, R.McDermott; *March Meeting of the American Physical Society Bulletin*, 2018, Los Angeles, CA. (2018). [Syracuse University]
- “Two-dimensional Nanopore and Nanoporous Devices for Molecular Sensing and Ion Selectivity”; Danda, Gopinath; University of Pennsylvania, PhD Thesis (2018). [University of Pennsylvania]
- “Ultrafast optical study of surface acoustic waves up to 50 GHz on patterned layered nanostructures”; Daly, B.; Colletta, M.; Gachuhi, W.; Szwed, E.; Antonelli, G.; Cui, W.; Team, B.; *APS Meeting Abstracts* (2018). [Vassar College]
- “Ultrasonic Fourier Transform Analog Computing Apparatus, Method and Applications”; Amit Lal; Docket No.7368-03-US, Country of Filing; United States, App Type; MPR - Manuscript Provisional, App Status; Filed Date; 5/23/18, App#; 62/675,415 (2018). [Cornell]
- “Ultrasonic Horn Actuated Microprobes based Self-Calibrating Viscosity Sensor”; R.Abhishek, A.Lal; Docket No.4948-03-US, Country of Filing; United States, App Status; Issued, Filing Date; 4/30/13, App#; 13/810,648, Patent Number & Issue Date; 9,970,853, 5/15/18 (2018). [Cornell University]
- “Ultrasound Transducer Probe and Methods”; S.Gelber, G.Lewis Jr., G.Lewis, Sr., W.Olbricht; Docket No.4848-03-US, Country of Filing; United States, App Status; Issued, Filing Date; 8/15/14, App#; 14/110,866, Patent Number & Issue Date; 10,092,271, 10/9/18 (2018). [Cornell University]
- “Understanding nanocatalysts’ ‘talk’ could better inform design”; P.Chen; *Cornell Chronicle*, March 26, 2018 (2018). [Cornell]
- “UniChip enables long-term recirculating unidirectional perfusion with gravity-driven flow for microphysiological systems”; Wang, Ying I.; Shuler, Michael L.; *Lab on a Chip*, Vol.18, Issue 17, p.2563-2574, DOI:10.1039/c8lc00394g (2018). [Cornell]
- “Using scanning plasmonic heating for nanoscale imaging of magnetization”; Jason Bartell, Jonathan Karsch, Colin Jermain, Jack Brangham, Fengyuan Yang, Daniel Ralph, and Gregory D.Fuchs; *March Meeting of the APS*, Los Angeles, CA 2018 (2018). [Cornell University]

- “UV-Triggered Transient Electrospun Poly(propylene carbonate)/ Poly(phthalaldehyde) Polymer Blend Fiber Mats”; Shi, Chengjian; Leonardi, Amanda; Zhang, Yiren; Ohlendorf, Peter; Ruyack, Alexander; Lal, Amit; Ober, Christopher K.; *Acs Applied Materials & Interfaces*, Vol.10, Issue 34, p.28928-28935, DOI:10.1021/acssami.8b06051 (2018). [Cornell University]
- “Vaporizable and Destickikng Polymer for Surface Coating”; Amit Lal, Amanda Leonardi, Christopher Ober, Alexander Ruyack; Docket No.8189, App Status; UnFiled Date; 3/28/18, App#; Invention (2018). [Cornell]
- “Versatile, Cost-effective, and Flexible Wearable Devices for Sweat Collection, Sweat Monitoring, and Personalized Nutrition”; A.Abbaspourrad, Z.Zhang; Docket No.8211, App Status; Filed Date; 4/6/18, App#; Invention (2018). [Cornell]
- “Vortex Microwave Response in High Kinetic Inductance Superconducting Thin Films”; Plourde, Britton; Landau Institute for Theoretical Physics, Chernogolovka, Russia, Workshop on Localization, Interactions and Superconductivity, July 2018 (2018). [Syracuse University]
- “Wafer-Based Charged Particle Accelerator; Wafer Components, Methods and Applications”; S.Ardanuc, V.Basavarajappa, Q.Ji, A.Lal, A.Persaud, T.Schenkel, P.Seidl, W.Waldron; Docket No.7390-03-US, Country of Filing; United States, App Type; US from PCT, App Status; Filed Date; 11/2/18, App#; 16/098,537 (2018). [Cornell University]
- “Wafer-scale Fabrication of Recessed-channel PtSe<sub>2</sub> MOSFETs with Low Contact Resistance and Improved Gate Control”; K.Xiong; 2018 Graphene & Beyond, poster, State College, PA, USA, May 2018; K.Xiong; EuMC, paper, Madrid, Spain, Sep.2018; K.Xiong; IMWS-AMP, paper, Ann Arbor, MI, USA, Jul.2018; L.Li, K.Xiong, R.J.Marstell, A.Madjar, and N.C.Strandwitz, J.C.M.Hwang, N.McEvoy, J.McManus, G.Duesberg, A.Goritz, M.Wietstruck, and M.Kaynak; Graphene Week, San Sebastian, Spain, Sep.2018; L.Li, K.Xiong, R.J.Marstell, A.Madjar, N.C.Strandwitz, J.C.M.Hwang, N.McEvoy, J.McManus, G.Duesberg, A.Goritz, M.Wietstruck, and M.Kaynak; Nano Applications Workshop, Bundeswehr U., Munich, Germany, 2018 Sep (2018); Li, L.; Xiong, K.; Marstell, R.J.; Madjar, A.; Strandwitz, N.C.; Hwang, J.C.M.; McEvoy, N.; McManus, J.B.; Duesberg, G.S.; Goeritz, A.; Wietstruck, M.; Kaynak, M.; *IEEE Transactions on Electron Devices*, Vol.65, Issue 10, p.4102-4108, DOI:10.1109/TED.2018.2856305 (2018). [Lehigh University]
- “Wafer-scale Fabrication of Recessed-channel PtSe<sub>2</sub> MOSFETs”; L.Li, K.Xiong, R.J.Marstell, A.Madjar, N.C.Strandwitz, J.C.M.Hwang, N.McEvoy, J.McManus, G.Duesberg, A.Goritz, M.Wietstruck, and M.Kaynak; NSF EFRI 2-DARE, NewLAW Joint Grantees Meet., San Diego, CA, Oct.2018 (2018). [Lehigh University]
- “Wafer-scale Material-device Correlation of Tellurene MOSFETs”; K.Xiong, L.Li, R.J.Marstell, A.Madjar, N.C.Strandwitz, J.C.M.Hwang, G.Qiu, Y.Wang, W.Wu, P.D.Ye, A.Görizt, M.Wietstruck, and M.Kaynak; Graphene and Beyond Workshop, University Park, PA, May 2018 (2018). [Lehigh University]
- “Wafer-scale material-device correlation of tellurene MOSFETs”; K.Xiong, L.Li, R.J.Marstell, A.Madjar, N.C.Strandwitz, J.C.M.Hwang, G.Qiu, Y.Wang, W.Wu, P.D.Ye, A.Görizt, M.Wietstruck, and M.Kaynak; *IEEE MTT-S Int.Microwave Workshop Series Advanced Materials Processes (IMWS-AMP)*, Ann Arbor, MI, USA, Jul.2018 (2018). [Lehigh University]
- “Wafer-scale material-device correlation of tellurene MOSFETs”; K.Xiong, L.Li, R.J.Marstell, A.Madjar, N.C.Strandwitz, J.C.M.Hwang, G.Qiu, Y.Wang, W.Wu, P.D.Ye, A.Görizt, M.Wietstruck, and M.Kaynak; *IEEE MTT-S Int.Microwave Workshop Series Advanced Materials Processes (IMWS-AMP)*, Ann Arbor, MI, USA, Jul.2018, pp.1-3. (2018). [Lehigh]
- “Waferscale Electrostatic Quadrupole Array for Multiple Ion Beam Manipulation”; Vinayakumar, K.B.; Persaud, A.; Ji, Q.; Seidl, P.; Schenkel, T.; Lal, A.; 2018 IEEE Micro Electro Mechanical Systems (mems), p.820-823 (2018). [Cornell University]
- “Water at surfaces with tunable surface chemistries”; Sanders, Stephanie E.; Vansalous, Heather; Petersen, Poul B.; *Journal of Physics-Condensed Matter*, Vol.30, Issue 11, p.113001, DOI:10.1088/1361-648X/aaab5 (2018). [Cornell University]
- “Waveguide for Use in Distributive Sensing”; H.Bai, S.Li, R.Shepherd, Y.Tu; Docket No.8067-01-US, Country of Filing; United States, App Type; EPR - Enhanced Provisional, App Status; Converted, Filing Date; 3/13/18, App#; 62/642,407 (2018); H.Bai, S.Li, R.Shepherd, Y.Tu; Docket No.8067-02-PC, Country of Filing; Not Applicable (PCT App), App Type; PCT - Patent Cooperation Treaty, App Status; Filed Date; 11/29/18, App#; PCT/US18/63173 (2018). [Cornell University]
- “Waveguides for Use in Sensors or Displays”; H.Bai, R.Huang, S.Li, R.Shepherd, H.Zhao; Docket No.7179-03-US, Country of Filing; United States, App Type; US from PCT, App Status; Filed Date; 8/24/18, App#; 16/079,798 (2018); H.Bai, R.Huang, S.Li, R.Shepherd, H.Zhao; Docket No.7179-04-CA, Country of Filing; Canada, App Type; FOR - Foreign, App Status; Filed Date; 8/27/18, App#; 3015906A1 (2018); H.Bai, R.Huang, S.Li, R.Shepherd, H.hao; Docket No.7179-05-CN, Country of Filing; China, App Type; FOR - Foreign, App Status; Filed Date; 10/25/18, App#; 2.0178E+11 (2018). [Cornell]
- “Wide Dynamic Range Detector Suitable for Large Pulses”; Sol Gruner, Hugh Philipp, Prafull Purohit, Katherine Shanks, Mark Tate, Joel Weiss; Docket No.8204, App Status; UnFiled Date; 4/4/18, App#; Invention (2018). [Cornell University]
- “Wide-bandgap gold-free E-mode p-channel HFET based on GaN/ AlN 2D hole gas”; Samuel James Bader, R.Chaudhuri, K.Nomoto, A.Hickman, H.G.Xing and D.Jena; Submitted. (2018). [Cornell]
- “Wireless, Optically-Powered Inorganic Optoelectronics for Cell-Scale Sensors”; Alejandro Cortese, Sunwoo Lee, Paul McEuen, Alyosha Molnar; Docket No.8107, App Status; Filed - by Cornell, Filing Date; 1/17/18, App#; Invention (2018). [Cornell]
- “Wireless, Optically-Powered Optoelectronics Sensors”; Alejandro Cortese, Sunwoo Lee, Paul McEuen, Alyosha Molnar; Docket No.8107-01-US, Country of Filing; United States, App Type; MPP - Manuscript Plus Provisional, App Status; Converted, Filing Date; 2/8/18, App#; 62/628,190 (2018). [Cornell]
- “Wireless, Optically-Powered Optoelectronics Sensors”; A.Cortese, S.Lee, P.McEuen, A.Molnar; Docket No.8107-02-US, Country of Filing; United States, App Type; MPP - Manuscript Plus Provisional, App Status; Converted, Filing Date; 10/2/18, App#; 62/740,326 (2018). [Cornell University]
- “X-ray absorption spectroscopy study of annealing process on Sr<sub>1-x</sub> La<sub>x</sub> CuO<sub>2</sub> electron-doped cuprate thin films”; Galdi, A.; Orgiani, P.; Sacco, C.; Gobaut, B.; Torelli, P.; Aruta, C.; Brookes, N.B.; Minola, M.; Harter, J.W.; Shen, K.M.; *Journal of Applied Physics*, Vol.123, Issue 12, p.123901 (2018). [Cornell University]
- “Young’s modulus and thermal expansion of tensioned graphene membranes”; Storch, I. De Alba, R.; Adiga, V.P.; Abhilash, T.S.; Barton, R.A.; Craighead, H.G.; Parpia, J.M.; McEuen, P.L.; *Physical Review B*, Vol.98, Issue 8, DOI:10.1103/PhysRevB.98.085408 (2018). [Cornell University]
- “Zero-Power Sensor Apparatus, Method and Applications”; Amit Lal, Alyosha Molnar; Docket No.7221-03-US, Country of Filing; United States, App Type; US from PCT, App Status; Filed Date; 4/12/18, App#; 15/767,913 (2018). [Cornell University]

# Common Abbreviations & Meanings

|  |   |
|--|---|
| μl. .... microliter  | CH <sub>4</sub> ..... methane                                       |
| μm. .... micron, micrometer                                      | CHESS ..... Cornell High Energy Synchrotron Source                  |
| μN. .... micro-Newtons   | CHF <sub>3</sub> ..... trifluoromethane                             |
| μs ..... microsecond   | Cl ..... chlorine   |
| Ω ..... Ohm  | Cl <sub>2</sub> ..... chlorine gas                                  |
| < ..... is less than   | Cl <sub>2</sub> /SF <sub>6</sub> ..... chlorine sulfur hexafluoride |
| > ..... is greater than  | cm. .... centimeter   |
| ~ ..... approximately  | CMOS. .... complementary metal oxide semiconductor                  |
| 1D. .... one-dimensional   | CMP ..... chemical mechanical polishing                             |
| 2D. .... two-dimensional   | CNF. .... Cornell NanoScale Science & Technology Facility           |
| 2DEG. .... two-dimensional electron gas                          | Co ..... cobalt   |
| 3D. .... three-dimensional                                       | CO <sub>2</sub> ..... carbon dioxide                                |
| <sup>3</sup> He ..... helium-3                                   | Co <sub>3</sub> O <sub>4</sub> ..... cobalt oxide                   |
| α-Al <sub>2</sub> O <sub>3</sub> ..... sapphire                  | CoFeAl ..... cobalt iron aluminum                                   |
| α-Si ..... amorphous silicon                                     | CoFeB. .... cobalt iron boron                                       |
| AC ..... alternating current                                     | CoP ..... cobalt porphyrin  |
| AFM ..... atomic force microscopy/microscope                     | CPC ..... colloidal photonic crystal                                |
| AFOSR ..... Air Force Office of Scientific Research              | CPD ..... contact potential difference                              |
| Ag ..... silver  | CpG ..... cytosine-phosphate-guanine                                |
| Al ..... aluminum  | Cr ..... chromium   |
| Al <sub>2</sub> O <sub>3</sub> ..... aluminum oxide              | CRDS ..... cavity ring-down spectrometer                            |
| ALD ..... atomic layer deposition                                | cryoSAXS ..... cryogenic small angle x-ray scattering               |
| AlGaAs ..... aluminum gallium arsenide                           | CTE ..... coefficients of thermal expansion                         |
| AlGaN ..... aluminum gallium nitride                             | CTL ..... confinement tuning layer                                  |
| Ar ..... argon   | Cu ..... copper   |
| ARC ..... anti-reflective coating                                | CVD ..... cardiovascular disease                                    |
| ArF ..... argon fluoride   | CVD ..... chemical vapor deposition                                 |
| As ..... arsenic   | CW ..... continuous wave  |
| atm ..... standard atmosphere (as a unit of pressure)            | CXRF ..... confocal x-ray fluorescence microscopy                   |
| Au ..... gold  | DARPA ..... Defense Advanced Research Projects Agency               |
| AuNPs ..... gold nanoparticles                                   | DC ..... direct current   |
| B ..... boron  | DCB ..... double cantilever beam                                    |
| <i>B. subtilis</i> ..... <i>Bacillus subtilis</i>                | DCE ..... 1,2-dichloroethane  |
| Bi ..... bismuth   | DCM ..... dichloromethane   |
| BOE ..... buffered oxide etch                                    | DEP ..... dielectrophoresis   |
| Br ..... bromine   | DFT ..... density functional theory                                 |
| C ..... carbon   | DFT ..... discrete Fourier transform                                |
| C ..... centigrade   | DI ..... de-ionized   |
| C-V ..... capacitance-voltage                                    | DMF ..... dimethyl formamide  |
| C <sub>3</sub> N <sub>4</sub> ..... carbon nitride               | DNA ..... deoxyribonucleic acid                                     |
| CaCl <sub>2</sub> ..... calcium chloride                         | DNP ..... dynamic nuclear polarization                              |
| CaCO <sub>3</sub> ..... calcium carbonate                        | DOE ..... United States Department of Energy                        |
| CAD ..... computer-aided design                                  | DPPC ..... 1,2-dipalmitoyl-sn-glycero-3-phosphocholine              |
| CaF <sub>2</sub> ..... calcium fluoride                          | DRAM ..... dynamic random access memory                             |
| CCMR ..... Cornell Center for Materials Research                 | DRIE ..... deep reactive ion etch                                   |
| Cd ..... cadmium   | DSA ..... directed self assembly                                    |
| CdS ..... cadmium sulfide  | dsDNA ..... double-stranded DNA                                     |
| CdSe ..... cadmium selenide                                      | DUV ..... deep ultraviolet  |
| CDW ..... charge-density-wave                                    | e-beam ..... electron beam lithography                              |
| Ce ..... cerium  | <i>E. coli</i> ..... <i>Escherichia coli</i>                        |
| CF <sub>4</sub> ..... carbon tetrafluoride or tetrafluoromethane | EBL ..... electron-beam lithography                                 |
| CFD ..... computational fluid dynamics                           | EDS ..... energy dispersive spectroscopy                            |

|                                      |  |  |   |
|--------------------------------------|--|--|---|
| EELS .....                           | electron energy loss spectroscopy  | hcp .....                                  | hexagonal close packing   |
| EG.....                              | ethylene glycol  | He.....                                    | helium  |
| EIS.....                             | electrochemical impedance spectroscopy   | HEMTs.....                                 | high electron mobility transistors  |
| ELISA.....                           | enzyme-linked immunosorbent assays   | Hf.....                                    | hafnium   |
| EO.....                              | electro-optic  | HF.....                                    | hydrofluoric acid   |
| EOT.....                             | equivalent oxide thickness   | HfB <sub>2</sub> .....                     | hafnium diboride  |
| EPICs.....                           | electronic photonic integrated circuits  | HFES.....                                  | hydrofluoroethers   |
| Er.....                              | erbium   | HfO <sub>2</sub> .....                     | hafnium dioxide   |
| ErAs.....                            | erbium arsenide  | Hg.....                                    | mercury   |
| ESM.....                             | effective screening medium   | high-κ.....                                | high dielectric constant  |
| EUV.....                             | extreme ultraviolet  | HMDS.....                                  | hexamethyldisilazane  |
| <i>ex situ</i> .....                 | Latin phrase which translated literally as 'off-site' -- to examine the phenomenon in another setting than where it naturally occurs | HRS.....                                   | high resistance state   |
| <i>ex vivo</i> .....                 | Latin for "out of the living" -- that which takes place outside an organism  | HSQ.....                                   | hydrogen silsesquioxane   |
| F.....                               | fluorine   | HSQ/FOX.....                               | negative electron beam resist<br>hydrogen silsesquioxane  |
| FDA.....                             | United States Food & Drug Administration   | Hz.....                                    | Hertz   |
| FDMA.....                            | fluorinated perfluorodecyl methacrylate  | I-V.....                                   | current-voltage   |
| Fe.....                              | iron   | I/O.....                                   | input/output  |
| Fe <sub>2</sub> O <sub>3</sub> ..... | iron oxide   | IARPA.....                                 | Intelligence Advanced Research Projects Activity  |
| FeCl <sub>3</sub> .....              | iron(III) chloride, aka ferric chloride  | IC.....                                    | integrated circuit  |
| FeGe.....                            | iron germanium   | ICP.....                                   | inductively coupled plasma  |
| FEM.....                             | finite element method  | ICP-MS.....                                | inductively coupled plasma mass spectroscopy  |
| FET.....                             | field-effect transistor  | ICP-RIE.....                               | inductively coupled plasma reactive ion etcher  |
| FFTs.....                            | fast Fourier transforms  | IFVD.....                                  | impurity free vacancy diffusion   |
| fg.....                              | femto gram   | IID.....                                   | impurity induced disordering  |
| FIB.....                             | focused ion beam   | IIEI.....                                  | ion implant enhanced interdiffusion   |
| FIR.....                             | far infrared   | In.....                                    | indium  |
| fj.....                              | femto Joules   | <i>in situ</i> .....                       | Latin phrase which translated literally as 'in position' -- to examine the phenomenon exactly in place where it occurs  |
| FM.....                              | frequency modulation   | <i>in vitro</i> .....                      | Latin for "within glass" -- refers to studies in experimental biology that are conducted using components of an organism that have been isolated from their usual biological context in order to permit a more detailed or more convenient analysis than can be done with whole organisms |
| FMR.....                             | ferromagnetic resonance  | <i>in vivo</i> .....                       | Latin for "within the living" -- experimentation using a whole, living organism   |
| FOTS.....                            | fluorosilane, tridecafluoro-1,1,2,2-tetrahydrooctyltrichlorosilane   | InAlN.....                                 | indium aluminum nitride   |
| FTIR.....                            | Fourier transform infrared spectroscopy  | InAs.....                                  | indium arsenide   |
| Ga.....                              | gallium  | InAs NWS.....                              | indium arsenide nanowires   |
| Ga <sub>2</sub> O <sub>3</sub> ..... | gallium(III) trioxide  | INDEX.....                                 | Institute for Nanoelectronics<br>Discovery and Exploration  |
| GaAs.....                            | gallium arsenide   | InGaAsN.....                               | indium gallium arsenide nitride   |
| GaAsN.....                           | gallium arsenide nitride   | InGaZnO <sub>4</sub> .....                 | indium gallium zinc oxide   |
| GaInAs.....                          | gallium indium nitride arsenide  | InP.....                                   | indium phosphide  |
| GaN.....                             | gallium nitride  | IPA.....                                   | isopropyl alcohol   |
| GaP.....                             | gallium phosphide  | IR.....                                    | infrared  |
| GaSb.....                            | gallium antimonide   | IrO <sub>2</sub> or IrO <sub>x</sub> ..... | iridium oxide   |
| Gd.....                              | gadolinium   | ITO.....                                   | indium tin oxide  |
| Ge.....                              | germanium  | JP-8.....                                  | Jet Propellant 8  |
| GFET.....                            | graphene field effect transistor   | κ.....                                     | dielectric constant   |
| GHz.....                             | gigahertz  | K.....                                     | Kelvin (a unit of measurement for temperature)  |
| GI.....                              | gastrointestinal   | K.....                                     | potassium   |
| GMR.....                             | giant magnetoresistance  | KFM.....                                   | Kelvin force microscopy   |
| GPa.....                             | gigapascal   | kg.....                                    | kilogram  |
| GPS.....                             | global positioning system  | kHz.....                                   | kilohertz   |
| h.....                               | hours  | KOH.....                                   | potassium hydroxide   |
| H.....                               | hydrogen   |  |   |
| H <sub>2</sub> O <sub>2</sub> .....  | hydrogen peroxide  |  |   |
| HBAR.....                            | high-overtone bulk acoustic resonator  |  |   |
| hBN.....                             | hexagonal boron nitride  |  |   |
| HBr.....                             | hydrogen bromide   |  |   |

|                          |   |                         |   |
|--------------------------|---|-------------------------|---|
| La .....                 | lanthanum   | NPs .....               | nanopores   |
| LED .....                | light-emitting diode                                  | ns .....                | nanosecond  |
| LER .....                | line edge roughness                                   | NSF .....               | National Science Foundation   |
| Li .....                 | lithium   | NV .....                | nitrogen-vacancy  |
| low- $\kappa$ .....      | low dielectric constant                               | NVM .....               | non-volatile memory   |
| LPCVD .....              | low pressure chemical vapor deposition                | NW FETs .....           | nanowire field-effect transistors   |
| lpm .....                | liter per minute                                      | O .....                 | oxygen  |
| LRS .....                | low resistance state                                  | O <sub>3</sub> .....    | trioxygen   |
| Lu .....                 | lutetium  | OFET .....              | organic field effect transistor   |
| LWR .....                | line width roughness                                  | OLED .....              | organic light-emitting diode  |
| MBE .....                | molecular beam epitaxy                                | ONO .....               | oxide/nitride/oxide   |
| MEMS .....               | microelectromechanical systems                        | ONR-MURI ..             | Office of Naval Research Multidisciplinary<br>University Research Initiative                              |
| MFMR .....               | microfabricated micro-reactors                        | OPV .....               | organic photovoltaic cells  |
| MgO .....                | magnesium oxide                                       | OTFT .....              | organic thin-film transistor  |
| MGs .....                | molecular glasses                                     | Pa .....                | Pascals   |
| MHz .....                | megahertz   | PAB .....               | post-apply bake   |
| micron .....             | micrometer, aka $\mu\text{m}$                         | PaC .....               | Parylene-C  |
| min .....                | minutes   | PAG .....               | photoacid generator   |
| ml .....                 | milliliter  | Pb .....                | lead  |
| mm .....                 | millimeter  | PBG .....               | photonic bandgap  |
| mM .....                 | millimolar  | PbS .....               | lead sulfide  |
| Mo .....                 | molybdenum  | PBS .....               | phosphate-buffered saline   |
| MOCVD .....              | metal oxide chemical vapor deposition                 | PbSe .....              | lead selenide   |
| MOS .....                | metal oxide semiconductor                             | PC .....                | persistent current  |
| MoS <sub>2</sub> .....   | molybdenum disulfide                                  | PC .....                | photocurrent  |
| MoSe <sub>2</sub> .....  | molybdenum diselenide                                 | PCN .....               | photonic crystal nanocavity   |
| MOSFET .....             | metal oxide semiconductor field effect transistor     | Pd .....                | palladium   |
| MRAM .....               | magnetic random access memory                         | PD .....                | photodetector   |
| MRFM .....               | magnetic resonance force microscopy                   | PDMS .....              | polydimethylsiloxane  |
| MRI .....                | magnetic resonance imaging                            | PEB .....               | post-exposure bake  |
| ms .....                 | millisecond   | PEC .....               | photoelectrochemical  |
| MSM .....                | metal-semiconductor-metal                             | PECVD .....             | plasma enhanced chemical vapor deposition   |
| mTorr .....              | millitorr   | PEDOT:PSS ..            | poly(3,4-ethylenedioxythiophene):<br>poly(styrenesulfonate)   |
| mV .....                 | millivolt   | PEG .....               | polyethylene glycol   |
| MVD .....                | molecular vapor deposition                            | PEI .....               | polyethyleneimine   |
| M $\Omega$ .....         | megaohms  | pFET .....              | p-channel field-effect transistor   |
| N .....                  | nitrogen  | PFM .....               | piezo-response force microscopy   |
| N <sub>2</sub> .....     | nitrous oxide   | PGMA .....              | poly(glycidyl methacrylate)   |
| nA .....                 | nanoAmperes   | pH .....                | a measure of the activity of hydrogen ions<br>(H <sup>+</sup> ) in a solution and, therefore, its acidity |
| NaCl .....               | sodium chloride                                       | Ph.D. ....              | doctorate of philosophy   |
| NASA .....               | National Aeronautics & Space Administration           | PhC .....               | photonic crystal  |
| Nb .....                 | niobium   | PL .....                | photoluminescence   |
| Nb <sub>3</sub> Sn ..... | triniobium-tin  | pL .....                | picoliter   |
| NCS .....                | nanocrystals  | PLD .....               | pulsed laser deposition   |
| Nd .....                 | neodymium   | PMMA .....              | poly(methyl methacrylate)   |
| NEMS .....               | nanoelectromechanical systems                         | poly-Si .....           | polycrystalline silicon   |
| NH <sub>4</sub> F .....  | ammonium fluoride                                     | PS .....                | polystyrene   |
| Ni .....                 | nickel  | PS- <i>b</i> -PMMA ..   | polystyrene- <i>block</i> -poly(methyl methacrylate)  |
| NIH .....                | National Institutes of Health                         | Pt .....                | platinum  |
| NIR .....                | near-infrared   | Pt/Ir .....             | platinum/iridium  |
| nL .....                 | nanoliter   | PtSe <sub>2</sub> ..... | platinum diselenide   |
| nm .....                 | nanometer   | PV .....                | photovoltaic  |
| NMP .....                | n-methyl-2-pyrrolidone                                | PVD .....               | physical vapor deposition   |
| NNCI .....               | National Nanotechnology<br>Coordinated Infrastructure | Py .....                | permalloy, Ni <sub>81</sub> Fe <sub>19</sub>  |
| NPs .....                | nanoparticles   |                         |   |

|                                  |  |                   |   |
|----------------------------------|--|-------------------|---|
| Q.                               | quality factor                                       | Ti                | titanium                                |
| QD                               | quantum dots   | TiN               | titanium nitride                        |
| QW                               | quantum well   | TiO <sub>2</sub>  | titanium dioxide                        |
| RA                               | resistance-area                                      | TM                | transverse magnetic                     |
| REU                              | Research Experience for Undergraduates Program       | TXM               | transmission x-ray microscopy           |
| RF                               | radio frequency                                      | UHV               | ultra-high vacuum                       |
| RF MEMS                          | radio frequency microelectromechanical systems       | USDA              | United States Department of Agriculture |
| RIE                              | reactive ion etch                                    | UV                | ultraviolet                             |
| RMS or rms                       | root mean square                                     | UV-Vis            | ultraviolet-visible                     |
| RNA                              | ribonucleic acid                                     | V                 | vanadium                                |
| RTA                              | rapid thermal anneal                                 | V                 | voltage                                 |
| RTD                              | resistance temperature device                        | vdW               | van der Waals                           |
| RTD                              | resonant tunneling diodes                            | VLS               | vapor-liquid-solid                      |
| Ru                               | ruthenium  | VRMs              | voltage regulator modules               |
| s                                | seconds  | VSM               | vibrating sample magnetometry           |
| S                                | sulfur   | W                 | tungsten                                |
| SAMs                             | self-assembled monolayers                            | WDM               | wavelength-division multiplexing        |
| SAXS                             | small angle x-ray scattering                         | WSe <sub>2</sub>  | tungsten diselenide                     |
| Sb                               | antimony   | XeF <sub>2</sub>  | xenon difluoride                        |
| Sc                               | scandium   | XPM               | cross-phase modulation                  |
| sccm                             | standard cubic centimeters per minute                | XPS               | x-ray photoelectron spectroscopy        |
| scCO <sub>2</sub>                | supercritical carbon dioxide                         | XRD               | x-ray diffraction                       |
| SDS                              | sodium dodecyl sulfate                               | XRR               | x-ray reflectivity                      |
| Se                               | selenium   | ZMW               | zero-mode waveguide                     |
| sec                              | seconds  | Zn                | zinc                                    |
| SEM                              | scanning electron microscopy/microscope              | ZnCl <sub>2</sub> | zinc chloride                           |
| SERS                             | surface enhanced Raman spectroscopy                  | ZnO               | zinc oxide                              |
| SF <sub>6</sub>                  | sulfur hexafluoride                                  | ZnO:Al            | zinc aluminum oxide                     |
| Si                               | silicon  | ZnS               | zinc sulfide or zinc-blende             |
| Si <sub>3</sub> N <sub>4</sub>   | silicon nitride                                      | Zr                | zirconium                               |
| SiC                              | silicon carbide                                      | ZrO <sub>2</sub>  | zirconium dioxide                       |
| SiH <sub>4</sub>                 | silane   | ZTO               | zinc tin oxide                          |
| SiN                              | silicon nitride                                      |                   |   |
| SiO <sub>2</sub>                 | silicon dioxide, silica                              |                   |   |
| Sn                               | tin  |                   |   |
| SnO <sub>2</sub>                 | tin oxide  |                   |   |
| SnSe <sub>2</sub>                | tin selenide or stannous selenide                    |                   |   |
| SOL                              | silicon-on-insulator                                 |                   |   |
| SPR                              | surface plasmon resonance                            |                   |   |
| SQUID                            | superconducting quantum interference device          |                   |   |
| Sr <sub>2</sub> RuO <sub>4</sub> | strontium ruthenate                                  |                   |   |
| SRC                              | Semiconductor Research Corporation                   |                   |   |
| SrTiO <sub>3</sub>               | strontium titanate                                   |                   |   |
| STEM                             | scanning transmission electron microscopy/microscope |                   |   |
| <i>t</i> -BOC                    | <i>tert</i> -butoxycarbonyl                          |                   |   |
| Ta                               | tantalum   |                   |   |
| Ta <sub>2</sub> O <sub>5</sub>   | tantalum pentoxide                                   |                   |   |
| TaN                              | tantalum nitride                                     |                   |   |
| TAO <sub>x</sub>                 | tantalum oxide                                       |                   |   |
| Te                               | tellurium  |                   |   |
| TEM                              | transmission electron microscopy/microscope          |                   |   |
| TFET                             | tunnel field effect transistor                       |                   |   |
| TFT                              | thin-film transistor                                 |                   |   |
| Tg                               | glass transition temperature                         |                   |   |
| THz                              | terahertz  |                   |   |

## PHOTOGRAPHY CREDITS

The cover image is used with permission from CNF User, Bugao Zou; CNF Project 2458-16, "Development of Single and Double Layer Anti-Reflective Coatings for Astronomical Instruments", Principal Investigator, Gordon Stacey. Bugao's full report begins on page 146.

The 2019 CNF Annual Meeting photographs were taken by Cornell University Photo, and photographer, Gary Hodges. More meeting photos are online at [http://cnf.cornell.edu/events/annual\\_meeting](http://cnf.cornell.edu/events/annual_meeting)

The CNF TCN photographs on page xi were taken by Sam Wright, CNF staff.

The CNF REU photographs on pages xii were taken by Don Tennant, Director of Strategic Initiatives.

The photographs on page xiii are a mix of Cornell University Photo, and photographer, Robyn Wishna.

The full color research images on pages xiv-xv are individually credited to their research group.

***Cornell NanoScale Science  
& Technology Facility  
(CNF)***

**2018-2019**

**Research**

**Accomplishments**

# Investigating the Effect of Environment Shape on Bacteria Growth at the Microscale

**2019 CNF REU Intern: Jacob Baker**

**2019 CNF REU Intern Affiliation: Biomedical Engineering, University of Arizona**

*CNF Project: 2019 Cornell NanoScale Science & Technology Facility Research Experiences for Undergraduates Program*

*CNF REU Principal Investigator(s): Guillaume Lambert, Applied and Engineering Physics, Cornell University*

*CNF REU Mentor(s): Matthew Henriques, Applied Physics, Cornell University*

*Primary Source of CNF REU Funding: National Science Foundation*

*via the National Nanotechnology Coordinated Infrastructure (NNCI) Grant No. NNCI-1542081*

*Contact: jacob baker@email.arizona.edu, lambert@cornell.edu, mdh324@cornell.edu*

*Website(s): <https://lambertlab.io/>, <http://cnf.cornell.edu/education/reu/2019>*

*Primary CNF Tools Used: ABM contact aligner, Hamatech wafer processor develop 1, P10 profilometer*

## Abstract:

*Escherichia coli* (*E. coli*) bacteria are sensitive to pressures exerted by their physical environment. The constraints that differently shaped growth chambers have on cell populations over time are a significant extension of this fact and play a part in characterizing bacteria growth. By utilizing the resources of the Cornell NanoScale Facility, we created a microfluidic device that features a large central fluid distribution chamber and hundreds of tiny growth chambers designed to grow bacteria at a 1  $\mu\text{m}$  height display to view different test geometries and analyze their growth patterns. The device was produced by spinning micrometer thick layers of negative photoresist onto a silicon wafer and exposing to create a pattern designed in L-Edit CAD software. The wafer served as the mold for the actual device, which we then cast in PDMS. This created reproducible devices with channels for bacteria and nutrients to flow through and grow. A type of *E. coli* was genetically engineered to produce fluorescent bacteria that don't produce biofilms and were grown separately before being injected into the device. The results of this experiment play a part in widening the pool of knowledge for under what conditions bacteria thrive or stagnate, crucial data towards solving World Health Organization global health challenges such as antimicrobial resistance. Characterizing bacteria growth is one of the primary ongoing objectives of biological research. By expanding the pool of information available about how bacteria grow in different environments, application-based research on bacterial diseases, biofuels as an alternative to fossil fuels, and plasmid genetic engineering is optimized.

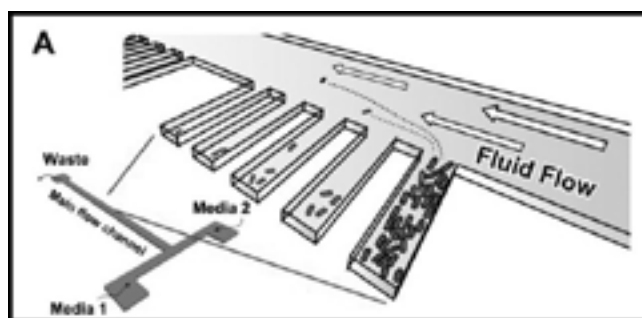


Figure 1: Microfluidic device to culture E.Coli.

## Summary of Research:

We chose to focus on characterizing how *E. coli* bacteria responds to environmental conditions, specifically how the geometry containing the starting sample of bacteria limits or bolsters the growth of bacteria over time. In this preliminary qualitative research, we utilized the resources of the CNF to produce a microfluidic device, a device that would allow us to monitor bacteria growth in growth chambers one micrometer thick, while being pumped nutrients through a pneumatic system.

This microfluidic device provides a unique environment in which the bacteria and nutrients exhibit non-laminar flow, meaning that these structures can be assessed on

their contribution to osmosis-based interaction with nutrients and bacteria. The microfluidic device was fabricated by developing two layers on a silicon wafer. The first layer contained a one micrometer thick etching of the entire design, notably including four growth chambers with different geometries. The first layer was purposely thin, so that the bacteria growth could be viewed efficiently, and the only effect on bacteria diffusion was the basic two dimensional geometry.

To produce this first layer, negative AZ2020 photoresist was spun onto the 4-inch silicon wafer for an even coating of resist, and then the wafer was baked at 110°C, cooled,

and then exposed to a contact aligner for 3.5 seconds for a total energy exposure of 41 mJ of energy. The wafer was then baked once more and run through the Unaxis 770 deep etch and Aura 1000 resist strip to complete the etching.

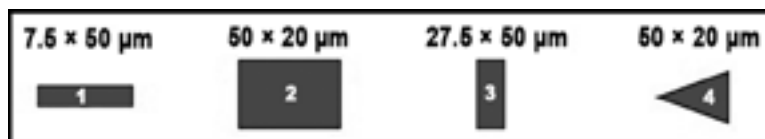


Figure 2: Geometries of four devices on the fluidic chip.

The second layer was 25  $\mu\text{m}$  thick, and alternatively, we spun 2020 SU-8 photoresist on top of the wafer, which was baked at 95°C, exposed for 12 seconds for 140 mJ of energy, and then developed with SU-8 developer, completing the device. The second layer extended the height of the main flow channel.

The device itself was a long T-shape in which bacteria and nutrients could flow starting at the top of the T (Figure 1) and exited through the waste at the end of the channel. Along the main channel were a couple hundred growth chambers for each of the four geometries: a long skinny rectangle with dimensions 7.5  $\times$  50  $\mu\text{m}$  (device 1), a rectangle with dimensions 50  $\times$  20  $\mu\text{m}$  (device 2), a thick but shallow rectangle with dimensions 27.5  $\times$  50  $\mu\text{m}$  (device 3), and an isosceles triangle with dimensions 50  $\times$  20  $\mu\text{m}$  (device 4, Figure 2). Device 4 was specifically designed to study the effects of a growth chamber with smaller surface area for starter bacteria to grow than the surface area exposed to the main channel.

When hypothesizing the growth chamber geometries that would result in the highest change in cell count over time, we decided that the two largest contributing factors to the success of the designs would be the amount of surface area at the back of the device and the amount of surface area exposed to the main channel. This idea was grounded in the observation of similar microfluidic device bacteria growth experiments, where a few starter bacteria stay at the back of the device and serve as the main progenitors of new bacteria over the course of the trial period.

From the qualitative results we received in the form of pictures before the experiment began and two hours after (Figure 3, a and b), Device 1 was the only one to experience major growth, while Devices 2 and 4 had a net loss in bacteria, and Device 3 was too malformed to draw conclusions. We expected Device 4 to have poor growth due to its combination of low surface area at the back of the device and high surface area facing the main channel, but we were surprised at the lack of growth from Device 2 compared to the high growth in Device 1. We had overestimated the importance of surface area for growth at the back of the device versus the adverse effects of diffusion.

### Acknowledgements:

The 2019 CNF REU Program and National Science Foundation funding via the NNCI Grant No. NNCI-1542081.

### References:

- [1] G Lambert, E Kussell, "Quantifying Selective Pressures Driving Bacterial Evolution Using Lineage Analysis." *Physical Review X* 5, 011016 (2015).
- [2] G Lambert, A Bergman, Q Zhang, D Bortz, RH Austin, "Physics of biofilms: the initial stages of biofilm formation and dynamics." *New J. of Physics* 16 (4), 045005 (2014).
- [3] "Soft Lithography: Glass/PDMS Bonding." Elveflow, [www.elveflow.com/microfluidic-tutorials/soft-lithography-reviews-and-tutorials/how-to-get-the-best-process/soft-lithography-glass-pdms-bonding/](http://www.elveflow.com/microfluidic-tutorials/soft-lithography-reviews-and-tutorials/how-to-get-the-best-process/soft-lithography-glass-pdms-bonding/).

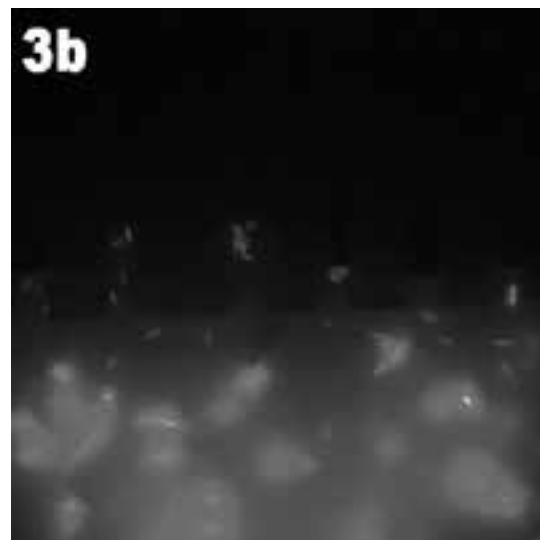
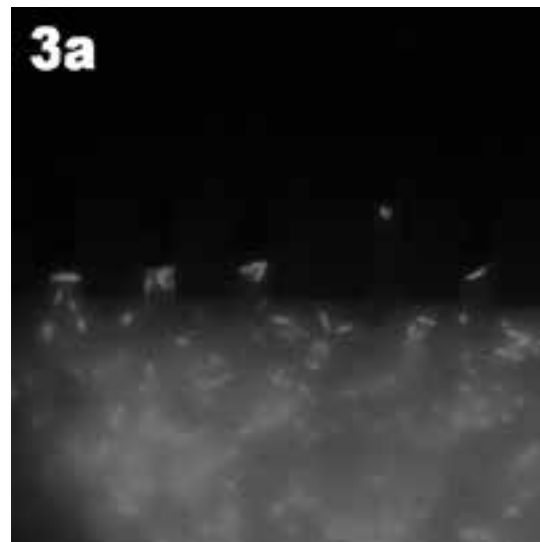


Figure 3, a and b: Fluorescent bacteria grow in Device 1 after two hours. (Find in full color on pages xiv-xv.)

# Microfluidic Chip Manufacturing for Point-of-Care Sepsis Diagnosis

**2019 CNF REU Intern: Katie Munechika**

**2019 CNF REU Intern Affiliation: Biomedical Engineering, University at Buffalo SUNY**

*CNF Project: 2019 Cornell NanoScale Science & Technology Facility Research Experiences for Undergraduates Program*

*CNF REU Principal Investigator(s): Dr. David Erickson, Mechanical and Aerospace Engineering, Cornell University*

*CNF REU Mentor(s): Taylor Oeschger, Biomedical Engineering, Cornell University*

*Primary Source of CNF REU Funding: National Science Foundation*

*via the National Nanotechnology Coordinated Infrastructure (NNCI) Grant No. NNCI-1542081*

*Contact: km854@cornell.edu, de54@cornell.edu, tmo55@cornell.edu*

*Website: <http://cnf.cornell.edu/education/reu/2019>*

*Primary CNF Tools Used: ABM contact aligner, Hamatech wafer developer, UNAXIS 770 deep silicon etcher, Anatech resist strip, PDMS casting station*

## Abstract:

Sepsis is a life threatening condition affecting the immune system that causes the body to damage its own organs. The current diagnostic standard, consisting of monitoring organ dysfunction with a cell culture, is ineffective as it can take days, while sepsis can cause death within hours. The goal of the project is to develop a point of care microchip that can provide an accurate diagnosis from a drop of blood in 30 minutes or less by measuring the level of expression of white blood cell antigens associated with sepsis. The device utilizes a lysing and quenching process to destroy red blood cells while preserving white blood cells, and then captures white blood cells containing target antigens on antibody-coated pillars. Research has been focused on optimizing the lysing and quenching process, with a secondary goal of redesigning the pillar arrangement to maximize cell capture. In on-bench experiments, we have been able to achieve nearly 100% red blood cell lysis while maintaining less than 10% white blood cell lysis. Initial testing of cell capture on the pillars has resulted in a new design containing less pillars to increase the ease of imaging, manufacturing, and flow.

## Summary of Research:

**Introduction.** Contributing to over 250,000 deaths per year in the US alone, sepsis alters the body's immune response to infection, leading to organ damage and immunosuppression [1]. The current diagnostic standard for sepsis includes a cell culture and a scoring system known as the Sequential Organ Failure Assessment (SOFA), which involves measuring a collection of non-specific clinical symptoms for levels of organ dysfunction [2]. This current method of diagnosis is ineffective, partly due to its lack of specificity, and because it can take days to obtain results, whereas the survival rate for sepsis decreases by 7.7% each hour that administration of antimicrobials is delayed [3]. The objective of this research is to create a microchip that can provide an accurate septic or non-septic diagnosis within 30 minutes using a drop of whole blood.

**Design and Fabrication.** The design of the microchip contains S-shaped channels and a section of antibody-coated pillars (Figure 1). When blood enters the channels, it mixes with a lysing buffer, which lyses the red blood cells allowing for easier passage of white blood cells through the device. After the blood and lysing buffer have

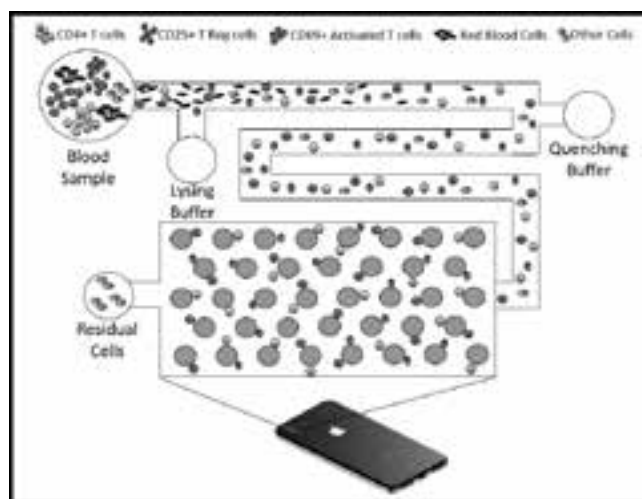


Figure 1: A simplified representation of the processing of blood and capturing of specific white blood cells on pillars in the microchip.

mixed for a few seconds, a quenching buffer is added to halt the lysing process before the white blood cells are damaged. The white blood cells enter the pillar section,

and cells containing the target antigens corresponding to the pillar antibodies adhere to the pillars. The use of fluorescent antibodies allows for fluorescence smartphone imaging of the captured cells. The measured fluorescence corresponds to the level of expression of the target antigens, correlating to the presence of sepsis. To manufacture the device, first a mold is made from deep etching a silicon wafer. The mold is then cast in polydimethylsiloxane (PDMS) and plasma bonded to a glass slide. A pump system is attached via tubing to move fluid through the device.

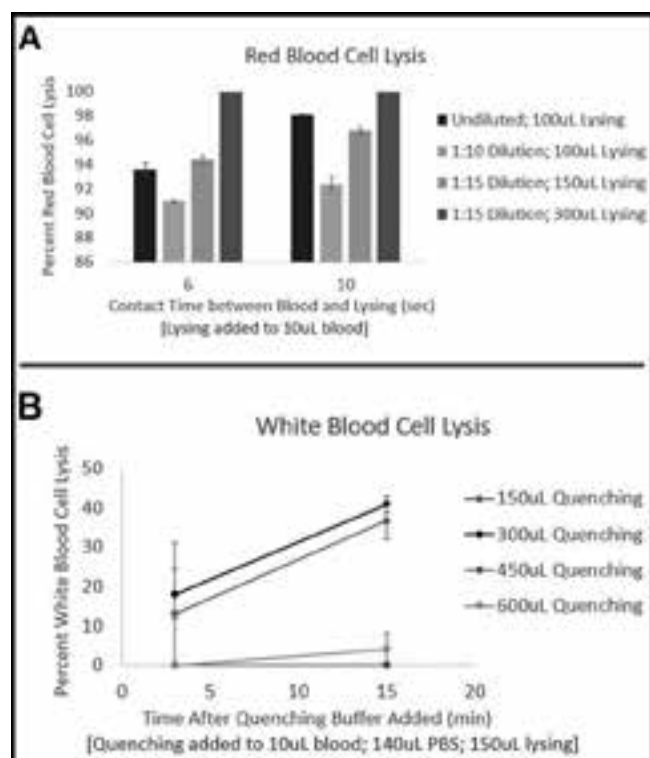


Figure 2: A) Percentage of red blood cell lysis at differing blood to lysing volume ratios for undiluted and diluted blood. B) Percentage of white blood cell lysis over time for differing quenching volumes after quenching buffer is added to diluted blood and lysing buffer.

## Results and Conclusions:

A lysing buffer consisting of formic acid and saponin and a quenching buffer with sodium carbonate and phosphate buffered saline (PBS) were selected [4]. We tested various ratios of lysing buffer and quenching buffer on the bench to determine the most effective proportions to lyse the red blood cells, while limiting the damage to white blood cells. As Figure 2A shows, we were able to achieve 100% red blood cell lysis using 10  $\mu$ L of blood diluted 1:15 in PBS and a lysing volume twice as large as the volume of diluted blood. We determined that the quenching volume must be at least three times that of the lysing volume to achieve less than 10% white blood cell lysis over time (Figure 2B). Based on our results, we redesigned the device with longer channels to increase contact time between the blood and buffers (Figure 3B).

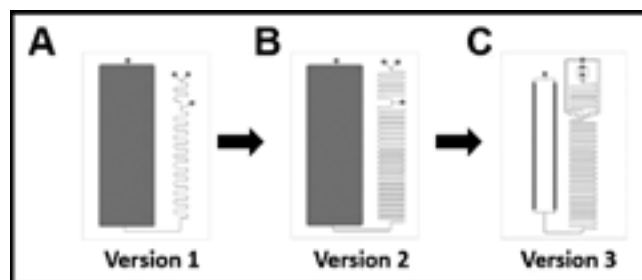


Figure 3: CAD drawings of the three versions of microchip designs.

The third version of the chip contains two channels and four channels extending from the lysing inlet and quenching inlet respectively to ensure that sufficient amounts of the buffers mix with the blood (Figure 3C). From a preliminary test of cell capture on the pillars, we determined that the large number of pillars was inhibiting fluid flow through the chip. Version 3 contains only 30,000 pillars, compared to the 400,000 pillars in the previous versions, and the pillar chamber is broken into two sections to allow for easier fluid flow and imaging of the device.

From an initial on-chip lysing test using Version 3, we obtained nearly 99.5% red blood cell lysis with a flow rate of 10  $\mu$ L per minute, however further testing is needed to determine the accuracy of these results.

## Future Work:

Further research includes testing of the on-chip lysing and quenching process using Version 3 devices, as well as optimizing and imaging the capture of CD3+ T cells, CD4+ helper T cells, CD25+ T regulatory cells, and CD69+ activated T cells on the chip. Future work also includes incorporating a low-cost, effective pumping system to replace the current 3-syringe pump system.

## Acknowledgements:

Special thanks to Taylor Oeschger, Dr. David Erickson, Melanie-Claire Mallison, and the CNF staff. This work was performed in part at the CNF as part of the 2019 Cornell NanoScale Science and Technology Facility Research Experiences for Undergraduates (CNF REU) Program. The CNF is a member of the National Nanotechnology Coordinated Infrastructure (NNCI), which is supported by the National Science Foundation (Grant NNCI-1542081).

## References:

- [1] Rhee, et al. (2017). JAMA, 318(13), 1241.
- [2] Gül, et al. (2017). TJAR, 45(3), 129-138.
- [3] Kumar, et al. (2006). Crit Care Med, 34(6), 1589-1596.
- [4] Hassan, et al. (2017). Nat Commun, 8(1), 15949.

# Developing Microfluidic Devices for Assisted Reproductive Technologies

**2019 CNF REU Intern: Darien Nguyen**

**2019 CNF REU Intern Affiliation: Chemistry, Winthrop University**

*CNF Project: 2019 Cornell NanoScale Science & Technology Facility Research Experiences for Undergraduates Program*

*CNF REU Principal Investigator(s): Alireza Abbaspourrad, Food Science and Technology, Cornell University*

*CNF REU Mentor(s): Amir Mokhtare, Food Science and Technology, Cornell University*

*Primary Source of CNF REU Funding: National Science Foundation*

*via the National Nanotechnology Coordinated Infrastructure (NNCI) Grant No. NNCI-1542081*

*Contact: nguyend4@winthrop.edu, alireza@cornell.edu, am2964@cornell.edu*

*Website: <http://cnf.cornell.edu/education/reu/2019>*

*Primary CNF Tools Used: ABM contact aligner, Class II resist spinners (SU-8), plasma cleaner/PDMS casting room*

## Abstract:

The gaining popularity of Assisted Reproductive Technologies (ART) such as *in vitro* Fertilization (IVF) and Intracytoplasmic Sperm Injection (ICSI) calls for the introduction of more affordable and less tedious processes rather than the typical manual operations. In order for ICSI to occur, the Cumulus Oocyte Complexes (COCs) retrieved from the ovaries must be processed in order to remove the tightly-packed cumulus cells surrounding them. As of yet, this tedious and unstandardized process is being done manually by skilled embryologists, which result in variability and unavailability. The focus of this project is to develop microfluidic devices to denude the COCs for ICSI in order to reduce the tyranny of manual operations and push towards automated reproducible operations. However, many microfluidic devices are fabricated through conventional PDMS microfluidic processes that can be potentially harmful and result in loss of the precious oocytes. Herein, we report the fabrication and testing of a non-PDMS and reversibly-bonded microfluidic device using artificial eggs similar to COCs.

## Summary of Research:

In order to reduce the tyranny of the current tedious, manual processes in Assisted Reproductive Technologies (ART), microfluidic devices emerge as a plausible solution. Microfluidic devices have been recently used in a few parts of the ART procedure such as sperm selection, insemination, etc. However, microfluidics has rarely been applied to improve the processing of oocytes for ICSI, which calls for the removal of the tightly-packed cumulus cells surrounding the oocyte. This research aims at developing microfluidic devices to denude cumulus cells from oocytes to not only reduce manual operations but also to increase the standardization within the ART process.

First of all, we used AutoCAD 2019 to prepare a variety of designs for the denudation of the COCs. They range from a simple single inlet/outlet port in which jagged walls intend to denude the cumulus cells off the COCs to more complex designs intending to vacuum the cumulus cells off the COCs. These designs were constructed for bovine COCs, which have a size of 400-500  $\mu\text{m}$  and an oocyte size of about 150-200  $\mu\text{m}$ .

We employed photolithography fabrication methods for making PDMS microfluidic devices. SU-8 molds were developed on a silicon wafer and coated with parylene to act as a mold release. PDMS was then casted on the wafer and slowly peeled from the wafer to ensure channels remain intact. The PDMS channels were then punched for the inlet and outlet ports and bonded to glass slides using a plasma oxygen bonding method.



*Figure 1: Equipment set-up for testing microfluidic devices. Figure 1a shows the magnetic valves and also the Fluigent pump. Figure 1b shows the Arduino microcontroller controlling the magnetic valves. Figure 1c shows the observation deck for the microfluidic devices.*

In order to test these PDMS microfluidic devices, we developed an automated system consisting of a microcontroller and a set of solenoids that are connected to the computer and controlled through a graphical user interface (Figure 1). Different programs were coded for the microcontroller for each desired design. Porous, partially-crosslinked polymeric beads, dispersed in water, were used to simulate COCs and were successfully run through the channels in the PDMS microfluidic devices. However, many challenges were revealed along with this individual success.

The particles tended to stick together when traveling from the transferring tube to the microfluidic device, causing them to clog the channels. Therefore, designs were modified to a two-inlet port design where one inlet was used to only flow the media, while the other flows the particles. Although this reduced the number of clog incidents, it did not fully resolve the problem. A new microfluidic device (Figure 2) was fabricated on acrylic using the CNC Milling Machine, in order to not only prevent COCs from sticking together, but also expose them to hyaluronidase, a chemical used in oocyte processing to break down the cumulus cells.

PDMS itself is known to be deformable, allow absorption, and permit leaching, which could be harmful to cells; therefore, it potentially has a very low chance to be applied in the real and large scale. In addition, the conventional PDMS microfluidic device relies on permanent bonding to glass, which could result in damages or wasting an egg if the process were to go wrong. A new design requiring two layers of SU-8 was proposed that would apply a vacuum in order to seal the channels to a substrate that could be reversed if needed. The masks were also reverse polarized so that the channels would be etched into SU-8. The SU-8 channels were enclosed using a flat slab of PDMS and a vacuum was applied to fully enclose the channels (Figure 3).

Finally, the polymeric beads did not accurately simulate eggs due to their hydrophilic properties and the lack of an outer layer that could be removed to simulate the cumulus cells. A microfluidic device was created in order to create artificial eggs from hydrogel (Figure 4). A solid particle, acting as the oocyte, would be encapsulated in loosely-bonded hydrogel, acting as the cumulus cells.

**Results, Conclusion, and Future Work:**

A working, reversibly-bonded, non-PDMS microfluidic device was fabricated in order to denude COCs. Artificial eggs were produced from hydrogel through another designed microfluidic device. In the future, the non-PDMS microfluidic device would be tested using actual bovine COCs to determine the effectiveness of the denudation and physical stress towards the oocyte. This would be compared to the current physical processes of denudation and be determined to be advantageous or not. In addition, further development on making the microfluidic device more automated would be in action.

**Acknowledgements:**

National Nanotechnology Coordinated Infrastructure, 2019 Cornell NanoScale Science and Technology Facility Research Experiences for Undergraduates (CNF REU) Program, NSF grant no. NNCI-1542081, PI: Alireza Abbaspourrad, Mentor: Amir Mokhtare, CNF REU Program Coordinator and Staff.

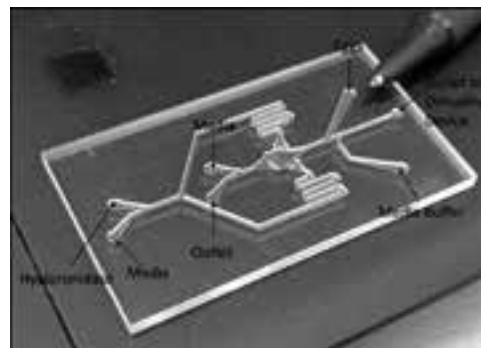


Figure 2: Acrylic microfluidic device aimed at exposing and separating the COCs.



Figure 3: SEM of the SU-8 reversible vacuum design.

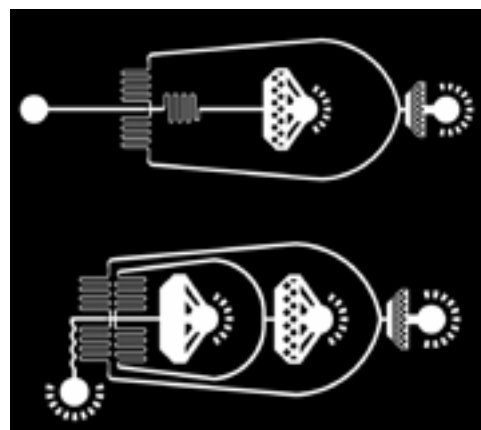


Figure 4: Mask designs for microfluidic hydrogel particle maker.

**References:**

[1] L. Weng, G. Y. Lee, J. Liu, R. Kapur, T. Toth, and M. Toner, Lab Chip, 2018, 18, 3892.

# Measuring Non-Equilibrium RNA Dynamics One Molecule at a Time with SU-8 Microfluidics

**CNF Project Number: 692-98**

**Principal Investigator(s): Lois Pollack**

**User (s): Alexander Plumridge**

*Affiliation(s): Applied and Engineering Physics, Cornell University*

*Primary Source(s) of Research Funding: National Institute of Health*

*Contact: lp26@cornell.edu, ap866@cornell.edu*

*Website: <https://pollack.research.engineering.cornell.edu/>*

*Primary CNF Tools Used: ABM contact aligner, class 2 resist room, VersaLaser, Heidelberg mask writer (2000)*

## Abstract:

Here we report the design, fabrication and implementation of an SU-8 based microfluidic mixing device to enable non-equilibrium single-molecule fluorescence measurements. The device allows rapid initiation of biological reactions, and, in a subsequent region, probing with fluorescence microscopy at times from 10ms-5s after mixing is complete. This device is used to probe the conformational dynamics of regulatory RNA molecules as they sense and bind their target and non-target ligands.

## Summary of Research:

Non-equilibrium measurements are powerful tools to study biological interactions [1]. The rapid initiation of biological reactions and examination of their evolution in time, exposes information that is hidden in simple equilibrium experiments. This technique provides details on short lived intermediates, folding pathways and transition states.

Whilst the benefits of non-equilibrium measurements are numerous, such techniques are rarely applied when compared to their equilibrium counterparts. The major bottle-neck is the lack of commercially available systems to perform these experiments. Only the stopped-flow technique is widely used, but requires high sample volumes, limiting the number of kinetic measurements that have been made. Additionally, in cases where kinetic measurements are applied, the experiments report bulk averages. Therefore, sparse or short-lived intermediates are challenging to identify, and careful analysis is required to resolve the presence of intermediate states along reaction pathways [2].

Coupling microfluidic mixing to single-molecule fluorescence circumvents the above challenges. Examination of single molecules allows resolution of individual subpopulations within a sample, nanomolar concentrations are used, and ~millisecond timescales are accessible using microfluidics, with sparse sample consumption [3]. We previously designed and fabricated microfluidic mixing devices to perform such

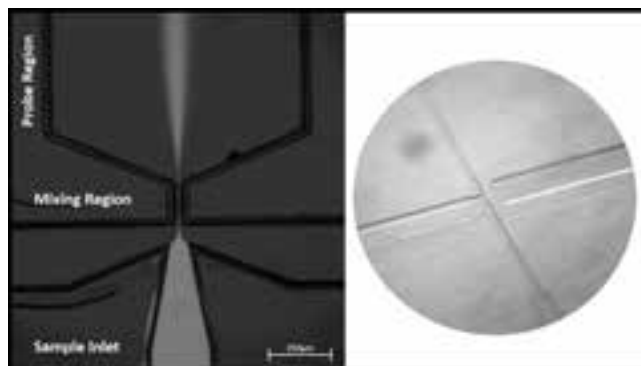


Figure 1: Two images of the SU-8 microfluidic mixing device are shown. At left, a fluorescence image is shown. Fluorescent dye (light grey), enters the sample inlet, and is compressed by flanking buffer streams through the mixing region. Here, the sample stream thins to the micron length scale, allowing rapid diffusion into the sample from the side streams. After mixing, the flow is expanded to allow probing (flow direction bottom to top). The right image shows a stereoscope image of a functional device.

measurements (Figure 1) applying photolithography to pattern a hard material, SU-8.

In brief, a 100  $\mu\text{m}$  thick layer of SU-8 2050 is spun on borofloat, after which it is baked, cured with the ABM contact aligner and developed to yield fluidic channels. A thin sealing layer of SU-8 2005 is next deposited over the top of the fluidic channels, and standard 170  $\mu\text{m}$

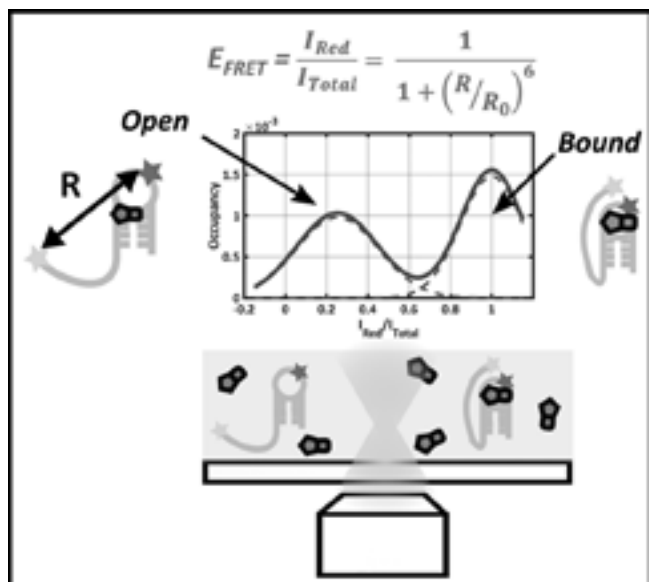


Figure 2: Single-molecule fluorescence measurements use a pair of dyes (represented as stars) to enable FRET. The relative emission of the red dye to the total emission of the dye pair is dependent on the inter-dye distance ( $R$ ). When suitable positions are found for the dyes, different conformational states of RNA can be distinguished (left and right cartoons). Bound states of regulatory RNAs can be identified (in this case) by EFRET values of 1.

thick glass cover slides attached to produce a stack. The stack is baked, and the sealing SU-8 layer cured. Development removes residual SU-8 that may have entered the channels. The result is a sealed microfluidic device consisting of channel geometries defined by SU-8 sandwiched between two glass layers. The use of SU-8 significantly improves device lifetime and chemical compatibility over traditional soft polymer approaches, allowing extended experiment time with a single device.

With this device we follow regulatory ribonucleic acids (RNAs) as they bind their ligand partners. These RNA elements are labelled with two fluorescent dyes of differing colors, green and red, that form a FRET pair (Figure 2). We excite the green dye with green laser light, and measure the fluorescence emission from the red dye

as a ratio of the total emission (sum of green and red dye emission), which yields the FRET efficiency value EFRET. The red emission depends on the inter-dye distance, with smaller inter-dye distances yielding EFRET values that are closer to 1. Probing single-molecules at a time, a distribution of inter-dye distances (EFRET) can be built that resolves subpopulations within our RNA sample. When bound to their ligand partners, a value close to one is expected; unbound states have larger inter-dye distances, and thus a lower EFRET value.

Pairing our microfluidic mixing device with single-molecule fluorescence measurements, we can rapidly introduce different ligand partners to our RNA sample, and watch the conformational transitions at varying times after mixing is complete. The resulting picture illustrates transitions between conformational states in the sample, and furthermore, provides quantitative measurement of rates and bound fractions for differing conditions. The results (Figure 3), show differences in the rates between two ligand partners for this particular RNA. Binding of the target (native) PreQ1 ligand occurs in  $\sim 500$  ms, whilst the off-pathway Guanine binds in  $\sim 5000$  ms.

The conformational re-arrangements required to transition from the unbound to the bound state are much more energetically favorable in the case of PreQ1 than for Guanine. The small differences in chemical composition of these two partners speaks to the highly evolved specificity of this RNA for its native ligand [4].

## References:

- [1] Al-Hashimi, H. M.; Walter, N. G. *Curr. Opin. Struct. Biol.* 2008, 18 (3), 321-329.
- [2] Daniels, K. G.; Suo, Y.; Oas, T. G. *Proc. Natl. Acad. Sci.* 2015, 112 (30), 9352-9357.
- [3] Wunderlich, B.; Nettels, D.; Benke, S.; Clark, J.; Weidner, S.; Hofmann, H.; Pfeil, S. H.; Schuler, B. *Nat. Protoc.* 2013, 8 (8).
- [4] Plumridge, A.; Pollack, L. In preparation 2019.

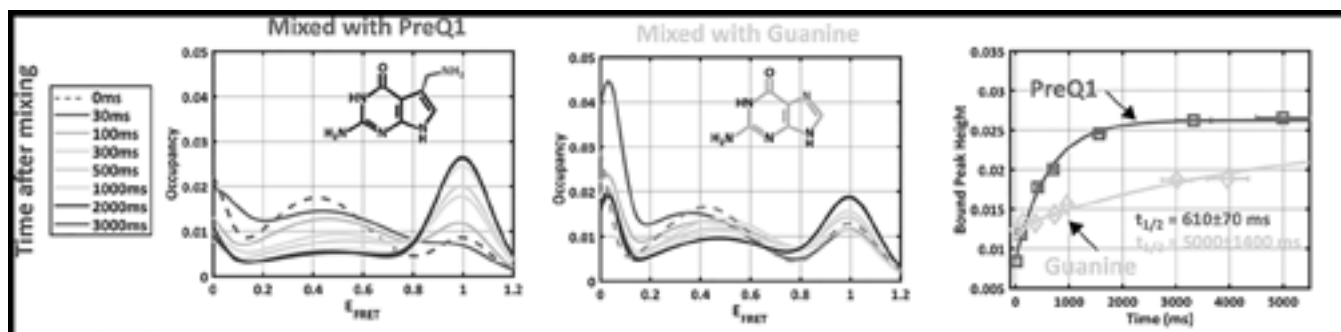


Figure 3: Pairing microfluidic mixing with single-molecule fluorescence allows us to observe RNA transitions from open to bound states at various times after mixing with ligand. In this case we probe transitions after mixing the on path (native) PreQ1, and the off path Guanine (non-native) ligands. Plotting the bound peak height as a function of time after mixing (far right) shows large differences in rates for this conformational change, despite the similar structure of these two ligands (chemical structures shown inset left panels)

# Body-on-a-Chip Systems for Drug Development

**CNF Project Number: 731-98**

**Principal Investigator(s): Michael Shuler**

**User(s): Danielle LaValley**

*Affiliation(s): Nancy E. and Peter C. Meinig School of Biomedical Engineering, Robert Frederick Smith School of Chemical and Biomolecular Engineering; Cornell University*

*Primary Source(s) of Research Funding: National Center for Advancing Translational Sciences, National Science Foundation, National Institutes of Health*

*Contact: MLS50@cornell.edu, DJL339@cornell.edu*

*Primary CNF Tools Used: VersaLaser cutting and engraving CO<sub>2</sub> laser*

## Abstract:

**This research involved creating a pumpless, unidirectional body-on-a-chip microfluidic device for anti-cancer drug testing. The body-on-a-chip device contains individual organ chambers representing a colon tumor, liver, and bone marrow tissue connected by microfluidic channels in a relevant physiological order. The microfluidic channels were designed with specialized valves to promote fluid flow in only one direction without backflow, mimicking blood circulation in the body.**

## Summary of Research:

The body-on-a-chip device was fabricated out of poly(methyl methacrylate) (PMMA) and silicone layers using the VersaLaser cutting and engraving CO<sub>2</sub> laser. The layered design consists of a silicone layer for cell culture, a PMMA channel layer, a sealing silicone gasket, and outer PMMA housing units (Figure 1). Once assembled, the device was placed onto a rocker platform for pumpless operation, thereby allowing easier operation and eliminating the need to external tubing and pumps. This work has been submitted for publication in *Lab on a Chip* [1].

## References:

- [1] LaValley DJ, Miller PG, Shuler ML. (2019). Pumpless, unidirectional microphysiological system for testing metabolism-dependent chemotherapeutic toxicity. Submitted to *Lab on a Chip*.

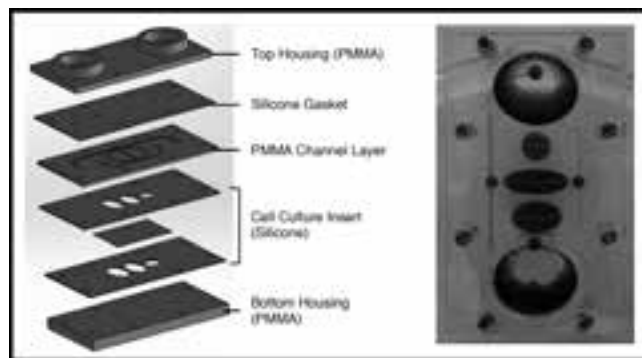


*Figure 1: (Left) A schematic of the layered design for the body-on-a-chip device consisting of alternating PMMA and silicone layers. (Right) An image of the assembled device filled with blue dye to visualize the organ chambers and microfluidic channels.*



# Body-on-a-Chip Systems for Drug Development

**CNF Project Number: 731-98**

**Principal Investigator(s): Michael L. Shuler, Harold G. Craighead**

**User(s): Ying Wang, Paula Miller, Danielle LaValley**

*Affiliation(s): Nancy E. and Peter C. Meinig School of Biomedical Engineering, Robert Frederick Smith School of Chemical and Biomolecular Engineering; Cornell University*

*Primary Source(s) of Research Funding: National Center for Advancing Translational Sciences, National Science Foundation, National Institutes of Health*

*Contact: mls50@cornell.edu, hgc1@cornell.edu, ying.wang@cornell.edu, pgm6@cornell.edu, djl339@cornell.edu*

*Primary CNF Tools Used: VersaLaser engraver/cutter tool, ABM contact aligner, PDMS casting station, Samco UV/Ozone stripper, hot press, ObJetPro 3D printer*

## Abstract:

**Body-on-a-chip (BOC) microphysiological systems combine biomaterials, microfluidics, microfabrication, and stem cell technologies to recreate organ structure and functionality as well as the dynamic organ-organ interactions *in vitro* [1]. They are powerful next-generation tools for human disease modeling and drug screening [2]. Here we describe two of the BOC systems that are being developed in our lab. They are fabricated with tools at CNF and designed to be used to study cancer cell extravasation and model cancer cell metastasis, and simulate immune responses.**

## Summary of Research:

Liver sinusoidal vascular chip for modeling colon cancer extravasation. We have designed and constructed a gravity-driven microfluidic platform for modeling the human liver sinusoidal microenvironment and investigating the extravasation of liver metastatic colorectal cancer (CRC) cells.

The device was fabricated in poly(methyl methacrylate) (PMMA). PMMA layers of desired thickness were patterned using a CO<sub>2</sub> laser (VersaLaser VLS3.50), and were bond together using a hot press at CNF after a 15 min UV/Ozone (Samco UV and Ozone stripper) exposure. We have also developed an apparatus to overcome the issue of sediment and aggregation of CRC cells in the feed reservoirs by introducing a propeller stirring device driven by a small stir bar on a magnetic stirrer. The propeller stirring device was designed in Inventor and fabricated using the ObJetPro 3D printer at CNF. We have tested different combinations varying in the propeller design, the positioning in the reservoir, and the stirring speed, and formulated an optimize stirring scheme that produced minimal cell sediment while preserving maximal cell viability.

We currently focus on characterizing the phenotype of liver sinusoidal endothelial cells in our microfluidic model and comparing CRC cell interactions with human liver sinusoidal endothelial cells versus human umbilical vascular endothelial cells.

## Lung-on-a-Chip:

We describe a multiorgan (lung, liver and breast cancer) microphysiological system ("Body-on-a-Chip") designed to mimic both inhalation therapy and/or intravenous therapy. Microfluidic channels, chambers and medium reservoirs were etched into a layer of PMMA with the VersaLaser VLS3.5 cutting and engraving CO<sub>2</sub> laser (Universal Laser Systems, Scottsdale, Arizona) at the CNF. Clear silicone gaskets were also cut/etched to help seal the device and provide support for the polycarbonate membranes. This system is "pumpless" and self-contained using a rocker platform for fluid (blood surrogate) bidirectional recirculation. Our lung compartment is constructed to maintain an air-liquid interface and contained a "breathable" component that was designed to mimic breathing by simulating gas exchange, contraction and expansion of the "lung" using a reciprocating pump.

## References:

- [1] Wang YI, Carmona C, Hickman JJ, Shuler ML. Multiorgan Microphysiological Systems for Drug Development: Strategies, Advances, and Challenges. *Adv Healthc Mater* 2018;7:1701000. <https://doi.org/10.1002/adhm.201701000> (2018).
- [2] Sung JH, Wang YI, Narasimhan Sriram N, Jackson M, Long C, Hickman JJ, et al. Recent Advances in Body-on-a-Chip Systems. *Anal Chem* 2019;91:330-51. <https://doi.org/10.1021/acs.analchem.8b05293> (2019).

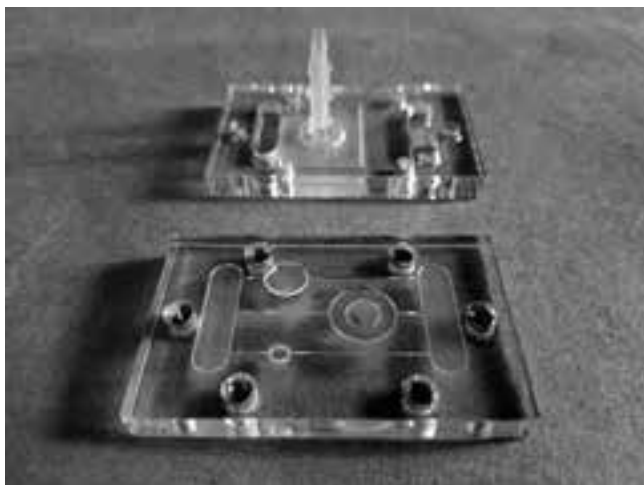


*Figure 1: Actual photograph of the top and bottom frame of the microphysiological system with the breathable lung chamber.*

# Silicon Nitride Cantilevers for Muscle Myofibril Force Measurements

**CNF Project Number: 1255-04**

**Principal Investigator(s): Walter Herzog**

**User(s): Timothy Leonard, Andrew Sawatsky**

*Affiliation(s): Faculty of Kinesiology, University of Calgary, Calgary, Canada*

*Primary Source(s) of Research Funding: Natural Sciences and Engineering Research Council of Canada, Canadian Institutes of Health Research and the Canada Research Chair for Cellular and Molecular Biomechanics*

*Contact: wherzog@ucalgary.ca, leonard@ucalgary.ca, ajsawats@ucalgary.ca*

*Website: www.ucalgary.ca/knes*

*Primary CNF Tools Used: GCA 5X stepper, Photolith spinners, Oxford 81 ion etcher*

## Abstract:

Spastic cerebral palsy (CP) is associated with increased passive muscle stress/stiffness in muscles, fascicles and fibres. However, crucial information on passive stress/stiffness on the sarcomere/myofibril level is missing. Previous research has shown that the sarcomere, the basic contractile unit of skeletal muscle, is overstretched in spastic muscle tissue compared to normal, and operates at long sarcomere lengths. At these increased lengths, the overstretched sarcomeres would have low active force-generating capacity and high passive forces, which agrees with the clinical situation whereby muscles are not only tight but also weak. Adductor longus muscle biopsies from children with CP and from typically developing children were analyzed for their *in vivo* sarcomere lengths, passive stress/stiffness, titin isoforms, and titin abundance and we found *in vivo* sarcomere lengths were increased and passive stress/stiffness and titin abundance were reduced, in CP muscle compared to controls. We conclude CP myofibrils are more compliant than control myofibrils, contrary to reports at higher structural levels. This increased compliance is caused by a reduction in the abundance of titin in CP sarcomeres. Because of the increased *in vivo* sarcomere length in CP, passive forces at functional muscle/sarcomere lengths are greater in children with CP compared to controls. Titin loss appears to be an adaptive response reducing high passive forces in CP muscles, but is insufficient to bring passive stresses to control levels, *in vivo*.

To measure muscle forces in the nano-Newton range, silicon nitride cantilever pairs were manufactured using the GCA 5x-stepper photolithography system and the Oxford 81 ion etching system at the CNF, and then used in our lab in Canada.

## Summary of Research:

The aim of this research was to investigate passive properties of single CP myofibrils to see if an increase in passive stress/stiffness mirrors what has been previously reported in CP muscles, fascicles and fibres. The isolated myofibril is devoid of passive structural elements outside of the sarcomere, such as the extracellular matrix (including collagen), and so this preparation provides crucial insight into the mechanics of sarcomeres and titin in CP. The molecular spring titin is an important structural element within the sarcomere, tethering the thick filament (myosin) to the Z-discs. This protein centers the thick filament within the sarcomere and is thought to account for the majority of passive force generated when sarcomeres are stretched [1].

## Methods:

Biopsies of operated adductor longus muscle were obtained and either held at the *in vivo* length for later *in vivo* sarcomere length determination, stored in a special rigor solution for generation of myofibrils, or frozen for titin analysis.

To obtain myofibrils, samples were homogenized and placed in the testing chamber [2]. The testing protocol was a ramp-hold-return design and every myofibril was lengthened (0.1  $\mu\text{m}$ /sarcomere/second) from slack length (< 2.0  $\mu\text{m}$ ) to a sarcomere length (SL) of 2.4, 2.8, 3.2, 3.6 and 4.0  $\mu\text{m}$ , sequentially. Steady-state stress and SL were measured at the end of a 1-minute hold. The cantilevers used were manufactured at the CNF and had a stiffness of 75 nN/ $\mu\text{m}$ .

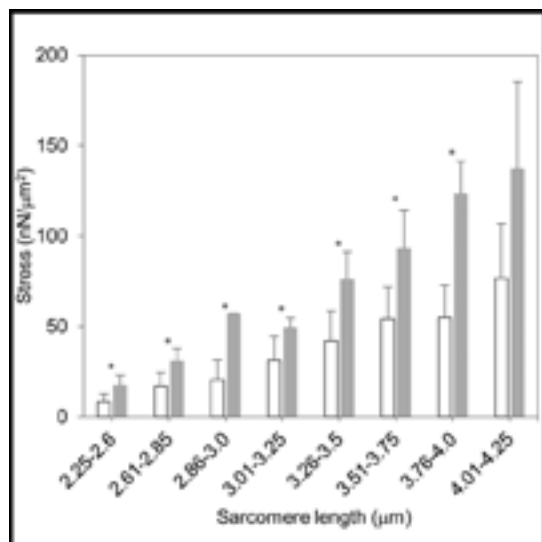


Figure 1: Passive stress generation versus sarcomere length for CP and control adductor longus. Mean stress  $\pm$  SD for CP (white) and control (grey) are significantly different at all sarcomere lengths tested, except for the longest range ( $> 4 \mu\text{m}$ ). ( $*p < 0.05$ ). The non-significant result at the longest sarcomere lengths is explained by the reduced number of observations.

Titin isoforms were determined using 2% agarose-strengthened polyacrylamide electrophoresis gels. To assess the total titin content in the tissues, a ratio of titin to nebulin was calculated. Nebulin is a large protein found in association with the thin filament; a single nebulin molecule spanning each thin filament, thus the titin/nebulin ratio provides a measure of the abundance of titin relative to the contractile thick and thin filaments in a sarcomere.

### Results:

For the CP participants, 46 adductor longus myofibrils were isolated and analyzed. For the controls, 8 myofibrils were isolated and analyzed. At all matched sarcomere length ranges ( $< 4 \mu\text{m}$ ) passive steady-state stress was significantly lower in CP compared to control myofibrils (Figure 1). The elastic modulus for CP was  $98 \pm 45\text{kPa}$ , significantly lower than in controls ( $166 \pm 22\text{kPa}$ ,  $p = 0.0005$ ).

Titin molecular weights for CP and control tissues were  $3611 \pm 41\text{kDa}$  and  $3615 \pm 8\text{kDa}$ , respectively (no difference:  $p = 0.76$ ). The ratio of titin-nebulin content for CP was  $1.47 \pm 0.37$  and for control was  $3.26 \pm 0.16$  ( $p = 0.004$ ). This difference is indicative of a reduced titin content relative to an unchanged nebulin content within the sarcomeres of the CP muscle. *In vivo* sarcomere lengths were much greater in CP than in typically developing children ( $3.6 \mu\text{m}$  versus  $2.7 \mu\text{m}$ ).

### Discussion and Conclusions:

Passive stresses are much lower in CP myofibrils compared to typically developing control myofibrils. This finding is in contrast to results found on the single fibre, fascicle and muscle level, and as such, appears to be an adaptation to reduce an already excessive passive force in spastic muscles. Despite the much lower stresses in CP compared to control myofibrils at matched sarcomere lengths, passive stresses at *in vivo* sarcomere lengths are much greater in CP than in typically developing children because the CP sarcomeres are over-stretched ( $3.6 \mu\text{m}$  versus  $2.7 \mu\text{m}$ ). A loss in titin content in CP muscle was found to be associated with decreases in the passive peak stress and elastic modulus of CP sarcomeres, which may be an adaptive response resulting in a more compliant myofibril, to partially offset the high passive stresses experienced at long *in vivo* sarcomere lengths of CP patients [3].

### References:

- [1] Bartoo, M. L., Linke, W. A., and Pollack, G. H. Basis of passive tension and stiffness in isolated rabbit myofibrils. *Am. J. Physiol.* 273, C266-276 (1997).
- [2] Joumaa, V., Rassier, D.E., Leonard, T.R., Herzog, W. The origin of passive force enhancement in skeletal muscle. *Am. J. Physiol. Cell Physiol.* 294, C74-78. <https://doi.org/10.1152/ajpcell.00218.2007> (2008).
- [3] Smith, L. R., Lee, K. S., Ward, S. R., Chambers, H. G., and Lieber, R. L. Hamstring contractures in children with spastic cerebral palsy result from a stiffer extracellular matrix and increased *in vivo* sarcomere length. *J. Physiol.* 589, 2625-2639 (2011).

# Unzipping an Array of DNA Molecules by Resonator Based Nanophotonic Tweezers

**CNF Project Number: 1738-08**

**Principal Investigator(s): Michelle D. Wang**

**User(s): Fan Ye**

*Affiliation(s): a) Department of Physics, Cornell University; b) Howard Hughes Medical Institute*

*Primary Source(s) of Research Funding: Howard Hughes Medical Institute*

*Contact: mdw17@cornell.edu, fy72@cornell.edu*

*Website: <http://wanglab.lassp.cornell.edu/>*

*Primary CNF Tools Used: ASML deep ultraviolet stepper, Oxford 100 plasma etcher, Unaxis 770 deep Si etcher, Heidelberg mask writer DWL2000, SÜSS MA6-BA6 contact aligner, Gamma automatic coat-develop tool, LPCVD Nitride - B4 furnace, Wet/Dry Oxide - B2 furnace, AJA sputter deposition, CVC sputter deposition, GSI PECVD, Oxford PECVD, SC4500 odd-hour evaporator, Zeiss Supra and Ultra SEMs*

## Abstract:

Optical trapping has become a major technique widely used in biological and materials sciences, on size scales ranging from the single molecule to the cellular level, and force scales ranging from sub piconewton (pN) to tens of pN [1]. The rapid development of nanofabrication techniques in the past few decades has bolstered the emergence of nanophotonic evanescent-field traps. The ability of nanostructures to direct and confine light beyond the diffraction limit enables miniaturized, on-chip devices with abilities beyond traditional microscope-based optical tweezers [2]. The Wang lab has developed and implemented such an on-chip device based on Si or Si<sub>3</sub>N<sub>4</sub> waveguides, coined a nanophotonic standing-wave array trap (nSWAT), that allows for controlled and precise manipulation of trapped single biomolecule (such as DNA) arrays via microparticle handles [3-6]. We present here the latest development of the nSWAT platform based on a resonator design that achieves large enough manipulation forces for unzipping an array of DNA molecules. This benchmark achievement is one step closer to the full realization of nanophotonic tweezers' capabilities, promising increased accessibility and expansion of these platforms to a wide range of biological and biomedical research topics.

## Summary of Research:

Over the past decade, the Wang lab has demonstrated a high-throughput, near-field nanophotonic trapping platform that achieves stable trapping and precision manipulation of microparticles [3-6]. The kernel of this platform is the formation of standing waves along a nanophotonic waveguide: by counter propagating two coherent laser beams along a single-mode nanophotonic waveguide. The antinodes of the standing wave form an array of stable optical traps. We call this type of trap a nanophotonic standing-wave array trap (nSWAT). By tuning the phase difference between the two counter-propagating laser beams via thermo-optic effect, the antinode locations can be precisely repositioned, and consequently, the optical trap positions can be precisely manipulated. The nSWAT platform holds the capability for high throughput precision measurements for single biomolecules.

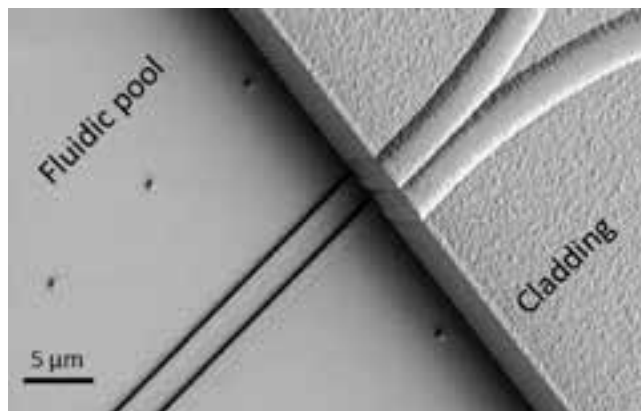


Figure 1: A tilted-angle SEM image of the step boundary of the fluidic pool region. Inside the fluidic pool region, the two parallel Si<sub>3</sub>N<sub>4</sub> waveguides trap two arrays of polystyrene microbeads (380 nm diameter) with DNA molecules tethered in between. The dot arrays near the parallel waveguides are fiducial markers for local position tracking.

In 2018, we have implemented a major upgrade of the nSWAT platform, including the following three aspects: (1) We have implemented a resonator based design for ultimate local intensity enhancement into the nSWAT devices. Compared to previous designs, this resonator design gives the highest force enhancement factor, limited only by the total scattering loss of the trapped beads onto the waveguide. We have measured around three times force enhancement, larger than our previous force-double design [5]. (2) We have implemented a balanced layout and differential operation mode for the micro heaters. This greatly reduced the response time of the micro heaters (from  $\sim 30 \mu\text{s}$  to  $\sim 1 \mu\text{s}$ ). This is shown to be crucial for maintaining high trapping forces for a trapped bead under strong biased forces under single molecule manipulations. (3) We have also designed a special sample holder for the nSWAT chip that can greatly reduce (by two orders of magnitude) the thermal drift of the sample caused by the micro heaters. This greatly enhanced the thermal stability of the nSWAT devices. Thanks to the above described improvements, we have achieved DNA unzipping on the nSWAT devices for the first time

In the past year, we have continued optimizing the nSWAT platform to achieve our final goal of unzipping an array of DNA molecules. We have further optimized the flow chamber design of the nSWAT devices to achieve better DNA molecule trapping efficiency. We have also implemented SU-8 layer as the anti-corrosion protection layer for the nSWAT device that works significantly better

than the  $\text{Si}_3\text{N}_4$  protection layer we used before [4]. With all these improvements, we are looking forward to the achievement of trapping and unzipping an array of DNA molecules in the near future.

Our development and improvement of the nSWAT platform has led to five publications in the past few years [2-6], and more to come later this year.

### References:

- [1] J. L. Killian, F. Ye, M. D. Wang, "Optical Tweezers: A Force to Be Reckoned With" *Cell* 175 (6), 1445-1448 (2018).
- [2] J. E. Baker, R. P. Badman, and M. D. Wang, "Nanophotonic trapping: precise manipulation and measurement of biomolecular arrays" *WIREs Nanomed Nanobiotechnol.* e1477 (2017).
- [3] M. Soltani, J. Lin, R. A. Forties, J. T. Inman, S. N. Saraf, R. M. Fulbright, M. Lipson, and M. D. Wang, "Nanophotonic trapping for precise manipulation of biomolecular arrays" *Nature Nanotechnology* 9(6), 448-452 (2014).
- [4] F. Ye, R. P. Badman, J. T. Inman, M. Soltani, J. L. Killian, and M. D. Wang, "Biocompatible and high stiffness nanophotonic trap array for precise and versatile manipulation" *Nano Letters* 16(10), 6661-6667 (2016).
- [5] F. Ye, M. Soltani, J. T. Inman, and M. D. Wang, "Tunable nanophotonic array traps with enhanced force and stability" *Optics Express* 25 (7) 7907-7918 (2017).
- [6] R. Badman, F. Ye, W. Caravan, and M. D. Wang, "High Trap Stiffness Microcylinders for Nanophotonic Trapping" *ACS Appl. Mater. Interfaces* (2019) <https://doi.org/10.1021/acsami.9b10041> (published online).

# Development of a Salivary Microfluidic Diagnostic Device using Hot Embossing

**CNF Project Number: 1872-10**

**Principal Investigator(s): David Erickson**

**User(s): Elizabeth Rey**

*Affiliation(s): Sibley School of Mechanical and Aerospace Engineering, Cornell University*

*Primary Source(s) of Research Funding: National Science Foundation*

*Contact: de54@cornell.edu, egr42@cornell.edu*

*Primary CNF Tools Used: Hot press, photolithography room, ABM contact aligner, Unaxis 770 deep Si etcher, Microdrill, Objet30 3D Printer*

## Abstract:

Point of care diagnostic devices allow people to get fast, accurate information about their health and well-being without the need to go to a clinic or hospital. The device that we are designing will determine the concentration of cortisol from a sample of the user's saliva. Cortisol is a steroid hormone associated with stress levels and expressed in human saliva [1,2]. This microfluidic device contains a microbead-based immunoassay that we are optimizing to determine the cortisol content from a saliva sample. The device is manufactured using a hot embossing process, which uses a silicon master made with traditional lithographic processes. The device is made from a thermoplastic called Zeonor 1020R, which is a transparent, semi-rigid plastic that can be used in large-scale manufacturing processes such as injection molding and hot embossing. Nearly all the fabrication of the device is being done in the Cornell NanoScale Facility.

## Summary of Research:

The microfluidic device is made using a hot embossing process, which involves the high-temperature pressing of a mold into a piece of thermoplastic. The mold that we use in our process is made of silicon and is fabricated using photolithographic processes. The design for the mold is made using L-Edit and transferred to a photomask using the Heidelberg mask writer (DWL2000). This mask is then used to transfer a pattern to a photoresist on a silicon wafer. The photoresist (SPR-220-7.0) is spun onto a bare silicon wafer, which has been previously primed in the YES vapor prime oven, to a thickness of approximately 7  $\mu\text{m}$ . After spinning, the photoresist is soft baked on a 115°C hot plate for 2 minutes and 30 seconds. The wafer is allowed to sit for an hour and then exposed using the mask and the ABM contact aligner. The wafer is again allowed to sit for an hour and then is developed using the Hamatech Steag wafer processor. The pattern is now developed and can be used to etch the silicon wafer.

We etched the wafer using the Unaxis 770 deep Si etcher to a depth of 50  $\mu\text{m}$ . We monitored the etch depth and etch rate using the P10 profilometer. Upon reaching the desired depth, we removed the photoresist in the chemical strip bath. We then used the Unaxis 770 again to deposit a thin layer of fluoropolymer onto the wafer in order to prevent sticking in the hot emboss process. Our

masters were then ready to be used in the hot emboss process.

The hot emboss process uses the CRC Prepreg Mini Test Press, which applies heat and even pressure. The silicon master is adhered to a glass backing, for strength, and then the plastic piece is placed on top of the master, with another glass piece on top of that. This whole stack is placed in the hot press once the hot press reaches the desired temperature and pressed for several minutes. The setup is allowed to cool below the glass transition temperature of the plastic and then the pressure is released and the plastic is de-embossed. The pattern is transferred from the master to the plastic. We then drill through-holes in a blank piece of plastic using the custom-made micro drill. In our own lab, we perform a photografting procedure to increase hydrophilicity of the Zeonor surfaces and improve bonding. This blank piece is then thermally bonded to the patterned piece to create the microfluidic device in the hot press. Our microfluidic device is now complete and ready to be turned into an immunoassay. An example can be seen in Figure 1(a).

We can now flow differently sized beads into the device to create areas for antibody-antigen-fluorophore interaction. The channels after the beads are successfully

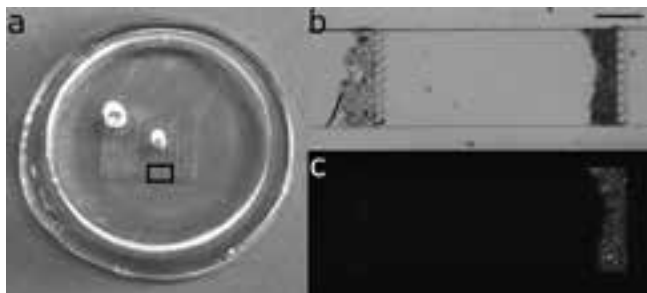


Figure 1: Microfluidic chip. a.) Completed microfluidic chip with inlet at center and outlet on the left. Box depicts pillar/bead zone. b.) Microscope image of channels, pillars, and different sized bead zones c.) Microscope image of fluorescence on beads after flowing of AlexaFluor488 through chip.

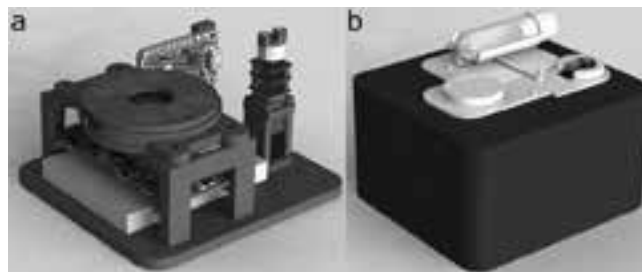


Figure 2: Rendering of 3D-printed imaging and pumping device. a.) Interior assembly including Raspberry Pi Zero W, optical components, geared motor, custom peristaltic pump head, lithium-ion battery, and Powerboost 1000C. b.) Exterior of device with disposable cassette attached via snap fit.

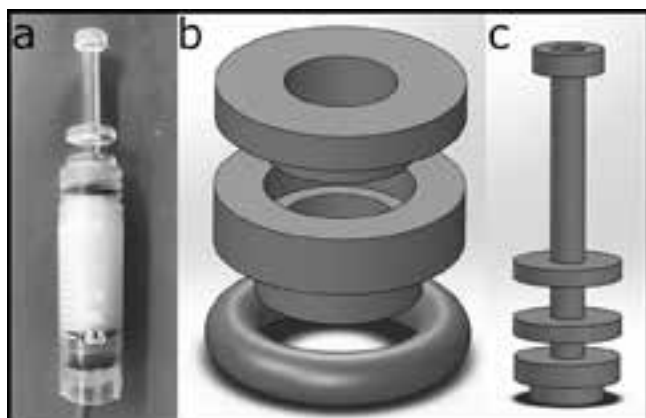


Figure 3: Saliva filtration setup. a.) Image of complete filtration setup. b.) Custom filter holder with two pieces that hold a circular filter between them and an O-ring beneath. c.) Plunger to compress saliva swab and push saliva through filter.

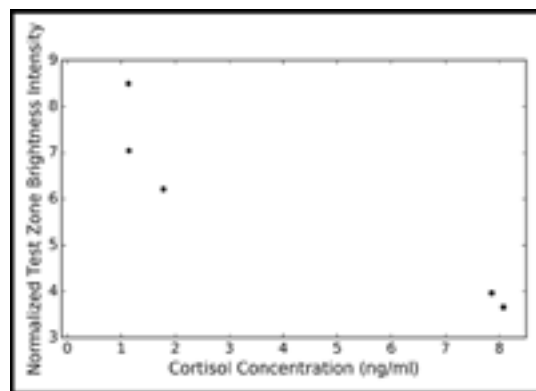


Figure 4: Preliminary fresh filtered saliva results. n=1.

added can be seen in Figure 1(b). The differently-spaced pillars allow two zones with beads with different antibodies to be separated by size. We then flow fluid with cortisol and AlexaFluor488-labeled antibodies through the device using a custom microfluidic peristaltic pump and measure the brightness of the fluorescence at the bead zones with a microscope or with our portable imaging and pumping device. A microscope image of the two bead zones with attached fluorophores can be seen in Figure 1(c). The portable imaging device is a Raspberry Pi Zero W with a camera attached, fluorescent optics, a lithium-ion battery, LEDs, and a custom peristaltic pump setup, all assembled in a 3D-printed light-tight case. This case is printed using the Objet30 Pro 3D printer and can be seen with all parts assembled in Figure 2.

Saliva samples were collected from human participants with approval from Cornell's Institutional Review Board,

and then stored at 4°C until analysis. These samples were analyzed using a commercial ELISA kit to determine the concentration of cortisol in each. These samples were also filtered using a custom 3D-printed filter setup (Figure 3) and then flowed through the microfluidic chips and imaged. Some preliminary results from some samples can be seen in Figure 4.

### References:

- [1] Kirschbaum C, Hellhammer DH Salivary cortisol in psychoneuroendocrine research: recent developments and applications. *Psychoneuroendocrinology*, 1994 - Elsevier.
- [2] Umeda T, Hiramatsu R, Iwaoka T, et al. Use of saliva for monitoring unbound free cortisol levels in serum. *Clin Chim Acta* 110:245-253. doi: 10.1016/0009-8981(81)90353-3 (1981).

# An *in vacuo* Microfluidic Mixer for Biological X-Ray Solution Scattering

**CNF Project Number: 1940-10**

**Principal Investigator(s): Richard E. Gillilan**

**User(s): Christopher Flynn**

*Affiliation(s): Macromolecular Diffraction Facility of the Cornell High Energy Synchrotron Source (MacCHESS); Cornell High Energy Synchrotron Source; Department of Physics, Fort Lewis College, Durango, Colorado*

*Primary Source(s) of Research Funding: National Institutes of Health GM-103485*

*Contact: reg8@cornell.edu, csflynn@fortlewis.edu*

*Website: www.macchess.cornell.edu/MacCHESS/bio\_saxs.html*

*Primary CNF Tools Used:*

## Abstract:

Small angle x-ray scattering (SAXS) is an important tool for probing the structure and interactions of biological molecules under realistic physiological-like conditions. Fabrication of plastic microfluidic chips for time resolved small angle x-ray solution scattering (TR-SAXS) involves embedding various thin, fragile x-ray transparent window materials within a polymer matrix. This continuous-flow mixer utilizes chaotic laminar flow that is designed to reach multiple timescales down to a millisecond. High flow rates of water-based samples though the cell induces high pressures that present design challenges. Our current cell design utilizes relatively deep 500  $\mu\text{m}$  channels for fluid flow combined with either polyimide or synthetic mica x-ray windows. Synthetic mica is more rigid than polyimide, resulting in less flexing of x-ray windows under pressure. Mica also has the advantage of fewer x-ray scattering artifacts and its hydrophilic nature lends itself to bonding.

## Summary of Research:

Biological small angle x-ray solution scattering (BioSAXS) is a popular technology for extracting structural information from biomolecules under realistic physiological-like solution conditions. Given that many studies in structural biology today rely heavily on crystalline and/or frozen samples, the ability to probe solution behavior is more critical than ever. Many important biological phenomena change on timescale ranging from 1 ms to several seconds [1]. Time-resolved SAXS methods have been developed in the literature that can reach these timescales, but the techniques are difficult to implement and still require intensive effort by specialists in the field. High-volume, repeated experiments required for use in a general user facility are currently impractical. The focus of this work is to make TR-SAXS more easily accessible to the general biology community by developing disposable microfluidic mixing cells that can be easily replaced to handle the high-volume, continuous duty of a user facility.

Our fabrication method uses the recently developed SUEX film (DJ Microlaminates, Sudbury, MA) to create a 500  $\mu\text{m}$  thick layer containing deep microfluidic channels (Figure 1a). The x-ray window is bonded

to a poly(methyl methacrylate) (PMMA) base using epoxy then overlaid with SUEX, exposed and developed by standard photolithography techniques. A second x-ray window (4, in Figure 1B) covering all the liquid channels, is sandwiched between the underlying SUEX layer and an outer PMMA support. While thin 7  $\mu\text{m}$  polyimide has been used for some time in x-ray work, it is easily deformed resulting in irreproducible scattering absorption and undesirable scattering background. High quality synthetic mica is now available with superior rigidity and low background scatter (fluorophogopite, Great Wall Mineral, Shijiazhuang, China). Bench testing subjected layers to pressures of approximately 4500 bar, though pressure downstream of the mixing zone was estimated to be much lower (130-70 mbar).

## References:

- [1] Panine, P., S. Finet, T. M. Weiss and T. Narayanan (2006). "Probing fast kinetics in complex fluids by combined rapid mixing and small-angle x-ray scattering." *Advances in Colloid and Interface Science* 127(1): 9-18.

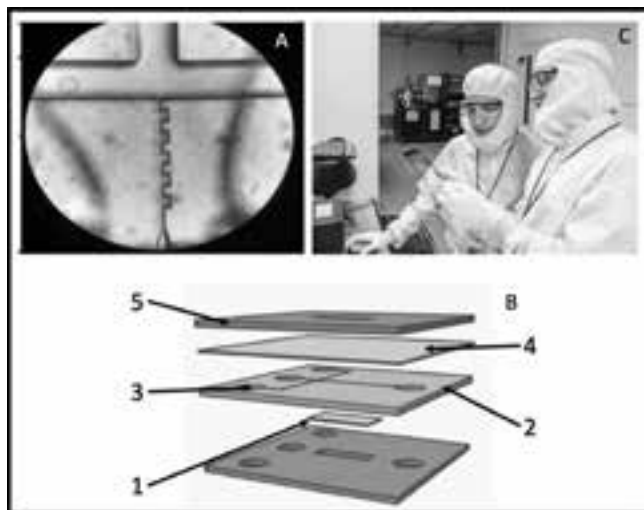


Figure 1: Microfluidic TR-SAXS chip. (A) Closeup view of mixing region. (B) Schematic of layer design: 1. x-ray window, 2. SUEX layer, 3. Input port, 4. x-ray window, 5. PMMA layer. (C) Christopher Flynn, Fort Lewis, Colorado, SunRise program for Summer students, together with CHESS scientist Richard Gillilan examining their latest photolithography mask.

## Biomechanics of Bacteria

**CNF Project Number: 1970-10**

**Principal Investigator(s): Christopher J. Hernandez**

**User(s): Christine E. Harper, Melanie F. Roberts**

*Affiliation(s): Sibley School of Mechanical and Aerospace Engineering,  
Meinig School of Biomedical Engineering; Cornell University*

*Primary Source(s) of Research Funding: National Science Foundation 1463084*

*Contact: cjh275@cornell.edu, ceh272@cornell.edu, mfr75@cornell.edu*

*Website: hernandezresearch.com*

*Primary CNF Tools Used: ASML, Oxford 100, AJA sputter deposition, VersaLaser, MOS clean anneal*

### Abstract:

**The mechanical properties of the bacterial cell envelope influence cell growth, cell division and subcellular localization of membrane proteins. Here we demonstrate the ability to apply mechanical loads to live bacteria, the first step toward determination of mechanical properties of bacterial components *in vivo*. Additionally, we show that devices based on the same concept have the ability to separate bacterial species/strains from one another based on the cell mechanical phenotype.**

### Summary of Research:

In bacteria, the ability to resist mechanical forces is necessary for survival and growth, allowing cells to withstand osmotic pressures while maintaining cell shape, cell growth and division. Hence, the mechanical properties of bacteria and bacterial structural components influence species competition and resistance to toxins and antibiotics. Our work involves the use of micro/nano fabricated devices as tools for mechanical testing of live bacteria. Within our devices individual bacteria are flowed into tapered channels and trapped. The point at which the cell becomes trapped reflects the whole cell stiffness, more stiff cells are trapped earlier in the channels and less stiff cells are able to travel further into the channels (Figure 1).

Key advantages of this microfluidic platform for profiling the biomechanical properties of bacteria include: minimal sample preparation, no chemical immobilization or labeling, and the ability to analyze hundreds of cells at once.

In our first series of experiments we manufactured devices on silica glass wafers using deep UV photolithography to achieve nano-scale features (250 nm smallest dimension). These glass on glass devices were manufactured using the ASML, Oxford 100, AJA sputter deposition, VersaLaser, and MOS clean anneal tools at the Cornell NanoScale Science and Technology Facility.

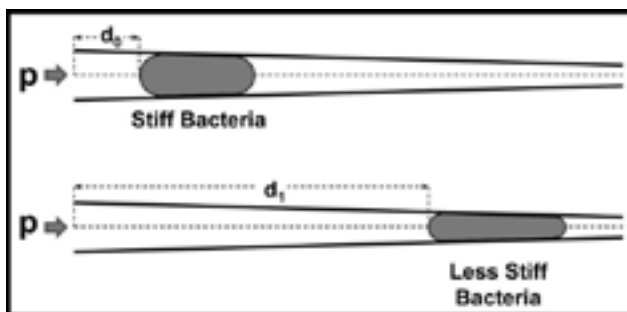


*Figure 1: Bacteria under fluid pressure ( $p$ ) are forced into tapered channels. The distance a cell travels into a tapered channel depends on cell stiffness with more compliant cells traveling further into the channels. The distance traveled by a cell into the tapered channel ( $d_1$ ) is therefore an indicator of cell stiffness. Viewing the deformation of a cell under two different applied pressures can be used to determine the mechanical properties of the cell envelope.*

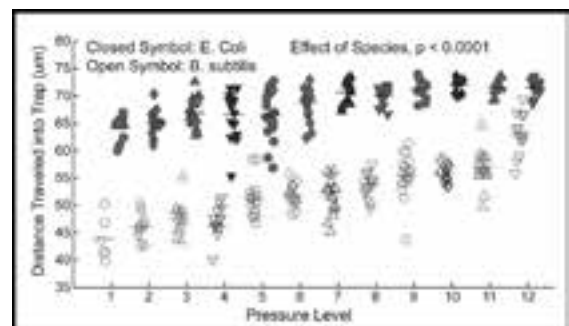


*Figure 2: The position of bacteria occupying trap channels at twelve different pressure levels (where level 1 is lowest and level 12 is greatest) in a single experiment are shown. Horizontal lines indicate averages at each pressure level. *E. coli* travel further into the traps than *B. subtilis* overall ( $p < 0.0001$ , ANCOVA) as well as at each individual pressure level ( $p < 0.0001$ ,  $t$  tests). (Find full color on pages xiv-xv.)*

In the first device design bacteria in liquid culture were submitted to up to 12 different applied pressures to establish the biomechanical profile of two model organisms, *E. coli* and *B. subtilis*.

Our results demonstrated differences in stiffness between *E. coli* and *B. subtilis* (Figure 2) and suggested that a device with a shorter channel length would allow transport of *E. coli* but not *B. subtilis*, potentially allowing for separation of bacteria based on the biomechanical properties [1]. When combined with theoretical mechanics models, it allowed us to determine the stress distribution within individual bacteria and study their response to mechanical stimulation [2].

In our recent work we have explored the effects of mechanical loads on the assembly/disassembly of multicomponent efflux pumps. Multicomponent efflux pumps are three-part channels that cross the inner membrane, periplasm and outer membrane of bacteria and are used to remove toxins including excessive metal ions and antibiotics. Our data suggests that the assembly and function of multicomponent efflux pumps is sensitive to mechanical stress and strain. Increased octahedral shear stress due to increased pressure in our microfluidic device was shown to promote disassembly of multicomponent efflux pumps as well as decreasing cell elongation rate (Figure 3), suggesting metal resistance of mechanically stressed cells may be reduced [4].

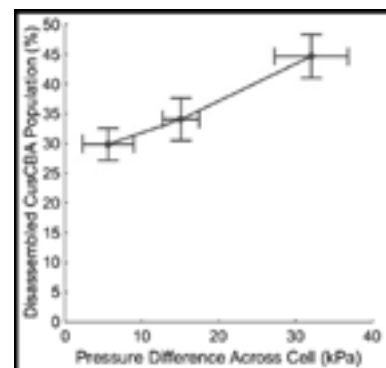


Figure 3: Bacteria trapped within tapered channels experience a difference in pressure across the cell length. Increased pressure difference across the cell was shown to increase disassembly of the multicomponent efflux pump CusCBA.

## References:

- [1] Sun, X., Weinlandt, W.H., Patel, H., Wu, M., Hernandez, C.J. (2014) "A Microfluidic Platform for Profiling Biomechanical Properties of Bacteria." *Lab Chip*. 14 (14), 2491-2498. NIHMS600175.
- [2] M. F. Roberts, A. Srivastava, X. Sun, L. Kreminski, L. Ling, L. Wang, P. Chen, C-Y. Hui, C. J. Hernandez. "A Microfluidic Platform for Generating Non-Uniform Mechanical Stress in Cell Envelopes of Live Bacteria," American Society of Microbiology Annual Meeting, Boston, MA, USA. 2016.
- [3] M.F. Roberts, A. Srivastava, L.M. Wang, C-Y Hui, L.A. Genova, P. Chen, C.J. Hernandez, "A microfluidic system for mechanical characterization and stimulus of individual bacteria," European Society of Biomechanics 2017.
- [4] L.A. Genova, M.F. Roberts, Y.C. Wong, C.E. Harper, A.G. Santiago, B. Fu, A. Srivastava, W. Jung, L.M. Wang, Krzemiski, X. Mao, X. Sun, C.Y. Hui, P. Chen, C. J Hernandez. "Mechanical stress compromises multicomponent efflux complexes in bacteria". *BioRxiv* preprint 2019.

# Design and Application of Microfluidic Devices to Study Cell Migration in Confined Environments

**CNF Project Numbers: 2065-11**

**Principal Investigator(s): Jan Lammerding**

**User(s): Aaron Windsor**

*Affiliation(s): Meinig School of Biomedical Engineering, CNF, Weill Institute; Cornell University*

*Primary Source(s) of Research Funding: National Institutes of Health award R01 HL082792; National Institutes of Health award 1U54 CA210184; Department of Defense Breast Cancer Research Program Breakthrough Award BC150580; National Science Foundation CAREER award CBET-1254846*

*Contact: jan.lammerding@cornell.edu, ajw49@cornell.edu*

*Website: <http://lammerding.wicmb.cornell.edu/>*

*Primary CNF Tools used: Heidelberg DWL 2000 mask writer, ABM contact aligner, SÜSS MA6 contact aligner, Plasma-Therm 770, Anatech SCE-110-RF resist stripper, Trion Minilock III ICP etcher, Tencor P-10 profilometer, MVD*

## Abstract:

For multicellular organisms, cell migration can act as a double-edged sword. While being vital for embryonic development, wound healing, and immune responses, wayward cells may also disrupt essential biological processes that can detrimentally affect the long-term survival of a life form. This is particularly true for the ability of metastatic cancer cells to translocate from the primary tumor, invade into surrounding tissues, and colonize distant organs. Metastatic cancer cells are able to penetrate through tight interstitial spaces of only 1-30  $\mu\text{m}$  in diameter. The squeezing through such confined spaces places substantial physical stress on the cell nucleus, leading to nuclear envelope ruptures, chromatin herniation, and significant DNA damage. To study these processes in more detail, we created a microfluidic device that models the tight 3D constrictions that metastatic cancer cells may encounter during the metastatic process. The device gives us a high-throughput method for observing the short- and longer-term effects mechanically induced nuclear deformation has on the tumor cells. Originally, we constructed our intricate PDMS microfluidic devices from SU-8 molds, which lacked reliability and inconsistently reproduced the most critical features of our designs. Thus, we shifted the nanofabrication process to deep-reactive-ion etching (DRIE) and reactive-ion etching (RIE) of silicon. This revised approach has enabled us to improve the fidelity of our critical features, while also reducing the fabrication time and costs. The precision of silicon etching has opened doors for creating more complex microfluidic designs and other novel ideas. For example, we recently created a set of five devices that mimic different densities of the extracellular collagen fiber networks that form in many tissues. These devices are now finding use in the study of cancer cell migration and immune cell motility in confined spaces. We also have explored the use of fluorinated ethylene propylene (FEP Teflon®) as a substitute for PDMS molded devices. Nanoimprinted FEP has a reflective index near that of water and could give our devices the capability of super-resolution microscopy. Taken together, these examples illustrate new uses of the available nanofabrication technologies to create improved *in vitro* models to study cancer cell migration.

## Summary of Research:

For decades, cell biologists have relied on two-dimensional (2D) migration assays for their convenience and seamless integration with many common imaging tools [1]. While being impactful in the field of cell biology, 2D studies are limiting for studying cancer cell migration [2], as they do not accurately depict how a cancer cell moves *in vivo* [3]. In order for cells to move throughout the body, they must navigate three-dimensional (3D) matrixes of different compositions, pore sizes and stiffnesses. Our goal was to design polydimethylsiloxane (PDMS) based microfluidic devices that recreate the confining 3D environment cells encounter *in vivo*, using approaches that provide precisely controlled and consistent geometries, and that enable high resolution imaging of the cells as they migrate through the devices [4]. These devices support a wide range of cell lines, and enable high-quality fluorescence imaging of nuclear lamina bucking, chromatin strain, DNA damage and nuclear rupture/blebbing and repair [4,5].

Over the past two years, we have explored alternate nanofabrication methods for the microfluidic migration devices. SU-8 was effective in creating these migration devices,

but suffered from a few common fabrication issues. First, the reproducibility of the fine ( $\sim 1 \mu\text{m}$ ) features was difficult to achieve consistently, which led to an overuse of the few successful device wafers. The repeated molding and removal of PDMS would overtime weaken the SU-8/silicon substrate bond, eventually resulting in the delaminating of features and device failure. In order to reliably reproduce and preserve our most critical features, we decided to forgo SU-8 and instead etch the fine constrictions of the devices directly into the silicon substrate. We accomplished this “bottom-down” approach by using a negative photoresist mask and deep-reactive ion etching (DRIE). Not only were the critical dimension sizes reproduced with fidelity (Figure 1), but the fabrication time was cut in half.

Another advantage to this process was the ease of creating 1  $\mu\text{m}$  features through contact lithography with photoresist compared to SU-8. With this in mind, we revisited some of our alternative migration device designs. One design that was now achievable with DRIE was creating large ( $\sim 25 \text{ mm} \times 25 \text{ mm}$ ) arrays of randomly spaced 5  $\mu\text{m}$  diameter circular pillars, mimicking collagen matrixes with different densities (Figure 2). While the

DRIE process successfully created the desired geometries, we noticed that the holes etched into the silicon wafer to mold the 5  $\mu\text{m}$  PDMS pillars frequently contained remnants of the PDMS pillars after molding. We determined that the scalloped-sidewalls from the DRIE etch likely contributed to this problem, and that smoother sidewalls were required to facilitate removal of the PDMS replicas. To achieve this, we developed a reactive-ion etching (RIE) protocol, which was subsequently used for all device fabrication. The photonics etch on the Plasma-Therm Unaxis SLR 770 was chosen for its unique capability to produce smooth anisotropic sidewalls in silicon and compatibility with our original DRIE lithography. As another demonstration of the versatility of the new RIE approach, we created another migration design for the observation of single cells passing a precisely defined constriction (Figure 3). We highly recommend this process to other researchers aiming to produce microfluidic devices with smooth walls, feature heights of several micrometers, and width in the sub-micrometer range.

Another major breakthrough this past year was discovering a method to remove SU-8 features from silicon wafers, which enables reusing wafers when the SU-8 structures have become damaged after repeated use. The weakest point to any SU-8 device is its substrate adhesion, especially after repeated PDMS molding. For our migration devices, the silicon wafers contain the fine featured etched into the wafer using the RIE approach described above, and additional larger SU-8 features for the fluid handling. Typically, the wafers have to be discarded after any SU-8 component begins to delaminate from the wafer. To overcome this issue, we developed two techniques that can remove all the remaining SU-8 from our wafers while not affecting the fine photonics etch features. This approach enabled us to spin on a new layer of SU-8 and reuse the fine silicon etched wafer. Intriguingly, this process can also be used to produce and liftoff designs entirely made from SU-8 (Figure 4), which could find future use in the fabrication of small micrometer-sized parts.

Lastly, we investigated PDMS substitutes for molding our microfluidic devices for super-resolution applications that require imaging through media that matches the refractory index of water, i.e.,  $n = 1.33$  [6]. The cured PDMS typically used for microfluidic devices has a refractive index of 1.41 [7], which is not well suited for the lattice light sheet imaging. Instead, we chose to use fluorinated ethylene propylene (FEP) as an alternative material for the device fabrication. FEP is a highly transparent copolymer of hexafluoropropylene and tetrafluoroethylene with a refractive index of 1.334 (<https://holscot.com/glossary/fep/>), closely matching that of water. We were able to emboss thin FEP sheets with micrometer resolution and minimum damage to our existing molds with the Nanonex 2500 nanoimprint tool. The most accurate representations of our both DRIE and RIE master wafers were achieved slightly below the melting point of FEP (260°C - 265°C) (Figure 5). Ongoing work is focused on optimizing thermal or chemical bonding of FEP sheets to each other or to glass substrates to create complete microfluidic devices.

## References:

- [1] Wu, P., Gilkes, D. M., and Wirtz, D. Annual Review of Biophysics, 47(1), 549-567. doi:10.1146/annurev-biophys-070816-033854 (2018).
- [2] Van Horsen, R. V., and Hagen, T. L. J of Cellular Physiology, 226(1), 288-290. doi:10.1002/jcp.22330 (2010).
- [3] Lautscham, L., et al. Biophysical Journal, 109(5), 900-913. doi:10.1016/j.bpj.2015.07.025 (2015).
- [4] Davidson, P. M., Sliz, J., Isermann, P., Denais, C., and Lammerding, J. Integrative Biology, 7(12), 1534-1546. doi:10.1039/c5ib00200a (01 December 2015).
- [5] Denais C.M., Gilbert R.M., Isermann P., McGregor A.L., te Lindert M., Weigelin B., Davidson P.M., Friedl P., Wolf K., Lammerding J. Science. 352(6283):353-8. doi: 10.1126/science.aad7297 2016 Apr 15.
- [6] Bashkatov, A. N., and Genina, E. A. Saratov Fall Meeting 2002: Optical Technologies in Biophysics and Medicine IV, 5068, 393-395. doi:10.1117/12.518857 (13 October 2003).
- [7] Dow Corning Technical Data Sheet SYLGARD™ 184 Silicone Elastomer. Retrieved May 6, 2019, from <https://consumer.dow.com/content/dam/dcc/documents/en-us/productdatasheet/11/11-31/11-3184-sylgard-184-elastomer.pdf?iframe=true> (2017).

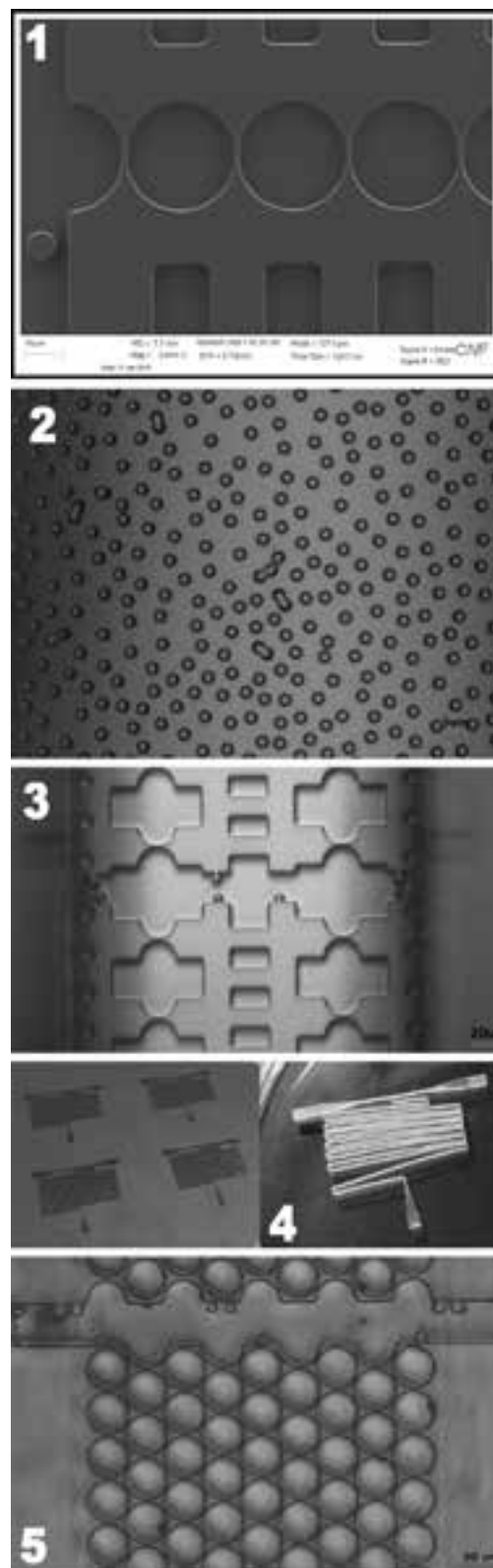


**Figure 1:** SEM image of a row of 1  $\mu\text{m}$  constrictions created by etching 5  $\mu\text{m}$  into Si by DRIE. **Figure 2:** An example of DRIE 5  $\mu\text{m}$  diameter holes intended for PDMS molding pillars to mimic collagen (50x). **Figure 3:** Single cell migration device with 1  $\mu\text{m}$  constriction gaps. **Figure 4:** Left: Four SU-8 microfluidic devices  $\approx 170 \mu\text{m}$  tall on a four-inch silicon wafer. Right: A microfluidic device detached from the silicon substrate. **Figure 5:** Nanoimprinted fluorinated ethylene propylene (FEP) with 5  $\mu\text{m}$  DRIE master @ 265°C (20x).

# Electrochemical Lasso for Trapping Biomolecules inside Zero-Mode Waveguides

**CNF Project Number: 2214-13**

**Principal Investigator(s): Meni Wanunu<sup>1</sup>**

**User(s): Mohammad Amin Alibakhshi<sup>1</sup>, Fatemeh Farhangdoust<sup>2</sup>**

*Affiliation(s): 1. Physics Department, 2. Bioengineering Department; Northeastern University*

*Primary Source(s) of Research Funding: NIH/National Human Genome Research Institute award no. HGO09186*

*Contact: wanunu@neu.edu, m.alibakhshi@northeastern.edu, f.farhangdoust@northeastern.edu*

*Website: <http://www.northeastern.edu/wanunu/>*

*Primary CNF Tools Used: Electron-beam lithography, e-beam evaporation and lift-off*

## Abstract:

Single molecule real time (SMRT) sequencing technology developed by Pacific Biosciences is a robust single molecule DNA sequencing method in which DNA strand replication by an individual DNA polymerase is imaged using fluorescently labeled nucleotides [1-2]. SMRT sequencing, however, suffers from inefficient loading of DNA molecules into the zero-mode waveguides (ZMWs), a sequencing unit that provides the smallest available volume for light detection. In addition, ZMWs are biased towards diffusion-based entry of short DNA templates. To overcome these challenges, our lab introduced two powerful tools, i.e., nanopore ZMW (NZMW) [3] and porous ZMW (PZMW) [4], to electrokinetically capture DNA fragments inside ZMWs. The efficiency of voltage-induced DNA loading into these waveguides is length-independent and is 6-7 orders of magnitude larger than diffusion-based SMRT sequencing. Although NZMW and PZMW are effective tools for capturing long DNAs in picogram levels, they are fabricated on top of free-standing ultrathin membranes, which makes them fragile and difficult to scale up. In this work, we introduce a new technique in order to draw DNA fragments inside ZMWs fabricated on fused silica substrates.

## Summary of Research:

The working principle of our design relies on embedding metallic electrodes (platinum, Pt) under the waveguides to create an electric field. This electrode film is separated from the ZMWs made of aluminum, by a dielectric layer. Application of a voltage to the electrode layer with the use of proper electrolyte allows efficient electrophoretic DNA capture at picogram levels. Electron-beam lithography, e-beam evaporation, and lift-off are used to fabricate 100 nm ZMW arrays in wafer scale. Our new device eliminates the need for free-standing membranes and enables scaled-up fabrication, reduces the background optical noise, and improves the DNA loading efficiency by several orders of magnitude.

We have continued to fabricate these devices for DNA sequencing experiments. Figure 1 shows PtZMWs' fabrication process and Figure 2 is scanning electron microscope image of the top view and cross-section of an array of ZMWs.

## References:

- [1] Levene, M. J.; Korlach, J.; Turner, S. W.; Foquet, M.; Craighead, H. G.; Webb, W. W., Zero-mode waveguides for single-molecule analysis at high concentrations. *science* 2003, 299 (5607), 682-686.
- [2] Eid, J.; Fehr, A.; Gray, J.; Luong, K.; Lyle, J.; Otto, G.; Peluso, P.; Rank, D.; Baybayan, P.; Bettman, B., Real-time DNA sequencing from single polymerase molecules. *Science* 2009, 323 (5910), 133-138.
- [3] Larkin, J.; Foquet, M.; Turner, S. W.; Korlach, J.; Wanunu, M., Reversible positioning of single molecules inside zero-mode waveguides. *Nano letters* 2014, 14 (10), 6023-6029.
- [4] Jadhav, V.; Hoogerheide, D. P.; Korlach, J.; Wanunu, M., Porous Zero-Mode Waveguides for Picogram-Level DNA Capture. *Nano letters* 2018, 19 (2), 921-929.

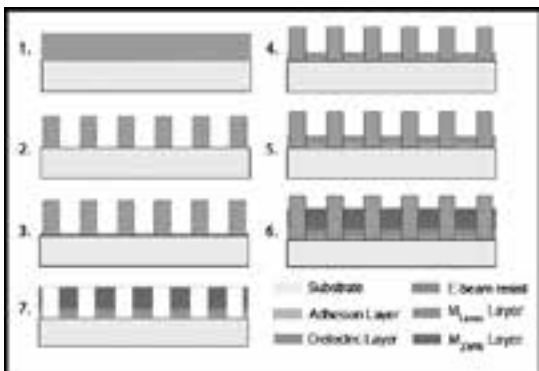


Figure 1: Schematic representation of ZMW fabrication process: 1. Spincoat negative e-beam resist and bake. 2. Expose using e-beam lithography and develop resist. 3. E-beam evaporation of an adhesion layer on the fused silica substrate, followed by deposition of Pt layer (electrode), alumina (dielectric layer), and 100 nm aluminum (cladding layer of ZMWs). 4. Lift-of-resist using 1165 stripper.

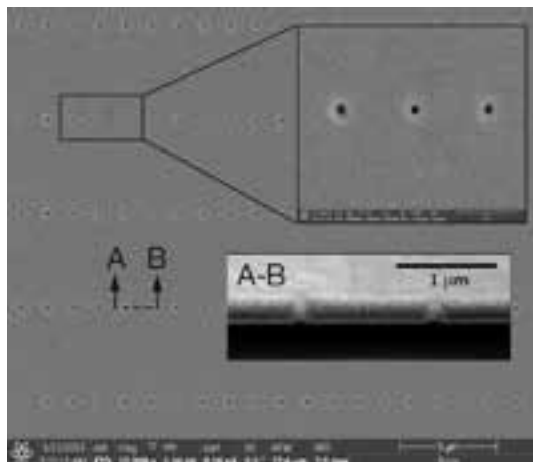


Figure 2: SEM of an array of 100 nm diameter ZMWs. Cross-section of the ZMWs shown in the bottom inset demonstrates that the cladding layer (aluminum) is separated from the electrode (Pt) by a dielectric layer ( $Al_2O_3$ ).

# Zero-Mode Waveguides Fabrication for DNA Nucleosome Sequencing Application

**CNF Project Number: 2214-13**

**Principal Investigator(s): Meni Wanunu**

**User(s): Pengyu Zheng**

*Affiliation(s): Department of Physics, Northeastern University*

*Primary Source(s) of Research Funding: NIH/NHGRI R01*

*Contact: wanunu@neu.edu, zheng.p@husky.neu.edu*

*Website: <http://www.northeastern.edu/wanunu/index.php>*

*Primary CNF Tools Used: JEOL 6300 electron-beam lithography system*

## Abstract:

**Cost-effective deoxyribonucleic acid (DNA) sequencing has been one of the most important goal in this era of biological and health science study. Zero-mode waveguide (ZMW) has been proven to be a promising technology for single DNA sequencing [1]. This research aims to apply this technology on directly reading DNA nucleosome sequence while detecting nucleosome modification in parallel. This could be a new innovative means of probing for epigenetics [2].**

## Summary of Research:

ZMW is essentially a  $\sim 100$  nm size well that allows a confined region of laser illumination at its bottom. Once a DNA/polymerase complex is immobilized in the ZMW, the sequence can be read by imaging the incorporation of fluorescence-labeled nucleotides [1]. In our research, we plan to use it on DNA nucleosome complex instead of a simple single strand DNA. Thus the information of histone modification can be probed at the same time as we sequence the DNA, and the modification site can be located in the genome.

The proposed structure for ZMW chips is an array of  $\sim 100$  nm holes on a thin film of aluminum on top of a glass wafer, similar to other designs under the same

CNF project. We have finished a few trainings for some necessary fabrication tools, but haven't yet started the fabrication. Meanwhile colleagues Mohammad Alibakhshi and Fatemeh Farhangdoust are working on optimizing the protocol for glass wafer based ZMW fabrication.

## References:

- [1] Levene, M. J.; Korlach, J.; Turner, S. W.; Foquet, M.; Craighead, H. G.; Webb, W. W. *Science* 2003, 299, 682-686.
- [2] Shema, Efrat, et al. "Single-molecule decoding of combinatorially modified nucleosomes." *Science* 352.6286 (2016): 717-721.



# Dual-Gradient Microhabitat Platform for Microalgae Growth

**CNF Project Number: 2262-13**

**Principal Investigator(s): Dr. Mingming Wu**

**User(s): Fangchen Liu**

*Affiliation(s): Department of Biological and Environmental Engineering*

*Primary Source(s) of Research Funding: United State Department of Agriculture  
- National Institute of Food and Agriculture*

*Contact: mm272@cornell.edu, FL373@cornell.edu*

*Website: <http://biofluidics.bee.cornell.edu/>*

*Primary CNF Tools Used: Heidelberg mask writer DWL2000, ABM contact aligner, P10 profilometer, MVD 100*

## Abstract:

**The occurrence of harmful algal blooms (HABs) is increasing at an alarming rate worldwide, threatening water resources and aquatic ecosystems. Nutrients are known to trigger the onset of HABs and systematic investigation at cellular level is lacking. To study the combination effects of multiple nutrients on microalgae growth in a high throughput way, a dual-gradient microhabitat platform was designed, fabricated, and characterized.**

## Summary of Research:

Harmful algal blooms, or HABs, are serious environmental problems, where a sudden growth of algae or cyanobacteria poses threat to freshwater and marine ecosystems. HABs deteriorate drinking water quality and have huge environmental and economical costs. Nutrient enrichment is believed to be the fundamental cause of HABs, and climate change may further intensify the problem [1]. However, there lacks a quantitative/mechanistic understanding of the roles of environmental factors in the onset of HABs at cellular level. The goal of this project is to investigate the synergistic roles of multiple environmental factors in the growth of cyanobacteria.

Environmental conditions known to affect algae growth include nutrients, mainly nitrogen (N) and phosphorous (P), light intensity and temperature. These conditions are hard to control in nature, and also cannot be quantified in a high throughput way in flasks and chemostats. Previously, an high throughput array microhabitat platform has been developed in our lab that is suitable for monitoring growth of photosynthetic microbes [2]. This platform is capable of generating a stable single nutrient gradient. Using this platform, we discovered that the growth rates of *Chlamydomonas reinhardtii* in the presence of  $\text{NH}_4\text{Cl}$  gradient fit into a modified Monod kinetics model with the half saturation constant of  $\text{NH}_4\text{Cl}$  to be  $1.2 \pm 0.3 \mu\text{M}$ .

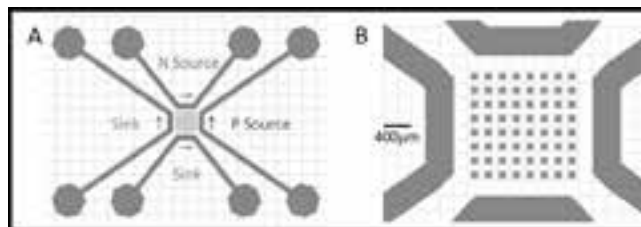


*Figure 1: Dual-gradient microfluidic platform design. A. Top view of a device. B. A zoomed-in view of microhabitats and channel. The  $8 \times 8$  array of  $100 \mu\text{m}$  cubic habitats are separated by  $100 \mu\text{m}$  from each other. These habitats are surrounded by four channels with width of  $400 \mu\text{m}$  and height of  $200 \mu\text{m}$ . N source and P source runs through the top and right channel respectively, and the other channels are sink channels. A gradient is generated for each chemical species in the microhabitat array region through molecular diffusion.*

In this project, we developed a microhabitat platform that can provide dual nutrient gradients to facilitate a more realistic condition found in nature. The design of our device is shown in Figure 1, which consists of 64 microhabitats in the form of an  $8 \times 8$  array and each habitat is  $100 \mu\text{m} \times 100 \mu\text{m} \times 100 \mu\text{m}$ . The microhabitat array is surrounded by two sets of side channels each with the width of  $400 \mu\text{m}$  and height of  $200 \mu\text{m}$ . In each set of side channels, we can run source media (with N, or P) and blank media respectively, and a stable gradient can be simultaneously generated along vertical and horizontal directions.

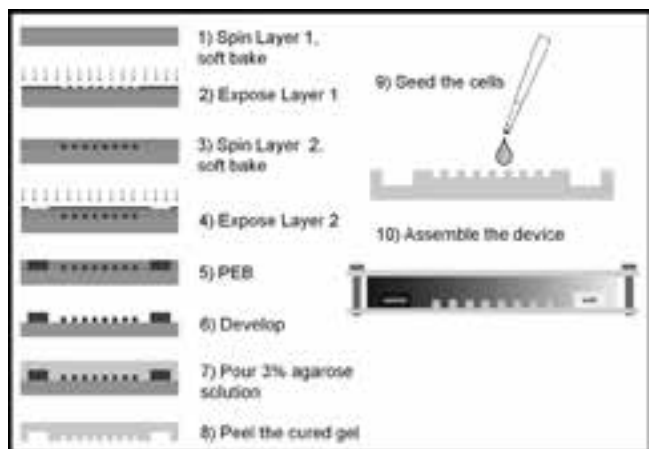


Figure 2: Schematics of a two-layer SU-8 photolithography procedure and the final microfluidic device assembly. First, a 100  $\mu\text{m}$  resist layer was spun on wafer, soft baked and exposed. Then, another 100  $\mu\text{m}$  layer was spun on top and baked together overnight, followed by the second exposure and post exposure bake (PEB) for the 200  $\mu\text{m}$  structures. The unexposed resist was then developed and the structures went through hard bake. For device assembly, the pattern was imprinted on an agarose gel, and cells were seeded in the microhabitats. The gel was then sandwiched between glass slide and manifolds and tightened by screws.

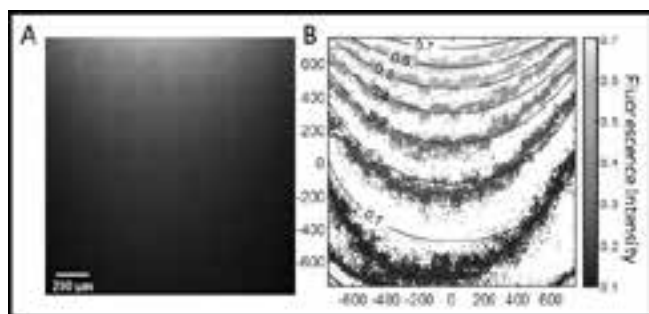


Figure 3: Characterization of the device using fluorescein (FITC) dye. A. FITC solution was introduced to top channel and buffer solution without FITC were introduced in the other three channels at  $t = 0$ . The fluorescence image is taken at the middle where the microhabitats are at  $t = 60$  min. B: Contour plot of simulated (lines) and experimental (dots) concentration fields at  $t = 60$  min. Concentration is scaled such that the concentration in source channel is 1 and sink channel 0.

Soft lithography was used to make this dual-gradient microhabitat platform, which involves fabricating the silicon master mold and molding the pattern onto agarose gel for device assembly. Schematics of the step by step procedure are shown in Figure 2. The silicon master mold was fabricated using two layer SU-8 negative resist photolithography, since the channels are 200  $\mu\text{m}$  high and the microhabitats are 100  $\mu\text{m}$  high. The post exposure bake (PEB) of the first layer of photo resist was combined with the soft bake of the second layer of the photo resist. Also, it was found that slow temperature ramping and relaxation time after each bake is critical to minimize internal stress in order to prevent resist detachment problem. After developing, the height of the feature were measured using P10 profilometer and a layer of FOTS was deposited using molecular vapor deposition (MVD100) to increase the surface hydrophobicity for easier demolding of agarose gel. To transfer the pattern, boiled 3% agarose solution was poured on the silicon master and peeled once it cured.

The gradient behavior of this dual-gradient platform was characterized using Fluorescein (FITC) dye (Figure 3). 50  $\mu\text{M}$  FITC was flown through the top channel, and blank media in the other channels at  $t = 0$ , and the stable gradient was established via molecular diffusion through the agarose gel. A fluorescence image at 60 min was plotted together with results from a 2D COMSOL simulation, which uses Fick's second law for diffusion and fixed concentrations at the channels as boundary conditions. In Figure 4B, the experimental field matches the simulated concentration field, which indicates the establishment of both gradients. Currently, microalgal growth in both nitrogen and phosphorous gradient are being studied at the same time in this platform.

## References:

- [1] Paerl, Hans W., et al. Environmental Science and Technology (2018): 5519-5529.
- [2] Kim, Beum Jun, et al. Lab on a Chip 15.18(2015): 3687-3694.

# Shear-Rate Controlled Microfluidic Devices to Examine von Willebrand Factor-Mediated Platelet Deposition

**CNF Project Number: 2349-15**

**Principal Investigator(s): Brian J. Kirby**

**User(s): Anjana Jayaraman, Junhyuk (Andrew) Kang**

*Affiliation(s): Sibley School of Mechanical and Aerospace Engineering, Cornell University*

*Primary Source(s) of Research Funding: NIH Project # HL089456, NSF contract # CBET-1706518*

*Contact: kirby@cornell.edu, aj597@cornell.edu, jk2829@cornell.edu*

*Website: <http://blogs.cornell.edu/kirbyresearch/>*

*Primary CNF Tools Used: ABM contact aligner, Class II resist spinners (SU-8), Heidelberg mask writer (DWL 2000), Hamatech mask chrome etch 1, resist hot strip bath, SU-8 hot plates, P10 profilometer*

## Abstract:

Ventricular Assist Devices (VAD) have been known to cause thrombosis, or the formation of clots in blood vessels due to the pumping of blood at high shear rates. Thrombi are formed when platelets aggregate together as a result of many blood-borne agonists and processes. The purpose of our research is to study how strain rates influence how platelets aggregate and adhere to vessel walls. We will be using microfluidic devices to mimic platelet deposition at clinically relevant shear rates, and use fluorescence microscopy to visualize the thrombi.

## Summary of Research:

Our research focus has been to study VAD-related thrombosis. Thrombosis is a process by which platelets aggregate and adhere to blood vessels. This can lead to major health problems, such as nutrient deficiency, higher blood pressure, and stroke [1]. The mechanism through which platelets function is dependent on hemodynamic shear stresses [2,3].

When a ventricular assist device is implanted, it generates supra-physiological shear rates that uncoils a normally globular glycoprotein named von Willebrand Factor. When the protein chain unfolds, it reveals several binding sites that enable tethering to both collagen and platelets [2]. This tether gives platelets sufficient time and contact to collagen to activate via the GP IIb/IIIa integrin and activates the platelets, releasing more prothrombogenic biochemical agonists such as adenosine diphosphate, thromboxane A<sub>2</sub>, and thrombin [5,6]. Our group's objective is to study this mechanism using microfluidic chips made of polydimethylsiloxane (PDMS) that allow for precise strain rate control.

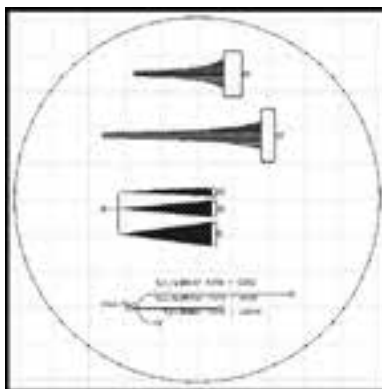


*Figure 1: Computer aided design of channel geometries: (from top to bottom) short and long hyperbolic channels, expansion channels (5°, 10°, 15°), standard width channels (40  $\mu\text{m}$ , 30  $\mu\text{m}$ , 20  $\mu\text{m}$ ).*

The design features three different channel geometries (Figure 1). One channel comprises a single inlet that diverges into three channels, each with a different width (40, 30 and 20  $\mu\text{m}$ ) in order to examine platelet deposition at a constant shear rate. Next, there are three channels that expand gradually at angles of 5°, 10°, and 15°. This design helps us study platelet deposition at constantly varying shear rates.

The third design is a hyperbolic expansion channel. We have incorporated hyperbolic channels of two different lengths; however, in both cases, along the central axis, the flow is extensionally dominated. In both the

standard and hyperbolic expansions, there are square-shaped microposts that exist serve as a dual purpose of preventing channel collapse and for examining the effects of different obstacle geometries and orientations with respect to the flow direction on platelet deposition.

In order to implement our design into a device, we first used the Heidelberg DWL 2000 mask writer to generate

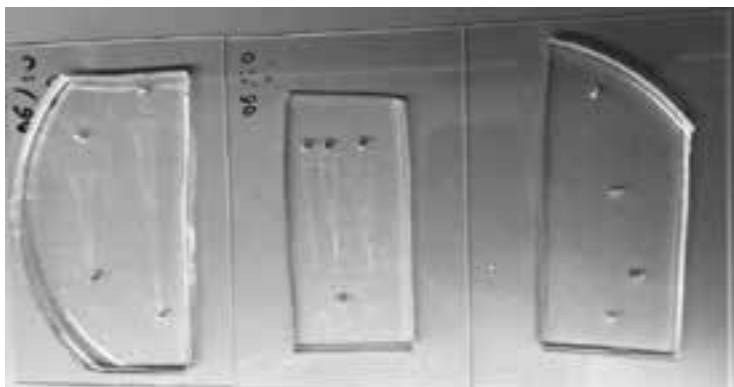


Figure 2: Microfluidic devices made of PDMS plasma bonded to glass surface.

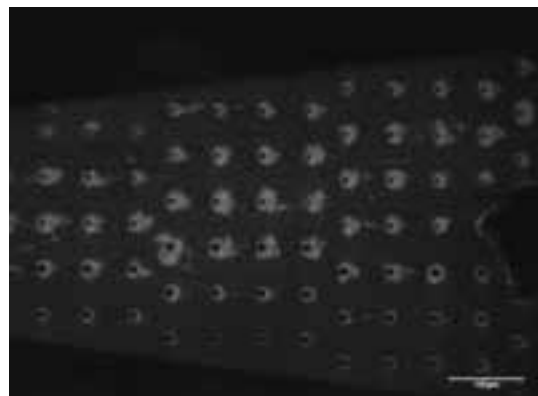


Figure 3: Mepacrine-labelled platelets depositing during perfusion through the 15° expansion channel. Flow rate is 18.8  $\mu\text{L}/\text{min}$  from left to right.

our microfluidic channel design on a chrome-coated glass plate. The chrome sputtered layer was etched on the chrome using the Hamatech Mask Chrome Etch 1, and the resist was stripped using a strip bath. In the class II photolithography room, we spin-coated SU-8 photoresist to a thickness of 50  $\mu\text{m}$ . Bake times and exposure times were calculated based on recommendations provided by experienced CNF personnel [7]. We used the ABM contact aligner with our patterned chrome-coated plate and SU-8 coated wafer to expose the channel features onto the wafer. Following a post-exposure bake and SU-8 developer bath, the features were generated on the silicon wafer. Finally, to check our feature dimensions, we used the P10 profilometer to check the channel thickness.

In order to turn this wafer into a usable device, we poured a 9:1 mixture of Dow Corning Sylgard 184 silicone elastomer and curing agent onto the wafer and used a vacuum pump to create a bubble-free, rigid set of channels. The PDMS was then baked in an oven at 60°C for 150 minutes. Finally, the devices were plasma bonded onto glass slides.

In order to use these devices for imaging platelet deposition, we mix citrated ovine whole blood with mepacrine, a fluorophore taken up by platelets that allows them to be visualized using fluorescent light. We coat the channels with a collagen solution to create a thrombogenic surface so that the platelets can adhere to the glass. In our preliminary work, we have flowed blood through the channels at a constant flow rate and observed platelet deposition over several minutes (Figure 3).

### References:

- [1] Eckman, P. M., and John, R. Bleeding and Thrombosis in Patients With Continuous-Flow Ventricular Assist Devices. *Circulation*. <https://doi.org/10.1161/circulationaha.111.040246> (2012).
- [2] Casa, L. D. C., Deaton, D. H., and Ku, D. N. Role of high shear rate in thrombosis. *Journal of Vascular Surgery*. <https://doi.org/10.1016/j.jvs.2014.12.050> (2015).
- [3] Selgrade, B. P., and Truskey, G. A. Computational Fluid Dynamics Analysis to Determine Shear Stresses and Rates in a Centrifugal Left Ventricular Assist Device. *Artificial Organs*. <https://doi.org/10.1111/j.1525-1594.2011.01416.x> (2012).
- [4] Yang, F., Kormos, R. L., and Antaki, J. F. High-speed visualization of disturbed pathlines in axial flow ventricular assist device under pulsatile conditions. *Journal of Thoracic and Cardiovascular Surgery*. <https://doi.org/10.1016/j.jtcvs.2015.06.049> (2015).
- [5] Maxwell, M. J., Westein, E., Nesbitt, W. S., Giuliano, S., Dopheide, S. M., and Jackson, S. P. Identification of a 2-stage platelet aggregation process mediating shear-dependent thrombus formation. *Blood*. <https://doi.org/10.1182/blood-2006-07-028282> (2007).
- [6] Kragh, T., Schaller, J., Kertzsch, U., Affeld, K., Reininger, A., and Spannagl, M. Platelet adhesion, aggregation, and embolism on artificial surfaces in non-parallel blood flow. *Microfluidics and Nanofluidics*. <https://doi.org/10.1007/s10404-015-1557-5> (2015).
- [7] Cornell NanoScale Facility. SU-8 Processing Suggestions [PDF file]. Retrieved from <https://www.cnfusers.cornell.edu/sites/default/files/Equipment-Resources/SU8%20processing%20suggestions.pdf> (2013).

# Handheld Chem/Biosensor Combining Metasurfaces and Engineered Sensor Proteins to Enhance Surface Plasmon Resonance (SPR)

**CNF Project Number: 2430-16**

**Principal Investigator and User(s): Lori Lepak**

*Affiliation(s): Phoebus Optoelectronics, LLC*

*Primary Source(s) of Research Funding: Department of Defense*

*Contact: llepak@phoebusopto.com*

*Website: www.phoebusopto.com*

*Primary CNF Tools Used: DWL2000 photomask writer, ASML DUV stepper, SC4500 evaporators, Oxford 81 etcher, Zeiss SEM, DISCO dicing saw*

## Abstract:

Since 2003, Phoebus Optoelectronics has enabled custom R&D solutions in the fields of Plasmonics, Metamaterials, Antennas, and Sensors. We work closely with our customers throughout device development, from prototype realization to small volume manufacturing. Our R&D portfolio spans the spectral ranges of visible light, infrared, terahertz, and microwave radiation, for applications in high resolution infrared imaging systems, wavelength and polarization filtering, tunable optical components, beam forming and steering, solar cells and renewable energy devices, and chemical and biological toxin sensors. Our agile team makes extensive use of the resources at the CNF for our nano/micro fabrication and testing, to provide cost efficiency and rapid turnaround.

In the present report, we discuss recent efforts to develop a chem/bio toxin detection system, which provides the state-of-the-art sensitivity of a typical benchtop system with the superior SWaP performance of a handheld system. Our surface plasmon resonance (SPR)-based sensor is expected to be capable of detecting ng/mL concentrations of selected toxins in under five minutes.

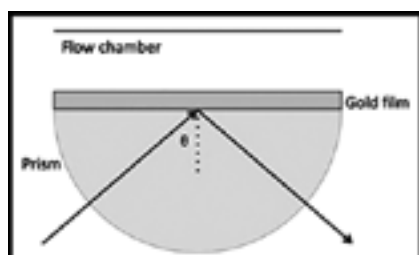


Figure 1: Surface plasmon resonance spectroscopy schematic. Reproduced from reference [8].

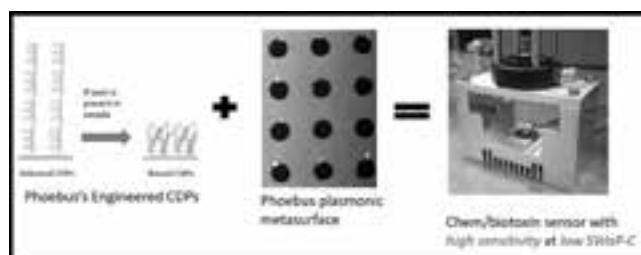


Figure 2: Phoebus-engineered sensor system combines; (a) Designed CDPs that undergo extreme conformational changes upon binding target, (b) Gold metasurface, patterned to maximize transmission at SPR resonant wavelength into (c) a high sensitivity, low SWaP-C chem/biotoxin sensor system.

## Summary of Research:

SPR is a highly sensitive, label-free optical detection technique, whose underlying physics is illustrated in reflection mode in Figure 1. A laser passes through a prism, at an incident angle  $\theta$ , on a gold film which is in contact with an analyte solution on its opposite side. The illumination produces an evanescent wave (surface plasmon), which significantly reduces the reflectance at a resonant angle. The resonant angle is

strongly dependent on the local refractive index, within a few tens of nanometers of the gold surface, and thus is extremely sensitive to enzyme-substrate or antibody-antigen binding events near the surface. The resonance is independent of the geometric configuration of the optical elements (see [8] for mathematical derivation.), such that these results also apply to devices that operate in transmission mode.

As illustrated in Figure 2, Phoebus has combined two recently developed technologies to enable an SPR sensor system that provides enhanced sensitivity at lower SWaP, relative to technologies currently on the market.

First, Phoebus detects toxins using Computationally Designed Proteins (CDP's), engineered to undergo an exceptionally large conformational change upon binding their specific target. This conformation change increases the density of the protein layer, thereby locally increasing the effective refractive index, which in turn enhances the SPR signal by a factor of 1000x competing systems.

Second, Phoebus uses the resources of the CNF to fabricate plasmonic chips patterned with a metamaterial surface to enable Extraordinary Optical Transmission (EOT), a phenomenon unique to metastructures in which light is transmitted through apertures much smaller than the incident wavelength, at anomalously large intensities relative to the predictions of conventional aperture theory. EOT was first observed by T.W. Ebbesen in 1998 [1]. Since its founding in 2003, Phoebus has successfully harnessed EOT by incorporating metasurfaces into devices used to perform light filtering [2-3], photon sorting [4-5], polarimetric detection [6], high speed optical detection [7], and most recently, in our SPR plasmonic sensor chips [8].

These two innovations are combined by attaching the engineered CDP's to the patterned gold metasurface using standard thiol-based attachment chemistry, to make a disposable sensor chip. As shown in Figure 3, this chip is inserted into the complete 3D printed module. All of the optical elements are already assembled in-line as indicated, for a transmission based detection system. Except for Phoebus's disposable sensor chip, all of the optical components are inexpensively commercially available, which helps to make our overall system a highly cost-effective toxin sensing solution.

Our most recent generation of metasurface chips, shown in a scanning electron microscope (SEM) image in Figure 4, consist of an array of holes in a gold film, which serve both to bind the CDPs and to undergo SPR. To make the chip, we patterned the wires using the ASML deep ultraviolet photolithography system, evaporated Cr/Au, and performed a liftoff. This process is capable of consistently producing holes down to  $\sim 200$  nm in diameter, with smooth enough sidewalls for an operable optical device.

#### References:

- [1] Ebbesen, T.W., et al., "Extraordinary optical transmission through sub-wavelength hole arrays." *Nature*, (1998). 391(6668): p. 667-669.
- [2] Crouse, D. "Numerical modeling and electromagnetic resonant modes in complex grating structures and optoelectronic device applications." *Electron Devices, IEEE Transactions on* 52.11 (2005): 2365-2373.
- [3] Crouse, D., and Keshavareddy, P. "Polarization independent enhanced optical transmission in one-dimensional gratings and device applications." *Optics Express* 15.4 (2007): 1415-1427.
- [4] Lansey, E., Crouse, D., et al. "Light localization, photon sorting, and enhanced absorption in subwavelength cavity arrays." *Optics Express* 20.22 (2012): 24226-24236.
- [5] Jung, Y.U; Bendoy, I; Golovin, A.B; and Crouse, D.T. "Dual-band photon sorting plasmonic MIM metamaterial sensor." *Proc. SPIE 9070, Infrared Technology and Applications XL, 90702X* (June 24, 2014); doi:10.1117/12.2050620.
- [6] Crouse, D., and Keshavareddy, P. "A method for designing electromagnetic resonance enhanced silicon-on-insulator metal-semiconductor-metal photodetectors." *Journal of Optics A: Pure and Applied Optics* 8.2 (2006): 175.
- [7] Mandel, I.; Gollub, J.; Bendoy, I; Crouse, D. Theory and Design of A Novel Integrated Polarimetric Sensor Utilizing a Light Sorting Metamaterial Grating. *Sensors Journal, IEEE*, (2012): Vol. PP, 99
- [8] Lepak, L., et al. "Handheld chem/biosensor using extreme conformational changes in designed binding proteins to enhance surface plasmon resonance (SPR)" *Proc. SPIE 9862, Advanced Environmental, Chemical, and Biological Sensing Technologies XIII, 9862-7* (April 17, 2016); doi:10.1117/12.2222305.



Figure 3: a) Complete Phoebus handheld biosensor system, b) removable module with plasmonic chip.

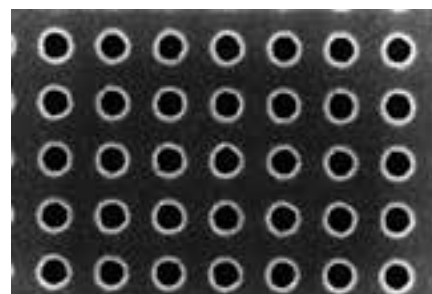


Figure 4: SEM image of a metasurface used in disposable biosensor chip.

# Metasurface Enhanced Infrared Spectroscopy for Live Cells

**CNF Project Number: 2472-16**

**Principal Investigator(s): Gennady Shvets**

**User(s): Steven He Huang, Junlan Lu, Robert Delgado**

*Affiliation(s): Applied and Engineering Physics, Cornell University*

*Primary Source(s) of Research Funding: Cornell University internal funding*

*Contact: gs656@cornell.edu, hh623@cornell.edu, jl3286@cornell.edu, rd377@cornell.edu*

*Website: <http://shvets.aep.cornell.edu>*

*Primary CNF Tools Used: JEOL 9500, SC4500 evaporator, Zeiss Supra SEM, PDMS casting station, Anatech resist strip*

## Abstract:

**Infrared (IR) spectroscopy is a powerful tool for biological analyses since it is a label-free, non-invasive technique that provides information on molecular composition. IR spectroscopy of live cells, however, remains challenging due to the strong attenuation of mid-IR light in water. In our lab, we are investigating the use of metasurface-enhanced infrared spectroscopy (MEIRS) to measure live cells in cell culture. The cells are grown on a nanoplasmonic metasurface and we utilize the strong near-field hotspot of the plasmonic nanoantennas to collect IR spectra from the cells. We have demonstrated the spectral imaging of cells adhered on the metasurface as well as spectroscopically probing the response of the cells to different drugs.**

## Summary of Research:

Infrared (IR) spectroscopy, in which materials are identified through their molecular vibration fingerprints, has a wide range of applications in chemistry, geology, and material sciences. Applied to biological tissues, IR spectroscopy can be used as a histology or cytopathology tool, identifying tumor tissues from normal tissues and looking at the effect of chemotherapeutics on cancer cells. We have developed a new technique, using surface-enhanced infrared absorption (SEIRA) from plasmonic metasurfaces to probe the IR absorption of biomolecules and cells. This technique, which we named metasurface-enhanced infrared spectroscopy (MEIRS), had been used to measure protein monolayers [1], as well as fixed cancer cells [2]. Our current work involves further extending this technique to the measurement of live cells grown on the metasurface, in particular focusing on the spectroscopic investigation of different drugs and stimuli on these cells.

We fabricate our plasmonic metasurface in the CNF cleanroom. Starting from an IR-transparent  $\text{CaF}_2$  substrate, we define the patterns on poly(methyl methacrylate) (PMMA) using electron-beam lithography with the JEOL 9500 system. This is followed by gold evaporation and lift off in acetone to create a working metasurface device. Scanning electron microscopy (SEM) image of our plasmonic metasurface is shown in Figure 1. In order to grow the cells on this metasurface and deliver different drugs as needed, we use a polydimethylsiloxane (PDMS) microfluidic cell culture, which is also fabricated at the CNF.

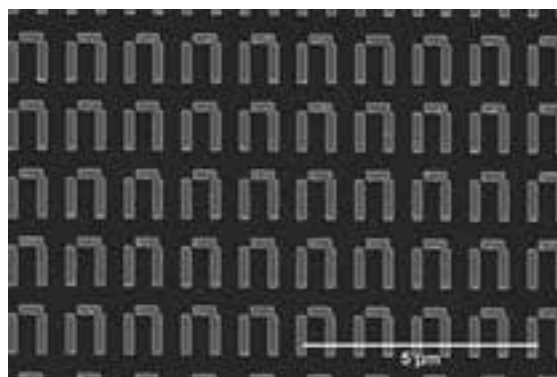


*Figure 1: SEM micrograph of the plasmonic metasurface. The metasurface nanoantennas are fabricated in an array covering approximately  $250\ \mu\text{m} \times 250\ \mu\text{m}$ . These nanoantennas are designed to have specific optical resonances, matching the molecular vibrations of the biomolecules of interest (primarily lipids and proteins). Scale bar:  $5\ \mu\text{m}$ .*

To measure live cells, the metasurface is treated with fibronectin and the cells are initially seeded on the metasurface in a multi-well dish. After the cells are adhered on the metasurface, the metasurface is assembled on a PDMS microfluidic cell culture chamber and measured in reflection mode with an IR microscope coupled to a Fourier Transform IR (FTIR) spectrometer. Our plasmonic metasurface has optical resonances in the

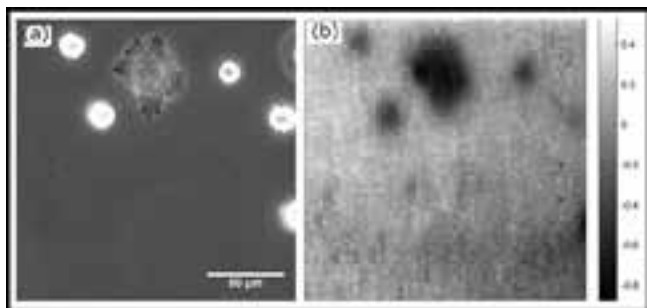


Figure 2: IR spectroscopic imaging using MEIRS combined with a focal plane array detector. (a) Phase contrast microscopy of HeLa cells grown on a metasurface. (b) The same metasurface imaged through MEIRS. The score of a principal component from PCA is plotted here. The MEIRS image reflects the cell's adhesion to the metasurface. Scale bar: 50  $\mu\text{m}$ .

mid-IR, and when probed by IR light, it generates intense plasmonic “hotspots” in the vicinity of these plasmonic nanoantennas, with a penetration depth of 50-100 nm into the surrounding. Sensing cells with our metasurface relies on the spatial overlap between the cells and these plasmonic hotspots, and thus our signal is very sensitive to the degree of cell adhesion on the metasurface. Figure 2 shows a comparison between an image of HeLa cells on the metasurface obtained with phase contrast microscopy and the same cells imaged through MEIRS using an IR focal plane array detector. The MEIRS image was obtained by processing the spectra using principal component

analysis (PCA). The distribution and morphology of the cells seen with the two techniques agree well, and this demonstrates that we can clearly see cells adhered on the metasurface through MEIRS.

We have applied MEIRS to the study of chemotherapeutic drugs on cancer models. Here, we measured the spectroscopic response of feline carcinoma cells to four drug combinations, control (no drug), salinomycin, doxorubicin, and a combination of both salinomycin and doxorubicin. Salinomycin is a known inhibitor of multidrug resistance protein 1 in cancer cells, and although it does not lead to high cytotoxicity alone, it increases the potency of doxorubicin when administered in combination. Figure 3 shows the MEIRS spectra measured from these cells after 2-days drug treatment. Cells treated with the combination treatment had much lower IR absorption due to proteins and lipids, and this is attributed to the cell detachment from the metasurface caused by doxorubicin-induced apoptosis. This result agrees with what we expect from salinomycin acting as a sensitizer for doxorubicin. The spectra were further analyzed by PCA and the score plot for the 1<sup>st</sup> and 2<sup>nd</sup> principal components (PCs) is shown in Figure 4. From the PCA score plot, clear separation between the cells with different treatment can be seen, even for treatments that do not significantly affect cell viability (control vs. salinomycin).

## References:

- [1] Wu, C., et al. Fano-resonant asymmetric metamaterials for ultrasensitive spectroscopy and identification of molecular monolayers. *Nat. Mater.* 11, 69-75 (2011).
- [2] Kelp, G., et al. Application of metasurface-enhanced infra-red spectroscopy to distinguish between normal and cancerous cell types. *Analyst* 144, 1115-1127 (2019).

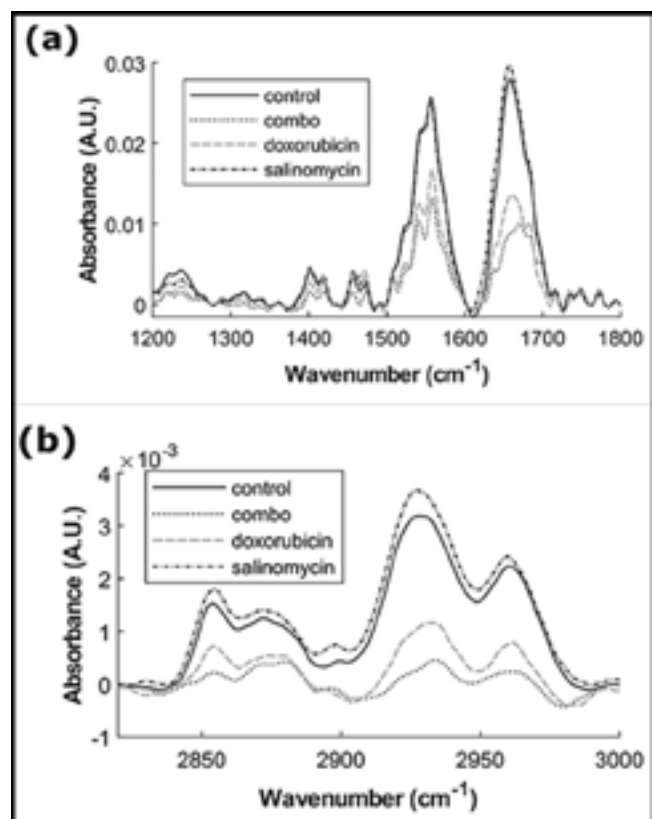


Figure 3: MEIRS spectra for feline carcinoma cells with different drug treatments. (a) Fingerprint region and (b) Lipid absorption region.

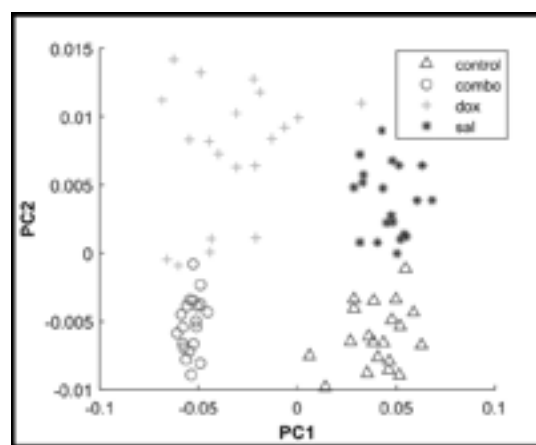


Figure 4: PCA score plot of the IR absorbance spectra from cells with different drug treatments. Data points for cells with the same treatment cluster among themselves, and cells with different drug treatment can be clearly distinguished from each other.

## Retinal Implant Project

**CNF Project Number: 2504-16**

**Principal Investigator(s): Douglas Shire, Ph.D.**

**User(s): Marcus Gingerich, Ph.D.<sup>1,4</sup>, Douglas Shire, Ph.D.<sup>1,3,4</sup>, Patricia Wong<sup>2,4</sup>**

*Affiliation(s): 1. Dept. of Electrical Engineering, Cornell University; 2. Dept. of Neuro-Ophthalmology, Massachusetts Eye and Ear Infirmary; 3. VA Cleveland Healthcare System; 4. Bionic Eye Technologies, Inc.*

*Primary Source(s) of Research Funding: NIH/NIBIB U01EB018873; NIH/NIBIB R01EB022013, Massachusetts Lions Eye Research Fund, DoD W81XWH-16-2-0015*

*Contact: dbs6@cornell.edu, mdg37@cornell.edu, pwong@bionicvisiontechnologies.com*

*Website: <http://www.bostonretinalimplant.org>*

*Primary CNF Tools Used: PT-72, lithography toolset/MA6, DWL2000, evaporators, AJA sputter, Gamma spray coater, SEMs, gold electro-plating, Class 2 lithography toolset, Oxford PECVD, Oxford 100 etcher, Glenn 1000, YES polyimide oven, VersaLaser*

### Abstract:

The purpose of the Retinal Implant Project is to restore useful vision to patients who are blind with degenerative retinal diseases. The primary illnesses we hope to treat are retinitis pigmentosa (a primary cause of inherited blindness) and age-related macular degeneration (the leading cause of blindness in the developed world). Both these diseases cause the eventual destruction of the photoreceptor cells — rods and cones — in the retina, leaving intact the ganglion cells that transmit electrical impulses (and hence visual information) to the brain. The ganglion cells may be stimulated, however, with biphasic current pulses from a microfabricated electrode array. Blind surgical volunteers have consistently described visual percepts that resulted from such stimuli, and this has led our team to develop a wireless, implantable retinal prosthesis.

### Summary of Research:

The implanted portion of our device consists of power and data secondary receiving coils, and in a sealed titanium (Ti) can a small number of discrete components, and a custom designed application specific integrated circuit (ASIC) that consists of circuitry for clock and data recovery, current drivers for electrodes in a stimulating electrode array, and a programmable function generator capable of stimulating with a wide range of pulse widths and amplitudes. The current outputs drive high-charge capacity sputtered iridium oxide film (SIROF) stimulating electrodes, which in turn give rise to the visual percepts mentioned above.

CNF-fabricated components of this system have included various proof-of-concept test structures and tools used in the research effort and an integrated combination flexible circuit and stimulating electrode array. Si wafers serve as carriers for these freestanding films during processing. The electrode leads are fabricated inside of 'sandwiches' of polyimide and amorphous silicon carbide (SiC), while the SIROF electrodes are reactively sputter-deposited.

Assembly of the intraocular components of the prosthesis is accomplished by flip chip solder ball bonding of the IC and solder attachment of discrete components onto an internal flexible circuit board that is hermetically sealed into an ultraminiature Ti can. The RF coils are soldered and glued to the integrated external flex-array that is in turn thermosonically bonded to the hermetic feedthrough of the Ti can. Finally, the thermosonic bonds are protected and insulated with an over-mold. An external patient interface unit, will consist of a video camera for capturing images, a digital signal processor, and a radio frequency (RF) transmitter and coil to relay power and data to the implanted device.

Scientific challenges still remain in realizing a chronically implantable retinal prosthesis. While our first-generation device was primarily encapsulated in polymers for short term proof-of-concept implant studies, our second-generation system focused on a system that would last many years *in vivo*. Our more recent efforts have focused on developing a device with 256+ stimulation channels,

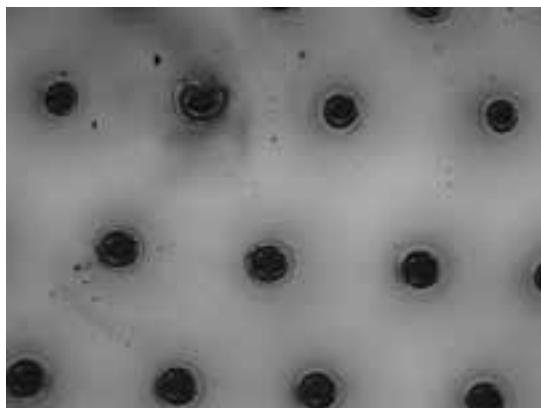


Figure 1: A image of through-wafer holes in a fused silica wafer made with the CNF VersaLaser.

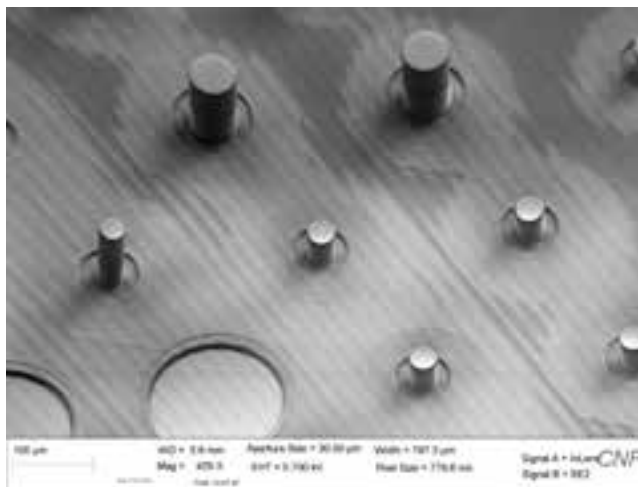


Figure 2: An SEM image of an electrode array of SU-8-based penetrating electrodes and planar electrodes fabricated on the same flexible substrate.

which is still small enough and of a configuration to be easily implanted in the ocular orbit and continue to function for many years *in vivo*. Thus, a major effort has been the development of a technological platform to build a robust, hermetically packaged, high-density subretinal visual prosthesis with a lifetime of > 10 years in biological saline that is scalable to hundreds of I/O channels.

Recent efforts in the CNF have included developing improvements to bonding of electrode arrays to Pt-pin ceramic feedthroughs by electroplating Au onto the surface of the platinum (Pt) pins. This has increased the reliability of the bonds between the electrode array and the ceramic feedthrough. Improvements in assembly techniques, underfilling, overmolding and final parylene-C protection have yielded a passive retinal implant system that has been successfully implanted in an animal model for several months with no significant adverse effects.

Other efforts in the CNF have included developing a fabrication process for indwelling electrodes for long-term implantation in brain tissue. The process currently utilizes low-stress silicon-nitride as the protective layer whereas it is expected that this will transition to silicon-carbide as the material of choice in the future. An economic means of producing a fused-silica feedthrough was also explored utilizing the VersaLaser to create through-wafer holes as shown in Figure 1, but it is not yet clear that this method is capable of producing devices with the necessary hermeticity.

The project has substantially completed the implementation of a microfabrication process to incorporate SU-8-based 3D electrodes into a hybrid electrode array to achieve a more optimal interface between the electrode and the target neural cells. Fabrication work at the CNF has included process development required for such high aspect structures including the challenges of lithography with the presence of extreme topography. Many of these lithographic processes have been successfully realized using the Gamma spray coating tool. Figure 2 shows such an SEM image of an electrode array containing different geometries of SU-8-based penetrating electrodes as well as planar electrodes on the same flexible substrate. The latest microfabrication processes utilize numerous CNF tools including the Heidelberg 2000 mask writer, MA6 aligner, polyimide YES curing oven, PT72 RIE, SC4500 evaporator, Gamma Spray Coater, Au electroplating station, K & S Au ball bonder, Oxford PECVD, Oxford 100 etch tool, Parylene coater, as well as numerous metrology tools.

#### References:

- [1] J. F. Rizzo, J. Wyatt, J. Loewenstein, S. Kelly, and D. Shire, "Methods and Perceptual Thresholds for Short-Term Electrical Stimulation of Human Retina with Microelectrode Arrays," *Investigative Ophthalmology and Visual Science*, vol. 44, no. 12, Dec. 2003, pp. 5355-5361.

# Characterizing the Role of Tumor-Derived Extracellular Vesicles in Breast Cancer

**CNF Project Number: 2580-17**

**Principal Investigator(s): Claudia Fischbach, Lara Estroff**

**User(s): Aaron Chiou, Rupal Khaitan, Minjee Kang**

*Affiliation(s): Meinig School of Biomedical Engineering, Cornell University*

*Primary Source(s) of Research Funding: National Institutes of Health*

*Contact: cf99@cornell.edu, lae37@cornell.edu, aec267@cornell.edu, rk545@cornell.edu, mk2546@cornell.edu*

*Website(s): fischbachlab.org, estroff.mse.cornell.edu*

*Primary CNF Tools Used: Malvern NS300 Nanosight*

## Abstract:

Breast cancer frequently metastasizes to bone, leading to osteolytic bone degradation and poor clinical prognosis. Therapeutic options are largely ineffective as the mechanisms underlying this process remain unclear. Increasing evidence suggests that primary tumors release soluble factors and extracellular vesicles (EVs) that can systemically prime distant organs for eventual metastasis. We have previously shown that primary breast tumors can alter bone materials properties even prior to secondary tumor formation, suggesting possible interference with bone mineralization pathways [1]. However, it remains unclear whether EVs directly contribute to alterations in the bone microenvironment prior to metastasis, whether their generation depends on tumor malignancy, and whether these vesicles differ in content and function. Our project investigates the connections between EV generation, breast cancer malignancy, the functional effect of EVs on stromal cells present in metastatic sites such as the bone.

## Summary of Research:

Tumor-derived EVs, such as microvesicles (0.2-2  $\mu\text{m}$  in size) shed from the plasma membrane and exosomes (30-100  $\mu\text{m}$ ) derived from multi-vesicular bodies, are emerging as critical yet distinct mediators of cell-cell communication in cancer. We are exploring the role of EVs in breast cancer metastasis to bone by isolating EVs from a panel of breast cancer cell lines representing varying degrees of malignancy to 1) characterize the amount and size distribution of EVs generated, and 2) evaluate their interaction with bone-mimetic microenvironments, and 3) evaluate their effects on stromal cells present in the bone microenvironment. By studying these phenomena, we hope to identify novel insights on bone metastasis progression that may inform the development of more effective treatments.

To investigate these questions, we have begun by culturing breast cancer cell lines of varying malignant potential and collecting the EVs shed by these cell lines. We are using the Nanosight instrument to analyze the size distributions and measure concentrations of EVs shed by these cell lines.

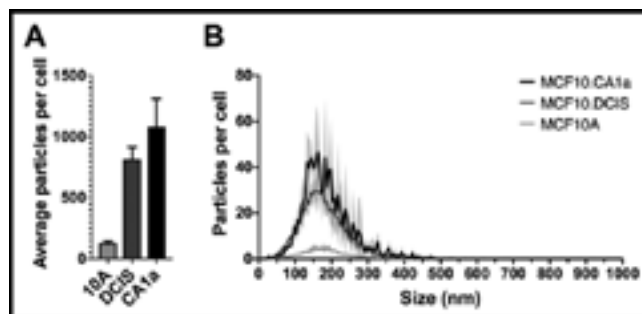


Figure 1: EV concentration and size distributions as measured by Nanosight. (a) Average number of EVs shed per cell increases with breast cancer cell malignancy potential (in increasing order: MCF10A, MCF10.DCIS, MCF10.CA1a). (b) Histograms of EV size distribution indicate increasing amounts of both microvesicles and exosomes shed by cells of increasing malignancy potential.

Our findings in Figure 1 indicate that compared to their benign counterparts, cell lines that represent more invasive and metastatic potential shed a greater amount of EVs per cell, with increases in both microvesicles and exosomes.

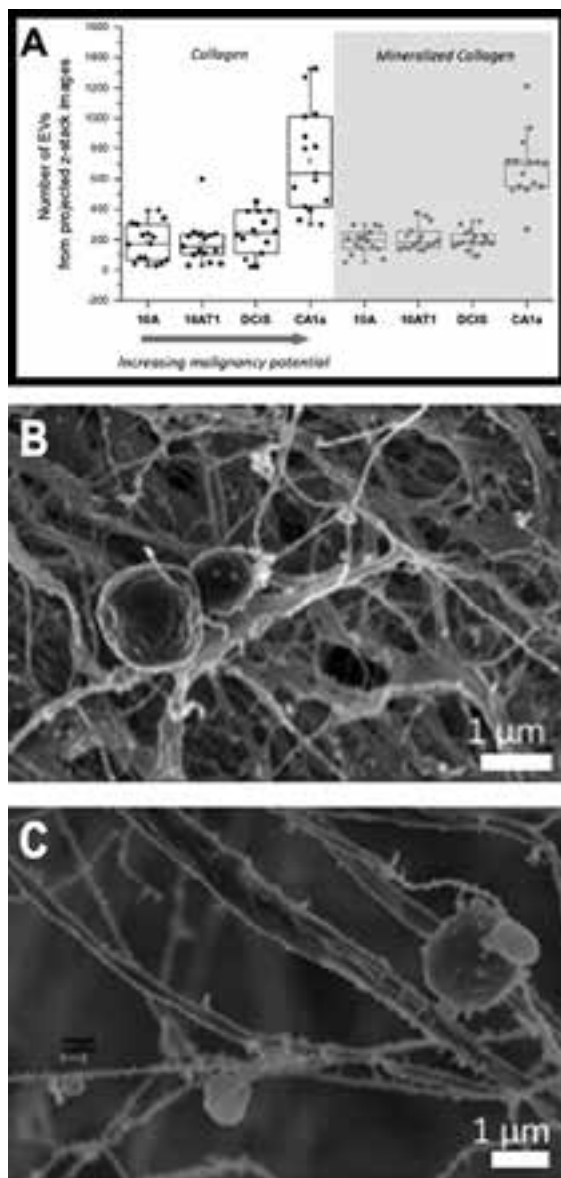


Figure 2: EVs within non-mineralized and mineralized collagen scaffolds analyzed via confocal imaging and SEM. (a) EVs shed from more malignant breast cancer cells (MCF10CA1a) show better binding ability than those shed from less malignant cells both in microenvironments. (b,c) Representative SEM images of MCF10CA1a cell-shed EVs bound to (b) collagen fibrils and (c) mineralized collagen fibrils.

Next, we have also labelled these EV populations and incubated them into collagen scaffolds with and without mineralization to examine their interactions with bone-mimetic microenvironments. As shown in Figure 2, we have imaged these EVs via confocal microscopy and found that the number of EVs bound to these bone-mimetic matrices was 3-8 fold greater when derived from more malignant cells compared to less malignant cells. Using scanning electron microscopy (SEM), we can visualize EVs from malignant cells bound to the non-mineralized and mineralized collagen fibrils in the bone-mimetic microenvironments.

These findings suggest that tumor-shed EVs, in particular those from more malignant tumor cells, can effectively bind to components of the bone microenvironment, and thus may play a role in priming the bone for subsequent metastasis. We are pursuing further investigation of the mechanisms by which these EVs bind to the bone microenvironment, as well as the effects of these EVs on bone-resident stromal cells and tumor cells within bone-mimetic microenvironments.

#### References:

- [1] He F, Chiou AE, Loh HC, Lynch ME, Seo BR, Song YH, Lee MJ, Hoerth R, Bortel E, Willie B, Duda G, Estroff LA, Masic A, Wagermaier W, Fratzl P, Fischbach C. Multiscale characterization of the mineral phase at skeletal sites of breast cancer metastasis. *Proceedings of the National Academy of Sciences*, 114(40), 10542-10547. <https://doi.org/10.1073/pnas.1708161114> (2017).

# Circulating Extracellular Vesicles and Physical Stress in ME/CF

**CNF Project Number: 2590-17**

**Principal Investigator(s): Maureen R. Hanson**

**User(s): Adam O'Neal, Ludovic Giloteaux**

*Affiliation(s): Department of Molecular Biology and Genetics, Cornell University, Ithaca, NY 14853*

*Primary Source(s) of Research Funding: National Institutes of Health*

*Contact: mrh5@cornell.edu, ajo39@cornell.edu, lg349@cornell.edu*

*Website: <https://neuroimmune.cornell.edu/research/vesicles-and-signaling/>*

*Primary CNF Tools Used: Malvern NS300 Nanosight*

## Abstract:

**Myalgic Encephalomyelitis/Chronic Fatigue Syndrome (ME/CFS) is a chronic, complex, multisystemic condition characterized by long-term fatigue that does not improve with rest, persists for more than six months, and other associated symptoms, and cannot be explained by any other underlying medical condition. The cause of ME/CFS remains unknown, and no established diagnostic tests, nor universally effective treatment are available.**

## Introduction:

A hallmark of ME/CFS is a distinctive Post-Exertional Malaise (PEM), which occurs following physical or cognitive exertion and can last from days to weeks. Research on the physiological responses to exercise in ME/CFS subjects supports disruptions and disturbances in the central nervous system, cardiovascular and immune system with impaired muscular energy metabolism. Following exercise challenge, skeletal muscle can impact the whole body physiology through secretion of diverse biomolecules into exosomes (exersomes) such as muscle-derived humoral factors (myokines) and exercise-induced humoral factors (exerkines) in a regulated and targeted manner.

Extracellular vesicles (EVs), once ignored, are now receiving increasing attention as various roles in signaling in cancer, nervous system disorders, innate immunity, pregnancy, and stress responses have become evident [1,2]. Several types of extracellular vesicles have been described, as well as identifying markers [1]. Exosomes, a specific type of EV, are small membrane-bound vesicles that are 30-120 nm in diameter that are released into the extracellular environment by various cell types when internal bodies fuse with the plasma membrane. Exosomes contain cargo such as proteins, lipids, hormones, and RNAs (especially miRNAs) that

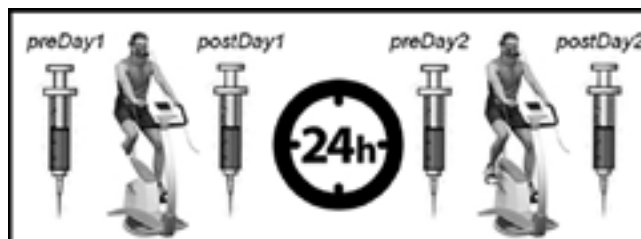


*Figure 1: ME/CFS patients and age- and gender-matched sedentary controls will perform two successive CPETs, separated by 24 hours. EVs will be characterized in blood samples taken at four different time points, preDay1, postDay1, preDay2, and postDay2.*

can influence the function of the cells with which they fuse. One possibility is that exosomes and other types of EVs are involved in cell-to-cell signaling that results in abnormalities in ME/CFS patients' immune function and metabolism at baseline but particularly after any exertion (see Figure 1). In healthy individuals, exercise is known to result in the release of exosomes [3], but there are no published studies on the effect of exercise on EVs in ME/CFS. The size distribution and concentration of isolated exosomes/EVs will be performed using Nanoparticle Tracking Analysis on the Malvern NS300 Nanosight instrument.

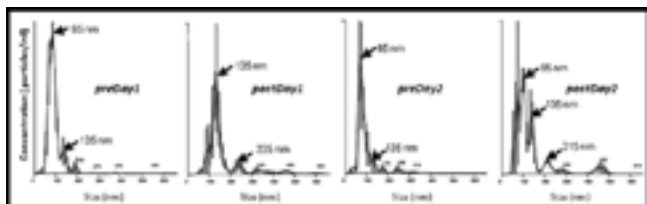


Figure 2: Changes in EV size distribution before and after two exercise challenges on consecutive days, as measured by Nanoparticle Tracking Analysis.

### Summary of Research:

We examined EV size and concentration in plasma from 35 ME/CFS patients and 35 healthy controls. By performing NTA with the Malvern NS300 Nanosight, we found that the concentration of the exosome size class was increased in the patient plasma, though the concentration of the total EV population was not significantly different. The aforementioned plasma was collected the same day as the blood draw. We used a second population in which blood was shipped overnight before plasma was collected.

In this second population, we observed that the concentration of all size classes of EVs and the average size of the EVs were significantly increased in the patient plasma. A pilot experiment with blood taken at four time points is shown in Figure 2 and demonstrates the expected increase in size and concentration after exercise.

### References:

- [1] Yanez-Mo M, Siljander PR, Andreu Z, Zavec AB, Borrás FE, Buzas EI, Buzas K, Casal E, Cappello F, Carvalho J, Colas E, Cordeiro-da Silva A, Fais S, Falcon-Perez JM, Ghojri IM, Giebel B, Gimona M, Graner M, Gursel I, Gursel M, Heegaard NH, Hendrix A, Kierulf P, Kokubun K, Kosanovic M, Kralj-Iglic V, Kramer-Albers EM, Laitinen S, Lasser C, Lener T, Ligeti E, Line A, Lipps G, Llorente A, Lotvall J, Mancek-Keber M, Marcilla A, Mittelbrunn M, Nazarenko I, Nolte-'t Hoen EN, Nyman TA, O'Driscoll L, Olivan M, Oliveira C, Pallinger E, Del Portillo HA, Reventos J, Rigau M, Rohde E, Sammar M, Sanchez-Madrid F, Santarem N, Schallmoser K, Ostefeld MS, Stoorvogel W, Stukelj R, Van der Grein SG, Vasconcelos MH, Wauben MH, De Wever O (2015) Biological properties of extracellular vesicles and their physiological functions. *J Extracell Vesicles* 4: 27066.
- [2] Desrochers LM, Antonyak MA, Cerione RA (2016) Extracellular Vesicles: Satellites of Information Transfer in Cancer and Stem Cell Biology. *Dev Cell* 37: 301-309.
- [3] Safdar A, Saleem A, Tarnopolsky MA (2016) The potential of endurance exercise-derived exosomes to treat metabolic diseases. *Nat Rev Endocrinol* 12: 504-517.

# Development of Microfluidic Device for Protein Synthesis and Modification

**CNF Project Number: 2641-18**

**Principal Investigator(s): Susan Daniel**

**User(s): Zachary Manzer**

*Affiliation(s): Smith School of Chemical and Biomolecular Engineering, Cornell University*

*Primary Source(s) of Research Funding: National Science Foundation*

*Contact: sd386@cornell.edu, zam42@cornell.edu*

*Primary CNF Tools Used: Heidelberg DWL66fs mask writer, ABM contact aligner, Unaxis 770 deep Si etcher, Anatech resist strip, MVD 100, P10 profilometer, FilMetrics F50-EXR*

## Abstract:

Current biological production limits our ability to produce and study tailored biological therapeutics. Many important targets need post-translational modifications that are necessary for maintaining proper structure and function [1]. The cell naturally uses membrane-bound enzymes to do this in a regulated and compartmentalized way. We aim to create a microfluidic device that can recreate this cellular assembly line in a synthetic system while still maintaining the natural biological environment. The first step in this process is the protein synthesis, which we have shown in this work. Since the flow characteristics, channel dimensions, and the local environment are readily controlled, this platform gives us a way to easily mimic and manipulate the local environment to efficiently produce a protein of interest. Future work will focus on the incorporation of the enzymes into a supported membrane in the device.

## Summary of Research:

Previous work in cell-free protein synthesis has been done in static reaction conditions [2]. We aim to build on this body of work and build a platform with continuous flow protein synthesis in conjunction with the selective patterning of necessary enzymes to modify them in a precise way. To design the microfluidic device, first a negative mask for a prototype microfluidic design was created using the Heidelberg DWL66fs mask writer and used with the ABM contact aligner to pattern photoresist that was spun onto a silicon wafer. After development, the profile of the patterns was analyzed on the P10 profilometer. Optimization of the process was conducted to produce consistent and even films, as measured by the profilometer and the FilMetrics F50-EXR. Once this was done, the exposed silicon was etched using the Unaxis 770 deep Si etcher. Photoresist on the channels was removed by oxygen plasma cleaning in the Anatech resist strip. A final hydrophobic coating (FOTS) was applied using molecular vapor deposition to allow for PDMS molds to be easily removed once cast.

Once the mold was fabricated, Sylgard 184 was poured over the mold and cured. This could then be removed and bonded to a glass coverslip by using oxygen plasma cleaning on both surfaces.

The first step in creating this device is the successful synthesis of a model protein. By collecting the cellular

machinery, proteins can be produced in an *in vitro* environment [3]. We isolate a plasmid encoding the green fluorescent protein (GFP) and a cell lysate, and by mixing them together, we produce GFP.

As seen in Figure 1, we can inject each of them independently and through the mixing in the channels, GFP is produced as they proceed through the channels. The small volume of the microfluidic gives tighter temperature control by limiting heat transfer and enhances diffusion to give a higher rate of synthesis as compared to the test tube.

Future work will involve the synthesis of more relevant protein targets as well as the incorporation of enzymes into the supported membrane for modification of the proteins produced.

## References:

- [1] Defaus, S., Gupta, P., Andreu, D., and Gutiérrez-Gallego, R. Mammalian protein glycosylation - structure versus function. *Analyst* 139, 2944-2967 (2014).
- [2] Swartz, J. R. Advances in Escherichia coli production of therapeutic proteins. *Curr. Opin. Biotechnol.* 12, 195-201 (2001).
- [3] Mohr, B. P., Retterer, S. T., and Doktycz, M. J. While-you-wait proteins? Producing biomolecules at the point of need. *Expert Rev. Proteomics* 13, 707-709 (2016).

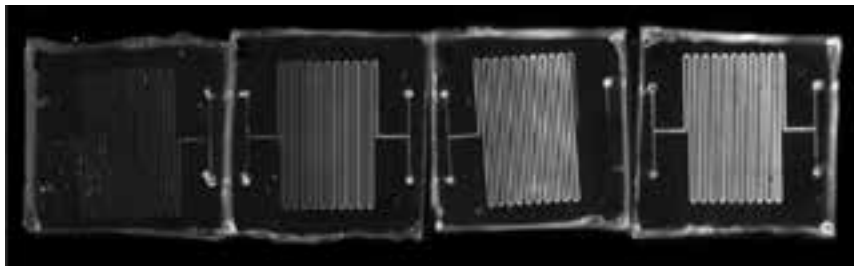


*Figure 1: Series of microfluidic devices that were used to produce GFP in a cell-free continuous flow reaction. DNA and cell lysate are introduced independently on the left side and mix as they enter the first device. The increase in fluorescence across the image is seen as the protein increases in concentration through the length of the channels.*

# Development of a Heparin-Based Coacervate Loaded Liposomes as Non-Invasive Therapy for Myocardial Infarction

**CNF Project Number: 2754-18**

**Principal Investigator(s): Yadong Wang**

**User(s): Chia-Wei Yeh**

*Affiliation(s): Biomedical Engineering, Cornell University*

*Primary Source(s) of Research Funding: Cornell Startup Funds*

*Contact: yw839@cornell.edu, cy465@cornell.edu*

*Primary CNF Tools Used: ABM contact aligner*

## Abstract:

Cardiovascular disease is one of the major leading causes of death worldwide. Specifically, myocardial infarction (MI), generally known as heart attack, is the main cause of death in cardiovascular disease. Among them, the major cause of death of MI is due to the myocyte necrosis and heart failure. Therefore, it is of particular importance to prevent myocyte necrosis after MI as well as induce infarcted heart tissue to regenerate.

## Introduction:

Coacervate is an electrostatically bound complex between cationic and anionic polyelectrolytes. In the extracellular matrix (ECM), glycosaminoglycan such as heparan sulfate proteoglycan (HSPG) binds with several growth factors (GFs) to form HSPG-GF complex. This complex not only serves as reservoir for bonding and stabilization of GFs but also potentiates GFs responsible for maintaining normal cellular function. Due to the similar mechanism of protein-extracellular matrix interaction, it has been shown that heparin-based coacervate is a promising candidate for drug delivery system in biomedical and tissue engineering applications. However, coacervate complex is unstable in the blood stream owing to the relatively weak electrostatic interaction within coacervate droplets, leading to the difficulty to systemically administer coacervate via intravenous injection.

To solve this problem, we aim to encapsulate heparin-based coacervate complex into liposome, namely coacervosomes, for a non-invasive therapy for MI. In this study, polyanion heparin is utilized to complex with vascular endothelial growth factors C (VEGF-C) to form heparin-growth factor complex, which is then mixed with synthetic polycation, ploy(ethylene arginyl aspartate diglyceride) (PEAD) to construct VEGF-C loaded coacervate droplets. In order to enhance coacervate complex stability in the blood stream, an on-chip microfluidic device is used to generate coacervosomes by encapsulating VEGF-C loaded coacervates into liposomes in a well-defined manner. The therapeutic effect of the coacervosomes will be evaluated on rat myocardial infarction model.

## Summary of Research:

The microfluidic device is designed to generate liposomes encapsulated with coacervate complex in different size by using different flow rate among outer aqueous phase (OA), inner aqueous phase (IA), and lipid carried organic phase (LO), as shown in Figure 1. OA contains 15% (vol/vol) glycerol and 5% (w/v) P188 in water, IA contains 15% (vol/vol) glycerol and 20  $\mu\text{g}/\text{mL}$  FITC-heparin water, and LO contains 0.2% (wt/vol) DOPC in 1-octanol. Liposomes are successfully generated via microfluidic device, and the flow rate is 5  $\mu\text{L}/\text{min}$  for each phase, as shown in Figure 2. At this time point, the size distribution is wide — the diameter of liposome ranges from 10 to 200  $\mu\text{m}$ .

Next, FITC-heparin is successfully encapsulated into DOPC liposomes, and the flow rate is 0.1  $\mu\text{L}/\text{min}$  for each phase, as shown in Figure 3. The diameter of FITC-heparin encapsulated DOPC liposome ranges from few microns to 10  $\mu\text{m}$ . The encapsulation efficiency is 40% to 50% at this time point. In order to generate liposomes in different size, two different flow rate are used to generate DOPC liposomes (0.1  $\mu\text{L}/\text{min}$  and 5  $\mu\text{L}/\text{min}$  for each phase, as shown in Figure 4), and the diameter is different. However, detailed size distribution is not tested at this time point.

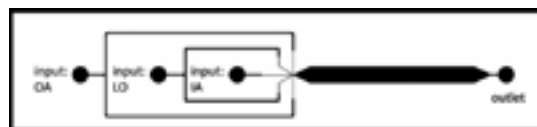


Figure 1: Water-in-oil-in-water double emulsion chip for generating liposome encapsulated with coacervate. OA: outer aqueous phase; IA: inner aqueous phase; LO: lipid carried organic phase.

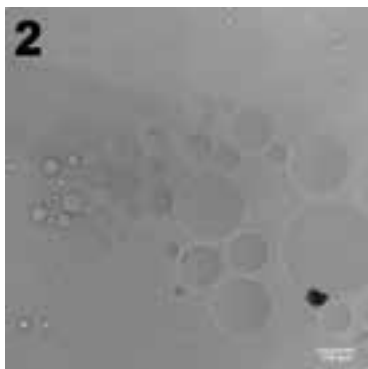


Figure 2: DOPC liposomes generated via microfluidic device. Scale bar: 100  $\mu\text{m}$ .



Figure 3: FITC-heparin encapsulated DOPC liposomes, gray scale and fluorescent images. Scale bar: 50  $\mu\text{m}$ .

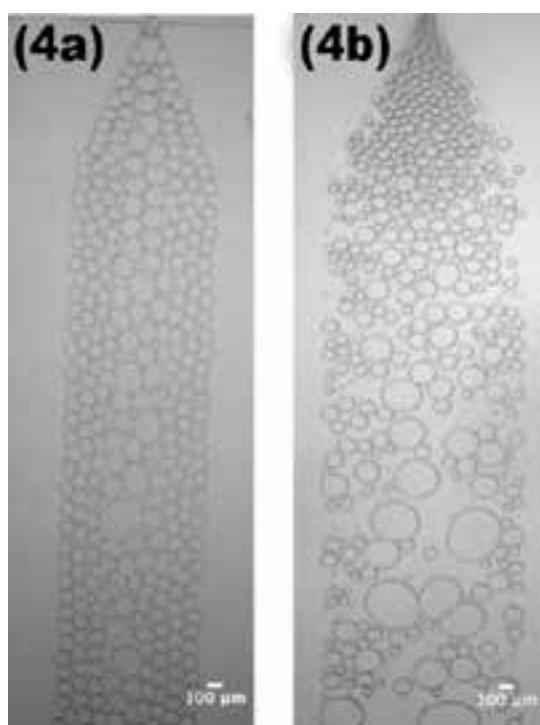


Figure 4: DOPC liposomes generated via microfluidic device. (a) flow rate: 0.1  $\mu\text{L}/\text{min}$  for each phase. (b) flow rate: 5  $\mu\text{L}/\text{min}$  for each phase. Scale bar: 100  $\mu\text{m}$ .

### References:

- [1] Deshpande, Siddharth, and Cees Dekker. "On-chip microfluidic production of cell-sized liposomes." *Nature protocols* 13.5 (2018): 856.
- [2] Deshpande, Siddharth, et al. "Spatiotemporal control of coacervate formation within liposomes." *Nature communications* 10.1 (2019): 1800.

## Phytophthora Zoospore Chemotaxis

**CNF Project Number: 2774-19**

**Principal Investigator(s): Denis S. Willett**

**User(s): Bo Holladay**

*Affiliation(s): Department of Entomology, Cornell AgriTech (New York State Agricultural Experiment Station)*

*Primary Source(s) of Research Funding: Cornell University Start-Up*

*Contact: deniswillett@cornell.edu, bh542@cornell.edu*

*Primary CNF Tools Used: Photolithography, mask writing, spinner*

### Abstract:

***Phytophthora* oomycetes (greek for 'plant destroyer') cause devastating losses to many food crops and are responsible for the Irish potato famine in the 1800s. *Phytophthora* can attack plants with single-celled zoospores. These zoospores respond to chemical cues released by plants to decide where to attack. This project evaluates zoospore response to chemical cues to prevent *Phytophthora* infection.**

### Summary of Research:

*Phytophthora* is perhaps the most devastating plant pathogen affecting the human food system and is a major pathogen affecting vegetable production (squash, pumpkin, cucumber, pepper, eggplant, tomato, and snap beans) in NY State. *Phytophthora capsici* is now established in 25 NY counties and has been detected in 100% of irrigation sources in two regions of the state. Management currently relies on intensive fungicide regimes, but left unmanaged, *Phytophthora* losses can reach 100%. *Phytophthora* infection spreads through travel of single-celled swimming zoospores, which use flagella to propel themselves through aqueous media. These zoospores can travel relatively long distances under their own power and respond to chemical cues in their environment. These cues include volatiles released by plants; *Phytophthora* zoospores can be repelled or attracted by these cues and can choose to move toward or away from them. Using a combination of single-cell microfluidic chip bioassays, analytical chemistry techniques, microcosm bioassays, and field experiments we seek to evaluate chemical cues for controlling and preventing *Phytophthora* zoospore infection.

Previous work has determined zoospore motile ability and suggested specific plant volatiles as potential attractants and repellents. This work will focus on evaluating these cues for applications to New York vegetable crops. These chemical ecology based techniques will provide producers with a potent tool for managing devastating *Phytophthora* infection in the high-value vegetable crops of New York State.

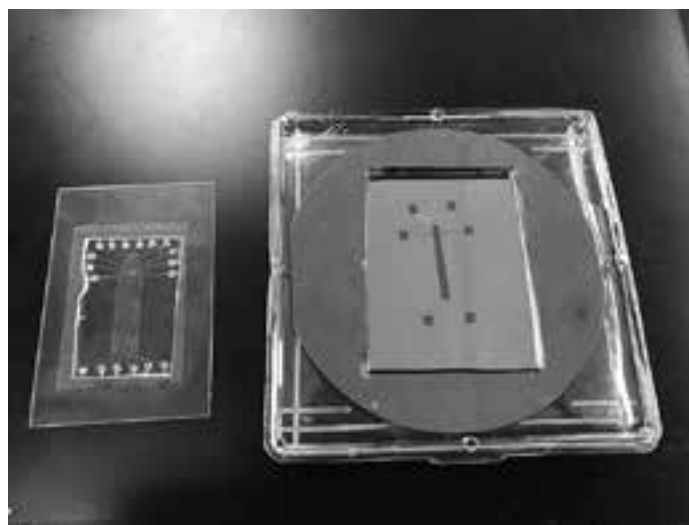


Figure 1: Microfluidic chips made to study *Phytophthora* zoospore chemotaxis.



## Characterization of Cancer Microvesicles

**CNF Project Number: 2780-19**

**Principal Investigator(s): Cynthia Leifer, Tracy Stokol**

**User(s): Christopher Wan, Jingyi Chen**

*Affiliation(s): Microbiology and Immunology, and Population Medicine and Diagnostic Sciences,  
College of Veterinary Medicine, Cornell University*

*Primary Source(s) of Research Funding: Physical Sciences Oncology Center Pilot Project*

*Contact: cynthia.leifer@cornell.edu, ts23@cornell.edu, cw685@cornell.edu, jc2876@cornell.edu*

*Website: <https://www.leiferlab.com/>*

*Primary CNF Tools Used: Malvern NS300 Nanosight*

### Abstract:

Pathologic activation of hemostasis in cancer is associated with systemic thrombotic events and transformation, growth and metastasis of various tumors [1,2]. Tissue factor (TF), the main activator of coagulation, is over-expressed in breast tumors *in situ* and in breast cancer cell lines, particularly triple negative cells [3,4] and expression in patient tumors is correlated with a poor prognosis [3]. Cancer-associated TF produces coagulation factor complexes that trigger thrombosis and induce cell signaling via protease-activated receptors (PARs). Macrophages are recruited from bone marrow-derived cells and blood monocytes and play key roles in pathologic hemostasis. Exposure to cancer cells and the tumor microenvironment induces a protumorigenic, pro-angiogenic, and immunosuppressive phenotype in tumor-associated macrophages [9]. However, it is unknown whether breast cancer cell-generated TF-coagulation complexes and PARs regulate macrophage recruitment to tumors or whether they subsequently modulate macrophage behavior in tumors. This is important since macrophage recruitment and regulation contributes to angiogenesis, metastasis and tumor progression [10-12].

### Introduction:

We hypothesize that breast cancer-associated hemostatic components regulate macrophage recruitment and their inflammatory, angiogenic and hemostatic activity. To investigate this question, we have demonstrated that conditioned media from a mouse breast cancer cell line enhances procoagulant activity of mouse macrophages. To determine the active component of the conditioned media, we isolated the microvesicles by ultracentrifugation and showed they had intrinsic procoagulant activity and conferred procoagulant activity to macrophages. We used the Nanosight NS300 to characterize the microvesicle populations purified from cancer cell-conditioned and control media.

Data obtained using the Nanosight NS300 confirmed that we isolated particles < 100 nm, compatible with exosomes. Altogether, our data show that breast cancer-derived microparticles confer procoagulant activity to macrophages, which may play a key role in the connection between coagulation and inflammation to regulate tumor growth and anti-tumor immunity.

### Summary of Research:

In this project, we tested the procoagulant activity of a mouse breast cancer cell line and found that the cells accelerated clotting in mouse plasma. We isolated the microvesicle fraction shed from the mouse breast cancer cell line into conditioned media using ultracentrifugation and tested the procoagulant activity of the isolated microvesicle fraction. We found that the microvesicle fraction also demonstrated procoagulant activity. Overnight incubation of a mouse macrophage cell line with the isolated microvesicle fraction from tumor-conditioned, but not cell-free, media increased the procoagulant activity of the mouse macrophage cell line. This supports our hypothesis that tumor cells upregulate procoagulant activity in macrophages. Our goal with using the Cornell NanoScale Facility was to characterize the size distribution of the obtained microparticles, using cell-free media as a negative control. For this we used the Nanosight NS300 instrument. We found that the microvesicle fraction consisted of a dominant population of particles < 100 nm, supporting successful isolation of exosomes shed from tumor cells (Figure 1).

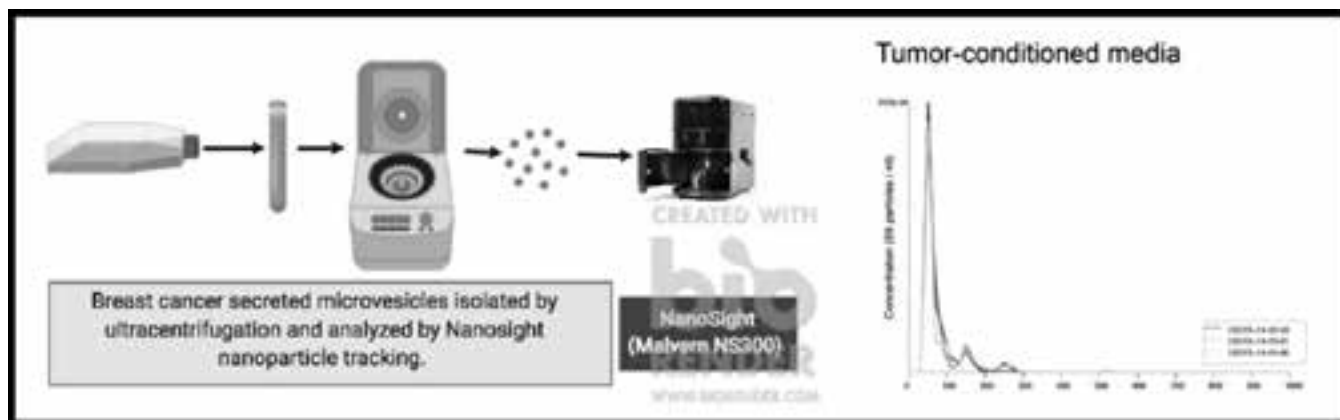


Figure 1: Schematic for nanoparticle isolation and analysis using the Nanosight. Example results of nanoparticle tracking analysis of microvesicles isolated by ultracentrifugation from mouse breast cancer cell tumor-conditioned media. A high concentration of particles < 100 nm, compatible with exosomes, was found in the tumor-conditioned media preparation.

## References:

- [1] Khan UT, Walker AJ, Baig S, et al. Venous thromboembolism and mortality in breast cancer: cohort study with systematic review and meta-analysis. *BMC Cancer* 2017;17:747.
- [2] Cole M, Bromberg M. Tissue factor as a novel target for treatment of breast cancer. *Oncologist* 2013;18:14-18.
- [3] Vrana JA, Stang MT, Grande JP, et al. Expression of tissue factor in tumor stroma correlates with progression to invasive human breast cancer: paracrine regulation by carcinoma cell-derived members of the transforming growth factor beta family. *Cancer Res* 1996;56:5063-70.
- [4] Che SPY, Park JY, Stokol T. Tissue Factor-Expressing Tumor-Derived Extracellular Vesicles Activate Quiescent Endothelial Cells via Protease-Activated Receptor-1. *Front Oncol* 2017;7:261.
- [5] Versteeg HH, Schaffner F, Kerver M, et al. Inhibition of tissue factor signaling suppresses tumor growth. *Blood* 2008;111:190-9.
- [6] Bourcy M, Suarez-Carmona M, Lambert J, et al. Tissue Factor Induced by Epithelial-Mesenchymal Transition Triggers a Procoagulant State That Drives Metastasis of Circulating Tumor Cells. *Cancer Res* 2016;76:4270-4282.
- [7] Palumbo JS, Talmage KE, Massari JV, et al. Tumor cell-associated tissue factor and circulating hemostatic factors cooperate to increase metastatic potential through natural killer cell-dependent and -independent mechanisms. *Blood* 2007;110:133-141.
- [8] Eftekhari R, de Lima SG, Liu Y, et al. Microenvironment proteinases, proteinase-activated receptor regulation, cancer and inflammation. *Biol Chem* 2018;399:1023-1039.
- [9] Aras S, Zaidi MR. TAMEless traitors: macrophages in cancer progression and metastasis. *Br J Cancer* 2017;117:1583-1591.
- [10] Gil-Bernabé AM, Ferjancic S, Tlalka M, et al. Recruitment of monocytes/macrophages by tissue factor-mediated coagulation is essential for metastatic cell survival and premetastatic niche establishment in mice. *Blood* 2012;119:3164-3175.
- [11] Lin L, Chen Y-S, Yao Y-D, et al. CCL18 from tumor-associated macrophages promotes angiogenesis in breast cancer. *Oncotarget* 2015;6:34758-34773.
- [12] Su S, Liu Q, Chen J, et al. A positive feedback loop between mesenchymal-like cancer cells and macrophages is essential to breast cancer metastasis. *Cancer Cell* 2014;25:605-620.

# Sample Preparation for Single-Electron Spin Detection

**CNF Project Number: 863-00**

**Principal Investigator(s): John A. Marohn**

**User(s): Peter (Hanyu) Sun**

*Affiliation(s): Department of Chemistry and Chemical Biology, Cornell University*

*Primary Source(s) of Research Funding: Army Research Office*

*Contact: jam99@cornell.edu, hs859@cornell.edu*

*Website: marohn.chem.cornell.edu*

*Primary CNF Tools Used: CVC SC4500 e-gun evaporation system*

## Abstract:

**Magnetic resonance force microscopy (MRFM) is a scanning probe microscopy technique that aims to achieve high force sensitivity and sub-nanometer resolution of magnetic spins through spatially resolved magnetic resonance. This report discusses a recent study on methods of preparing MRFM samples at the Cornell NanoScale Science and Technology Facility (CNF) that will improve sample preparation techniques and progress us towards the goal of single electron detection and imaging in an MRFM microscope.**

## Summary of Research:

In MRFM, nuclear magnetic resonance or electron spin resonance are detected as a force or force gradient on the tip of a microscopic cantilever. The Marohn group prepares attonewton-sensitivity nanomagnet-tipped cantilevers using a method previously developed at the CNF.

In recent test experiments, the sample is a 200 nm thick layer of polystyrene doped with an electron radical spin probe, 4-amino-TEMPO. This polystyrene sample is spin-coated on a coplanar waveguide (10 mm by 2 mm by 0.5 mm). A 12 nm gold film is then deposited on top of the polystyrene by electron-beam vapor deposition and wire-bonded to the ground plane.

It has been shown that with the gold film, surface non-contact friction from the sample can be sufficiently reduced to achieve signal to noise ratio necessary for single electron detection. However, comparing recent measurements of them MRFM-ESR signal to numerical simulations suggests the existence of a 20 nm layer at the top of the sample in which the 4-amino-TEMPO does not contribute to the signal.

Bulk ESR measurements suggest the reduction in signal may be due to sample damage induced by e-beam vapor deposition of the gold layer.

In this study we investigated an alternative hypothesis, that magnetic field fluctuations from the metal film reduced the spin-lattice relaxation time  $T_1$  of electron radical spins to a degree that made them undetectable via MRFM.

Thermal motion of electrons in materials produce small magnetic fields. Near the surface of conductive materials such as metals, these charge fluctuations can produce enough magnetic field fluctuations at the electron Larmor frequency to produce electron relaxation. In their 2018 paper, Ariyaratne, et al., develop equations to quantify this relaxation effect and use the  $T_1$  relaxation of nitrogen-vacancy (NV) centers as a detector of conductivity in metal films (85 nm thick Ti, Al and Ag films) [1]. The induced relaxation rate is proportional to the conductivity of the metal thin film and related to the distance between the targeted spin and the metal film.

The work done at the CNF allows us to predict the effect of our 12 nm gold film on the MRFM sample. The test sample was a 200 nm polystyrene film spin-coated on a silicon chip identical in size to our coplanar waveguide. A 12 nm gold film was deposited on top of the polystyrene film with the CVC SC4500 e-gun evaporation system at the CNF. The resulting samples were wired bonded and the resistivity of the gold film was measured

using Quantum Design 14T “Blue” Physical Property Measurement System (PPMS) at the Cornell Center for Materials Research (CCMR). The resistivity was profiled at 4.2 K and  $10^{-5}$  Torr, conditions closely resembling MRFM operating conditions. The preliminary data shows a resistivity of 116 n $\Omega$ -m for the 12 nm gold film on polymer, suggesting that the relaxation rate of electron spins in the polystyrene sample due to the gold film would be minimal.

We expect to further explore the behavior of metal films with different parameters with the help of CNF in the coming year. This information will help us to improve sample design and how best to reduce noise due to sample dielectric fluctuations without reducing our ability to detect sample spins.

### **References:**

- [1] Ariyaratne, A. et al.; Nat Commun, 2018, 9, 2406.

# Investigation of Area Selective Atomic Layer Deposition with Microreactor and *in situ* Surface Analysis

**CNF Project Number: 1239-04**

**Principal Investigator(s): James R. Engstrom**

**User(s): Taewon Suh, Colleen Lawlor**

*Affiliation(s): Robert Frederick Smith School of Chemical and Biomolecular Engineering, Cornell University*

*Primary Source(s) of Research Funding: Semiconductor Research Corporation*

*Contact: jre7@cornell.edu, ts695@cornell.edu, ccl233@cornell.edu*

*Website: <http://engstromgroup.cbe.cornell.edu>*

*Primary CNF Tools Used: Acid hood, atomic layer deposition (ALD)*

## Abstract:

Atomic layer deposition (ALD) is a technique capable of precise control of film thickness and conformal film growth due to self-limiting nature of the precursors. Engstrom research group (ERG) has built a microreactor through which reactants of ALD are delivered and confined in a small region for deposition. This microreactor is coupled to an ultra high vacuum (UHV) chamber for surface characterization such that the deposited film is transferred *in vacuo*, without an air break, to the analysis chamber. In addition to the two reactants used in conventional ALD: ALD precursor and co-reactant, a third species called “co-adsorbate” is introduced for possible area selective deposition to act as a site-blocking layer.

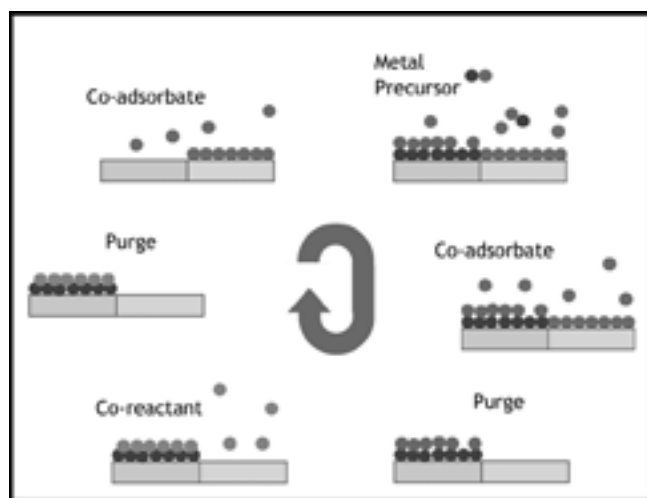


Figure 1: Schematic of an ALD cycle with co-adsorbate molecules.

## Summary of Research:

In continuous downscaling of semiconductor devices, ALD has emerged as a potential approach capable of meeting required criteria of next generation technologies. The self-limiting nature of ALD precursors brings about two major advantages unique to the technique: precise control of thickness of deposited film and conformal growth [1]. ALD is sequential binary gas-phase reaction separated by purge steps to prevent any unwanted parasitic reactions between the precursor and co-

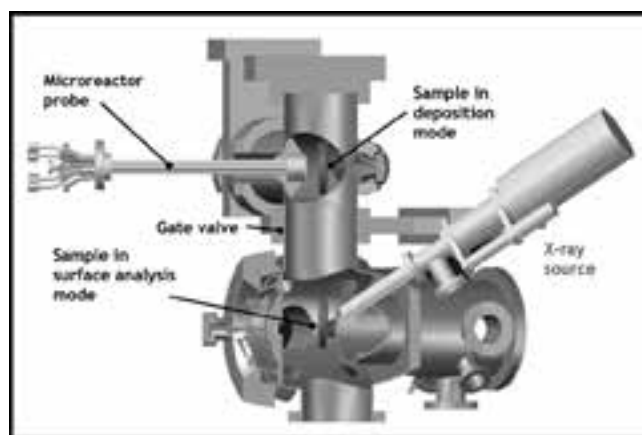


Figure 2: CAD rendering of the microreactor and UHV surface analysis chamber.

reactant. ERG takes this deposition technique a step further to study fundamental mechanisms involved in potential area-selective ALD. Co-adsorbate molecules are introduced within a conventional cycle of ALD: before, during, and after precursor pulse as in Figure 1, to investigate how this third species potentially allows for area selective deposition. The deposited film is transferred *in vacuo* to and characterized in a UHV chamber coupled with the microreactor using XPS.

The thickness of deposited film (~ a few nm) is often in the range that is most effectively probed with surface-sensitive characterization techniques that require UHV,  $p < 10^{-9}$  Torr. Conventional ALD is typically conducted at low to medium vacuum conditions ( $p \sim 10^{-3}$ - $10^{-2}$  Torr), thus in most cases UHV based analysis of the deposited thin films occurs in a separate chamber, requiring an air break that may significantly alter the surface composition, oxidation state, structure of the deposited film, and/or underlying substrate. Avoiding this air break is critical for fundamental studies of the growth of ultrathin films, particularly in the early stages. Figure 2 describes how a sample is exposed to precursors at the upper stage and transferred down to the lower stage of the chamber without exposure to air for post-deposition characterization.

In this report, we investigate a mechanism that can possibly achieve area-selective deposition with ALD by employing co-adsorbate molecules. Two substrates of different composition are used as initial surfaces: chemical oxide and metallic copper. Substrate preparation for the dielectric is conducted in the acid hood of CNF at Cornell University. This wet chemical etch includes submerging Si <100> wafer in buffered oxide etch (BOE) (6:1) for two minutes that produces hydrogen-terminated Si, confirmed by hydrophobicity of the surface. The substrate is then immersed in nanostrip for 15 minutes, which generates hydroxyl group termination with a known density of  $\sim 5 \times 10^{-14}$  OH/cm<sup>2</sup> [2]. This cycle of removing native oxide and generating chemical oxide is repeated twice. OH-terminated SiO<sub>2</sub> and copper substrates are loaded into the vacuum chamber within a sample holder which allows simultaneous exposure of substrates to reactants such that gas-surface reactions will occur under identical+ experimental conditions.

In area-selective ALD experiments, substrates are annealed to substrate temperature of 180°C for an hour prior to exposure. Then co-adsorbate species, unsaturated hydrocarbon in this report, is introduced to surfaces to form site-blocking layer to prevent incoming ALD precursor from adsorbing on non-growth surfaces. The co-adsorbate molecules are present at relatively high ratio compared to ALD precursor before, during, and after the precursor pulse to ensure excess co-adsorbate molecules are present for competitive adsorption. After purge of the precursor and co-adsorbate, pulse and purge of co-reactant occurs, just like the second half cycle in conventional ALD. Deposited metal oxide films are characterized with *in situ* x-ray photoelectron spectroscopy (XPS) using several parameters: photoionization cross section, inelastic mean free path, and kinetic energy, etc. [3]. The absolute atomic density of metal atom is calculated using calibration of semi-infinite Au film and methods described elsewhere [4].

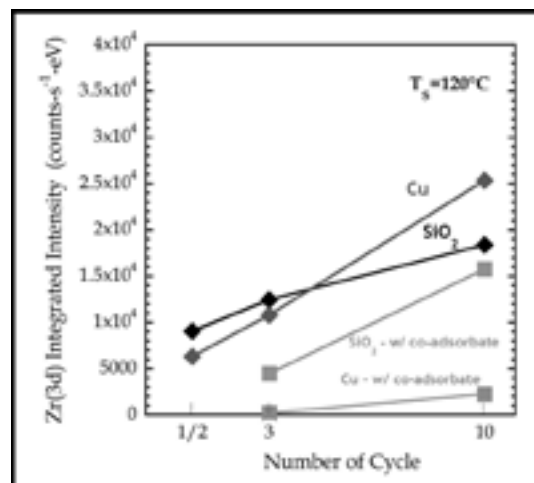


Figure 3: Sample holder capable of holding two coupon samples.

Results from preliminary AS-ALD experiments with an unsaturated hydrocarbon as the co-adsorbate species are summarized in Figure 3. The top two curves represent the integrated intensity of Zr(3d) detected in 1/2, 3, and 10 ALD cycles of Zr-containing precursor with an oxidant. As expected for an ALD process, the amount of transition metal within the deposited thin film is linearly proportional to the number of cycles. Density functional theory (DFT) calculations demonstrate that the co-adsorbate species has stronger affinity towards Cu than SiO<sub>2</sub>. Experimental results show good correlation with the theoretical calculations; in Figure 3, the two bottom curves represent the amount of Zr(3d) detected on SiO<sub>2</sub> and Cu from 3 and 10 ALD cycles in presence of the co-adsorbate.

In the three-cycle experiment with the co-adsorbate, complete inhibition of Zr adsorption is obtained, most likely due to competitive adsorption between the co-adsorbate and ALD precursor for surface active sites. In the ten-cycle experiment, some Zr(3d) is detected, but the amount of Zr on SiO<sub>2</sub> compared to Zr on Cu is greater by approximately a factor of 10.

#### References:

- [1] S. M. George, "Atomic layer deposition: An overview," *Chem. Rev.*, vol. 110, pp. 111-131, 2010.
- [2] L. T. Zhuravlev, "Concentration of hydroxyl groups on the surface of amorphous silicas," *Langmuir*, vol. 3, no. 3, pp. 316-318, 1987.
- [3] J. H. Scofield, "Hartree-Slater subshell photoionization cross-sections at 1254 and 1487 eV," *J. Electron Spectros. Relat. Phenomena*, vol. 8, no. 2, pp. 129-137, 1976.
- [4] K. J. Hughes and J. R. Engstrom, "Interfacial organic layers: Tailored surface chemistry for nucleation and growth," *J. Vac. Sci. Technol. A Vacuum, Surfaces, Film.*, vol. 28, no. 5, p. 1033, 2010.

# Thin Film, Laser-Etched Sorbent Sheets for Spatially Resolved and High Throughput Analysis of Volatiles

**CNF Project Number: 2513-16**

**Principal Investigator(s): Gavin Sacks**

**User(s): Jessica Rafson, Madeleine Bee**

*Affiliation(s): Department of Food Science, Cornell University*

*Primary Source(s) of Research Funding: United States Department of Agriculture, National Institute of Food and Agriculture (USDA-NIFA) Award #2017-67007-25940*

*Contract: gls9@cornell.edu, myb8@cornell.edu, jr2255@cornell.edu*

*Website: <http://blogs.cornell.edu/winechemistry/>*

*Primary CNF Tools Used: VersaLaser engraver/cutter tool*

## Abstract:

The analysis of trace-level volatiles responsible for odor of foods, beverages, and other systems is challenging because of their low concentrations, often down to part-per-trillion (nanogram-per-liter) levels. Because of this, trace volatile analyses often require pre-concentration and extraction steps, followed by lengthy analysis on gas chromatography — mass spectrometry (GC-MS). Often, analyses require 30 min per sample. Using tools available through the Cornell NanoScale Facility (CNF), we have prepared etched sorbents sheets. These sheets can be used to extract multiple samples in parallel, either from multiwell plates or other planar surfaces. The etched geometry of the sheets facilitates their direct coupling with mass spectrometers, and allows for very rapid analyses of trace volatiles — up to 24 samples in 17 min, or over 10-fold faster than conventional approaches. Additionally, because the extraction step preserves the spatial distribution of volatiles, it can also be used for imaging analyses of volatiles.

## Summary of Research:

The odors associated with common foods, beverages, and fragrances are due to range of odorants, many present at concentrations as low as a part-per-trillion (nanogram-per-liter, or ng/L). Because of these low concentrations, analysis of these trace volatiles often requires initial steps to concentrate them and remove interferences, followed by analysis by techniques like gas chromatography — mass spectrometry (GC-MS).

GC-MS analyses often require 30 min per sample and represent a common bottleneck in characterization of large numbers of samples. So-called “ambient-ionization” — MS techniques like direct analysis in real time (DART) — are much faster than GC-MS, but coupling automated extraction approaches to DART-MS has not been straightforward. To overcome this, our group developed an approach called Solid Phase Mesh Enhanced Sorption from Headspace (SPMESH), which is readily coupled to DART-MS, as shown in Figure 1.

Our group used the VersaLaser cutting tool at the CNF to generate mesh patterns on poly(dimethylsiloxane) (PDMS) sheets shown in Figure 2. We could then position the sheets over multiwell plates pre-loaded with samples, e.g. macerated grapes. The silicone sheets then absorbed the volatiles in the headspace above each well in parallel.

Following extraction, the SPMESH sheet with extracted volatiles is then transferred to an automated positioning stage. Using three representative odorants, we were able to use SPMESH-DART-MS to analyze 24 samples in 17 min with detection limits in the ng/L range, shown in Figure 3 [1]. We also showed that the approach had excellent day-over-day repeatability (< 25% in signal over two weeks).

In a follow-up study [2], we reported that SPMESH absorption could also be performed from headspace of other planar surfaces, including samples spotted on thin-layer chromatography (TLC) plates. The use of TLC plates greatly enhanced the extraction rate, such that extraction only required 2-3 min to reach equilibrium. We also demonstrated that spatial distribution of volatiles could be preserved during imaging, allowing SPMESH to be used for imaging of volatiles from a surface, as shown in Figure 4.

In summary, laser-etched SPMESH sheets can be used for both high-throughput extraction and analysis of trace volatiles, as well as imaging of the spatial distribution of volatiles.

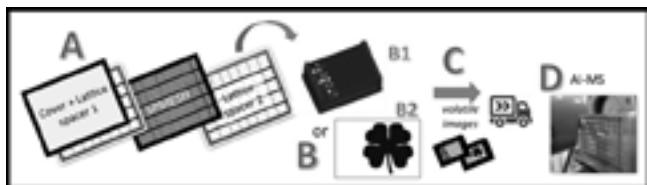


Figure 1: Overview of new approach to volatile analyses. Sorbent coated laser-etched meshes (SPMESH, A), are situated between inert lattice spacers, and positioned over well plates for high-throughput quantification (B1) or over an intact sample for imaging analyses (B2). Following parallel headspace extraction to create volatile images (C), the SPMESH sheet can be rapidly analyzed by ambient ionization - mass spectrometry (AI-MS, e.g., DART-MS (D)).

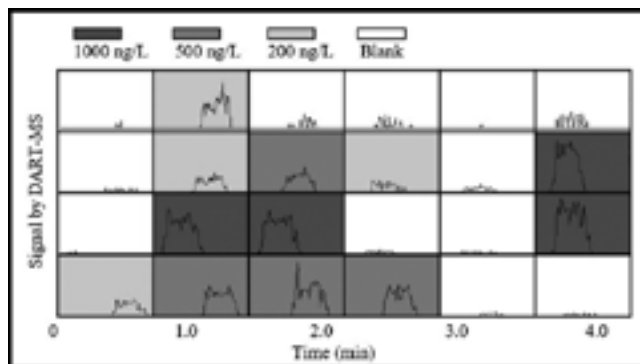


Figure 3: High-throughput SPMESH-DART-MS analyses of a trace level volatile (IBMP, "green pepper aroma") from a multi-well plate. Each cell represents a sample on a 24-well plate, containing 0-1000 ng/L IBMP.



Figure 2: Etched silicone SPMESH sheet produced at the CNF. The grid size is 0.5 mm × 0.5 mm.

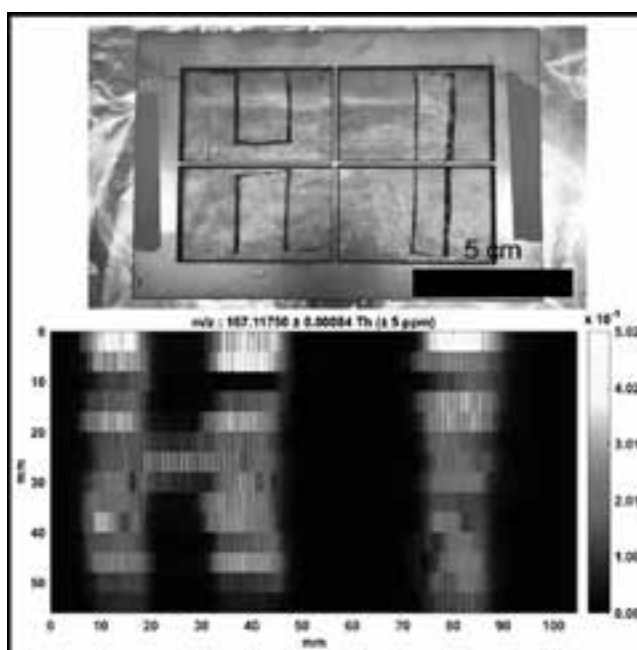


Figure 4: Spatially resolved image (bottom) of a volatile deposited on a polyethylene film (top) using SPMESH-DART-MS.

## References:

- [1] Bee MY, Jastrzembki JA and Sacks GL. Parallel headspace extraction onto etched sorbent sheets prior to ambient-ionization mass spectrometry for automated, trace-level volatile analyses. *Analytical Chemistry*. 90, pp. 13806-13813. <https://pubs.acs.org/doi/10.1021/acs.analchem.8b04465> (2018).
- [2] Rafson J, Bee MY, Sacks GL. Spatially resolved headspace extractions of trace-level volatiles from planar surfaces for high-throughput quantitation and mass spectral imaging. *Journal of Agricultural and Food Chemistry*. <https://pubs.acs.org/doi/10.1021/acs.jafc.9b01091> (2019).

# Fabrication of Graphene Microelectrodes

**CNF Project Number: 2618-17**

**Principal Investigator(s): Prof. Héctor D. Abruña**

**User(s): Dr. Matej Velický**

*Affiliation(s): Department of Chemistry and Chemical Biology, Cornell University*

*Primary Source(s) of Research Funding: European Union/European Commission*

*Contact: hda1@cornell.edu, mv337@cornell.edu*

*Website: <https://abruna.chem.cornell.edu>*

*Primary CNF Tools Used: Anatech resist strip, Nikon L200 eclipse microscope, Heidelberg mask writer DWL2000, ABM contact aligner, SC4500 odd-hour evaporator, YES vapor prime oven*

## Abstract:

**We present a method of graphene microelectrode fabrication, which we designed to be able to study the electrochemical properties and applicability of graphene in energy storage, sensing, and electrocatalysis. The fabrication scheme consists of mechanical exfoliation of graphene/graphite crystals, photolithographic patterning of their surface, and metal deposition of electrical contacts.**

## Summary of Research:

The electrochemistry of two-dimensional (2D) materials such as graphene has been of significant interest to researchers hoping to apply these materials in energy storage, sensing, and electrocatalysis [1]. However, a limited understanding of the fundamental electrochemical properties of graphene has hindered the recent progress, mostly due to lack of well-defined single-crystal graphene samples. Our aim was to fabricate microscale opening within an insulating layer of a polymer in order to study the electrochemical properties of single-crystal graphene/graphite microelectrodes. To that end, we exfoliated bulk graphite onto an insulating substrate and used polymer-based photolithography and metal deposition to create an electrical contact to graphene/graphite and to fabricate the microelectrode opening over the material.

First step in the fabrication process is the mechanical exfoliation of bulk graphite onto an oxidized silicon wafer ( $\text{SiO}_2/\text{Si}$ ). The wafers are sonicated in acetone and isopropanol (IPA) in order to remove surface contamination. To maximize the adhesion between the graphite and the wafer, the latter is cleaned by plasma ashing in the Anatech resist strip (at 900 W for 5 min), immediately prior to the graphite exfoliation. The tape used for exfoliation is peeled away, leaving some graphite/graphene crystals on the wafer surface. Examination under the Nikon L200 eclipse microscope reveals crystal of different thickness, readily identified by their optical contrast, as shown in Figure 1.

We then designed and wrote a quartz/chrome photomask (courtesy of Alejandro J. Cortese, McEuen group) using the Heidelberg mask writer DWL2000, to be used with our two-step photolithographic process. Poly(methyl methacrylate) (PMMA) (950K 4% in anisole) was used as the photoresist polymer material for both steps, using the 220 nm mirror, 60 min exposure, and methylisobutyl ketone/IPA (1:3) developer. First, the mask was manually aligned to a selected graphene/graphite crystal and exposed using the ABM contact aligner. This was done in a way such that a window in the PMMA was created, exposing a small portion of the crystal as shown in Figure 2.

Next, the SC4500 odd-hour evaporator was used to deposit a layer of 7 nm Cr and 50 nm Au. The PMMA and top-surface Au/Cr were then removed by a lift-off procedure in acetone (assisted by a methyl methacrylate undercut layer). This resulted in the exposed portion of the crystal in contact with the Au/Cr layer, as shown in Figure 3.

In the second photolithographic step, another PMMA layer was used to cover the entire wafer, another pattern on the mask was aligned to the alignment marks from the previous metal deposition step and exposed using the ABM contact aligner. This resulted in a microelectrode disk opening in the PMMA, exposing the graphene/graphite surface in the final device shown in Figure 4. We then contacted the Au layer to metal wire and erected

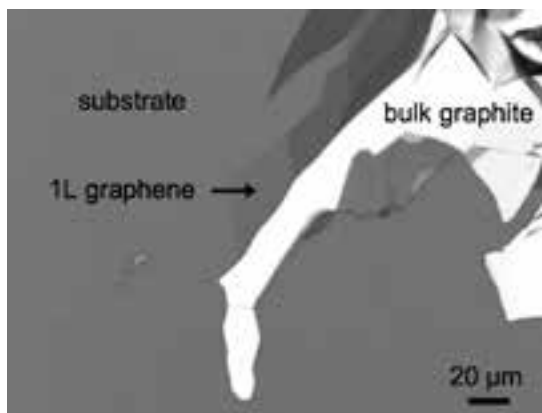


Figure 1: Optical image of graphene/graphite crystals exfoliated on 290 nm  $\text{SiO}_2/\text{Si}$  substrate.

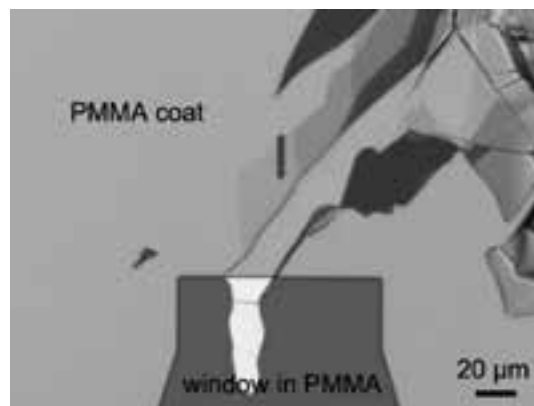


Figure 2: Optical image showing the first photolithographic step with a window in the PMMA exposing a part of the graphite crystal.



Figure 3: Optical image showing the deposited Au/Cr layer contacting the graphite crystal.

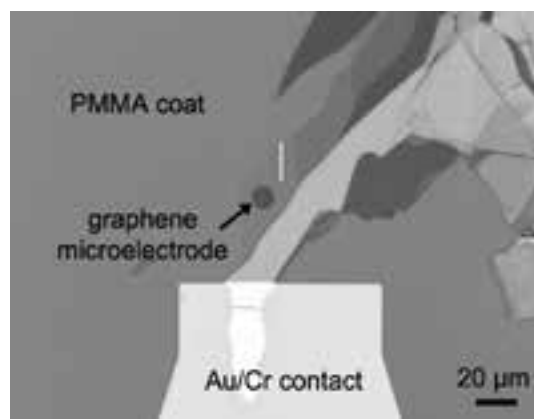


Figure 4: Optical image showing the final device with a 10  $\mu\text{m}$  diameter opening in PMMA exposing a monolayer graphene crystal microelectrode.

an electrochemical cell around this opening made of a several-mm thick polydimethylsiloxane (PDMS), which has previously been set over a silicon wafer surface primed with hexamethyldisilazane using the YES Vapor Prime Oven. The PDMS “pool” has been filled with the liquid solution of interest in order to carry out the electrochemical experiments.

To date, we have not been able to achieve satisfying electrochemical behavior of our devices. Specifically, we either observed no current upon application of voltage or current-voltage characteristics significantly deviating from the behavior expected for the device geometry. We suspect that there are several factors contribute to this discrepancy, namely contamination of the microelectrode from the photolithographic process and either pinholes in PMMA or poor adhesion between the PMMA and the  $\text{SiO}_2/\text{Si}$  substrate, resulting in the liquid “creeping” between the two.

In summary, we succeeded in designing a fabrication scheme, which can produce graphene/graphite electrodes of diameters between 5-100  $\mu\text{m}$ . We currently work towards resolving the aforementioned issues affecting the electrochemical measurement of these devices. We envisage that once these technical obstacles are resolved, we will be able to study some of the fundamental relationships, namely the effect of the electric field upon the electron transfer rate between a graphene electrode and a redox molecule in solution. Such fundamental insights will facilitate exploration of graphene and other 2D materials in the electrochemical energy storage/conversion, sensing, and electrocatalysis.

#### References:

- [1] Velick, M. and Toth, P. S. From Two-Dimensional Materials to Their Heterostructures: An Electrochemist's Perspective. *Appl. Mater. Today* 2017, 8, 68-103.

# Small Molecule Photoresists for EUV Lithography

**CNF Project Number: 2656-18**

**Principal Investigator(s): Emmanuel Giannelis, Christopher Kemper Ober**

**User(s): Wenyang Pan**

*Affiliation(s): Materials Science and Engineering, Cornell University*

*Primary Source(s) of Research Funding: JSR*

*Contact: epq2@cornell.edu, cko3@cornell.edu, wp222@cornell.edu*

*Primary CNF Tools Used: ASML 300C DUV stepper, ABM contact aligner, Zeiss Ultra SEM*

## Abstract:

**We are developing novel small molecule photoresists that are compatible with the state-of-art extreme ultraviolet (EUV) lithography, and represent under 10 nm resolution.**

## Summary of Research:

In the Giannelis group and the Ober group, we are developing a class of novel photoresists that are small enough for the current EUV lithography [1,2]. These photoresists are small molecules that crosslink upon exposure under DUV or EUV.

We normally develop the chemistry in our labs at MSE, Cornell. Once we have got a new recipe, we expose our thin film using the contact aligner and DUV stepper at certain wavelengths in CNF. We also rely heavily on CNF SEM to check our resolution. Certain chemistry would also be evaluated for e-beam lithography, which is performed by another colleague in Ober group.

## References:

- [1] Sakai, Kazunori, et al. "Development of metal organic cluster EUV photoresists." *Advances in Patterning Materials and Processes XXXVI*. Vol. 10960. International Society for Optics and Photonics, 2019.
- [2] Sakai, Kazunori, et al. "Metal organic cluster photoresists: new metal oxide systems." *Advanced Etch Technology for Nanopatterning VIII*. Vol. 10963. International Society for Optics and Photonics, 2019.

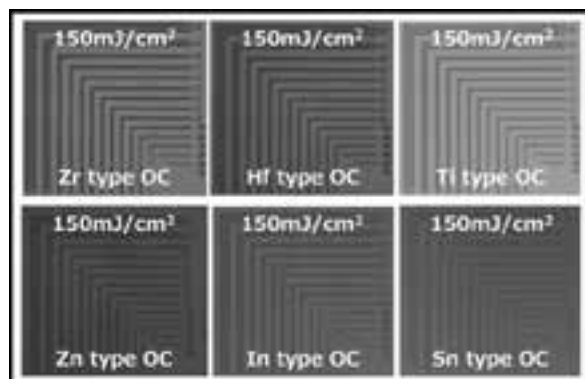


Figure 1: Micron-scale patterning results from contact aligner in CNF, of several resists.

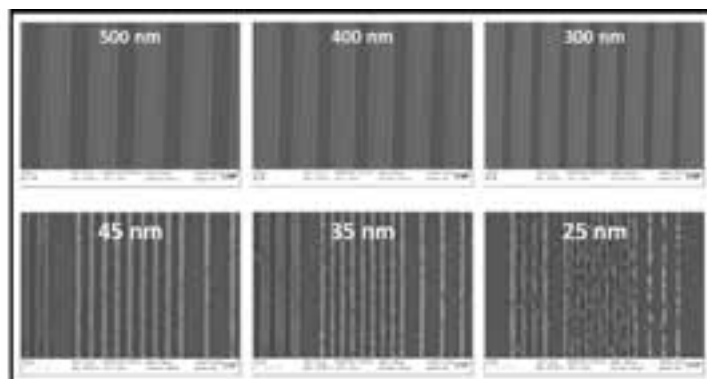


Figure 2: DUV exposure (upper), in CNF, and further evaluation using finer masks (lower) exposure one organic cluster resist.



# Power Electronic Devices Based on Ga<sub>2</sub>O<sub>3</sub>

**CNF Project Number: 2307-14**

**Principal Investigator(s): Huili Grace Xing**

**User(s): Wenshen Li, Zongyang Hu, Jui-Yuan Hsu, Anni Wu**

*Affiliation(s): Electrical and Computer Engineering, Material Science and Engineering; Cornell University*

*Primary Source(s) of Research Funding: NSF DMREF Program under Grant 1534303 AFOSR under Grants FA9550-17-1-0048, FA9550-18-1-0529 and FA9550-18-1-0479*

*Contact: grace.xing@cornell.edu, WL552@cornell.edu, zh249@cornell.edu, jh2627@cornell.edu, jw2472@cornell.edu*

*Website: <http://grace.engineering.cornell.edu>*

*Primary CNF Tools Used: Oxford PECVD and ALD, odd-even hour evaporation, AJA sputtering tool, PT-770 etcher*

## Abstract:

Gallium(III) trioxide (Ga<sub>2</sub>O<sub>3</sub>) is an ultra-wide bandgap semiconductor material with excellent breakdown electric field and the availability of melt-grown substrates, thus very promising for power electronic devices. Employing a vertical device topology, we have been able to successfully demonstrate Ga<sub>2</sub>O<sub>3</sub> power diodes and transistors with excellent device performance, including a breakdown voltage exceeding 2 kV, as well as state-of-the-art on-state performance. Through electrostatic engineering and process optimization, we are pushing toward the limit of this material, which could surpass the performance of current power devices based on SiC and GaN.

## Summary of Research:

β-Ga<sub>2</sub>O<sub>3</sub> has attracted considerable interests as a promising wide-bandgap semiconductor material for power devices. Aside from the availability of melt-grown substrates, the sizable bandgap value of 4.5-4.7 eV allows for a large critical electric field exceeding 5 MV/cm as observed experimentally. Aided by the excellent field strength, high breakdown voltage exceeding 1 kV has been demonstrated in both diodes and transistors. In addition, a Baliga's figure-of-merit (BFOM) of around 0.5 GW/cm<sup>2</sup> has been achieved in both lateral and vertical Schottky barrier diodes (SBDs), which already exceeded the unipolar limit of Si.

Vertical power devices can provide higher current density than the lateral counterparts. With the incorporation of fin-channels, vertical enhancement-mode Ga<sub>2</sub>O<sub>3</sub> transistors with good gate-control [1,2] as well as vertical Ga<sub>2</sub>O<sub>3</sub> trench Schottky barrier diodes with reduced reverse leakage current [3,4] have been realized by our group.

The fabrication process for the Ga<sub>2</sub>O<sub>3</sub> trench Schottky barrier diodes is as follows: First, reactive ion etch (RIE) based on BCl<sub>3</sub> and Ar was performed on the backside of the wafer to facilitate ohmic contact using the PT-770 etcher; After that, Ti (50 nm)/Au (125 nm) was evaporated on

the backside as the cathode contact followed by a rapid thermal anneal (RTA) for 1 min under N<sub>2</sub> ambient; Next, Ni/Pt were deposited and patterned by a lift-off process on the top surface, serving as the Schottky contact as well as the hard mask for the subsequent etching for trench formation; Trenches with a depth of 1-2 μm were etched using RIE; Subsequently, a 100-nm Al<sub>2</sub>O<sub>3</sub> dielectric layer was deposited by atomic layer deposition (ALD) using the Oxford ALD tool; Next, the dielectric was opened by dry etching to expose the Ni/Pt Schottky contact, followed by a deposition of Cr/Pt over the sidewall by sputtering using the AJA sputtering tool.

The fabrication process for the Ga<sub>2</sub>O<sub>3</sub> vertical fin transistors is as follows: Si ion implantation and activation was performed in the top 50 nm of the drift layer; Pt metal masks were then patterned by electron beam lithography and deposited by electron beam evaporation on the sample surface to define position and size of the FET channels; Vertical Fin-channels were etched in the PT-770 etcher with a target width/height of 0.3/1.0 μm, respectively; Then, a 30 nm Al<sub>2</sub>O<sub>3</sub> was deposited by atomic layer deposition (ALD) as the gate dielectric, followed by a 50 nm thick Cr sputtered as the gate metal; A photoresist planarization process was used

to selectively etch away the gate metal/dielectric on top of the  $n^+$ -Ga<sub>2</sub>O<sub>3</sub> source; Then, a 200 nm SiO<sub>2</sub> was deposited by plasma-enhanced chemical vapor deposition (PECVD) using the Oxford PECVD tool and a second planarization process was used to etch away the SiO<sub>2</sub> on top of the  $n^+$  source; Finally, source ohmic contacts were formed by depositing Ti/Al/Pt, and device isolation was realized by etching away SiO<sub>2</sub> and Cr between active devices.

The trench Schottky barrier diodes have a specific on-resistance of 10<sup>-11</sup> mW·cm<sup>2</sup>. In comparison with the regular Schottky barrier diode, the trench diodes possess not only a lower leakage current, but also a higher breakdown voltage. In a number of 1- $\mu$ m and 2- $\mu$ m channel devices, the leakage current is below our measurement noise floor (1  $\mu$ A/cm<sup>2</sup>) even at a voltage of more than 2 kV. The reduction of the leakage current directly translates to the reduction of the off-state power loss.

All the vertical Ga<sub>2</sub>O<sub>3</sub> MISFETs exhibit normally-off operation. The drain current reaches  $\sim$  300-500 A/cm<sup>2</sup> with an associated differential on-resistance of  $\sim$  13-18 mW·cm<sup>2</sup> in devices with a channel width of 300 nm. In devices with a channel width of 400 nm, the current density reaches over 1000 A/cm<sup>2</sup>.

At off state, the device records very low drain and gate leakage currents. The 3-terminal breakdown voltage is over 1 kV. The breakdown is identified to be due to field crowding at the device periphery. With improved edge termination designs, the breakdown voltage is expected to be much higher.

In summary, we have demonstrated kV-class Ga<sub>2</sub>O<sub>3</sub> power diodes and transistors. These initial device results showed a great potential of Ga<sub>2</sub>O<sub>3</sub> as a promising material for power electronics applications.

## References:

- [1] Z. Hu, K. Nomoto, W. Li, N. Tanen, K. Sasaki, A. Kuramata, T. Nakamura, D. Jena, and H. G. Xing, IEEE Electron Device Lett. 39, 869 (2018).
- [2] Z. Hu, K. Nomoto, W. Li, Z. Zhang, N. Tanen, Q. T. Thieu, K. Sasaki, A. Kuramata, T. Nakamura, D. Jena, and H. G. Xing, Appl. Phys. Lett. 113, 122103 (2018).
- [3] W. Li, Z. Hu, K. Nomoto, Z. Zhang, J. Y. Hsu, Q. T. Thieu, K. Sasaki, A. Kuramata, D. Jena, and H. G. Xing, App. Phys. Lett. 113, 202101 (2018).
- [4] W. Li, Z. Hu, K. Nomoto, R. Jinno, Z. Zhang, T. Q. Tu, K. Sasaki, A. Kuramata, D. Jena, and H. G. Xing, 2018 IEEE International Electron Devices Meeting (IEDM), pp. 8.5.1, 2018.

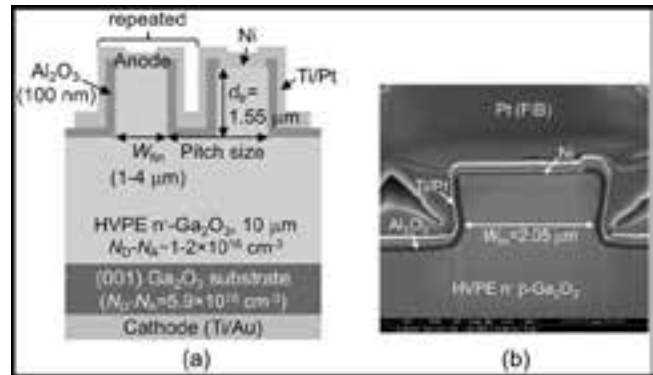


Figure 1: Schematic and SEM cross-section of the Ga<sub>2</sub>O<sub>3</sub> trench Schottky barrier diodes.

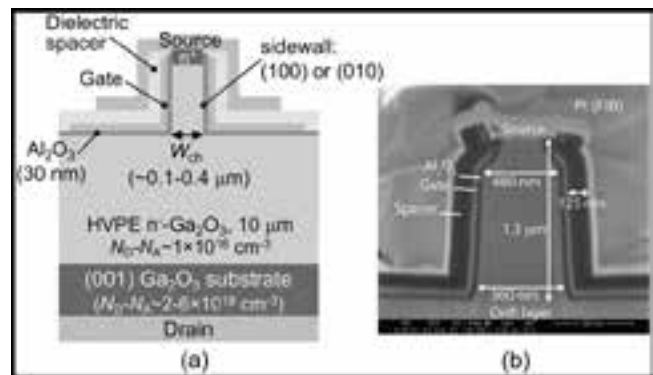


Figure 2: Schematic and SEM cross-section of the Ga<sub>2</sub>O<sub>3</sub> vertical fin transistors.

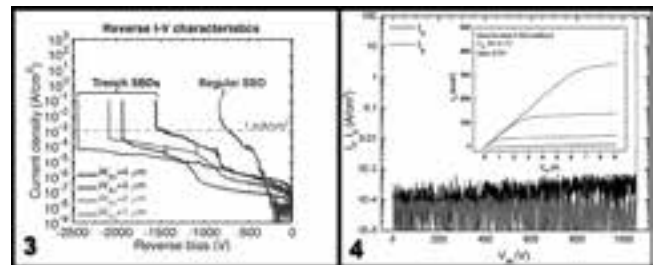


Figure 3, left: Reverse I-V characteristics of the Ga<sub>2</sub>O<sub>3</sub> trench Schottky barrier diodes. Figure 4, right: Output I-V characteristics (inset) and reverse I-V characteristics of the Ga<sub>2</sub>O<sub>3</sub> vertical fin transistors.

# WSe<sub>2</sub> RF MOSFETs and CMOS Integration

**CNF Project Number: 2509-16**

**Principal Investigator(s): James C.M. Hwang**

**User(s): Kuanchen Xiong, Lei Li**

*Affiliation(s): Department of Electrical and Computer Engineering, Lehigh University*

*Primary Source(s) of Research Funding: This work was supported in part by the U.S. Office of Naval Research under Grant N00014-14-1-0653 and the Air Force Office of Scientific Research and the National Science Foundation EFRI 2-DARE Grant No. 1433459-EFMA*

*Contact: jhoo@lehigh.edu, kux214@lehigh.edu, lel216@lehigh.edu*

*Primary CNF Tools Used: ABM contact aligner, Autostep I-line stepper, PT720-740 etcher, SC4500 odd-hour evaporator, P10 profilometer*

## Abstract:

We've demonstrated that it is practical and promising to integrate TMDs or other 2D materials into current CMOS process based on large-scale transferred CVD MoS<sub>2</sub>, dispensed liquid-exfoliated MoS<sub>2</sub>, and temperature assisted converted PtSe<sub>2</sub> [1-4]. Of all two-dimensional (2D) atomic-layered materials, WSe<sub>2</sub> is particularly attractive for electronic applications because it has a sizable bandgap, a high carrier mobility, and can be grown on large scale by chemical vapor deposition (CVD). Additionally, both p-type and n-type conductions have been demonstrated, making it possible to realize complimentary logic in WSe<sub>2</sub>. In the present experiment, CVD-grown millimeter-sized WSe<sub>2</sub> flakes were etchant-free transferred onto Al gates covered by 30-nm-thick Al<sub>2</sub>O<sub>3</sub> gate insulation. With Al<sub>2</sub>O<sub>3</sub> passivation, the fabricated WSe<sub>2</sub> MOSFETs were found stable for more than five months. The Al<sub>2</sub>O<sub>3</sub> passivation had the additional benefit of enhancing the current capacity of the MOSFETs by two orders of magnitude. Temperature-dependent small-signal microwave measurements showed that both the forward current-gain cut-off frequency ( $f_T$ , Figure 1a) and the maximum frequency of oscillation ( $f_{MAX}$ , Figure 1b) of the MOSFETs tend to peak near room temperature, with  $f_T \sim 600$  MHz and  $f_{MAX} \sim 2$  GHz (Figure 1c) [5].

## Summary of Research:

**Fabrication.** The main difference of the fabrication between this work and [1] is in the material preparation part. In this work, multilayer tungsten diselenide (WSe<sub>2</sub>) films were synthesized on c-plane sapphire substrate through a multi-step gas source chemical vapor deposition (CVD) process [6]. After CVD growth, the film was transferred onto the target chip by an etchant-free transfer method [7].

**Passivation Result.** The transfer curves of the device at row 5 column 8 (Device 0508) before and after passivation are shown in Figure 2(a). With passivation, the transfer curve, under drain-source bias ( $V_{DS}$ ) of 1 V, shows current capacity increased by more than two orders of magnitude from  $\sim 1$  nA/ $\mu$ m to  $\sim 200$  nA/ $\mu$ m. Although the on/off ratio decreased, the resulting transconductance still increased from  $\sim 0.5$  nS/ $\mu$ m to  $\sim 30$  nS/ $\mu$ m. In five months, the transfer characteristics did not show noticeable change compared with the characteristics directly after passivation.

**DC & RF Thermal Dependence.** Figure 2(b) and (c) shows the output and transfer characteristics under different temperature ranging from 223 K to 373 K, of the device at row 3 column 10 (Device 0310). From Figure 2(b), higher temperature leads to saturation at lower  $V_{DS}$  because the increasing phonon scattering lowered the mobility and saturation velocity of the electrons. The drain current decreased with increasing temperature under the same biases. The output curves also indicated that when  $V_{DS} < 1$  V, the device characteristics were dominated by large resistances, which were probably the contact resistances at drain and source. From Figure 2(c), with increasing temperature, the hysteresis first increased and then decreased until at 373 K, the device showed p-type conduction, which suggested that temperature as high as 373 K could effectively anneal the sample and even change the conduction carrier type.

Figure 1(a) and (b) show the current gain and power gain of Device 0310 separately after de-embedding under different temperature. The  $f_T$  and  $f_{MAX}$  peak near room temperature (Figure 1c). The reason  $f_T$  and  $f_{MAX}$  peak near room temperature is probably due to competing temperature effects. For example, contact resistance, carrier mobility, and saturation voltage all decrease with increasing temperature. These competing effects are being characterized and will be incorporated into a device model to evaluate their combined effect.

**Future Direction.** First, the uniformity of device performances across the same chip based on single CVD film can be improved. Other than film uniformity itself, direct growth should also help as in the transfer process, the stress introduced by wrinkles during transfer is different at different locations. Second, better interface can be formed if the process can be done in connected ultra-high vacuum (UHV) chambers. This can help to rule out the ambient environment effects in the analysis and make results more reproducible. Third, hexagonal boron nitride can be used as both dielectric and passivation buffer layer to offer better interface and possibly better thermal stability. Finally, introducing contact bias and gate-length dependence study to truly understand the 2D channel.

## References:

- [1] K. Xiong, et al., "CMOS-compatible batch processing of monolayer MoS<sub>2</sub> MOSFETs," *J. Phys. D: Appl. Phys.*, vol. 51, no. 15, pp. 15LT02-1-15LT02-6, Mar. 2018.
- [2] K. Xiong, et al., "Large-scale fabrication of RF MOSFETs on liquid-exfoliated MoS<sub>2</sub>," in *European Microwave Conf. (EuMC)*, Madrid, Spain, Sep. 2018, pp. 1.4.
- [3] K. Xiong, et al., "Improvement by channel recess of contact resistance and gate control of large-scale spin-coated MoS<sub>2</sub> MOSFETs," *IEEE Electron Device Lett.*, vol. 39, no. 9, pp. 1453-1456, Sep. 2018.
- [4] L. Li, et al., "Wafer-scale fabrication of recessed-channel PtSe<sub>2</sub> MOSFETs with low contact resistance and improve gate control," *IEEE Trans. Electron Devices*, vol. 65, no. 10, pp. 4102-4108, Oct. 2018.
- [5] K. Xiong, et al., "Temperature Dependence of Al<sub>2</sub>O<sub>3</sub>-Passivated WSe<sub>2</sub> RF MOSFETs," *IEEE Electron Device Lett.*, in preparation.
- [6] X. Zhang, et al., "Diffusion-Controlled Epitaxy of Large Area Coalesced WSe<sub>2</sub> Monolayers on Sapphire," *Nano Lett.*, vol. 18, no. 2, pp. 1049-1056, Jan. 2018.
- [7] F. Zhang, et al., "Etchant-free transfer of 2D nanostructures," *Nanotechnology*, vol. 29, no. 2, pp. 025602-1-025602-5, Dec. 2017.

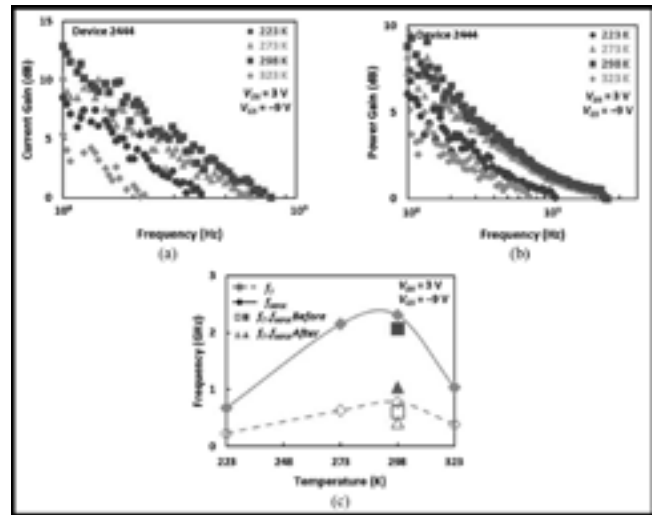


Figure 1: Temperature dependence of de-embedded small-signal (a) current gain, (b) power gain, and (c) cutoff frequencies. (Find full color on pages xiv-xv.)

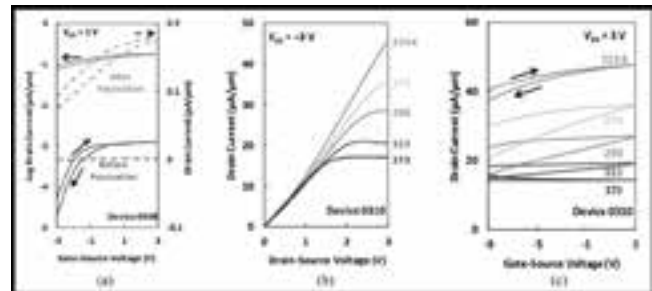


Figure 2: (a) Drain current under different gate-source voltages in log and linear scale,  $V_{DS} = 1 V$ , (b) output curves ( $V_{GS} = -3 V$ ) and (c) transfer curves ( $V_{DS} = 3 V$ ) of device 0310 under different temperatures (223, 273, 298, 323, 373 K).

# Fully Transparent Oxide Thin-Film Transistor with Record Current and On/Off Ratio

CNF Project Number: 2543-17

Principal Investigator(s): Darrell Schlom

User(s): Jisung Park

Affiliation(s): Department of Material Science and Engineering, Cornell University, Ithaca, NY 14853, USA

Primary Source(s) of Research Funding: Air Force Office of Scientific Research - DOD

Contract: schlom@cornell.edu, gp359@cornell.edu

Primary CNF Tools Used: PT720/740, PVD75 sputter deposition, Oxford ALD FlexAL, Autostep i-line stepper

## Abstract:

Here we report making a fully depleted micrometer-scale barium tin oxide ( $\text{BaSnO}_3$ )-based fully transparent TFT that sources over  $1.6 \text{ mA}/\mu\text{m}$  of current with an on/off ratio over  $10^8$  and a peak mobility of  $68 \text{ cm}^2\text{V}^{-1}\text{s}^{-1}$  at room temperature. Further scaling of these TFTs is expected to provide performance rivaling today's most advanced and scaled transistors. Our results demonstrate the tremendous potential of  $\text{BaSnO}_3$  for the future of transparent oxide electronics.

## Summary of Research:

A fully transparent oxide TFT based on  $\text{BaSnO}_3$  has been fabricated with record drain current and on/off current ratio. This breakthrough is made possible by (1) high mobility bare films in combination with (2) the development of a micrometer-scale etching method for  $\text{BaSnO}_3$  that preserves the surface roughness, conductivity, resistivity and mobility of  $\text{BaSnO}_3$  films. These results demonstrate the tremendous potential of  $\text{BaSnO}_3$  for the future of transparent electronics.

## References:

- [1] Zhou, H., Maize, K., Qiu, G., Shakouri, A., and Ye, P. D.  $\beta$ -Ga2O3 on insulator FET with drain currents exceeding  $1.5 \text{ A}/\text{mm}$  and their self-heating effect. *Appl. Phys. Lett.* 111, 092102 (2017).
- [2] Kim, U., et al. All-perovskite transparent high mobility field effect using epitaxial  $\text{BaSnO}_3$  and  $\text{LaInO}_3$ . *APL Mater.* 3, 036101 (2015).
- [3] Kim, H. J., et al. High mobility in a stable transparent perovskite oxide. *Appl. Phys. Exp.* 5, 061102 (2012).
- [4] Park, C., et al. High mobility FET based on  $\text{BaSnO}_3$  with  $\text{Al}_2\text{O}_3$  gate oxide. *Appl. Phys. Lett.* 105, 203503 (2014).
- [5] Kim, Y. M., et al. High- $\kappa$  perovskite gate oxide  $\text{BaHfO}_3$ . *APL Mater.* 5, 016104 (2017).
- [6] Kim, Y. M., et al. High-mobility  $\text{BaSnO}_3$  thin-film transistor with  $\text{HfO}_2$  gate insulator. *Appl. Phys. Exp.* 9, 011201 (2016).
- [7] Mun, H., et al. Large effects of dislocations on high mobility of epitaxial perovskite  $\text{Ba}_{0.96}\text{La}_{0.04}\text{SnO}_3$  films. *Appl. Phys. Lett.* 102, 252105 (2013).
- [8] Kim, U.  $\text{BaSnO}_3$ : thin films growth, transport properties, devices, and interfaces. PhD dissertation, Seoul National University, Department of Physics and Astronomy, August (2015).

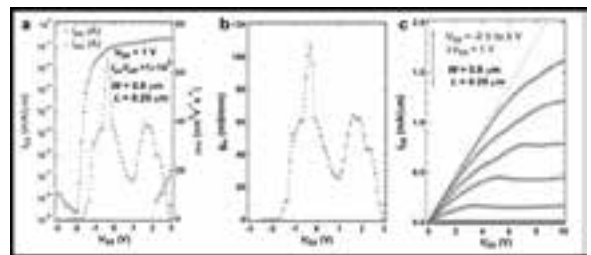


Figure 1: Thin-film transistor based on  $\text{La-BaSnO}_3$ . a, The transfer characteristic of the TFT in the linear region ( $V_{\text{DS}} = 1\text{V}$ ) and the transconductance. The peak field-effect mobility is  $68 \text{ cm}^2\text{V}^{-1}\text{s}^{-1}$  and the on-off ratio is over  $10^8$ . The subthreshold swing is  $0.1 \text{ V}/\text{dec}^{-1}$ . b, Transconductance of the device at  $V_{\text{DS}} = 1\text{V}$ . The maximum transconductance is  $10^7 \text{ mS}/\text{mm}$ . c, The output characteristic of the device at  $V_{\text{GS}} = -2, -1, 0, 1, 2, 3, 4, 5 \text{ V}$ . The maximum drain current exceeds  $1.6 \text{ mA}/\mu\text{m}$ .

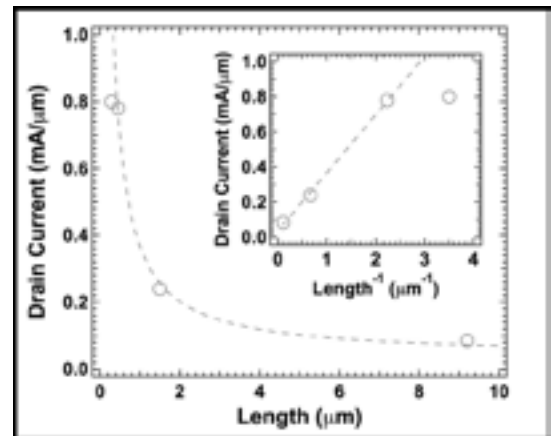


Figure 2: Drain current dependence on channel length ( $L$ ) when  $V_{\text{GS}} = 3 \text{ V}$  and  $V_{\text{DS}} = 10 \text{ V}$ . The drain current ( $I_{\text{D}}$ ) is inversely proportional to the overall channel length except at the shortest channel length, showing little degradation with respect to device scaling. The deviation from linear behaviour in the inset at the shortest channel length is consistent with a velocity saturation effect: the degradation of the mobility and thus the drain current as the carrier velocity is limited by increased scattering rate at the high electric field at short channel length.



# Injectable Micro-Scale Opto-Electrically Transduced Electrodes (iMOTES)

**CNF Project Number: 2578-17**

**Principal Investigator(s): Prof. Alyosha C. Molnar**

**User(s): Sunwoo Lee, Alejandro J. Cortese**

*Affiliation(s): Electrical and Computer Engineering, Cornell University*

*Primary Source(s) of Research Funding: National Institute of Health*

*Contract: AM699@cornell.edu, SL933@cornell.edu*

*Website: <https://molnargroup.ece.cornell.edu/>*

*Primary CNF Tools Used: ABM contact aligner, AJA sputter, Westbond 7400A ultrasonic wire bonder, Oxford 100 / 81 / 82, Unaxis deep Si etcher, Oxford PECVD, Oxford ALD, Anatech, P7 profilometer, ZEISS Ultra and Supra SEMs*

## Abstract:

Recording neural activity in live animals *in vivo* poses several challenges. Electrical techniques typically require electrodes to be tethered to the outside world directly via a wire, or indirectly via an RF Coil [1], which is much larger than the electrodes themselves. Tethered implants result in residual motion between neurons and electrodes as the brain moves, and limits our ability to measure from peripheral nerves in moving animals, especially in smaller organisms such as zebra fish or fruit flies. On the other hand, optical techniques, which are becoming increasingly powerful, are nonetheless often limited to subsets of neurons in any given organism, impeded by scattering of the excitation light and emitted fluorescence, and limited to low temporal resolution [2]. Here we present the electronics for an untethered electrode unit, powered by, and communicating through a microscale optical interface, combining many benefits of optical techniques with high temporal-resolution recording of electrical signals, named Injectable Micro-scale Opto-electrically Transduced Electrodes (iMOTES).

## Summary of Research:

Our fabrication starts with a 5mm × 5mm, conventional 180 nm CMOS die, which contains the electronics for signal amplification, encoding, and transmission. The CMOS die is then integrated with AlGaAs diode, which acts as a photo-voltaic (PV) as well as light emitting diode (LED), hence the diode is abbreviated as PVLED. The PVLED provides an optical link that powers the electronics and transmits encoded signals in optical pulses. The MOTE utilizes pulse position modulation (PPM) for signal encoding for its high information-per-photon efficiency, where the spacing between the output pulses is proportional to the measured electric field of neuronal signals across the measurement electrodes.

Figure 1 depicts a conceptual deployment and simplified schematic of described iMOTE [3].

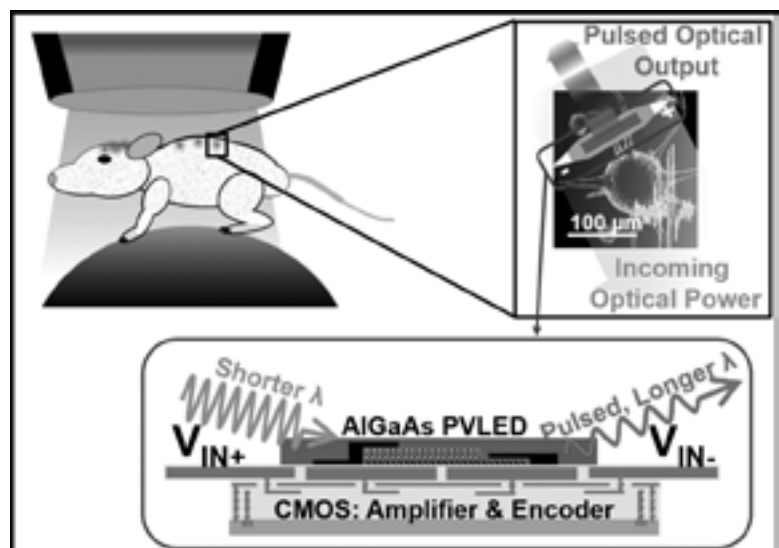


Figure 1: An envisioned implementation of the iMOTE along with a simplified system description.

The AlGaAs diodes are first fabricated on a sapphire wafer, to be later released from the sapphire substrate with a sacrificial poly(methyl methacrylate) (PMMA) polymer. Once the PMMA-coated AlGaAs diodes are transferred onto the CMOS die, the Oxford 81 plasma etcher is used to remove the sacrificial PMMA, leaving only the diodes array intact on the CMOS die. To establish the electrical contact between the PVLED and CMOS, we have used the CNF ABM contact aligner for photolithography with AZ nLof2020 UV photoresist for efficient lift-off process that ensues after metal deposition. After the contact fabrication, the contacts of CMOS and PVLED are connected via similar photolithography process, and to maximize the conformality of the metal routing, we employ AJA sputter.

Following the routing step, each iMOTE is encapsulated using Oxford ALD and PECVD for  $\text{SiO}_2$  and  $\text{Si}_3\text{N}_4$  deposition, followed by dielectric etching using Oxford 100 and Unaxis deep reactive ion etch (DRIE) for release. Figure 2 described the fabrication sequence described herein.

It should be noted that before making much changes are made in fabrication flow, to confirm the functionality of each module (CMOS and the diode), we use Westbond 7400A ultrasonic wire bonder for board-level test. ZEISS Ultra and Supra scanning electron microscopes (SEMs) are also used to inspect the fabricated iMOTE for debugging purposes.

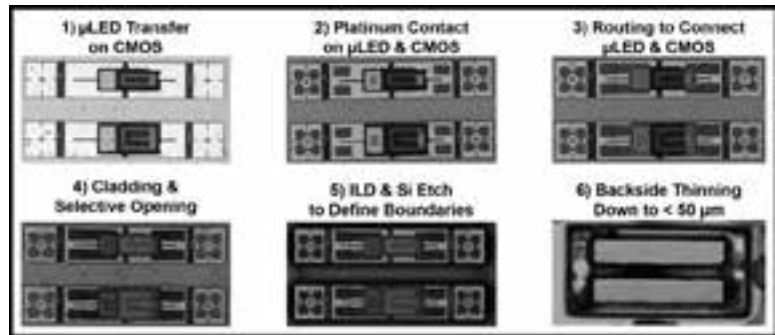


Figure 2: Fabrication flow of iMOTE integration where AlGaAs PVLED is integrated on CMOS. 1) Micro-scale PVLED is transferred on CMOS, 2) platinum contacts fabricated on both PVLED and CMOS, 3) platinum routing is added to connect the contacts made in 2), 4) iMOTEs are passivated with  $\text{SiO}_2$  and  $\text{Si}_3\text{N}_4$  except for its input electrodes openings, 5) using dielectric etching and deep silicon etching, iMOTEs are 'cookie-cut', 6) backside etching allows thinning-down below  $50 \mu\text{m}$ .

## References:

- [1] R. R. Harrison, et al., "A Low-Power Integrated Circuit for a Wireless 100-Electrode Neural Recording System," in IEEE J. Solid-State Circuits, vol. 42, no.1, pp. 123-133, Jan. 2007.
- [2] W. Yang and R. Yuste, "In vivo imaging of neural activity," Nature Methods, vol. 14, no. 4, pp. 349-359, April 2017.
- [3] S. Lee, et al., "A  $250 \mu\text{m} \times 57 \mu\text{m}$  Microscale Opto-electronically Transduced Electrodes (MOTEs) for Neural Recording," IEEE Transactions on Biomedical Circuits and Systems, vol. 12, no. 6, pp. 1256-1266, December 2018.

# Trench Formation and Filling in Silicon Carbide

**CNF Project Number: 2755-18**

**Principal Investigator(s): Zeynep Dilli**

**User(s)): Aysanew Abate**

*Affiliation(s): CoolCAD Electronics, LLC*

*Primary Source(s) of Research Funding: National Aeronautics and Space Administration (NASA)*

*Contact: zeynep.dilli@coolcadelectronics.com, aysanew.abate@coolcadelectronics.com*

*Primary CNF Tools Used: Oxford Cobra etcher, PT770 etcher (left chamber), Logitech Orbis CMP*

## Abstract:

The two main objectives of our time in the CNF was to form deep trenches in silicon carbide and to planarize our polysilicon trench fill material.

## Summary of Research:

Our first objective was to etch deep trenches in silicon carbide. In order to achieve this, a patterned metal mask was used since photoresist and oxide have poor etch selectivity relative to SiC in fluorine-based reactive ion etches (RIE).

A metal layer was first deposited on to the bare SiC surface. Photoresist was then applied and lithographically patterned on the metal layer. The trench pattern was then etched into the metal using a chlorine ICP etcher, the PT770, exposing the SiC. Finally, the Oxford Cobra ICP was then used to etch the deep trenches into the exposed SiC using SF<sub>6</sub>-based chemistry. The depth of the trench features were measured using the P10 profilometer.

Thick undoped polysilicon was then deposited to fill the deep trenches. In order to remove the polysilicon from non-trench areas and also to planarize the polysilicon over the trenches, chemical-mechanical polishing (CMP) was used.

Additional work still needs to be completed in order to determine whether this process was satisfactory, such as using a scanning electron microscope (SEM) to determine whether the trenches have been completely filled. In addition to this, metal line test features need to be deposited over the array of deep trenches and electrically tested to confirm that they are shorted across the array, verifying that they are not breaking over the trenches.

## References:

- [1] Bashir, R., and Hebert, F. PLATOP: A novel planarized trench isolation and field oxide formation using poly-silicon. IEEE Electron Device Letters, 17(7), 352-354. doi:10.1109/55.506364 (1996).
- [2] Voldman, S. H. The Influence of a Novel Contacted Polysilicon-Filled Deep Trench (DT) Biased Structure and Its Voltage Bias State on CMOS Latchup. 2006 IEEE International Reliability Physics Symposium Proceedings, 151-158. doi:10.1109/relphy.2006.251208 (2006).

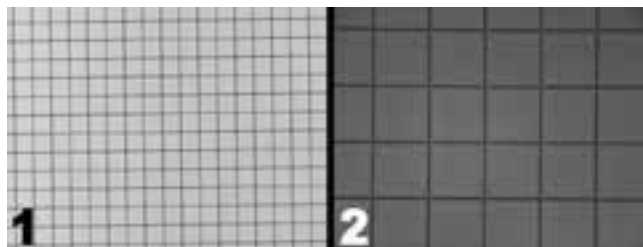


Figure 1, left: Trench features etched into the metal mask. Figure 2, right: Trench features etched into the SiC wafer, no metal mask present.

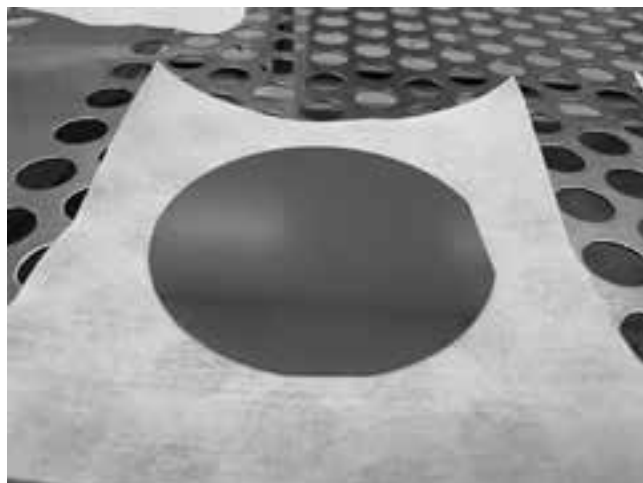


Figure 3: Thick polysilicon on SiC.

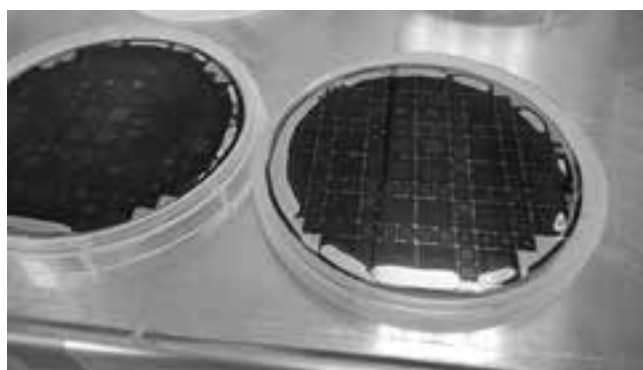


Figure 4: Post-polysilicon CMP.

# Emerging III-Nitride Devices for Terahertz Electronics

**CNF Project Number: 2800-19**

**Principal Investigator(s): Huili Grace Xing, Debdeep Jena**

**User(s): Jimmy Encomendero, Austin Hickman, Samuel Bader**

*Affiliation(s): Electrical and Computer Engineering, Cornell University*

*Primary Source(s) of Research Funding: Office of Naval Research under the DATE MURI Program*

*Contact: grace.xing@cornell.edu, djena@cornell.edu, jje64@cornell.edu, alh288@cornell.edu, sjb353@cornell.edu*

*Primary CNF Tools Used: Veeco AFM, ABM contact aligner, YES Asher, odd-hour evaporator, PT770 etcher, P10 and P7 profilometer, Oxford ALD, Oxford 81 etcher, AJA sputtering*

## Abstract:

In the present work, we report the design, fabrication and demonstration of emerging III-nitride electronic devices that hold the promise for the manufacture of high-power ultra-fast electronic amplifiers and complementary logic based solely on nitride semiconductors. A novel design of a quantum well transistor is presented and its power performance is assessed employing the Johnson figure-of-merit. The complementary III-nitride p-channel transistor is also studied here, showing record performance in terms of on-current and carrier density. Finally, vertical resonant tunneling transport is also studied in III-nitride heterostructures. By introducing an analytical quantum transport model for III-nitride resonant tunneling diodes (RTDs), we reproduce all the features of the experimentally measured tunneling current. These advances pave the way for the design all-nitride high-power ultra-fast amplifiers and digital integrated circuits.

## Summary of Research:

III-nitride materials have emerged as a promising platform for the development of electronic devices capable of meeting the increasing demand for high-power ultra-fast amplifiers for communication networks, and complementary transistors for computing applications. This revolutionary family of wide bandgap semiconductors has already enabled the manufacture of high-power electronic switches, harnessing the internal polarization fields for the generation of highly dense two-dimensional electron gases (2DEG) [1]. However, digital applications require the manufacture of the complementary 2D hole gas (2DHG) switch, which would unleash the full potential of III-nitride semiconductors for digital applications.

In this report, we present important advances in the design, fabrication and understanding III-nitride switches that can be employed for the development of the nitride-based complementary logic for computation, and ultra-fast resonant tunneling diodes (RTDs) that hold the promise for the development of future nitride-based terahertz electronics.

Polarization-induced high-electron mobility transistors (HEMTs) are the workhorse of nitride electronics. HEMTs harness the high electron density of the 2DEG induced at the AlGa<sub>N</sub>/Ga<sub>N</sub> heterointerfaces.

In the present work, we report a novel design in which a 2DEG is engineered employing AlN as the buffer layer,

thus taking advantage of the higher thermal conductivity of the AlN platform. The 2DEG confinement is provided by a 30-nm GaN quantum well sandwiched between the AlN buffer region and a 2-nm AlN top barrier as shown in Figure 1(a). Transistors are fabricated employing a realigned last-gate process with non-alloyed ohmic contacts [2]. Figure 1(b) shows the output characteristics measured at room temperature, revealing a saturation current of 2A/mm and a low on-resistance of 1.3 Ωmm. The transfer curve for this quantum-well HEMT design is displayed in Figure 1(c), showing a current modulation that spans four orders of magnitude with a peak transconductance of 0.6 S/mm. To assess the high-power performance of these devices, breakdown voltage is measured in multiple devices, resulting in a maximum breakdown voltage of 591 Volts.

In addition to III-nitride quantum well HEMTs, the complementary p-type transistor, enabled solely by polarization engineering, is also introduced here. The heterostructure is grown by molecular beam epitaxy (MBE) atop an AlN-template substrate [3]. The MBE-grown layers comprise an AlN buffer layer, an unintentionally (UID)-doped GaN layer extending 5 nm and a 10 nm p-type GaN layer that facilitates the formation of ohmic contacts [See Figure 2(a)]. Enhancement mode p-channel field-effect transistors (pFETs) are fabricated employing a gate-recess process. The transistor characteristics are displayed in Figure

2(b), revealing a record-high on-current of 10 mA/mm and a 640- $\Omega$ mm on-resistance. Figure 2(c) shows that the drain current is modulated over four orders of magnitude with a maximum transconductance of 1.5 mS/mm. These results constitute a significant improvement in state-of-art III-nitride pFETs, raising hopes for the demonstration of nitride-based digital ICs.

So far we have discussed the DC operation of III-nitride switches, however high-data rate communication networks also require ultra-fast amplifiers that operate at frequencies approaching the terahertz band. To push the cutoff frequencies of III-nitride high electron mobility transistors (HEMTs) towards this frequency band, parasitic management techniques and highly-scaled fabrication processes have been recently employed [4,5]. However, amplification at frequencies > 1 THz is yet to be demonstrated; in this scenario, alternative gain mechanisms such as resonant tunneling injection, have been proposed to achieve terahertz power amplification [6]. The recent successful engineering of resonant tunneling injection in III-nitride heterostructures [7] has led to an invigorated effort to harness the multiple advantages of nitride-based resonant tunneling devices. Because of their noncentrosymmetric crystal structure, sheets of polarization charge are induced at the heterointerfaces of nitride heterostructures, which lead to a redistribution of free carriers across the active region and surrounding contacts. To get a further insight into the effects of the internal polarization fields, we have recently introduced a quantum transport model that captures the physics of resonant tunneling transport across polar heterostructures.

To experimentally study resonant tunneling transport, we fabricate a series of resonant tunneling diodes (RTDs) with the device structures shown in Figure 3(a). Reflection high-energy electron diffraction (RHEED) is employed to monitor the incorporation of single atomic monolayers to the AlN tunneling barriers [8]. Devices are fabricated employing a self-aligned process and the current-voltage characteristics are measured at room temperature as shown in Figure 3(b). Clear and repeatable negative differential conductance is measured in each of the fabricated samples. Figure 3(b) shown the exponential relationship between the barrier thickness and the resonant tunneling current. Finally, we develop a comprehensive quantum transport model that completely captures all the experimentally measured features of the tunneling current. This model provides a clear insight into the polar RTD current-voltage characteristics and its connection with the heterostructure design parameters. This theory can be employed for the design of nitride resonant tunneling devices exhibiting efficient current injection and improved tunneling dynamics as required in practical applications.

## References:

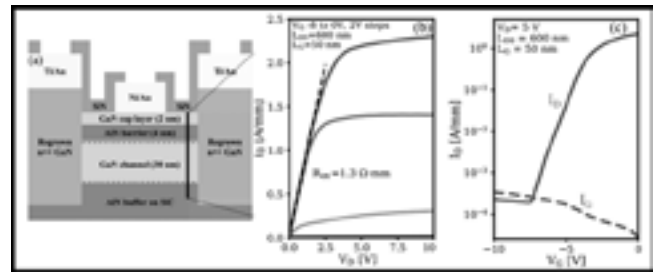


Figure 1: (a) Schematic cross section of the quantum well high-electron mobility transistor (HEMT). (b) and (c) Output and transfer characteristics of the device fabricated at CNF.

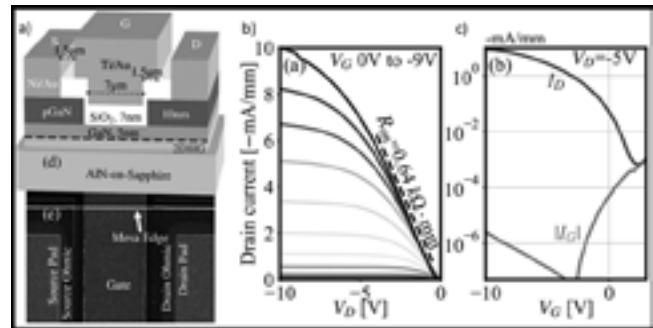


Figure 2: (a) Schematic cross section of the III-nitride p-type field effect transistor (pFET) fabricated in CNF. (b) Room-temperature current-voltage output characteristics show a record-high saturation current of 10 mA/mm and low on-resistance. (c) Transfer characteristics showing four orders of drain current modulation and a peak transconductance of 1.6 mS/mm.

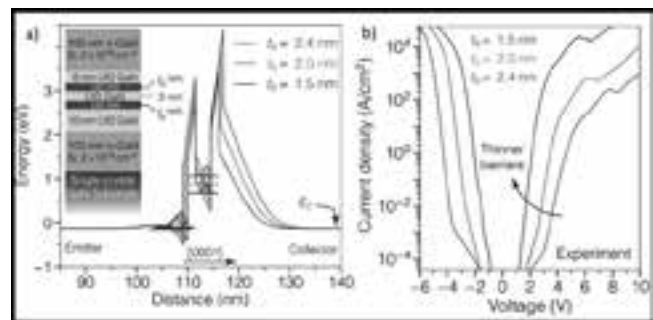


Figure 3: (a) Schematic cross section and band diagram of three resonant tunneling diodes grown by molecular beam epitaxy on single-crystal GaN substrates. (b) Room-temperature current-voltage characteristics for each of the fabricated diodes showing the exponential modulation of the tunneling current as a function of barrier thickness.

- [1] T. Suemitsu, IEICE Electronics Express 12, 20152005 (2015).
- [2] A. Hickman, et al., IEEE Electron Device Letters, in press (2019),
- [3] S. Bader, et al., IEEE Elec. Device Letters, 39, 12, 1848-51 (2018).
- [4] Y. Tang, et al., IEEE Electron Device Letters 36, 549 (2015).
- [5] Y. Yue, et al., Japanese J. of Applied Physics 52, 08JN14 (2013).
- [6] B. Sensale-Rodriguez, et al., IEEE Transactions on Terahertz Science and Technology 3, 200 (2013).
- [7] J. Encomendero, et al., Phys. Rev. X 7, 041017 (2017)
- [8] J. Encomendero, et al., Phys. Rev. Applied 11, 034032 (2019).

# Fully Passivated InAlN/GaN HEMTs on Silicon with $f_T/f_{MAX}$ of 144/141 GHz

CNF Project Number: 2800-19

Principal Investigator(s): Huili Grace Xing, Debdeep Jena

User(s): Kazuki Nomoto

Affiliation(s): School of Electrical and Computer Engineering, Cornell University

Primary Source(s) of Research Funding: ComSenTer

Contact: grace.xing@cornell.edu, kn383@cornell.edu

Primary CNF Tools Used: Autostep i-line stepper, Heidelberg mask writer DWL2000, P7 profilometer, FilMetrics, AFM Veeco Icon, Zeiss SEM, PT770, Oxford81, Oxford PECVD, Oxford ALD, odd-hour evaporator, AJA sputter deposition, RTA AG610, JEOL9500

## Abstract:

Depletion-mode high-electron mobility transistors (HEMTs) based on a quaternary barrier  $\text{In}_{0.17}\text{Al}_{0.83}\text{N}$ /AlN/GaN heterostructure on a Si substrate were fabricated. The 87 nm long gate device shows a dc drain current density of 2.48 A/mm, a peak extrinsic transconductance of 450 mS/mm, and balanced current gain cutoff frequency  $f_T$  and maximum oscillation frequency  $f_{MAX}$  are 144 and 141 GHz, respectively.

## Summary of Research:

Gallium nitride (GaN)-based high electron mobility transistors (HEMTs) have demonstrated great potential for high-speed, high power RF applications [1] and next-generation power electronics [2]. In addition, the adoption of a Si substrate would pave the way for low cost and high-performance GaN electronics.

We report the fabrication and DC and RF characteristics of fully passivated InAlN/GaN high-electron mobility transistors (HEMTs) on Si substrates with balanced  $f_T$  and  $f_{MAX}$  (144/141 GHz).

The InAlN/AlN/GaN HEMT structure consists of a 10 nm  $\text{In}_{0.17}\text{Al}_{0.83}\text{N}$  barrier, a 1 nm AlN spacer (total barrier thickness: 11 nm), a 800 nm unintentionally doped GaN channel, and AlGaIn/AlN buffer and nucleation layers on a 6" Si substrate, grown by a Propel<sup>®</sup> HVM MOCVD system at Veeco Instruments. Room temperature Hall-effect measurements prior to device fabrication showed a 2DEG sheet concentration of  $2.4 \times 10^{13}/\text{cm}^2$  and electron mobility of  $1310 \text{ cm}^2/\text{V}\cdot\text{s}$ , corresponding to a sheet resistance of  $196 \Omega/\text{sq}$ .

A schematic cross-section of the InAlN/AlN/GaN HEMT device with regrown  $n^+$  GaN contacts is shown in Figure 1(a). The device fabrication process started with patterning of a  $\text{SiO}_2$  mask for  $n^+$ GaN ohmic regrowth by PA-MBE. The prerogrowth etch depth into the HEMT

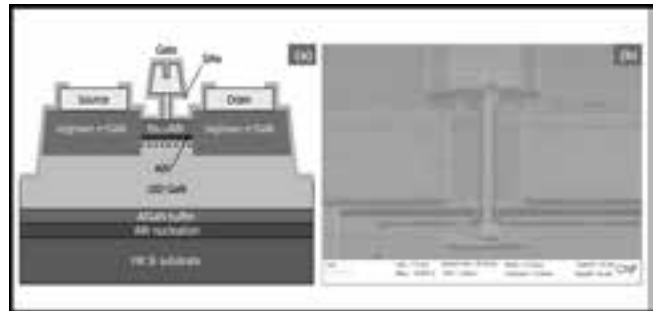


Figure 1: (a) Schematic cross-section of fully passivated InAlN/AlN/GaN HEMTs on Si with regrown  $n^+$ GaN contacts. (b) An angled SEM image of a fabricated InAlN/AlN/GaN HEMT with an EBL T-gate.

structure was 40 nm, and regrown  $n^+$ GaN was 100 nm with a Si doping level of  $7 \times 10^{19}/\text{cm}^3$ . Non-alloyed ohmic contact of Ti/Au/Ni was deposited by e-beam evaporation. T-shaped Ni/Au (40/200 nm) gates were formed by electron-beam lithography, followed by liftoff. The devices were finally passivated by a 50 nm PECVD  $\text{SiN}_x$ . TLM measurements yielded a contact resistance of  $0.19 \Omega\cdot\text{mm}$ . The device presented here has a regrown  $n^+$ GaN source-drain distance  $L_{sd}$  of 800 nm, a gate width of  $2 \times 25 \mu\text{m}$ , and a gate length  $L_g$  of 87 nm. Figure 1(b) shows an angled-SEM image of the fabricated InAlN/AlN/GaN HEMT.

Figure 2(a) shows the family  $I$ - $V$  curves of the device, measured for  $V_{ds} = 0$  to  $8$  V and  $V_{gs} = 1$  to  $-8$  V. The device has a saturation drain current  $I_{dss} = 2.48$  A/mm and an on-resistance  $R_{on} = 1.07$   $\Omega$ ·mm extracted at  $V_{gs} = 1$  V. The transfer curves are shown in Figure 2(b). A peak extrinsic transconductance  $g_m$  is  $\sim 0.45$  S/mm at  $V_{ds} = 5$  V. Figure 3(a) shows the current gain  $|h_{21}|^2$  and unilateral gain  $U$  of the device as a function of frequency at the peak  $f_T$  bias condition,  $V_{ds} = 5$  V, and  $V_{gs} = -4.6$  V. The extrapolation of both  $|h_{21}|^2$  and  $U$  with  $-20$  dB/dec slope gives the current gain cutoff frequency/maximum oscillation frequency  $f_T / f_{MAX}$  of 144/141 GHz after de-embedding. The  $f_T$  and  $f_{MAX}$  of the device are summarized in Figure 3(b). Figure 3(b) shows how the results of this device compare with the early state-of-art results of GaN HEMTs on Si substrates [3,4].

**References:**

- [1] Y. Yue, et al., "InAlN/AlN/GaN HEMTs with regrown ohmic contacts and  $f_T$  of 370 GHz," IEEE Electron Device Lett., vol. 33, no. 7, pp. 988-990, Jul. 2012.
- [2] M. Zhu, et al., "1.9-kV AlGaIn/GaN lateral Schottky barrier diodes on silicon," IEEE Electron Device Lett., vol. 36, no. 4, pp. 375-377, Apr. 2015.
- [3] O. Laboutin, et al., ECS Transactions, 41 (8) 301-311 (2011).
- [4] W. Xing, et al., IEEE EDL, Vol. 39, No. 1, 75-78 (2018).

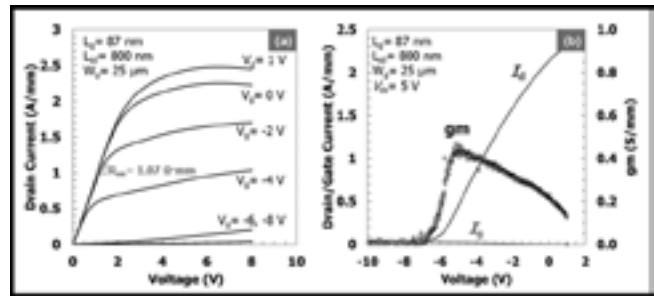


Figure 2: (a) Family  $I$ - $V$  curves and (b) transfer characteristics of the device with  $L_g = 87$  nm and  $L_{sg} = 800$  nm.

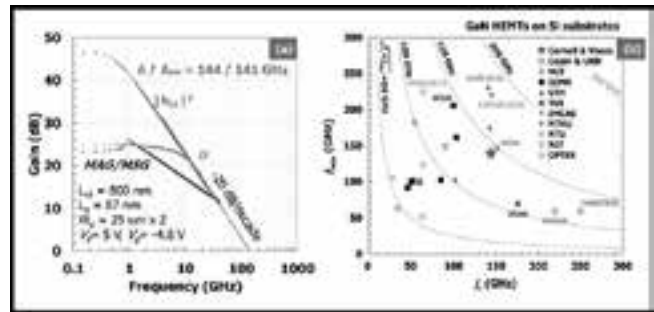


Figure 3: (a) Current gain and unilateral gain of the device with  $L_g = 87$  nm, showing  $f_T / f_{MAX} = 144/141$  GHz. (b) Comparison of the measured  $f_T$  and  $f_{MAX}$  of GaN HEMTs on Si substrates.

# Area-Selective Deposition to Enable Single-digit nm Fabrication

**2019 CNF REU Intern: James M.H Tran**

**2019 CNF REU Intern Affiliation:**

**Electrical Engineering, The University of Texas at Dallas**

*CNF Project: 2019 Cornell NanoScale Science & Technology Facility Research Experiences for Undergraduates Program*

*CNF REU Principal Investigator(s): Prof. James R. Engstrom, Chemical and Biomolecular Engineering, Cornell University*

*CNF REU Mentor(s): Taewon Suh and Colleen C. Lawlor, Chemical and Biomolecular Engineering, Cornell University*

*Primary Source of CNF REU Funding: National Science Foundation via*

*the National Nanotechnology Coordinated Infrastructure (NNCI) Grant No. NNCI-1542081*

*Contact: tranj@utdallas.edu, jre7@cornell.edu, ts695@cornell.edu, ccl233@cornell.edu*

*Website: <http://cnf.cornell.edu/education/reu/2019>*

*Primary CNF Tools Used: Photolithography spinners and hot plates, GCA AS200 stepper, Oxford 81/82 (80+) RIE etchers, Anatech resist strip, CVC SC4500 e-beam evaporator (odd), Logitech Orbis CMP*

## Abstract:

As semiconductor manufacturing approaches single-digit nm feature sizes, there is an increasing difficulty in reliably patterning critical device features. A major obstacle is that conventional top-down techniques suffer from issues with alignment of device features during the manufacturing process. Area-selective deposition (ASD) seeks to remedy this by a bottom-up technique; selectively depositing films only on defined growth areas and not on non-growth regions, creating a “self-aligned” feature. We produce line and space patterned wafers of metal and dielectric, copper and silicon dioxide in this study, to serve as a substrate for ASD experiments. We use various characterization techniques, such as optical microscopy and scanning electron microscopy (SEM), to evaluate our wafers. We also discuss intended uses of these wafers in ASD experiments.

## Introduction:

For decades, top-down manufacturing has been the method of choice for fabricating semiconductor devices. However, as we approach single-digit nm feature sizes, device patterning becomes problematic. At this scale, pattern misalignment can severely affect device functionality and operation. This misalignment is known as the “edge placement error” [1], which is defined as the distance between the actual and intended position of a patterned feature. ASD could achieve device patterning at the single-digit nm scale by utilizing a bottom-up approach, selectively depositing thin films using atomic layer deposition (ALD) or chemical vapor deposition (CVD) on defined deposition areas. By depositing thin films only on intended areas, any possibility of misalignment could be eliminated, because a “self-aligned” feature is created. In addition to resolving feature misalignment, ASD also introduces advantages such as uniform, conformal, and Angstrom level thickness controlled deposition of thin films.

In this study, 10, 5, 3, and 1  $\mu\text{m}$  line and space patterns of Cu and  $\text{SiO}_2$  were fabricated to study ASD of thin films. Alternating metal and dielectric patterns allow investigation of ASD of thin films on Cu and not on  $\text{SiO}_2$ , or vice versa. Variable widths of Cu and  $\text{SiO}_2$  enable study of how film growth varies with different feature sizes.

The pattern also has equal line and space widths of Cu and  $\text{SiO}_2$ , producing a 50/50 area coverage of metal and dielectric for *in situ* x-ray photoelectron spectroscopy (XPS) studies.

## Experiment Details:

500 nm  $\text{SiO}_2$  on 100 mm Si wafers were utilized. Wafers were cleaned in a Hamatech automated wafer processor with piranha solution before spin coating. Brewer Science WiDE-C 15C bottom anti-reflective coating (BARC) was spun at 3000 RPM for 60 seconds before a two-step bake on a 190°C proximity hotplate for 60 seconds, followed by a 160°C vacuum hotplate for 60 seconds. OiR 620-7i photoresist was spun at 5000 RPM for 60 seconds followed by a pre-exposure 90°C vacuum hotplate bake for 60 seconds. Exposure was performed on a GCA AS200 stepper, followed by a post-exposure bake on a 115°C vacuum hotplate. Etching was performed using the Oxford 80+ reactive ion etcher. BARC was etched using an  $\text{O}_2$  and Ar mixture for six minutes.  $\text{SiO}_2$  was etched with a mixture of  $\text{CHF}_3$  and Ar for 6:30 minutes to etch ~ 220 nm into the  $\text{SiO}_2$ . Resist and BARC were stripped using an Anatech  $\text{O}_2$  plasma dry strip, followed by a piranha clean. A CVC SC4500 e-beam evaporator was then used to deposit 25 nm of Ta as an adhesion layer, followed by

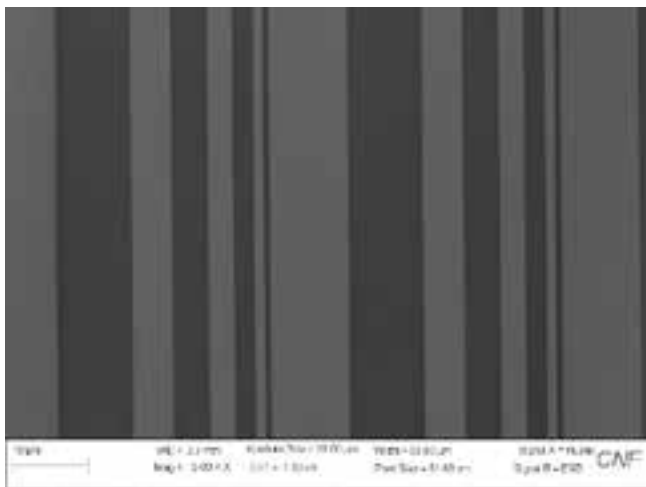


Figure 1: Top-down optical microscope image of 10, 5, 3, and 1  $\mu\text{m}$  widths of Cu and  $\text{SiO}_2$ . Bright areas correspond to Cu and dark blue to  $\text{SiO}_2$ .

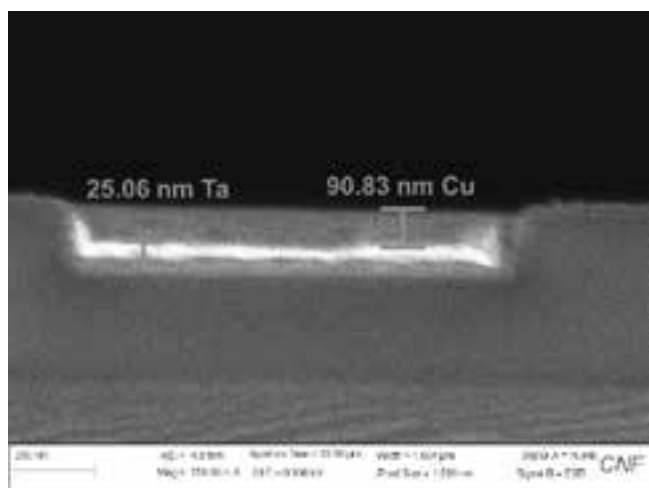


Figure 2: Cross-sectional SEM image of a 1  $\mu\text{m}$  width trench filled with 90.83 nm Cu on top of 25.06 nm Ta.

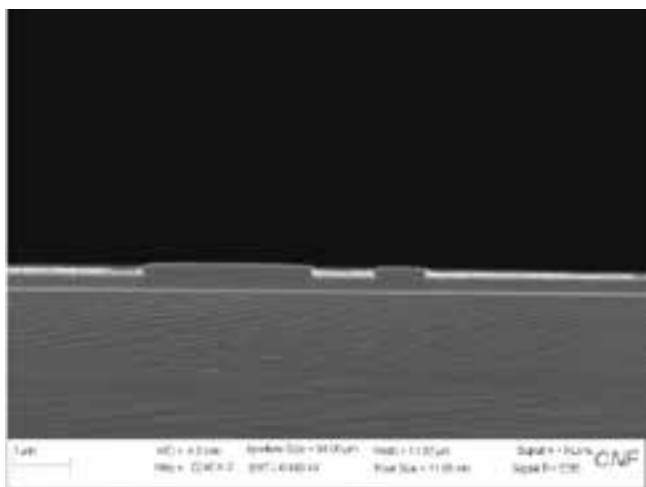


Figure 3: Etch uniformity across varying feature sizes.

300 nm Cu. Logitech-Orbis CMP was finally used to planarize the surface and remove Cu overburden at 4 psi down and 30 psi back pressure for 1:50 minutes. A Hamatech was then used again to clean the wafer of CMP debris.

### Results and Discussion:

Optical microscope images showed a definite line and space pattern of Cu and  $\text{SiO}_2$ . Images confirm enough Cu overburden was polished away to reveal the desired pattern, as shown in Figure 1. Cross-sectional SEM images show the anisotropic etch profile, and the Cu and Ta layers deposited in Figure 2. Ta was deposited as an adhesion layer between the Cu and the  $\text{SiO}_2$ . Without Ta, Cu would rip out of the trenches during the CMP step due to its poor adhesion to  $\text{SiO}_2$ . No metal was seen on top of the  $\text{SiO}_2$ , and the Cu line was level with the  $\text{SiO}_2$  space. Etch depth and anisotropic profile was consistent across varying feature sizes, as shown in Figure 4. The depth of Cu was kept greater than 70 nm, thick enough to serve as a substrate layer for surface-sensitive analysis techniques such as XPS.  $\text{CHF}_3$  and Ar was chosen as the etch chemistry for its anisotropic etch profile. The gas mixture combines physical etching from Ar and chemical etching from  $\text{CHF}_3$ .  $\text{CHF}_3$  provides F radicals that etch  $\text{SiO}_2$  [2,3].  $\text{Ar}^+$  ions etch the  $\text{SiO}_2$  by breaking its crystal bonds.  $\text{Ar}^+$  also desorbs the fluoropolymer film generated by the  $\text{CHF}_3$  radicals, exposing horizontal surfaces to the etch gases [2]. The fluoropolymer keeps the etch directional, by passivating the sidewalls of the  $\text{SiO}_2$  preventing lateral etching.

### Conclusions:

We successfully developed a robust and reproducible process to fabricate patterned line and space wafers. The ability to perform experiments on a patterned wafer will greatly enhance our understanding of area selective deposition.

### Acknowledgements:

Thanks to ERG and CNF staff for insight and helpful discussion. This work was performed in part at the Cornell NanoScale Facility via the 2019 CNF REU Program. The CNF is a member of the National Nanotechnology Coordinated Infrastructure (NNCI), which is supported by the National Science Foundation (Grant NNCI-1542081).

### References:

- [1] Mackus, A.J.M., M.J.M. Merx, and W.M.M. Kessels. "From the Bottom-Up: Toward Area-Selective Atomic Layer Deposition with High Selectivity." *Chemistry of Materials* 31, no. 1: 2-12. <https://doi.org/10.1021/acs.chemmater.8b03454> (January 8, 2019).
- [2] Fuller, Lynn, "Plasma Etching", *Microelectronic Engineering*, Rochester Institute of Technology.
- [3] Kunimasa Takahashi, et al. 1994 *Jpn. J. Appl. Phys.* 33 4745.

# Metal-Organic Hybrid Photoresists

**CNF Project Number: 386-90**

**Principal Investigator(s): Christopher Kemper Ober**

**User(s): Kazunori Sakai, Seok-Hyon Jung, Wenyang Pan**

*Affiliation(s): Materials Science and Engineering, Cornell University*

*Primary Source(s) of Research Funding: JSR Corporation*

*Contact: christoper.ober@cornell.edu, ks2288@cornell.edu, sj736@cornell.edu, wp222@cornell.edu*

*Primary CNF Tools Used: Zeiss Supra SEM, ASML 300C DUV stepper, ABM contact aligner*

## Abstract:

While extreme ultraviolet (EUV) lithography is being investigated for patterning under 20 nm half pitch pattern size, further improvement is needed for achieving high volume manufacturing. EUV lithography uses a wavelength of 13.5 nm and this brings about the biggest problem of EUV lithography that a typical EUV power source is incapable of generating enough photons compared to other light sources. In this circumstance, materials enabling use of fewer EUV photons have been investigated. In this report, microscale patterning results of metal-organic cluster resists with high EUV absorption composition and EUV exposure results of zinc organic cluster resist on different underlayer are described.

## Summary of Research:

While continuous effort has been dedicated to the extreme ultraviolet (EUV) lithography to follow Moore's law, further improvement is needed for achieving high volume manufacture.

One of the reasons why manufacturing by EUV lithography has taken a longer time to develop than other lithography techniques is typical EUV sources provide fewer numbers of photons than other light sources. In terms of materials, photoresists including higher EUV absorption and better underlayer materials absorbing EUV transmitted through the photoresist and assisting additional generation of acid have been investigated. Inorganic elements possess higher EUV absorption than organic elements and EUV photoresist, including metal oxide nanoparticles or metal complexes have been attracting interest.

We developed hafnium and zirconium oxide nanoparticle resist and have recently focused on developing zinc-organic cluster resist with controlled molecular weight and size distribution [1].

In this report, the lithography performance of other metal-organic cluster resists and the effect of underlayer

for EUV lithography performance are discussed. The micro-scale patterning results are shown in Figure 1.

Transition metals such as Group 4 metals, cobalt and nickel and non-transition metals such as indium and tin are available. Especially, cobalt and nickel are expected to absorb more EUV light, and further study will be investigated.

The EUV exposure results of zinc-organic cluster resist on the different underlayer are summarized in Figure 2. The introduction of underlayer has improved the sensitivity with the almost same LWR value. The mechanism based on this phenomenon will be elucidated.

## References:

- [1] Xu, H., Sakai, K., Kasahara, K., Yang, K., Herbol, H. C., Odent, J., Clancy, P., Giannelis, E. P., Ober, C. K., Metal-Organic Framework-inspired metal-containing building units for high resolution patterning, *Chem. Mater.* 2018, 30, 4124-4133.

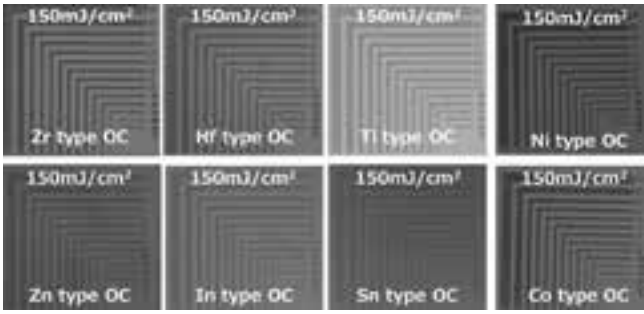


Figure 1: Optical microscope images of micro-scale patterning using the ABM contact aligner.

| Resist       | Sample-A  | Sample-A   | Sample-A   | Sample-A   |
|--------------|---|--|--|--|
| Substrate    | Bare-Si   | UL-A   | UL-B   | UL-C   |
| Image @16mLS | <br>47mJ/cm <sup>2</sup><br>LWR 5.6nm | <br>28mJ/cm <sup>2</sup><br>LWR 5.2nm | <br>33mJ/cm <sup>2</sup><br>LWR 5.6nm | <br>34mJ/cm <sup>2</sup><br>LWR 5.2nm |

Figure 2: SEMs of EUV exposure results with zinc organic cluster resists.

# Transient Laser Heating Derived Mesoporous Materials Directed by Gyroidal Templates from Block Copolymer Self-Assembly

**CNF Project Number: 1356-05**

**Principal Investigator(s): Ulrich Wiesner**

**User(s): Qi Zhang, Fei Yu**

*Affiliation(s): Department of Materials Science and Engineering, Cornell University*

*Primary Source(s) of Research Funding: National Science Foundation (DMR-1719875)*

*Contact: ubw1@cornell.edu, qz224@cornell.edu, fy84@cornell.edu*

*Website: <http://wiesner.mse.cornell.edu/>*

*Primary CNF Tools Used: TFT N+/P+ Polysilicon Furnace - A4, Oxford 81 etcher*

## Abstract:

Equilibrium thin-film gyroidal carbon was fabricated from co-assembly of an amphiphilic triblock terpolymer and resorcinol-formaldehyde resols through solvent vapor annealing. Upon crosslinking the resols and carbonizing the thin films, mesoporous carbon templates were obtained. Low-pressure chemical vapor deposition (LPCVD) was utilized to deposit amorphous silicon into the templates. Pulsed excimer laser irradiation melted and crystallized the deposited silicon through a non-equilibrium nanosecond-scale process that preserves the underlying organic template. Finally, after removing the carbon template, we successfully prepared 3D continuous crystalline silicon with the inverse gyroidal nanostructure.

## Summary of Research:

Templates enable the manufacturing of objects with intricate and complicated structures. Templates at the nanoscale allow for fabrication of nanomaterials that could find applications in catalysis or microelectronics. Block copolymer self-assembly offers bottom-up pathways to complex nanostructured templates, which can be combined with laser annealing for pattern transfer to produce porous ordered nanomaterials after template removal.

We first prepared such nanoscale organic templates derived from block copolymer in co-assembly with carbon precursors. To this end, poly(isoprene)-*block*-poly(styrene)-*block*-poly(ethylene oxide) (PI-*b*-PS-*b*-PEO, or ISO) was synthesized via sequential anionic polymerization as described elsewhere [1]. The resorcinol-formaldehyde resols, i.e. the carbon precursors, are hydrogen bonded to the PEO block of the amphiphilic ISO terpolymer. Through solvent vapor annealing, the resols were structure-directed by ISO and they formed an equilibrium co-continuous structure known as alternating gyroids on silicon wafers [2]. After the resols were crosslinked and carbonized at high temperatures, mesoporous carbon thin-film templates with gyroidal nanostructures were prepared (Figure 1).

These thin films derived from organic precursors are stable and amenable to nanomaterials fabrication and

processing techniques, a prerequisite for any structure-directing template. We used LPCVD in the A4 Polysilicon Furnace at CNF to backfill the mesopores with undoped Si (Figure 2). Following TFT MOS cleaning procedures, the native oxide layer between the carbon templates and silicon wafers was removed by dipping them in diluted 20:1 hydrofluoric acid (HF) without compromising the ordered mesostructure of the organic templates. The resulting thin films have small grains of silicon filling the pores with a silicon overlayer on top.

In order to achieve conformal backfilling with crystalline materials, carbon templates with amorphous silicon deposited were subject to pulsed laser annealing at ambient atmosphere. Previous research [3] has demonstrated that shortening heating times promotes the thermal stability of organic materials. Transient excimer laser irradiation for 40 ns delivered enough energy to melt the silicon (melting temperature around 1250°C). The resulting crystallized silicon displayed polycrystallinity, with the carbon template remaining intact after the heating process.

A combination of dry and wet etching was utilized to remove the carbon template from the carbon/silicon hybrid. Using the Oxford 81 etcher at CNF, reactive ion etching was carried out with CF<sub>4</sub> and oxygen, and brief dipping in HF exposed the carbon template to the outside.

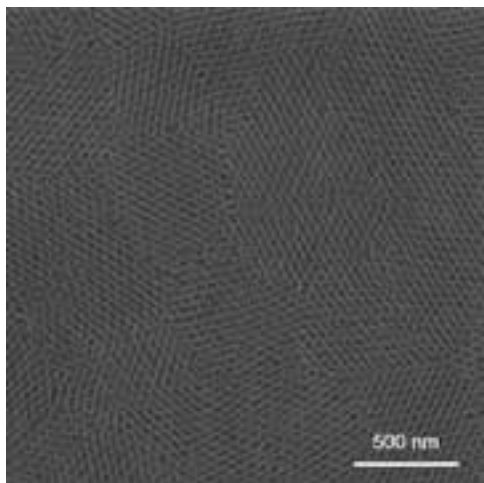


Figure 1: Scanning electron microscopy (SEM) plan view of the mesoporous gyroidal carbon template, derived from ISO-resols hybrid carbonized at 450°C.

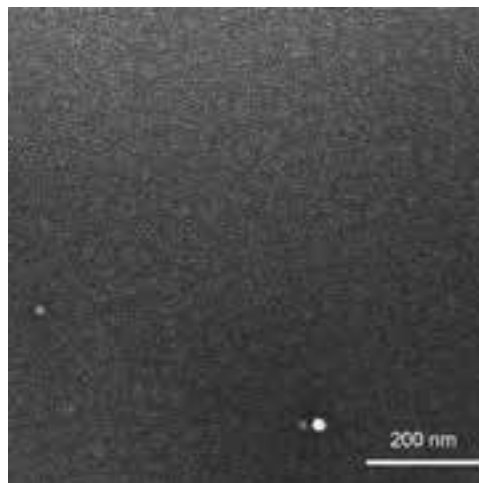


Figure 2: SEM plan view of the carbon template with Si deposited through LPCVD. There is a Si overlayer on top of the template, showing grains of silicon.

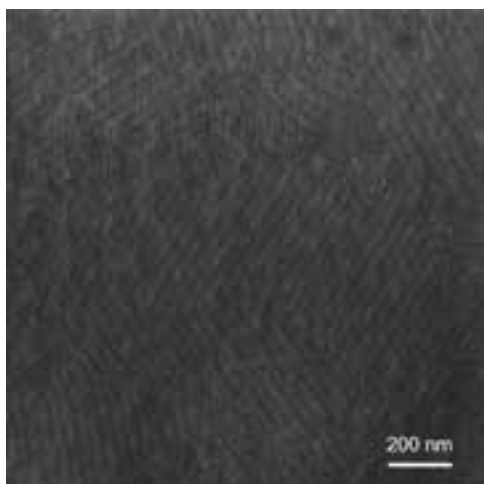


Figure 3: SEM plan view of crystalline silicon nanostructures after template removal, leaving behind interconnected trenches.

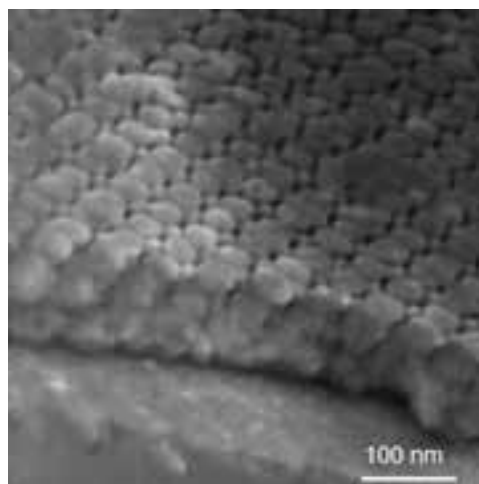


Figure 4: SEM cross-section view of crystalline silicon nanostructures after template removal, leaving behind interconnected trenches.

We subsequently immersed the samples in piranha solution at elevated temperatures to decompose the carbon template. The 3D continuity of gyroids ensures complete removal of the template. Periodically ordered crystalline silicon with the inverse nanostructure of the carbon template was finally obtained via brief dipping in HF to remove silicon oxide (Figures 3 and 4).

Our fabrication route makes compatible the processing of organic soft materials and inorganic semiconductors and capitalizes on the highly non-equilibrium nature of transient laser heating. This same strategy can be expanded to other materials, such as metals and compound semiconductors, to be backfilled into the template.

The resulting mesoporous crystalline materials could allow us to explore interesting functionalities in areas including sensing, catalysis, and microelectronics.

#### References:

- [1] Bailey, T. S. et al. A Noncubic Triply Periodic Network Morphology in Poly (Isoprene-*b*-Styrene-*b*- Ethylene Oxide) Triblock Copolymers. *Macromolecules* 35, 7007-7017 (2002).
- [2] Zhang, Q. et al. Pathways to Mesoporous Resin/Carbon Thin Films with Alternating Gyroid Morphology. *ACS Nano* 12, 347-358 (2018).
- [3] Jung, B. et al. Kinetic Rates of Thermal Transformations and Diffusion in Polymer Systems Measured during Sub-millisecond Laser-Induced Heating. *ACS Nano* 6, 5830-5836 (2012).

# Three-Dimensional Printing with Silica Cages

CNF Project Number: 1645-08

Principal Investigator(s): Tobias Hanrath

User(s): Jen-Yu Huang

Affiliation(s): Robert F. Smith School of Chemical and Biomolecular Engineering, Cornell University

Primary Source(s) of Research Funding: National Science Foundation

Contact: th358@cornell.edu, jh2486@cornell.edu

Primary CNF Tools Used: SEMs (Supra and Ultra), Leica supercritical dryer, AFM

## Abstract:

Material scientists have now developed an extensive library of nano-sized building blocks, offering a vast panel of properties (optic, magnetic, plasmonic, catalytic, etc.). Nevertheless, combining these building blocks for the realization of multifunctional materials while controlling their structure from the nano- to the micro- and all the way to the macroscale still remains an open challenge in order to fully exploit their potential. In parallel, new material processing techniques such as 3D printing technologies are emerging for the fabrication of macroscopic highly engineered parts and devices. In this work, newly discovered silica nanocages are combined with digital light processing 3D printing technique for the rapid fabrication of mesoporous parts with arbitrary shapes and tunable internal structures. Complementary strategies are then deployed for the implementation and deliberate positioning of various functionalities throughout 3D printed objects with high control on the microstructure and macroscopic architecture of the superstructures. This approach paves the road for innovative device concepts and designs, that will benefit from the unique properties of nanomaterials and from the micro- and macroscale manufacturing capability of 3D printers.

## Summary of Research:

In this work, the silica cages were made compatible with digital light processing 3D printing, through their functionalization with methyl methacrylate groups (Figure 1). In a previous study, calculations suggested that as part of their formation mechanism, the cages vertices and struts deform the surface of the micelles, with positively charged surfactant molecules wrapping the negatively charged inner surface of the cages. As illustrated in the inset of Figure 1a, this soft-template approach allows to distinguish the inner and outer surfaces of the cages, forcing the functional group to attach predominantly on the outer surface. Later in the synthesis process, the surfactant micelles were removed from the inside of the cages by dialysis in an acidic ethanol solution, causing the cages to precipitate in aqueous solution.

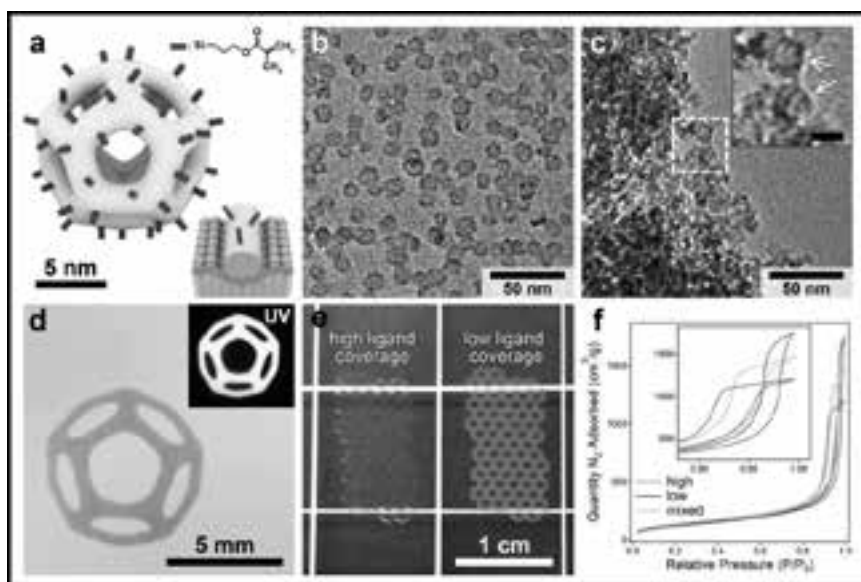


Figure 1: Illustration (a) and TEM image (b) of silica cages functionalized with methyl methacrylate groups (inset in a: illustration of a cage strut before removal of the surfactant micelle, in blue). (c) TEM image of a piece of a printed part (inset: zoom in, white arrows point to clearly visible cage structures, scale bar 10 nm). (d) Photograph of a pattern printed on a glass substrate with dye functionalized cages (inset: photograph under UV irradiation). (e) Photograph of parts printed with silica cages with high (left) and low (right) methyl methacrylate surface coverage. (f) Nitrogen sorption isotherms of parts printed with high and low methyl methacrylate coverage, and with mixed samples (inset: zoom in the hysteresis range). (Find full color on pages xiv-xv.)

Although the original silica cage synthesis was upscaled 30 times in order to make the printing of large parts affordable, the transmission electron microscope (TEM) image in Figure 1b shows that cage structures were obtained with this modified method.

In Figure 1e, larger and free-standing parts exhibiting a honeycomb structure were printed with different ligand coverages and dried with Leica critical point dryer in CNF. For the part with low ligand coverage, the cages were functionalized with 2.5 times less than for the high ligand coverage. Although these two parts have the same dimensions, the low coverage one is 1.7 times lighter than the high coverage one. This important difference in density suggests different internal microstructures. These parts have relatively similar specific surface area, specifically  $438 \text{ m}^2\text{g}^{-1}$  and  $450 \text{ m}^2\text{g}^{-1}$  for the high and low coverage parts respectively, as determined by the Brunauer-Emmett-Teller (BET) method. Nevertheless, the hysteresis of the nitrogen sorption measurements (Figure 1f) show important difference in adsorption-desorption behavior.

The broader hysteresis of the high coverage part suggests that mesopores access is more restricted in this case, whereas in the low coverage part the mesopores access is facilitated by the presence of large pores and channels. This is also supported by the direct visual inspection of

these parts (Figure 1e). While the high coverage part appears relatively transparent, the low coverage one is more translucent due to light scattering by larger pores. To induce significant Mie scattering, these larger pores should be at least few tens of nanometers in size and can only correspond to interparticle pores because the intraparticle pores, i.e. core of the cages, are less than 10 nm. Since the parts have similar specific surface area regardless of the ligand coverage, these large interparticle pores do not contribute significantly to the total surface area.

Instead, this property mostly derives from the intraparticle pores of the cage structures and from the microporosity of silica itself. Thus, varying the ligand coverage of cage-based PLIC inks is a powerful tool to purposefully tune the porosity and internal structure of 3D printed objects. Additionally, a PLIC ink was prepared by mixing the two cage samples in equivalent proportion. The isotherms of the resulting printed part, denoted as 'mixed' (Figure 1f), shows an intermediate behavior between those obtained with either purely high or low coverage, hence offering an additional knob to tune the microstructure of these macroscopic objects.

As an interesting feature, these parts can also be calcined in order to remove the organic component, yet fully preserving their fine microstructure.

# Fabricating Advanced Characterization Platforms for Polyelectrolyte Brushes

**CNF Project Number: 1757-09**

**Principal Investigator(s): Christopher Kemper Ober**

**User(s): Nilay Duzen**

*Affiliation(s): Materials Science and Engineering, Cornell University*

*Primary Source(s) of Research Funding: National Science Foundation*

*Contact: cko3@cornell.edu, nd387@cornell.edu*

*Primary CNF Tools Used: ASML 300C DUV stepper, SC4500 evaporator, Oxford PlasmaLab 80+ etch system, ZEISS SEM, Oxford ALD FlexAL, Unaxis 770 deep silicon etcher, Veeco Icon AFM*

## Abstract:

Polyelectrolyte brushes are a special class of polymer brushes with charges present along the backbone. They have unique properties and promising applications as stimuli responsive smart surfaces for numerous areas [1]. However, a greater fundamental understanding of the behavior and stability of these brush systems in different environments is still needed. Advanced characterization tools such as neutron scattering are helpful for this purpose. Here we report the development of a novel platform that has been used in neutron scattering studies of polyelectrolyte brushes. This design enabled the growth of brushes laterally from sidewalls of trenches of patterned silica surfaces and helped us to gain insight on the relationship between the backbone and charged group on polyelectrolyte brushes.

## Summary of Research:

We employed a top-down process starting with patterning a silicon wafer. In order to prevent polymer brush growth from the top and bottom of the trenches, we decided to cover those parts with chromium film (about 5 nm thickness). However, since we don't want to have chromium residue on the sidewalls, we first deposited a sacrificial SiO<sub>2</sub> layer on the grating with atomic layer deposition (ALD). Then this layer is selectively removed from only the top and bottom of the trenches by reactive ion etching (RIE) followed by the deposition of chromium layers on these flat surfaces with atomic layer deposition. Potential chromium residue on the sidewalls is removed by hydrofluoric acid, which results in the desired grating design where the flat surfaces are covered with chromium to prevent polymerization, whereas sidewalls are covered with SiO<sub>2</sub> to be ready for lateral brush growth. Figure 1 summarizes the fabrication process.

After finishing the fabrication, poly(dimethyl aminoethylmethacrylate) (PDMAEMA) brushes with different thickness were grown from the sidewalls of the grating. Since the top of the brushes do not feel steric repulsion due to the lack of confinement [2], the polymer chain stretching is the highest at the bottom of the grating and thickness decreases towards the top.

A schematic of the platform design with the polymer brush is shown in Figure 2. The neutron scattering studies that have been done with the help of our collaborators at the University of Sheffield showed good fit between the model and experimental specular data. Using these fits as input, we will further investigate brush profile by using off-specular data.

We are also planning to use the Cornell NanoScale Science and Technology Facility (CNF) for our new polyelectrolyte brush architecture that incorporates well defined charged side groups via peptoid structures. We are studying these brushes to see the effect of charge type and proximity to the backbone on brush behavior. We will use nanopatterning through CNF as a tool for controlling the geometric confinement and we will continue to fabricate the advanced platforms for further characterization of these new brush types.

## References:

- [1] *Macromolecules* 2017, 50 (11), 4089-4113.
- [2] *Macromolecules* 2017, 50 (12), 4715-4724.

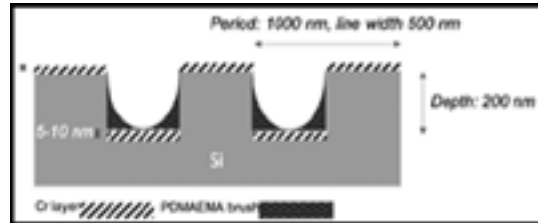
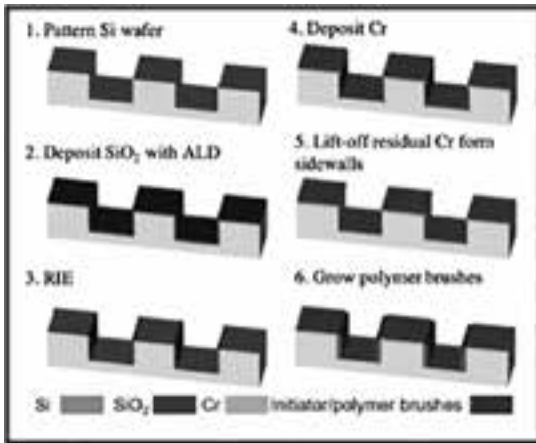


Figure 1, left: Fabrication process for advanced characterization platform.

Figure 2, above: Design details schematic of the platform showing polymer brush growth from sidewalls.

# Nanometer-Scale Area-Selective Formation of Polymer Brushes

**CNF Project Number: 1757-09**

**Principal Investigator(s): Christopher Kemper Ober<sup>2</sup>**

**User(s): Yuming Huang<sup>2</sup>, Hai Quang Tran<sup>1,2</sup>**

*Affiliation(s): 1. School of Chemical and Biomolecular Engineering,  
2. Department of Materials Science and Engineering; Cornell University*

*Primary Source(s) of Research Funding: National Science Foundation*

*Contact: cko3@cornell.edu, yh839@cornell.edu*

*Website: <http://cober.mse.cornell.edu/index.html>*

*Primary CNF Tools Used: E-beam resist spinners, JEOL 9500, FilMetrics F50-EXR,  
Oxford 81 etcher, Zeiss Ultra SEM, optical microscope*

## Abstract:

The topological control of polymer brushes can be realized via surface-initiated polymerization on a pattern fabricated by electron-beam (e-beam) lithography, which is known for its fine resolution and precision. Patterned polymer brushes were produced on silicon wafers by selective deposition of initiator, using patterned e-beam resists as the masks. As a result, cone-like polymer brushes with a height of ~ 60 nm and diameter of ~ 60 nm were formed in the desired pattern. This platform has several potential uses, including cytoskeleton mimicry and molecular recognition.

## Summary of Research:

**Introduction.** Polymer brushes have a unique molecular structure with one end of the polymer chain covalently bonded to a substrate, such as a silicon wafer. Fabricating these brushes has been one of the main areas of focus in polymer science in recent decades and has demonstrated interesting applications in many fields [1]. The precise, nanometer-scale patterning of e-beam lithography can be incorporated with surface-initiated polymerization to provide a novel pathway in the area-selective placement of polymer brushes on hard substrates. This results in surfaces with anisotropic properties, unique chemical functionality, and responsive behavior under different stimulations.

**Fabrication.** The polymer brushes were patterned on a silicon wafer by depositing polymerization initiators selectively on desired areas. This was accomplished by patterning the e-beam resist (~150nm) through JEOL 9500 and using it as the mask for deposition. Before depositing the initiator, the surface of the substrate was etched ~ 10 nm to remove residual debris. The deposition of a silane initiator was carried out in the vapor phase, followed by the removal of the resist. Subsequently, surface-initiated ring-opening polymerization was carried out under vacuum and elevated temperature [2]. A schematic illustration of the fabrication process is shown in Figure 1.

**Characterization and Results.** The thickness of the e-beam resist was found using FilMetrics F50-EXR after spin-coating. After the exposure and developing process, the e-beam resist was analyzed by Zeiss Ultra SEM (Figure 2). The patterned polymer brushes were characterized using atomic force microscopy (AFM) in Cornell Center for Materials Research (Figure 3) for height measurement, and Zeiss Ultra scanning electron microscope (SEM) for topological analysis (Figure 4).

**Conclusions.** We demonstrated that e-beam lithography can be used to precisely control the spatial arrangement of polymer brushes. In the near future, we plan to explore the use of these surfaces for biological applications, such as cell membrane support and molecular recognition.

## References:

- [1] Chen, W.-L.; Cordero, R.; Tran, H.; Ober, C. K. 50<sup>th</sup> Anniversary Perspective: Polymer Brushes: Novel Surfaces for Future Materials. *Macromolecules* 2017, 50 (11), 4089-4113.
- [2] Wang, Y.; Chang, Y. C. Preparation of Unidirectional End-Grafted  $\alpha$ -Helical Polypeptides by Solvent Quenching. *J. Am. Chem. Soc.* 2003, 125 (21), 6376-6377.

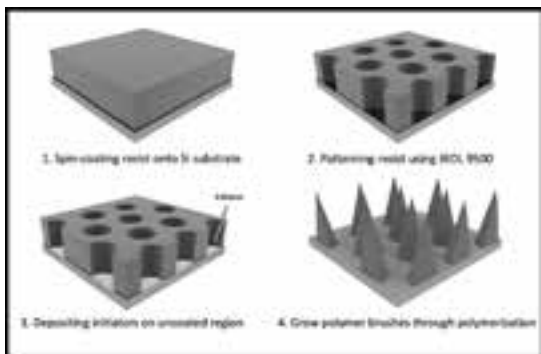


Figure 1: Schematic illustration of the fabrication process.

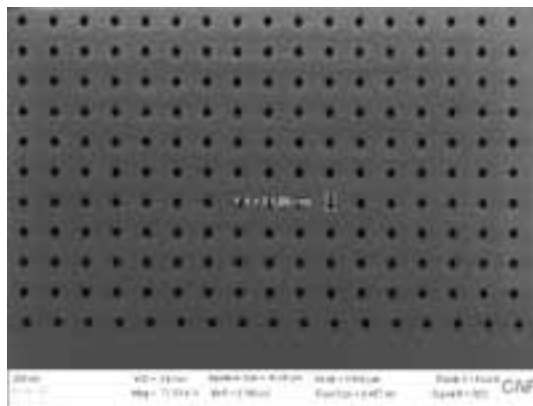


Figure 2: The e-beam pattern after the exposure and developing processes.

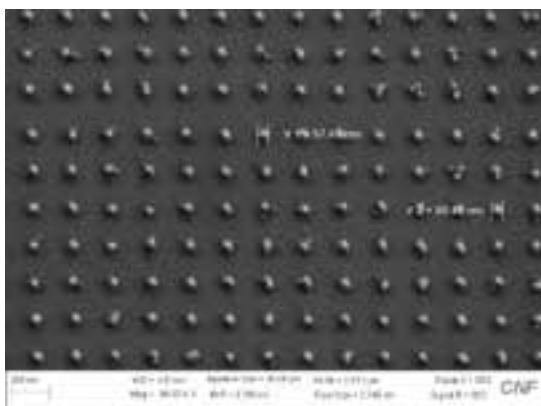


Figure 3: An SEM image of the polymer brushes. The diameter is around 60 nm.

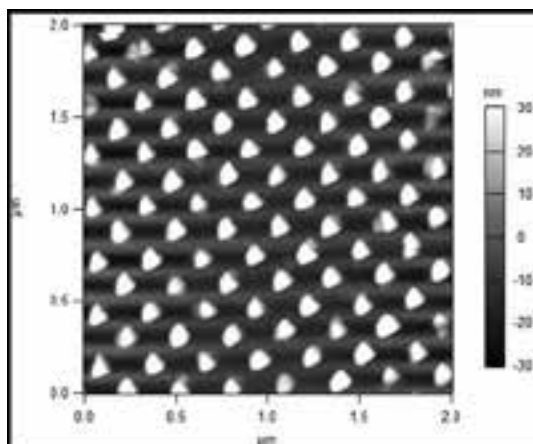


Figure 4: An AFM image of the polymer brushes. The height is around 60 nm.

# Engineering Transport in Confined Environments of Stable Radical Polymers

**CNF Project Number: 2091-11**

**Principal Investigator(s): Gregory D. Fuchs**

**User(s): Albert M. Park**

*Affiliation(s): Applied Physics, Cornell University*

*Primary Source(s) of Research Funding: Department of Energy*

*Contact: gdf9@cornell.edu, amp356@cornell.edu*

*Primary CNF Tools Used: GCA 5X stepper, wet stations, CVC evaporators, Heidelberg mask writer DWL 2000, DISCO dicing saw*

## Abstract:

We study properties of a doped radical polymer with a conjugated backbone, which is a promising potential material for an organic radical battery electrode. To compensate the exponential decay of conductivity caused by steric hindrance from covalently attached stable radical, we dope the conjugated backbone using either iodine or 2,3,5,6-tetrafluoro-7,7,8,8-tetracyanoquinodimethane (F4-TCNQ). We characterize the electrical properties as we vary the pendent radical concentration. Transport measurements confirm that doping increases the conductivity by a few to several orders of magnitude, depending on the dopant. Additionally, we use electron paramagnetic resonance (EPR) to investigate the interplay between polarons and stable radical electrons.

## Summary of Research:

For enhanced performance of radical polymer based energy storage materials, a high conductivity and a large volume density of electroactive radical electrons are required for efficient current collection and increased capacity, respectively. Our first study in this line of works was to confirm the intrinsic conductivity of poly(2,2,6,6-tetramethyl- piperidinyloxy-4-yl methacrylate (PTMA), which is one of the model polymers suggested for energy storage [1].

In this work we found that without alternative conduction channels, such as swelling of the polymers with an ionic liquid, the conductivity of non-conjugated radical polymers are closer to that of an insulator than to organic semiconductors. Next, we tried including alternative conductive channels by attaching pendent radical (2,2,6,6-tetramethylpiperidin-1-yl)oxyl (TEMPO) to the conductive conjugated backbone poly(3-hexylthiophene-2,5-diyl) (P3HT) [2].

In this study we were able to achieve increased conductivity, however, we discovered that there is an exponential decrease in conductivity as we increase the number of pendant radicals due to the disorder they create in stacking. In other words, we found a tradeoff between conductivity and the volume density of radical electrons.

As a natural extension to these works, we've focused on doping of the conjugated backbone to increase the conductivity relative to what we found in the intrinsic polymers. In our experiment we chose two dopants: iodine and F4-TCNQ.

The low sublimation point and volatility of iodine allows an easy doping process at room temperature. We were able to see more than five orders of magnitude increase of conductivity for the P3HT control sample that did not have pendent radicals. This trend continued for the polymers with different fractions of pendent radicals showing that the entire curve is shifted upward in conductivity with doping. (Figure 1.) However, iodine also imposes some technical challenges such as dedoping at ambient condition and chemical reaction with metal that composes crucial parts of experimental setup. Thus, while iodine as a dopant for P3HT-TEMPO is very effective at increasing conductivity, at the same time it has limited technical applications due to its volatility and reactivity.

One alternative dopant, which does not suffer from this problem, is F4-TCNQ. When mixed with conjugated backbone polymer in solution state, it is known to form a rigid and semicrystalline charge transfer complex that creates polarons. Due to the rigid formation of a charge transfer complex, it also makes it easier to trace polarons using solution-state EPR.

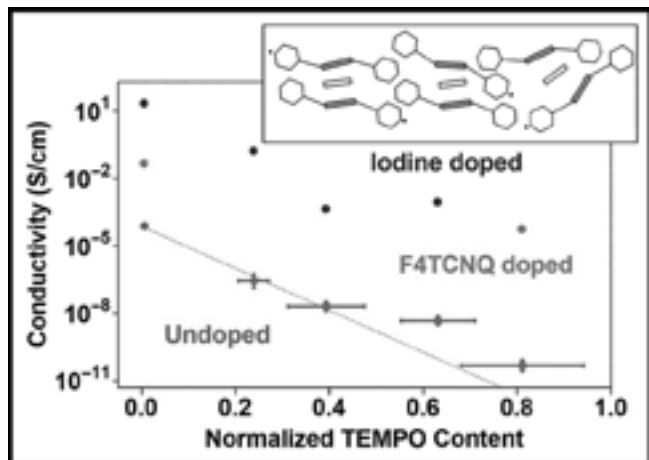


Figure 1: Trend of conductivity as a function of normalized TEMPO content. Blue dots and magenta dots correspond to iodine and F4-TCNQ doped P3HT-TEMPO. Inset shows a schematic of steric hindrance in system of conjugated backbone (orange) with pendent radical (hexagon) in presence of dopants (yellow). (Find full color on pages xiv-xv.)

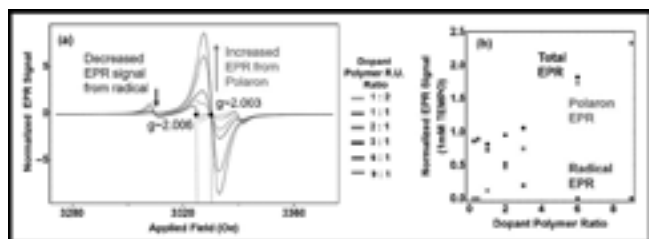


Figure 2: (a) EPR curve of doped conjugated polymer with pendent radical obtained from varying ratio of dopant molecule to polymer repeating unit. (b) Relative contribution of polaron and radical electron to total EPR signal size as a function of dopant polymer ratio. (Find full color on pages xiv-xv.)

In our experiment we've used in-solution doping where we simply mix conjugated polymer and F4-TCNQ in a vial for EPR results. We then cast the dopant on a conjugated polymer film for electrical transport measurement.

The effect of doping of conjugated radical polymer in EPR is clearly visible in Figure 2 (a). In this system, the first source of EPR signal is pendent radicals. Due to hyperfine coupling in the nitroxide radical, we observe a triplet signal when the radicals are isolated from each

other. When two or more radical molecules are brought in close distance, exchange coupling become dominant and singlet signal with broader linewidth is observed. Thus, when we vary the percentage of stable radicals that are pendent to the backbone, we get a statistical combination of triplet and singlet. The additional source of EPR signal we introduce from doping of the backbone is polarons. Since polarons are mobile radicals unaffected by hyperfine coupling, they show a singlet lineshape.

These two signals can be distinguished from each other because they have different g-factors and therefore different resonant fields at the same frequency. By fitting the data with known EPR curves for radical electron and polaron, we can quantitatively extract the contribution each component. In Figure 2 (b) we see that the polaron contribution increases linearly with increasing dopant concentration while the radical electron signal decreases. This shows that there is electron transfer between pendent radicals and polarons formed in the backbone.

Finally, with F4-TCNQ doped P3HT-TEMPO we get around 2~3 orders of magnitude increase in conductivity (Figure 1, magenta points, see page XX for full color). While conductivity increase is not as large as iodine doped case, F4-TCNQ is more stable doping technique, which have negligible dedoping at ambient air and no reaction problem with metal. The consistent trend of decreasing conductivity for higher ratio of pendent stable radical shows that steric hindrance still plays a role in conductivity of thin film doped conjugated polymers (Figure 1, Inset).

## References:

- [1] Y. Zhang, et al., "Impact of the Synthesis Method on the Solid-State Charge Transport of Radical Polymers." *J. Mater. Chem. C* 6 (1), 111-118 (2017).
- [2] Y. Zhang, et al., "Charge Transport in Conjugated Polymers with Pendent Stable Radical Groups." *Chem. Mater.* 30 (14), 4799-4807 (2018).

# Production of Beta-Tungsten as a Function of Sputtering Pressure

**CNF Project Number: 2103-12**

**Principal Investigator(s): Shefford Baker<sup>1</sup>**

**User(s): Nathaniel Rogers<sup>2</sup>**

*Affiliation(s): 1. Department of Materials Science and Engineering,*

*2. Sibley School of Mechanical and Aerospace Engineering; Cornell University*

*Primary Source(s) of Research Funding: National Science Foundation Grant DMR 1411024*

*Contact: shefford.baker@cornell.edu, ngr27@cornell.edu*

*Website: <https://baker.mse.cornell.edu/>*

*Primary CNF Tools Used: MOS hood, AJA sputtering system #2, FleXus film stress measurement system*

## **Abstract:**

Metastable phases of tantalum and tungsten that are only present in thin film form are technologically important for the microelectronics industry and show promise for new magnetic memory applications with exhibition of the Giant Spin Hall Effect. Nonetheless, there has been considerable debate about the crystal structural and formation mechanism of these beta phases. Recent advances in the understanding of beta-tantalum provide a road map for how to bring similar clarity to beta-tungsten. A series of five films were made at varying Ag sputter pressures in the CNF AJA #2 sputtering system (3, 5, 6.8, 7, 7.8 mTorr). Substrate curvature was measured before and after each deposition to estimate the average film stress. Theta-2-theta XRD scans were used to examine the resulting crystal structure. Preliminary results show that highly tensile films (made at the higher sputtering pressures) were nearly entirely beta-tungsten, while the other films had significantly more of the alpha phase. While we have conclusively produced beta-tungsten, precise indexing of the theta-2-theta peaks will require higher precision XRD measurements and finer control over film stress generation.

## **Summary of Research:**

This research on tungsten is inspired by recent work our group has done on tantalum [1]. Like tantalum, tungsten can form two phases, either alpha or beta. The alpha phases of both metals have a BCC crystal structure, are present in bulk form, have good electrical conductivity, and are relatively ductile [1]. The beta phases are metastable, found in only some thin films, and are brittle with poor electrical conductivity [2-6]. Both phases of tantalum are technologically important for the microelectronics industry. Additionally, the beta phases of both materials show strong Giant Spin Hall Effect (GSHE), which could be used in advanced magnetic memory devices [5-9]. Yet, even though tantalum has been studied for decades, the formation mechanism and crystal structure for beta-tantalum was only recently well established [1]. Reviewing the literature, it is interesting to note that the historical debates about the formation mechanisms of the metastable beta phases for each material mirror each other closely. Beta-tungsten, like beta-tantalum, for some

time was believed to be an oxide rather than a distinct phase [2,6]. At other times, researchers believed that the beta phases of the two metals may share the A15 crystal structure [1,2,6]. In order to sort out the confusion, very carefully controlled deposition experiments need to be performed to understand the role of both sputter pressure and impurity atoms (especially oxygen). Eventually, it was shown that the actual crystal structure of beta-tantalum is a distorted Frank-Kasper sigma structure ( $P\bar{4}2_1m$ ) and requires a template of tungsten oxide to form [1].

Our goal in this research is to explore the formation of beta-tungsten and determine if a similar formation mechanism exists as was discovered for beta-tantalum. The first step in this process is to determine deposition parameters that would reliably produce beta-Tungsten. To do this, the AJA #2 sputtering system was used. Five four-inch wafers were MOS cleaned (but retained the native oxide layer) and sputtered with a 99.995% pure tungsten

target at 450 Watts at argon sputtering pressures of 3, 5, 6.8, 7, and 7.8 mTorr. These pressures were chosen based on the CNF supplied process data that showed that films in this pressure range could be expected to vary their stress widely from highly compressive (3 mTorr) to highly tensile (7 mTorr). Each wafer's curvature was measured with the CNF Flexus stress measurement system immediately before and after deposition to determine the average film stress. The films' thickness was then measured via contact profilometry and its out-of-plane texture was investigated with XRD theta-2-theta scans to look for the presence of BCC alpha-tungsten or a more complex beta-tungsten crystal structure.

Preliminary results show that the 3 mTorr sample did develop compressive stress with little to no evidence of beta-tungsten. The other films produced high tensile stresses, with the films in the 6.8 to 7.8 mTorr regime possibly being composed almost entirely of the beta phase. It is hard to say with certainty in this preliminary data since the  $\langle 110 \rangle$  and  $\langle 220 \rangle$  alpha peaks are nearly identical in location to the  $\langle 210 \rangle$  and  $\langle 420 \rangle$  beta peaks which creates some ambiguity. However, we believe that these peaks can be indexed by carefully controlling film stress and shifting them through their stress-free positions. Previous work by Ellis, et al., in 2018 [1] showed that a peak can be unambiguously indexed by tracking its position as film stress changes and noting that it moves through the equilibrium position of a peak corresponding to one phase but not the other.

Future work will include both a sputtering pressure series to first be able to unambiguously index all the observed diffraction peaks, and then an oxygen partial pressure series to determine the amount of oxygen necessary for the formation of beta-tungsten.

### References:

- [1] Ellis, E. A., et al., Effect of sputter pressure on Ta thin films: Beta phase formation, texture, and stresses. *Acta Mater.* 150, 317-326 (2018).
- [2] Petroff, P., and Reed, W. Resistivity behavior and phase transformations in  $\beta$ -W thin films. *Thin Solid Films* 21, 73-81 (1974).
- [3] Read, M. H., and Altman, C. A new structure in tantalum thin films. *Appl. Phys. Lett.* 7, 51-52 (1965).
- [4] Desai, P. D., et al. Electrical Resistivity of Selected Elements. *J. Phys. Chem. Ref. Data* 13, 1069-1096 (1984).
- [5] Hao, Q., et al.  $\beta$ -tungsten thin films: Structure, electron transport, and giant spin Hall effect. *Appl. Phys. Lett.* 106 182403 (2015).
- [6] Liu, J., and Barmak, K. Topologically close-packed phases: Deposition and formation mechanism of metastable  $\beta$ -W in thin films. *Acta Mater.* 104 223-227 (2016).
- [7] Pai, C.-F., et al. Spin transfer torque devices utilizing the giant spin Hall effect of tungsten. *Appl. Phys. Lett.* 101 122404 (2012).
- [8] Liu, L., et al. Spin-Torque Switching with the Giant Spin Hall Effect of Tantalum. *Science.* 80, 336 (2012).
- [9] Hao, Q., and Xiao, G. Giant Spin Hall Effect and Switching Induced by Spin-Transfer Torque in a W / Co 40 Fe 40 B 20 / MgO Structure with Perpendicular Magnetic Anisotropy. *Phys. Rev. Appl.* 3 34009 (2015).

# Nanotube Transistor Arrays on a TEM Substrate

**CNF Project Number(s): 2486-16, 2719-18**

**Principal Investigator(s): Jonathan S. Alden, Paul L. McEuen**

**User(s): Jonathan S. Alden, Joshua S. Alden**

*Affiliation(s): Esper Biosciences Inc; Department of Physics, Cornell University*

*Primary Source(s) of Research Funding: National Institutes of Health, National Science Foundation*

*Contact: jonathan.alden@gmail.com, mceuen@ccmr.cornell.edu, ja698@cornell.edu*

*Primary CNF Tools Used: Low pressure chemical vapor deposition (LPCVD) furnaces (oxide, nitride), Autostep i-line stepper, ABM contact aligner, SC4500 evaporators, Oxford 80 RIE*

## Abstract:

We use photolithography to fabricate nanotube transistor devices on substrates with thin nitride windows, which can be imaged using transmission electron microscopy (TEM). Our device architecture permits us to characterize a given nanotube both electrically, and by high-resolution TEM. In low-dimensional systems, such as nanotubes, where nanoscale surface and defect structure can have profound influences on the electrical properties, we expect this combined nanoscale imaging and electrical characterization to yield insights that will inform the design of nanoscale sensors.

## Summary of Research:

The study of low-dimensional materials, such as carbon nanotubes, graphene, and molybdenum disulfide, has been an area of growing interest over the past decades, in part due to their promise as molecular sensors. Due to their one-to-few-atom thickness, the properties of such materials often depend sensitively on surface adsorbates, substrate-surface interaction and defect structure.

Improving sample cleanliness, for example, enabled the first observations of spin-orbit coupling in carbon nanotubes [1] and, more recently, the fractal quantum Hall effect, known as Hofstadter's butterfly, in graphene [2]. In order to understand these nanoscale structures and subsequently design improved sensors, a device architecture is needed which combines the atomic-level characterization afforded by TEM with the electronics characterization ability enabled by a gated, transistor-like geometry.

We demonstrate that we can produce arrays of gated nanotube sensors devices, with reasonably high yield that can be characterized afterwards by TEM. Our design

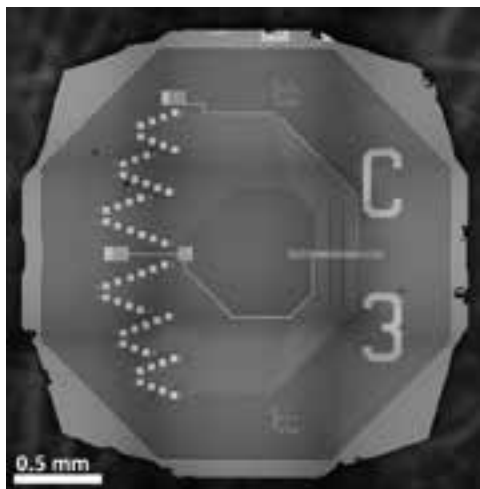


*Figure 1: Optical image of microfabricated TEM grid with 26 pairs of source-drain electrodes, a top gate, and a thin nitride window for TEM imaging after top-gate is removed via chemical etching.*

also keeps parasitic capacitance from our electrodes to the highly resistive silicon substrate low enough to enable electronic measurements of our transistors at MHz bandwidth.

We fabricate nanotube devices on TEM grids using a combination of photolithography and standard nanotube growth and transfer techniques [3]. Figure 1 shows one of such devices, having 26 source-drain electrode pairs and two top gates. Between a few of the electrode pairs are individual nanotubes, which have been transferred prior to the deposition of a gate dielectric, and top-gate. The device fabrication involves using nine masks to define the various structures, which have been designed to yield nanotube

devices with good gating characteristics, as well as low capacitive coupling between nearby electrodes.

The outline of the fabrication procedure is as follows. We begin by using low pressure chemical vapor deposition (LPCVD) to deposit the low-stress nitride on a 300  $\mu\text{m}$ -thick silicon substrate, which will ultimately become our TEM window. We later deposit electrodes, and use backside alignment followed by reactive ion etching

(RIE) to expose rectangles on the back of the wafer, which will later be used for a potassium hydroxide (KOH) through-etch. Arrays of parallel nanotubes are grown by CVD on a separate quartz substrate, coated with poly(methyl methacrylate) (PMMA), lifted off with KOH, and transferred onto the device substrate [3], where unwanted areas are patterned and etched using RIE. We use atomic layer deposition (ALD) to deposit a gate dielectric, after which we pattern and evaporate a gold top-gate. The surface is then coated with a KOH protection layer, and the devices are placed in hot KOH, which etches the silicon exposed on the back, to both release individual grids and to etch the silicon away from behind the nitride window. Later, the nanotube devices will be imaged through this window using TEM. The protection layer is then removed, and the grids are cleaned with oxygen plasma. Our fabrication process typically yields at least one electrically-connected, gated nanotube on 75% of the TEM grids.

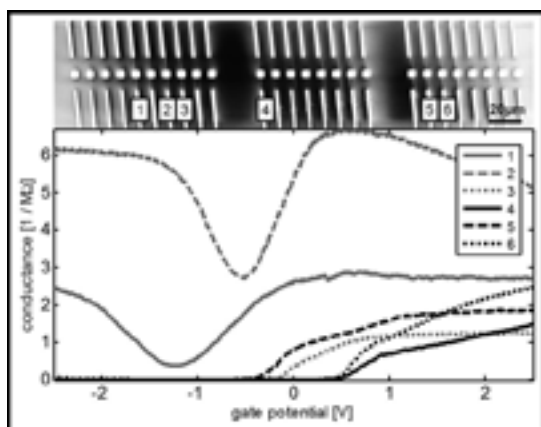


Figure 2: Upper: Scanning electron microscope image of nanotubes between source-drain electrodes, passing over thin nitride windows. Lower: Corresponding conductance measurements as a function of top gate voltage showing six conducting nanotubes with varying characteristics.

Figure 2 shows an SEM image of nanotubes patterned between the source-drain electrode pairs, imaged prior to top-gate deposition. The squares in the center are thin nitride windows for low-background TEM imaging. After completion of the device fabrication, these nanotubes are characterized electrically, shown in the lower portion of Figure 2. All of these nanotubes can be gated to have resistance lower than  $1 \text{ M}\Omega$  ( $50 \text{ k}\Omega/\mu\text{m}$ ) showing that they have a low defect density, and good coupling to the top gate. Nanotubes 1 and 2 can be seen to be metallic, while nanotubes 3-6 are semiconducting.

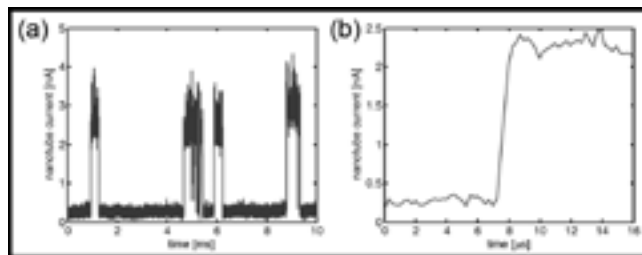


Figure 3: High-speed measurement of nanotube random telegraph signal showing (a) fluctuations in nanotube current and (b) measured rise time of less than  $1 \mu\text{s}$ .

Furthermore, we can probe the electrical characteristics at high speeds in the MHz range. Previous research has shown that single charge fluctuations in a dielectric can be detected by semiconducting carbon nanotubes as random telegraph signals [4]. As shown in Figure 3, our devices are also capable of measuring such signals, but at higher speeds with rise times less than  $1 \mu\text{s}$ .

After characterizing the nanotubes electronically, we can etch away the gold top-gate, and image them by TEM to determine, for example, the nanotube diameter. Figure 3 shows one such nanotube, which can be seen to be single-walled (single dark lines running parallel to the arrows), and 4 nm in diameter (the width between those lines).

In principle, our fabrication procedure can be applied to many different CVD-grown low-dimensional materials with only minor modifications, and may lead to the development of improved nanoscale sensors capable of high-speed molecular sensing.

## References:

- [1] F. Kuemmeth, et al., Nature 452 448-452 (2008).
- [2] C. R. Dean, et al., Nature 497, 598-602 (2013).
- [3] L. Jiao, et al., J. Am. Chem. Soc. 130, 12612-12613 (2008).
- [4] T. Sharf, et al., Nano Lett. 14 (9) 4925-4930 (2014).

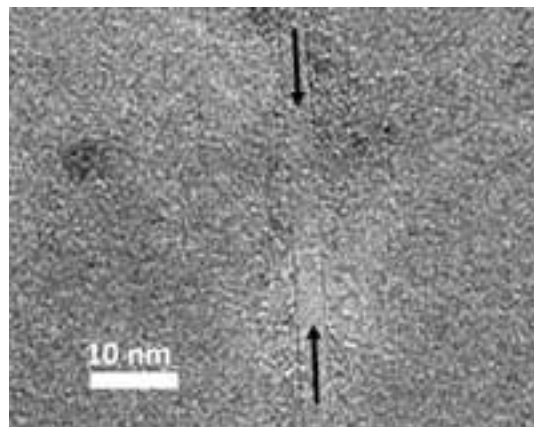


Figure 4: TEM image of a nanotube imaged through a thin nitride window, after top-gate removal.

# Inertial Spreading and Imbibition of a Liquid Drop Through a Porous Surface

**CNF Project Number: 2565-17**

**CNF Principal Investigator(s): Michel Louge**

**User(s): Shilpa Sahoo**

*Affiliation(s): Mechanical and Aerospace Engineering, Cornell University*

*Primary Source(s) of Research Funding: NSF-CBET-1637531*

*Contact: michel.louge@cornell.edu, ss3624@cornell.edu*

*Primary CNF Tools Used: Goniometer and the availability of other wonderful tools at CNF*

## Summary of Research:

The project that has been accomplished in Cornell NanoScale Science and Technology Facility (CNF) is a part of the ISS imbibition project with NASA. The ISS project requires capillary plates with hydrophilic coatings.

To get a hydrophilic surface, the capillary plates need to be coated with SAM coating. For feasible and strength purposes, the capillary plates must be made of metal. The plate must first be coated with a thin layer of gold after the metal plate has been machined to the required roughness. Because SAM is stable on gold but rarely on other metals, gold plating must first be applied.

All the gold coated plates were then coated with self-assembled-monolayer (SAM) coatings in Professor Susan Daniel's Lab (<https://chemistry.cornell.edu/susan-daniel>).

Thiols 6-Mercapto-1-Hexanol, 6-Mercaptohexanoic Acid 90% and 8-Mercaptooctanoic Acid 95% were used. The contact angles were measured in CNF's Rame 500 Goniometer to record the resulting contact angles and their hysteresis. Corresponding hydrophilic angles of 26°, 46°, and 68° were obtained for 6-Mercapto-1-Hexanol, 6-Mercaptohexanoic Acid 90% and 8-Mercaptooctanoic Acid 95% respectively.



# Fabrication of Graphene-Encapsulated Photocathodes

**CNF Project Number: 2584-17**

**Principal Investigator(s): Melissa A. Hines**

**User(s): William J.I. DeBenedetti**

*Affiliation(s): Chemistry and Chemical Biology, Cornell University*

*Primary Source(s) of Research Funding: Center for Bright Beams, a NSF-funded Science and Technology Center (STC)*

*Contact: melissa.hines@cornell.edu, wjd74@cornell.edu*

*Primary CNF Tools Used: SC4500 odd-hour evaporator*

## Abstract:

**A new technique for the fabrication of graphene-encapsulated photocathodes is being developed. The monolayer-thick graphene film will protect the photocathode from oxidation by residual gases or the atmosphere while having only a small effect on the intensity and brightness of the generated electron beam.**

## Summary of Research:

Photocathodes are materials that eject electrons under illumination. By their very nature, high-performance photocathodes must be made from materials that lose electrons easily — in other words, materials that are easily oxidized. For example, many photocathodes are either coated with alkali metals (e.g., Cs/GaAs) or comprised of alkali metals (e.g., Cs<sub>3</sub>Sb). This presents a technical challenge, as exposure to even trace amounts of O<sub>2</sub> or H<sub>2</sub>O will destroy or degrade the photocathode. For highest performance, the photocathodes must also be atomically flat and extremely homogeneous.

To meet these challenges, we are developing a technique to produce a graphene-encapsulated photocathodes. The key challenge in this project is ensuring that every step of the fabrication leaves no residue on the surface, as even monolayer levels of contamination could significantly reduce photoelectron transmission and beam brightness.

In the first step of fabrication, commercial graphene monolayers, which are grown on a copper foil, are coated with a thin gold layer in the SC4500 evaporator. The copper foil is then removed with an aqueous etchant, allowing the graphene side of the gold-coated graphene to be adhered to a low energy substrate. The gold film is then removed by a second aqueous etch. As shown in Figure 1, we have successfully transferred intact, single-layer-thick graphene films to cm-size substrates as confirmed by both optical microscopy and Raman analysis. The near-atomic cleanliness of the transferred films has been quantified using photoelectron spectroscopy.

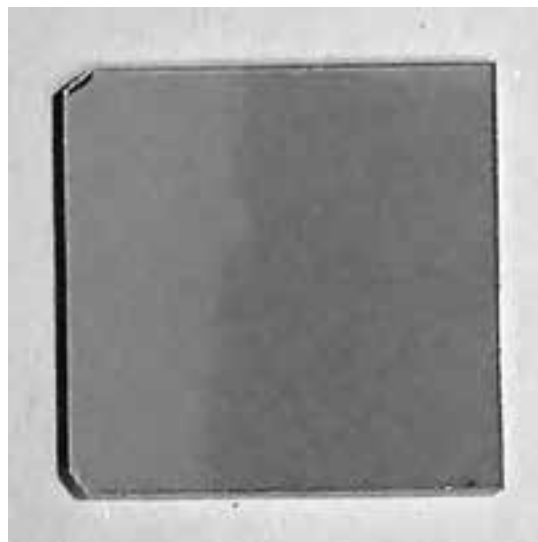


*Figure 1: Optical image of a transparent substrate with a graphene monolayer deposited on the right half of the substrate. The graphene monolayer causes a small decrease in the transmission of visible light.*



# Al<sub>2</sub>O<sub>3</sub> Deposition and Characterization on III-Nitride Surfaces for Improvement of Dielectric/Semiconductor Interface Properties and Device Reliability

**CNF Project Number: 2684-18**

**Principal Investigator(s): Fatemeh Shahedipour-Sandvik**

**User(s): Benjamin McEwen**

*Affiliation(s): Colleges of Nanoscale Science and Engineering, SUNY Polytechnic Institute*

*Primary Source(s) of Research Funding: Army Research Laboratory*

*Contact: sshahedipour-sandvik@sunypoly.edu, bmcewen@sunypoly.edu*

*Primary CNF Tools Used: Oxford FlexAL ALD, Woollam spectroscopic ellipsometer*

## **Abstract:**

We investigate the use of atomic layer deposition (ALD) to deposit Al<sub>2</sub>O<sub>3</sub> and the effect of a post deposition forming gas anneal on the structural properties of the dielectric. Scanning transmission electron microscopy (STEM) and energy dispersive x-ray spectroscopy (EDS) indicate that after low temperature (350°C) anneal in forming gas, the oxide bulk structure and interface do not undergo significant change.

## **Summary of Research:**

Gallium nitride (GaN) is considered as an excellent candidate for the high voltage device platform because of its superior material properties. It has the potential for lower power losses, higher efficiency, and smaller system volume and weight [1,2]. The next generation of reliable and enhancement mode AlGaIn/GaN based high electron mobility transistors (HEMTs) requires further development of high quality passivation and gate dielectric materials. Passivation dielectric is used to reduce current collapse, and gate dielectric is used to reduce gate-leakage current. However, the introduction of a dielectric layer leads to issues associated with the dielectric/(Al)GaN interface trap states, bulk trap states within the dielectric, and surface defect states. Device properties depend on the dielectric used and the density of these interface, bulk, and surface states associated with the dielectric. Decreasing the density of these trap states is essential for good device quality.

Unintentionally doped (UID) GaN was grown on c-plane sapphire using metal-organic chemical vapor deposition (MOCVD). 20 nm of Al<sub>2</sub>O<sub>3</sub> was deposited using the Oxford FlexAL ALD system at CNF. Trimethylaluminum (TMA) was used as the aluminum precursor and water as the oxidant; the substrate was maintained at 300°C during the deposition. After the oxide deposition, the thickness of the layer was confirmed using the Woollam spectroscopic ellipsometer at CNF. A piece of the wafer was then cleaved off and subjected to annealing in forming gas (95% N<sub>2</sub>/5% H<sub>2</sub>) ambient at 350°C for 10 minutes.

Lamellae were cut from the as-deposited Al<sub>2</sub>O<sub>3</sub>-on-GaN and the annealed Al<sub>2</sub>O<sub>3</sub>-on-GaN samples using focused ion beam (FIB). STEM imaging and EDS mapping were used to evaluate structural evolution in the Al<sub>2</sub>O<sub>3</sub>, especially at the interface with GaN, as a result of the anneal. Figure 1 shows a high angle annular dark field (HAADF) image of the as-deposited Al<sub>2</sub>O<sub>3</sub>. As expected, the interface between the Al<sub>2</sub>O<sub>3</sub> and GaN is abrupt since the ALD process is surface reaction limited and no additional processes were performed after the deposition. Figure 2 shows a HAADF image of the annealed sample. Additionally, Figures 3a and 3b show the EDS mapping of aluminum and oxygen, respectively in the annealed sample.

From these images, it can be concluded that at moderate temperatures of 350°C or less, the structure of the Al<sub>2</sub>O<sub>3</sub>/GaN interface is stable, and minimal interdiffusion between the dielectric and semiconductor are observed.

Additionally, metal-insulator-semiconductor (MIS) capacitors were fabricated. Capacitance-voltage (C-V) characteristics were measured to evaluate the effects of forming gas anneal on the electrical properties of the dielectric/semiconductor interface. Both frequency dispersion and C-V hysteresis were reduced in the sample that underwent the anneal, compared to the as-deposited sample, indicating that the density of interface states was reduced as a result of the forming gas anneal.

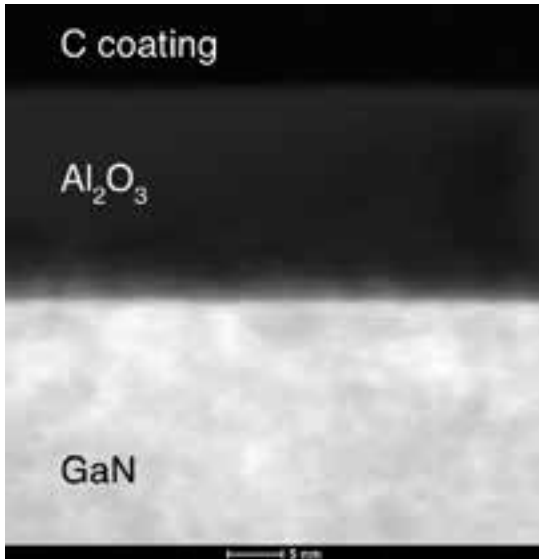


Figure 1: HAADF image of as-deposited  $\text{Al}_2\text{O}_3$ -on-GaN. The apparent thickness of the interface is most likely due to roughness of the surface of the GaN.

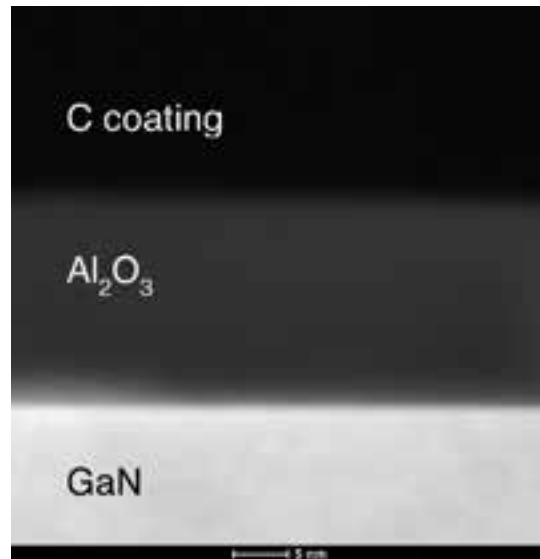


Figure 2: HAADF image of  $\text{Al}_2\text{O}_3$ -on-GaN subjected to annealing in forming gas at  $350^\circ\text{C}$  for 10 min.

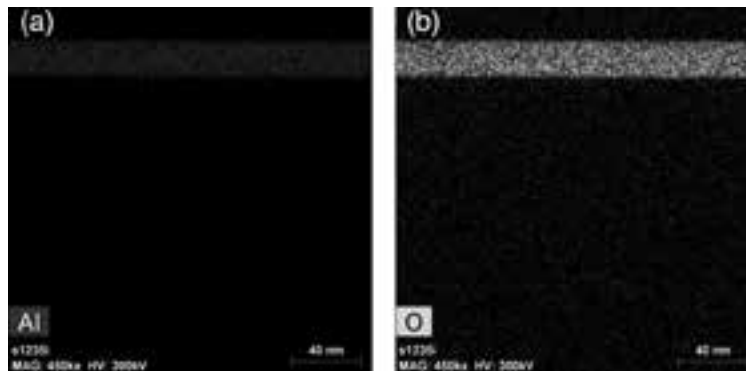


Figure 3: (a) EDS map of Al and (b) EDS map of O from  $\text{Al}_2\text{O}_3$ -on-GaN subjected to annealing in forming gas at  $350^\circ\text{C}$  for 10 min. The Al and O are segregated to the oxide layer and no interdiffusion between the  $\text{Al}_2\text{O}_3$  and GaN is observed. (Find full color on pages xiv-xv.)

### References:

- [1] K. Shenai, R. S. Scott and B. J. Baliga, "Optimum Semiconductors for High-Power Electronics," Transactions on Electron Devices, vol. 36, no. 9, pp. 1811-1823, 1989.
- [2] M. Bhatnagar and B. J. Baliga, "Comparison of 6H-SiC, 3C-SiC, and Si for power devices," Transactions on Electron Devices, vol. 40, no. 3, pp. 645-655, 1993.

# Thermal and Electrical Properties of Quasi-1D van der Waals Nanowires

**CNF Project Number: 2698-18**

**Principal Investigator(s): Deyu Li**

**User(s): Yang Zhao, Lin Yang**

*Affiliation(s): Department of Mechanical Engineering, Vanderbilt University*

*Primary Source(s) of Research Funding: National Science Foundation*

*Contact: deyu.li@vanderbilt.edu, yang.zhao@vanderbilt.edu, lin.yang@vanderbilt.edu*

*Primary CNF Tools Used: Heidelberg mask writer DWL2000, Autostep i-line stepper, LPCVD Nitride - B4, GSI PECVD, AJA sputter deposition, AJA ion mill*

## Abstract:

Using the CNF cleanroom, we have successfully fabricated microdevices for nanowire electrical and thermal conductivity measurements. These microdevices allow for experimental studies of the transport properties of various types of van der Waals nanowires, including  $\text{NbSe}_3$  and  $\text{Ta}_2\text{NiSe}_5$ . Interesting observations such as record long ballistic phonon transport in  $\text{NbSe}_3$  nanowires have been obtained. Systematic studies are being conducted to understand the underlying physical mechanisms.

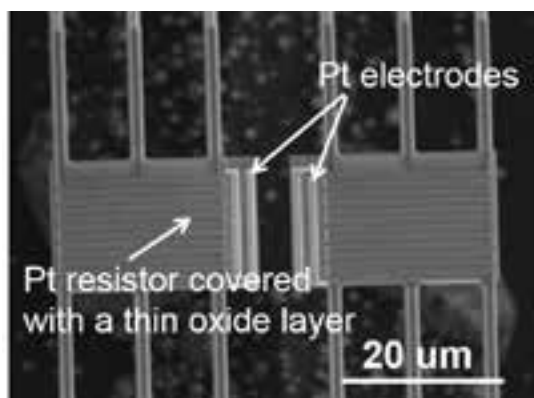


*Figure 1: A scanning electron microscopy (SEM) image of the microdevice consisting of two suspended membranes integrated with serpentine Pt coils as both resistance heaters and thermometers for transport property measurements of individual nanowires.*



*Figure 2: An SEM micrograph of an individual 135 nm-diameter  $\text{NbSe}_3$  nanowire placed between the two suspended membranes.*

## Summary of Research:

Two Ph.D. students, Yang Zhao and Lin Yang have been trained and used CNF cleanroom facilities to fabricate microdevices as shown in Figure 1. The microdevice consists of two side-by-side suspended  $\text{SiN}_x$  membranes integrated with serpentine Pt coils serving as both resistance heaters and thermometers. Yang Zhao made three trips to CNF and spend a total of about five weeks to fabricate the devices while Lin Yang only joined the first trip and spent about ten days at CNF.

The nanofabrication process involves LPCVD  $\text{SiN}_x$  film growth, sputtering deposition of Pt films, PECVD  $\text{SiO}_2$  film deposition, photolithography and etching, and the students have got extensive experience of using various nanofabrication tools to prepare the microdevices. In about half year time frame, the students have successfully fabricated a few wafers of devices, which have been used to measure the electrical and thermal conductivities of  $\text{NbSe}_3$  and  $\text{Ta}_2\text{NiSe}_5$  nanowires.

To measure the electrical and thermal properties of nanowires, individual nanowire samples are placed to bridge the two suspended membranes as shown in Figure 2. The device is then put into a cryostat for electrical and thermal transport measurements, during which one suspended membrane is heated up by resistance Joule heating and a portion of the heat is transferred to the other suspended membrane. Through monitoring the resistance change of the Pt coils, the temperature of both membranes can be simultaneously obtained. This allows for extraction of the thermal conductivity of the nanowire. In addition, the four extra Pt electrodes at the inside of the two membranes allow for four-point measurements of the nanowire electrical conductivity.

Our group has used this approach to conduct extensive measurements of various nanowires, nanotubes and nanoribbons. To date, the newly fabricated microdevices have been adopted to study thermal properties of two kinds of van der Waals nanowires made of NbSe<sub>3</sub> and Ta<sub>2</sub>NiSe<sub>5</sub>. van der Waals nanowires are a class of materials composed of covalently bonded molecular chains assembled together via weak van der Waals interactions, which renders interesting electrical and thermal transport properties as demonstrated by some of our recent studies [1,2].

For example, the measured thermal conductivity of a 135 nm-diameter NbSe<sub>3</sub> nanowire is displayed in Figure 3 together with the contributions from both electron and phonon as energy carriers. NbSe<sub>3</sub> nanowires demonstrate two spontaneous charge density waves (CDW) as the temperature drops to 145 K and 59 K, respectively, which correspond to condensation of a large portion of free electrons and lead to variations in their electrical conductivity and electron contribution to the thermal conductivity. The unusual peaks in the lattice thermal conductivity are attributed to electron-phonon scattering, which provide direct and

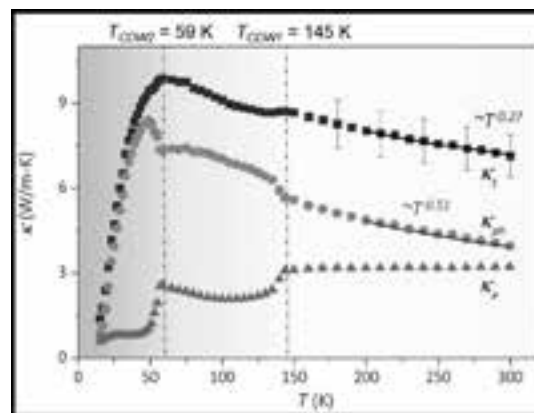


Figure 3: Distinct signatures of electron-phonon scattering in the lattice thermal conductivity of a 135 nm-diameter NbSe<sub>3</sub> nanowire in the temperature range of 15-300 K. The electron and phonon contributions are labelled as  $\kappa_e$  and  $\kappa_{ph}$  respectively, and the total thermal conductivity is denoted as  $\kappa_t$ .

unambiguous evidence for the importance of electron-phonon scattering in lattice thermal transport, which has been lacking so far. In addition, we have used the newly fabricated devices to probe ballistic transport of phonons in NbSe<sub>3</sub> nanowires and observed record long ballistic transport distance and currently we are probing the underlying physical mechanisms for this unexpected ballistic phonon transport.

## References:

- [1] Q. Zhang, C. Liu, X. Liu, J. Liu, Z. Cui, Y. Zhang, L. Yang, Y. Zhao, T. T. Xu, Y. Chen, J. Wei, Z. Mao, and D. Li, "Thermal Transport in Quasi-1D van der Waals Crystal Ta<sub>2</sub>Pd<sub>3</sub>Se<sub>8</sub> Nanowires: Size and Length Dependence," ACS Nano 12, 2634-2642 (2018).
- [2] L. Yang, Y. Tao, J. Liu, C. Liu, Q. Zhang, M. Akter, Y. Zhao, T. T. Xu, Y. Xu, Z. Mao, Y. Chen, and D. Li, "Distinct Signatures of Electron-Phonon Coupling Observed in the Lattice Thermal Conductivity of NbSe<sub>3</sub> Nanowires," Nano Lett. 19, 415-421 (2019).

# Fabricating Lithographically Designed Cylindrical Colloidal Particles

**CNF Project Number: 2704-18**

**Principal Investigator(s): Prof. Fernando Escobedo**

**User(s): Prajwal Bangalore Prakash**

*Affiliation(s): Chemical and Biomolecular Engineering, Cornell University*

*Primary Source(s) of Research Funding: Escobedo Funding*

*Contact: fe13@cornell.edu, pb526@cornell.edu*

*Primary CNF Tools Used: Spinners and hot plates in Class-II resist room, AutoStep i-line stepper*

## Abstract:

Materials with characteristic structural features on the colloidal scale (10 nm to 10  $\mu\text{m}$ ) are potentially important for applications in electronics, optics, high density memory, microelectromechanical machines, and tissue engineering. In this project, we are exploring our understanding to allow for rational design of desired materials from colloidal building blocks. For this purpose, we have exploited a class of colloidal particles formed by photolithography in a polymeric photoresist (SU-8) [1-3]. The objective of the current project is to study the equilibrium assembled structures formed by the cylindrical colloidal particles under confinement. These structures are predicted using Monte Carlo simulation model; and we are now focusing on validating the assembly behavior using experiments.

## Summary of Research:

Our first step was to fabricate micron-sized monodisperse cylindrical particles using the photolithography technique. We used the epoxy-based negative photoresist, SU-8 2001 and adopted the following procedure to achieve the target dimension [2]:

(1) Spin coating of the SU-8 2001 photoresist on top of a sacrificial layer (OmniCoat™) on a silicon substrate achieving the desired average height of 0.98  $\mu\text{m}$ . For a 0.98  $\mu\text{m}$  layer, SU-8 can be spun at 500 rpm for 10s, immediately followed by a step at 3000 rpm for 30s.

(2) Exposure of the wafer through a Cr photomask with round holes using a 5X stepper (GCA Autostep i-line). The average diameter of the particle ( $\sim 1.605 \mu\text{m}$ ) is controlled by exposing the resist to the ultraviolet light (365 nm) through a photomask with rounded holes with a focus value of  $-1.4 \mu\text{m}$  and exposure time = 0.22s.

(3) Post-exposure bake of the SU-8 layer: the wafer was placed on a vacuum hotplate at 65°C for 1 min and 95°C for 2 min to crosslink the exposed photoresist. The wafer was allowed to cool to ambient temperature before proceeding to the next step. Next, the wafer is then placed in  $\sim 100 \text{ mL}$  of SU-8 developer for 1 min and then rinsed with IPA.

(4) The particles are then released by using Remover PG and sonication in an ultrasonic cleaner.

Before placing the particles in the buffered solutions of surfactants, a sample of particles in DI water was redeposited on a silicon wafer and imaged by SEM (Zeiss Supra 55VP or Zeiss Ultra 55). The average and standard deviation of the heights and diameters of the particles were measured on the images (Figure. 2). We estimated about 6.3% and 4.7% polydispersity in height and diameter, respectively. We note in Figure 1 that the two ends of the cylinders were not identical: one end had sharp edges that were globally flat (although not smooth); the other end had more rounded edges (arrow). The flat end was the one that was in contact with the OmniCoat sacrificial layer. We obtained the size distributions by analysis of scanning electron micrographs. The fabricated SU-8 particles are then dispersed in water and Tergitol NP70 surfactant solvent medium.

## References:

- [1] Badaire, Stéphane, Cécile Cottin-Bizonne, and Abraham D. Stroock. "Experimental investigation of selective colloidal interactions controlled by shape, surface roughness, and steric layers." *Langmuir* 24.20 (2008): 11451-11463.
- [2] Badaire, Stéphane, et al. "Shape selectivity in the assembly of lithographically designed colloidal particles." *Journal of the American Chemical Society* 129.1 (2007): 40-41.
- [3] Hernandez, Carlos J., and Thomas G. Mason. "Colloidal alphabet soup: Monodisperse dispersions of shape-designed lithoparticles." *The Journal of Physical Chemistry C* 111.12 (2007): 4477-4480.

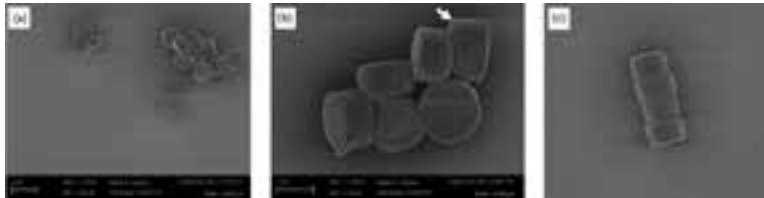


Figure 1: (a)-(c) Structure of the SU-8 particles obtained using scanning electron micrographs. Arrow (white) shows the curvature of edge of one of the particles. (c) The column arrangement of the particles shows variation in particle diameter.

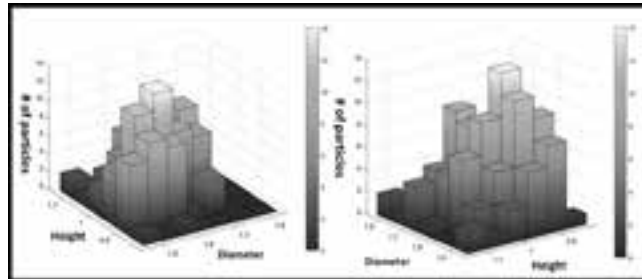


Figure 2: Histogram of height and diameter of the particles. The statistics is taken for ~200 particles diameter and height data. The skewness in diameter is about 0.056 in diameter and 0.305 in height. This indicates an approximate symmetric distribution in the profile.

# Development of Microsensors for Air Quality Monitoring

**CNF Project Number: 2728-18**

**Principal Investigator(s): Alex Deyhim**

**User(s): Nicole Chu, Jin Luo, Chuan-Jian Zhong, Shanana Yan**

*Affiliation(s): Materials Science and Engineering, Cornell University*

*Primary Source(s) of Research Funding: MEng Materials Science and Engineering FlexSurfaces/CCMR Jumpstart*

*Contact: akd9@cornell.edu, nc537@cornell.edu*

*Primary CNF Tools Used: Metal film deposition, photolithography, mask making equipment, optical pattern generator, ABM contact aligner, wafer processors*

## Abstract:

Air pollution is a major problem that is dangerous not only to the environment but to the health and safety of humans. Due to the increase in air pollution in recent years there has in turn been a decline in health. Particularly conditions such as respiratory and cardiovascular diseases have seen a rise in prevalence. People who had preexisting conditions have seen their conditions worsen due to this rise and there has been a rise in prevalence of health defects such as headaches, dizziness, trouble breathing, damage to the liver and in some cases cancer. As such there is a need for a device to monitor air pollution levels for personalized use. Existing technology lacks sensitivity and selectivity as well as cost efficiency and are not equip for personalized use. Gold nanoparticles fabricated into microelectrode array devices allow for the selectivity and sensitivity need to make these sensors. Working with company FlexSurfaces and the Cornell NanoScale Science and Technology Facility, we have used the clean room facilities to begin developing the technology for low-cost sensors with high sensitivity for use in portable and wearable air quality monitoring systems.

## Summary of Research:

The design of the sensors is very important. The parameters and shape of the microelectrode used in the array impacts its performance when measuring air quality. The composition of the nanostructure thin film also has a large impact on the performance of the sensor to detect VOCs. Current array measurements are made of combinations of the following, finger width (FW, 5  $\mu\text{m}$ , 10  $\mu\text{m}$ ), finger space (FS, 5  $\mu\text{m}$ , 10  $\mu\text{m}$ ), and finger length (FL, 100  $\mu\text{m}$ , 200  $\mu\text{m}$ ). Previously gathered sensor array response data shows that smaller parameter values for width, length and space typically result in a higher response sensitivity when tested and exposed to various VOCs. (See Figure 1.)

Flexible devices use a similar mask design and parameters as the glass substrates. (See Figure 2.) The material used in the flexible design is Kapton also known as polyimide. This material is both flexible and inexpensive making it perfect for this application. This design while testing and

optimized for glass array devices still needs alterations to maximize ability on flexible substrates. This is currently being tested and studied.

The photos in Figure 3 demonstrate the diminished finger space as seen in the first photo the finger space is so small you cannot see it and in the second is disappearing. The final photo shows what a well-made finger space should look like. This problem with the disappearing and diminishing of the devices parameters was predicted to be one of two problems — over exposure or loose contact. Several experiments were carried out to find a solution to these problems.

The possible problem of a loose contact was addressed by cleaning the mask more thoroughly before contact with the substrate. While the problem of overexposure was dealt with in a more expansive method.

| Design # | FS ( $\mu\text{m}$ ) | FW ( $\mu\text{m}$ ) | FL ( $\mu\text{m}$ ) | Design | W ( $\mu\text{m}$ ) | Space ( $\mu\text{m}$ ) | L ( $\mu\text{m}$ ) |
|----------|----------------------|----------------------|----------------------|--------|---------------------|-------------------------|---------------------|
| 1        | 10 (I)               | 10 (I)               | 100 (I)              | 1      | 5                   | 5                       | 100                 |
| 2        | 10 (I)               | 5 (I)                | 200 (I)              | 2      | 5                   | 10                      | 100                 |
| 3        | 5 (I)                | 10 (I)               | 200 (I)              | 3      | 10                  | 5                       | 100                 |
| 4        | 5 (I)                | 5 (I)                | 100 (I)              | 4      | 10                  | 5                       | 200                 |
|          |                      |                      |                      | 5      | 10                  | 10                      | 100                 |
|          |                      |                      |                      | 6      | 10                  | 10                      | 400                 |

Figure 1: Device parameters for glass samples (right) and polyimide samples (left).

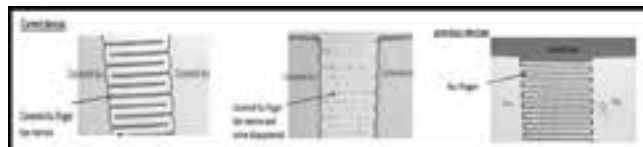


Figure 3: The finger spaces between first devices and older devices. As can be seen in the photos on the left, the finger space has been diminished.

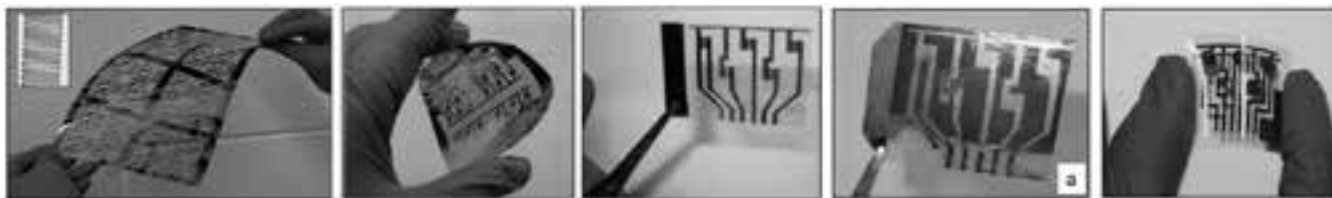


Figure 2: Examples of flexible devices. Devices are very versatile as demonstrated in the photographs.

In order to address overexposure a single substrate was taken and exposed at six different exposure times. Exposure times from 4-11 seconds were tested. The image below shows an example of what one of these test samples would look like. One can see in the images the finger of a sample produced at six seconds, nine seconds and eleven seconds. From these images one can already see how the finger parameters are affected by the exposure time. The sample at eleven seconds has a much smaller finger space than the sample at six seconds. After etching and careful observations under the microscope it could be seen that six seconds was the exposure time that developed the optimal device parameters for flexible substrates. All future tests were carried out with flexible substrates at six seconds exposure times.

Testing of the array devices is done at Binghamton University. Where further processing of the wafers is first conducted. The interdigitated microelectrode devices are first coated with a sensing tin film which is prepared by molecularly-mediated assembly of nanoparticles. Samples were then housed in Teflon® chambers and hooked to computer-interfaced multimeters, resistance was measured. Vapor sources and N<sub>2</sub> were connected via tubing. Vapor concentration in ppm moles per liter was calculated from partial vapor pressure. N<sub>2</sub> is used as the reference gas, and all experiments were performed at room temperature, 22 ± 1°C.

The graphs in Figure 4 are examples of glass and polyimide device response profiles to benzene and or hexane. The images show that both the glass and flexible devices show somewhat similar response profiles. This means that only slight adjustments will need to be made to the device parameters in order to maximize their ability on the polyimide substrate.

### Conclusions:

Through this project we have developed a process for fabricating interdigitated microelectrodes on flexible polyimide substrates. This development process differed from the one used on glass substrates in order to ensure the optimal parameters. Particularly within the process the exposure time needed adjustments for flexible

substrates. Tests conducted so far have shown that the microfabricated IMEs on both glass and polyimide substrates worked well, showing similar response profiles to certain VOC's.

Further testing is still being carried out to evaluate the performance of these sensors. Experiments into other possible substrates such as paper are being considered. A systematic study is underway to evaluate the device parameters. As we gather more information, we are beginning to develop a prototype sensor device to be used in air quality monitoring.

### References:

- [1] Wang L, et al. Sensing Arrays Constructed from Nanoparticle Thin Films and Interdigitated Microelectrodes. *Sensors (Basel)*. 2006;6(6):667-679. Published 2006 Jun 22.
- [2] Craft, Elena. "Microsensors Help Map Crowdsourced Pollution Data." *GreenBiz*, GreenBiz Group Inc., 26 June 2013, [www.greenbiz.com/blog/2013/06/26/microsensing-measure-air-pollution-palm-your-hand](http://www.greenbiz.com/blog/2013/06/26/microsensing-measure-air-pollution-palm-your-hand).
- [3] "A Brief Guide to Atmospheric Pollutants." *Compound Interest*, Compound Interest, 8 May 2015, [www.compoundchem.com/2015/05/05/atmospheric-pollutants/](http://www.compoundchem.com/2015/05/05/atmospheric-pollutants/).
- [4] Knox, A., et al. "Air Pollution Air Pollution Monitoring Air Pollution Monitoring and Sustainability Air Pollution Sustainability." *Encyclopedia of Sustainability Science and Technology*, 2012, pp. 167-203., doi:10.1007/978-1-4419-0851-3\_373.
- [5] "Air Conditions", *Bloomberg Pursuits*, April 15, 2019.
- [6] "Indoor Air Quality." EPA, Environmental Protection Agency, 16 July 2018.

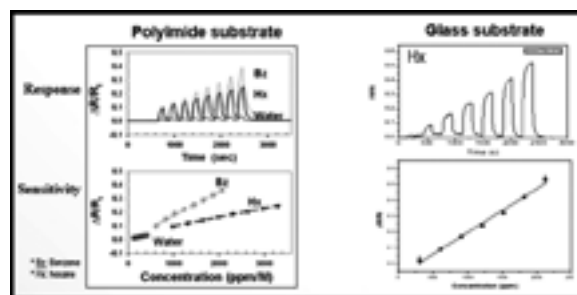


Figure 4: Response profiles for polyimide (left) and glass (right) substrates to hexane and for polyimide benzene vapors.

# Scissionable Polymer Photoresist for Extreme Ultraviolet Lithography

**CNF Project Number: 2751-18**

**Principal Investigator(s): Christopher Kemper Ober**

**User(s): Abhaiguru Ravirajan**

*Affiliation(s): Materials Science and Engineering, Cornell University*

*Primary Source(s) of Research Funding: INTEL Corporation*

*Contact: christoper.ober@cornell.edu, ar2362@cornell.edu*

*Primary CNF Tools Used: ASML 300C DUV stepper, ABM contact aligner, JEOL-9500 e-beam lithography, P10 profilometer*

## Abstract:

Researchers across the globe are intensively working on photoresists that can show high resolution down below 10 nm in a single-step process. Extreme ultraviolet (EUV) and electron-beam (e-beam) lithography are the most prominent candidates to create such small structures in resists. The difficulty in achieving such small feature size arises due to the RLS tradeoff, where the resists must simultaneously satisfy the resolution, line width roughness and sensitivity requirements. Also, another major concern with EUVL is the problem of stochastics due to lesser number of photons. Through our work, we believe that chemically amplified photoresists based on scissionable polymers are potential candidates to overcome these challenges. Our work focuses on polyaldehydes based low ceiling temperature ( $T_c$ ) polymers that unzip upon exposure to DUV (deep ultraviolet)/EUV light sources due to main chain cleavage of the polymer backbones. So far, we have synthesized polyphthalaldehyde (PPA) based photoresists and studied their performances with the incorporation of various photoacid generators (PAGs) and base quencher.

## Summary of Research:

One of the limitations with EUV light source is that there are much less photons available for the photochemical reactions of the photoresists. Either low or uneven light radiation energy across the exposed region can cause random defects during the lithography processes. Thus, it is desirable to pursue multimechanism photoresists that involves intrinsically depolymerizable polymers and the concept of chemical amplification. This approach shares some feature of the scissionable photoresist using main chain cleavage, but in contrast makes effective use of limited light exposure through the chain depolymerization of the resist polymer. The chain scissionable polymers usually have low ceiling temperatures ( $T_c$ ) and contain weak chemical bonds, which can be cleaved by external triggers and thus starting the depolymerization process [1]. Due to their interesting properties, they have been widely utilized as sacrificial components in many areas, such as resist imaging, fabrication of porous materials, and transient electronics.

In our study, we focus on the synthesis of one kind of chain scissionable polymers, polyphthalaldehydes, via metal-free anionic polymerization of aldehyde monomers that are promoted by superbases bases with alcohol

initiators [2]. Not only can this method produce linear PPA with tunable molecular weights and low dispersity, but also provides the possibility to introduce extra functional groups at the chain ends. Later, the PAGs can be introduced into the side chains using highly efficient post-polymerization reactions [3].

## Materials and Methods; Synthesis:

Photoresist solution containing 5 wt.% PPA in cyclohexanone blended with common ionic and nonionic PAG's, for example, triphenylsulfonium triflate was prepared in varying ratios of 2-10 wt.% to PPA. Further base quenchers were introduced to these PPA-PAG blends [4]. The solution was then spin coated onto a silicon wafer at 3000 rpm for 1 min and post apply baked at 90°C for 1 min to remove excess solvent.

## Results and Discussions:

The PAG blended polymer solution was exposed to 254 nm mid-UV radiation through a mask containing

patterns using ABM contact aligner. The pattern on the exposed resist was then directly observed through Nikon Microscope Cameras in CNF without the use of any developer or post-exposure processing techniques at different times after exposure. As shown in Figure 1, the image pattern continued to develop gradually over time.

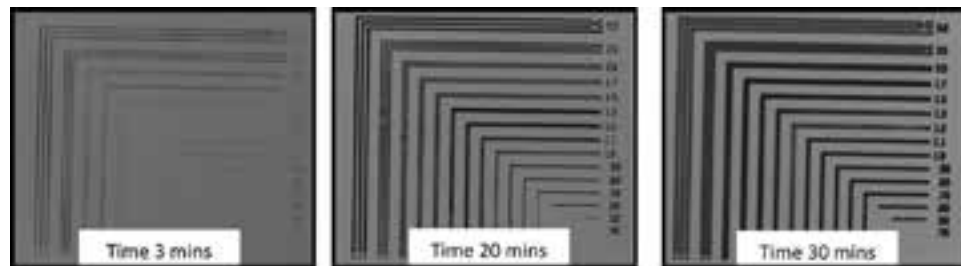


Figure 1: Optical microscope images of PAG blended PPA resist observed at different times after exposure to  $1 \text{ mJ/cm}^2$  mid-UV radiation using ABM contact aligner.

This is mainly because of the vaporization of monomers due to the main chain depolymerization under mid-UV radiations. Further the resist solution containing PAG, Base quencher blend was exposed to mid-UV radiations. As seen in Figure 2, good quality pattern was observed compared to the PAG only blended polymer patterns and the self-development of pattern was found to be more controlled.

Similar performance of these photoresists was also observed when exposed to 248 nm DUV radiation using ASML 300C DUV stepper. Well-defined 1:1-line spaced positive tone patterns were observed for an exposure dosage in the range of  $1\text{-}4 \text{ mJ/cm}^2$  without any use of post-exposure. Further, these resists were evaluated under e-beam lithography using CNF JEOL 9500 Lithography tool. While large amounts of residues can be easily found at exposed areas, good 1:1 line patterns with feature sizes from  $1000\text{-}400 \text{ nm}$  were obtained for exposure dosage in the range of  $75\text{-}100 \text{ }\mu\text{C/cm}^2$  by atomic force microscopy (AFM), as shown in Figure 3.

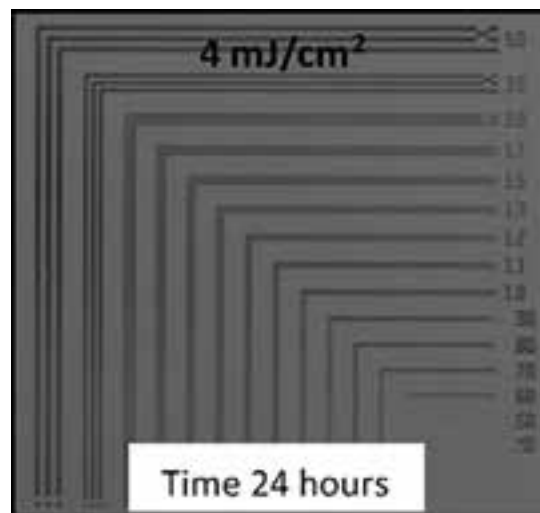


Figure 2: Optical microscope image of PAG, base quencher blended PPA resist observed at 24 hours after exposure to mid-UV radiation showing enhanced image quality.

### Summary:

In summary, photocleavable polymer photoresists show promising results when introduced to mid-UV, DUV and e-beam lithography. By introducing an optimized percentage of PAG and base quencher into resist solution, high contrast patterns under extremely low exposure dosages can be achieved. With these preliminary findings, PAG functionalized derivatives of PPA will be introduced to lithography, and the performances will be evaluated for achieving improved resolution and LER.



Figure 3: 1:1-line space patterns with feature size: (a)  $600 \text{ nm}$  (b)  $400 \text{ nm}$  observed under AFM after exposure to  $75 \text{ }\mu\text{C/cm}^2$  e-beam radiation.

### References:

- [1] Sasaki, T., et al., Photoinduced depolymerization in poly(olefin sulfone) films comprised of volatile monomers doped with a photobase generator. *Journal of Polymer Science Part A: Polymer Chemistry*, 2012. 50(8): p. 1462-1468.
- [2] Wang, F. and C.E. Diesendruck, Polyphthalaldehyde: Synthesis, Derivatives, and Applications. *Macromol Rapid Commun*, 2018. 39(2).
- [3] Hernandez, H.L., et al., Triggered transience of metastable poly(phthalaldehyde) for transient electronics. *Adv Mater*, 2014. 26(45): p. 7637-42.
- [4] Natsuda, K., et al., Study of Acid-Base Equilibrium in Chemically Amplified Resist. *Japanese Journal of Applied Physics*, 2007. 46(11): p. 7285-7289.

# Quantum Materials for Communication, Computing, and Storage

**CNF Project Number: 2801-19**

**Principal Investigator(s): Debdeep Jena, Huili Grace Xing**

**User(s): John Wright, Phillip Dang, Zexuan Zang, Jashan Singhal, Hyunjea Lee**

*Affiliation(s): 1. Materials Science and Engineering, 2. Applied and Engineering Physics,  
3. Electrical and Computer Engineering; Cornell University*

*Primary Source(s) of Research Funding: ONR-DJ*

*Contact: djena@cornell.edu, grace.xing@cornell.edu, jgw92@cornell.edu, pd382@cornell.edu,  
zz523@cornell.edu, js3452@cornell.edu, hl2255@cornell.edu*

*Primary CNF Tools Used: Autostep 2000 I-Line stepper, JEOL 6300, AJA sputter, Veeco AFM, DISCO dicing saw*

## **Abstract:**

**The integration of new material properties into electronics devices creates new possibilities for device performance, architecture, and function. We therefore investigate the fabrication and applications of materials with exceptional properties, including superconductivity, ferromagnetism, ferroelectricity, and topologically non-trivial electronic states.**

## **Summary of Research:**

Two-dimensional (2D) materials, which allow the extreme scaling down of transistors with their atomically thin structure, are a promising candidate for the next generation electronics. One of the challenges for these applications is complementary metal oxide semiconductor (CMOS) devices. For CMOS, there should be a complementary pair of n-type and p-type field effect transistors (FETs) whose mobility and threshold voltage are well matched. There have been many studies about n-type 2D materials that make n-type field effect transistors (FETs), but p-type 2D materials with sizable band gap have not been well explored. For a pMOS option, we have investigated tungsten diselenide ( $\text{WSe}_2$ ).  $\text{WSe}_2$  is a good candidate for CMOS applications since it shows ambipolar behavior as well as relatively high hole mobility. We have been making p-type FETs using exfoliated  $\text{WSe}_2$  flakes. The Autostep stepper is used to make the substrate for 2D material transfer, the JEOL 6300 is used to define patterns for metal contacts, and the AJA sputtering system is used to deposit metals. The I-V characteristics of representative device is shown in Figure 1(a) and 1(b). Maximum drive current reaches more than  $20 \mu\text{A}/\mu\text{m}$ , the on/off current ratio is more than seven decades, and the upper bound of contact resistance is around  $75 \text{k}\Omega\cdot\mu\text{m}$ , which is comparable to some of the best results in literature [1].

Spin-orbit torque (SOT) is a physical phenomenon where a material with large spin-orbit coupling can exert a torque on the magnetic moment of an adjacent ferromagnet (FM). This effect is applicable to magnetic memory, where information can be stored in the magnetization direction of the FM, and SOT can be used to control that magnetization direction. The efficiency of magnetic manipulation by SOT is dependent on the types of materials used and the quality of the interface between them. Topological insulators (TI) are a class of materials with strong spin-orbit coupling, an inversion of the band structure, and surface states where the spin and momentum of electrons are interdependent. These attributes can lead to more efficient SOTs and make FM/TI bilayers very promising for magnetic memory devices [1]. However, in many reports, at least one material of the FM/TI bilayer is sputtered [1-3]. To further enhance the performance of FM/TI bilayer, we grow FM/TI structures using molecular beam epitaxy (MBE) in one shot without exposure to air. Here, we report our advances in the MBE growth and characterization of TIs and FMs bilayers that are applicable to SOT devices.

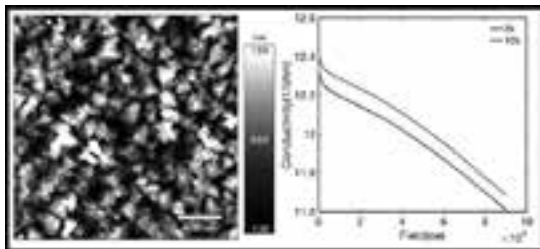


Figure 1: AFM surface height map of  $\text{Bi}_2\text{Se}_3$  grown on GaAs, showing  $< 1\text{ nm}$  RMS roughness (left) and magnetoresistance of  $\text{Bi}_2\text{Se}_3$  grown on GaAs (right).

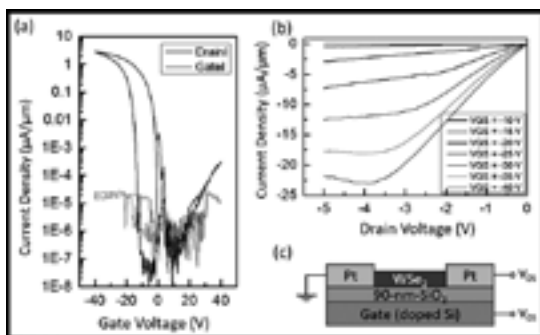


Figure 2: (a) Transfer curve of  $\text{WSe}_2$  pFET, (b) Output curve of  $\text{WSe}_2$  pFET, and (c) Cross-sectional image of  $\text{WSe}_2$  pFET.

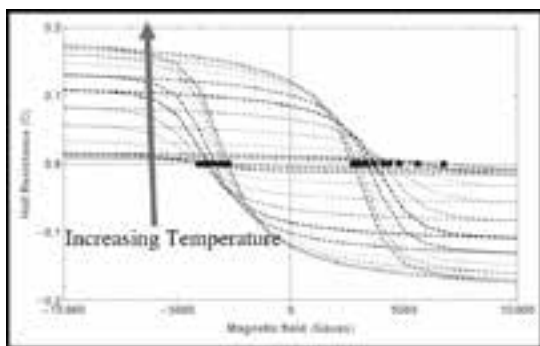


Figure 3: Temperature-dependent AHE measurement from 10K - 300K for  $\text{Mn}_4\text{N}$  film on  $\text{MgO}$  (001). The saturation Hall resistance increases with temperature. (Find full color on pages xiv-xv.)

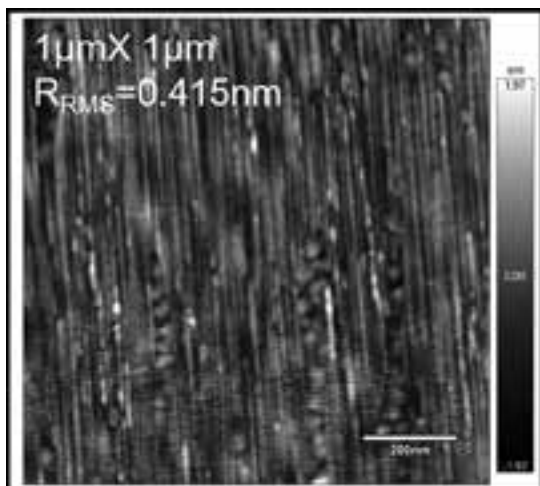


Figure 4: AFM surface height map of  $\text{NbN}/\text{AlN}/\text{NbN}$  heterostructure grown on 6H-SiC by MBE.

Recently, room temperature switching of the magnetization of a FM using  $\text{Bi}_2\text{Se}_3$  as the TI have been reported [2,3], revealing the merits of using  $\text{Bi}_2\text{Se}_3$  in FM/TI structures. We are now optimizing growth condition of  $\text{Bi}_2\text{Se}_3$  on different substrates including GaAs and sapphire. Thanks to the weak VdW interaction between  $\text{Bi}_2\text{Se}_3$  and substrates, high quality single crystal  $\text{Bi}_2\text{Se}_3$  have been successfully grown on both substrates with smooth surface (RMS  $< 1\text{ nm}$ ), as shown in the atomic force microscopy (AFM) image shown in Figure 1. However, it is found that bulk states exhibit metallic electrical transport characteristics, as shown by the temperature-dependent resistance in Figure 2. Topological insulators should be insulating in the bulk, so the metallic behavior indicates that the Fermi level is not in the bulk band gap of  $\text{Bi}_2\text{Se}_3$ . Tuning the Fermi level into the bulk bandgap of  $\text{Bi}_2\text{Se}_3$  by electrostatic gating or doping the film could also lead to higher SOT efficiency.

For the ferromagnetic layer in our FM/TI structure, we are exploring  $\text{Mn}_4\text{N}$ , one of the few known magnetic nitride materials. We are optimizing the MBE growth of  $\text{Mn}_4\text{N}$  on various substrates such as  $\text{MgO}$ ,  $\text{STO}$  and  $\text{GaN}$ . Through measurement techniques such as vibrating sample magnetometry and anomalous Hall effect (AHE) measurements, we have confirmed perpendicular magnetization and low saturation magnetization which are both beneficial for magnetic memory device applications. To make our samples suitable for these measurements, we use the dicing saw and metal deposition systems such as the CHA thermal evaporator. The shape of the AHE signal, as shown in Figure 3, nearly forms a parallelogram and is indicative of perpendicular magnetic anisotropy, which is desirable for higher-density magnetic memory.

The phenomena of superconductivity and the integration of superconducting materials with normal state materials are utilized in applications such as quantum computing and single flux quantum computing. We investigate the possibility of realizing epitaxial integration of III-N semiconductors with metallic superconducting materials such as  $\text{NbN}$  through the growth of thin film heterostructures by molecular beam epitaxy. We have demonstrate that epitaxial  $\text{NbN}/\text{AlN}/\text{NbN}$  heterostructures can be grown on 6H-SiC substrate with RMS roughness less 0.5 nm. Measurements to observe the Josephson effect in these structures are ongoing.

## References:

- [1] H. C. P. Movva et al., ACS Nano 9, 10402-10410 (2015).
- [2] Melnik, A. R., et al. "Spin-transfer torque generated by a topological insulator." Nature, 511(7510), 449-451 (2014).
- [3] Han, Jiahao, et al. "Room-temperature spin-orbit torque switching induced by a topological insulator." Physical review letters 119.7 (2017): 077702.
- [4] Mahendra, D. C., et al. "Room-temperature high spin-orbit torque due to quantum confinement in sputtered  $\text{Bi}_2\text{Se}_3$ -x films." Nature materials 17.9 (2018): 800.

# Responsive Liquid Crystal Micro Actuators for Microrobotic Applications

**2019 CNF REU Intern: Anna Alvarez**

**2019 CNF REU Intern Affiliation:  
Mechanical Engineering, University of Illinois at Urbana Champaign**

*CNF Project: 2019 Cornell NanoScale Science & Technology Facility Research Experiences for Undergraduates Program*

*CNF REU Principal Investigator(s): Prof. Itai Cohen, Department of Physics, Cornell University*

*CNF REU Mentor(s): Qingkun Liu, Department of Physics, Cornell University*

*Primary Source of CNF REU Funding: National Science Foundation via  
the National Nanotechnology Coordinated Infrastructure (NNCI) Grant No. NNCI-1542081*

*Contact: itai.cohen@cornell.edu, ql59@cornell.edu*

*Website: <http://cnf.cornell.edu/education/reu/2019>*

*Primary CNF Tools Used: ABM contact aligner, MVD 100, Oxford 81, Unaxis 770 deep Si etcher,  
Heidelberg mask writer - DWL2000*

## Abstract:

**Multifunctional micro-sized soft robotics are poised to revolutionize drug delivery, surgical operation and many other biomedical applications. However, building such microrobots with a variety of functionalities is challenging due to the lack of fabrication technologies for responsive materials at the microscale. In this research, we developed a scalable microfabrication technology to build light and thermal activated microrobots using liquid crystal (LC) polymers, which are known for their facile response to relatively weak stimuli. First, an ultraviolet light curable precursor containing LC oligomers was developed, allowing for patterning of the LC microrobots via photolithography. Second, fluoroctyl-trichlorosilane-coated silicon microgrooves were used to establish unidirectional alignment in LC microactuators. Finally, heat was applied to confirm the LC microactuators could properly contract along the alignment direction as expected when experiencing a phase transition from the LC to its isotropic phase. These LC microactuators could further bend as hinges if an athermal photoresist was patterned on top, allowing 2D patterned films to fold into 3D objects. Fabricating these LC-based responsive microrobots in a scalable way will provide a powerful platform for dynamically reconfigurable micro-sized origami-robots.**

## Summary of Research:

The field of microrobotics presents a promising future for advancements in sensing, surgery, and drug delivery. However, current microrobots are only capable of performing simple functions, such as self-propulsion or particle encapsulation [1]. In order to evolve into multifunctional, controllable devices, it is necessary to develop a new actuation system. In this work, we propose to use of photopatternable responsive liquid crystal (LC) polymer to fabricate micro-scale devices from.

The initial challenge of this project was to develop an ultraviolet (UV) curable LC precursor compatible with photolithography technology. The precursor contained a photoinitiator, a 3:1 molar ratio of LC diacrylate to butylamine, and chloroform as the solvent. To test precursor performance, the substance was spin coated at 1000 rpm, yielding a thickness of 2.5  $\mu\text{m}$ . Exposure to UV light in the ABM contact aligner excited the photoinitiator and a postbake at 90°C released free radicals to complete polymerization [2]. From successful samples,

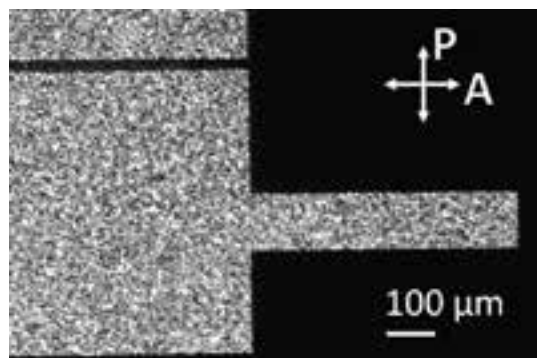


Figure 1: A well-developed LC pattern viewed between crossed polarizers (A and P).

features 50  $\mu\text{m}$  and smaller can be observed. However, photopatterning the LC polymer with no initial alignment results in a speckled image when viewed through crossed polarizers (Figure 1). Given no set direction to follow, the LC mesogens align themselves in random orientations.

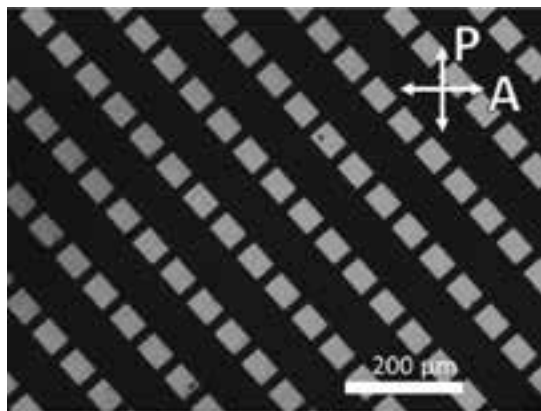


Figure 2: Well aligned LC patterns oriented 45° relative to the polarizers.

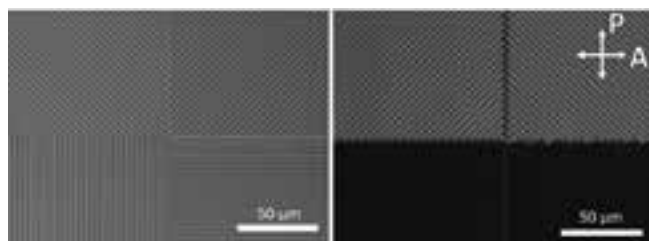


Figure 3: (a) 1.5  $\mu\text{m}$  wide and 1.4  $\mu\text{m}$  deep Si grooves with four orientations. (b) Aligned LC on top of etched Si grooves. Birefringent materials appear brightest when aligned 45° relative to the polarizer and darkest when 0° or 90° relative to the polarizer. The black lower half of the image suggests near perfect alignment.

For an LC polymer actuator to work, it is crucial that the mesogens display predesigned alignment. LC polymers will expand along the direction of average molecular alignment and contract in the perpendicular when transitioning from isotropic to LC phase. Altering the surface architecture was accomplished through two methods. In the first, the substrate was spin-coated with polyimide PI-2555 and physically rubbed with a velvet cloth after a 30 minute-long bake at 170°C. The LC polymer achieved planar anchoring and aligned along the rubbing orientation. This method proved to be a reliable technique and resulted in few defects (Figure 2). While suitable for aligning simple patterns, such as cantilever beams, it is unable to align the LC polymer in differing orientations. Fabricating a micro robot that can actuate hinges in various directions requires a more versatile micropatterning technique. In the second method, fluoroctyl-trichlorosilane-coated silicon microgrooves, 1.5  $\mu\text{m}$  wide and 1.4  $\mu\text{m}$  deep, were etched to establish an arbitrary alignment (Figure 3a). The LC once again can be aligned planarly along the groove geometry, as visible in Figure 3b.

The final challenge of this work was inducing actuation of the aligned LC polymer in response to heat. Patterned cantilevers were released from the substrate during development in IPA and exposed to 90°C while still submerged in the solution. LC can only expand and

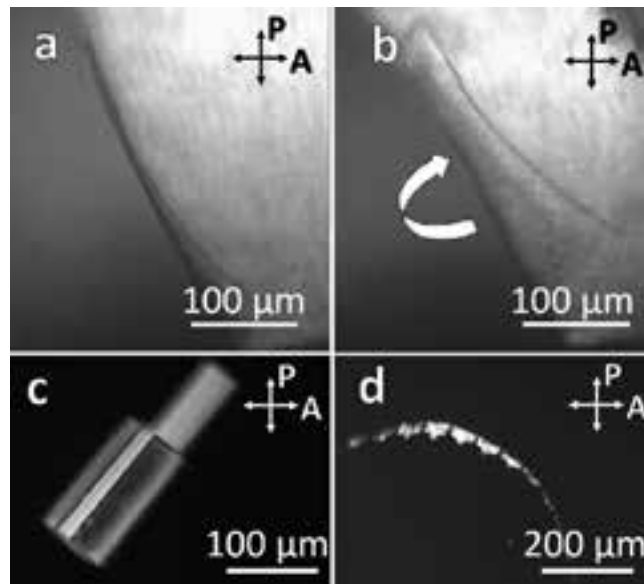


Figure 4: (a) Cantilever edge at 60°C. (b) Cantilever edge at 90°C. (c) A curled cantilever pattern. (d) A connected chain of released cantilevers.

contract in the 2D plane when experiencing a phase transition. However, the combination of athermal polymer PI-2555 and LC coating proved to be an efficient bimorph, allowing the 2D patterned films to fold into 3D shapes (Figure 4a,b) in response to the elevated temperature. Successful actuations thus far (Figure 4c) have a measured radius of curvature of 25  $\mu\text{m}$ . To further improve the quality of the LC-patterned films, an oxygen plasma etch was required to remove fringes of excess polymer before IPA development. This is to prevent a chain of adhering cantilevers (Figure 4d). Continued work will focus on doping the LC precursor with a photoresponsive dye to induce actuation via light exposure.

The use of responsive LC films is a promising platform for microrobotic actuation. Not only has this work shown it is possible to fabricate LC films with available nanofabrication technology, but it is possible to align the polymers through patternable microgrooves as well. Future development of these actuators may lead to new fields of reconfigurable origami-based microrobots.

#### Acknowledgements:

I would like to thank Professor Itai Cohen, Qingkun Liu, and the CNF staff for their support this summer. This work was carried out as part of the 2019 CNF REU Program and supported by the National Science Foundation (Grant No. NNCI-1542081).

#### References:

- [1] M. Medina-Sánchez, V. Magdanz, M. Guix, V.M. Fomin, O.G. Schmidt, O. G. Adv. Funct. Mater. 28, 1707228, 2018.
- [2] T. H. Ware, T. J. White, Polym. Chem. 6, 4835, 2015.

# ALD for Membranes, Metamaterials, and Mechanisms

**CNF Project Number: 900-00**

**Principal Investigator(s): Paul L. McEuen<sup>1,2</sup>, Itai Cohen<sup>1,2</sup>**

**User(s): Tanner Pearson<sup>3</sup>, Kyle Dorsey<sup>3</sup>, Edward Esposito<sup>1</sup>, Sierra Russell<sup>4</sup>, Baris Bircan<sup>3</sup>**

*Affiliation(s): 1. Laboratory of Atomic and Solid State Physics, Cornell University; 2. Kavli Institute for Nanoscale Science, Cornell University; 3. School of Applied and Engineering Physics, Cornell University; 4. College of Nanoscale Sciences, SUNY Polytechnic Institute*

*Primary Source(s) of Research Funding: NSF grant DMR-1435829, Air Force Office of Scientific Research (AFSOR) multidisciplinary research program of the university research initiative grant FA2386-13-1-4118, Cornell Center for Materials Research (CCMR) through NSF MRSEC program (DMR-1719875), ARO grant W911NF-18-1-0032, National Science Foundation (NSF) Major Research Instrumentation Award DMR-1429155, NNCI Grant No. NNCI-1542081, and the Kavli Institute at Cornell for Nanoscale Science*

*Contact: plm23@cornell.edu, itai.cohen@cornell.edu, tgp34@cornell.edu, kjd96@cornell.edu, epe3@cornell.edu, srussell@sunypoly.edu, bb625@cornell.edu*

*Primary CNF Tools Used: Oxford FlexAL ALD, Arradance ALD, Autostep AS200 i-line stepper, CVC e-beam evaporators, Oxford 81/82 etchers, PT770 and PT740 etchers, Anatech Asher, Zeiss SEMs, Veeco AFM, Tencor P7 profilometer, Filmetrics UV, Woollam ellipsometer, DISCO dicing saw, Heidelberg DWL2000, AJA sputterer*

## Abstract:

**Bending and folding techniques such as origami and kirigami enable the scale-invariant design of three-dimensional structures, metamaterials, and robots from two-dimensional starting materials. Such techniques have been used in everything from deployable spacecraft solar panel arrays [1], soft robots [2], and microelectromechanical systems (MEMS) [3]. These design principles are especially valuable for small systems because most micro- and nanofabrication involves lithographic patterning of planar materials. Ultra-thin films of inorganic materials serve as an ideal substrate for the fabrication of flexible microsystems because they possess high intrinsic strength, are not susceptible to plasticity, and are easily integrated into microfabrication processes [4]. In recent work, we employed atomic layer deposition (ALD) to synthesize films down to 2 nm thicknesses to create membranes, metamaterials, and machines with micron scale dimensions [5]. In this thickness limit, ALD films behave elastically and can be fabricated with femtojoule-scale bending stiffnesses. Further, ALD membranes are utilized to design micron-scale mechanical metamaterials and magnetically actuated three-dimensional devices. These results establish thin ALD films as a scalable basis for micron-scale actuators and robotics.**

## Summary of Research:

ALD is an ideal technique for scaling mechanical systems to micron-scale dimensions. We have developed an entire fabrication strategy around ALD, including lithography, etching, release, and integration. ALD films are grown conformally on a sacrificial layer of aluminum, as shown schematically in Figure 1. The devices consist of lithographically patterned regions of ALD membranes and thicker panels of other materials that provide rigid structure and additional functions such as mirrors or magnets. The devices are fabricated at wafer scales at yields exceeding 90%. The wafer is diced and devices are released by immersing in dilute base, followed by rinsing in water. Upon release, all experiments are carried out in aqueous environments, often with added surfactant, to avoid stiction of the free membranes.

We investigated the mechanical properties of these films by measuring the bending stiffness of over 60 magnetically actuated glass hinges. Ferromagnets with a saturated in-plane moments are patterned on panels at the ends of the hinges. The panels are deflected when we apply an out-of-plane magnetic field  $B$  (Figure 2a). Figure 2b shows the measured hinge deflection angles for ALD films of two different thicknesses, 5 and 8 nm, as a function of the magnetic field  $B$ . The hinges are deflected reversibly with no observable hysteresis. By equating the magnetic torque to the opposing mechanical torque due to the bending stiffness of the film, we deduce a linear relationship between the deflection angle and the applied field. The bending stiffness of each individual hinge can be extracted from the slope of this relationship.



Figure 1: Schematic of the fabrication and release processes.

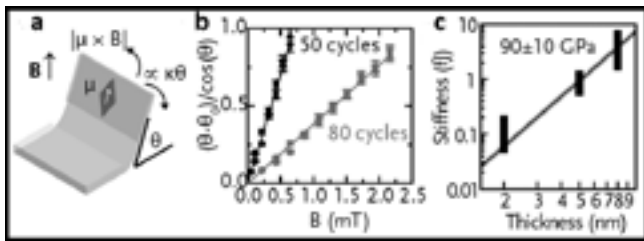


Figure 2: Mechanical characterization of ALD glass hinges.

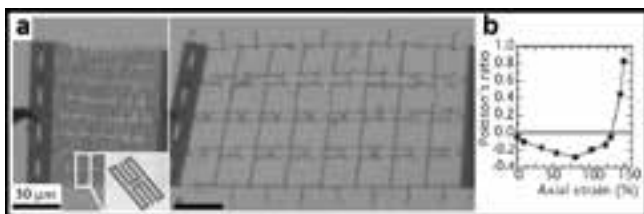


Figure 3: Auxetic mechanical metamaterial made of ALD Pt.

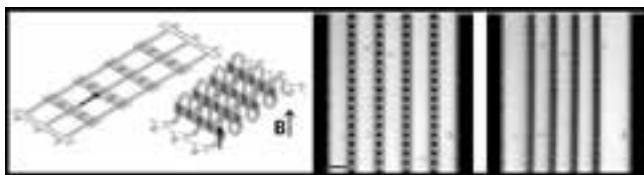


Figure 4: Magnetically actuated muscle-like device.

Scaling the thickness from 2 nm to 8 nm, we find bending stiffnesses spanning nearly two orders of magnitude in the femtojoule range (Figure 2c). We extract the Young's modulus of ALD glass from the fit in Figure 2c, finding  $Y = 90 \pm 10$  GPa. This value is comparable to values for bulk material (70-80 GPa), indicating that even at 2 nm thickness, the films behave mechanically similar to macroscopic counterparts.

We additionally use ALD membranes to fabricate mechanical metamaterials through in-plane and out-of-plane patterning. The sheet can become stretchable by cutting patterns that allow parts of the sheet to bend/buckle out of its fabrication plane. A metamaterial with

a negative Poisson's ratio, also known as an auxetic, is shown in Figure 3a. This material is patterned from 5 nm-thick sheet of ALD platinum. Under application of an axial strain, the sheet expands in the transverse direction, yielding a negative Poisson's ratio (Figure 3b).

These ultra-thin materials can also be used for micron-scale actuators and machines that function with exquisitely small forces and torques. The device shown in Figure 4 is a magnetically actuated mechanism that contracts to bear a load. The magnetic panels are attached to linear springs. Upon application of an external field, the panels rotate out of the plane and move laterally closer to each other while applying a load on the springs in a fashion analogous to a muscle.

The mechanical properties and fabrication protocols for ALD membranes and metamaterials facilitates their potential application in very sophisticated micromechanical systems. For example, the low processing temperatures and fabrication compatibility enable ALD actuators to be added to silicon-based integrated circuits for smart microsystems and machinery. In addition, the diverse materials palette offered by ALD enables bimorph actuators of dissimilar materials while still maintaining a low bending stiffness for the film stack. These actuators can be leveraged to create self-assembled and environmentally responsive three-dimensional structures and actuators. An additional benefit of ultra-thin versions of bulk materials is that the surface chemistry of many ALD films is well-studied. This enables chemical functionalization and patterning, enabling the coupling between chemical sensitivity and mechanical responsiveness. Combination of these capabilities may be used for sensors, self-assembled devices, optical devices, and microscale robotic systems.

## References:

- [1] S. A. Zirbel, B. P. Trease, M. W. Thomson, R. J. Lang, S. P. Magleby, L. H. Howell in *Micro- and Nanotechnology Sensors, Systems, and Applications VII*, Vol. 9467, International Society for Optics and Photonics, 2015, pp. 94671C-1.
- [2] D. Rus, M. T. Tolley, *Nature* 2015, 521, 467.
- [3] N. T. Eigenfeld, J. M. Gray, J. J. Brown, G. D. Skidmore, S. M. George, V. M. Bright, *Adv. Mater.* 2014, 26, 3962.
- [4] M. Z. Miskin, K. J. Dorsey, B. Bircan, Y. Han, D. A. Muller, P. L. McEuen, I. Cohen, *Proc. Natl. Acad. Sci. U.S.A.* 2018, 113, 466.
- [5] K. J. Dorsey, T. G. Pearson, E. Esposito, S. Russell, B. Bircan, Y. Han, M. Z. Miskin, D. A. Muller, I. Cohen, P. L. McEuen, *Adv. Mater.*, doi: 10.1002/adma.201901944, 2019.

# Localized Microfluidic Actuation and Mixing Using Planar Fresnel Type Gigahertz Ultrasonic Transducer

**CNF Project Number: 1121-03**

**Principal Investigator(s): Amit Lal**

**User(s): Adarsh Ravi**

*Affiliation(s): Electrical and Computer Engineering, Cornell University*

*Primary Source(s) of Research Funding: Intelligence Advanced Research Projects Activity (IARPA) - Trusted Integrated Chips (TIC) program, and National Science Foundation (NSF) - Emerging Frontiers in Research and Innovation (EFRI) program*

*Contact: amit.lal@cornell.edu, ar2256@cornell.edu*

*Website: <http://sonicmems.ece.cornell.edu/>*

*Primary CNF Tools Used: Heidelberg mask writer - DWL2000, Westbond 7400A ultrasonic wire bonder, ABM contact aligner, SU-8 Hotplates, YES Polyimide Bake Oven, Optical Microscopes, CorSolutions microfluidic probe station, Harrick plasma generator, high-temperature PDMS curing oven, low-temp PDMS vacuum oven, Tencor P7 profilometer*

## Abstract:

**We report on an AlN-based gigahertz (GHz) frequency ultrasonic transducer for microparticle actuation and microfluidic mixing. The device uses focusing transducers placed in a Fresnel lens configuration, which generates bulk acoustic waves through the silicon substrate adding in phase at the focus. The device is planar and is fabricated with a CMOS compatible process, with no thin-film release steps. Peak displacement of 250 pm was achieved at the focus with 5 V<sub>p</sub>, 1.06 GHz RF input. Owing to high absorption at gigahertz, vortices with streaming velocities > 2.6 mm/s in water were generated, and localized mixing of blue dye and water with 90% efficiency was observed.**

## Introduction:

Among the contactless microparticle manipulation mechanisms, optical and acoustic techniques are the most common. The laser based optical technique can produce a few pico-Newton of trapping force, but cannot control larger biological objects and operate in a medium of high optical opacity [1,4]. On the other hand, acoustic devices can be more easily integrated with the microfluidic channel and have been shown to handle biological particles better because of longer wavelengths and higher forces [1-3].

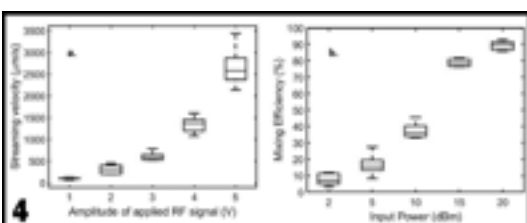
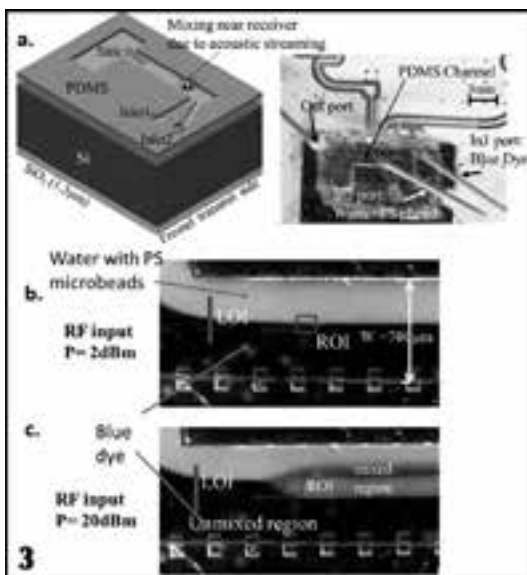
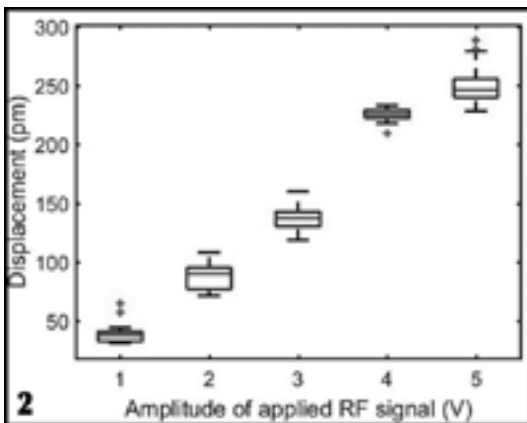
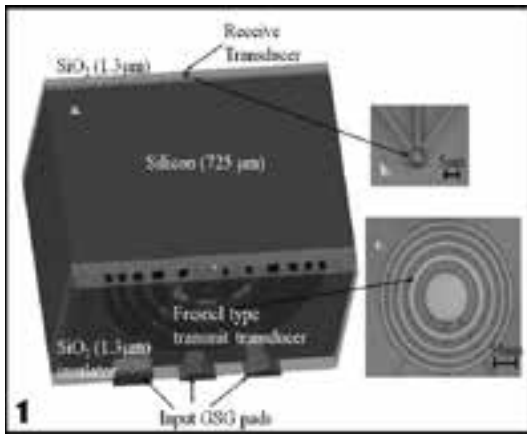
Efficient and rapid mixing of laminar fluid flows is critical for several microfluidic applications such as drug screening, chemical synthesis, genetic analysis, protein folding studies, etc. [3-5]. Traditional macroscopic fluidic mixing strategies employing long channels, mechanical or magnetic stirring elements become impractical for microscale mixing. Furthermore, as microfluidic flow lies in the laminar regime, mixing is dominated by diffusion, which is slow and prevents mixing in channel lengths compatible with microfluidic chip dimensions [2,4].

To improve the mixing time and homogeneity, various approaches have been employed. These approaches can be classified into passive and active mixing based on the absence or presence of an external energy source. Active

mixers generally outperform the passive counterparts with respect to mixing time, efficiency, and required channel length. Active microfluidic mixers employing external electrical, thermal, magnetic or acoustic energy sources have been reported [5]. However, acoustic mixers are advantageous as they perform contactless fluidic mixing without any restriction on the electrical properties of the fluids.

Acoustic mixers perturb the streamlined flow in the microfluidic channel by employing bulk acoustic wave (BAW), surface acoustic wave (SAW) or membrane transducers. For efficient mixing, strong acoustic streaming forces are required. The body force that generates streaming vortices at the edges of the acoustic fields in fluids scales as  $F_B \propto f^4$ , where  $f$  is the frequency. As a result, much interest is being showed in developing ultra-high frequency SAW and BAW based microfluidic actuators and mixers [4,5]. However, most of these actuators reported thus far require > 10 V<sub>p</sub> drive voltage and are fabricated using non-CMOS compatible materials such as ZnO, LiNbO<sub>3</sub>, LiTaO<sub>3</sub> or PZT [4].

Furthermore, in most of these devices, the fluid is placed on the same side of these transducers. This then forces considerable chip area dedicated to isolate electrical



interconnects from the fluidic sample. These factors can result in increased device area, expense of fabrication, and electronics complexity in the generation and amplification of high voltages at ultra-high frequencies.

### Summary of Research:

The acoustofluidic micro-mixer and actuator presented here uses gigahertz focused ultrasonic beam to create localized streaming vortices in the microchannel. The device is fabricated without any thin-film release steps, using CMOS compatible materials like aluminum nitride solidly mounted to silicon substrate. Further, the placement of the transducers on the opposite side of fluidics enable easier integration of distributed CMOS electronics with AlN transducers on one side, and the fluidic system on the opposite side. The cross-sectional sketch of the simplified GHz transducer stack with planar FZP shaped AlN transducer on the transmit side and a small circular AlN transducer on the receive side is shown in Figure 1. AlN in the regions without transduction are not shown here for simplicity. Figure 2 shows the peak displacements at the point of focus for different RF drive voltages.

A PDMS microfluidic channel with two inlet ports and an outlet port was fabricated using standard soft lithography process. The molds for the PDMS channel were made using 325 μm thick SU-8-100 photoresist spun onto a clean silicon wafer. The photo resist was patterned using UV contact lithography to make a 700 μm wide channel. PDMS resulting by mixing Sylgard-184 elastomer base and curing agent in the mass ratio 10:1 was poured onto the silicon wafer with SU-8 master. The cured PDMS stamp was then peeled off from the silicon wafer to make a microfluidic channel. The surfaces of the PDMS channel and the AlN-Si transducer stack were modified using a room temperature plasma cleaner before bonding. The image of the PDMS channel bonded onto the AlN-Si transducer substrate is shown in Figure 3. Figure 4 shows the results from the mixing activity and the streaming velocities for different drive voltages.

### References:

- [1] C. Lee, et al., "Single microparticle manipulation by an ultrasound beam," IEEE International Ultrasonics Symposium, 849-852, 2010.
- [2] B. W. Drinkwater, "Dynamic-field devices for the ultrasonic manipulation of microparticles," Lab Chip, 16, 2360, 2016.
- [3] A. Sarvazyan, et al., "Stirring and mixing of liquids using acoustic radiation force," The Journal of the Acoustic Society of America 125, 3548, 2009.
- [4] A. Ravi, et al., "CMOS compatible GHz ultrasonic Fresnel microfluidic actuator," Technical Digest of the 2018 Solid-State Sensor and Actuator Workshop, Hilton Head Isl, SC, 2018.
- [5] A. Ravi, et al., "Localized Microfluidic mixer using planar Fresnel type GHz ultrasonic transducer," IEEE International Ultrasonic Symposium, Japan, 2018.

**Figure 1:** Cross sectional schematic of the AIN-Si stack (a) and images of the Fresnel lens transmit (c) and circular receive (b) transducers post fabrication. **Figure 2:** Plot of surface displacement at the point of focus against different applied voltages. **Figure 3:** a. image of the GHz acoustofluidic micro-mixer after bonding. Image captures showing: negligible mixing activity near the receive transducer when RF input power is 2 dBm (a) and localized mixing when RF input power is 20 dBm (c) (LOI - Line of interest; ROI - region of interest for mixing efficiency calculation). **Figure 4:** a. Box plot of streaming velocity versus applied voltage. b. Box plot of mixing efficiency vs. applied RF input.

# N-Z Power NEMS Electrostatic RF Wakeup Receiver with Pt Contact

**CNF Project Number: 1262-04**

**Principal Investigator(s): Amit Lal**

**User(s): Alexander Ruyack**

*Affiliation(s): Electrical and Computer Engineering, Cornell University*

*Primary Source(s) of Research Funding: Defense Advanced Research Projects Agency (DARPA) project:  
Near Zero Power RF and Sensor Operations (N-ZERO)*

*Contact: amit.lal@cornell.edu, arr68@cornell.edu*

*Primary CNF Tools Used: ASML 300C DUV stepper, Heidelberg mask writer DWL2000, Gamma automatic coat-develop tool, Zeiss Ultra SEM, Zeiss Supra SEM, Oxford 81, 82 etchers, Oxford 100 etcher, AJA ion mill, Hamatech hot piranha, Primaxx Vapor HF etcher, Plasma-Therm deep Si etcher, Uniaxis 770 deep Si etcher, DISCO dicing saw, wire bonder, Aura 100, Zygo, furnaces, ResMap, Nanostrip Bath*

## Abstract:

**This work reports a nanoelectromechanical systems (NEMS) electrostatic RF switch usable as a near-zero power wake-up receiver capable of detection sensitivity reaching -25 dBm off resonance with sub-pW passive power consumption at less than 1.5V DC operation. The switch utilizes a multielectrode design allowing for a mechanical contact gap to be held just outside thermal oscillations and the radio frequency (RF) input to physically close the switch. This allows for operation away from pull-in and improves RF sensitivity. A focused ion beam (FIB) patterned platinum-platinum contact point enables the low DC bias requirement and improves contact resistance and longevity. The potential for on-resonance operation provides a pathway forward for improved RF sensitivity in the future.**

## Introduction:

With the advent of RF connectivity between sensors and the subsequent proliferation of wireless sensor nodes, power consumption and battery management of distributed sensor networks has become a bottleneck for widespread implementation. With applications spanning smart cities, agricultural monitoring and military scenarios, replacing batteries for increasing size sensor arrays is becoming costly, time consuming with significant downtimes, and potentially dangerous for reaching sensors in remote locations. Beyond advancements in battery technology and power reduction of active components, asleep-yet-aware sensors provide a means for reducing power consumption and significantly extending sensor node lifetime. These sensors work by operating in a low power, or near zero power, mode (typically comparable to battery leakage) but remain triggerable by signals of interest, turning on higher power electronics (like communications or signal processing) only when this signal is perceived and only for the duration required. For sensing applications in which signals of interest are infrequent, this modality can improve sensor operational lifetime by orders of magnitude.

These schemes have been implemented in a wide variety of physical sensors including accelerometers, microphones and magnetic field sensors, among others [1,2]. Near-zero power RF wake-up sensors have been widely developed using CMOS, but state of the art has

struggled to push powers lower than single digit nW at -60 to -70 dBm RF sensitivity [3,4]. MEMS based RF wake-up sensors are much less have the distinct advantage of extremely low power draw but are much less common due to complications in design and fabrication limiting their sensitivity [5,6].

In order to maintain this lower power but improve RF sensitivity, we have improved upon a near-KT lateral NEMS switch that showed 300  $\mu$ V switching at 50V DC bias [7]. This is accomplished by utilizing a multielectrode design to enable device switching without pull-in. Additional fabrication changes including, but not limited to, a compliant contact and FIB post-processing device contact areas, have also been implemented to reduce the DC bias requirement and improve device longevity.

## Summary of Research:

The switch is operated primarily by a set of DC bias electrodes and a single RF electrode, all of which electrostatically actuate a released shuttle and move it towards a contact electrode biased with a small voltage. The switch also contains a reset electrode that applies an electrostatic force in the opposite direction to the DC and RF electrodes, ensuring a means of un-sticking the switch if necessary. Figure 1 shows the general layout and the relevant switch components.

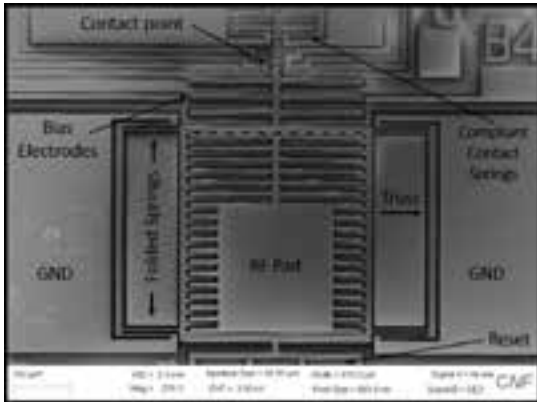


Figure 1: SEM micrograph of NEMS switch from above showing important electrical contacts and features.

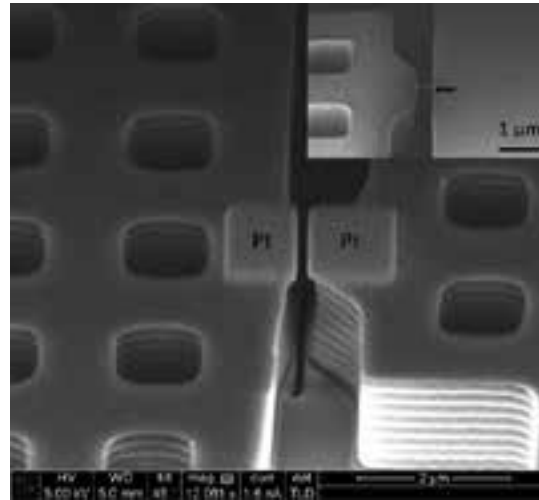


Figure 2: SEM micrograph of switch contact after Pt deposition using FIB.

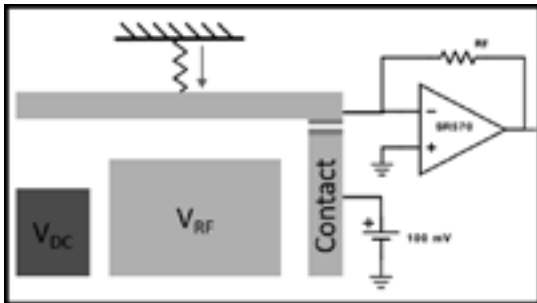


Figure 3: Simplified schematic of switch components showing biasing electrodes and TIA for detection.

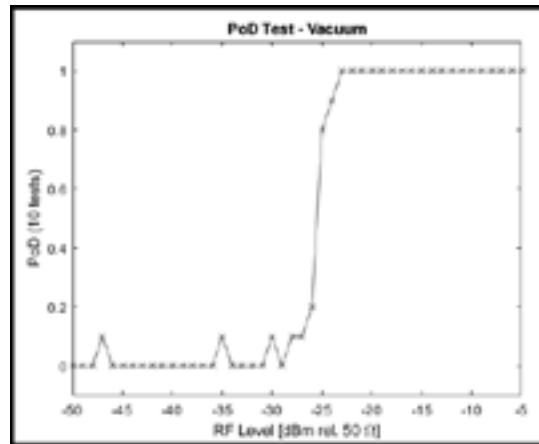


Figure 4: Probability of detection test showing 100% detection (out of 10 tests) for RF amplitudes of -25 dBm and greater.

Device fabrication follows a typical one mask SOI micromachining process with a vapor HF release. A full description of the device fabrication is available in last year's CNF technical report or [8]. Figure 2 shows an SEM image of the device contact area modified with Pt from a FIB process.

For operation, the switch is first pre-biased using the DC electrodes to bring the shuttle nearly into contact. The device is designed such that pull-in is not reached during this step. After pre-biasing, the RF wake-up signal is then applied to the RF electrode, which closes the switch the rest of the way. A TIA is used to read out a voltage when the switch closes. Figure 3 depicts a simplified schematic of the switch after DC pre-biasing and awaiting an RF input.

Testing is accomplished with a custom vacuum probe station with Python code managing a control loop running a MAXIM 5318 18-bit DAC, SR570 TIA and R&S SMC100A RF source. RF Probability of Detection (PoD) and False Alarm testing is accomplished using this automated code, described in [9]. Figure 4 shows a successful PoD test with -25 dBm sensitivity. Typical power consumption is 0.2 pW with a DC bias requirement of less than 1.5V. Ongoing work aims to operate the switch on resonance by modulating the RF signal at the device resonance.

## References:

- [1] V. Pinrod, et al., "PZT lateral bimorph-based sensor cuboid for near zero power sensor nodes," IEEE Sensors, 2017.
- [2] S. Gupta, et al., "Vibration powered RF-transponder for sensing low frequency motion events," PowerMEMS, 2016.
- [3] S. Bdiri, et al., "An 868 MHz 7.5  $\mu$ W wake-up receiver with 0.60 dBm sensitivity," J. Sens. Sens. Syst., vol. 5, pp. 433-46, 2016.
- [4] P. Wang, et al., "A near-zero-power wake-up receiver achieving 0.69-dBm Sensitivity," IEEE Solid-State Circuits, vol. 53, no. 6, pp. 1640-52, 2018.
- [5] T. Wu, et al., "Design and Fabrication of AlN RF MEMS Switch for Near-Zero Power RF Wake-Up Receivers," IEEE Sensors, 2017.
- [6] W. Vitale, et al., "RF MEMS power sensors for ultra-low power wake-up circuit applications," IEEE ESSDERC, 2013.
- [7] K. Amponsah, et al., "Near-kT switching-energy lateral NEMS switch," IEEE NEMS, 2010.
- [8] A. Ruyack, et al., "NEMS Electrostatic RF Wakeup Switch with Pt FIB Contact," PowerMEMS, 2018.
- [9] A. Ruyack, et al., "NEMS Electrostatic Resonant Near-Zero Power Resistive Contact RF Wake-up Switch with Pt FIB Contact," IEEE MEMS, 2019.

# Boiling Heat Transfer Enhancement by Coupling Nanoscale Evaporation in Buried Nanochannels

**CNF Project Number: 2123-12**

**Principal Investigator(s): Shalabh C. Maroo**

**User(s): An Zou, Sidharth P. Raut, Manish Gupta**

*Affiliation(s): Department of Mechanical and Aerospace Engineering, Syracuse University, Syracuse, NY 13244*

*Primary Source(s) of Research Funding: National Science Foundation Career Award NO. 1454450*

*Contact: scmaroo@syr.edu, azou@syr.edu, spraut@syr.edu, magupta@syr.edu*

*Website: <http://maroo.syr.edu>*

*Primary CNF Tools Used: Heidelberg mask writer DWL 2000, manual photoresist spinner, GAC auto stepper, YES image reversal oven, ABM contact aligner, SÜSS MA6-BA6 contact aligner, e-beam evaporator, Oxford PECVD, GSI PECVD, Glen 1000 Plasma, Anatech resist strip, Oxford 81/82 etcher, optical microscope, scanning electron microscope, atomic force microscope*

## Abstract:

We explicitly coupled pool boiling with nanoscale evaporation by using buried nanochannels to enhance boiling critical heat flux (CHF) by ~105%. This enhancement is attributed to the formation of extra menisci and contact line in nanochannels. The work reported here is part of a journal article which is currently under review.

## Summary of Research:

Boiling and evaporation are two distinct forms of liquid-to-vapor phase change, which is an efficient mechanism to move heat from a solid surface. Boiling has been used in a multitude of residential and industrial applications such as refrigerators, heat exchangers, boilers, etc. However, pool boiling is limited by occurrence of critical heat flux (CHF), the maximum stable heat flux a system can be operated at. Heat flux higher than CHF can irreversibly damage the surface due to a sudden and dramatic temperature increase. CHF occurs when liquid fails to quickly rewet the surface creating dry regions for extended periods of time, with typical values of  $\sim 80 \text{ W/cm}^2$  for water on silicon dioxide ( $\text{SiO}_2$ ) surface. On the other hand, nanoscale evaporation has recently [1] been shown the capability to remove transient heat flux  $\sim 8000 \text{ W/cm}^2$  for the same water-silicon dioxide combination over a very short time span in a single 2D nanochannel.

In this work, we combine these two techniques of pool boiling and nanoscale evaporation to increase CHF of pool boiling. The coupling is attained by creating buried 1D nanochannels underneath the surface where wicking in the channels maintains the surface wet, and creates additional evaporating menisci. Thus, nanoscale evaporation occurs in channels and pores, while boiling happens on the surface above.

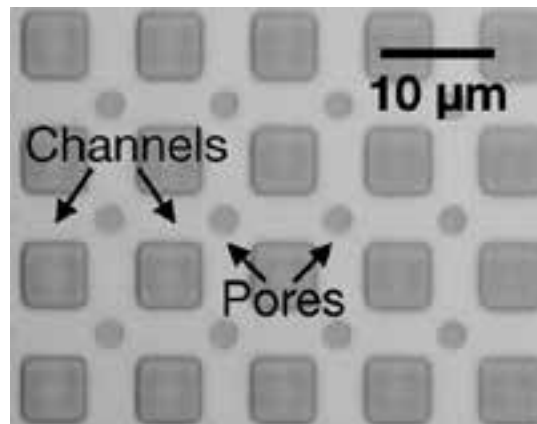


Figure 1: Optical microscope image of the sample with buried nanochannels.

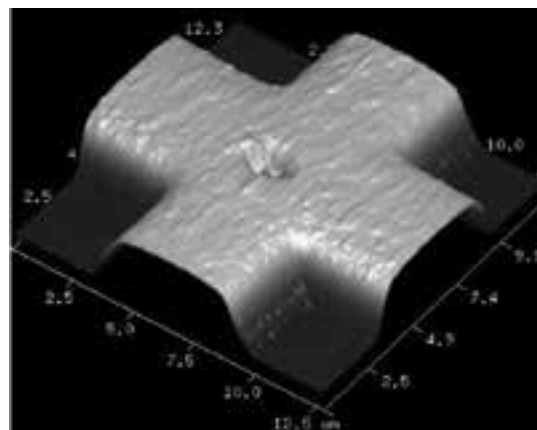


Figure 2: Atomic force microscope (AFM) image of the profile of channels and pores.

The buried cross-connected nanochannels were fabricated on a Si substrate by etching patterned sacrificial metal layers buried under a 300 nm thick SiO<sub>2</sub> film from plasma enhanced chemical vapor deposition (PECVD). The channel geometry was determined by the pattern of sacrificial layers, which was attained by a lift-off process. The cross-connected channels, made from two sets of channels perpendicular to each other, allow for ease of liquid exchange inside the channels. Further, at each intersect of the channels, a 2- $\mu$ m pore was fabricated allowing liquid present above the surface to flow into the channels. Figure 1 shows an image of these nanochannels (width: 5  $\mu$ m, spacing: 5  $\mu$ m, height: 728 nm) from optical microscope. Due to the conformal deposition of PECVD SiO<sub>2</sub>, trenches of depth same as channel height formed on the top surface between adjacent channels, Figure 2 shows an atomic force microscope (AFM) image of the surface.

The pool boiling experiments were conducted at atmospheric pressure under saturated conditions using deionized (DI) water. The experiment setup consists of a polycarbonate water bath and a thermal insulated copper block. Five cartridge heaters are embedded in the copper block allowing for a maximum power input of 1250 W (heat flux of 1250 W/cm<sup>2</sup>). The heat input to the copper block is controlled with a variable alternating current (AC) to AC transformer. Four equally spaced K-type thermocouples are inserted into the center axis of the copper block to measure the temperature gradient. In water bath, four immersion heaters and a resistance temperature detector (RTD) is used to maintain bulk water at its saturated temperature. In experiments, the sample with buried nanochannels was bonded on the top of the copper block using solder paste to ensure good attachment with minimal thermal contact resistance.

The sample was immersed in a pool of DI water, which was degassed by boiling it for 30 minutes and maintain its temperature at 97-100°C for another 30 minutes. Boiling on sample was achieved by increasing the output voltage

of the variable transformer. To obtain the boiling curve, the output of the variable transformer was increased in small increments. The temperature readings were recorded after reaching steady state, which is determined by the criterion that the temperature changes from all thermocouples were less than 0.5°C over one minute. The steady state was reached usually in 10-15 minutes after changing the output power. CHF was obtained when an incremental increase of power supplied resulted in dramatic increase of surface temperature, and its value was taken as the last stable heat flux recorded during experiments. The heat flux was obtained from measured temperature gradient using Fourier's law; while the surface temperature was obtained from the reading from the thermocouple closest to the top surface, also using Fourier's law. ~ 105% CHF enhancement was obtained with an absolute value of  $177.40 \pm 2.43$  W/cm<sup>2</sup>.

This enhancement is attributed to nanoscale evaporation from additional menisci inside the nanochannels formed by passive wicking of liquid. This CHF value is in good agreement (within 5% error) to the CHF model, which predicts CHF enhancement when surface force gets augmented due to elongated and/or additional contact line.

In summary, we achieved ~ 105% pool boiling CHF enhancement by explicitly coupling boiling with nanoscale evaporation using nanochannels. This enhancement is mainly contributed by the additional menisci and contact line created by the wicking flow in the nanochannels. The obtained boiling enhancement can be increased by optimizing the nanochannel geometry as well as potentially using 2D nanochannels.

#### References:

- [1] Y. Li, M.A. Alibakhshi, Y. Zhao, and C. Duan, "Exploring ultimate water capillary evaporation in nanoscale conduits," *Nano Letters*, vol. 17, pp. 4813-4819, 2017.

# Fabrication of AlN HBAR Devices for Spin Manipulation of Diamond NV Centers

**CNF Project Number: 2126-12**

**Principal Investigator(s): Gregory Fuchs<sup>1</sup>**

**User(s): Johnathan Kuan<sup>2</sup>, Huiyao Chen<sup>3</sup>**

*Affiliation(s): 1. Applied and Engineering Physics, 2. Department of Physics, 3. Department of Physics; Cornell University  
Primary Source(s) of Research Funding: DARPA-Driven and Nonequilibrium Quantum Systems (DRINQs)*

*Contact: gdf9@cornell.edu, jk2788@cornell.edu, hc846@cornell.edu*

*Website: <http://fuchs.research.engineering.cornell.edu>*

*Primary CNF Tools Used: AJA sputter, OEM Endeavor M1, GCA 5X stepper, Westbond 7400A ultrasonic wire bonder*

## Abstract:

Previous work with nitrogen-vacancy (NV) centers in diamond have demonstrated coupling between the NV spins and strain. Harmonic strain can be introduced into diamond lattice with transducers such as high-overtone bulk acoustic resonators (HBAR), which introduce a stress wave into the diamond. This strain can be used to coherently control the NV center spins. We describe our current work in fabricating HBAR devices using aluminum nitride (AlN) as the piezoelectric and characterize the performance of our device, which uses a 2  $\mu\text{m}$  film of AlN. With our AlN HBAR device, we find resonance modes from 300 MHz to 3.5 GHz with quality factors ranging from 800 to 1700.

## Summary of Research:

The diamond NV-center consists of vacancy in the diamond lattice that is adjacent to a substitutional nitrogen. The goal of our research is the manipulation of the spin states of NV center through strain. Strain is introduced into the diamond lattice with piezoelectric transducers, such as high-overtone bulk acoustic resonators (HBAR). Examples of previous work with HBAR devices and diamond include coupling of the NV center spins with strain [1], coherent control over magnetically forbidden transitions of NV centers [2], continuous dynamical decoupling [3], and cooling of a mechanical resonator with a high-density NV ensemble [4].

In our current work at CNF, we are working on process development of HBARs that use AlN as the piezoelectric film with the aim of applying these resonators for control of NV spins for quantum metrology applications such as angle sensing [5]. Previously, we would have to have to AlN film deposited externally from CNF, but with the recent addition of the OEM Endeavor M1 tool, we are able to do the entire fabrication in-house.

We fabricate these HBAR devices using AlN as the piezoelectric layer through the following process. The substrate that we work with is a 3 mm by 3 mm diamond piece. On top of the substrate, we sputter a layer of Ti/Pt (103 nm total thickness) to act as the bottom electrode of the device using the AJA sputter deposition tool at

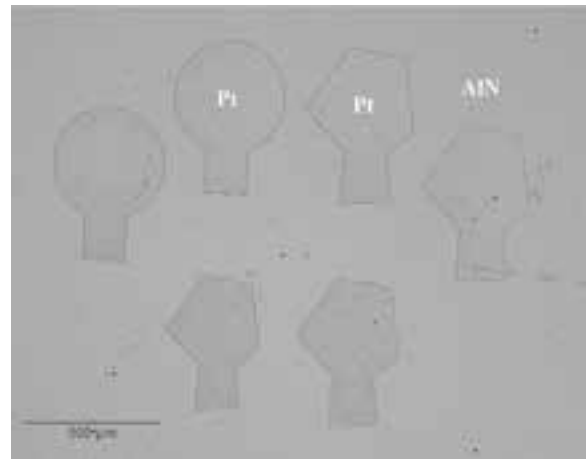


Figure 1: Final HBAR devices on the optical-grade diamond substrate. The devices are approximately 500  $\mu\text{m}$  large. The top electrode, which defines the HBAR, consists of a Ti/Pt film and made through lift-off. These electrodes sit on the AlN layer which is 2  $\mu\text{m}$  thick.

CNF. Following this, we sputter the piezoelectric layer of AlN (2  $\mu\text{m}$ ) using the OEM Endeavor M1 tool. To finish the fabrication, we define the shape of the top electrode through photolithography with the 5X stepper and sputter a Ti/Pt film (10nm/180nm) again with the AJA sputter deposition. The excess metal film on the top layer is

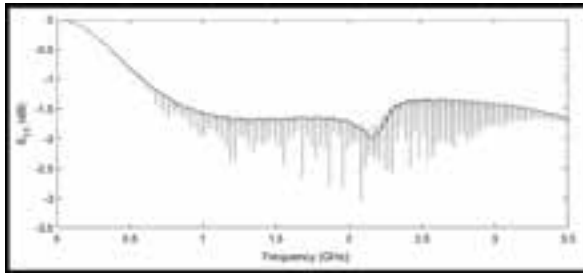


Figure 2:  $S_{11}$  measurement of the AlN HBAR device fabricated on optical-grade diamond. HBAR resonances modes are present in the  $S_{11}$  measurement in a frequency range of approximately 500 MHz to 3.5 GHz.

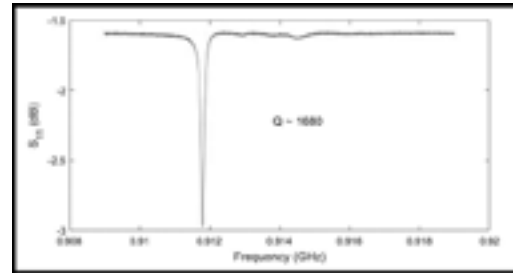


Figure 3: VNA Measurement single resonance mode of AlN HBAR device fabricated on optical-grade diamond. The quality factor that is extracted from fitting to Q-circle model is approximately 1680.

removed through lift-off, leaving behind the top electrode on the piezoelectric layer. In Figure 1, we see the final HBAR devices that are fabricated on diamond. These devices are approximately 500  $\mu\text{m}$  large.

We tested the electromechanical response of our HBAR device with a vector network analyzer. The devices presented here are fabricated on optical-grade diamond, with a thickness of 287  $\mu\text{m}$  and a variation of approximately 1  $\mu\text{m}$  across 3 mm. Minimizing the thickness variation of the substrate is important for these devices as the top and bottom surfaces of the substrate act as planar mirrors for the stress wave injected into the substrate by the HBAR. The planar surfaces allow for an acoustic standing wave in the substrate. Having a large thickness variation is detrimental to the quality factor of our resonator. Using the vector network analyzer, we looked at the  $S_{11}$  response of our HBAR device. When the HBAR is resonant with the applied power, less power is reflected, which is seen as a dip in the  $S_{11}$  measurement. As seen in Figure 2, from the  $S_{11}$  measurement, we find that the resonance modes of our device span from 500 MHz to 3.5 GHz, with quality factors in the range of 800 to 1700. In Figure 3, we see a resonance mode with a quality factor of 1680 which was extracted using the Q-circle method [6].

Further work in being done to improve the performance and the consistency of these devices and to optimize the

fabrication process. For example, the quality of the AlN piezoelectric layer limits the quality of the device. In our current process, we use a TMAH developer to define the top electrode area. However, TMAH etches the surface of the AlN film, increasing the surface roughness of the film, which lowers the performance of the device.

#### References:

- [1] E. R. MacQuarrie, T. A. Gosavi, N. R. Jungwirth, S. A. Bhawe, and G. D. Fuchs, Mechanical spin control of nitrogen-vacancy centers in diamond, *Phys. Rev. Lett.* 111, 227602 (2013).
- [2] E. R. MacQuarrie, T. A. Gosavi, A. M. Moehle, N. R. Jungwirth, S. A. Bhawe, and G. D. Fuchs, Coherent control of a nitrogen-vacancy center spin ensemble with a diamond mechanical resonator, *Optica* 2, 233 (2015).
- [3] E. R. MacQuarrie, T. A. Gosavi, S. A. Bhawe, and G. D. Fuchs, Continuous dynamical decoupling of a single diamond nitrogen-vacancy center spin with a mechanical resonator, *Phys. Rev. B* 92, 224419 (2015).
- [4] E.R. MacQuarrie, M. Otten, S.K. Gray, and G.D. Fuchs, Cooling a mechanical resonator with nitrogen-vacancy centres using a room temperature excited state spin-strain interaction *Nature Communications* 8, 14358 (2017).
- [5] Ashok Ajoy and Paola Cappellaro. Stable three-axis nuclear gyroscope in diamond, *Phys. Rev. A* 86, 062104 (2012).
- [6] D. A. Feld, R. Parker, R. Ruby, P. Bradley, and S. Dong, in *IEEE International Ultrasonics Symposium (IUS)*, Beijing, 2008 (IEEE, Piscataway, NJ, 2008), p. 431.

# NanoThermoMechanical Logic Thermal Gates

**CNF Project Number: 2357-15**

**Principal Investigator(s): Sidy Ndao**

**User(s): Ahmed Hamed**

*Affiliation(s): Mechanical and Materials Engineering, University of Nebraska-Lincoln*

*Primary Source(s) of Research Funding: This work was supported by the National Science Foundation (NSF) through the Nebraska Materials Research Science and Engineering Center (MRSEC) (grant No. DMR-1420645). This work was performed in part at the Cornell NanoScale Science & Technology Facility (CNF), a member of the National Nanotechnology Coordinated Infrastructure (NNCI), which is supported by the National Science Foundation (Grant NNCI-1542081)*

*Contact: sndao2@unl.edu, a.hamed@huskers.unl.edu*

*Primary CNF Tools Used: Heidelberg mask writer DWL2000, ASML 300C DUV, e-beam SC4500 odd evaporator, Oxford PECVD, Oxford 81 etcher, Unaxis 770 etcher, Tencor P7 profilometer*

## Abstract:

Today's electronics cannot perform in harsh environments (e.g., elevated temperature and ionizing radiation environments) found in many engineering applications. Thermal computing, data processing based on heat instead of electricity, is proposed as a practical solution and opens a new scientific area at the interface between thermal and computational sciences. We designed and modeled thermal AND, OR and NOT logic gates, achieved through the coupling between near-field thermal radiation (NFTR) and MEMS thermal actuation [1]. In the process, we also developed two novel non-linear thermal expansion designs of microstructured chevron beams. Using in-cleanroom standard microfabrication techniques in CNF, we successfully fabricated the designed thermal AND and OR gates.

## Summary of Research:

Due to the success and feasibility shown by modeling the designed thermal gates, we were interested in fabricating and characterizing the proposed micro-structured thermal logic gates. In general, the microdevices that intended to be fabricated consist of chevron beams hold suspended plates, all are thermally actuated by platinum microheaters above the silicon microstructures. So, we designed three photolithography masks: platinum microheaters, silicon front side microstructures, and silicon backside etching. The microdevices are fabricated using in-cleanroom standard microfabrication techniques in CNF starting with a four-inch-diameter <100> silicon-over-insulator (SOI) wafer. The SOI wafer consists of a 400  $\mu\text{m}$  thick handle silicon substrate, a 1  $\mu\text{m}$  thick buried silicon dioxide layer, and a 20  $\mu\text{m}$  thick boron-doped silicon device layer.

Figure 1 shows the steps followed through the microfabrication process flow adopted for the thermal gates' fabrication. Following a cleaning step of the wafers, a 0.5  $\mu\text{m}$  thick silicon dioxide film (acts as an electrical insulator) is thermally grown by wet oxidation in a furnace at 1100°C (Figure 1b) on both sides of the wafer. On the substrate's backside, an additional 3  $\mu\text{m}$  thick film of silicon dioxide is deposited via plasma enhanced

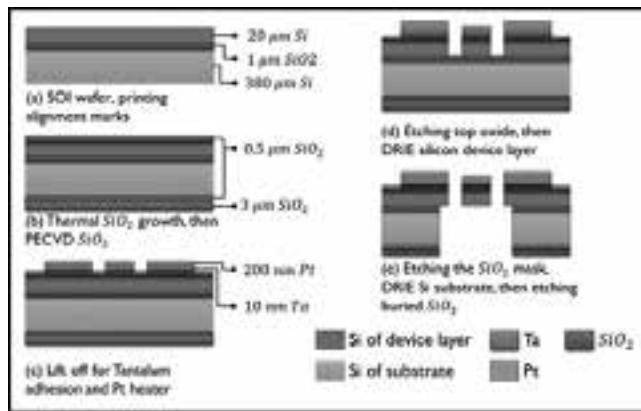


Figure 1: Fabrication steps of the two novel thermal expansion mechanisms (the reducing and the amplification mechanisms).

chemical vapor deposition (tool: Oxford PECVD) to serve as an etching mask in subsequent backside etch steps. The microheaters (200 nm thick platinum and 10 nm thick tantalum as adhesion layer) are formed on top of the device layer using lift-off and e-beam evaporation (tool: SC4500 odd evaporator) as shown in Figure 1c. Following the formation of the microheaters, the suspended structures of the NanoThermoMechanical



# Making a Microfluidic Device to Mimic Flow Through Porous Medium

**CNF Project Number: 2385-15**

**Principal Investigator(s): Brian J. Kirby**

**User(s): Katherine Polhemus**

*Affiliation(s): Mechanical and Aerospace Engineering, Cornell University*

*Primary Source(s) of Research Funding: IGERT Program for Earth Energy*

*Contact: kirby@cornell.edu, kcp44@cornell.edu*

*Primary CNF Tools Used: Photolithography tools, hot press, deep reactive ion etcher, CorSolutions*

## **Abstract:**

With the rapid depletion of known oil reserves, detecting properties of the oil reservoirs and optimizing oil extraction is critical. By measuring the aqueous properties of the reservoirs, decisions can be made on which reservoirs to drill and the available quantity of oil to extract, with minimal environmental impact. Utilizing hairy nanoparticles in testing can provide a variety of information about the reservoir. The objective of the proposed work is to characterize the behavior of hairy nanoparticles at the oil-water interface in order to optimize their use as subsurface sensors. In order to complete the optimization, a microfluidic model for the environment needs to be developed. This past year's work involves making microfluidic devices to mimic water flowing through the subsurface and oil trapped in pores. The design and mold to make the mold was developed in the CNF first using photolithography to create a mold with negative photoresist which was used to make microfluidic channels out of polydimethylsiloxane and later using positive photoresist and etching to create a mold to make microfluidic channels out of polypropylene.

## **Summary of Research:**

This work in the CNF has consisted of using micro-fabrication techniques to make a microfluidic device. Using the cad software L-Edit, we make patterns to transfer to a mask using the Heidelberg mask writer. In the past year, we have made two types of masks: one for positive photoresist and the other for negative photoresist.

The first set of microfluidic devices made used the negative photoresist (SU-8) to make a mold. The process of making a mold with photoresist (photolithography) consist of the steps: 1) pour and spin photoresist onto a wafer (using CNF spinner), 2) bake photoresist (using CNF hot plates), 3) wait time, 4) expose photoresist (using ABM contact aligner), 5) second wait time, and 6) development of photoresist. At the end of the process, we have a mold out of SU-8 on top of a wafer. In our research group's lab, we made microfluidic devices by pouring PDMS on top of the mold and baking then attaching the molded PDMS to a glass slide through plasma cleaning.

Unfortunately for this application, we need the PDMS to be very hydrophobic and PDMS was not hydrophobic

enough for our experiments. Therefore, we switched to making devices out of a polypropylene — a much more hydrophobic material. To make molded polypropylene pieces we used hot embossing, which is done on the CNF hot press. Because of the large pressure applied during embossing, we needed a stronger mold than SU-8, so we switched to making molds out of silicon. To make a mold out of silicon, a positive photoresist is spun instead of negative and after the photolithography process, the wafer is etched on the Deep Reactive Ion etcher in the CNF. The mold is used in the CNF Hot Press to hot emboss the pattern onto polypropylene. Another piece of polypropylene is pressed to a thinner thickness using the hot press. Finally, the device is bonded together using the hot press.

We also used the CorSolutions as a connection method for tubes to the device, which allows us to flow oil and particles into the device.

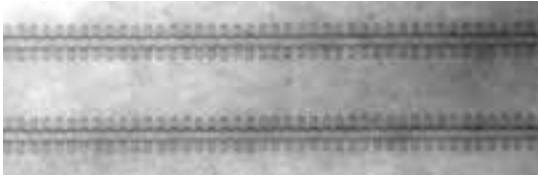


*Figure 1: Oil-water contact line in polypropylene device.*



*Figure 2: Device on CorSolution station.*

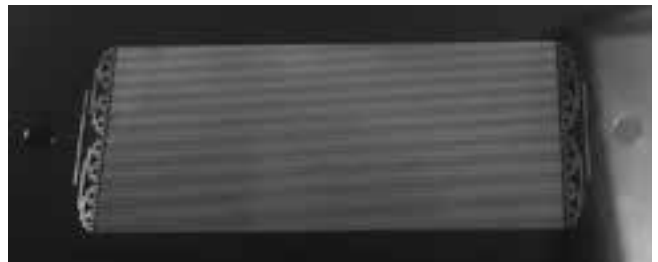


*Figure 3: Etched silicon mold for hot pressing.*

# Atomically Thin Metamaterial Robots, Origami, and Artificial Flagella

**CNF Project Number: 2416-16**

**Principal Investigator(s): Itai Cohen, Paul L. McEuen**

**User(s): Qingkun Liu, Baris Bircan, Wei Wang, Tianyu Ma**

*Affiliation(s): Kavli Institute at Cornell for Nanoscale Science, School of Applied and Engineering Physics, Laboratory of Atomic and Solid-State Physics, Department of Physics; Cornell University*

*Primary Source(s) of Research Funding: National Science Foundation, Contract: DMR-1719875; DMR-1435829 Army Research Office, Contract: W911NF-18-1-0032*

*Contact: itai.cohen@cornell.edu, plm23@cornell.edu, ql59@cornell.edu, bb625@cornell.edu, ww459@cornell.edu, tm478@cornell.edu*

*Primary CNF Tools Used: Oxford ALD FlexAL, Arradiance ALD Gemstar-6, Oxford 81 etcher, Oxford 100 etcher, ABM contact aligner, SC 4500 odd-hour, AJA sputter, AJA ion mill, Oxford Cobra ICP etcher, Heidelberg DWL2000*

## Abstract:

The ability to actuate an object at the microscale is an important technological aspect of manufacturing micro-robots and micro-machines. Here we demonstrate that micro-actuators made by atomically thin layers of metals and dielectrics could bend in response to electrical or chemical signals. These actuators could be designed into bidirectional bending modes, enabling chemically responsive micro-scale complex origami structures. By harnessing the electrical controllability and bidirectional folding structures, a mechanical metamaterial microrobot has been fabricated, allowing remotely controllable robotic sheets with large degree of freedom of motion.

## Summary of Research:

Using commercial semiconductor processing techniques, our team has developed methods to deposit and pattern atomically thin films that can bend in response to chemical and electrical stimuli. This approach makes it possible to create complex structures, machines, and microrobots by using origami design principles at the microscale.

Our team first demonstrated an electrically responsive micro cantilever with an ultra small bending radii of

1-2  $\mu\text{m}$ . The microcantilever has a bimorph structure comprising of 5 nm platinum (Pt) and 2 nm silica ( $\text{SiO}_2$ ), both of which are deposited by atomic layer deposition (ALD). The exposed platinum surface expands at a low voltage of -0.2V in a buffer solution due to the hydronium ( $\text{H}_3\text{O}^+$ ) adsorption on the platinum surface, bending the bimorph structure toward the silica layer. Based on this actuation mode of platinum/ $\text{SiO}_2$  bimorph, we fabricated artificial flagella that could swing and drive the small particles to move in a buffer solution, as shown in Fig. 1.

Our team has also demonstrated a technique to create micron scale folds using ultra-thin bending actuators composed of 2 nm of ALD grown  $\text{SiO}_2$  and a sheet of monolayer graphene. These actuators are driven by ion exchange reactions, where larger  $\text{H}_3\text{O}^+$  ions take the place of smaller  $\text{Na}^+$  ions in the  $\text{SiO}_2$  layer, causing swelling and creating a strain mismatch that produces unidirectional bending action.

Photolithographically defining fold patterns and localizing the bending using 1  $\mu\text{m}$  thick panels of rigid SU-8 polymer enables the fabrication of elementary folded structures like cubes and tetrahedra [1].

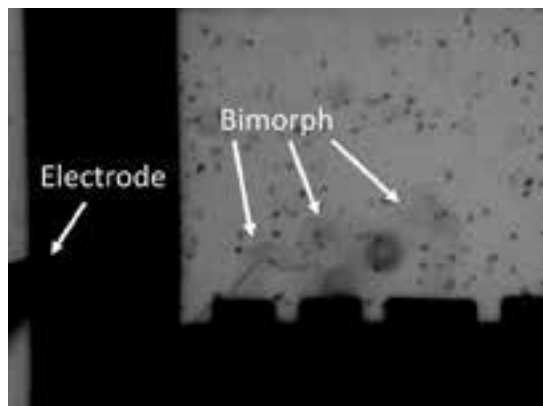


Figure 1: Electrically driven artificial flagella made by atomically thin Pt/ $\text{SiO}_2$  bimorph structure swing in the buffer solution.

Since origami design principles can be used to map any arbitrary shape to a crease pattern with fold angles ranging from  $-180^\circ$  to  $+180^\circ$ , bidirectional bending action is needed to create a complete platform for origami-based self-assembly at the microscale. The basic idea is that if one type of bimorph stack bends upwards, the order of the stack can be inverted to produce downward bending. To achieve this, our group has developed a method for growing and stitching together all ALD grown  $\text{Si}_3\text{N}_4$ - $\text{SiO}_2$  bimorph stacks. Replacing graphene with ALD  $\text{Si}_3\text{N}_4$  not only makes the fabrication more easily scalable, but also eliminates the need for any additional functionalization step that would be required to perform ALD on graphene. This strategy makes it possible to design and fabricate origami devices of variable complexity that can sense changes in pH and change configurations from flat to folded according to prescribed mountain-valley folds.

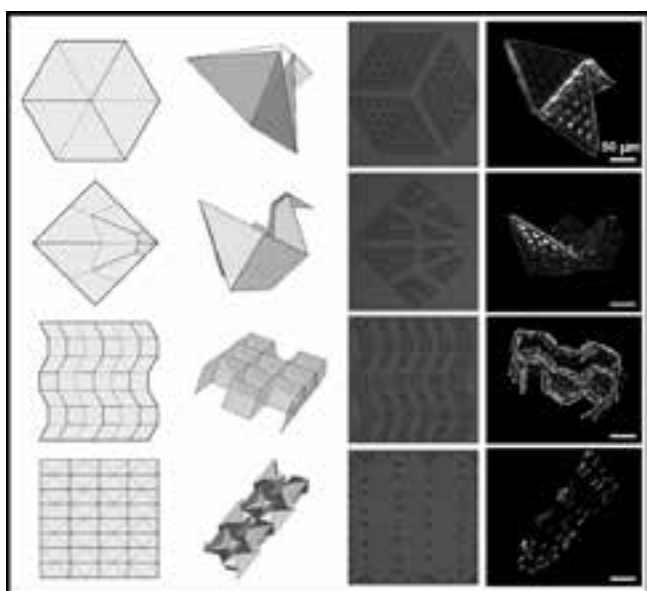


Figure 2: Origami designs of variable complexity constructed at the microscale using all-ALD bimorphs. Columns from left to right: Origami crease patterns, computer models of folded shapes, micro-origami devices (unfolded), micro-origami devices (folded). Scale bars are  $50 \mu\text{m}$ .

Figure 2 shows a variety of origami designs fabricated using this method, ranging from relatively simple ones with six folds to more complex structures with more than 100 folds. The origami bird made using our approach is less than half the size of the current state of the art [2]. Having established a complete platform for micro-origami with ion exchange actuated bimorphs, our group is preparing to develop bimorphs consisting of atomic layer deposition Pt and  $\text{SiO}_2$ , which will make it possible for us to achieve bidirectional bending action through electrical actuation.

By harnessing the electrical controllability and bidirectional folding structure, our team designed and fabricated

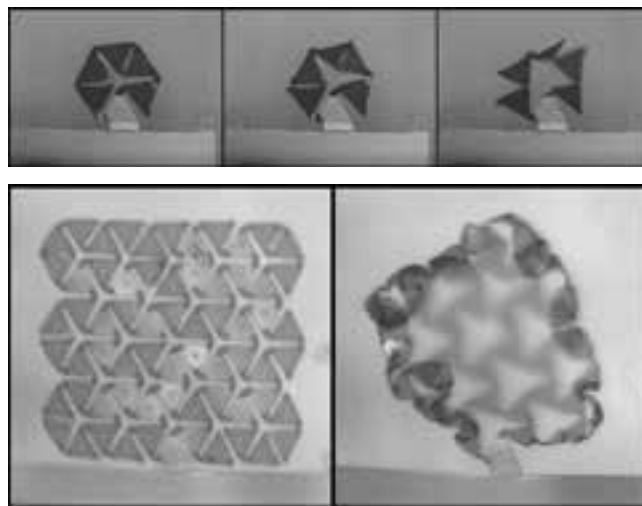


Figure 3, top: Three images from a movie showing voltage-based actuation of nm thin hinges of a six-panel metamaterial sheet.

Figure 4, bottom: A flat mechanical metamaterial microrobotic sheet (left) shows expansion and wrapping modes (right).

metamaterial robots that could locally expand and change its Gaussian curvature. Once integrated with electronics, such robots will be able to locomote, wrap, and encapsulate synthetic and biological materials. To generate local expansion of the metamaterial robot it is necessary to create hinges that allow panels to splay. The three folding actuators with opposite bending directions are connected to two panels. The middle hinge can bend at an angle of  $180^\circ$ , while the two side hinges can bend at an angle of  $90^\circ$  in the opposite direction.

Having determined that this design was mechanically feasible, we fabricated, using alternating layers of ALD grown Pt and sputtered Ti that are 7 nm thin, the first bidirectional surface electrochemical actuators. We used these voltage-driven actuators to implement a proof of principle scaffold for the metamaterial robot (Figure 3). Integrating these building blocks into a sheet structure, we fabricated mechanical metamaterial-based microrobots with large degree of freedom (Figure 4). This sheet-like microrobot could expand into three-dimensional structure, wrap the target object and shrink its size, opening the door to diverse applications in medical treatment and drug delivery.

## References:

- [1] Miskin, M., Dorsey, K., Bircan, B., Han, Y., Muller, D., McEuen, P., and Cohen, I. Graphene-based bimorphs for micron-sized autonomous origami machines. *Proceedings of the National Academy of Sciences*, 115: 466-470 (2018).
- [2] Bircan, B., Miskin, M., Dorsey, K., McEuen, P. and Cohen, I., Bidirectional Folding with Nanoscale Sheets for Autonomous Micro-Origami, 2018.

# A MEMS Microphone Using Levitation Force

**CNF Project Number: 2446-16**

**Principal Investigator(s): Shahrzad Towfighian, Ronald N. Miles**

**User(s): Mehmet Ozdogan**

*Affiliation(s): Mechanical Engineering Department, State University of New York at Binghamton*

*Primary Source(s) of Research Funding: National Science Foundation Project ECCS grant # 1608692 titled "A new Approach to Capacitive Sensing: Repulsive Sensors"*

*Contact: stowfigh@binghamton.edu, rmiles@binghamton.edu, mozdoga1@binghamton.edu*

*Website: <https://www.binghamton.edu/labs/mems/>*

*Primary CNF Tools Used: LPCVD N+/P+ Polysilicon-Wet Oxide-CMOS Nitride, MOS clean anneal, Heidelberg mask writer DWL2000, AS200 i-line stepper, Plasma-Therm deep Si etcher, Oxford 80+-100 etchers, Oxford PECVD, Zeiss Ultra SEM, dicing saw, Leica critical point dryer*

## Abstract:

We report fabrication and preliminary experimental results of a microelectromechanical systems (MEMS) microphone using a levitation force-based electrode configuration. This electrode scheme causes the sensing electrode (attached to a diaphragm) to move away from the biasing electrode as DC source is applied. The devices employing this scheme benefit from pull-in free behavior. Main objective of this work is to fabricate a MEMS microphone whose sensitivity could be improved simply by increasing the bias voltage, without suffering from pull-in instability. The microphone was fabricated at CNF and tested in Binghamton University anechoic chamber. The output of the chip at various bias voltages are measured using a read-out circuit. Experimental results show that the sensitivity of the device increases with increasing bias voltages from 40 volts to 100 volts. The ability to design electrostatic sensors without concerns about pull-in failure can enable a wide range of promising sensor designs.

## Summary of Research:

A microphone is an acoustic sensor that converts mechanical motions generated by sound pressure waves into electrical signals. Every year, billions of MEMS microphones have been produced and integrated into consumer products such as smartphones, laptops, hearing aids, smart wireless speakers etc. The sensitivity of the microphone is one of the most important parameters that defines the quality of a microphone. In general, the sensitivity is proportional to the applied bias voltage. However, usual electrode configurations (one fixed and one moving electrode) mostly suffer from pull-in instability, which causes the device stop functioning after some certain DC bias values. The levitation (repulsive) electrode configuration has been widely investigated and shown to be pull-in safe [1-3], which enables MEMS devices to have large travel ranges and proper functioning at high DC loads. This method utilizes fringe electrostatic field to generate a net force that pushes the diaphragm away from the substrate which eliminates the pull-in possibility. The microphone design consists of fixed and moving electrodes which are attached to a rotating diaphragm, see Figure 1. The design includes three sets of electrodes: grounded sensing electrodes, grounded fixed electrodes and biasing electrodes. The moving and fixed electrodes are vertically separated.

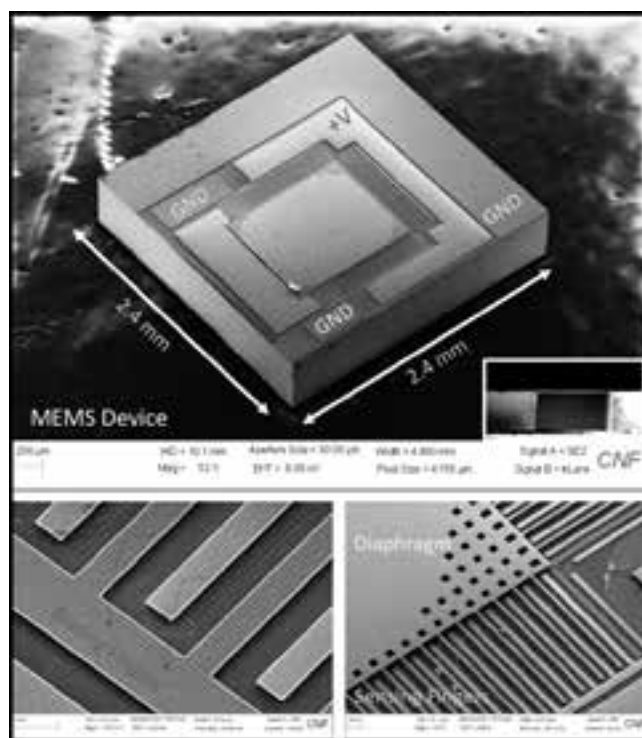


Figure 1: Images of the fabricated device. (Top) SEM image of the microphone and the cross section of the released chip. (Bottom Left) Biasing fixed fingers. (Bottom Right) Moving Finger and the diaphragm.

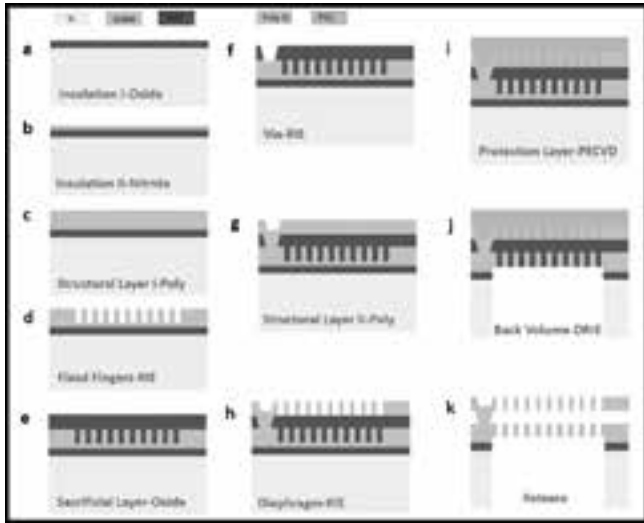


Figure 2: Fabrication process flow of the sensor.

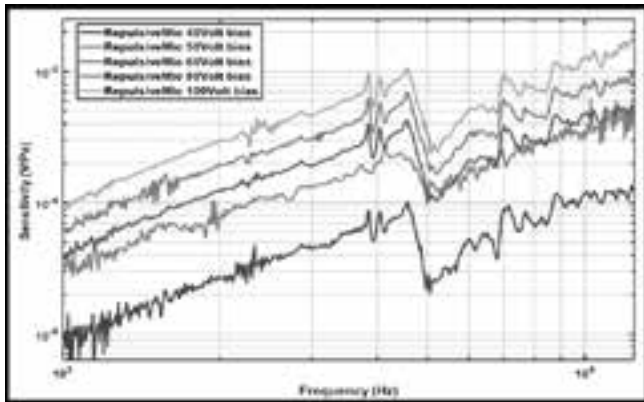


Figure 3: Experimental results. Shows the change of sensitivity of the microphone as the DC bias increases.

Process flow for the fabrication of the MEMS microphone is depicted in Figure 2. We started with 100 mm silicon wafers and grew 1  $\mu\text{m}$  thick LPCVD silicon dioxide as an insulation layer. Following this step LPCVD low stress silicon nitride was deposited on top of the oxide layer. On top of the insulation layers 2  $\mu\text{m}$  thick polysilicon layer was deposited and annealed using LPCVD furnace. This layer was etched using Unaxis 770 silicon etcher to form fixed fingers, Figure 3. On top of the fingers, 4  $\mu\text{m}$  thick sacrificial layer of LPCVD high-temperature-oxide (HTO) was deposited. Then, Logitech Orbis chemical mechanical polisher (CMP) was used to remove half of the oxide layer which yielded around 2  $\mu\text{m}$  vertical gap between fixed and moving electrodes. Then, Oxford 100 etcher is used to create vias on this sacrificial layer. Later, second 2  $\mu\text{m}$  thick polysilicon layer was deposited and annealed to reduce the residual film stresses. This layer was etched to form the diaphragm and the sensing electrodes.

Next, we deposit phosphosilicate glass (PSG) using Oxford PECVD tool. This layer mechanically supported the diaphragm while etching the back-volume of the device. The back volume was created by etching the bulk silicon using Plasma-Therm deep silicon etcher. Then, wafers were diced into 2.4 mm by 2.4 mm chips, which are then released in HF:HCl mixture and critical-point-dried.

After the microphone was released the chip was glued on a printed-circuit-board (PCB) and wire-bonded. A charge amplifier-based read-out circuit was used to obtain electrical signals. The acoustic tests for the microphone were performed in the anechoic chamber at Binghamton University. We applied various DC voltages to the biasing electrodes. This DC voltage created an out-of-plane motion to the diaphragm and increased the initial gap between the diaphragm and the fixed electrodes. The sound pressure was created by a loudspeaker by sweeping a broad range of pure tone signals (100 Hz-20 KHz). The incident pressure measured using a Bruel&Kjaer 4138 reference microphone. The electronic output from the chip was detected using a charge amplifier read-out circuit. The circuit consisted of an operational, capacitors and feedback-resistors. The sensitivity plot was obtained by measuring the output voltage relative to the sound pressure. The signals were acquired using a National Instruments Data Acquisition System.

Figure 3 shows the measured electrical response of the microphone for a wide range of bias voltages. It is shown that levitation electrode concept improves the sensitivity of a MEMS microphone simply by increasing the DC bias voltage without any pull-in failure.

This approach can enable designs that employ large bias voltages without adversely impacting the diaphragm's mechanical response.

### References:

- [1] S. He and R. B. Mrad, "Design, Modeling, and Demonstration of a MEMS Repulsive-Force Out-of-Plane Electrostatic Micro Actuator," in *Journal of Microelectromechanical Systems*, vol. 17, no. 3, pp. 532-547, June 2008.
- [2] Towfighian S, He S, Ben Mrad R. "A Low Voltage Electrostatic Micro Actuator for Large Out-of-Plane Displacement.," *ASME. IDETC/CIE*, Vol. 4: doi:10.1115/DETC2014-34283.
- [3] Ozdogan M, Daeichin M, Ramini A, Towfighian S, "Parametric Resonance Of A Repulsive Force MEMS Electrostatic Mirror.," *Sensors and Actuators A: Physical*, Volume 265, 2017, Pages 20-31.
- [4] Daeichin M, Ozdogan M, Towfighian S, Miles R, "Dynamic Response Of A Tunable MEMS Accelerometer Based On Repulsive Force.," *Sensors and Actuators A: Physical*, Volume 289, 2019, Pages 34-43.

# Carbon Dioxide as Thermal Fluid in Micro Systems

**CNF Project Number: 2474-16**

**Principal Investigator(s): Dr. Yoav Peles**

**User(s): Mostafa Asadzadeh, Anatoly Parahovnik**

*Affiliation(s): Mechanical and Aerospace Engineering, University of Central Florida (UCF)*

*Primary Source(s) of Research Funding: Office of Naval Research (ONR)*

*Contact: yoav.peles@ucf.edu, asadzade@knights.ucf.edu, tolik@knights.ucf.edu*

*Primary CNF Tools Used: AJA sputter deposition, chemical mechanical polishing (CMP)*

## Summary:

Carbon dioxide (CO<sub>2</sub>) is a natural coolant that present an alternative for environmentally hazardous coolants like hydrocarbons. The highest potential of CO<sub>2</sub> is in the trans critical region where it's thermophysical properties exhibit largest variations. For example, CO<sub>2</sub> viscosity lowers significantly during transition from liquid to supercritical phase, such reduction enables to reduce the pressure drop inside a micro channel and to achieve higher mass fluxes leading to a better heat removal. The project goal is to fabricate a microfluidic device that will enable to better understand thermal behavior of CO<sub>2</sub> in the vicinity of the critical point — a temperature and pressure of 31.4°C and of 7.37 MPa, respectively. This requires the microfluidic device to function under high pressure.

The part that was fabricated at CNF is shown in Figure 1. It has heaters and resistor temperature detectors (RTDs) depicted as the white and brown layer, respectively. These layers were deposited using AJA sputter deposition tool, and then separated and sealed using silicon oxide that was applied using plasma enhanced chemical vapor deposition (PECVD).

To achieve good sealing of the microdevice, the top surface was polished using chemical-mechanical polishing process. The wafer was then placed in a DISCO dicing saw to separate the devices. With the AJA sputter tool and the help of the CNF staff we were able to achieve very high repeatability in respect to electrical resistance. To minimize fluid leakage, the top surface was polished to an average roughness of 150 nm. This helped ensure a leakage of several orders of magnitude smaller than the intended mass flow inside the device.

Figure 2 presents the microdevice assembly where the bottom substrate has the control components (i.e., the heaters and the RTDs) and the top substrate has the microchannel. The top substrate is made of fused silica to allow optical access to the microchannel.

Figure 3 presents an image of flow patterns at different phases — gas, liquid, and supercritical. The applied heat flux is 17 W/cm<sup>2</sup>, the inlet temperature is 23°C, and the mass flux is 500 kg/m<sup>2</sup>s for all images. The pressures are 5.34 MPa, 6.6 MPa and 8 MPa for gas, liquid and supercritical respectively. For the liquid phase there is formation of bubbles inside the channel which corresponds to heat removal by boiling. Bubble inside pressure is inversely proportional to its diameter,

Therefore, due to high operating pressure the bubbles are small. In the images of the gas and supercritical phases, vertical lines can be seen. The lines correspond to equal density, which are dependent on the refraction index, and therefore visible using the camera. For the supercritical phase the lines are more distinct corresponding to larger variation of the density due to local heating. These density variations promote mixing, and therefore, enhance the heat transfer at the supercritical phase. It was found that the heat transfer coefficient of supercritical phase was enhanced by approximately 20% compared to the gas phase.

Our future work includes further investigation of heat transfer patterns at the trans-critical region. Gaining better understanding of the mechanisms controlling the heat transfer process will enable to have more efficient thermal control in microsystems.

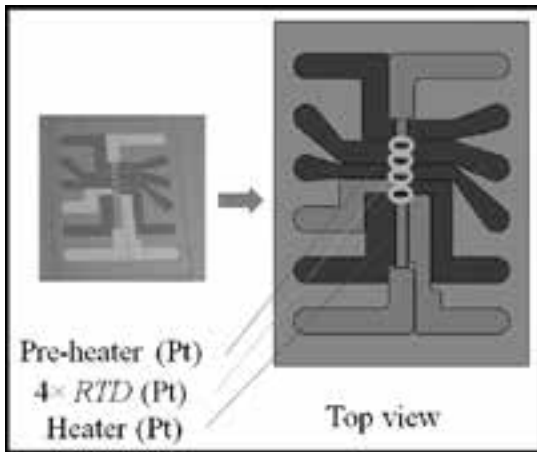


Figure 1: The microfabricated piece.

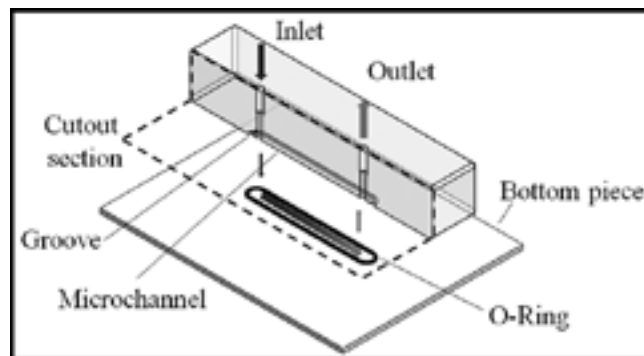


Figure 2: Microdevice assembly.

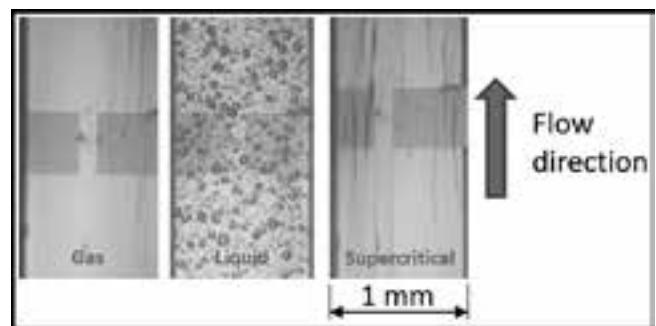


Figure 3: Heat transfer patterns at for different phases of  $CO_2$ .

# Fabricating Vitreous Silica Micropillars for Uniaxial Compression with *in situ* Raman Spectroscopy

**CNF Project Number: 2632-18**

**Principal Investigator(s): Shefford Baker**

**User(s): Zachary Rouse**

*Affiliation(s): Materials Science and Engineering Department, Cornell University*

*Primary Source(s) of Research Funding: Corning, Inc.*

*Contact: spb14@cornell.edu, zvr6@cornell.edu*

*Website: <https://baker.mse.cornell.edu/>*

*Primary CNF Tools Used: Autostep i-line stepper, PT770 etcher, Oxford 100 etcher, Oxford 81 etcher*

## **Abstract:**

**In silicate glasses, the interplay between glass structure and plastic deformation is not well understood. To address this, high-quality SiO<sub>2</sub> micropillars were fabricated through a reactive-ion etching based method which were then tested in compression while characterizing the structure of the glass *in situ* using Raman spectroscopy. These experiments provide direct observation of how the structure of the glass changes in response to a well-known uniaxial stress and strain state. The SiO<sub>2</sub> micropillar fabrication process, as well as considerations for optimizing pillar geometry are described.**

## **Summary of Research:**

Silicate glass is a vital component in countless applications such as display screens, solar panels, and vehicle windshields and as such its fabrication has become a near trillion-dollar industry. Although silicate glasses are macroscopically brittle materials, in small volumes they can undergo extensive plastic deformation. The character of this deformation influences the stress field evolution and crack nucleation around mechanical contacts, ultimately dictating the bulk fracture of the glass. Despite this, very little is known about the underlying atomistic mechanisms leading to silicate glass plasticity.

A popular method of probing these mechanisms is to perform Raman spectroscopy of residual indentations *ex situ*. A basic understanding of how the glass network reconfigures during deformation can be acquired by associating spectral peaks with known glass network features and then observing the spectral shifts between a pristine and an indented region. However, the quantitative analysis of data acquired through this method is limited due to the poorly known and highly heterogeneous stress/strain states of the probed volumes underneath the indentations. Additionally, these *ex situ* tests only characterize the nature of the glass network due to residual deformation, rather than during deformation. To rectify this, we developed a novel experimental method in which Raman spectra are recorded *in situ* during uniaxial micropillar compression of SiO<sub>2</sub>.

This testing enables us to probe the structure of a glass that is being subjected to well-known, homogeneous, and easily tunable stress and strain-states.

The success or failure of this method is entirely dependent on the ability to fabricate numerous high-quality SiO<sub>2</sub> micropillars with highly vertical side walls and minimal structural damage. To accomplish this, a new reactive-ion etching based process was developed at CNF. In this process first a thick (> 1.25 μm) chromium film is sputtered onto a standard SiO<sub>2</sub> wafer using the CVC 601 sputtering tool. An anti-reflective coating (ARC) followed by photoresist is then spun coat on top of the chromium. A reticle with a grid of circles with various diameters is then used for the resist exposure on the Autostep 200 stepper tool. After development (and oxygen plasma etching of the uncovered ARC), the residual discs of resist are used as a mask for a chlorine-based reactive-ion etch through the chromium film in the Plasma-Therm 770 etcher. After removal of the remaining resist, the residual discs of chromium are used as a mask for an extremely deep (6-10 μm) fluorine-based reactive-ion etch of the underlying SiO<sub>2</sub> wafer on the Oxford 100 etcher. The remaining chromium caps are dissolved with a chemical chromium etchant, and the passivating fluoropolymer layer left on the pillar sidewalls is stripped with an EKC solvent.

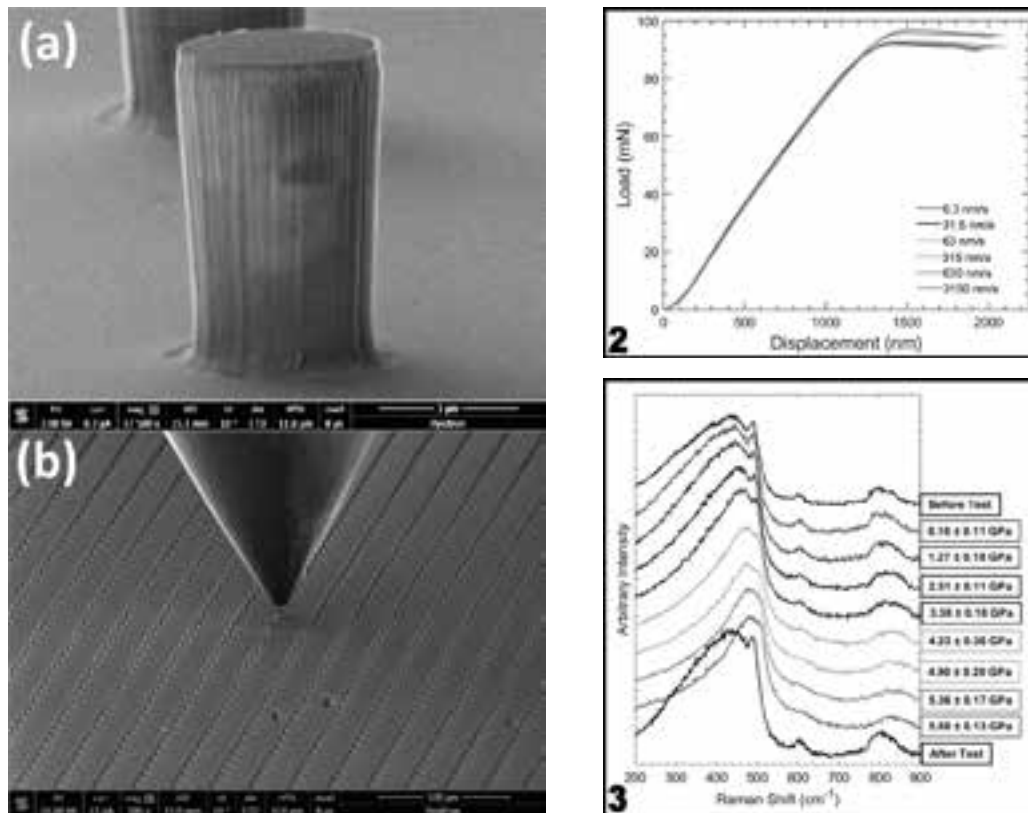


Figure 1, above: left (a) Scanning electron images of one typical silica micropillar and (b) a wide view of an array of micropillars as well as the diamond flat punch used to compress them. Figure 2, top right: Schematic of the utilized testing setup for micropillar compression with in situ Raman spectroscopy. Figure 3, bottom right: Ex situ and in situ Raman spectra taken during micropillar compression at various applied engineering stresses. Spectrum peaks are associated with specific, known SiO<sub>2</sub> network features.

This process leads to the creation of millions of pristine SiO<sub>2</sub> micropillars such as the one shown in Figure 1. Other SiO<sub>2</sub> micropillar compression studies made through analogous fabrication procedures have struggled with highly uneven pillar cross-sections [1,2]. This study's pillars are extremely dimensionally uniform and have only a slight negative taper angle of 1.8°. The tapering observed in other studies is largely caused by slanted side walls in the initial photoresist side walls, which transmits into the chromium (and then later into the SiO<sub>2</sub>) when the resist is used as a mask. To mitigate this, a stepper exposure tool (as opposed to a contact exposure tool) using carefully optimized exposure parameters was used. During the etching stages, obtaining a very high etch selectivity was also critical for mitigating the transmission of a taper from the masks to the substrates.

To compress these pillars, the wafers were cleaved into pieces which were then mounted on a nanoindenter system (Bruker) equipped with a diamond flat punch tip. The nanoindenter system was then incorporated into a confocal Raman microscope (Renishaw InVia) such that micropillars near the cleaved edges could be probed by the Raman laser while simultaneously being compressed by the indenter punch as shown in Figure 2. By repeatedly raising the applied stress and then pausing to acquire a

Raman spectrum, we can observe *in situ* Raman spectra as a function of a well-known uniaxial stress and strain for the first time ever (Figure 3).

From the dramatic peak shifts in these Raman spectra we can see that significant structural rearrangements occur with increasing applied stress, but surprisingly it is also observed that a large portion of these structural changes recover upon unloading of the pillar. This provides strong evidence that elastic deformation in SiO<sub>2</sub> significantly alters the glass network structure and provides a physical justification for silica's highly non-linear elastic behavior. By connecting the observed Raman peaks with SiO<sub>2</sub> network features, future quantitative analysis of these spectra will enable us to illuminate the fundamental atomic mechanisms of silicate glass deformation in a way that has never been possible before.

**References:**

[1] Kermouche, G., et al. (2016). "Perfectly plastic flow in silica glass." *Acta Materialia* 114: 146-153.  
 [2] Lacroix, R., et al. (2012). "Plastic deformation and residual stresses in amorphous silica pillars under uniaxial loading." *Acta Materialia* 60(15): 5555-5566.

# Construction of Microplasma Test Array

**CNF Project Number: 2762-19**

**Principal Investigator and User(s): Andrew Dickens**

**Affiliation(s): WildSpark Technologies LLC**

*Primary Source(s) of Research Funding: U.S. Department of Defense*

*Contact: andrew.dickens@wildsparktech.com*

*Website: WildSparkTech.com*

*Primary CNF Tools Used: ASML 300C gamma coat / develop tool, SC4500 deposition*

## Abstract:

Since 2016, WildSpark Technologies LLC has been working to develop and commercialize microplasma devices. Microplasma devices create and manipulate small regions of plasma from gas, solid, or liquid feedstock. These devices show promise for novel applications in electron devices, displays, medical devices, and flow control. Our lean and agile team uses the resources at the CNF to rapidly test concepts and construct prototype devices for test. In this report we discuss our efforts to build a system of electrodes and substrate stack to probe material and physical parameters which are used as building blocks for more complicated devices. The physical data extracted from these prototype devices is used to calibrate models used in multiphysics simulation to predict device performance in real world applications.

## Summary of Research:

We created patterns of electrodes on varying substrate materials. These patterns formed microplasma actuator elements and were windowed across a range of dimensions and physical designs. We then tested the devices using semiconductor parameter analyzers and were able to directly measure — for the first time — our microplasma cells in action. Our company constructed several devices with different material stacks and substrate composition to assess the impact of material parameters on performance. The electrical test data was used in combination with physical simulation in order to isolate physical parameters, in particular the Fowler-Nordheim tunneling equation coefficients for the material system.

We were concerned about the ability of our test devices to operate under high power densities for a long period of time. The results of these experiments demonstrated an ability to operate at power densities exceeding  $0.5\text{W}/\text{mm}^2$  for several minutes without degradation. This result exceeded our expectations and allows us to consider designs and power densities that we previously thought to be unattainable. While there are few comparable technologies in the literature, we believe this represents a milestone in terms of device endurance.

We chose CNF as a fabrication facility primarily because of the availability of the ASML 300C 248 nm stepper and

gamma coat / develop system. Our work requires us to pattern very fine structures with tight tolerances for both critical dimension (CD) and registration. It is very difficult to find production 248 nm lithography tools available for use by small businesses and our work would not be possible without these tools.

We extensively used the SC4500 deposition tools in order to deposit titanium electrodes as well as some proprietary surface coatings to our electrode / substrate sandwiches. Interconnects and bond pads were constructed using a metal liftoff technique with aluminum deposition.

Our future work at CNF will include further refinements of our test arrays to gain new insight into microplasma device physics and eventually to produce prototype products based on this knowledge.

## References:

- [1] Arakoni, R, et al., "H<sub>2</sub> Generation in Ar/NH<sub>3</sub> Microdischarges", J Phys. D: Appl. Phys. 40 (2007) 2476-2490.
- [2] Strong, F, et al., "Electrical discharge across micrometer-scale gaps for planar MEMS structures in air at atmospheric pressure", J. Micromech. Microeng. 18(2008) 075025, page 11.
- [3] Nishida, Y, et al., "Hydrogen Production from Hydrocarbons With Use of Plasma Discharges Under High Pressure Condition", IEEE Transactions on Plasma Science, Vol 42, No 12, December 2014.



# Self-Starting Lithium Niobate Soliton Microcombs

**CNF Project Number: 1997-11**

**Principal Investigator(s): Qiang Lin**

**User(s): Yang He, Rui Luo, Jingwei Ling**

*Affiliation(s): Department of Electrical and Computer Engineering, University of Rochester*

*Primary Source(s) of Research Funding: Defense Threat Reduction Agency-Joint Science and Technology*

*Office for Chemical and Biological, Defense (grant No. HDTRA11810047),*

*National Science Foundation under grants No. ECCS-1810169 and ECCS1610674*

*Contact: qiang.lin@rochester.edu, yhe26@ur.rochester.edu, ruiluo@rochester.edu, jling8@ur.rochester.edu*

*Primary CNF Tools Used: JEOL 9500, Yes Asher, AJA, DISCO dicing saw*

## Abstract:

**We report soliton generation in a high- $Q$  lithium niobate resonator. The photorefractive effect enables self-starting mode locking and is able to produce stable single solitons on demand that feature reversible switching between soliton states.**

## Summary of Research:

The recent demonstration of soliton mode locking in microresonators [1] represents a major turning point in the subject of frequency microcombs and many material systems and cavity geometries are being explored for various applications [2]. In this work soliton generation in a high- $Q$  lithium niobate (LN) resonator is observed for the first time. Moreover, on account of the intriguing properties of lithium niobate the soliton mode locked system is able to self-start. Specifically, soliton microcombs must be pumped at a frequency that is red detuned relative to a cavity resonance [2], but this regime is also unstable due to a thermo-optical nonlinearity [3]. As a result special techniques for pumping and triggering solitons have been developed [2]. Here the photorefractive property of LN is shown to allow stable operation and pumping on the red-detuned side of resonance. As a result, self-starting mode locking of soliton microcombs is demonstrated by a simple and reversible pump tuning process.

LN features a strong photorefractive effect, which causes an intensity-dependent decrease of refractive index [4]. Moreover, LN exhibits a negligible thermo-optic coefficient for the ordinary polarized light (around room temperature) [5], leading to a suppressed thermo-optic nonlinearity. The combination of these two effects results in a net decrease of refractive index with increased optical intensity. This behavior is opposite to that induced by thermo-optic and/or optical Kerr nonlinearities in conventional Kerr soliton microresonators [2]. The optical Kerr effect from the soliton shifts the resonance towards the red, while the photorefractive effect significantly shifts the resonance towards the blue. As a result, the soliton formation regime resides directly

within the laser detuning regime that is self-stabilized by the photorefractive effect, thereby enabling self-starting soliton mode locking.

To show this capability, we used a LN microresonator (shown as Figure 1), which has a radius of 100  $\mu\text{m}$ . The group velocity dispersion of the device is engineered to be slightly anomalous. The device was patterned by electron-beam lithography (JEOL 9500).

To produce Kerr combs, a pump power of 33 mW is coupled onto the chip. When the pump frequency is scanned into a cavity resonance from long wavelength, the average intracavity power readily shows clear discrete steps (Figure 2). Figure 3 shows the spectrum measured for the single soliton at the first power step, which exhibits a smooth hyperbolic sech-shaped spectral envelope.

## References:

- [1] T. Herr, et al., "Temporal solitons in optical microresonators," *Nature Photon.* 8, 145-152 (2014).
- [2] T. J. Kippenberg, A. L. Gaeta, M. Lipson, and M. L. Gorodetsky, "Dissipative Kerr solitons in optical microresonators," *Science* 361, 567 (2018).
- [3] T. Carmon, L. Yang, K J Vahala, et al., "Dynamical thermal behavior and thermal self-stability of microcavities," *Optics Express* 12, 4742-4750 (2004).
- [4] P. Gunter and J.-P. Huignard, eds., *Photorefractive Materials and Their Applications* 1, 2 (Springer, New York, 2006).
- [5] L. Moretti, M. Lodice, F. G. D. Corte, and I. Rendina, "Temperature dependence of the thermo-optic coefficient of lithium niobate, from 300 to 515 K in the visible and infrared regions," *J. Appl. Phys.* 98, 036101 (2005).

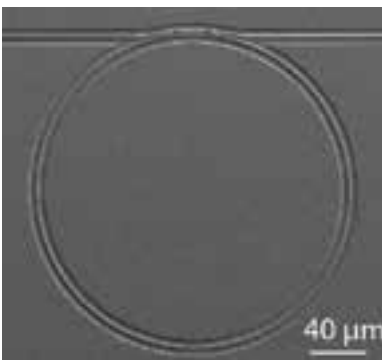


Figure 1: Scanning electron microscope image of a LN microring resonator.

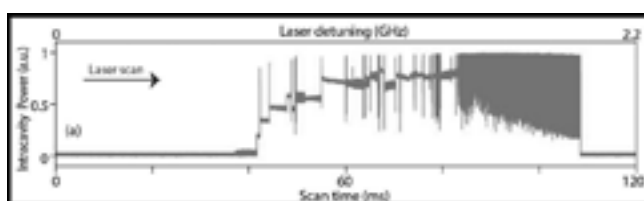


Figure 2: Intracavity power as a function of time when the laser is scanned from red to blue (long to short wavelength).

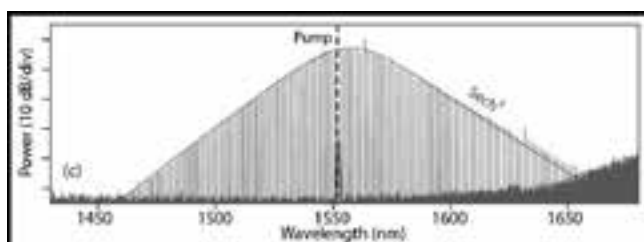


Figure 3: Optical spectrum of the single soliton state.

# High-Q Two-Dimensional Lithium Niobate Photonic Crystal Slab Nanoresonators

**CNF Project Number: 1997-11**

**Principal Investigator(s): Qiang Lin**

**User(s): Mingxiao Li**

*Affiliation(s): Electrical and Computer Engineering, University of Rochester*

*Primary Source(s) of Research Funding: National Science Foundation (NSF) (EFMA-1641099, ECCS1810169, and ECCS-1842691); the Defense Threat Reduction Agency-Joint Science and Technology Office for Chemical and Biological Defense (grant No. HDTRA11810047)*

*Contact: qiang.lin@rochester.edu, mli53@ur.rochester.edu*

*Primary CNF Tools Used: JEOL 9500, AJA ion mill*

## Abstract:

**We report a 2D LN PhC slab nanoresonators with high optical  $Q$  over  $3 \times 10^5$ . Such a high quality enables us to probe the intriguing anisotropy of nonlinear optical phenomena of LN never reported previously.**

## Summary of Research:

Photonic crystal (PhC) nanoresonators exhibit exceptional capability of controlling light confinement and light matter interactions in the sub-wavelength scale, which forms a crucial foundation for many applications [1,2]. Among various photonic crystal structures, two-dimensional (2D) photonic crystal slabs exhibit significant advantage in the engineering of the density of photonic states. These excellent characteristics have excited tremendous interest in recent years to develop 2D PhC slab nanoresonators on a variety of material platforms.

Lithium niobate (LN), exhibits outstanding electro-optic, nonlinear optical, acousto-optic, piezoelectric, photorefractive, pyroelectric, and photoconductive properties [5], promising for broad applications. The great application potential has attracted significant attention recently to develop LN photonic devices on chip-scale platforms [3,4,7]. However, realizing high-quality 2D LN PhC structures remains significant challenge [6], which becomes the major obstacle hindering the exploration of optical phenomena in the nanoscopic scale that would potentially result in intriguing device characteristics and novel functionalities inaccessible by conventional means.

In this paper, we demonstrate 2D LN PhC slab nanoresonators with optical  $Q$  up to  $3.51 \times 10^5$ , about three orders of magnitude higher than other 2D LN photonic crystal nanocavities reported to date [6].



*Figure 1: Scanning electron microscopic image of a fabricated 2D LN PhC slab. Figure 2: Zoom-in image of a section of the photonic crystal slab.*

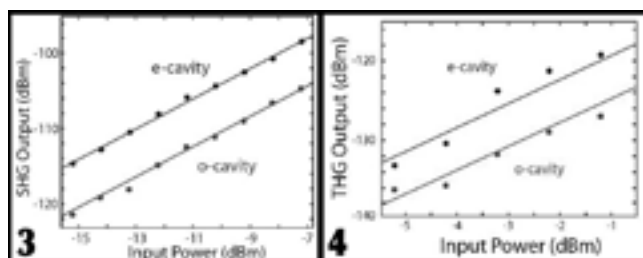


*Figure 3: Recorded power of the generated second harmonic wave as a function of that of the fundamental pump wave, where the dots are experimental recorded data for an e-cavity and o-cavity, respectively. The solid lines show quadratic fitting to the experimental data. Figure 4: Recorded power of the generated third harmonic wave as a function of the fundamental pump wave, where the dots are experimental recorded data for an e-cavity and o-cavity, respectively. The solid lines show cubic fitting to the experimental data.*

Devices are patterned by JEOL 9500. Such a pure polarization enables us to explore intriguing anisotropy of optical phenomena, by making the line-defect cavity either in parallel with or perpendicular to the optical axis. For convenience, we denote the one perpendicular to the optical axis as an e-cavity since the dominant electric field polarizes along the optical axis, corresponding to the extraordinary polarization. Accordingly, we denote the one in parallel with the optical axis as an o-cavity as the dominant cavity field polarizes along the ordinary polarization. In particular, the high optical  $Q$  together with the tiny effective mode volume supports extremely strong nonlinear optical interactions, which results in efficient third harmonic generation combined with cascaded second harmonic generation, for the first time in on-chip LN nanophotonic devices [3,4,7]. The demonstrated high- $Q$  2D LN PhC nanoresonators offer an excellent device platform for the exploration of extreme nonlinear and quantum optics at single-photon and few-photon level, opening up a great avenue towards future development of energy efficient nonlinear photonic and electro-optic signal processing.

In summary, we have demonstrated 2D LN PhC slab nanoresonators with optical  $Q$  up to  $3.51 \times 10^5$  that is about three orders of magnitude higher than other 2D LN PhC nanoresonators reported to date [6]. The high optical  $Q$  together with tight optical mode confinement results in intriguing nonlinear optical interactions. We have observed second-harmonic generation, particularly third harmonic generation that is the first time to be observed in on-chip LN nanophotonic devices [3,4,7].

Moreover, the devices exhibits pure polarization of the cavity modes, which enabled us to probe the intriguing anisotropy of nonlinear optical phenomena, which have never been reported previously.

### References:

- [1] E. Kuramochi, K. Nozaki, A. Shinya, K. Takeda, T. Sato, S. Matsuo, H. Taniyama, H. Sumikura, and M. Notomi, "Large-scale integration of wavelength-addressable all-optical memories on a photonic crystal chip," *Nature Photon.* 8, 474 (2014).
- [2] P. Lodahl, S. Mahmoodian, and S. Stobbe, "Interfacing single photons and single quantum dots with photonic nanostructures," *Rev. Mod. Phys.* 87, 347 (2015).
- [3] R. Luo, H. Jiang, H. Liang, Y. Chen, and Q. Lin, "Self-referenced temperature sensing with a lithium niobate microdisk resonator," *Opt. Lett.* 42, 1281 (2017).
- [4] C. Wang, X. Xiong, N. Andrade, V. Venkataraman, X.-F. Ren, G.-C. Guo, and M. Loncar, "Second harmonic generation in nanostructured thin-film lithium niobate waveguides," *Opt. Express* 25, 6963 (2017).
- [5] R. S. Weis and T. K. Gaylord, "Lithium niobate: Summary of physical properties and crystal structure," *Appl. Phys. A* 37, 191-203 (1985).
- [6] R. Geiss, S. Diziain, M. Steinert, F. Schrepel, E.-B. Kley, A. Tunnermann, and T. Pertsch, "Photonic crystals in lithium niobate by combining focused ion beam writing and ion-beam enhanced etching," *Phys. Stat. Sol. A* 211, 2421 (2014).
- [7] H. Liang, et al., "High-quality lithium niobate photonic crystal nanocavities," *Optica.* 4, 1251 (2017).

# Fabrication of Anti-Resonant Reflecting Optical Waveguides for On-Chip Raman Spectroscopy

**CNF Project Number: 2255-13**

**Principal Investigator(s): Jin Suntivich<sup>1,2</sup>**

**User(s): Chengyu Liu<sup>3</sup>**

*Affiliation(s): 1. Materials Science and Engineering Department, 2. Kavli Institute at Cornell for Nanoscale Science, 3. School of Applied and Engineering Physics; Cornell University*

*Primary Source(s) of Research Funding: Samsung Advanced Institute of Technology (SAIT)*

*Contact: js2765@cornell.edu, CL986@cornell.edu*

*Primary CNF Tools Used: AJA sputter deposition, Woollam spectroscopic ellipsometer, ABM contact aligner, SC4500 evaporator, Oxford PECVD*

## Abstract:

On-chip gas sensing technology has received extensive attention due to its potential applications in environmental and healthcare monitoring. Herein, we utilize hollow-core anti-resonant reflecting optical waveguides (ARROWs) in the near-infrared wavelength for on-chip Raman scattering for various chemical detections. In this work, we fabricate hollow-core ARROWs with Bragg reflectors made by tantalum oxide ( $\text{Ta}_2\text{O}_5$ ) and silicon dioxide ( $\text{SiO}_2$ ) film decks and characterize our device performance. The propagation loss is about 19 dB/cm at 780 nm wavelength, which is an advance for the next-generation integrated on-chip Raman sensors.

## Summary of Research:

On-chip sensing technology [1,2] has received extensive attention due to its potential applications in environmental and healthcare monitoring. On-chip spectroscopy methods such as on-chip infrared absorption spectroscopy have high sensitivity and selectivity; however, on-chip infrared devices still face challenges from the component complexity and cost. Herein, we use hollow-core anti-resonant reflecting optical waveguides (ARROWs) [3,4] in the near-infrared wavelength for on-chip Raman scattering for gaseous-molecule detections. The geometry of the hollow-core ARROWs confines the guided light in the air mode, where the optical field can efficiently overlap with the detected molecules. To demonstrate the proof of concept, we fabricate hollow-core ARROWs with alternating layers of  $\text{Ta}_2\text{O}_5$  and  $\text{SiO}_2$ , where the fabrication details will be discussed.

We first designed the Bragg reflector by alternating  $\text{Ta}_2\text{O}_5$  and  $\text{SiO}_2$  layers. A period of high index/low index dielectric film decks can provide a desirable reflectance over a certain range. We utilized the transfer matrix method to simulate the film decks with different design parameters. Considering the fabrication difficulty, we limit the  $\text{Ta}_2\text{O}_5/\text{SiO}_2$  period number to be three. We got the actual film thicknesses for each layer by Woollam ellipsometer and measured the reflectance of deposited

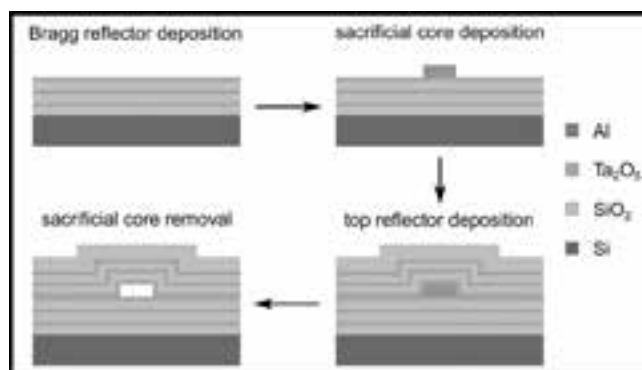


Figure 1: The fabrication process of ARROW waveguides.

film decks with UV/Vis/NIR optical spectrophotometer to verify our design (results not shown). The thicknesses used for each layer were optimized to reach the maximum reflection near 800 nm wavelength.

After that, we developed the fabrication process shown in Figure 1 for the ARROWs. We started with a silicon wafer. First, we deposited a stack of  $\text{Ta}_2\text{O}_5$  and  $\text{SiO}_2$  Bragg layers using sputtering ( $\text{Ta}_2\text{O}_5$  using reactive sputtering



Figure 2: An SEM image of the hollow core structure after aqua regia etching.

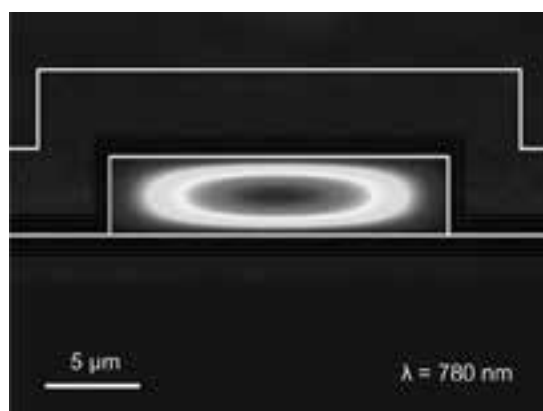


Figure 3: Calculated guiding mode profile of the ARROW waveguide at 780 nm.

and  $\text{SiO}_2$  using RF sputtering) based on our calibrated design parameters. Then, we did a contact lithography for waveguide sacrificial core patterning. A 3.5- $\mu\text{m}$  thick aluminum (Al) was evaporated into these patterned channels. Then, we did a lift-off to remove the unwanted Al to form the sacrificial channels. Similarly, a Bragg reflector by  $\text{Ta}_2\text{O}_5$  and  $\text{SiO}_2$  was deposited on top of the Al channels. A 3- $\mu\text{m}$  thick protective oxide cladding was added by PECVD. After a clean facet cleaving, Al sacrificial cores were removed by a two-day heated aqua regia etching in our lab.

Figure 2 shows a representative scanning electron micrograph (SEM) of the fabricated ARROW waveguide after aqua regia etching, which exemplifies a hollow core feature of our device.

We design the ARROWS by calculating the mode profile using the geometry estimated from SEM (Figure 2). The modal behavior was calculated from a commercial mode solver assuming that an air core inside. Figure 3 indicates that our fabricated ARROW waveguide supports a quasi-TE mode inside the air core, which provides the complete mode overlap between the pump mode and Stokes mode. In order to characterize this device's performance, we measured the propagation loss using a top-view camera method around 780 nm wavelength in air. Using the background-corrected signals, we fit the loss data to a regression model. The propagation loss of our device is about 19 dB/cm. To characterize the feasibility of the ARROW as a waveguide-based evanescent Raman sensor for gaseous molecule detection, we are incorporating a flow cell, where external gases can be applied to the device.

In conclusion, we propose a hollow-core ARROW structure by  $\text{Ta}_2\text{O}_5$  and  $\text{SiO}_2$  for on-chip Raman sensing especially for gas detection. We have fabricated the proposed ARROW waveguides with a clear hollow core and the device has been characterized. Future work will focus on the device application for gaseous molecule sensing.

## References:

- [1] Dhakal, A., Subramanian, A. Z., Wuytens, P., Peyskens, F., Le Thomas, N., and Baets, R. (2014). Evanescent excitation and collection of spontaneous Raman spectra using silicon nitride nanophotonic waveguides. *Optics letters*, 39(13), 4025-4028.
- [2] Evans, C. C., Liu, C., and Suntivich, J. (2016).  $\text{TiO}_2$  Nanophotonic sensors for efficient integrated evanescent Raman spectroscopy. *ACS Photonics*, 3(9), 1662-1669.
- [3] Yin, D., Schmidt, H., Barber, J. P., and Hawkins, A. R. (2004). Integrated ARROW waveguides with hollow cores. *Optics Express*, 12(12), 2710-2715.
- [4] Schmidt, H., Yin, D., Deamer, D. W., Barber, J. P., and Hawkins, A. R. (2004, October). Integrated ARROW waveguides for gas/liquid sensing. In *Nanoengineering: Fabrication, properties, optics, and devices* (Vol. 5515, pp. 67-81). International Society for Optics and Photonics.

# High Quality Factor PECVD $\text{Si}_3\text{N}_4$ Ring Resonators Compatible with CMOS Process

**CNF Project Number: 2364-15**

**Principal Investigator(s): Michal Lipson**

**User(s): Xingchen Ji, Samantha Roberts**

*Affiliation(s): Department of Electrical Engineering, Columbia University, New York, NY 10027;  
School of Electrical and Computer Engineering, Cornell University, Ithaca, NY 14853*

*Primary Source(s) of Research Funding: Defense Advanced Research Projects Agency*

*Contact: ML3745@columbia.edu, xj53@cornell.edu, spr2127@columbia.edu*

*Primary CNF Tools Used: PECVD, e-beam lithography, Oxford 100 etcher, AJA sputter deposition*

## Abstract:

**We demonstrate high-confinement  $\text{Si}_3\text{N}_4$  resonators with intrinsic quality factors more than one million using standard PECVD process. We show that by addressing scattering, the loss at 1.6  $\mu\text{m}$  can be as low as 0.4 dB/cm.**

## Summary of Research:

High quality factor silicon nitride ( $\text{Si}_3\text{N}_4$ ) ring resonators are critical for a variety of applications such as low threshold frequency combs [1-3], high precision sensing [4] and optical communications [5]. To date, high quality factor  $\text{Si}_3\text{N}_4$  ring resonators have been demonstrated almost solely using  $\text{Si}_3\text{N}_4$  films with high stress, deposited using low-pressure chemical vapor deposition (LPCVD), a high temperature process. Both the high stress of the films and the high temperature process make the fabrication of these devices in a standard foundry challenging.

Plasma-enhanced chemical vapor deposition (PECVD) is a standard, low temperature, commercial process for depositing low stress films. Indeed, achieving low waveguide losses in PECVD  $\text{Si}_3\text{N}_4$  has been challenging. There have been efforts to reduce losses in PECVD  $\text{Si}_3\text{N}_4$  films by substituting conventional precursors to deuterated precursors [6], which requires specialized tools and a series of complicated tests. Using standard PECVD, compatible with CMOS processes, the lowest propagation loss reported to date without a high temperature long furnace anneal are 1.6 dB/cm at 1.55  $\mu\text{m}$  and 2.5 dB/cm at 1.6  $\mu\text{m}$  [7,8].

Here we demonstrate  $\text{Si}_3\text{N}_4$  ring resonators with intrinsic quality factors of more than one million using a standard PECVD process. We show that processes addressing scattering losses such as optimized etch process, chemical-mechanical planarization (CMP) and multipass lithography can lead to quality factors above 700,000.

When combined with rapid thermal anneal (RTA) which reduces film absorption loss, quality factors can be more than one million. In contrast to furnace anneal, rapid thermal anneal has been successfully applied in the microelectronics industry. This has particular relevance for CMOS technology, specifically process steps such as implant annealing, oxidation, source and drain contact junctions [9].

We fabricated our devices on a thermally oxidized 4-inch silicon wafer.  $\text{Si}_3\text{N}_4$  is deposited using PECVD at 350°C in a single step. CMP, a standard CMOS process, is applied to  $\text{Si}_3\text{N}_4$  top surface in order to reduce scattering from top surface. The roughness before and after CMP is shown in Figure 1 and Figure 2. The roughness is reduced from 1.36 nm to 0.20 nm. In order to reduce the roughness from the sidewalls, we use a  $\text{SiO}_2$  hard mask deposited using PECVD after CMP and use a dry etching process with a higher oxygen flow. This etching process has been shown to reduce substantially the polymerization process during etching and decrease losses [3]. We pattern our devices with electron beam lithography using ma-N 2403 resist and use multipass to further reduce sidewall roughness from lithography. We clad the devices with 2  $\mu\text{m}$  of  $\text{SiO}_2$  using PECVD. After cladding, we applied RTA at 800°C for 5 mins to reduce absorption loss.

We have achieved an intrinsic quality factor of more than one million using the optimized process. The fabricated devices have radius of 115  $\mu\text{m}$ , height of

730 nm and width of 1500 nm coupled to a waveguide of the same dimensions. These dimensions ensure high confinement. The mode simulation and fabricated devices are shown in Figure 1. In order to test the devices, we launch a tunable laser source, transmitted through a fiber polarization controller, into the inverse nanotaper of our device using a lensed fiber and collect the output of the ring resonator through another inverse nanotaper with a collimating lens. We then monitor the output on a photodetector. Figure 3 shows the measured normalized transmission spectrum before RTA. The measured intrinsic quality factor around  $1.6 \mu\text{m}$  is 724,000, corresponding to a propagation loss of 0.42 dB/cm. Figure 4 shows the measured normalized transmission spectrum after RTA. The measured intrinsic quality factor around  $1.6 \mu\text{m}$  is 1.08 million, corresponding to a propagation loss of 0.28 dB/cm. Therefore, simply by addressing the surface roughness, we are able to achieve propagation loss as low as 0.42 dB/cm. After RTA, we achieve even lower loss of 0.28 dB/cm.

Utilizing CMOS compatible processes including etch optimization, CMP, multipass lithography and RTA, we are able to fabricate low loss waveguides and ring resonators. We have achieved high quality factor more than one million using a standard PECVD process. This work provides a platform for achieving low loss, crack-free  $\text{Si}_3\text{N}_4$  films, which could greatly benefit applications such as 3D photonic integration, telecommunications and nonlinear processing.

## References:

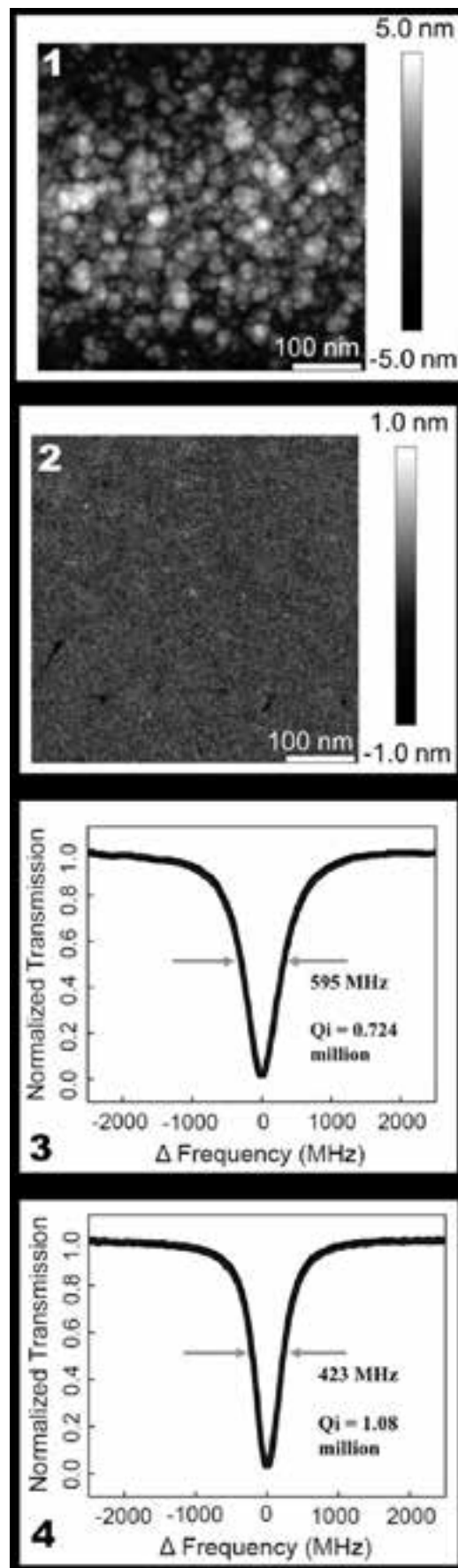
- [1] B. Stern, X. Ji, Y. Okawachi, A. L. Gaeta, and M. Lipson, *Nature* 562(7727), 401-405 (2018).
- [2] Y. Xuan, et al. *Optica* 3, 1171-1180 (2016).
- [3] X. Ji, et al. *Optica* 4(6), 619 (2017).
- [4] T. Kippenberg, A. L. Gaeta, M. Lipson, and M. L. Gorodetsky, *Science* 361 (6402), (2018).
- [5] P. Marin-Palomo, et al. *Nature* 546(7657), 274-279 (2017).
- [6] J. Chiles, et al. *Optics Letters* 43(7), 1527 (2018).
- [7] E. A. Douglas, et al. *Optical Materials Express* 6(9), 2892 (2016).
- [8] L. Wang, W. Xie, D. V. Thourhout, H. Yu, and S. Wang, *Optics Express* 26, 9645-9654.
- [9] M. J. Hart and A. G. R. Evans, *Semiconductor Science and Technology* 3(5), 421-436 (1988).
- [10] P. Rabiei, W. H. Steier, C. Zhang, and L. R. Dalton, *J. Lightwave Technol.* 20(11), 1968-1975 (2002).

Figure 1: AFM measurement of the top surface of  $\text{Si}_3\text{N}_4$  before CMP. Roughness of 1.36 nm.

Figure 2: AFM measurement of the top surface of  $\text{Si}_3\text{N}_4$  after CMP. Roughness of 0.20 nm.

Figure 3: Normalized transmission spectra of the same ring resonator before rapid thermal anneal (RTA). Resonance with 595 MHz linewidth corresponding to an intrinsic Q of 0.72 million.

Figure 4: Normalized transmission spectra of the same ring resonator after rapid thermal anneal (RTA). Resonance with 423 MHz linewidth corresponding to an intrinsic Q of 1.08 million.



## III-N UV Photonic Devices

**CNF Project Number: 2387-15**

**Principal Investigator(s): Debdeep Jena**

**User(s): Shyam Bharadwaj, Kevin Lee, Ryan Page, Jimmy Encomendero**

*Affiliation(s): Electrical and Computer Engineering, Materials Science Engineering; Cornell University*

*Primary Source(s) of Research Funding: National Science Foundation*

*Contact: djena@cornell.edu, sb2347@cornell.edu, kl833@cornell.edu, rlp238@cornell.edu, jje64@cornell.edu*

*Primary CNF Tools Used: ABM contact aligner, electron-beam evaporators, Plasma-Therm PT770*

### Abstract:

Our research goal is to improve and fabricate deep ultraviolet (DUV) and visible photonic devices such as light-emitting diodes (LEDs) and laser diodes (LDs). We grow the semiconductor thin films by molecular beam epitaxy (MBE). The III-nitride material system is ideal for such devices due to its wide range of direct bandgaps. For deep UV devices, AlN, GaN and AlGaIn are the typical materials. P-type transport is a major challenge in these materials; as such, we are focusing on improving this property through the use of InGaIn contact layers and polarization-doped AlGaIn cladding regions. The structure of the active region is also an important determinant of the external quantum efficiency (EQE) of the LEDs, so we are studying different active region thicknesses and compositions.

### Summary of Research:

We grow UV LED structures by plasma-assisted MBE (PA-MBE). These LEDs are grown on metal organic chemical vapor deposition (MOCVD)-grown AlN on sapphire template substrates. One study we performed involved a comparison of AlGaIn active region DUV LEDs to ultra-thin GaN active region ones. Ultra-thin GaN theoretically has a more favorable valence band alignment for light extraction, though AlGaIn active regions can be grown thicker (resulting in a larger active volume — a larger region in which radiative recombination can occur) while still emitting at the same wavelength. The structures that were grown are shown in Figure 1.

After growing the LED structures, they were processed in the CNF using contact photolithography. Positive tone photoresist was spun onto samples for the device isolation step. After developing, individual devices were defined through ICP-RIE etching in the PT770 tool. The electron-beam evaporators were used to deposit metal contacts for probing.

After the LEDs were fabricated, the electrical and optical characteristics were measured through current-voltage (IV) and electroluminescence (EL) measurements. The results of these measurements are shown in Figure 2 (IV) and Figure 3 (EL).

It can be seen that that the electrical performance of the devices are fairly similar between the two structures, with current densities reaching  $\sim 500$  A/cm<sup>2</sup> at 10V. The



Figure 1: Schematic structures of the UV LEDs grown in this study. On the left is the AlGaIn active region LED, and on the right is the ultra-thin GaN active region LED. The AlGaIn LED has one single quantum well, while the ultra thin GaN LED has 4 quantum wells separated by 2 nm AlN barriers.

biggest difference in device performance can be seen in the EL results: the measured EL intensity for the device with an AlGaIn active region is roughly 10x greater than the EL intensity from the device with GaN active region at the same current levels. This can be partly attributed to the difference in active volume: The AlGaIn device active area is roughly 7x greater than the GaN device active area. More work is being performed to quantify the difference in emission properties (such as the angle- and polarization-resolved emission patterns) of the two active regions.

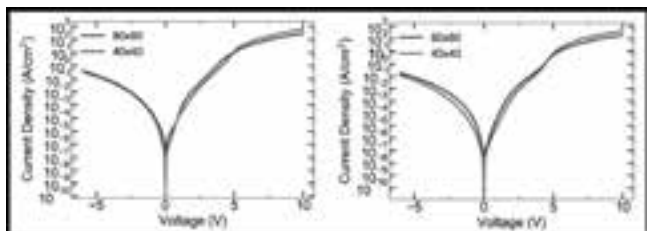


Figure 2: Log scale current-voltage characteristics of the two LEDs. The IV for the AlGaN active region LED is shown on the left, while the IV for GaN active region LED is on the right. Two different device areas were measured for each ( $80 \times 80$  square  $\mu\text{m}$ , and  $40 \times 40$  square  $\mu\text{m}$ ).

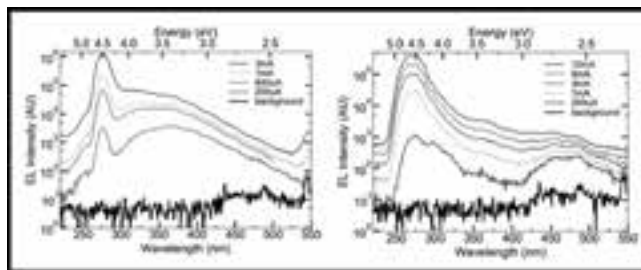


Figure 3: Log scale electroluminescence data for the two LEDs (AlGaN active region device on left, GaN active region device on the right). Both devices have emission peaks around 275 nm, though the AlGaN active region device has a larger broad peak around 375 nm (likely defect related). The AlGaN active region device has around 10x emission intensity as the GaN device for the same current levels.

# Development of Single and Double Layer Anti-Reflective Coatings for Astronomical Instruments

**CNF Project Number: 2458-16**

**Principal Investigator(s): Gordon Stacey<sup>1</sup>**

**User(s): Bugao Zou<sup>2</sup>, Nicholas Cothard<sup>2</sup>, Mahiro Abe<sup>3</sup>**

*Affiliation(s): 1. Department of Astronomy, 2. Department of Applied and Engineering Physics, 3. Department of Physics; Cornell University*

*Primary Source(s) of Research Funding: NASA Grant NNX16AC72G*

*Contact: stacey@cornell.edu, bz332@cornell.edu, nc467@cornell.edu, ma797@cornell.edu*

*Primary CNF Tools Used: ABM contact aligner, Oxford plasma-enhanced CVD, Anatech resist strip, Oxford 82 etcher, Hamatech-Steag wafer processors, manual resist spinners, resist hot strip bath, Heidelberg mask writer - DWL 2000, Plasma-Therm deep silicon etcher, Zygo optical profilometer, Zeiss Supra/Ultra SEM*

## Abstract:

We have been developing Fabry-Perot interferometers using silicon-based metal mesh filters for the far infrared and sub-millimeter astronomical instruments. The filters comprise gold meshes on one side and metamaterial anti-reflection coatings on the other side to both achieve wide bandwidth transmission and mitigate Fresnel reflection by the un-metalized substrate surface. In the past year we had a paper presented at SPIE Advances in Optical and Mechanical Technologies for Telescopes and Instrumentation III that demonstrates the performance of metal mesh reflectors and anti-reflection coated silicon surfaces by simulation and establishes standard procedures to fabricate these two parts. We are currently polishing the recipe of anti-reflection coatings by fabricating samples on high-resistivity silicon wafers. We will test the optical efficiency of samples fabricated at CNF using a Fourier transform spectrometer.

## Summary of Research:

The purpose of the project is to develop Fabry-Perot interferometers for use in the far infrared and sub-millimeter astronomical instruments. They are comprised of metal mesh reflectors and metamaterial anti-reflection coatings. The former part provides high reflectance over the frequency range of interest and controls the resolving power of interferometers while the latter part help mitigate strong Fresnel reflections of silicon and widen the bandwidth.

Our main job at CNF is the development of the fabrication methods of these two parts. We had some preliminary result about the fabrication of anti-reflection coatings published in Applied Optics a few years ago [1]. Last summer we had a paper presented at SPIE Advances in Optical and Mechanical Technologies for Telescopes and Instrumentation III [2] that summarizes the fabrication procedures for metal meshes and anti-reflection coatings and we continued to refine the recipe in order to improve the performance of samples.

Figure 1 shows two microscope images (taken by CNF's Olympus MX-50 Microscope) of metal mesh filters. We fabricate metal mesh filters using standard evaporation and lift-off lithography techniques. Negative lift-off

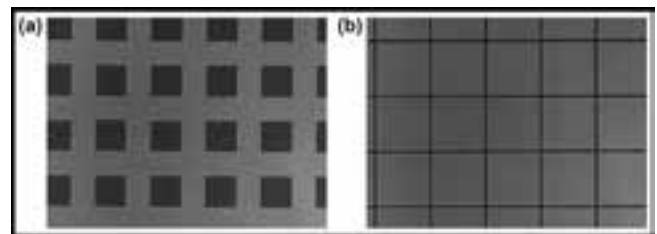


Figure 1: Microscope images of inductive (a) and capacitive (b) metal meshes fabricated by depositing 10 nm of gold on silicon.

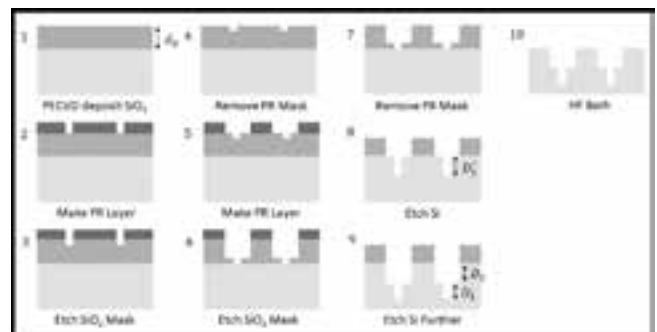


Figure 2: Process flow for fabricating a double-layer ARC on a silicon wafer. Grey represents the oxide. Dark grey represents the photoresist. Light grey represents the silicon wafer.

photoresist (AZ nLOF 2020) is exposed with the mesh pattern using an ABM contact aligner and then developed. The patterned resist is descummed using an Anatech resist strip. After that, 500 nm of gold are evaporated onto the patterned wafer using a CHA evaporator. Then the wafer is placed in a bath of Microposit 1165 remover and left for 24 hours to clean up the photoresist. Using contact lithography, feature sizes of 1  $\mu\text{m}$  can be achieved.

Figure 2 shows our current recipe for double-layer anti-reflection coatings. We start with depositing the silicon dioxide using an Oxford plasma-enhanced chemical vapor deposition (PECVD) tool. Then two photomasks are correspondingly patterned with oxide etch process in between to define the double-layer structure of anti-reflection coatings. The oxide etch process is achieved by a reactive ion etch tool Oxford 82 and those masks are removed using an Anatech resist strip. The lower layer is then etched using a Plasma-Therm deep silicon etcher. Besides, we add an external thermal oxidation step followed by a buffered oxide etch of hydrofluoric acid and an oxygen stripping step after each silicon etch to remove the passivation layer generated during silicon etch

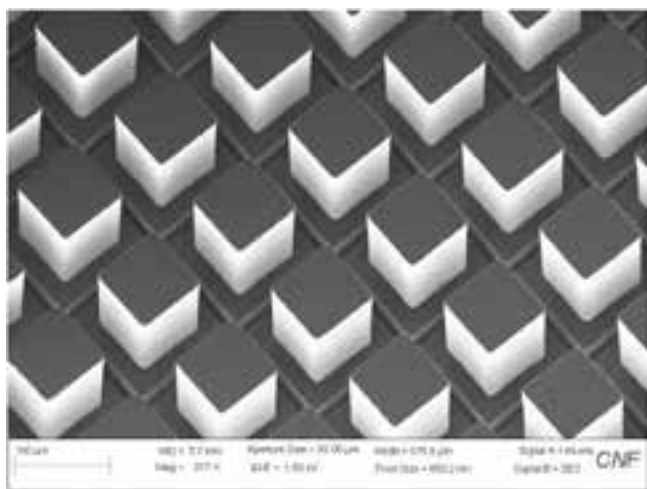


Figure 3: SEM image taken using CNF's Zeiss Ultra SEM showing successful fabrication of our two-layer metamaterial silicon anti-reflection coatings. (See cover.)

processes, which may form fence-like structure at the boundary of two silicon layers. Figure 3 shows an SEM image (taken by CNF's Zeiss Ultra SEM) of a successful result of this fabrication procedure.

The Fabry-Perot interferometers we have been developing will be used in the CCAT-prime telescope located at 5600 meters elevation on Cerro Chajnantor in the Atacama Desert in Chile [3]. One of the science goals of the CCAT-prime telescope is to study the Epoch of Reionization, a time around one billion years after the Big Bang when the first galaxies were assembling. The broad bandwidth of the silicon substrate Fabry-Perot interferometers can efficiently cover the far-IR frequencies required for an intensity mapping of the [CII] fine structure line to probe this era of the universe, and will provide information on the first star forming galaxies.

In the past year we have made great steps towards achieving our goals at CNF. We have demonstrated our ability to fabricate double-layer ARCs for different wavelengths and metal meshes with different feature sizes. We have used many of the fabrication and metrology tools at CNF. Our next steps are to better characterize our etched geometries and improve our metamaterial ARCs. We will be using Fourier transform spectrometers to measure our samples optical performance and using the results to iterate on our fabrication design.

#### References:

- [1] P.A. Gallardo, B.J. Koopman, N.F. Cothard, S.M.M. Bruno, G. Cortes-Medellin, G. Marchetti, K.H. Miller, B. Mockler, M.D. Niemack, G. Stacey, and E.J. Wollack, "Deep reactive ion etched anti-reflection coatings for sub-millimeter silicon optics," *Appl. Opt.* 56, 2796-2803 (2017).
- [2] N.F. Cothard, M. Abe, T. Nikola, G.J. Stacey, G. Cortes-Medellin, P.A. Gallardo, B.J. Koopman, M.D. Niemack, S.C. Parshley, E.M. Vavagiakis, and K. Vetter, "Optimizing the efficiency of Fabry-Perot interferometers with silicon-substrate mirrors," Presented at SPIE Advances in Optical and Mechanical Technologies for Telescopes and Instrumentation III (2018).
- [3] <http://www.ccatobservatory.org/>

# Fabricating All-Glass, 1 cm Diameter Metalens Working at Visible Wavelength

**CNF Project Number: 2471-16**

**Principal Investigator(s): Professor Federico Capasso**

**User(s): Joon-Suh Park**

*Affiliation(s): John A. Paulson School of Engineering and Applied Sciences, Harvard University*

*Primary Source(s) of Research Funding: Defense Advanced Research Projects Agency*

*Contact: capasso@seas.harvard.edu, parkj@g.harvard.edu*

*Website: <https://www.seas.harvard.edu/capasso>*

*Primary CNF Tools Used: Heidelberg DWL2000, Hamatech mask chrome etch 1, ASML 300C DUV stepper, Gamma automatic coat-develop tool, CVC sputter, CHA Mark 50 e-beam evaporator, Trion Minilock III ICP etcher, Oxford 81, Oxford 82, Oxford 100, P10 profilometer, Zeiss Ultra SEM*

## Abstract:

**Single-material, centimeter-scale metalens working in the visible wavelength is demonstrated in mass-manufacturing style. Using DUV stepper lithography, we show wafer-scale fabrication of a flat optical elements capable of diffraction-limited focusing at visible wavelength.**

## Summary of Research:

With the market growth of virtual reality (VR), augmented reality (AR), or mixed reality (MR) devices, aerial drone cameras, and on-board cameras for orbital satellites, the importance of payload for optical devices is evermore increasing. However, as such applications need large-aperture optics to meet its physical demands such as the size of the human eye's pupil, or to obtain better imaging in low-light conditions by increasing the amount of collected light. For conventional refractive optics, aperture size and the weight were in trade-off relations: The larger the aperture, the heavier the lens become at an undesirable rate. In addition, due to the nature of refractive optics where the optics relied on the refractive index of the lens material and its curvature at the material boundary, they were subject to spherical aberration (Figure 1). Such aberration was dealt with using expensive methods such as creating aspheric surfaces, cascading multiple lenses, choosing high-refractive materials, or using size-limiting variables such as using aplanatic point.

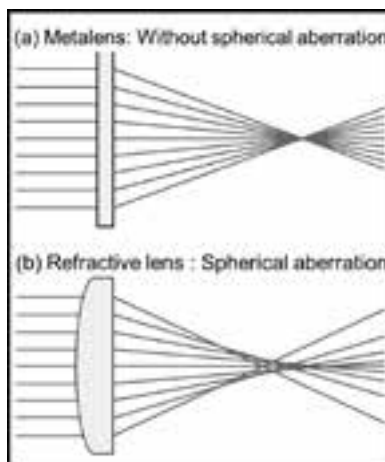


*Figure 1: Effect of spherical aberration to focusing profiles. (a) Metalens, without spherical aberration. (b) Refractive lens, with spherical aberration.*

In our previous reports [1,2], we have shown that metasurfaces, a new class of optics that rely on sub-wavelength structures capable of locally controlling the output phase, amplitude, and polarization, can pave way to an alternative solution for refractive optics. By placing sub-wavelength structures on a planar surface, one can design an optical component that resembles the functionality of a refractive optics counterpart. Many prior works presented in the field of metasurfaces used deposition of high-refractive index dielectrics, such as  $\text{TiO}_2$ ,  $\text{SiN}$ ,  $\text{GaN}$ , amorphous silicon, and such, to achieve such functionalities. In this research, we instead use fused silica ( $\text{SiO}_2$ ) wafer, a low-refractive index material, and demonstrate a metasurface lens (metalens) capable of focusing and imaging as a lens in the visible wavelength.

To fabricate such lens, we choose DUV (248 nm, KrF) stepper lithography so that we can create features smaller than the incident wavelength. At CNF, we use Heidelberg DWL 2000 mask writer to create a reticle of the metalens. After writing the mask design by exposing the photoresist with UV laser scanner on a chrome-coated quartz reticle blank, we develop the photoresist using Hamatech mask chrome etch 1. After optical inspection of the developed pattern on the reticle, we wet-etch the chrome layer with the patterned photoresist as etch mask. The reticle substrate is chosen to fit the ASML 300C DUV stepper.

The substrate on which the metalens is fabricated is chosen to be a 4-inch fused silica wafer, as most of the tools in CNF are set to work with 4-inch wafers. On top, we deposit a thin-layer of chrome, with either CVC sputter (decommissioned) or CHA Mark 50 e-beam evaporator. After coating AR3 ARC layer and DUV resist using GAMMA automatic coat-develop tool (GAMMA), we expose the substrate with the metalens pattern written on the reticle, using ASML 300C DUV stepper. The exposed wafer is then put through post-exposure bake, develop, rinse, and dry process with the GAMMA tool. After ensuring the focus-dose conditions with the DUV stepper, we perform descum and ARC layer etch using Oxford 81 or 82 etcher. Then, we transfer the pattern to the chrome layer by plasma etching, using Trion Minilock III ICP-etcher. When the metalens pattern is transferred to the chrome layer, we remove the DUV resist and the ARC layer using Oxford 81 or 82 etcher, using oxygen plasma. The  $\text{SiO}_2$  wafer is then plasma etched with the patterned chrome as etch mask, using Oxford 100 etcher until we reach the target etch depth. We inspect the fabrication results with P10 profilometer and Zeiss Ultra SEM. The fabrication of the metalens is completed when we then remove the chrome layer, leaving only  $\text{SiO}_2$  pattern (Figure 2). From our measurements, we observe that the fabricated metalens show diffraction-limited focusing in the visible wavelength (Figure 3), and high-quality imaging properties.

The results of this research are being prepared for publication.

## References:

- [1] A. She, S. Zhang, S. Shian, D.R. Clarke, and F. Capasso, "Large area metalenses: design, characterization, and mass manufacturing," *Opt. Express* 26, 1573-1585 (2018).
- [2] M. Khorasaninejad, W.T. Chen, R.C. Devlin, J. Oh, A.Y. Zhu, and F. Capasso, "Metalenses at visible wavelengths: Diffraction-limited focusing and subwavelength resolution imaging," *Science* 352, 1190 (2016).

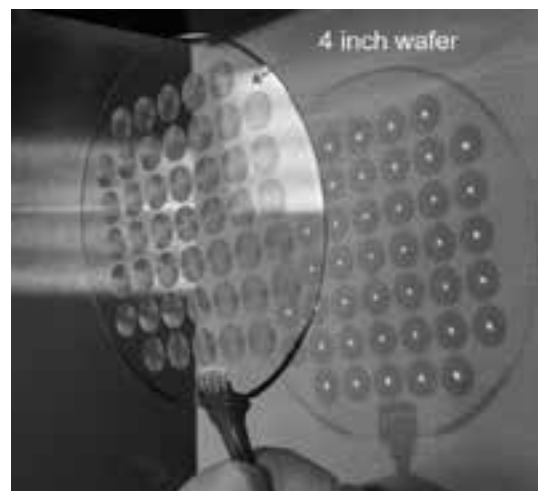


Figure 2: Photograph of fabricated metalens with diameter of 1 cm, on a 4-inch fused silica wafer.

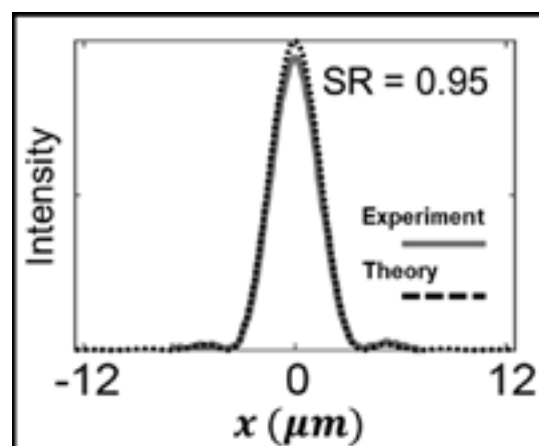


Figure 3: Focusing profile of the metalens.

# Metasurface-Based Infrared Optical Devices

**CNF Project Number: 2472-16**

**Principal Investigator(s): Gennady Shvets**

**User(s): Melissa Bosch, Minwoo Jung, Maxim Shcherbakov**

*Affiliation(s): School of Applied and Engineering Physics, Department of Physics; Cornell University*

*Primary Source(s) of Research Funding: Office of Naval Research (ONR) and National Science Foundation (NSF)*

*Contact: gs656@cornell.edu, mb2583@cornell.edu, mj397@cornell.edu, mrs356@cornell.edu*

*Website: <http://shvets.aep.cornell.edu>*

*Primary CNF Tools Used: JEOL 9500, CVC SC4500 evaporator, Zeiss Supra SEM*

## Abstract:

Planar metamaterials, or metasurfaces, provide strong and resonant light modulations both in near- and far-fields. We engineer several metasurface structures for near-to mid-infrared photonic applications. A plasmonic metasurface, for example, can be integrated with graphene to greatly enhance the absorption of incident radiation into graphene through ultrahigh field enhancement at its resonance. On the other hand, we also exploit low-loss dielectric metasurfaces with thermally tunable resonances to demonstrate tunable polarization control. These metasurface-based approaches are scalable and space-efficient, thereby promising versatile platforms for ultrathin optical devices.

## Summary of Research:

### High-Gain and High-Speed Mid-Infrared Graphene Photodetector with Plasmonic Metasurfaces.

Graphene, owing to its gapless and semi-metallic electronic dispersion, is a broadband photo-diode, and graphene photodetectors can be in principle operated at ultrahigh speeds up to hundreds of gigahertz thanks to its linear Dirac electrons traveling at a relatively high Fermi velocity [1]. High-gain operation, however, is not guaranteed in graphene itself due to its monolayer nature and weak absorption. Strong field enhancement via resonant metasurfaces can increase the absorption into graphene by an order of magnitude without sacrificing high-speed capability [2]. We aim for even more efficient high-gain configuration, by using the metasurface structures themselves as the electrodes—source and drain—of the photodetector. In this way, the gain is enhanced not only due to the plasmonic resonances, but also by reducing the distance that the photo-generated carriers travel to get to the electrodes.

Furthermore, as seen in Figure 1, the source and the drain are interdigitated, thus increasing the photo-absorption area by a factor of the number of metasurface unit cells. The device is fabricated in a total of five e-beam lithography steps: (1) alignment marks, (2) graphene patterning, (3) source deposition, (4) drain deposition, and (5) contact pads deposition. The source and the drain are deposited in separate steps for introducing different materials (Ti and Pd) for the adhesion layer between graphene and gold. Two different contact metals dope graphene at slightly different Fermi levels, enabling

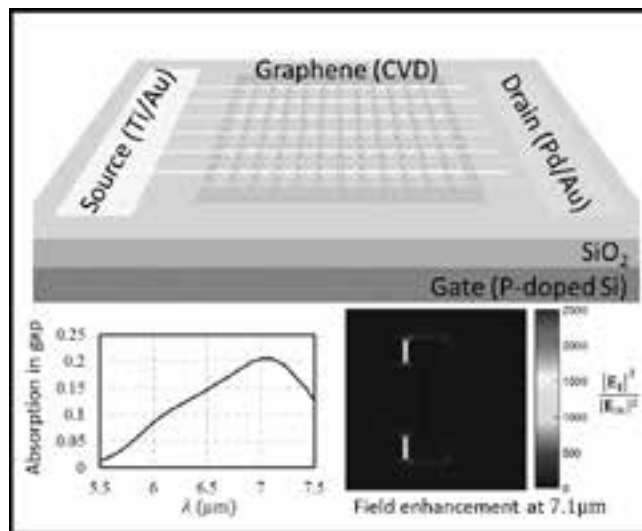


Figure 1: Top, Schematic of graphene photodetector integrated with a plasmonic metasurface. Bottom Left, Absorption of mid-infrared radiation into graphene in the gap region between the source and drain. Bottom Right, Field enhancement at the plasmonic resonance.

photo-voltaic mode operation at zero source-drain bias voltage.

Figure 2 shows an SEM image zoomed on a gap between the source and the drain. The fabricated device is currently under electrical and optical characterization. Our simulation predicts a photocurrent of  $\sim 0.1\text{A/W}$  at the resonance.

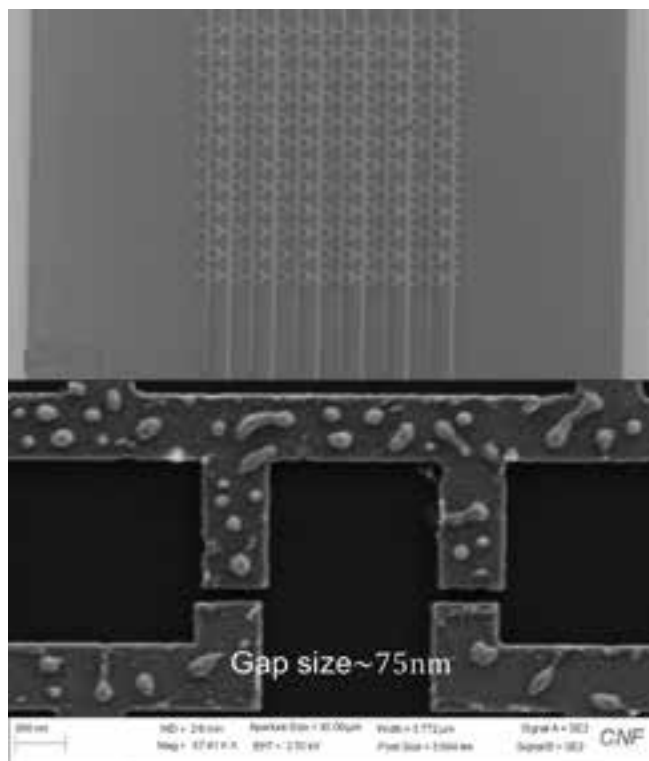


Figure 2: Top, Fabricated device imaged under optical microscope. Bottom, SEM image zoomed on a gap between the source and the drain.

**Polarization States Synthesizer Based on a Thermo-Optic Dielectric Metasurface.** The dynamic control of light polarization is ubiquitous to free-space and integrated photonics applications. Low-loss dielectric metasurfaces have recently emerged as an attractive platform for efficient polarization synthesizers, however most implementations exhibit static functionalities. Germanium (Ge), one of the most promising materials for nanophotonics [3] due to its infrared transparency and high refractive index, also has one of the largest thermo-optic coefficients in the mid-infrared range [4].

In our work, we exploit the thermo-optic properties of germanium to demonstrate a resonant dielectric metasurface that acts as a thermally-actuated polarization state generator. This is accomplished through the design of a germanium-based anisotropic resonant metasurface (ARM) which supports a spectrally-sharp (high- $Q$ ) resonance that can be excited by one of the principal linear polarizations of incident light. Enabled by the high thermo-optic coefficient of germanium, the central frequency of the high- $Q$  mode can be adjusted by almost its bandwidth within a 100°C window. Due to the anisotropic nature of the mode, light that is initially linearly polarized becomes elliptically polarized upon transmission through the ARM, with a polarization state that can be widely tuned by heating the sample. For device fabrication, we use the following procedure: a standard two-layer PMMA spin-coat, baking, and e-beam

exposure at 1000  $\mu\text{C}/\text{cm}^2$  (JEOL 9500); development in MIBK:IPA 1:3 for 90s; e-beam evaporation of 300 nm of Ge (CVC SC4500), and liftoff in room-temperature sonicated acetone for 60s.

Figure 3 presents an SEM image of the fabricated metasurface and its temperature-dependent transmittance spectra. An example of the experimental thermal polarization tuning is shown in Figure 4; by varying both temperature and the polarization angle of incident light, we find the full polarization tuning range of the device covers near 40% of the upper Poincare hemisphere surface.

### References:

- [1] Photodetectors based on graphene, other 2D materials and hybrid systems. F. Koppens, T. Mueller, P. Avouris, A. Ferrari, M. Vitiello and M. Polini; *Nature Nanotechnology* 9, 780-793 (2014).
- [2] High-Responsivity Mid-Infrared Graphene Detectors with Antenna-Enhanced Photocurrent Generation and Collection. Y. Yao, R. Shankar, P. Rauter, Y. Song, J. Kong, M. Loncar, and F. Capasso; *Nano Letters* 14(7), 3749-3754 (2014).
- [3] Mid-infrared photonics in silicon and germanium. Soref, Richard; *Nature photonics* 4.8 (2010): 495.
- [4] Temperature-dependent refractive index of silicon and germanium. Frey, B.J., D.B. Leviton, and T.J. Madison; *Optomechanical technologies for Astronomy*. Vol. 6273. International Society for Optics and Photonics, 2006.

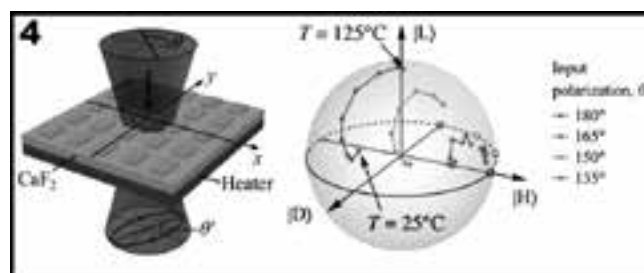
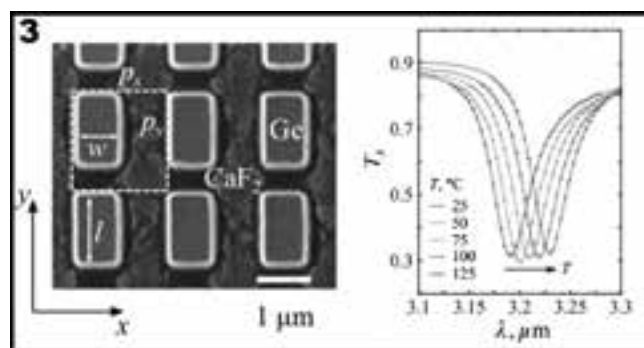


Figure 3, top: Left, An SEM image of the fabricated metasurface. Right, Experimental temperature-dependent mid-IR transmittance spectra of the metasurface, with  $Q$ -factor near 70.

Figure 4, bottom: Left, Schematic depicting the temperature-tunable polarization conversion of light transmitted through the ARM. Right, A Poincare sphere depicting the maps of experimental polarization modulation by the metasurface at a wavelength of 3.21  $\mu\text{m}$ , corresponding to the maximum Poincare sphere coverage. Individual curves describe the transformation of the transmitted polarization state with increasing metasurface temperature for different incident polarizations.

# Exploratory Etching and Electrodeposition Project

**CNF Project Number: 2527-17**

**Principal Investigator(s): Dr. David Crouse**

**User(s): Golsa Mirbagheri**

*Affiliation(s): Electrical and Computer Engineering Department, Clarkson University*

*Primary Source(s) of Research Funding: CFM, Clarkson University*

*Contact: dcrouse@clarkson.edu, mirbagg@clarkson.edu*

*Primary CNF Tools Used: Oxford 82, Oxford 100, ASML, Gamma, PECVD, Cobra*

## Abstract:

**This project is a continuing project. We will be finishing the fabrication of the hyperbolic metamaterial structure and designing a 2<sup>nd</sup> generation of the filter that uses more of a photonics crystal resonant material within a Bragg stack. Both the hyperbolic metamaterial structure and the 2<sup>nd</sup> generation devices have compelling properties. Both show very little dispersion — meaning that their performance is not affected by the angle of incidence to the optical signal.**

## Project Description:

During the last year, we have further designed the hyperbolic metamaterial device and have performed much more optimization and have taken into account practical design considerations. We are now fabricating the structure at the Cornell NanoScale Science and Technology Center (CNF). We have developed a fabrication plan and are now implementing the plan, with masks designed and fabrication processes in development. Based on what we have learned, we are now investigating a 2<sup>nd</sup> generation device that does not use metal wires, but uses resonant cavities in the three middle layers of the Bragg stack.

The resulting structure will have far less polarization dependence, will absorb less radiation, will be far easier to fabricate and manufacture, and will have a larger tuning range that allows for it to be used within pixelated wavelength filters for hyperspectral imaging applications.

We have been performing preliminary testing on the resonant cavities and have a preliminary design for operation in the midwavelength infrared range of 3-5  $\mu\text{m}$ . The Bragg stack will use silicon and silicon dioxide, and potentially silicon nitride — all CMOS compatible devices — as well as having all structure features with sizes amenable to optical lithography.

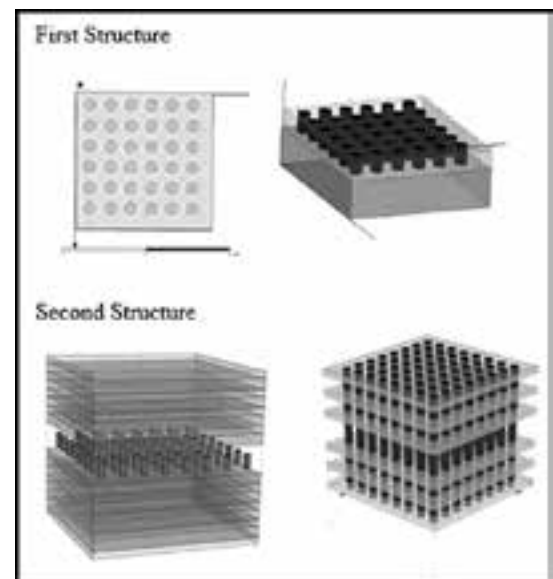


*Figure 1: First Structure: The 1.5  $\mu\text{m}$   $\text{SiO}_2$  film was deposited, patterned and etched. The holes were 0.5  $\mu\text{m}$ , electroplated with Cu. Second Structure: Alternative layers of  $\text{SiO}_2$  and Si are deposited, patterned and etched (all through the layers), then holes electroplated with Cu.*



# Metamaterial Spectrometer: A Low SWaP, Robust, High Performance Hyperspectral Sensor for Land and Atmospheric Remote Sensing

**CNF Project Number: 2661-18**

**Principal Investigator and User(s): Lori Lepak**

**Affiliation(s): Phoebus Optoelectronics LLC**

*Primary Source(s) of Research Funding: NASA*

*Contact: llepak@phoebusopto.com*

*Website URL (Optional): www.phoebusopto.com*

*Primary CNF Tools Used: DWL2000 photomask writer, ASML stepper, JEOL 9500 e-beam lithography, AJA sputter, Oxford PECVD, SC4500 evaporators, Oxford Cobra etcher, Oxford 81 etcher, Trion etcher, CMP, SEM, Woolam ellipsometer, DISCO dicing saw*

## Abstract:

Since 2003, Phoebus Optoelectronics has enabled custom R&D solutions in the fields of Plasmonics, Metamaterials, Antennas, and Sensors. We work closely with our customers throughout device development, from prototype realization to small volume manufacturing. Our R&D portfolio spans the spectral ranges of visible light, infrared, terahertz, and microwave radiation, for applications in high resolution infrared imaging systems, wavelength and polarization filtering, tunable optical components, beam forming and steering, solar cells and renewable energy devices, and chemical and biological toxin sensors. Our agile team makes extensive use of the resources at the CNF for our nano/micro fabrication and testing, to provide cost efficiency and rapid turnaround. In the present report, we discuss the ongoing development of a metamaterial-based hyperspectral imaging filter.

## Summary of Research:

Phoebus uses the resources of the CNF to fabricate plasmonic chips patterned with a metamaterial surface to enable Extraordinary Optical Transmission (EOT), a phenomenon unique to metastructures in which light is transmitted through apertures much smaller than the incident wavelength, at anomalously large intensities relative to the predictions of conventional aperture theory. EOT was first observed by T.W. Ebbesen in 1998 [1]. Since its founding in 2003, Phoebus has successfully harnessed EOT by incorporating metasurfaces into devices used to perform light filtering [2-3], photon sorting [4-5], polarimetric detection [6], high speed optical detection [7], and most recently, in our SPR plasmonic sensor chips [8].

Examples of metastructured optical devices previously fabricated by Phoebus at CNF are shown in Figures 1-3. In our first-generation IR polarimeter (Figure 1), which is currently commercially available, each pixel has four arrays of wires oriented at 0°, 45°, 90°, and 135° to each other. Each array is capable of acting as a graded index lens, to focus and collimate transmitted light. At the same time, the phase delay produced by the four arrays together allow the pixel as a whole to behave as a polarizer to control the phase of the light. A higher magnification image of a typical array (Figure 2) illustrates the high aspect ratios and smooth sidewalls which are essential

for the high-quality performance of our metasurface structures. A second generation of this design, which was fabricated by electron beam lithography and tailored to operate at a shorter wavelength, is shown in Figure 3.

In our current project, we are developing a hyperspectral imaging system, shown schematically in Figure 4. Our technology (Figure 4b) uses a metasurface to precisely target very narrow spectral bands of interest, enabling a significant reduction in the size and number of optical components relative to current state-of-the-art imaging systems (Figure 4a), which in turn will enable integration of our high-performance sensor onto weight-sensitive platforms (ie. satellites) far more readily than existing systems. The goal of our initial application is to detect and image trace gases in the Earth's atmosphere in the midwave infrared (MWIR) region, with a reduction to adjacent channel latency of less than 10 ms. In planned future research, the overall metasurface technology can be easily adapted to other spectral ranges, from the visible to the microwave, by substituting appropriate materials (most of which can be deposited in the CNF), and scaling feature sizes of the metastructures in proportion to the desired wavelength of imaging. Thus, our versatile Metamaterial Spectrometer technology is expected to be applicable to a much broader range of imaging and sensing applications.

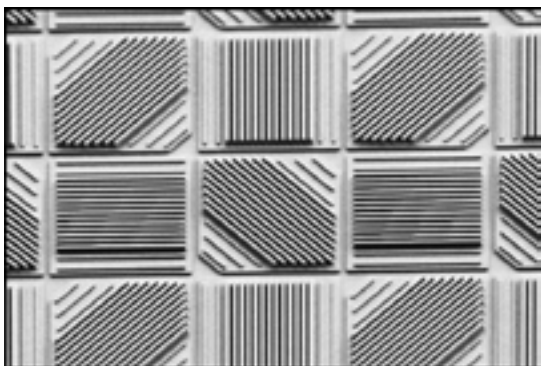


Figure 1: SEM image of metasurface-based IR polarimeter, currently commercially available from Phoebus, and initially developed at CNF using the ASML DUV stepper.

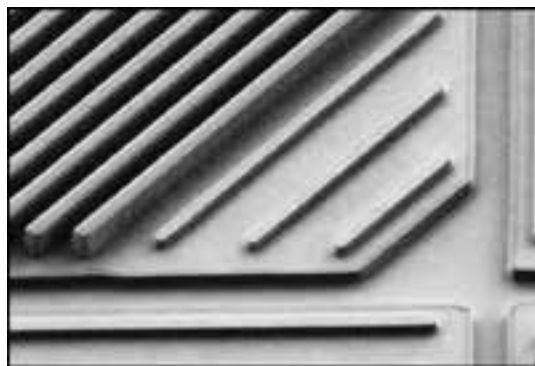


Figure 2: A single sub-pixel at higher magnification. These high aspect ratio features with smooth sidewalls were fabricated at CNF using the ASML DUV stepper and dry etch tools.

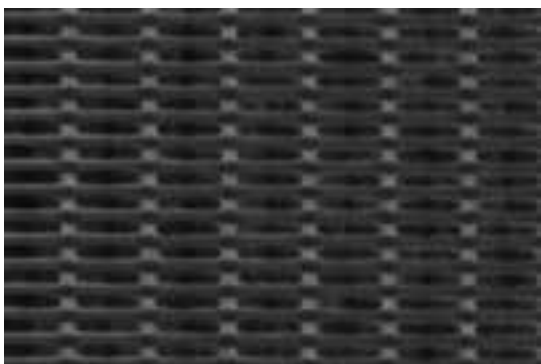


Figure 3: SEM image of another focusing polarimeter device developed by Phoebus at CNF, fabricated using the JEOL 9500 e-beam lithography system.

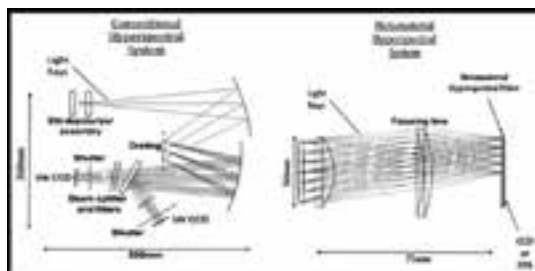


Figure 4: Phoebus's Metamaterial Spectrometer (MS) technology eliminates much of the size and weight of current hyperspectral spectrometer technologies.

## References:

- [1] Ebbesen, T.W., et al., "Extraordinary optical transmission through sub-wavelength hole arrays." *Nature*, 391(6668): p. 667-669 (1998).
- [2] Crouse, D. "Numerical modeling and electromagnetic resonant modes in complex grating structures and optoelectronic device applications." *Electron Devices, IEEE Transactions on* 52.11: 2365-2373 (2005).
- [3] Crouse, D., and Keshavareddy, P. "Polarization independent enhanced optical transmission in one-dimensional gratings and device applications." *Optics Express* 15.4: 1415-1427 (2007).
- [4] Lansy, E., Crouse, D., et al. "Light localization, photon sorting, and enhanced absorption in subwavelength cavity arrays." *Optics Express* 20.22: 24226-24236 (2012).
- [5] Jung, Y.U.; Bendoyim, I.; Golovin, A.B.; and Crouse, D.T. "Dual-band photon sorting plasmonic MIM metamaterial sensor." *Proc. SPIE 9070, Infrared Technology and Applications XL, 90702X*; doi:10.1117/12.2050620 (June 24, 2014).
- [6] Crouse, D., and Keshavareddy, P. "A method for designing electromagnetic resonance enhanced silicon-on-insulator metal-semiconductor-metal photodetectors." *Journal of Optics A: Pure and Applied Optics* 8.2: 175 (2006).
- [7] Mandel, I.; Gollub, J.; Bendoyim, I.; Crouse, D. Theory and Design of A Novel Integrated Polarimetric Sensor Utilizing a Light Sorting Metamaterial Grating. *Sensors Journal, IEEE: Vol. PP, 99* (2012).

# Ion Mill X-Ray Reflection Gratings

**CNF Project Number: 2692-18**

**Principal Investigator(s): Randall McEntaffer**

**User(s): Drew Miles**

*Affiliation(s): Astronomy and Astrophysics, The Pennsylvania State University*

*Primary Source(s) of Research Funding: National Aeronautics and Space Administration*

*Contact: rlm90@psu.edu, dmiles@psu.edu*

*Primary CNF Tools Used: AJA ion mill, Zeiss Ultra/Sigma SEMs*

## Abstract:

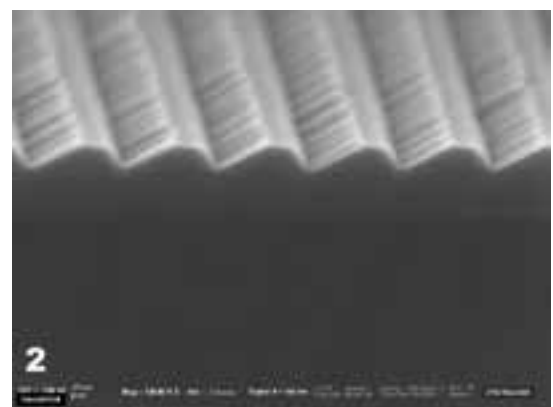
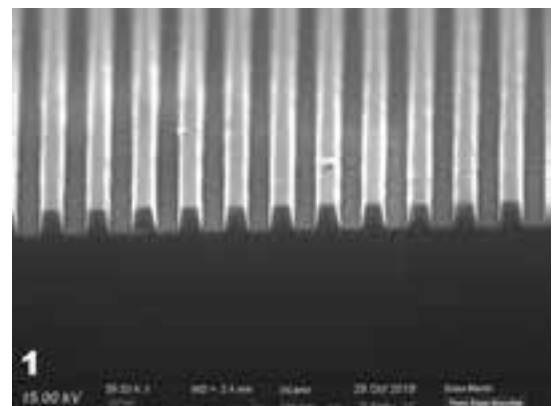
Astronomical x-ray diffraction gratings are a key technology under development for current and future NASA missions. X-ray reflection gratings, developed at Penn State University, have recently demonstrated both leading diffraction efficiency and high spectral resolving power. However, recent results are the result of different fabrication techniques and a single technique has not yet been developed to yield a grating that satisfies both the diffraction efficiency and resolving power required by future missions. Here we seek to leverage existing electron-beam lithographic techniques to produce a grating with a groove pattern capable of high resolving power. We then introduce ion-milling techniques to create custom groove profiles capable of high diffraction efficiency. The goal is to produce a radial groove pattern with precisely blazed facets that are customizable based on ion mill input parameters. The process should be insensitive to groove density (ranging from  $\sim 150$  nm to 400+ nm), facet size, and desired facet angle. Initial efforts in this study have concentrated on constraining various parameters in ion milling to fully characterize the effect of each parameter on the grating groove profile. We present here initial results and discuss experimental verification and future work.

## Summary of Research:

The research performed at the Cornell NanoScale Facility utilizes state-of-the-art x-ray gratings fabricated at Penn State University. The Penn State grating samples, which have a rectangular or sinusoidal groove profile as depicted in Figure 1, are transported to Cornell for directional ion beam etching using the AJA ion mill. The ion mill etches the gratings in an effort to convert the rectangular/sinusoidal grooves to a more triangular or sawtooth profile. The exact angle and dimensions of the triangular grooves depend on specific grating applications. Figure 2 shows an ion milled grating that has a facet angle of  $\sim 30$  degrees and groove spacing of  $\sim 170$  nm. The ideal grating facet would come to a sharp point, whereas the grating in Figure 2 has a plateau that is  $\sim 30$  nm wide; the plateau is the result of non-optimized fabrication conditions and represents a snapshot of the ongoing development of these processes.

*Figure 1, top right: An x-ray reflection grating with rectangular grooves. This grating is an example of a grating developed for ion milling.*

*Figure 2, bottom right: An x-ray reflection grating that has been exposed to the ion beam in the AJA ion mill. The formerly rectangular facets are now etched to the desired angle ( $\sim 30^\circ$ ). The plateau at the top of the features represents a shortcoming in development and will be eliminated by the culmination of the project.*





# Spin-Orbit Torque Switching of Magnetic Tunnel Junctions by Oxide Material

**CNF Project Number: 111-80**

**Principal Investigator(s): Robert A. Buhrman**

**User(s): Arnab Bose**

*Affiliation(s): Applied and Engineering Physics, Cornell University*

*Primary Source(s) of Research Funding: Department of Defense-Intelligence Advanced Research Projects Activity*

*Contact: buhrman@cornell.edu, ab2729@cornell.edu*

*Primary CNF Tools Used: 5x stepper, AJA sputtering, ASML, JEOL 6300, Oxford*

## **Abstract:**

Generation of spin-orbit torques (SOT) has remained one of the major aspects of spintronics for the past decade [1]. It has been shown that SOT can be efficiently created by the heavy metals such as Pt, Ta, W [1] and with their alloys [1]. It can be useful for magnetic memory application [1-2]. We recently studied SOT in oxide-based systems such as SrRuO<sub>3</sub> [2], IrO<sub>2</sub>, etc. We aimed to implement switching of magnetic tunnel junctions (MTJ) using the intrinsic spin Hall effect of oxide materials.

## **Summary of Research:**

To quantify SOT, the spin torque ferromagnetic resonance (ST-FMR) technique is used [1]. Basic device structure of an ST-FMR device and an MTJ are shown below (Figures 1 and 2). ST-FMR devices are fabricated by two-step optical lithography processes. Initially optical lithography is done on a film consisting of a ferromagnet/non-magnet bi-layer, followed by Ar-ion milling and lift off process. Another step of optical lithography is done to make contact pads on the small micron size devices, which also involves sputtering and lift-off process. The CNF 5x stepper is used for optical lithography and contact metallization is done by CNF-AJA sputtering instrument. MTJ fabrication is very complex and involves many steps — i.e. sputtering the MTJ film --> optical lithographys to make the channel (ASML) --> etching the channel --> lift off the resist --> electron-beam lithography (JEOL 6300)+plasma etching (Oxford) to make a pattern of the MTJ pillar on the channel --> selective Ar-ion etching to remove other material apart from the non-magnetic base or heavy metal --> SiO<sub>2</sub> evaporation (even hour evaporator) --> lift off the resist --> final layer of optical lithography (ASML) for contact pad patterning --> sputtering Ti(5nm)/Pt(60nm) by AJA at CNF --> lift off.

Characterization of the device fabrication is monitored by tapping mode AFM to confirm the existence of the channel and the pillar. Detailed method of the device fabrication can be found in reference [1]. Our devices are aimed to operate for fast and reliable magnetic memory application.

## **References:**

- [1] L. Liu, et al., Science 336, 555 (2012) and citations of this paper.
- [2] Y. Ou, et al., NanoLetters 19, 63663-3670 (2019).

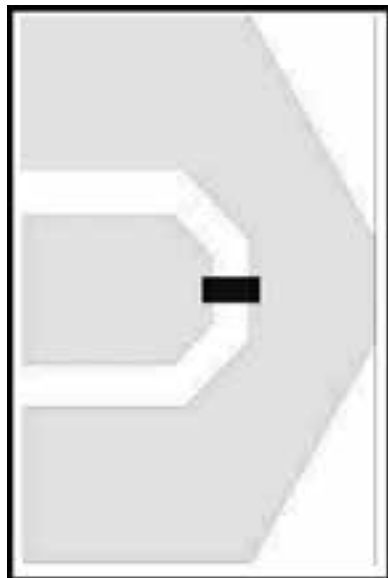


Figure 1: Schematics of an ST-FMR device.

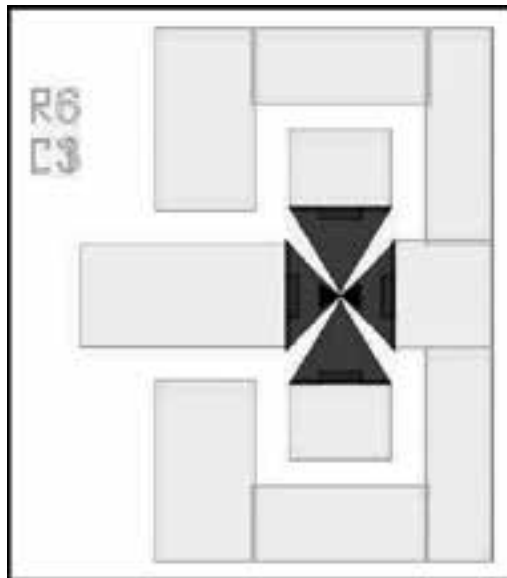


Figure 2: Schematics of an MTJ.

# Reducing Write Current of Three Terminal Magnetic Tunnel Junctions by Engineering the Spin Hall Channel Structures

CNF Project Number: 111-80

Principal Investigator(s): Robert A. Buhrman

User(s): Shengjie Shi

Affiliation(s): Applied and Engineering Physics, Cornell University

Primary Source(s) of Research Funding: Department of Defense -Intelligence Advanced Research Projects Activity

Contact: buhrman@cornell.edu, ss2882@cornell.edu

Primary CNF Tools Used: ASML, JEOL e-beam 6300FS, Veeco AFM

## Abstract:

Three terminal magnetic tunnel junctions (MTJs) are very good candidates for future cache memory applications due to their low energy consumption, fast switching characteristics, and reliable operation. To demonstrate the practicality of these structures being used in high density memory arrays, further reduced switching current is desired. In this report we show that by re-designing the layout of the spin Hall channel that is used to supply spin current that switches the MTJs, we can obtain significant reduction in switching voltage thanks to a dramatic decrease in the channel resistance caused by shortened length and a faster spread-out.

## Summary of Research:

One of the key advances in magnetic memory technologies is the utilization of the giant spin Hall effect to switch a nanomagnet free layer in a magnetic tunnel junction (MTJ) structure. Due to the separate read and write channel, different aspects of the device can be engineered independently to satisfy different needs. We have shown that the reduction of  $M_{eff}$  in the free layer can effectively reduce the switching current in the MTJs [1]. Another critical element of the MTJs is the spin Hall channel on which the switching voltage is applied where  $V = I \cdot R_{channel}$ . In order to further reduce the  $V$  needed to operate these MTJs, we now design a shorter and narrower channel that can scale down the  $R_{channel}$  significantly (Figure 1) with the accurate exposure from the ASML. This has enabled lower  $V_{c0}$  compared to previously reported for similar structures [2]. Excellent write error rate shows that these devices can be reliably used with infinite endurance, which is advantageous over other type of emerging memory technologies (Figure 2).

## References:

- [1] Shengjie Shi, Yongxi Ou, S. V. Aradhya, D. C. Ralph and R.A. Buhrman, Fast Low-Current Spin-Orbit-Torque Switching of Magnetic Tunnel Junctions through Atomic Modifications of the Free-Layer Interfaces. *Phys. Rev. Applied.* 9, 011002 (2018).
- [2] Aradhya, S. V., Rowlands, G. E., Oh, J., Ralph, D. C., and Buhrman, R. A. Nanosecond-Timescale Low Energy Switching of In-Plane Magnetic Tunnel Junctions through Dynamic Oersted-Field-Assisted Spin Hall Effect. *Nano Lett.* 16, 5987-5992 (2016).

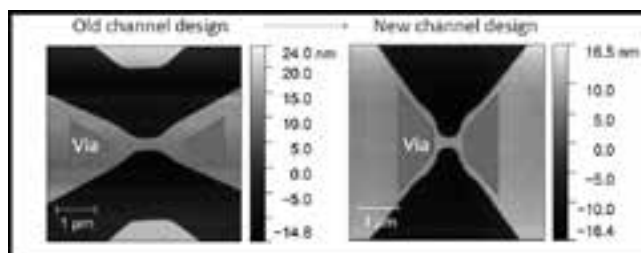


Figure 1: Schematic picture of the difference in the channel design.

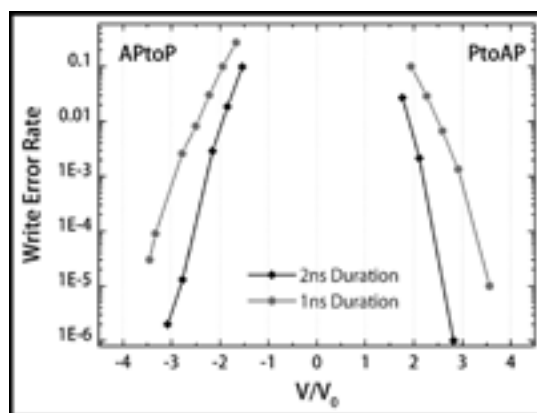


Figure 2: Write error rate measurement on a typical device made with the new mask design.



# Spin Currents and Spin Fluctuations in $\text{Fe}_x\text{Pt}_{1-x}$ Alloys and Heterostructures

CNF Project Number: 111-80

Principal Investigator(s): Robert A. Buhrman

User(s): Ryan Tapping

Affiliation(s): Applied and Engineering Physics, Cornell University

Primary Source(s) of Research Funding: The Office of Naval Research, Cornell Center for Materials Research, National Science Foundation

Contact: buhrman@cornell.edu, rct76@cornell.edu

Primary CNF Tools Used: GCA 5x stepper, AJA sputtering tool

## Abstract:

The spin Hall effect (SHE) is the conversion of a longitudinal charge current to a transverse spin current, often attributed to spin-orbit coupling. The magnetization of a thin film can be manipulated by spin-orbit torques (SOTs) generated by the SHE in an adjacent metallic layer, which has many promising applications in spintronics. Most research studying SOTs has focused on heavy metals such as Ta, Pt, and  $\beta$ -W, and more recently in alloys with other non-magnetic elements such as PtAu [1]. However, SOTs in systems with magnetic elements is not well understood. Recently it has been shown that the SOTs have a strong temperature dependence in  $\text{Fe}_x\text{Pt}_{1-x}$  alloys [2]. The strength of the SHE in these ferromagnetic alloys, as measured through the damping-like spin torque efficiency, are enhanced near the Curie temperature, where there are strong spin fluctuations. We also look at the results of Fe/Pt multilayer heterostructures, where the strength of the magnetism can be adjusted by tuning the thicknesses of the ferromagnetic and heavy metal layers. Additionally, our work is continued to show that the Curie temperature can be tuned to be above room temperature, at working temperatures for possible computing applications.

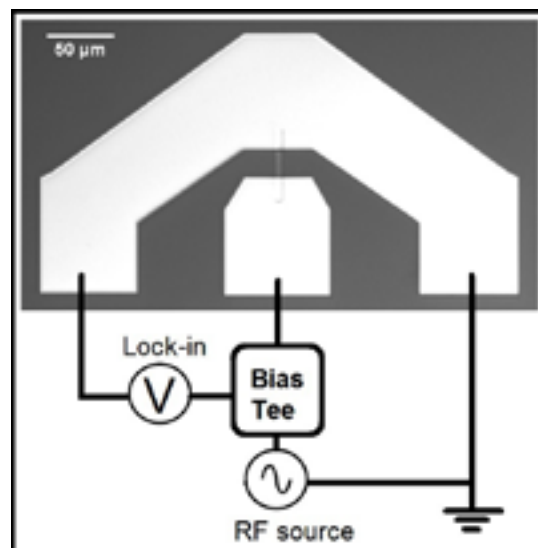


Figure 1: Microstrip after fabrication with top contacts and a schematic of the ST-FMR measurement.

## Summary of Research:

Thin film samples were deposited onto 100 mm silicon wafers using our magnetron sputtering system. Structures were composed of, from bottom to top, Ta(1)/ $\text{Fe}_x\text{Pt}_{1-x}$ (4)/FM(t)/MgO(2)/Ta(1) with numbers in parenthesis representing the thickness of the layer in nanometers and t, the thickness of the ferromagnetic layer (FM). Stacks were then patterned into  $60 \times 5 \mu\text{m}^2$  microstrips using photolithography with the 5X g-line stepper at CNF and etched using our own ion milling system. The contacts were made using the AJA sputtering system at CNF.

Resistivity measurements, using a four probe method, showed that the FePt resistance increased with Fe concentration. Resistivities ranged from  $40 \mu\Omega\cdot\text{cm}$  for pure Pt films to 88 and  $101 \mu\Omega\cdot\text{cm}$  for  $\text{Fe}_x\text{Pt}_{1-x}$  films with  $x = 0.23$  and  $0.35$ , respectively. This result is in agreement with previous reports and is indicative of the FM scattering impurities in the FePt [2]. Using Co as the FM layer, along with 0.4 nm of Pt spacer between the FePt and Co, the stacks have induced perpendicular magnetic anisotropy (PMA). When using FeCoB as the FM layer, the samples have in-plane anisotropy.

These two structures allow for different, independent measurements of the spin torque efficiency.

The spin torque efficiency ( $\xi$ ) in the in-plane samples was determined using spin-torque ferromagnetic resonance (ST-FMR) [3]. This technique works by driving a microwave frequency (RF) current through the microstrip, which induces magnetic precession in the ferromagnetic layer via the spin transfer torque. A magnetic field is swept at  $45^\circ$  to the microstrip and the voltage is measured by a lock-in amplifier. A lineshape analysis is done by fitting a Lorentzian function with symmetric (S) and antisymmetric (A) components as shown in Figure 2. The ratio of the prefactors S and A yield  $\xi_{\text{FMR}}$ . By fitting  $1/\xi_{\text{FMR}}$  vs  $1/t$ , the damping-like ( $\xi_{\text{DL}}$ ) and field-like ( $\xi_{\text{FL}}$ ) spin torque efficiencies can be extrapolated.

Additionally PMA samples with cobalt as the FM layer were measured using an out-of-plane second harmonic technique [4]. Measurements of the resistance of the microstrips as an in-plane field is swept can yield information about the anisotropy field. Then second harmonic measurements of the resistance and fields are swept parallel and perpendicular to the applied current yield information about  $\xi_{\text{DL}}$  and  $\xi_{\text{FL}}$  through effective field determinations.

We observe that  $\xi_{\text{DL}}$  and  $\xi_{\text{FL}}$  are in the FePt alloys having a large temperature dependence, specifically near the Curie temperature ( $T_c$ ). As shown in Figure 3 (published [2]), a large increase in the effective fields,  $H_{\text{DL}}$  and  $H_{\text{FL}}$  occurs near the ferromagnetic transition and the peak values are measured just above the Curie temperature, for two samples of different Fe concentration.

These results pave the way for future research and potential application of ferromagnetic systems with strong spin-orbit coupling and spin fluctuations.

## References:

- [1] L. Zhu, D.C. Ralph, and R.A. Buhrman, Phys. Rev. Applied 10, 031001 (2018).
- [2] Y. Ou, D. C. Ralph, and R. A. Buhrman, Phys. Rev. Lett. 120, 097203 (2018).
- [3] Chi-Feng Pai, Yongxi Ou, Luis Henrique Vilela-Leão, D.C. Ralph, and R.A. Buhrman, Phys. Rev. B. 92, 064426 (2015).
- [4] M. Hayashi, J. Kim, M. Yamanouchi, and H. Ohno, Phys. Rev. B 89, 144425 (2014).

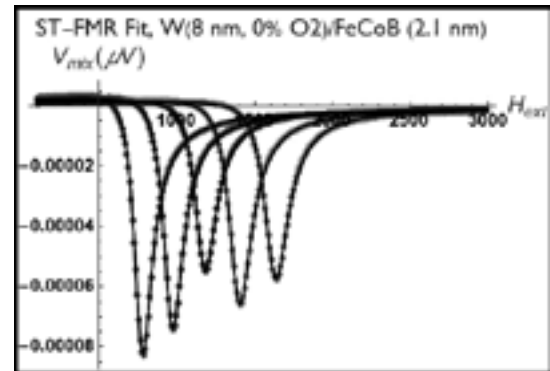


Figure 2: Example of voltage output from a magnetic field sweep from ST-FMR. Fits are also shown at 8, 9, 10, 11, and 12 GHz frequencies.

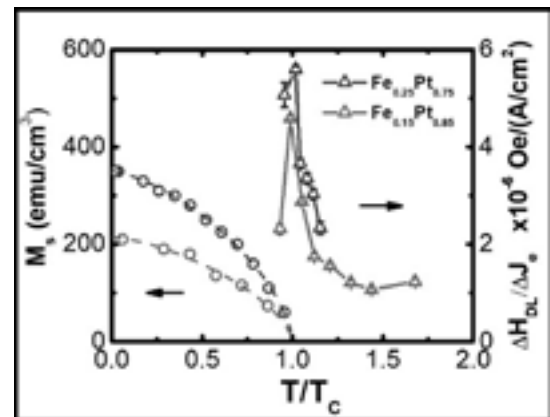


Figure 3: The temperature dependent magnetizations are plotted on the left for  $\text{Fe}_{0.15}\text{Pt}_{0.85}$  and  $\text{Fe}_{0.25}\text{Pt}_{0.75}$  samples, as a function of normalized temperature to the Curie temperature ( $T/T_c$ ). Damping-like effective fields are plotted on the right as a function of normalized temperature, with a large enhancement observed near  $T_c$ .

# Non-Local Spin Transport in Complex Oxide Thin Films

CNF Project Number: 598-96

Principal Investigator(s): Daniel Ralph

User(s): Ruofan Li, Tianxiang Nan

Affiliation(s): Physics, Cornell University

Primary Source(s) of Research Funding: Army Research Office (W911NF-15-1-0447)

Contact: dcr14@cornell.edu, rl643@cornell.edu, tn272@cornell.edu

Primary CNF Tools Used: JEOL JBX-6300FS 100 kV electron-beam lithography system, scanning electron microscope, Veeco Icon atomic force microscope for high resolution profilometry

## Abstract:

Magnon-mediated spin transport in magnetically-ordered insulators is of interest in the field of spintronics as it enables the transportation of spin information with ultra-low-dissipation compared with that by conduction electrons [1-4]. Recently, long-distance spin transport has been demonstrated in low-damping iron garnets, however the thicknesses of the iron garnet films that are required to possess low damping are typically over 100 nm. Efficient spin transport in low damping magnetic thin films with reduced thickness is essential for the integration of spintronic devices. In this work, we report long-distance spin transport in ultra-thin epitaxial films of magnesium aluminum ferrite ( $\text{MgAl}_{0.5}\text{Fe}_{1.5}\text{O}_4$ , MAFO). By exciting and detecting magnons by the spin Hall effect in Pt nanowires patterned on MAFO, we measured a magnon spin diffusion length of  $\sim 1 \mu\text{m}$ . This finding advances the study of magnon spin transport in the ultra-thin film regime.

## Summary of Research:

MAFO is a newly-developed spinel ferrite material that can be grown in thin films [5]. High quality MAFO thin films possess a small Gilbert damping parameter ( $\sim 0.0015$ ) that is comparable to that of the well-known low-damping material yttrium iron garnet (YIG) but with a much thinner film thickness. This ultra-thin, low-loss and low-damping MAFO thin film could provide a good platform for the study of magnon transport and devices.

In this study, magnon transport is characterized in a non-local geometry (Figure 1b) in which two Pt nanowires are separated by a certain distance, with one nanowire acting as a spin injector and another one as a spin detector. Owing to the strong spin-Hall effect in Pt, current passing through the spin injector gives rise to the spin accumulation at the interface that can excite the magnons in MAFO depending on the relative orientation between the spin polarization and magnetization directions. Reciprocally, the magnons are detected non-locally as a voltage via the inverse spin-Hall effect in the neighboring nanowire.

Our thin films of MAFO were grown by pulsed laser deposition on  $\text{MgAl}_2\text{O}_4$   $\langle 001 \rangle$  single crystal substrates in collaboration with the Yuri Suzuki group at Stanford. The nanowires were then defined using electron-beam

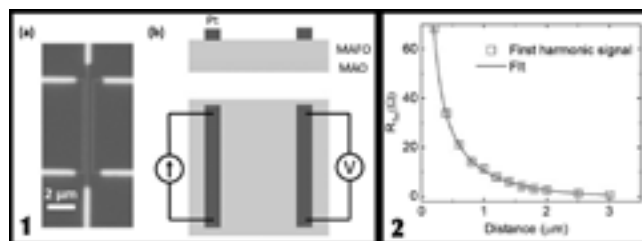


Figure 1, left: (a) Optical microscope image of a non-local Pt device on the MAFO thin film. (b) The device geometry and the measurement schematic.

Figure 2, right: The first-harmonic response of the non-local device as a function of the distance between the injector and the detector. The curve represents the fitting to a magnon diffusion model.

lithography (JEOL 6300) and the subsequent deposition and lift-off of a 10 nm Pt thin film. The Pt films were deposited by DC magnetron sputtering in an argon atmosphere with a base pressure  $< 3 \times 10^{-8}$  Torr. Finally, the metal contacts to the nanowires using Ti (5 nm)/Pt (100 nm) were patterned (JEOL 6300) and deposited (AJA sputtering system). The nanowire dimension is 200 nm wide and 10  $\mu\text{m}$  long with the wire separation ranging from 200 nm to 10  $\mu\text{m}$ . In Figure 1a, we show a finished device.

The non-local measurements were performed at room temperature in a magnetic probe station with an in-plane vector magnetic field. The non-local signal (both first and second-harmonic responses) was then measured as a function of angle  $\varphi$  between the nanowires and the in-plane magnetic field. A series of such nanowire pairs with different spacings between them were measured and their non-local resistances as a function of the separations are plotted as shown in Figure 2. Such decay of the non-local response can be well fitted to a magnon diffusion model [2]:

$$R = \frac{C}{\lambda} \frac{\exp(d/\lambda)}{1 - \exp(-d/\lambda)}$$

where  $C$  is a distance-independent constant,  $d$  is the injector-detector separation distance, and  $\lambda$  is the spin diffusion length of MAFO. The fitting gives a magnon spin diffusion length of 1  $\mu\text{m}$  for a 10-nm-thick MAFO thin film.

In conclusion, we studied the magnon diffusion length in the ultra-thin magnetic insulator, MAFO films, using non-local measurements with Pt nanowire pairs.

Our observed decay of magnons over distance fits well with the spin diffusion model, from which the spin diffusion length in MAFO was extracted to be around 1  $\mu\text{m}$ . This discovery demonstrates the potential of MAFO thin films as a new platform for energy-efficient spin transport.

#### References:

- [1] Kajiwara, Y. et al. Transmission of electrical signals by spin-wave interconversion in a magnetic insulator. *Nature* 464, 262-266 (2010).
- [2] Cornelissen, L. J., Liu, J., Duine, R. A., Youssef, J. Ben, and Van Wees, B. J. Long-distance transport of magnon spin information in a magnetic insulator at room temperature. *Nat. Phys.* 11, 1022-1026 (2015).
- [3] Lebrun, R. et al. Tunable long-distance spin transport in a crystalline antiferromagnetic iron oxide. *Nature* 561, 222-225 (2018).
- [4] Xing, W., Qiu, L., Wang, X., Yao, Y., and Ma, Y. Magnon Transport in Quasi-Two-Dimensional van der Waals Antiferromagnets. *Phys. Rev. X* 9, 11026 (2019).
- [5] Emori, S. et al. Ultralow Damping in Nanometer-Thick Epitaxial Spinel Ferrite Thin Films. *Nano Lett.* 18, 4273-4278 (2018).

# Photodiode Devices for Stimulation, Electrolysis, and Bubble Production

**CNF Project Number: 900-00**

**Principal Investigator(s): Paul L. McEuen<sup>1,2</sup>**

**User(s): Samantha L. Norris<sup>1</sup>, Michael F. Reynolds<sup>1</sup>, Alejandro J. Cortese<sup>1</sup>, Yanxin Ji<sup>1</sup>**

*Affiliation(s): 1. Laboratory of Atomic and Solid State Physics, Cornell University, Ithaca NY, USA;  
2. Kavli Institute at Cornell for Nanoscale Science, Cornell University, Ithaca NY, USA*

*Primary Source(s) of Research Funding: Cornell Center for Materials Research with funding from the NSF MRSEC program (DMR-1719875), Air Force Office of Scientific Research (AFSOR) multidisciplinary research program of the university research initiative Grant FA2386-13-1-4118*

*Contact: plm23@cornell.edu, sn588@cornell.edu, mfr74@cornell.edu, ajc383@cornell.edu, yj323@cornell.edu*

*Primary CNF Tools Used: Oxford Cobra ICP etcher, ABM contact aligner, Oxford 100 etcher, Xactix XeF<sub>2</sub> etcher, AJA sputter deposition Tool, Oxford PECVD*

## Abstract:

**We present photodiode devices that can be fabricated and released from the substrate in massive parallel using traditional photolithographic techniques. In this report, we discuss fabrication and characterization of these devices, and show some proof of concept measurements for applications in neural stimulation, as well as electrophoretic motion and gas bubble production based on electrolysis.**

## Summary of Research:

The ability to locally produce voltages and currents with a microscale device that is optically powered lends itself well to a variety of applications. For instance, a cell-scale device would be minimally invasive when inserted into neural tissue and could electrically stimulate surrounding neurons. In addition, these devices can perform electrolysis of the surrounding water, locally changing the pH near the electrodes. Finally, during electrolysis the creation of oxygen and hydrogen gas at the electrodes causes bubble formation, the flow of which can be controlled by the geometry of the device itself.

The entire process utilizes silicon-on-insulator substrates and traditional photolithographic techniques, which enables the production of these devices and their release from the substrate to be performed in massive parallel.

To create the silicon photodiode devices, we begin by selectively doping the top of the device layer with phosphosilicate glass to create a vertical PN junction. We then electrically isolate the photodiodes by dry etching to the underlying oxide layer in the Oxford Cobra inductively coupled plasma (ICP) etcher and connect them in series to apply voltages to two metal electrodes on either end of the device. The metal electrodes and

interconnects are platinum with a titanium adhesion layer deposited in the AJA sputter deposition tool. We encapsulate the photodiodes with silicon dioxide with the Oxford plasma enhanced chemical vapor deposition tool, leaving the metal electrodes protruding. Finally, we release the devices into solution using a combination of dry and wet etches.

In the presence of incident light, a voltage proportional to the number of photovoltaics wired in series is applied between the electrodes. The current flowing through the device is proportional to the incident light intensity, allowing the electrical characteristics of the device to be tuned *in situ*. The current and voltage characteristics for a 100  $\mu\text{m}$ , seven-photodiode device are shown in Figure 1. Such a device produces  $\sim 100 \mu\text{A}$  of current and  $\sim 4\text{V}$ .

These values correspond to those typically used for microstimulation of neurons [1]. We are currently working on inserting these devices onto flight steering muscles in *Drosophila melanogaster* for in-flight stimulation.

When in solution, these devices perform electrolysis of the surrounding water, locally increasing or decreasing the pH near the anode and cathode,

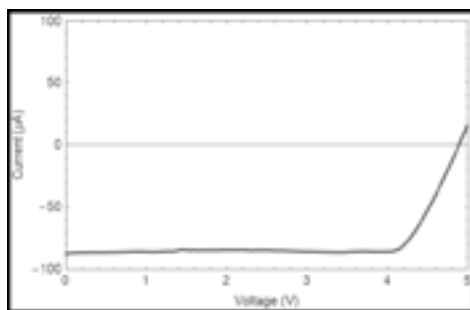


Figure 1: Current vs. bias voltage for a 100  $\mu\text{m}$ , 7-PV photodiode device under 100  $\text{nW}/\mu\text{m}^2$ , 532 nm laser illumination.

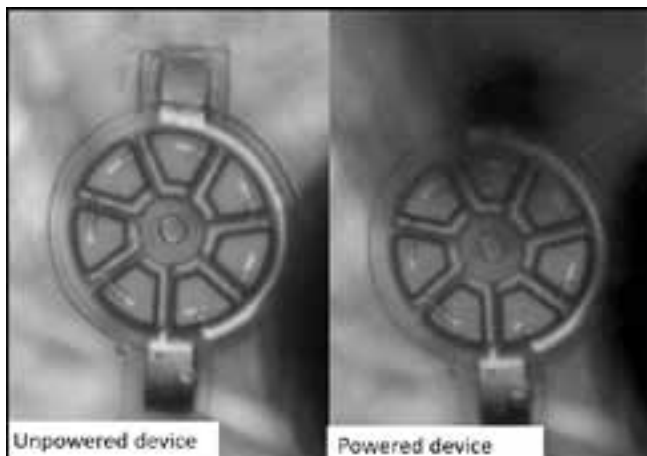


Figure 2: Unpowered and powered device in phenol red pH indicator dye. A darker color is indicative of a higher pH near the anode of the device.

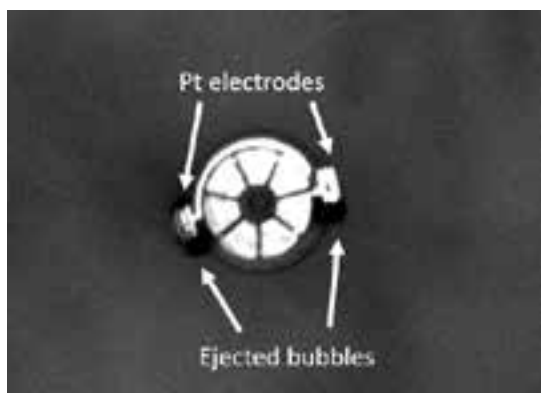


Figure 3: A typical photodiode device with tapered platinum electrodes for bubble production.

respectively. Figure 2 shows a local pH change imaged by adding a colorimetric pH indicator dye, phenol red. These devices could be used as optically powered voltage sources for local electrochemistry or electrophoretic pumps in microfluidic environments and other enclosed geometries.

During electrolysis, the electrodes also drive the conversion of water to hydrogen and oxygen gas at the cathode and anode, respectively. The size and flow of these bubbles can be tuned by changing the geometry of the electrodes. Inspired by previous works on bubble rockets [2], we fabricated devices with a hollow cylinder-like electrode geometry that is tapered to allow bubbles to be preferentially ejected in one direction. Future work includes tuning device geometry to cause self-propulsion by bubble ejection and using bubble production in an enclosed space to cause devices to be neutrally buoyant.

### References:

- [1] Ramasubbu, R. (2018). Dosing of Electrical Parameters in Deep Brain Stimulation (DBS) for Intractable Depression: A Review of Clinical Studies. *Frontiers in Psychiatry*.
- [2] Gallino, G., Gallaire, F., Lauga, E., and Michelin, S. (2018). Physics of Bubble-Propelled Microrockets. *Advanced Functional Materials*.

# Nanofabricated Superconducting Devices for Vortex Dynamics and Qubits

**CNF Project Number: 1314-05**

**Principal Investigator(s): Britton L.T. Plourde**

**User(s): Kenneth Dodge, Jaseung Ku, Yebin Liu, Michael Senatore**

*Affiliation(s): Department of Physics, Syracuse University*

*Primary Source(s) of Research Funding: Army Research Office*

*Contact: bplourde@syr.edu, krdodgej@syr.edu, jku102@syr.edu, yliu166@syr.edu, masenato@syr.edu*

*Website: <http://plourdelab.syr.edu>*

*Primary CNF Tools Used: ASML photostepper, JEOL 9500, Plasma-Therm 770*

## Abstract:

We fabricate superconducting microwave devices for studying the dynamics of vortices at low temperatures and for forming novel qubits. Vortices are quantized bundles of magnetic flux that thread many different superconductors over a particular range of applied magnetic field. By using disordered superconducting thin films for high kinetic inductance wires, we are able to build structures that can lead to qubits that are protected against decoherence.

## Summary of Research:

Superconducting microwave circuits play an important role in quantum information processing. Circuits composed of Josephson junctions and capacitors with superconducting electrodes can serve as qubits, the fundamental element of a quantum computing architecture. Various loss mechanisms limit the ultimate performance of these devices, including trapped magnetic flux vortices. Vortices can be trapped in the superconducting electrodes when background magnetic fields are present and contribute dissipation when driven with microwave currents [1]. Thus, techniques for controlling the trapping of vortices are critical to the development of large-scale quantum information processors with superconducting circuits. In addition, highly disordered superconducting films, including granular Al, can be used to form wires with a compact high kinetic inductance that can be combined with Al- $\text{AlO}_x$ -Al Josephson junctions to form the central element for novel qubit designs that are protected against decoherence [2,3].

We fabricate our microwave resonators from various superconducting films, including aluminum, deposited

onto silicon wafers in vacuum systems at Syracuse University. We define the patterns on the ASML stepper and transfer them into the films with a combination of reactive ion etching and liftoff processing. For defining Josephson junctions, we use the JEOL 9500 along with a dedicated deposition system at Syracuse University. We measure these circuits at temperatures of 100 mK and below in our lab at Syracuse University.

## References:

- [1] Song, C., Heitmann, T.W., DeFeo, M.P., Yu, K., McDermott, R., Neeley, M., Martinis, John M., Plourde, B.L.T.; "Microwave response of vortices in superconducting thin films of Re and Al"; *Physical Review B* 79, 174512 (2009).
- [2] Doucot, B., Ioffe, L.; "Physical implementation of protected qubits"; *Reports on Progress in Physics* 75, 072001 (2012).
- [3] Liu, Y., Dodge, K., Senatore, M., Zhu, S., Naveen, Shearrow, A., Schlenker, F., Klots, A., Faoro, L., Ioffe, L., McDermott, R., Plourde, B.; "Implementation of pi-periodic Josephson Elements for Topologically Protected Charge-Parity Qubits"; *Bull. Am. Phys. Soc.* 2019, <http://meetings.aps.org/Meeting/MAR19/Session/S26.11>.

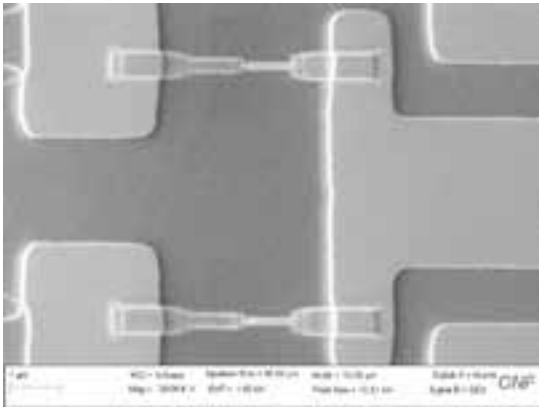


Figure 1: Scanning electron micrograph of Al-AIO<sub>x</sub>-Al Josephson junctions in protected qubit design.

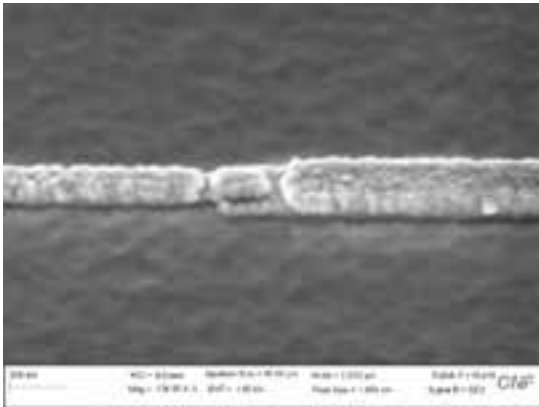


Figure 2: Scanning electron micrograph closeup image of Al-AIO<sub>x</sub>-Al Josephson junction on protected qubit element.

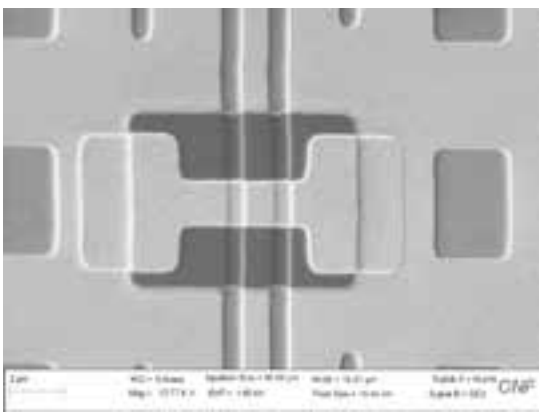


Figure 3: Scanning electron micrograph of Nb ground connection over SiO<sub>x</sub> spacer on protected qubit element.

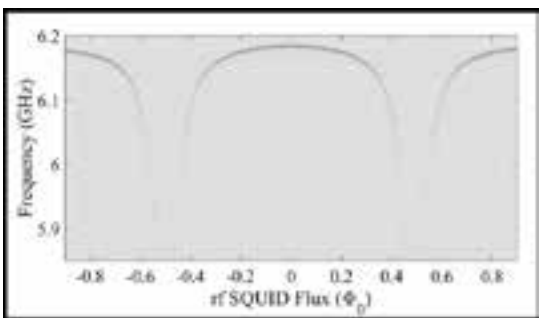


Figure 4: Measurement of magnetic flux modulation of microwave resonance from protected qubit element.

# Fabrication of Nanofluidic Cavities for Superfluid $^3\text{He}$ Studies

CNF Project Number: 1520-07

Principal Investigator(s): Jeevak M. Parpia

User(s): Abhilash Thanniyil Sebastian, Nikolay Zhelev

Affiliation(s): Department of Physics, Cornell University

Primary Source(s) of Research Funding: National Science Foundation

Contact: jmp9@cornell.edu, nizhelev@gmail.com, abhilashthanniyil@gmail.com

Website: <http://parpia.lassp.cornell.edu>

Primary CNF Tools Used: Oxide furnace, Oxford PECVD, Oxford and Plasma-Therm RIE, dicing saw

## Abstract:

We demonstrate nanoscale cavities that withstand 30 bar cooled to ultralow temperatures [1]. These structures have been utilized to observe an unexpected spatially modulated order parameter in superfluid  $^3\text{He}$  [2].

## Summary of Research:

Superfluid  $^3\text{He}$  is a unique system for study.  $^3\text{He}$  is a Fermion (like electrons), but its pairing into the superfluid state is more complex than its electronic counterparts producing a multiplicity of superfluid phases. In the bulk the anisotropic A phase and the isotropically gapped B phase emerge. Confinement favors the A phase over the B phase [2,3,4].

The superfluid state is attained between 0 and 35 bar and between 0.9 and 2.5 mK (respectively). Below the superfluid transition, pairs condense into the coherent superfluid state. The pairing length-scale (pair diameter) varies from  $\sim 80$  nm at 0 bar to 14 nm at high pressure. Confinement alters the phase diagram and as the  $^3\text{He}$  is progressively restricted to smaller sizes, the B phase should yield to the A phase and new phases should emerge.

A recent experiment [2], carried out by colleagues at Royal Holloway in London, explored the magnetic signatures of  $^3\text{He}$  confined in a  $1.1 \mu\text{m}$  tall chamber. Extracting signals from the  $\sim 70$  nL sample at temperatures well below 1 mK required using their highly sensitive SQUID NMR techniques.

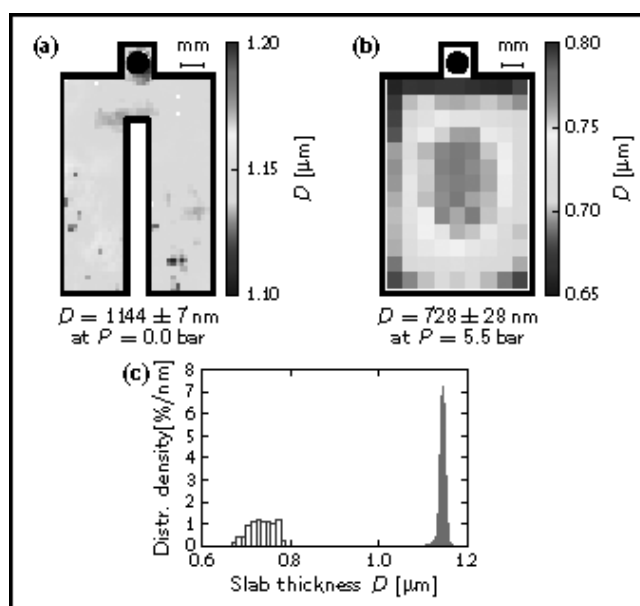


Figure 1: (a) Comparison of the heights within the new cell used in experiment [2] compared to (b) previous generation cell (at 5.5 bar pressure) using 3 mm thick silicon and glass. The addition of a “septum” to reduce the unsupported span results in a much more uniform spacing. The cavity dimensions are approximately  $7 \text{ mm} \times 11 \text{ mm}$ . (c) shows a comparison in height distributions of the two cells, the right one being the data from the newer cell, and the broader distribution at left, showing the height distribution measurement for the older cell.

To fabricate this device, a 1 mm thick silicon wafer was oxidized using the oxide furnace in CNF to grow thick oxide ( $> 2 \mu\text{m}$ ), then further oxide was deposited using the Oxford PECVD. The device was patterned using contact photolithography and the oxide removed using both dry plasma etch (Oxford and Plasma-Therm RIE) and wet etch (6:1 BOE). The wafer was further oxidized to create a step in the Si-SiO<sub>2</sub> interface (modified LOCOS process) and oxide removed using HF. The chips were then diced using CNF's dicing saw. Matching polished glass pieces were also diced.

The final step to make the cells was to remove oxide off Si pieces, clean in SC-1 solution and bond using custom made anodic bonding jig. The resulting bonded cell had a very uniform height distribution (Figure 1 a, c) in comparison to previous cells (Figure 1 b).

The experiments represent the melding of theory (experiments were initiated following a seminal theory result [5] that predicted stripes), the development of fabrication and sealing technology over several years [1], and a whole suite of experimental measurement techniques [2,3,4]. The final results that point to a "polka dot configuration" rather than the simpler proposed striped configuration have received wide publicity [6].

Former Physics Ph.D. students Nikolay Zhelev (now Corning Research), Roberto DeAlba (now INTEL), and post-doctoral scientist Abhilash Sebastian (now VTT Research Labs, Finland) fabricated these structures before they left Cornell. Results from these structures are now emerging or have been recently published.

## References:

- [1] Fabrication of microfluidic cavities using Si-to-glass anodic bonding; N. Zhelev, T. S. Abhilash, R. G. Bennett, E. N. Smith, B. Ilic, L. V. Levitin, X. Rojas, A. Casey, J. Saunders, and J. M. Parpia, *Rev. Sci. Instr.*, 073902-1-10, 89, <https://doi.org/10.1063/1.5031837> (2018).
- [2] Evidence for a Spatially Modulated Superfluid Phase of <sup>3</sup>He under Confinement; Lev V. Levitin, Ben Yager, Laura Sumner, Brian Cowan, Andrew J. Casey, John Saunders, Nikolay Zhelev, Robert G. Bennett, and Jeevak M. Parpia, *Phys. Rev. Lett.* 122, 085301, <https://journals.aps.org/prl/abstract/10.1103/PhysRevLett.122.085301> (2019).
- [3] Phase Diagram of the Topological Superfluid <sup>3</sup>He Confined in a Nanoscale Slab Geometry; L. V. Levitin, R. G. Bennett, A. Casey, B. Cowan, J. Saunders, D. Drung, Th. Schurig and J. M. Parpia, *Science*, 340 841-844, <https://science.sciencemag.org/content/340/6134/841> (2013).
- [4] The A-B transition in superfluid helium-3 under confinement in a thin slab geometry; N. Zhelev, T.S. Abhilash, E.N. Smith, R.G. Bennett, X. Rojas, L. Levitin, J. Saunders, and J.M. Parpia, *Nature Comm.* 8 15963, <https://www.nature.com/articles/ncomms15963> (2017).
- [5] Crystalline order in superfluid <sup>3</sup>He Films; J. A. Sauls, and A. B. Vorontsov, *Phys. Rev. Lett.* 98, 045301, <https://journals.aps.org/prl/abstract/10.1103/PhysRevLett.98.045301> (2007).
- [6] Viewpoint: A Polka-Dot Pattern Emerges in Superfluid Helium, Jochen Wosnitza, *Physics* 12, 20, <https://physics.aps.org/articles/v12/20>, February 27, 2019.

# Fabrication of Nanoscale Josephson Junctions for Quantum Coherent Superconducting Circuits

**CNF Project Number: 1735-08**

**Principal Investigator(s): Britton L.T. Plourde**

**User(s): Andrew Ballard, Caleb Howington, Indrajeet**

*Affiliation(s): Department of Physics, Syracuse University*

*Primary Source(s) of Research Funding: Army Research Office, National Science Foundation*

*Contact: bplourde@syr.edu, alballar@syr.edu, cjhowing@syr.edu, indraje@syr.edu*

*Website: <http://plourdelab.syr.edu>*

*Primary CNF Tools Used: ASML stepper, JEOL 9500, Plasma-Therm 770*

## **Abstract:**

**We fabricate nanoscale superconductor tunnel junctions and other structures for experiments involving quantum coherent circuits. Such circuits have shown great promise in recent years for explorations of quantum mechanics at the scale of circuits on a chip and for forming qubits, the foundational elements of a quantum computer. The quantum state of these superconducting qubits can be manipulated with microwave radiation at low temperatures. In addition, we are developing alternative techniques for probing the state of these qubits and controlling their quantum state using superconducting digital circuitry, as well as superconducting metamaterial structures with novel microwave mode spectra for coupling to superconducting qubits.**

## **Summary of Research:**

The unique properties of nanoscale Josephson junctions enable a wide range of novel superconducting circuits for investigations in many diverse areas. In recent years, circuits composed of such junctions have emerged as promising candidates for the element of a quantum computer, due to the low intrinsic dissipation from the superconducting electrodes and the possibility of scaling to many such qubits on a chip [1]. The quantum coherent properties of the circuits are measured at temperatures below 50 mK with manipulation of the qubit state through microwave excitation.

We are currently working on a variety of experiments involving these nanoscale Josephson junctions and other superconducting structures that allow us to probe novel quantum effects in our microwave circuits. We are fabricating superconducting circuits for forming low-temperature detectors of single microwave photons and for implementing a new scheme for the efficient readout of the quantum state of superconducting qubits [2,3]. We are also working with collaborators at the University of Wisconsin, Madison to develop hybrid quantum/classical superconducting chips that allow us to perform coherent quantum control of a superconducting qubit based on digital pulses from a Single Flux Quantum (SFQ) circuit [4,5].

In another effort, we are using particular combinations of superconducting lumped-circuit elements to engineer metamaterial transmission lines that exhibit novel mode structures characteristic of left-handed materials. We are fabricating such metamaterial transmission lines from Al and Nb films on Si and characterizing these at low temperatures [6]. We are working on experiments to couple these left-handed lines to superconducting qubits for experiments involving the exchange of microwave photons [7].

We pattern these circuits at the CNF with nanoscale structures defined with electron-beam lithography on the JEOL 9500 integrated with photolithographically defined large-scale features. The junctions are fabricated using the standard double-angle shadow evaporation technique, in which a resist bilayer of copolymer and PMMA is used to produce a narrow PMMA airbridge suspended above the substrate. Evaporation of aluminum (Al) from two different angles with an oxidation step in between forms a small Al-AlO<sub>x</sub>-Al tunnel junction from the deposition shadow of the airbridge. We have developed a process for defining these junctions with electron-beam lithography and we perform the aluminum evaporations in a dedicated chamber at Syracuse.

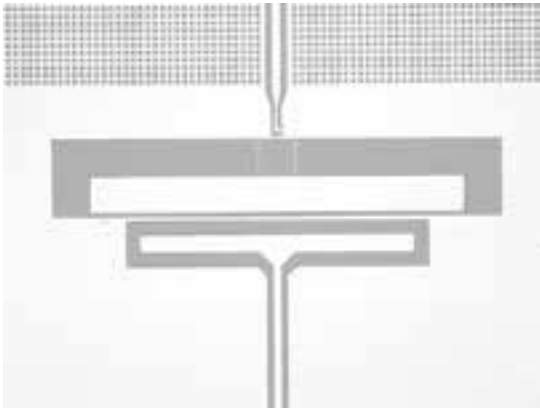


Figure 1: Optical micrograph of superconducting qubit for digital control experiments.

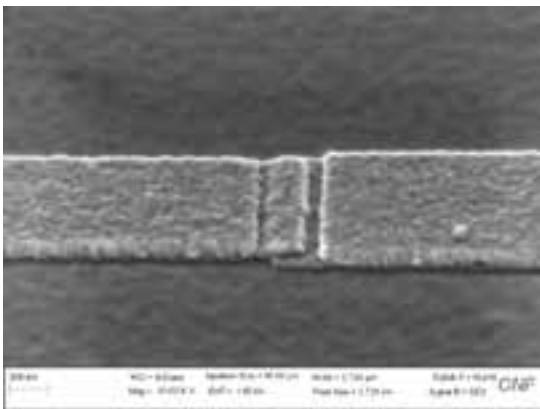


Figure 2: Scanning electron micrograph of Al-AlO<sub>x</sub>-Al Josephson junction for superconducting qubit.



Figure 3: Optical micrograph of superconducting metamaterial transmission line resonator fabricated from Nb thin film on Si.

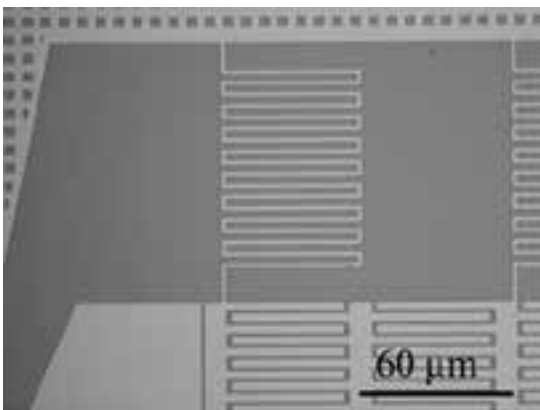


Figure 4: Optical micrograph of meander-line inductor and portion of interdigitated capacitor on metamaterial transmission line resonator fabricated from Nb thin film on Si.

We pattern large-scale features using the ASML stepper, with electron-beam evaporation of Al, sputter-deposition of Nb, and PECVD deposition of SiO<sub>2</sub>.

Measurements of these circuits are performed in cryogenic systems at Syracuse University, including dilution refrigerators for achieving temperatures below 30 mK.

### References:

- [1] Clarke, J. and Wilhelm, F.K.; "Superconducting quantum bits"; Nature, 453, 1031 (2008).
- [2] Govia, L.C.G., Pritchett, Emily J., Xu, Canran, Plourde, B. L. T., Vavilov, Maxim G., Wilhelm, Frank K., McDermott, R.; "High-fidelity qubit measurement with a microwave-photon counter"; Physical Review A 90, 062307 (2014).
- [3] Opremcak, A, Pechenezhskiy, I., Howington, C., Christensen, B.G., Beck, M.A., Leonard Jr, E., Suttle, J., Wilen, C., Nesterov, K.N., Ribeill, G.J., Thorbeck, T., Schlenker, F., Vavilov, M.G., Plourde, B.L.T., McDermott, R.; "Measurement of a Superconducting Qubit with a Microwave Photon Counter"; Science 361, 1239 (2018).
- [4] McDermott, R., Vavilov, M.; "Accurate Qubit Control with Single Flux Quantum Pulses"; Physical Review Applied 2, 014007 (2014).
- [5] Leonard, E., Beck, M., Nelson, JJ, Christensen, B., Thorbeck, T., Howington, C., Opremcak, A., Pechenezhskiy, I., Dodge, K., Dupuis, N., Ku, J., Schlenker, F., Suttle, J., Wilen, C., Zhu, S., Vavilov, M., Plourde, B., McDermott, R.. "Digital coherent control of a superconducting qubit"; Physical Review Applied 11, 014009 (2019).
- [6] Wang, H., Zhuravel, A., Indrajeet, S., Taketani, B., Hutchings, M., Hao, Y., Rouxinol, F., Wilhelm, F, LaHaye, M.D., Ustinov, A., Plourde, B.; "Mode Structure in Superconducting Metamaterial Transmission Line Resonators"; Physical Review Applied 11, 054062 (2019).
- [7] Indrajeet, S., Wang, H., Hutchings, M., LaHaye, M., Taketani, Bruno, Wilhelm, F., Plourde, B.; "Qubit Dynamics in a Multi-mode Environment with a Superconducting Metamaterial Resonator"; Bull. Am. Phys. Soc. 2019, <http://meetings.aps.org/Meeting/MAR19/Session/P26.4>.

# Spin Seebeck Imaging of Spin-Torque Switching in Antiferromagnetic Pt/NiO Heterostructures

CNF Project Number: 2091-11

Principal Investigator(s): Gregory D. Fuchs<sup>1</sup>

User(s): Isaiah Gray<sup>1</sup>, Gregory M. Stiehl<sup>2</sup>

Affiliation(s): 1. School of Applied and Engineering Physics, Cornell University, Ithaca, NY 14853;

2. Department of Physics, Cornell University, Ithaca, NY 14853

Primary Source(s) of Research Funding: Cornell Center for Materials Research from the National Science Foundation MRSEC Program, Grant No. DMR-1719875

Contact: gdf9@cornell.edu, ig246@cornell.edu, gms263@cornell.edu

Primary CNF Tools Used: GCA 5x stepper

## Abstract:

As electrical control of Néel order opens the door to reliable antiferromagnetic (AF) spintronic devices, understanding the microscopic mechanisms of AF switching is crucial. Spatially-resolved studies are necessary to distinguish multiple nonuniform switching mechanisms; however, progress has been hindered by the lack of tabletop techniques to image the Néel order. We demonstrate spin Seebeck microscopy as a sensitive table-top method for imaging antiferromagnetic order in thin films and apply this technique to study spin-torque switching in NiO/Pt and Pt/NiO/Pt heterostructures. We establish the interfacial antiferromagnetic spin Seebeck effect in NiO as a probe of surface Néel order. By imaging before and after applying current-induced spin torque, we resolve spin domain rotation and domain wall motion, acting simultaneously.

## Summary of Research:

Antiferromagnets (AFs) are attractive candidates for spintronic devices due to their lack of stray fields, their terahertz switching speeds, and their stability to magnetic field [1]. They are also notoriously difficult to read and write [2]. Recent demonstrations of electrical switching of Néel order [3-6] may provide a path to overcome this difficulty and potentially construct practical devices. However, AF switching is nonuniform and multiple switching mechanisms contribute simultaneously, making device-level readout difficult to interpret. Systematic imaging studies of AF switching are necessary to understand the microscopic mechanisms. The best-established technique for imaging Néel order — XMLD-PEEM7 — requires synchrotron facilities that are generally only available in 24-48-hour runs, therefore tabletop imaging techniques are necessary to better understand and optimize AF switching.

In this work [8] we demonstrate spin Seebeck microscopy as a sensitive tabletop probe of the Néel order and image current-induced spin-torque switching in antiferromagnetic Pt/NiO and Pt/NiO/Pt heterostructures.

Our technique is based on the interfacial antiferromagnetic longitudinal spin Seebeck effect (AF-LSSE) [9] in so-called *uncompensated* antiferromagnets such as the insulator NiO<111>, in which the spins in the interfacial layer are aligned parallel as shown schematically in Figure 1(a). A local thermal gradient at this interface generates a spin current that reports the Néel orientation of the interfacial spins. We generate local thermal gradients by focusing a pulsed laser to 650 nm spot size and detect the resulting spin current by transducing it into a charge current through the inverse spin Hall effect in the adjacent Pt layer. We therefore measure the in-plane component of the surface Néel orientation. Figure 1(b) shows an example AF LSSE image of a 20  $\mu\text{m}$ -wide Hall bar of 165 nm NiO<111>/ Pt on MgAl<sub>2</sub>O<sub>4</sub>. Blue and red  $V_{AF-LSSE}$  contrast represents spins pointing towards the right and left, respectively.

In contrast to an uncompensated AF, Figure 1(c) diagrams a *compensated* AF, in which the spins in the interfacial layer are anti-aligned. The spin current from this interface should cancel out to zero over the laser spot area. To test this prediction, in Figure 1(d) we image

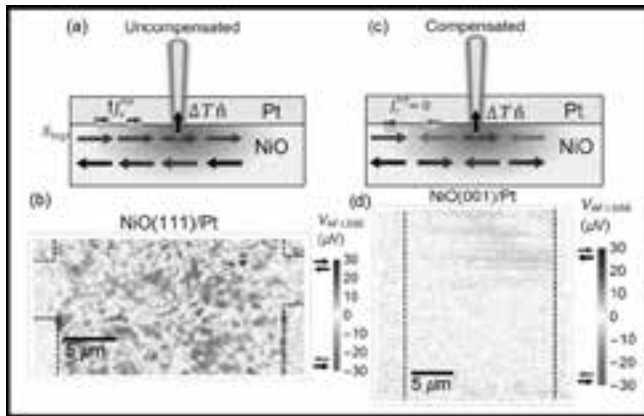


Figure 1: Demonstrating interfacial antiferromagnetic longitudinal spin Seebeck effect (AF LSSE). (a) Diagram of uncompensated NiO<111>/Pt, in which the spins on the top interface are aligned. A thermal gradient across this interface generates a spin current that reports the surface Néel orientation. (b) AF LSSE image of a 165 nm NiO<111>/Pt sample, showing AF domains. (c) Diagram of compensated NiO<001>/Pt, in which the spins on the top interface are anti-aligned and produce no net spin current. (d) AF LSSE image of a 136 nm NiO<001>/Pt sample, showing no measurable contrast. (Find full color on pages xiv-xv.)

another 20  $\mu\text{m}$ -wide Hall bar of 136 nm NiO<001>/Pt on MgO<001>, similar to the NiO<111>/Pt sample except that NiO<001> has a compensated interface. We obtain no measurable contrast from NiO<001> compared with NiO<111>, which confirms that the uncompensated interface is necessary and indicates that we indeed measure surface Néel order.

We then image spin-torque switching in a 10  $\mu\text{m}$ -wide device of Pt/6 nm NiO<111> in Figure 2. We image before and after applying  $7 \times 10^7 \text{A}/\text{cm}^2$  current density along the device and take the difference to show the changes in domain structure. Prominent regions of switching are highlighted in black dashed line. The lower portion of the difference image shows nearly uniform contrast, meaning different AF domains rotate by the same angle. The middle of the channel shows adjacent regions of blue and red, which indicate domain wall motion in response to current. Our findings are consistent with recently-developed models of spin-torque switching in NiO/Pt<sup>6</sup>.

In conclusion, we demonstrate spin Seebeck microscopy as a powerful tabletop technique for imaging surface

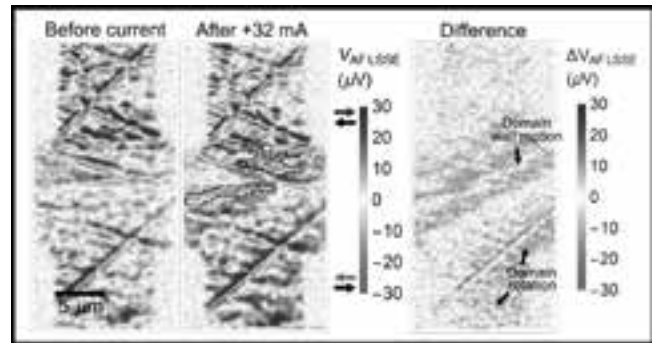


Figure 2: AF LSSE images of Pt/6 nm NiO<111> before and after applying  $7 \times 10^7 \text{A}/\text{cm}^2$  DC current. Prominent regions of switching are highlighted. The difference image shows switching both by rotation of AF domains and by domain wall motion. (Find full color on pages xiv-xv.)

Néel order in an antiferromagnetic insulator and apply this technique to image spin-torque switching in NiO/Pt heterostructures. We find that switching occurs by domain rotation and domain wall motion acting simultaneously. Our results provide critical insight into the complex processes in electrical control of antiferromagnetism and we expect our technique to generalize to a variety of antiferromagnetic insulators.

## References:

- [1] T. Jungwirth, et al., Nat. Nano. 11, 231-241 (2016).
- [2] C. Song, et al., Nanotechnology 29, 112001 (2018).
- [3] P. Wadley, et al., Science 351, 587-590 (2016).
- [4] T. Moriyama, et al., Scientific Reports 8, 14167 (2018).
- [5] X. Z. Chen, et al., Phys. Rev. Lett. 120, 207204 (2018).
- [6] L. Baldrati, et al., arXiv:1810.11326 (2018).
- [7] J. Stöhr, et al., Phys. Rev. Lett. 83, 1862 (1999).
- [8] I. Gray, et al., arXiv:1810.03997 (2018).
- [9] S. A. Bender, et al., Phys. Rev. Lett. 119, 056804 (2017).

# Fabrication and Measurements of Arrays of Constriction-Based Spin-Hall Nano-Oscillators

**CNF Project Number: 2091-11**

**Principal Investigator(s): Gregory D. Fuchs**

**User(s): Yanyou Xie**

*Affiliation(s): Applied and Engineering Physics, Cornell University*

*Primary Source(s) of Research Funding: National Science Foundation*

*Contact: gdf9@cornell.edu, yx322@cornell.edu*

*Primary CNF Tools Used: JEOL 9500, MA6 contact aligner*

## **Abstract:**

**Spin-Hall nano-oscillators (SHNOs) convert D.C. charge current to microwave frequency magnetic oscillations — enabling applications as highly agile microwave sources. The use of SHNOs for applications is still limited by the output microwave power and linewidth. The goal of this project is to synchronize SHNOs to generate larger power and narrower spectral linewidth. We are currently working on making arrays of SHNOs of different geometries and studying how they synchronize.**

## **Summary of Research:**

A spin-Hall nano-oscillator (SHNO) is a bilayer system containing a ferromagnetic layer and a metal layer with strong spin-orbit coupling [1], patterned as a nanowire or a nanoconstriction. SHNOs are based on spin-Hall effect, which converts a lateral charge current in the metal layer into a transverse pure spin current [2]. The spin current can provide sufficiently large spin transfer torque (STT) to the adjacent ferromagnetic layer to compensate the local spin wave damping, leading to auto-oscillations of the magnetic moment in the microwave regime [2]. For microwave oscillators, it is desirable to generate a larger power and a narrower spectral linewidth [3]. Arrays of synchronized SHNOs can reach these goals and the fabrication of arrays of constriction-based SHNOs is practical [1,3]. Here we fabricated arrays of two and four constriction-based SHNOs on  $20.5 \mu\text{m} \times 4 \mu\text{m}$  wires, with constriction width of 100 nm and 150 nm.

The fabrication process consists of three stages — sputtering, e-beam lithography and photolithography — as shown in Figure 1. We started by sputtering a bilayer of  $\text{Pt}_{0.75}\text{Au}_{0.25}$  (5 nm)/ $\text{Ni}_{81}\text{Fe}_{19}$  (5 nm) on a 2-inch sapphire wafer. Next, the SHNO devices were fabricated using e-beam lithography in JEOL 9500 to define constrictions with a 100 nm or 150 nm characteristic dimension. The SEM and AFM images of selected fabricated devices are shown in Figure 2 and 3. Finally, we fabricated gold bonding pads by photolithography. The process used the positive photoresist S1813 in the MA6 contact aligner. After developing, we evaporated Cr (10 nm)/Au (90 nm) and performed lift-off.

Figure 4 shows spin-torque ferromagnetic resonance (ST-FMR) [4] measurements on one of the 4-constriction devices. In a ST-FMR measurement, a microwave-frequency (rf) charge current is applied to the SHNO, generating an oscillating transverse spin current and thus oscillating STT [4]. The oscillating STT induces magnetization precession in  $\text{Ni}_{81}\text{Fe}_{19}$ , which results in an oscillating resistance due to the anisotropic magnetoresistance of  $\text{Ni}_{81}\text{Fe}_{19}$  [4]. Here we measure the generated D.C. differential voltage from the mixing of the rf current and the oscillating resistance [4],  $dV_{\text{mix}}/dH$ , as we sweep the external magnetic field. The occurrence of valley and peak (dark and light) combination indicates resonant excitation of spin wave eigenmodes [5]. Two significant valley and peak combination can be identified in Figure 4. By comparing with literature [5,6], we identified that at the same external magnetic field, the ones occurring at lower frequency are edge spin-wave modes, while the ones occurring at higher frequency are bulk spin-wave modes. The magnetization of the former mainly occurs near the edge of wire, while that of the latter mainly occurs in the interior of the wire [6]. To extract the mode profiles, we still need to perform micromagnetic simulations at the peak frequencies.

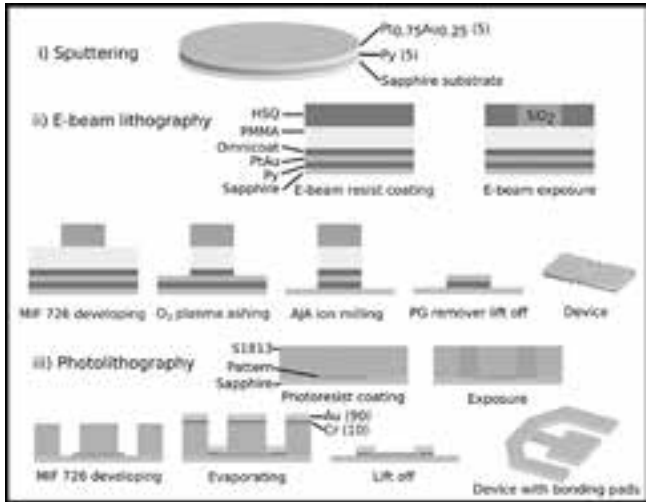


Figure 1: Fabrication process flow. (Find full color on pages xiv-xv.)

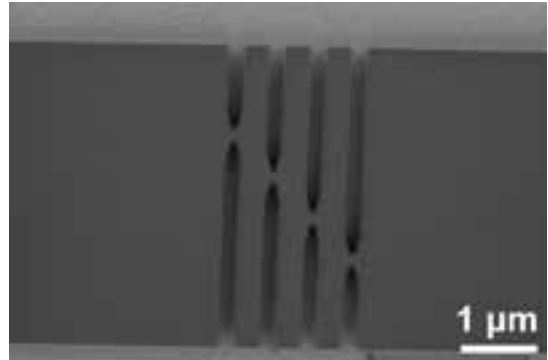


Figure 2: SEM image of one of the devices.

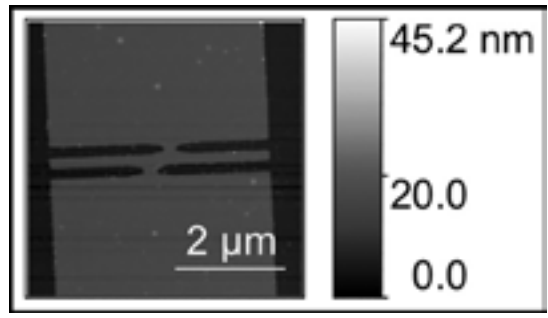


Figure 3: AFM image of one of the devices.

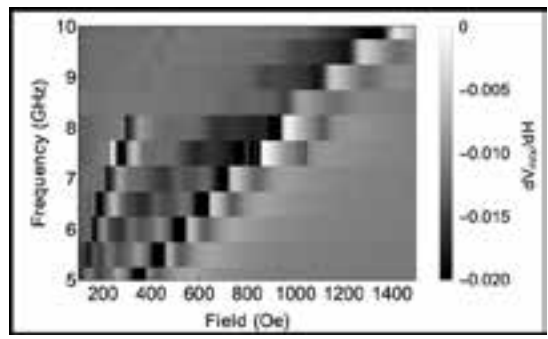


Figure 4: Density plot of spin-torque ferromagnetic resonance measurements sweeping along the external magnetic field. (Find full color on pages xiv-xv.)

**References:**

- [1] Kendziorczyk, T, and T. Kuhn. "Mutual synchronization of nanoconstriction-based spin Hall nano-oscillators through evanescent and propagating spin waves." *Physical Review B* 93, no. 13 (2016): 134413.
- [2] Dürrenfeld, Philipp, Ahmad A. Awad, Afshin Houshang, Randy K. Dumas, and Johan Åkerman. "A 20 nm spin Hall nano-oscillator." *Nanoscale* 9, no. 3 (2017): 1285-1291.
- [3] Demidov, V. E., S. Urazhdin, A. Zholud, A. V. Sadovnikov, and S. O. Demokritov. "Nanoconstriction-based spin-Hall nano-oscillator." *Applied Physics Letters* 105, no. 17 (2014): 172410.
- [4] Liu, Luqiao, Takahiro Moriyama, D. C. Ralph, and R. A. Buhrman. "Spin-torque ferromagnetic resonance induced by the spin Hall effect." *Physical review letters* 106, no. 3 (2011): 036601.
- [5] Duan, Zheng, Andrew Smith, Liu Yang, Brian Youngblood, Jürgen Lindner, Vladislav E. Demidov, Sergej O. Demokritov, and Ilya N. Krivorotov. "Nanowire spin torque oscillator driven by spin orbit torques." *Nature communications* 5 (2014): 5616.
- [6] Duan, Zheng, Carl T. Boone, Xiao Cheng, Ilya N. Krivorotov, Nathalie Reckers, Sven Stienen, Michael Farle, and Jürgen Lindner. "Spin-wave modes in permalloy/platinum wires and tuning of the mode damping by spin Hall current." *Physical Review B* 90, no. 2 (2014): 024427.

# Diamond and SiC Semi-Confocal Acoustic Resonator

CNF Project Number: 2126-12

Principal Investigator(s): Gregory D. Fuchs<sup>1</sup>

User(s): Huiyao Chen<sup>2</sup>

Affiliation(s): 1. School of Applied and Engineering Physics, 2. Department of Physics; Cornell University

Primary Source(s) of Research Funding: Office of Naval Research (Grants No. N000141410812 and No. N000141712290)

Contact: gdf9@cornell.edu, hc846@cornell.edu

Website: <http://fuchs.research.engineering.cornell.edu>

Primary CNF Tools Used: PT770 etcher, GCA 5x stepper, Heidelberg mask writer DWL2000, AJA sputtering deposition system, odd/even evaporator, YES Asher, P10 profilometer, Westbond 7400A ultrasonic wire bonder

## Abstract:

We report the design and fabrication of a semi-confocal high-overtone bulk acoustic resonator (SCHBAR) device on diamond (silicon carbide) with  $f \cdot Q > 10^{12}$  ( $> 10^{13}$ ) [1]. The semi-confocal geometry confines the phonon mode laterally below 10  $\mu\text{m}$ . The device also has integrated atomic-scale quantum defects, and is thus suitable for quantum control applications such as mechanical manipulation of the defect spin states.

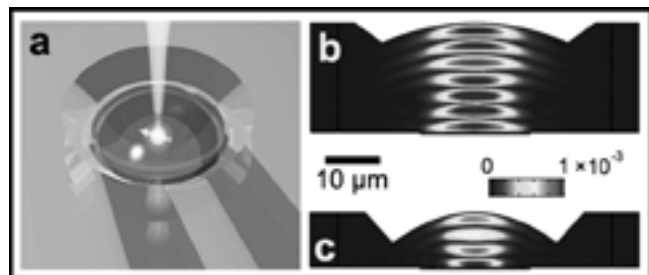


Figure 1: (a) Concept image of the semi-confocal HBAR device design. (b) and (c) are strain profiles of the diamond devices simulated by COMSOL for a 3 GHz mode, with a 1  $V_p$  voltage driving source.

## Summary of Research:

As illustrated in Figure 1, the device has a planar-convex structure. We design one side of the resonator with a curved surface, enabling it to confine three dimensional phonon modes with characteristic dimensions of 10  $\mu\text{m}$ . The radius of curvature of the curved surface is twice the thickness of the substrate in a semi-confocal geometry, giving rise to the device name, SCHBAR.

Compared to a planar cavity, the curved surface eliminates the requirement of boundary parallelism and, in principle, yields higher mechanical quality factors. Optically, the curved surface also acts as a solid immersion lens (SIL) [2]. It reduces substrate refraction and thus enhances light extraction from the defects inside the resonator. The defects are microns below the surface and thus are well-protected from fabrication damage and surface effects. On the planar side of the device, we fabricate an integrated piezoelectric transducer and a microwave antenna that

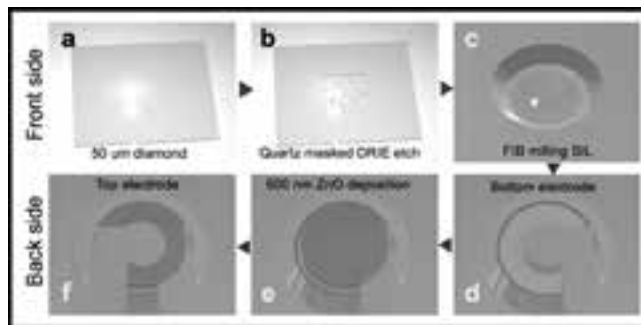


Figure 2: Fabrication process flow of the device starting from (a) a 50- $\mu\text{m}$ -thick double-side-polished diamond plate; (b) DRIE etch a diamond membrane down to 20  $\mu\text{m}$  or 10  $\mu\text{m}$  using  $\text{Ar}/\text{Cl}_2$  and  $\text{O}_2$  plasma, using a laser cut quartz mask; (c) Mill the parabolic SIL using focused Ga ion beam. (d-f) A ZnO piezoelectric transducer is fabricated on the backside of the SIL.

is aligned with the center of the resonator, allowing for acoustic and magnetic driving, respectively. The radius of the transducer has been designed to mode-match the waist of the confined acoustic wave, and the thickness of piezoelectric ZnO film is controlled to target a 3 GHz resonance mode, which allows stable confinement.

We fabricated SCHBAR devices from both diamond and 4H-SiC substrates. For simplicity, we restricted the process flow description to diamond (Figure 2). We start from a 50- $\mu\text{m}$ -thick, double-side polished single crystal diamond plate (nitrogen concentration  $< 1$  ppm). In the first step, we etch 5  $\mu\text{m}$  of diamond on each side of the substrate using  $\text{Ar}/\text{Cl}_2$  [3] and  $\text{O}_2$  [4] plasma as a stress-relief etch to eliminate the residual polishing damage. A laser-cut quartz shadow mask is then used to mask the

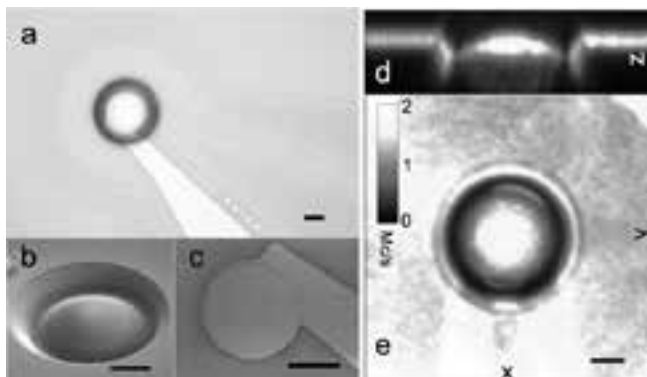


Figure 3: Micrographs and photoluminescence images of the finished device on an optical grade diamond substrate. (a) Device viewed from SIL side. (b) SEM of the milled solid immersion lens (radius of curvature 20  $\mu\text{m}$ ). (c) SEM of the transducer on the backside of the SIL. (d) and (e) show the photoluminescence image in a cross section view and a front view of the device (10  $\mu\text{m}$  thick), collected using a home-built confocal microscope. The scale bars in all figures are 10  $\mu\text{m}$  in length.

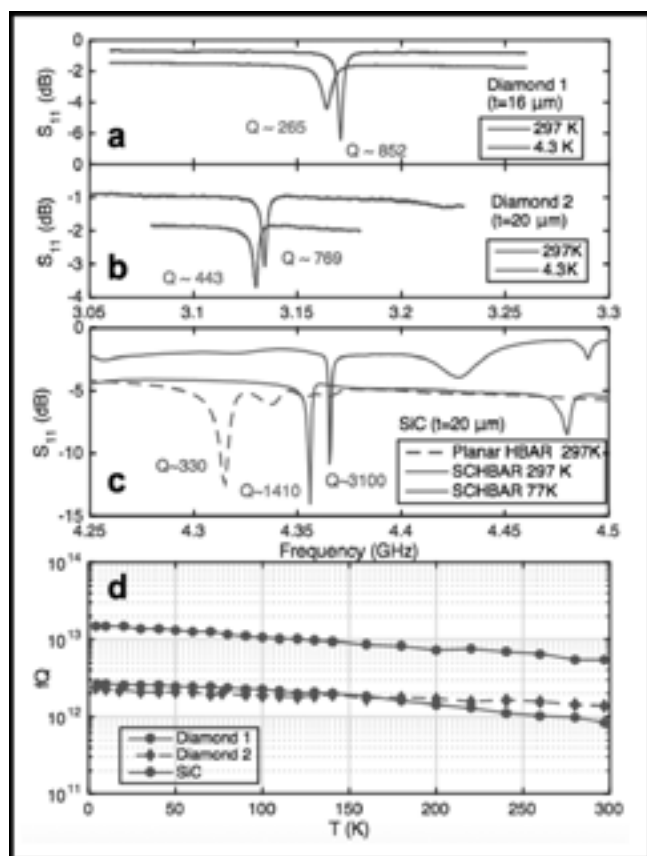


Figure 4: (a-c)  $S$ -parameters characterization of the device using a vector network analyzer. (d) Quality factors are extracted from the measured  $S$ -parameters as a function of temperature.

diamond for another 20- or 30- $\mu\text{m}$ -deep etch on one side of the sample (etch rate 5  $\mu\text{m}/\text{hr}$ ). After lifting the quartz mask, we end up with a 10  $\mu\text{m}$  or 20  $\mu\text{m}$  diamond membrane suspended in a 40  $\mu\text{m}$  frame. Atomic force microscopy (AFM) shows a surface roughness of < 0.3 nm.

A focused gallium ion beam (FIB, 30 kV, 20 nA) is used to mill the parabolic SIL structure on the diamond membrane. After FIB milling, the diamond surface is substantially graphitized and contains implanted gallium atoms (20 nm in depth). We then etch away the top 100 nm of damaged diamond using  $\text{Ar}/\text{Cl}_2$  plasma, followed by a 120 nm  $\text{O}_2$  plasma etch to oxygen terminate the diamond surface. A boiling tri-acid bath containing equal parts of sulfuric, nitric and perchloric acid is used to further clean off any residual contamination on the diamond. Optical profilometry and laser-scanning confocal microscopy have been used to confirm the profile accuracy of the SIL. The diamond membrane is then flipped with the planar side facing up. A piezoelectric zinc oxide (ZnO) transducer, consisting of bottom electrode (10 nm/90 nm Ti/Pt), 500 nm ZnO, top electrode (10 nm/180 nm Ti/Pt), and a microwave antenna are then lithographically defined and sputtered to finish the device fabrication.

We use a vector network analyzer (VNA) to characterize the scattering parameter ( $S$ -parameter) of the device. The mechanical quality factor of the device,  $Q$ , can be extracted from the VNA measurements. After mounting the devices in vacuum on a cold finger of a helium-flow cryostat, we perform electrical measurements as a function of temperature. The results are shown in Figure 4. The frequency and quality factor product is  $f \cdot Q > 10^{12}$  for a 20- $\mu\text{m}$ -thick diamond device at room temperature and  $f \cdot Q > 10^{13}$  for a 20- $\mu\text{m}$ -thick SiC device under cryogenic condition.

#### References:

- [1] Chen, H; Opondo, N. F; Jiang, B; MacQuarrie, E. R.; Daveau R. S.; Bhawe, S. A.; Fuchs G. D., arXiv: arXiv:1906.06309, 2019.
- [2] Hadden, J.; Harrison, J.; Stanley-Clarke, A.; Marseglia, L.; Ho, Y.-L.; Patton, B.; O'Brien, J.; Rarity, J. Applied Physics Letters 2010, 97, 241901.
- [3] Lee, C.; Gu, E.; Dawson, M.; Friel, I.; Scarsbrook, G. Diamond and Related Materials 2008, 17, 1292-1296.
- [4] Friel, I.; Clewes, S.; Dhillon, H.; Perkins, N.; Twitchen, D.; Scarsbrook, G. Diamond and Related Materials 2009, 18, 808-815.

# Coherent Spin-Magnon Coupling for Quantum-to-Quantum Transduction

CNF Project Number: 2126-12

Principal Investigator(s): Gregory D. Fuchs<sup>1</sup>

User(s): Hil Fung Harry Cheung<sup>2</sup>

Affiliation(s): 1. School of Applied and Engineering Physics, 2. Department of Physics; Cornell University

Primary Source(s) of Research Funding: Department of Energy (Grants No. DE-SC0019250)

Contact: gdf9@cornell.edu, hc663@cornell.edu

Website: <http://fuchs.research.engineering.cornell.edu>

Primary CNF Tools Used: GCA 5x stepper, AJA sputtering deposition system, P10 profilometer, Westbond 7400A ultrasonic wire bonder, Veeco Icon atomic force microscope, JEOL JBX-6300FS 100 kV electron-beam lithography system, PT770 etcher

## Abstract:

Nitrogen-vacancy (NV) centers possess long spin coherence lifetimes and coherent optical transitions at low temperatures. The combination of long-lived ground state spins and a narrow optical transition is useful for quantum-to-quantum transduction between spins and photons and quantum entanglement between NV spins and photons have been demonstrated. Here, we are developing an interface between magnons and NV spins, which is a key link in a quantum network.

## Summary of Research:

A key requirement in building a quantum network is the ability to transduce quantum information from one quantum system to another quantum system [1]. Diamond NV centers have long spin coherence time and a narrow linewidth optical transition, enabling both spin-photon entanglement [2,3] and spin-spin entanglement via photons [3]. NV centers are also suitable for quantum-to-quantum transduction between photons and magnons.

We are developing a platform that coherently couples microwave magnons to NV spins through magnetic dipole interaction. For this platform to perform quantum transduction, the magnons and spins decoherence rates need to be smaller than the coupling rate between magnons and spins. To enhance the coupling, the NV spin needs to be close ( $\sim 30$  nm) to the magnetic material (see Figure 1 for a schematic). To reduce magnon decoherence, we work with a low loss organic based magnetic material vanadium tetracyanoethylene ( $V[TCNE]_{x-2}$ ) [4] in collaboration with Prof. Johnston-Halperin's group at Ohio State University (OSU).

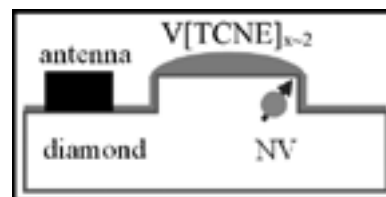


Figure 1: Schematic of coherent coupling between spins and magnons through an NV spin coupling to a magnon mode in  $V[TCNE]_{x-2}$ .

Diamond polishing results in a highly strained surface, which increases near surface NV centers decoherence. This can be mitigated by etching away the first several microns of diamond using reactive ion etch (RIE) [5,6]. We compare the diamond surface before and after the stress relief etch using the PT770 etcher and observe a significant decrease in polishing streaks and surface roughness (Figure 2).

The spin-magnon coupling strength is maximized when the NV is aligned with the magnon mode. One approach to improve alignment is to etch the diamond with disks like structures and the grown magnetic material will be automatically aligned with the diamond structure. In order to optimize disks dimension and material growth condition, we fabricate  $SiO_2$  arrays as test targets with diameters ranging from 200 nm to 8000 nm using electron beam lithography. The  $SiO_2$  disks will also be used as shadow masks for diamond etching. Our collaborators at OSU have grown  $V[TCNE]_{x-2}$  films on these disks showing nucleation free growth (Figure 3).

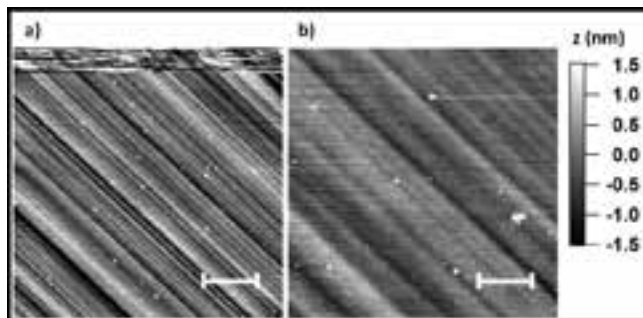


Figure 2: AFM image of the diamond before (a) and after (b)  $\text{Ar}/\text{Cl}_2$  reactive ion etch. Scale bar is  $1\ \mu\text{m}$ .

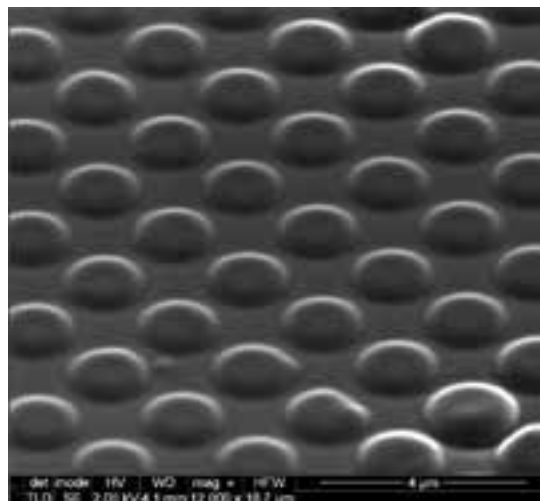


Figure 3: SEM of  $\text{V}[\text{TCNE}]_{x-2}$  grown on  $1\ \mu\text{m}$   $\text{SiO}_2$  disks.

### References:

- [1] H. J. Kimble, "The quantum internet" *Nature* 453, 1023 (2008).
- [2] E. Togan, et al. "Quantum entanglement between an optical photon and a solid-state spin qubit." *Nature* 466, 730 (2010).
- [3] B. Hensen, et al. "Loophole-free Bell inequality violation using electron spins separated by 1.3 kilometres" *Nature* 526, 682 (2015).
- [4] N. Zhu, et al. "Low loss spin wave resonances in organic-based ferrimagnet vanadium tetracyanoethylene thin films" *Appl. Phys. Lett.* 109, 082402 (2016).
- [5] Y. Chu, et al. "Coherent optical transitions in implanted nitrogen vacancy centers" *Nano Lett.* 14, 982 (2014).
- [6] S. Sangtawesin, et al. "Origins of diamond surface noise probed by correlating single spin measurements with surface spectroscopy" *ArXiv:* 1811.00144 (2018).

# Optical Properties of Locally Strained WSe<sub>2</sub> Monolayers

**CNF Project Number: 2126-12**

**Principal Investigator(s): Gregory D. Fuchs**

**User(s): Raphael Sura Daveau**

*Affiliation(s): Applied and Engineering Physics, Cornell University*

*Primary Source(s) of Research Funding: Air Force Office of Scientific Research*

*Contact: gdf9@cornell.edu, rsd228@cornell.edu*

*Website: <http://fuchs.research.engineering.cornell.edu>*

*Primary CNF Tools Used: JEOL 6300 electron-beam writer, GCA 5x stepper, Oxford 81 etcher*

## Abstract:

**We investigate spectral properties of locally strained tungsten diselenide (WSe<sub>2</sub>) monolayers. The local strain is created by layering the WSe<sub>2</sub> monolayer over a silicon dioxide (SiO<sub>2</sub>) substrate pre-patterned with 150 nm-wide nanopillars. From spectral measurements, we show that strain shrinks the band gap resulting in local wells that concentrate carriers and redshifts the exciton recombination energy. Low temperature measurements show that the strain gradient is so far insufficient to create quantum confinement of carrier to generate single-photon emission.**

## Summary of Research:

Monolayer transition metal dichalcogenides (TMD) are direct bandgap semiconductors with a very strong light-matter interaction, large excitonic effects and possessing a new electronic degree of freedom, known as valley, that locks excitons to a given photon helicity [1]. Tungsten diselenide (WSe<sub>2</sub>) is one such TMD, which has been shown to host quantum emitters [2]. Applications of quantum emitters inheriting valley properties are numerous, including dynamic generation of flying qubits with orthogonal polarization. While most reported emitters in WSe<sub>2</sub> monolayers are located at random, few reports show deterministic activation of quantum emitters via local strain by placing the WSe<sub>2</sub> monolayer over a patterned substrate [3]. The strain locally bends the band gap and creates quantum confinement of charge carriers, eventually leading to the emission of single photons upon recombination. Here, we report on the fabrication of nanopillar-patterned substrates, transfer and successful local straining of WSe<sub>2</sub> monolayers. We quantify the effect of strain on the band gap of WSe<sub>2</sub> at room temperature, while measurements at cryogenic temperatures remain elusive to resolve quantum emitters.

The nanopillars are fabricated on a SiO<sub>2</sub> substrate via electron-beam lithography (JEOL 6300) using hydrogen silsesquioxane (HSQ) negative resist. The nanopillars are cylindrical with equal height and diameter of 150 nm. The spacing between pillars is 3 μm, which gives enough room for the WSe<sub>2</sub> monolayer to both conform to the pillars while layering on the substrate. To place an exfoliated WSe<sub>2</sub> monolayer deterministically over the fabricated nanopillars, we employ an all-dry transfer

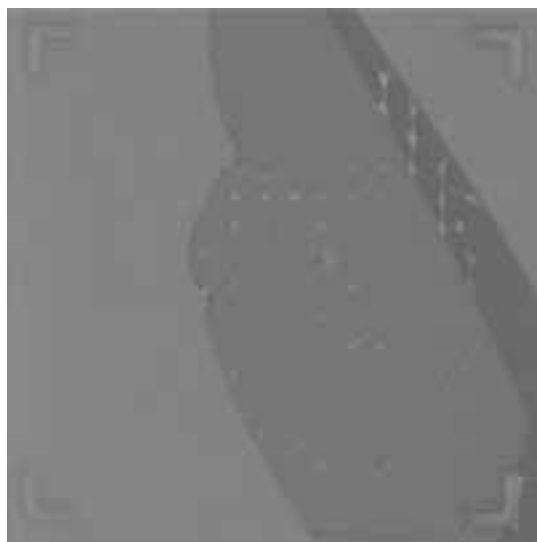


*Figure 1: Optical microscopy image of a WSe<sub>2</sub> monolayer transferred over an array of nanopillars. Bright spots indicate tenting sites resulting in local strain in the WSe<sub>2</sub> monolayer.*

technique using polydimethylsiloxane (PDMS) stamps. Figure 1 shows an optical microscopy image of a mechanically exfoliated WSe<sub>2</sub> monolayer transferred on top of a nanopillar array. The tenting of the monolayer over the pillars is visible as bright spots due to increased contrast. Atomic force microscopy imaging confirms the conforming of the monolayer to the substrate and nanopillars.

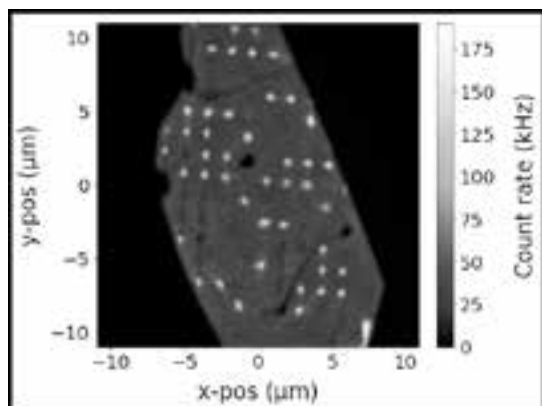


Figure 2: Room temperature photoluminescence scan of the  $WSe_2$  monolayer displaying brighter spots at the nanopillar sites.

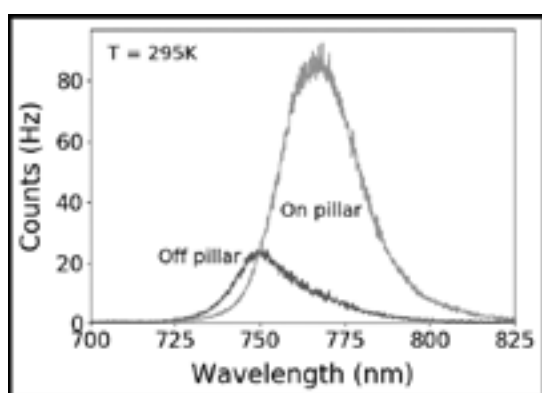


Figure 3: Spectrum of strained and unstrained  $WSe_2$  monolayer. Besides brightness increase, a clear redshift of the emission at the pillar indicates strain that shrinks the band gap.

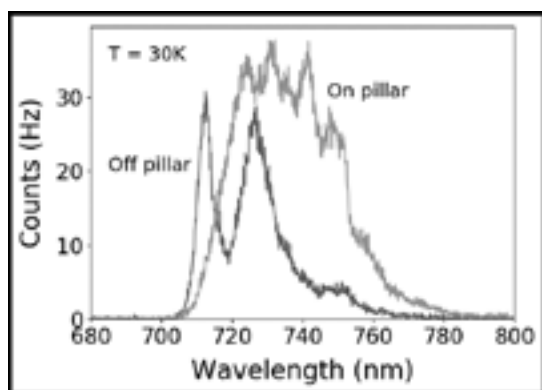


Figure 4: Spectrum of  $WSe_2$  monolayer at  $T = 30$  K. Besides the global redshift, no sharp features characteristic of quantum emitters are observed.

As-transferred  $WSe_2$  monolayers necessitate no further treatment to be investigated optically. We perform spectral and micro-photoluminescence measurements in a confocal setup. Charge carriers are excited with a continuous wave laser at 532 nm with a power density of about  $100 \text{ nW}/\mu\text{m}^2$ . In the photoluminescence scan of Figure 2, we see a clear brightness increase at the pillar sites, indicating a larger carrier concentration. The strain shrinks the bandgap at the nanopillar sites, thus creating a local well where carriers get concentrated. This is consistent with the results of Figure 3, which shows a redshift of the exciton recombination energy by 35 meV (16 nm) at strained sites compared to unstrained  $WSe_2$ . For comparison, this is twice the value reported by Palacios-Berraquero, et al., in [3], which is promising for obtaining quantum emitters.

Quantum emitters in  $WSe_2$  monolayers can only be resolved at cryogenic temperatures. We place the sample in a helium-flow cryostat and cool the sample to 30 K.

As shown in Figure 4, the emission of the unstrained  $WSe_2$  is composed of the neutral exciton at 715 nm, negatively charged excitons at 735 nm and an additional peak at longer wavelengths originating from impurity-bound excitons [3]. At the pillar sites where the  $WSe_2$  is strained, the spectrum is globally redshifted and is broadened towards longer wavelengths due to various local exciton traps naturally more populated at low temperatures. This data does not show correlation between strained sites and sharp emission lines characteristic of single quantum emitters. The temperature of the experiment is likely too high and resulting in a thermal depopulation of narrow exciton traps.

We conclude that the strain gradient created by the pillars is either too weak and/or too broad to confine a single exciton at 30 K but should be sufficient at temperatures below 10 K according to previous reports. Additionally, residual charging of the nanopillars from the electron beam during fabrication might quench the quantum emitters. Future generation of substrates will include electrical gating of the  $WSe_2$  monolayer to control the charge environment of the emitters.

#### References:

- [1] K. F. Mak and J. Shan, Nat. Photonics 10, 216 (2016).
- [2] A. Srivastava, M. Sidler, A. V. Allain, D. S. Lembke, A. Kis and A. Imamolu, Nat. Nanotechnology 10, 1038 (2015).
- [3] C. Palacios-Berraquero, D. M. Kara, A. R.-P. Montblanch, M. Barbone, P. Latawiec, D. Yoon, A. K. Ott, M. Loncar, A. C. Ferrari and M. Atature, Nat. Comm. 8, 15093 (2017).

# Micrometer-Scale Graphene-Based Hall Sensors with Tunable Sensitivity

CNF Project Number: 2361-15

Principal Investigator(s): Katja C. Nowack

User(s): Brian T. Schaefer

Affiliation(s): Laboratory of Atomic and Solid-State Physics, Department of Physics; Cornell University

Primary Source(s) of Research Funding: Cornell Center for Materials Research with funding from the NSF MRSEC program (DMR-1719875), National Science Foundation Graduate Research Fellowship under Grant No. DGE-1650441

Contact: kcn34@cornell.edu, bts72@cornell.edu

Website: <http://nowack.lasp.cornell.edu/>

Primary CNF Tools Used: Veeco Icon AFM, Zeiss Supra SEM/Nabity, Trion etcher, 5x stepper, Oxford 81, Plasma-Therm VersaLine, odd-hour evaporator

## Abstract:

We have fabricated high-quality graphene-based Hall sensors that can be tuned to maintain high magnetic field sensitivity at cryogenic temperatures, at room temperature, and in high background magnetic field. At best, we achieve a sensitivity of  $80 \text{ nT Hz}^{-1/2}$ , outperforming existing Hall sensor technologies. We will soon fabricate these devices into scanning probes to study magnetism and superconductivity via micrometer-scale magnetic imaging.

## Summary of Research:

In a Hall-effect sensor, the deflection of current in a small magnetic field  $B$  produces a voltage response that is linear in  $B$  and large at low carrier density. The noise in the Hall voltage measurement ultimately determines the magnetic field sensitivity and is typically limited by instrumentation, Johnson, and low-frequency charge noise [1,2]. The requirements for large voltage response and low noise suggest a material with low carrier density and high mobility [1,3]. Whereas mobility decreases at low carrier density in most two-dimensional electron systems, in graphene the mobility is enhanced in the absence of long-range impurity scattering [4]. We exploit tuning the carrier density in graphene through electrostatic gating to maintain sensitivity in a wide range of temperature and magnetic field conditions.

To obtain the cleanest possible graphene devices (Figure 1), we adopt recently developed strategies to achieve record-low charge inhomogeneity in graphene: encapsulation in hexagonal boron nitride (hBN) gate dielectrics [5] and few-layer graphite (FLG) gate electrodes [6]. The low charged defect density in hBN and FLG [6] improve carrier mobility [5] and have the potential to reduce noise [7]. We use electron-beam lithography (Zeiss Supra, Nabity), plasma etching (Trion),

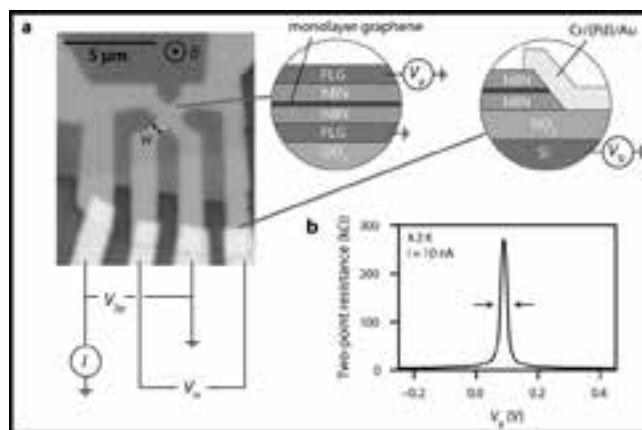


Figure 1: (a) Optical micrograph of a  $w = 1 \mu\text{m}$  Hall sensor. Upper inset: Layer structure consisting of graphene encapsulated with hexagonal boron nitride (hBN) and few-layer graphite (FLG). Lower inset: Edge contacts to part of the graphene extending outside of the FLG-gated region. (b) Top gate dependence of the two-point resistance  $R_{2p} = V_{2p}/I$ .

and electron-beam evaporation to define the device shape and deposit metal (Cr/Au) contacts. The two-point resistance of the device increases sharply as we apply top gate voltage  $V_g$  to tune the carrier density through charge neutrality point (Figure 1b).

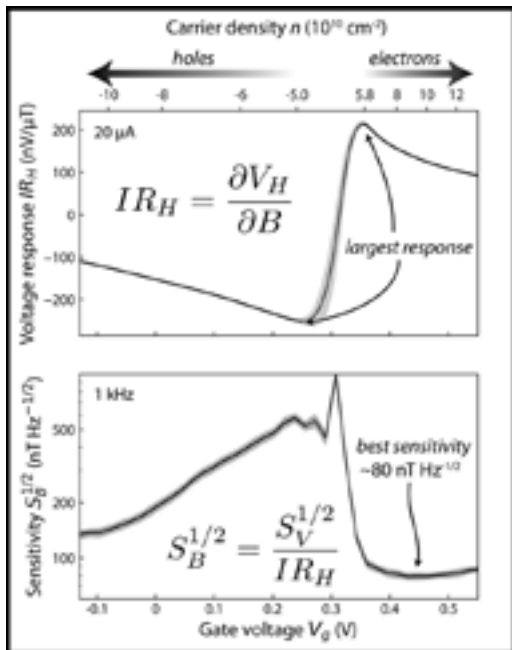


Figure 2: Gate voltage dependence of the Hall coefficient (top panel) and magnetic field sensitivity (bottom panel).

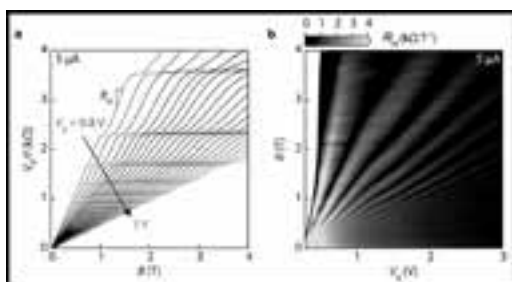


Figure 3: (a) Magnetic field dependence of the Hall resistance in the quantum Hall regime for a series of gate voltages. (b) Map of the Hall coefficient versus magnetic field and gate voltage.

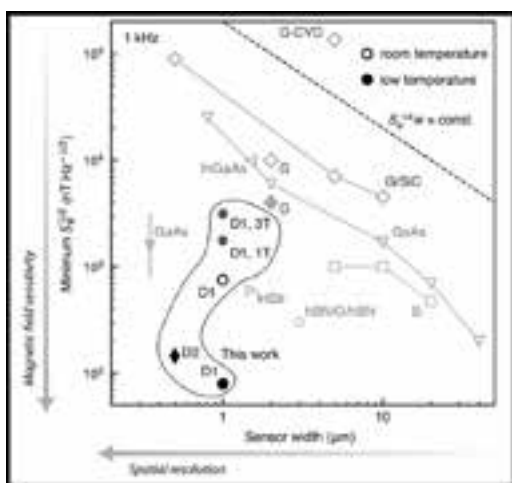


Figure 4: Magnetic field sensitivity  $S_B^{1/2}$  at 1 kHz compared against the width  $w$  of Hall sensors reported here and in the literature. Filled (open) markers correspond to liquid-helium (room) temperature. The outlined group of markers shows the best performance of our devices, and the other markers are estimates of the best performance of devices made from graphene and conventional semiconductor materials.

To properly characterize the sensitivity of the devices to small changes in magnetic field [1,3], we apply a DC bias current and determine the Hall coefficient  $R_H = I^{-1} [\partial V_H / \partial B]_{B=0}$  and Hall voltage noise spectral density  $S_V^{1/2}$ . The latter is dominated by flicker noise, which is pervasive in graphene-based microdevices [2] and decreases as  $1/f^{1/2}$  with frequency  $f$ . The noise at 1 kHz is largest at low carrier density, at which charge fluctuations are poorly screened and the device resistance is large.

Dividing the Hall voltage noise by the Hall coefficient, we estimate the magnetic field sensitivity  $S_B^{1/2} = S_V^{1/2} / IR_H$  (Figure 2, bottom panel). This quantity, when multiplied by the square root of the bandwidth of the measurement, represents the minimum detectable magnetic field. The best sensitivity —  $\sim 80 \text{ nT Hz}^{-1/2}$  — is found at an intermediate carrier density, indicating that the reduction in  $S_V^{1/2}$  from tuning away from charge neutrality is more important than tuning to the largest  $R_H$ .

We also demonstrate for the first time that magnetic field response can be maintained in a large background magnetic field. While at low magnetic field, the Hall voltage grows linearly with magnetic field, above  $\sim 500 \text{ mT}$  (at  $5 \mu\text{A}$  bias) the Hall voltage begins to develop plateaus, indicating a transition into the quantum Hall regime (Figure 3a). At each  $(B, V_g)$ , we calculate the effective Hall coefficient  $R_H = I^{-1}(\partial V_H / \partial B)$  and plot as a map in Figure 3b, in which dark bands indicate suppressed Hall coefficient due to the plateaus. At a fixed magnetic field, tuning the gate voltage into one of the white bands enables the sensor to maintain sensitivity in high magnetic field.

Finally, in Figure 4 we compare the noise measurements for our devices at low temperature and room temperature against similar measurements on leading micrometer-scale Hall sensors reported in the literature. Our devices, which combine high magnetic field sensitivity with small sensor size, lie towards the lower left corner of the plot, outperforming all other reported materials. Our work establishes a new standard for fabricating Hall sensors to engineer superior device performance. We anticipate that scanning graphene-based magnetic field probes will enable the first high-resolution, high-sensitivity imaging of localized magnetic fields under high temperature and magnetic field conditions.

**References:**

- [1] Dauber, J., et al. Ultra-sensitive Hall sensors based on graphene encapsulated in hexagonal boron nitride. *Appl. Phys. Lett.* 106, 193501 (2015).
- [2] Balandin, A. A. Low-frequency  $1/f$  noise in graphene devices. *Nat. Nanotechnol.* 8, 549-555 (2013).
- [3] Hicks, C. W., Luan, L., Moler, K. A., Zeldov, E., and Shtrikman, H. Noise characteristics of 100 nm scale GaAs/Al<sub>x</sub>Ga<sub>1-x</sub>As scanning Hall probes. *Appl. Phys. Lett.* 90, 133512 (2007).
- [4] Das Sarma, S., Adam, S., Hwang, E. H., and Rossi, E. Electronic transport in two-dimensional graphene. *Rev. Mod. Phys.* 83, 407-470 (2011).
- [5] Wang, L., et al. One-dimensional electrical contact to a two-dimensional material. *Science* 342, 614-617 (2013).
- [6] Zibrov, A. A., et al. Tunable interacting composite fermion phases in a half-filled bilayer-graphene Landau level. *Nature* 549, 360-364 (2017).
- [7] Stolyarov, M. A., Liu, G., Rumyantsev, S. L., Shur, M., and Balandin, A. A. Suppression of  $1/f$  noise in near-ballistic *h*-BN-graphene-*h*-BN heterostructure field-effect transistors. *Appl. Phys. Lett.* 107, 023106 (2015).

# Gigahertz Surface Acoustic Waves on Periodically Patterned Layered Nanostructures

**CNF Project Number: 2369-15**

**Principal Investigator(s): Brian C. Daly**

**User(s): Weili Cui**

*Affiliation(s): Physics Department, Astronomy Department; Vassar College, Poughkeepsie, NY*

*Primary Source(s) of Research Funding: National Science Foundation Award Division of Materials Research-1709521*

*Contact: brdaly@vassar.edu, weilicui@yahoo.com*

*Website: <http://pages.vassar.edu/ultrafast/>*

*Primary CNF Tools Used: E-beam lithography, CVD, thermal evaporation*

## Abstract:

We used the ultrafast pump-probe technique known as picosecond ultrasonics to generate and detect surface acoustic waves on nanoscale aluminum (Al) lines on silicon dioxide (SiO<sub>2</sub>) on silicon (Si). In all cases we identified a Rayleigh-like surface acoustic wave with wavelength equal to the pitch of the lines and frequency in the range of 5-24 GHz. In some samples, we detected additional, higher frequency surface acoustic waves or independent modes of the Al lines with frequencies close to 50 GHz. Our new focus is on the effect of the probe beam polarization on which modes are detected.

## Summary of Research:

In two recent papers, we have reported measurements of surface acoustic waves (SAWs) in periodically patterned nanostructures [1,2]. In these experiments we used an ultrafast optical pump-probe technique known as picosecond ultrasonics to generate and detect the SAWs. We then compared the experimental measurements to molecular dynamics simulations of the nanostructures in order to identify which modes we detected. In the second of these two papers, we measured samples that were fabricated at CNF and detected Rayleigh-like SAWs and Sezawa-like SAWs with wavelength equal to the pitch of Al lines that were etched on the sample. In some cases we also measured SAWs with wavelength equal to one-half or one-third of the pitch.

The ultrafast optical pump-probe experiment known as picosecond laser ultrasonics (PLU) has been described extensively in the literature [3]. We performed this experiment with a Ti:Sapphire oscillator operating at a 76 MHz repetition rate with pump wavelength of 800 nm and probe wavelengths of 800 nm or 400 nm. The 10 patterned samples that we studied are illustrated schematically in Figure 1. The samples were fabricated at the Cornell NanoScale Facility by the following process: thermal oxidation to produce the amorphous SiO<sub>2</sub> layer of thickness  $d = 60$  or  $112$  nm, thermal evaporation of 25 nm of Al, and e-beam lithography and dry etching to create the nanometer scale Al pattern. The lines were etched perpendicular to the [110] direction in the Si

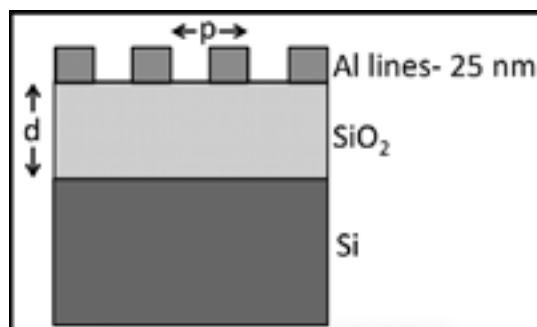


Figure 1: Schematic diagram of the samples. Film thickness  $d$  was either 60 nm or 112 nm as measured by picosecond ultrasonics. Al lines with pitch  $p$  varied from 1000 nm down to 140 nm. The duty cycle was close to 50% ( $\pm 10\%$ ) in all cases as measured by SEM imaging.

substrate, they varied in pitch  $p$  ranging from 140 nm up to 1000 nm, and they were all etched near 50% (ranging from 40-60%) duty cycle. The patterned samples were placed into the optical setup, where pump and probe beams were both focused onto the same 20  $\mu\text{m}$  diameter spot, so that anywhere from 20 to 140 periods of the pattern were strongly illuminated. The ultrafast pump pulses were absorbed by the Al lines, and the resulting rapid thermal expansion launched ultrasonic waves both

downward into the  $\text{SiO}_2$  film and Si substrate, and laterally as SAWs in the direction perpendicular to the line pattern. The ultrasonic waves can be detected by the time delayed probe pulses due to transient changes in the reflectivity  $\mu R$  that they cause. The sources of these transient changes include the dependence of the optical constants of the Al on strain as well as the changes in reflectivity of the optical grating produced by the nanostructure as it responds to the acoustic oscillations. In this work, we focus on the signals caused by laterally propagating ultrasound and not the signals caused by acoustic waves traveling normal to the sample surface.

The conclusions about the types of surface acoustic waves we detected are described in Ref. 2. The next step in this project is to determine the impact of the polarization of the probe beam on the detection mechanism.

Figure 2 clearly demonstrates that for certain nanostructure periodicities, the polarization can dramatically effect which modes are detected. We are currently exploring this question computationally using a finite difference frequency domain (FDFD) calculation, and experimentally on a new set of samples to be fabricated at CNF this summer. We will pattern the Al lines on a sapphire substrate rather than a silicon substrate. The use of a transparent substrate will simplify the optical interaction of the probe beam with the sample and give us more insight into the mechanism behind the polarization effect.

### References:

- [1] M.M. Bjornsson et al., J. Appl. Phys. 117, 095305 (2015).
- [2] M. Colletta, et al., Ultrasonics 87, 126 (2018).
- [3] C. Thomsen, H. T. Grahn, H. J. Maris, and J. Tauc, Phys. Rev. B 34, 4129 (1986).

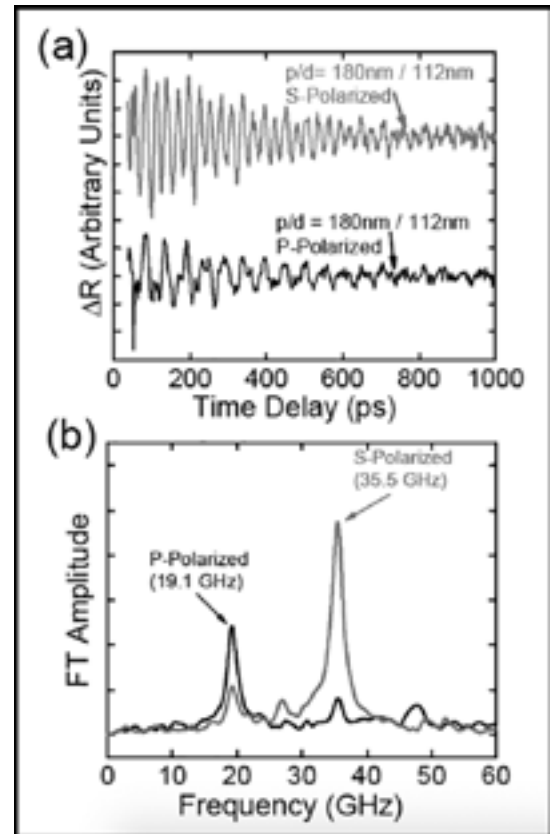


Figure 2: (a)  $\mu R$  for a sample with a pitch of 180 nm using 400 nm probe in the S-Polarized and P-polarized configurations. (b) Fourier transform amplitude of the signals in (a).

# Ultrafast Energy-Efficient Spin-Torque Magnetic Random Access Memories

**CNF Project Number: 2444-16**

**Principal Investigator(s): Robert A. Buhrman**

**User(s): Lijun Zhu**

*Affiliation(s): School of Applied and Engineering Physics, Cornell University*

*Primary Source(s) of Research Funding: Office of Naval Research*

*Contact: rab8@cornell.edu, lz442@cornell.edu*

*Primary CNF Tools Used: ASML stepper, Veeco Icon, JEOL JBX-6300FS, ASML stepper, AJA sputtering*

## Abstract:

Spin-orbit torques [1-5] have been a hot topic in the research and technology communities due to their great promise for magnetic memories, oscillators and logic of post-Moore era. Here we demonstrate ultrafast energy-efficient magnetic random access memories (MRAMs) [6,7] fabricated at the Cornell NanoScale Science and Technology Facility.

## Summary of Research:

We fabricated the spin-torque MRAM devices — schematically shown in Figure 1(a). The magnetic multilayer samples are patterned into three-terminal MRAM devices with a three-step procedure. First, we defined the spin Hall channel using DUV lithography (ASML stepper) and ion beam etching and measured the channel size to be  $300 \times 600 \text{ nm}^2$  by atomic force microscopy (Veeco Icon). We then defined the elliptical magnetic tunnel junction nanopillars with different aspect ratios and micron-size “via” pillars (as vertical connector between the bottom channel to top contact) onto the spin Hall channel with e-beam lithography (JEOL JBX-6300FS) and ion beam etching, and isolated the pillars with 80 nm thick  $\text{SiO}_2$  deposited by an e-beam evaporator. Finally, contacts of Ti 5/Pt 50 were deposited on the top of the magnetic tunnel junction pillars and “via” pillars for electrical measurements by combining the DUV lithography (ASML stepper), AJA sputtering, and liftoff processes.

Figure 1(b) shows the characteristic switching behavior of the MRAMs as the write current in the spin Hall channel is ramped quasi-statically. The MTJs show abrupt switching at write currents of  $20 \mu\text{A}$ . Since thermal fluctuations assist the reversal of a nanoscale MTJ device during slow current ramps, we carried out ramp rate measurements and determined that the zero-

temperature switching current is  $70 \mu\text{A}$ . The critical switching density in the Pt spin Hall channel is therefore  $j_{\text{co}} \approx 3.6 \times 10^7 \text{ A/cm}^2$ . Both the total critical switching and the low switching current density are the lowest yet reported for any spin-torque MRAMs. We also measured the fast switching behaviors of our spin-torque MRAMs and find deterministic switching even at 200 ps, which is also the fastest switching yet known.

## References:

- [1] L. Zhu, D.C. Ralph, R.A. Buhrman, Phys. Rev. Lett. 122, 077201 (2019).
- [2] L. Zhu, K Sobotkiewich, X. Ma, X. Li, D.C. Ralph, R.A. Buhrman, Adv. Funct. Mater. 29, 1805822 (2019).
- [3] L. Zhu, D.C. Ralph, R.A. Buhrman, Phys. Rev. B 99, 180404 (R) (2019).
- [4] L.J. Zhu, D.C. Ralph, R.A. Buhrman, Phys. Rev. B 98, 134406 (2018).
- [5] L. Zhu, D.C. Ralph, R.A. Buhrman, Phys. Rev. Appl. 10, 031001 (2018).
- [6] L. Zhu, L. Zhu, S. Shi, M. Sui, D. C. Ralph, R. A. Buhrman, Phys. Rev. Appl. 11, 061004 (2019).
- [7] L. Zhu, L. Zhu, S. Shi, D. C. Ralph, R. A. Buhrman, Energy-efficient Ultrafast SOT-MRAMs based on low-resistivity spin Hall metals  $\text{Au}_{0.25}\text{Pt}_{0.75}$ , in preparation.

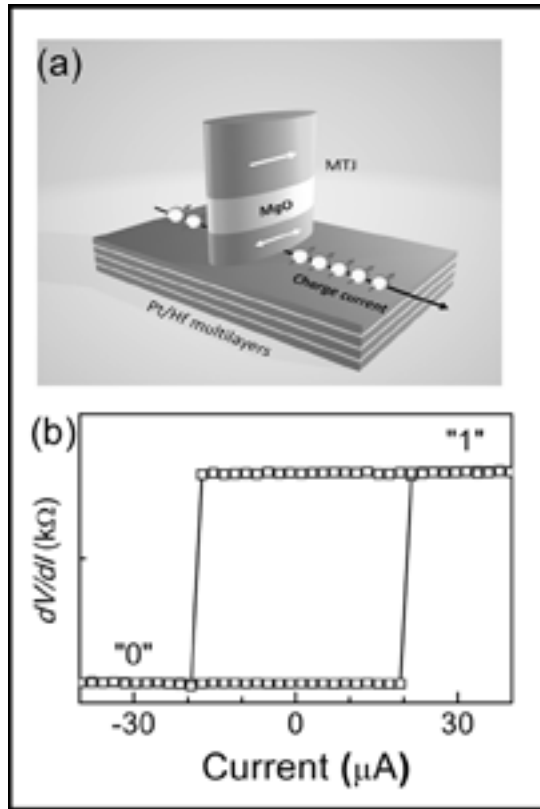


Figure 1: (a) Schematic of a spin-torque MRAM device;  
(b) Current-induced switching of the MRAMs.

# Low Loss Photonic Packaging Using Fusion Splicing

**CNF Project Number: 2524-17**

**Principal Investigator(s): Jaime Cardenas**

**User(s): Juniyali Nauriyal, Meiting Song**

*Affiliation(s): Department of Electrical and Computer Engineering, University of Rochester;  
The Institute of Optics, University of Rochester*

*Primary Source(s) of Research Funding: The Hajim School of Engineering and Applied Sciences, University of Rochester*

*Contract: jaime.cardenas@rochester.edu, j.nauriyal@rochester.edu*

*Primary CNF Tools Used: ASML stepper, Oxford 100, Oxford 82, Gamma, GSI, Furnace, Unaxis, Xetch, dicing saw*

## Abstract:

**We present a novel photonic packaging method for permanent optical edge coupling between a fiber and chip using fusion splicing. We demonstrate minimum loss of 1.0 dB per-facet with 0.6 dB penalty over 160 nm bandwidth from 1480-1640 nm.**

## Summary of Research:

One of the biggest challenges in the silicon photonics industry is to permanently attach an optical fiber to a photonic chip, with high optical coupling efficiency. Multiple packaging methods have been demonstrated to increase the coupling efficiency between an optical fiber and a chip while increasing throughput for high volume manufacturing. Some of these methods use grating couplers to couple light from the top of the chip, but grating couplers are fundamentally bandwidth-limited while edge couplers use a form of waveguide taper and/or lensed fiber and are inherently broadband but require access to the sides of a chip and have tight misalignment tolerances [1]. When used in packaging applications, individual fibers and fiber arrays are permanently placed over grating couplers using optical adhesive and fixtures or ferrules. Optical adhesives shrink during curing and alignment tolerances are tight, it becomes challenging to achieve lower losses with high scalability.

We present a novel photonic packaging method for permanent optical edge coupling between a fiber and a photonic chip using fusion splicing which is low-cost, low-loss and scalable to high volume manufacturing [2]. We introduce a cantilever-type silicon dioxide mode converter which is mode matched to a single mode fiber at the input facet and a silicon nitride waveguide at the output facet [3-5]. The silicon dioxide mode converter is permanently fused to the optical fiber using a CO<sub>2</sub> laser (Figure 1) [5]. As the main components of an optical fiber are silicon dioxide same as the silicon dioxide cladding on the photonic chip, it readily absorbs 10.6 μm of radiative power from the laser and forms a permanent bond between the two interfaces. This packaging method

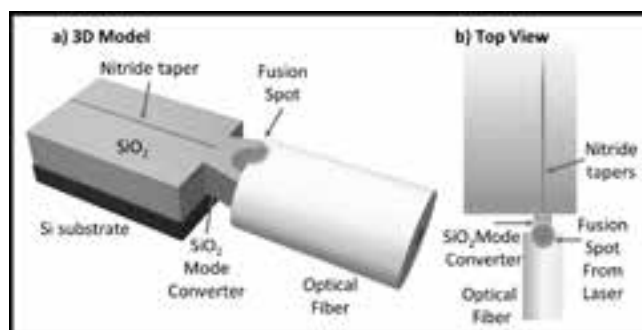


Figure 1: a) 3D model of a packaged device using silicon dioxide mode converter fused to SMF-28 fiber. It shows undercut silicon substrate which isolates the oxide mode converter from the chip, b) schematic representation of the top view of the method shows the fusion splicing spot from the CO<sub>2</sub> laser which improves the coupling efficiency.

is compatible with any photonic device with a cladding of silicon dioxide with different types of inverse nanotapers. The geometry of the oxide mode converter can be engineered to match the mode profile of the waveguide nanotaper. The proposed method is compatible with standard foundry processes and does not require any deviations from the standard fabrication process. The oxide mode converter uses two-stage mode conversion: first mode conversion from the waveguide (mode size < 1 μm) into the oxide mode converter and second, from the oxide mode converter to the optical fiber (mode size of 10.4 μm). The two sides of the oxide mode converter are engineered to maximize the coupling from the waveguide nanotaper to the cleaved optical fiber.

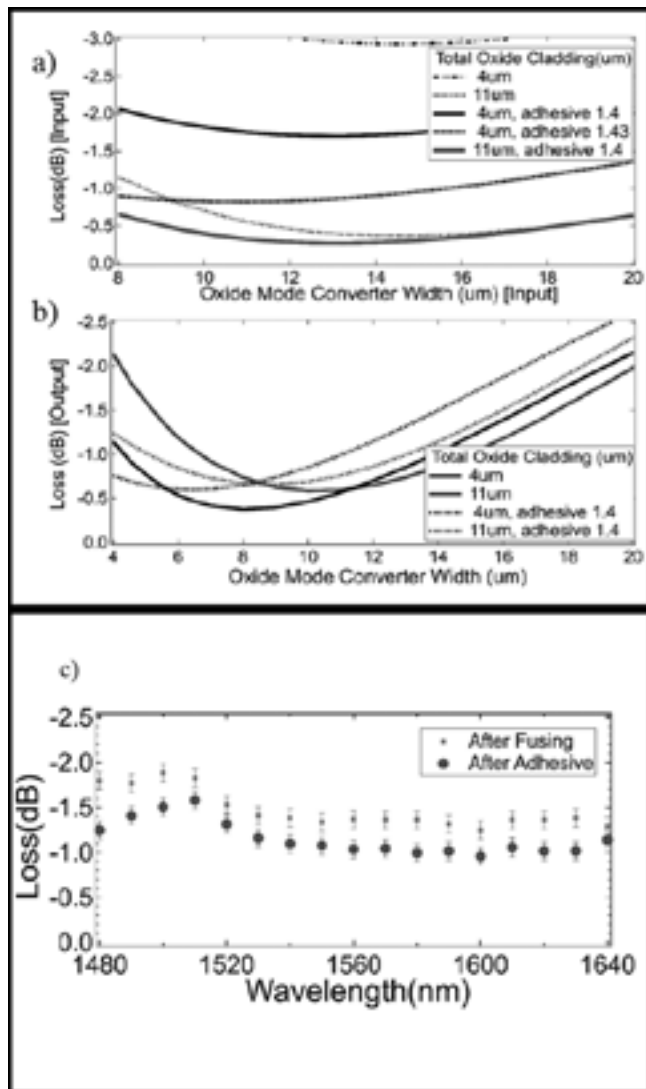


Figure 2: Coupling loss between the fiber and the mode converter as a function of oxide mode converter input width, a) at the input interface from the fiber to the mode converter, and b) from the mode converter into the waveguide. c) The coupling loss per-facet after fusing and after applying adhesive as a function of wavelength, a minimum loss of 1.0 dB is measured.

The width of the oxide mode converter is calculated with different total oxide cladding thickness ( $\mu\text{m}$ ) (Figure 2a and b) with a fixed nitride waveguide taper width. Our simulations also show that a minimum coupling loss of 0.3 dB can be achieved with 14  $\mu\text{m}$  oxide mode converter width and 11  $\mu\text{m}$  total (top plus bottom) oxide cladding thickness with an adhesive of refractive index 1.4. The waveguide nanotaper is made of silicon nitride and is 0.18  $\mu\text{m}$  wide at the tip and 100  $\mu\text{m}$  long with a linear profile. We also calculated the 1 dB penalty in misalignment tolerance between the fiber and the oxide mode converter, which is  $\pm 2.5 \mu\text{m}$  and  $\pm 2.4 \mu\text{m}$  in horizontal and vertical directions respectively.

The devices were fabricated using standard CMOS compatible, microfabrication techniques. The waveguides were patterned using standard DUV optical lithography at 248 nm, the devices were etched using inductively coupled plasma reactive ion etcher and cladded oxide using plasma enhanced chemical vapor deposition. After dicing, we remove the silicon substrate underneath the oxide mode converter to optically isolate it. We fuse the SMF-28 cleaved fiber to the oxide mode converter using a  $\text{CO}_2$  laser and reinforce the splice by adding an optical adhesive of suitable refractive index. Fusing the fiber and the chip together using radiative heating leaves no residue behind and forms a permanent bond.

We demonstrate a minimum loss of 1.0 dB per facet with a 0.6 dB penalty over 160 nm bandwidth near the C-band on a standard, cleaved SMF-28 fiber fused to the silicon nitride photonic chip (Figure 2c) [2]. We measure coupling loss after fusing and after the addition of optical adhesive of refractive index 1.3825.

We measure a -30.1 dB of optical return loss using a circulator for 1550 nm after fusing the optical fiber to the chip. The coupling loss before fusing was 2.1 dB with 0.4 dB of waveguide propagation loss. After fusing the fiber to the chip, the loss decreased to 1.3 dB on the fused facet and further decreases to 1.0 dB after the application of optical adhesive.

#### References:

- [1] T. Barwicz, et al., A Novel Approach to Photonic Packaging Leveraging Existing High-throughput Microelectronic Facilities, *IEEE J. Sel. Top. Quantum Electron.* 22 1-12. doi:10.1109/JSTQE.2016.2593637 (2016).
- [2] J. Nauriyal, M. Song, R. Yu, and J. Cardenas, "Fiber-to-chip fusion splicing for low-loss photonic packaging," *Optica*, OPTICA 6, 549-552 (2019).
- [3] L. Chen, et al., Low-Loss and Broadband Cantilever Couplers Between Standard Cleaved Fibers and High-Index-Contrast SiN or Si Waveguides, *IEEE Photonics Technol. Lett.* 22, 1744-1746. doi:10.1109/LPT.2010.2085040 (2010).
- [4] N. Shimizu, Fusion splicing between deposited silica waveguides and optical fibers, *Electron. Commun. Jpn. Part Commun.* 67, 115-122. doi:10.1002/ecja.4400670914 (n.d.).
- [5] P. Pal, W.H. Knox, Low loss fusion splicing of micron scale silica fibers, *Opt. Express.* 16, 11568-11573. doi:10.1364/OE.16.011568 (2008).

# Spin Tunnel Field-Effect Transistors Based on Two-Dimensional van der Waals Heterostructures

**CNF Project Number: 2633-18**

**Principal Investigator(s): Jie Shan, Kin Fai Mak**

**User(s): Lizhong Li, Shengwei Jiang**

*Affiliation(s): Laboratory of Atomic and Solid State Physics, Applied and Engineering Physics; Cornell University*

*Primary Source(s) of Research Funding: National Science Foundation under award DMR-1807810*

*for the sample and device fabrication, the Office of Naval Research under award N00014-18-1-2368*

*for the device characterization, and the Air Force Office of Scientific Research Hybrid Materials MURI under award FA9550-18-1-0480 for optical measurements*

*Contact: jie.shan@cornell.edu, kinfai.mak@cornell.edu, sj538@cornell.edu, ll646@cornell.edu*

*Primary CNF Tools Used: Autostep i-line stepper, Hamatech wafer processor develop, Heidelberg mask writer DWL2000, photolithography spinners, SC4500 odd/even-hour evaporator, DISCO dicing saw*

## Abstract:

Transistors based on control of spin orientations, if realized, can revolutionize modern electronics through the implementation of faster and more energy efficient performance and non-volatile data storage. Recent development in magnetic switching by a gate voltage and magnetic reading by the spin filtering effect in two-dimensional magnets has inspired a new operational principle for spin transistors. In this project, we demonstrate a spin tunnel field-effect transistor based on dual-gated graphene/CrI<sub>3</sub> tunnel junctions.

## Summary of Research:

Spin field-effect transistors (FETs) were first proposed by Datta and Das in 1990 [1]. These spin-based devices promise non-volatile data storage and faster and more energy-efficient performance than the current transistors. The original proposal that relies on electric-field-controlled spin precession in a semiconductor channel, faces significant challenges including inefficient spin injection, spin relaxation and spread of the spin precession angle. The recently discovered two-dimensional magnetic insulators [2,3] provide a unique platform to explore new spintronic device concepts. In this project, we develop a tunnel field-effect transistor (TFET) based on few-layer CrI<sub>3</sub> as a magnetic tunnel barrier to achieve spin-dependent outputs that are voltage controllable and reversible.

Figure 1 shows the device structure. It consists of a van der Waals heterostructure of bilayer graphene/bilayer CrI<sub>3</sub>/bilayer graphene with top and bottom gates. The vertical tunnel junction utilizes bilayer graphene as the source and drain contacts and bilayer CrI<sub>3</sub> as the magnetic tunnel barrier. The two nearly symmetric gates are made of few-layer graphene gate electrodes and hexagonal boron nitride (hBN) gate dielectrics. The gates tune the Fermi level of the nearest bilayer graphene contact effectively, which modulates the conductance of the junction through resonant tunneling.

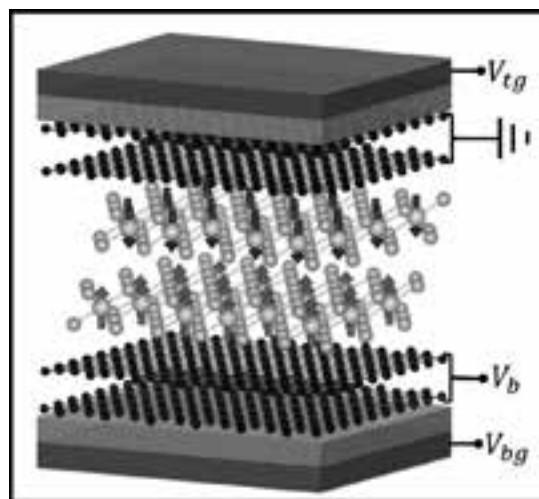


Figure 1: Operational principle of a spin TFET based on gate-controlled spin-flip transition in bilayer CrI<sub>3</sub> and spin filtering in the tunnel junction. Arrows indicate the spin orientation in CrI<sub>3</sub> layers.

The gates can also cause a significant modulation in the tunnel conductance by inducing a spin-flip transition in bilayer CrI<sub>3</sub> by an electric field or through electrostatic gating [4-6]. The conductance is high (low) when the spins in the two layers are aligned (misaligned) due to the spin-filtering effect [7,8]. A spin-TFET action is realized

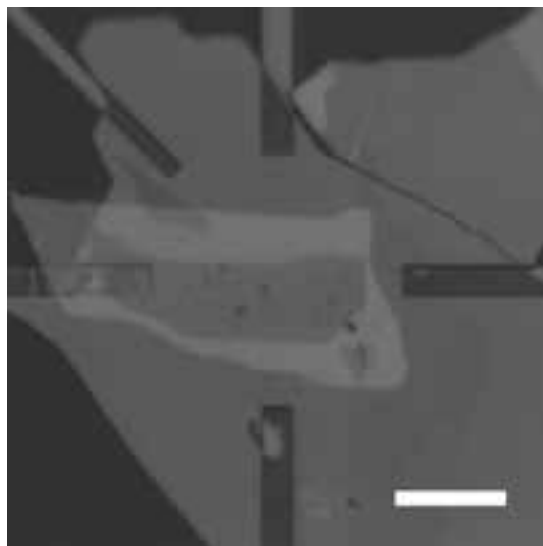


Figure 2: Optical images of a van der Waals heterostructure device deposited on pre-patterned electrodes.

through electrical switching of spins in the magnetic tunnel barrier.

Figure 2 is an optical image of a typical device. The Ti/Au electrodes were first patterned on Si/SiO<sub>2</sub> substrates by photolithography and metal evaporation. Atomically thin samples of CrI<sub>3</sub>, hBN, and graphene were first exfoliated from their bulk crystals onto silicon substrates covered with a 300 nm thermal oxide layer. The selected thin flakes of appropriate thickness and geometry were then picked up one-by-one by a stamp consisting of a thin layer of polycarbonate on polydimethylsiloxane. The complete stack was then deposited onto the substrates with pre-patterned Au electrodes.

An ambipolar transistor behavior with a zero conductance (i.e. off) state is observed for graphene tunnel junctions (solid line, Figure 3). This is a consequence of a sizable band gap opened in both bilayer graphene contacts by a built-in interfacial electric field from the asymmetric hBN/bilayer graphene/bilayer CrI<sub>3</sub> structure.

The TFET output is dependent on the magnetic state of the tunnel barrier. Under a vertical magnetic field of 1 T (dashed line, Figure 3), bilayer CrI<sub>3</sub> switches from an interlayer antiferromagnet to a ferromagnet. The gate dependence of the conductance shifts towards a slightly larger gate voltage, corresponding to a shift in the energy level alignment in the tunnel junction. The tunneling conductance increases over a large doping range.

We demonstrate the spin TFET action, i.e. control of the tunnel conductance by electrically switching the magnetic state of CrI<sub>3</sub>. To minimize the trivial conductance, change due to electrostatic doping, we choose a range of gate voltage, where the conductance is weakly gate dependent.

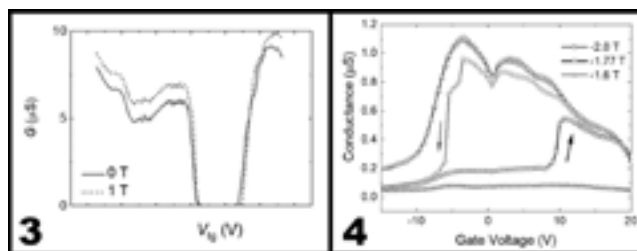


Figure 3, left: Gate dependence of the tunnel conductance in a bilayer CrI<sub>3</sub> device under an out-of-plane magnetic field of 0 T and 1 T [6]. Figure 4, right: Tunnel conductance of a TFET with a four-layer CrI<sub>3</sub> tunnel barrier is repeatedly switched by gating under a constant magnetic bias of -1.77 T. The top and bottom gate voltages are identical, and their sum is shown in the horizontal axis [6]. Results under -2.0 T and -1.6 T (corresponding to the barrier in the ferromagnetic and antiferromagnetic state, respectively) are included for comparison.

Figure 4 shows the result for a 4-layer CrI<sub>3</sub> device under a constant magnetic bias (-1.77 T), which is slightly above the spin-flip transition [9]. The gate voltage can repeatedly alter the TFET between a high and a low conductance state. As a reference, we also include the conductance under a bias magnetic field much above or below the spin-flip transition.

A relative change of ~ 400% in the tunnel conductance with a large hysteresis has been achieved through gating. The switching is originated from a gate-dependent spin-flip transition field.

In conclusion, a new type of spin transistors is achieved, which relies on the spin filtering effect to inject and detect spin, and electrical switching of the magnetization configurations in the tunnel barrier.

## References:

- [1] Datta, S., and Das, B. Applied Physics Letters 56, 665 (1990).
- [2] Huang, B., et al. Nature 546, 270 (2017).
- [3] Gong, C., et al. Nature 546, 265-269 (2017).
- [4] Jiang, S., Shan, J., and Mak, K. F. Nature Materials 17, 406 (2018).
- [5] Jiang, S., Li, L., Wang, Z., Mak, K. F., and Shan, J. Nature Nanotechnology 13, 549 (2018).
- [6] Huang, B., et al. Nature Nanotechnology 13, 544 (2018).
- [7] Song, T., et al. Science 360, 1214-1218 (2018).
- [8] Klein, D. R., et al. Science 360, 1218-1222 (2018).
- [9] Jiang, S., Li, L., Wang, Z., Shan, J., and Mak, K. F. Nature Electronics 2, 159 (2019).

# Non-Linear Anomalous Hall Effect in Few-Layer $\text{WTe}_2$

**CNF Project Number: 2633-18**

**Principal Investigator(s): Jie Shan, Kin Fai Mak**

**User(s): Kaifei Kang, Egon Sohn, Tingxin Li**

*Affiliation(s): Department of Applied and Engineering Physics, Cornell University*

*Primary Source(s) of Research Funding: Army Research Office, US Department of Energy (Office of Basic Energy Sciences), National Science Foundation*

*Contact: kinfai.mak@cornell.edu, kk726@cornell.edu, es799@cornell.edu, tl684@cornell.edu*

*Primary CNF Tools Used: Zeiss Supra SEM, Pt 720-740 reactive ion etcher, Autostep i-line stepper, SC4500 odd/even-hour evaporator*

## Abstract:

The Hall effect occurs only in systems with broken time-reversal symmetry, such as materials under an external magnetic field in the ordinary Hall effect and magnetic materials in the anomalous Hall effect (AHE). Here we demonstrate a new Hall effect in a non-magnetic material, few-layer  $T_d$ - $\text{WTe}_2$  under zero magnetic field. In this effect, the Hall voltage depends quadratically on the longitudinal current. Our results open the possibility of exploring topological effects in solids by nonlinear electrical transport and applications of the phenomenon in spin-orbit torque devices.

## Summary of Research:

The linear Hall effect is odd under time-reversal operation, it occurs only in systems with broken time-reversal symmetry (TRS). The second-order nonlinear effect, in which the Hall voltage depends on drive current quadratically, however, is even under time-reversal operation. It therefore does not require the application of an external magnetic field or the presence of magnetic order in the material. Furthermore, the effect is odd under space-inversion operation and is thus limited to systems with broken inversion symmetry. More specifically, the nonlinear anomalous Hall effect (AHE) has been predicted to exist in crystals with a polar axis and can be used to probe the topological properties of the solids such as the Berry curvature dipole [1]. The experimental studies of the nonlinear AHE remain elusive.

Here we investigate the nonlinear electrical properties of metallic few-layer  $T_d$ - $\text{WTe}_2$ . Atomically thin  $T_d$ - $\text{WTe}_2$  has one polar axis along the crystal b axis, and thus allows the nonlinear AHE. Figure 1 shows the images of samples employed in the experiment. Figure 1a is a sample in the Hall bar geometry and the Figure 1b shows a sample in the circular disk shape. To fabricate these devices, few-layer  $\text{WTe}_2$  and hexagonal boron nitride (hBN) were mechanically exfoliated from bulk crystals (HQ Graphene) onto silicon substrates. The hBN and  $\text{WTe}_2$  flakes were picked up by a stamp consisting of a thin film of polycarbonate (PC) on polydimethylsiloxane (PDMS). The stack was then released onto a Si substrate with pre-patterned Pt electrodes. For disk devices, the

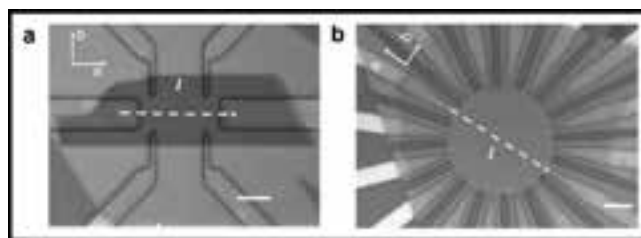


Figure 1: Optical image of a typical Hall bar (top) and circular disk (bottom) device used in this study. The scale bars are 5  $\mu\text{m}$ .  $\text{WTe}_2$  samples are in grey, Pt electrodes in orange, and the Si substrate in dark red-orange for the disk device, respectively. Dashed yellow lines indicate the current ( $I$ ) direction. a and b are the crystal axes.

completed stack was further patterned into a circular shape. To this end, a poly(methyl methacrylate (PMMA) mask with desired shape was first defined by standard e-beam lithography on top of the completed stack, it was then etched by reactive ion etching with  $\text{SF}_6$  gas. Finally the residual PMMA was removed in an acetone bath.

To measure the nonlinear anomalous Hall effect in few-layer  $\text{WTe}_2$  in the Hall bar devices, we apply an AC current along the crystal a-axis at a fixed frequency (137 Hz) and measure the longitudinal and transverse voltage drops at both the first and second-harmonic frequencies. The circular disk devices were measured in the same fashion. Current was injected from one of the 16 electrodes,

voltages parallel and perpendicular to the current injection were recorded. The angular dependence of the nonlinear anomalous Hall effect was carried out by rotating both current injection and voltage measurement simultaneously.

A second-harmonic transverse  $V_{\perp}^{2\omega}$  voltage was observed in both the Hall bar and circular disk devices. Its magnitude scales quadratically with the current. In the disk devices, the normalized nonlinear hall response  $V_{\perp}^{2\omega}/(V_{\parallel})^2$  (where  $V_{\parallel}$  is the linear longitudinal voltage) shows a one-fold angular dependence (Figure 2). It maximizes when the current is perpendicular to the mirror line (i.e. along the a-axis), and minimizes when the current is parallel to the mirror line (i.e. along the b-axis). The observed effect is fully consistent with the crystal symmetry of few-layer  $T_d$ -WTe<sub>2</sub>.

The microscopic mechanism of the observed effect was further examined by studying its scaling against scattering (conductivity  $\sigma$ ).

The normalized nonlinear Hall response

$$\frac{E_{\perp}^{2\omega}}{(E_{\parallel})^2}$$

(where  $E_{\perp}^{2\omega}$  and  $E_{\parallel}$  are the fields calculated from the corresponding voltages and the device dimensions) was observed to scale linearly with  $\sigma^2$  for a large range of temperature (Figure 3). Such a scaling law suggests that the observed nonlinear Hall effect can be understood as an anomalous Hall effect with electrically generated magnetization. Our result also indicates that both intrinsic Berry curvature dipole and extrinsic spin-dependent scatterings contribute to the observed nonlinear AHE.

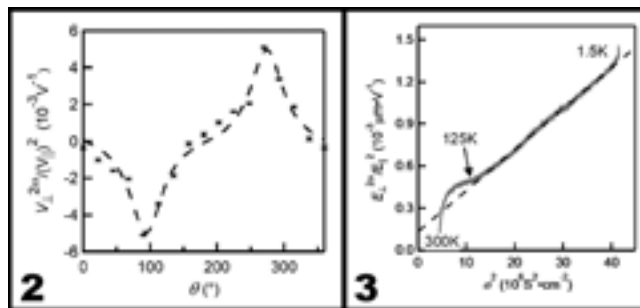


Figure 2, left: The nonlinear Hall effect as a function of current angle. Symbols are experimental data and the dashed line is a fit to the nonlinear response model including all second-order nonlinear susceptibilities allowed by the crystal symmetry. Figure 3, right: The normalized nonlinear Hall effect as a function of square of the longitudinal conductivity. The dashed line is a linear fit.

### References:

- [1] Sodemann, I., and Fu, L. Quantum Nonlinear Hall Effect Induced by Berry Curvature Dipole in Time-Reversal Invariant Materials. *Physical Review Letters* 115, 216806 (2015).

# Mass Transport on Graphene

**CNF Project Number: 2767-19**

**Principal Investigator(s): Scott Schiffres**

**User(s): Yingchun Jiang**

*Affiliation(s): Mechanical Engineering, Binghamton University*

*Primary Source(s) of Research Funding: Startup funding*

*Contact: sschiff@binghamton.edu, yjiang89@binghamton.edu*

*Primary CNF Tools Used: Photolithography tools, ABM contact aligner, Zeiss Ultra SEM*

## Summary of Research:

The development of nanotechnology requires versatile manipulation tools for atomic scale assembly and controlled material delivery. Scanning tunneling microscope (STM), atomic force microscope (AFM) have been demonstrated as powerful tools for manipulation atoms and molecules on clean surfaces. However, these tools suffer from low delivery efficiency: they are not capable to deliver nanometer scale features containing large amounts of atoms, and they cannot deliver atom efficiently to desired work area (sticky).

Carbon nanotubes and graphene have been suggested as possible nanoscale mass conveyors with electric field as source of applied force. Controllable and reversible atomic metal transportation along carbon nanotubes (CNTs) and transport of more than  $10^7$  atoms have been demonstrated [1-3]. Graphene is mechanically robust and chemically inert; it can sustain large current density similar to CNTs. It has advantage over CNTs that more complicated mass transport circuits can be designed with lithography techniques[4-7].

Despite experiments that show the Al plate transport along graphene in crossroad configuration, the more complicated transport circuit and the other type of transport species, and atomic scale transport are needed to be tested. Theoretical model on the nature of the driving mechanism will also be developed.

## References:

- [1] B.C. Regan, S. Aloni, R.O. Ritchie, U. Dahmen, A. Zetti, Carbon nanotubes as nanoscale mass conveyors, *Nature*. 428 924-927. doi:10.1038/nature02496 (2004).
- [2] Z. Ren, Y. Lan, Y. Wang, Subnanometer motion of cargoes driven by thermal gradients along carbon nanotubes, *Science* (80-. ). 7-43. doi:10.1007/978-3-642-30490-3\_2 (2012).
- [3] N. Mingo, L. Yang, J. Han, Current-induced forces upon atoms adsorbed on conducting carbon nanotubes, *J. Phys. Chem. B*. 105 11142-11147. doi:10.1021/jp011491s (2001).
- [4] S. Hertel, F. Kisslinger, J. Jobst, D. Waldmann, M. Krieger, H.B. Weber, Current annealing and electrical breakdown of epitaxial graphene, *Appl. Phys. Lett.* 98 2009-2012. doi:10.1063/1.3592841 (2011).
- [5] A. Barreiro, R. Rurali, E.R. Hernández, A. Bachtold, Structured graphene devices for mass transport, *Small*. 7 775-780. doi:10.1002/sml.201001916 (2011).
- [6] J. Moser, A. Barreiro, A. Bachtold, Current-induced cleaning of graphene, *Appl. Phys. Lett.* 91 1-4. doi:10.1063/1.2789673 (2007).
- [7] D. Solenov, K.A. Velizhanin, Adsorbate transport on graphene by electromigration, *Phys. Rev. Lett.* 109 1-5. doi:10.1103/PhysRevLett.109.095504 (2012).



# Superconducting Thin Film Growth and Post Laser Annealing

**CNF Project Number: 2779-19**

**Principal Investigator(s): Matthias Liepe**

**User(s): Zeming Sun**

*Affiliation(s): Cornell Laboratory for Accelerator-based Sciences and Education, Cornell University*

*Primary Source(s) of Research Funding: National Science Foundation under Grant No. PHY-1549132*

*Contact: mul2@cornell.edu, zs253@cornell.edu*

*Website: <https://physics.cornell.edu/matthias-liepe>*

*Primary CNF Tools Used: Oxford FlexAL atomic layer deposition system, Arradance Gemstar-6 atomic layer deposition system, Woollam spectroscopic ellipsometer, Zygo optical profilometer, P10 profilometer.*

## Abstract:

**Superconducting radio frequency (SRF) cavities are important in accelerating charged particle beams in broad applications such as colliders, neutron sources, and light sources. Niobium tin and magnesium diboride superconductors are the most promising candidates for the next generation SRF cavities. However, their thin film growth is still challenging due to grain boundaries, defects generation, surface roughness, and surface oxidation. Thus, this project investigates the growth mechanisms of superconducting films and explores post processing techniques, such as laser annealing and surface passivation, to mitigate the crystal defects, surface roughness, and oxidation.**

## Summary of Research:

This report is based on the work done since April 1st, 2019 when Zeming became a user of Cornell NanoScale Science and Technology Facility.

The project has focused on (1) reduction of surface roughness for niobium substrates, (2) deposition and optimization of titanium nitride film as a laser absorber, and (3) deposition of aluminum nitride film for passivating magnesium diboride surface.

(1) Reducing surface roughness of starting niobium substrates is critical for the following deposition of superconducting films since the roughness could negatively affect the nucleation process. Mechanical polishing was exploited, and Zygo optical profilometer was used to monitor the roughness. As shown in Figure 1, the final roughness of niobium substrates are reduced to  $R_a = 72$  nm.

(2) Laser annealing technique has been explored to enable the epitaxial growth of niobium tin grains and also

reduce the film surface roughness. Preliminary results showed that niobium tin surface failed to absorb sufficient laser energy using a 120 W, 1064 nm wavelength  $\text{CO}_2$  laser and a 250 W, 980 nm wavelength diode laser. In order to enhance the laser light absorption, a titanium nitride film was deposited using thermal atomic layer deposition system. The film thickness and refractive index are important for achieving the anti-reflection. Both parameters were determined by the ellipsometer as shown in Figure 2 and 3.

(3) Magnesium diboride superconducting thin film is easily oxidized in air which hinders its wider application. An aluminum nitride film is deposited on the magnesium diboride film using plasma-enhanced atomic layer deposition. This dielectric film is expected to passivate the magnesium diboride film surface. Further investigations are ongoing.

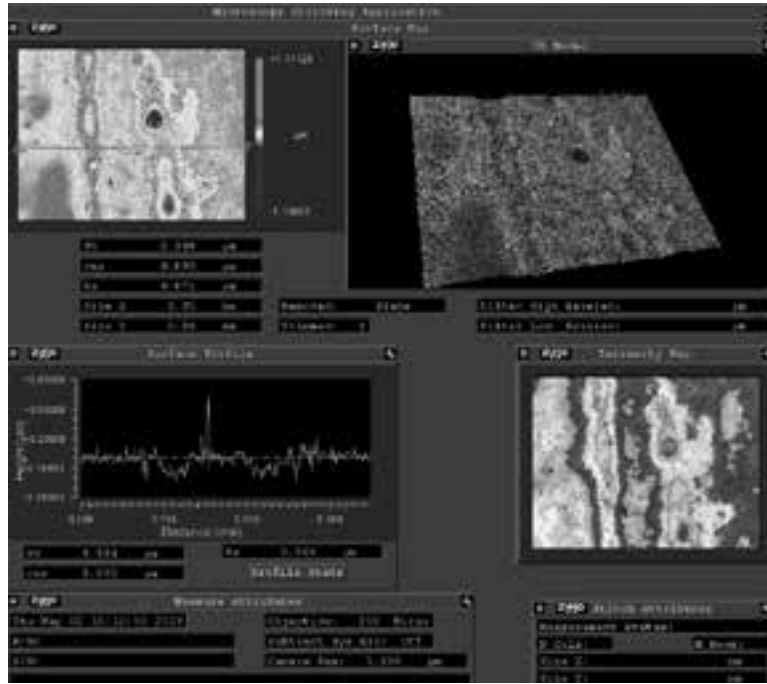


Figure 1: Surface roughness of niobium substrate after mechanical polishing. (Find full color on pages xiv-xv.)

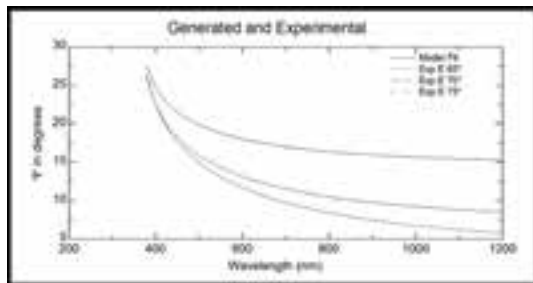


Figure 2: Ellipsometry modeling for determining the thickness of titanium nitride deposited by thermal atomic layer deposition.

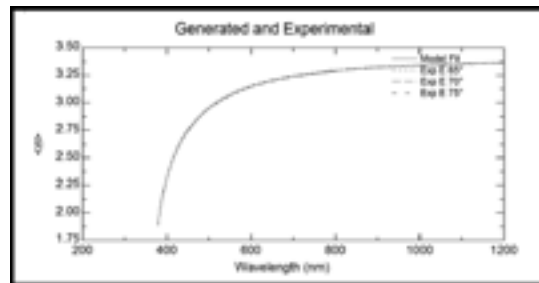


Figure 3: Refractive index of atomic layer deposited titanium nitride film.

# Directed Self Assembly of a Stable Radical Polymer

**CNF Project Number: 386-90**

**Principal Investigator(s): Prof. Christopher Kemper Ober**

**User(s): Mohit R. Khurana, Alicia Cintora**

*Affiliation(s): Materials Science and Engineering, Cornell University*

*Primary Source(s) of Research Funding: Department of Energy Office of Basic Energy Science (Grant DE-SC0014336)*

*Contact: cko3@cornell.edu, mrk263@cornell.edu, ac2467@cornell.edu*

*Website: <https://ober.mse.cornell.edu>*

*Primary CNF Tools Used: ASML DUV stepper, Oxford 80+ etcher, Oxford ICP Cobra etcher*

## Abstract:

We use graphoepitaxy and solvent vapor annealing (SVA) for directed self-assembly of a stable radical block copolymer composed of blocks of poly(2,2,6,6-tetramethylpiperidinyloxy methacrylate) (PTMA) and poly(2,2,2-trifluoroethyl methacrylate) (PTFEMA). We report lamellar and cylindrical morphologies formed by SVA. Silicon substrate is topographically modified to form trenches with two different trench depths. Narrow and deep trenches are shown to assemble the blocks parallel to the trench direction, however with defects. By using a neutral underlayer, we show alignment of the blocks perpendicular to the trench direction. This ordering is further improved by increasing film thickness. Lastly, we study morphologies by using gold sidewalls instead of the silicon sidewalls for chemically heterogeneous graphoepitaxy. We thus demonstrate control over placement of stable radical groups in nanostructures controlled for further electrical characterizations and device fabrication.

## Summary of Research:

**Introduction.** Microphase separation of the block copolymers (BCP) result in the formation of chemically discrete domains ordered in various geometries [1]. Recently, stable radical BCPs have been studied in order to place these stable radical groups in such geometries and study charge transport in these polymers [2,3]. Commonly explored BCP morphologies include the cylindrical (hcp), lamellar, and spherical (bcc) microphases, which can be ordered in the scale of microns. Lamellar morphology BCPs are often utilized in BCP lithography, but their self-assembly typically results in a finger-print like pattern rather than unidirectional order [4]. Directed self-assembly (DSA) has been studied extensively to attain this unidirectional order in lamellar and down-lying cylindrical BCPs. Two common DSA techniques used are graphoepitaxy, which uses topographically patterned substrates and chemoepitaxy, which uses chemically modified substrates [5]. We use graphoepitaxy here to unidirectionally order the two blocks parallel and perpendicular to the trenches using the strategies shown in Figure 1.

**Methods.** The trenches and gold sidewall are formed by deep UV (DUV) lithography process. Antireflective coating (ARC) DUV42P was first spin-coated followed by the resist UV210. DUV exposures were performed using

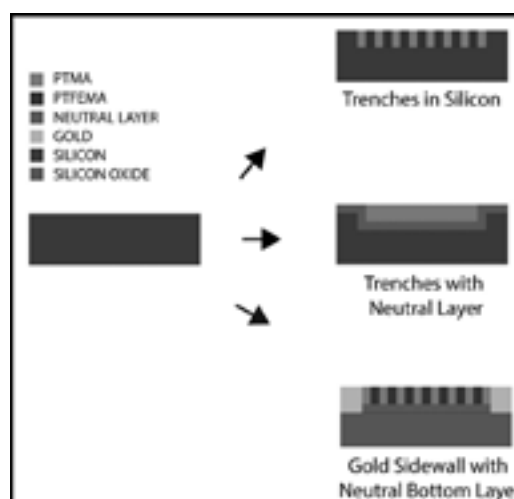


Figure 1: Epitaxial strategies used for direct self-assembly.

ASML 300C stepper. The dose was adjusted to achieve the desired trench width at a depth of focus of  $-0.1 \mu\text{m}$ . The exposed films were then baked at  $130^\circ\text{C}$  for 90s and developed using AZ MIF 726.

The ARC was then etched using Oxford 80+ etcher by using  $\text{CF}_4$  and  $\text{O}_2$  plasma. The silicon was then etched in Oxford Cobra ICP etcher using an HBr chemistry. The resist was then stripped using Anatech resist strip. Gold sidewalls were prepared using a lift-off process. A 300 nm thick  $\text{SiO}_2$  layer was grown on the silicon wafer by PECVD. The line and space patterns were created using the lithography process as mentioned above. ARC layer was then etched as mentioned above. A 5 nm layer of titanium and 100 nm film of gold were deposited on the patterned photoresist using an electron beam evaporator. The metal deposited on the photoresist was lifted off using MICROPOSIT 1165 solution. The BCP had a PTMA block molecular weight of 21,700 g/mol and PTFEMA block molecular weight of 14,300 g/mol having a dispersity of 1.21 when measured by GPC. AFM images were taken using Asylum-MFP3D-Bio-AFM-SPM in tapping mode.

### Results and Discussion:

The block copolymer when annealed using chloroform vapor for three hours exhibited a lamellar morphology as shown in Figure 2. The lamella showed short-range order in a fingerprint-like pattern and thus to enable DSA, we used trenches in the silicon wafer with a trench depth of 120 nm as well as gold sidewalls (100 nm thick). The AFM images are summarized in Figure 3. All films except the one shown in Figure 3e were annealed for six hours. The blocks align parallel to the silicon trenches but with defects as shown in Figure 3a and 3b. The defects exist due to weakly preferential wetting of silicon by PTMA. By grafting a neutral underlayer, we align the blocks perpendicular to the trenches (as shown in Figure 3c and 3d) with an improvement in the alignment with a thicker film. A short-range ordered parallel alignment is also obtained using gold sidewalls due to low vapor pressure annealing for three hours (Figure 3e).

Thus, we demonstrate directed self-assembly of the stable radical containing block copolymer in morphologies parallel and perpendicular to the trench direction. This opens up the possibility to elucidate charge transport in stable radical polymers and relate polymer structure to the electrical properties.

### References:

- [1] F. S. Bates and G. H. Fredrickson, "Block copolymers-designer soft materials," *Phys. Today*, vol. 52, no. 2, pp. 32-38, 1999.
- [2] C. Liedel, A. Moehle, G. D. Fuchs, and C. K. Ober, "Block copolymers with stable radical and fluorinated groups by ATRP," *MRS Commun.*, vol. 5, no. 3, pp. 441-446, 2015.
- [3] C. Liedel and C. K. Ober, "Nanopatterning of Stable Radical Containing Block Copolymers for Highly Ordered Functional Nanomeshes," *Macromolecules*, vol. 49, no. 16, pp. 5884-5892, 2016.
- [4] D. Sundrani, S. B. Darling, and S. J. Sibener, "Guiding Polymers to Perfection: Macroscopic Alignment of Nanoscale Domains," *Nano Lett.*, vol. 4, no. 2, pp. 273-276, 2004.
- [5] R. A. Segalman, "Patterning with block copolymer thin films," *Mater. Sci. Eng. R Reports*, vol. 48, no. 6, pp. 191-226, 2005.

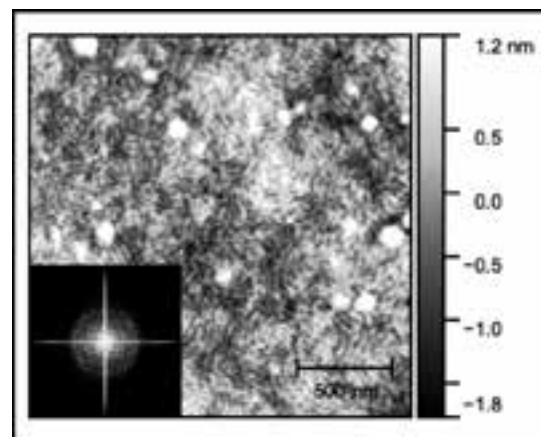


Figure 2: AFM topography image and its 2DFFT (inset) when annealed for three hours.

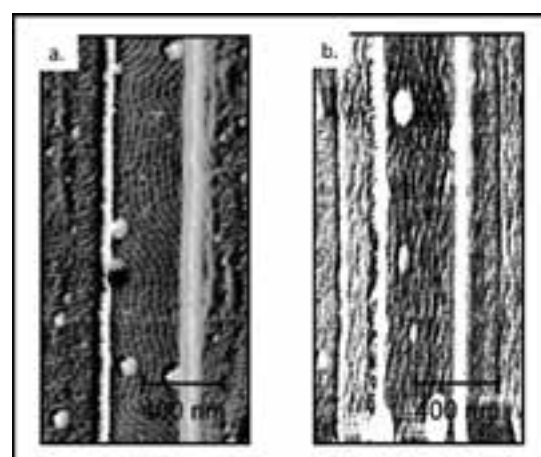


Figure 3: AFM phase images of the thin lm on (a) Si trench (width 480 nm) (b) Si trench (width 448 nm).

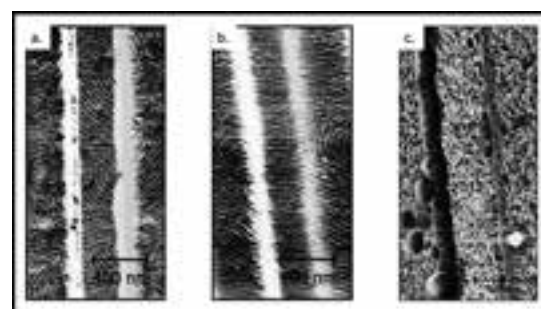


Figure 4: AFM phase images of the thin lm on (a) and (b) Si trench (width 480 nm) and (c) gold sidewall (width 448 nm).

# Nanoscale Periodic Pillar Feature Process Survival

**CNF Project Number: 2217-13**

**Principal Investigator(s): Ioannis Kymissis**

**User(s): Tanya Cruz Garza**

*Affiliation(s): Department of Electrical Engineering, Columbia University, New York, NY*

*Primary Source(s) of Research Funding: National Science Foundation*

*Contact: johnkym@ee.columbia.edu, tanyacruzgarza@gmail.com*

*Website: <http://kymissis.columbia.edu>*

*Primary CNF Tools Used: ASML 300C DUV, GCA 5x Autostep i-line stepper, SEMs*

## Abstract:

The ASML 300C DUV and GCA 5x Autostep i-line stepper have been used in previous years to produce pillar and hole features with diameters ranging from 232 nm to 446 nm on fused silica and silicon wafers. In recent years hole features have been favored over pillar features because pillars are more likely to break during further front and backside wafer processing. It has been found that pillar features give optical performance up to 3.5 times higher than the hole features in spectral applications. For this reason, pillar feature fabrication with further front and backside wafer processing is explored that gives initial wafer yield of 50% compared to previous hole feature wafer yield of 70%.

## Summary of Research:

In previous years a process for patterning nanophotonic pillar and hole structures was developed at CNF that used the ASML 300C DUV stepper as well as the GCA 5x Autostep i-line stepper. These features were etched into the substrate material using the patterned resist as an etch mask. The ASML 300C DUV stepper process has been used to pattern 4-inch borosilicate float glass wafers ("borofloat"), 4-inch fused silica wafers, and 4-inch silicon wafers. Pillar features like those shown in Figure 1 were fabricated with diameters ranging from 232 nm to 816 nm. Hole features like those shown in Figure 2 were fabricated with design diameters ranging from 306 nm to 446 nm. Optimal depth of focus (DOF), exposure dose, and etch time were determined for nanophotonic patterns in fused silica by varying these parameters incrementally and examining the resultant features. Photonic crystal geometry was examined in the SEM and photonic crystal performance was assessed optically via extraction of waveguided light.

The DUV process previously developed to pattern fused silica wafers with nanophotonic pillar and hole structures was expanded to include automated backside alignment on the ASML 300C DUV stepper. Work done to enable backside alignment was achieved for up to three out of four ASML alignment marks etched into bare fused silica to a depth of 150 nm.

For recent applications, nanophotonic patterning was mainly focused on holes versus pillars because pillars are more likely to break during further processing and wafer handling. In recent years processing steps have been added to the wafer after nanophotonic crystal patterning to include both front and backside aluminum reflector layers as shown in Figure 3. These added layers can be combined with black, opaque absorber layers on both sides to make a monolithic optical bench on a chip ideal for spectrometer applications. These added steps with the dicing of the wafer makes the pillars more exposed to handling that could damage them. It has been found that pillars designed to the same diameter of corresponding holes give spectral responsively between 50% - 350% higher over a range of inputs between 400-1000 nm for designs with a diameter of 446 nm. It is because pillars give such a greater spectral responsively, that they have again been investigated for the monolithic optical bench die design.

This past year, nanophotonic pillar structures with diameters of 612 nm and 816 nm were made in fused silica wafers with the intent of seeing how they would survive further processing to produce the monolithic optical bench die design. These pillars were patterned on fused silica wafers with the ASML 300C DUV and etched into the substrate using the resist as an etch

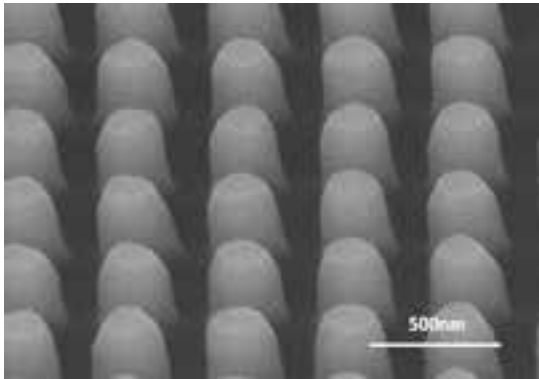


Figure 1: SEM image of photonic crystal pattern, nominally with 270 nm pillar features, fabricated fused silica with process developed with ASML 300C DUV stepper.

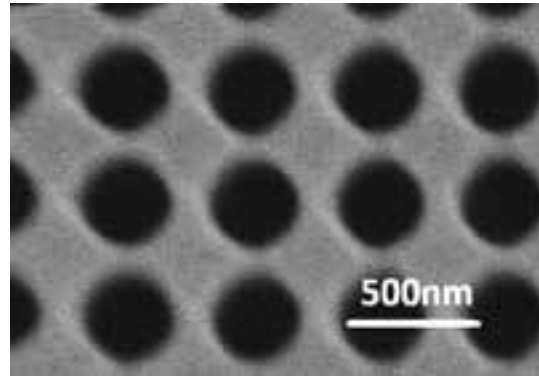


Figure 2: SEM image of photonic crystal pattern, nominally with 306 nm hole features, fabricated in fused silica with a process developed with ASML 300C DUV stepper.

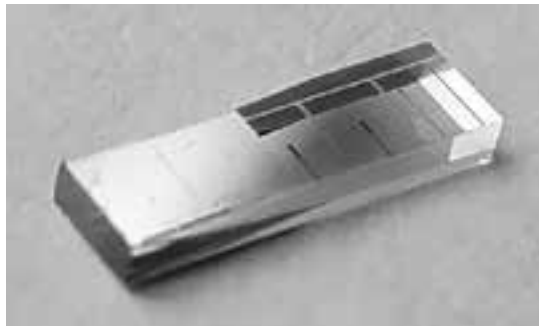


Figure 3: Diced fused silica die with patterned Al reflectors on both sides in addition to the nanophotonic pattern.



Figure 4: Green (gray) light being scattered through a 306 nm diameter nanophotonic pattern illuminating pillar damage.

mask. The wafers then had aluminum sputtered onto the front and backside, which was patterned via contact lithography plus liftoff and plasma etch respectively. The wafer was then coated with a protective resist layer, diced, and solvent cleaned. The resulting dies were inspected by waveguiding green light into the edge of the die and inspecting the nanophotonic crystal pattern in a microscope to check for defects. Pillar damage from handling is apparent in the example given in Figure 4. Nanophotonic patterns may also be rejected for other kind of defects. An example of a yield for a recent 446 nm diameter hole pattern wafer was 70.5% while the yield for a 612 nm diameter pillar wafer fabricated this year was 50%. Percent yield for a monolithic optical bench die with pillar nanophotonic patterns gives significantly lower yield due to the added aluminum layer processing steps after nanophotonic patterning.

In summary, a process to fabricate nanophotonic pillar structures with diameters of 612 nm and 816 nm has been used to make dies to have further processing including front and backside aluminum patterns. Although pillar features tend to be more fragile when it comes to further wafer processing, these features tend to give higher optical throughput in spectral scattering applications in spectrometer systems. Results of optically imaging of 306 nm diameter patterns with post-processing including front and backside aluminum layers as well as dicing shows a total die yield of 50% for pillars which is quite a bit lower than the normal yield for holes which can be around 70%.

## Size Characterization of Plasma Membrane Vesicles, Virus Particles, and Synthetic Vesicles

**CNF Project Number: 2575-17**

**Principal Investigator(s): Susan Daniel**

**User(s): Tiffany Tang, Miya Bidon**

*Affiliation(s): Chemical and Biomolecular Engineering, Cornell University*

*Primary Source(s) of Research Funding: National Science Foundation*

*Contact: sd386@cornell.edu, tt528@cornell.edu, mrb346@cornell.edu*

*Primary CNF Tools Used: Nanosight*

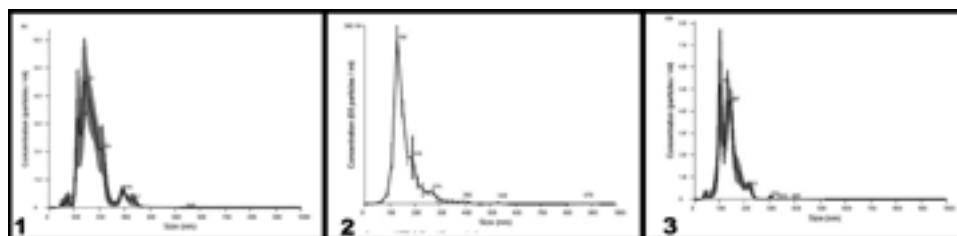


Figure 1, left: Concentration vs size (nm) distribution plot for pseudotyped virus particles. Figure 2, center: Concentration vs size (nm) distribution plot for plasma membrane vesicles. Figure 3, right: Concentration vs size (nm) distribution plot for synthetic vesicles.

### Abstract:

**Nanosight was used to determine the concentration and size distribution of various biologically relevant particles, including viruses and plasma membrane vesicles.**

### Summary of Research:

Our research investigates interactions of biologically relevant particles (viruses, microvesicles, plasma membrane vesicles) on a supported lipid bilayer and with synthetic vesicles.

Most of the particles used are generated in-house and as such, it is important to characterize them (diameter,

size distribution, concentration of particles) to ensure that we are using the similar quality and concentration of particles across various experiments for consistency. The concentration is especially important as too much or too little of the plasma membrane vesicles used to form the supported lipid bilayer will influence the bilayer's diffusivity and patchiness and varying concentration of viral particles may impact fluorescent dye incorporation.

Typical sizes of viruses, plasma membranes vesicles, and synthetic vesicles that we use range from 100-200 nm and typical values of concentration are on the order of  $10^8$  particles/mL for plasma membrane particles,  $10^{10}$  particles/mL for viruses and  $10^{12}$  particles/mL for synthetic vesicles.



# Nanoslit Silicon Nitride Fabrication for Virus Filtration

**CNF Project Number: 2660-18**

**Principal Investigator(s): James Roussie**

**User(s): Joshua Miller**

*Affiliation(s): SiMPore Inc.*

*Primary Source(s) of Research Funding: National Institutes of Health*

*Contact: jroussie@simpore.com, jmiller@simpore.com*

*Website: www.simpore.com*

*Primary CNF Tools Used: ASML 300C DUV stepper, SÜSS MicroTec Gamma Cluster Tool*

## Abstract:

Existing and widely used 0.2/0.22  $\mu\text{m}$  polymer filters are not well-suited for sterilizing larger non-protein biological therapeutics during their production, as these filters entrap these molecules, thus contributing to significant yield loss. Here, we report on the fabrication of nanoslit silicon nitride (NSN) membranes with isoporous sub-0.2  $\mu\text{m}$  rectangular “pores” for addressing the need for improved biological therapeutic sterile filtration. For this project, we used CNF’s SÜSS MicroTec Gamma Cluster Tool and the ASML 300C DUV 4x reduction stepper, as well as various tools at Rochester Institute of Technology (RIT) Semiconductor and Microsystems Fabrication Laboratory (SMFL) to produce novel NSN sterile filters.

## Summary of Research:

SiMPore produces a variety of suspended thin film membranes both porous and non-porous. For this project, the capability of the ASML 300C was explored for the fabrication of 200 nm wide slits. Capability for patterning this feature size is not available at SiMPore’s home cleanroom (RIT SMFL). Prior to this project, SiMPore offered nanomembrane filters with either pore sizes ranging from 500 nm - 8  $\mu\text{m}$  or sub-70 nm by way of SiMPore’s NanoPorous silicon nitride (NPN) membranes, but the range in-between has been missing from SiMPore’s offerings.

In this work, the SÜSS MicroTec was used to spin on 60 nm DUV 42P anti-reflective coating (ARC), then approximately 500 nm UV210 positive photoresist over 200 nm low stress silicon nitride on 150 mm diameter, 310  $\mu\text{m}$  thick double side polished (DSP) wafers. The mask designed for this project had four iterations: 1:1 pitch 200 nm slits, 1:2 pitch 200 nm slits, 1:3 pitch 200 nm slits, and finally 1:2 pitch 150 nm slits. These sizes allowed exploration of strength vs. fluency as well as the ability to make slightly different sizes via over exposure, if desired. The ASML 300C was then used to expose each pattern by Focus Exposure Matrix (FEM). The resultant FEM features were then etched into the nitride, the

feature sizes were measured with a Zeiss Auriga scanning electron microscope, and the optimal conditions were extrapolated. Once the conditions were selected, additional wafers were coated, exposed continuously across the entire frontside of the wafer, developed at CNF, and then taken back to RIT SMFL for further processing.

At RIT SMFL, the ARC was removed by a low power reactive ion etch (RIE) in a Trion and then the 200 nm SiN was etched via plasma etch in a LAM 490. The wafers were then stripped of the residual resist using Piranha and protected on the frontside with a silicon oxide derived from tetraethylorthosilicate (TEOS) using an AMAT Precision 5000 system. The wafers were then flipped to expose a backside pattern, etched in a similar fashion as the slit features, and then stripped. This backside pattern defined SepCon membrane chips with four (4) 0.3 mm by 3 mm porous membranes and a total chip size of 5.4 mm by 5.4 mm. Finally, the silicon wafers were bulk-etched from the backside with a crystallographic etchant and the frontside protective oxide was removed with buffered oxide etchant (BOE). See Figure 1 for process flow, and Figure 2 for scanning transmission electron microscope (STEM) images of the nanoslits.

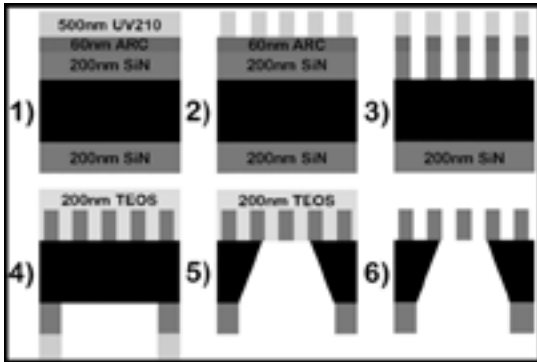


Figure 1: Process flow for NSN chips; 1) ARC plus Resist application, 2) Exposure with ASML 300C, 3) RIE of ARC and nitride to form nanoslits, 4) Frontside protection with TEOS and backside patterning, 5) Backside crystallographic etch to free-stand membranes, 6) Final porous membrane chips.



Figure 2: 25kX magnification STEM of 200 nm slits with 1:1 pitch.

One of the challenges faced in this work was the limited depth of focus (DOF) for these feature sizes. 200 nm slits are the practical limit of the 248 nm DUV light source on the ASML 300C. Due to this, we are operating at the maximum NA and Sigma, which further narrows the DOF. Another difficulty we experienced stemmed from the thinness of our wafers. The 310  $\mu\text{m}$  thick wafers used for this process have considerable flex when held by a vacuum chuck (as the ASML does during exposures). The result of this is a significant loss of real estate on the final wafer, as the flexed portions of the wafer were out of focus and their features under-exposed. To combat this, our current tests use 675  $\mu\text{m}$  thick wafers, and following frontside patterning, will be backside-ground and re-polished to 310  $\mu\text{m}$  for subsequent bulk-etching.

The resulting patterned features are significantly more uniform across the entire surface of the wafer. While there were still some aberrations; the use of ultra-flat wafers in the future may be necessary for complete and uniform exposures across a full 150 mm wafer.

In the next year, we will continue to pursue complete uniformity across these wafers, trying with tighter specified flatness, with the goal of fully useable wafers. Additionally, we will attempt using the same mask for slightly larger features to see if that will help alleviate some of the DOF issue. Our preliminary evidence suggests the 150 nm slits, when over exposed produce viable 200 nm slits at roughly 1:1 pitch.

# *CNF 2018-2019 Research Accomplishments*

# INDEX

## Reports by CNF Project Number

|                                    |                       |                        |
|------------------------------------|-----------------------|------------------------|
| 2019 CNF REU..... 2, 4, 6, 76, 110 | 2214-13 ..... 26, 28  | 2578-17 ..... 68       |
|                                    | 2217-13 ..... 202     | 2580-17 ..... 40       |
| 111-80 ..... 158, 160, 162         | 2255-13 ..... 140     | 2584-17 ..... 96       |
| 386-90 ..... 78, 200               | 2262-13 ..... 30      | 2590-17 ..... 42       |
| 598-96 ..... 164                   | 2307-14 ..... 62      | 2618-17 ..... 58       |
| 692-98 ..... 8                     | 2349-15 ..... 32      | 2632-18 ..... 132      |
| 731-98 ..... 10, 12                | 2357-15 ..... 122     | 2633-18 ..... 192, 194 |
| 863-00 ..... 52                    | 2361-15 ..... 184     | 2641-18 ..... 44       |
| 900-00 ..... 112, 166              | 2364-15 ..... 142     | 2656-18 ..... 60       |
| 1121-03 ..... 114                  | 2369-15 ..... 186     | 2660-18 ..... 206      |
| 1239-04 ..... 54                   | 2385-15 ..... 124     | 2661-18 ..... 154      |
| 1255-04 ..... 14                   | 2387-15 ..... 144     | 2684-18 ..... 98       |
| 1262-04 ..... 116                  | 2416-16 ..... 126     | 2692-18 ..... 156      |
| 1314-05 ..... 168                  | 2430-16 ..... 34      | 2698-18 ..... 100      |
| 1356-05 ..... 80                   | 2444-16 ..... 188     | 2704-18 ..... 102      |
| 1520-07 ..... 170                  | 2446-16 ..... 128     | 2719-18 ..... 92       |
| 1645-08 ..... 82                   | 2458-16 ..... 146     | 2728-18 ..... 104      |
| 1735-08 ..... 172                  | 2471-16 ..... 148     | 2751-18 ..... 106      |
| 1738-08 ..... 16                   | 2472-16 ..... 36, 150 | 2754-18 ..... 46       |
| 1757-09 ..... 84, 86               | 2474-16 ..... 130     | 2755-18 ..... 70       |
| 1872-10 ..... 18                   | 2486-16 ..... 92      | 2762-19 ..... 134      |
| 1940-10 ..... 20                   | 2504-16 ..... 38      | 2767-19 ..... 196      |
| 1970-10 ..... 22                   | 2509-16 ..... 64      | 2774-19 ..... 48       |
| 1997-11 ..... 136, 138             | 2513-16 ..... 56      | 2779-19 ..... 198      |
| 2065-11 ..... 24                   | 2524-17 ..... 190     | 2780-19 ..... 50       |
| 2091-11 ..... 88, 174, 176         | 2527-17 ..... 152     | 2800-19 ..... 72, 74   |
| 2103-12 ..... 90                   | 2543-17 ..... 66      | 2801-19 ..... 108      |
| 2123-12 ..... 118                  | 2565-17 ..... 94      |                        |
| 2126-12 ..... 120, 178, 180, 182   | 2575-17 ..... 204     |                        |

• • •

## CNF Principal Investigators & Users

### A

|                           |     |
|---------------------------|-----|
| Abate, Aysanew            | 70  |
| Abbaspourrad, Alireza     | 6   |
| Abe, Mahiro               | 146 |
| Abruña, Héctor D.         | 58  |
| Alden, Jonathan S.        | 92  |
| Alden, Joshua S.          | 92  |
| Alibakhshi, Mohammad Amin | 26  |
| Alvarez, Anna             | 110 |
| Asadzadeh, Mostafa        | 130 |

### B

|                            |                    |
|----------------------------|--------------------|
| Bader, Samuel              | 72                 |
| Baker, Jacob               | 2                  |
| Baker, Shefford            | 90, 132            |
| Ballard, Andrew            | 172                |
| Bangalore Prakash, Prajwal | 102                |
| Bee, Madeleine             | 56                 |
| Bharadwaj, Shyam           | 144                |
| Bidon, Miya                | 204                |
| Bircan, Baris              | 112, 126           |
| Bosch, Melissa             | 150                |
| Bose, Arnab                | 158                |
| Buhrman, Robert A.         | 158, 160, 162, 188 |

### C

|                        |               |
|------------------------|---------------|
| Capasso, Federico      | 148           |
| Cardenas, Jaime        | 190           |
| Chen, Huiyao           | 120, 178      |
| Chen, Jingyi           | 50            |
| Cheung, Hil Fung Harry | 180           |
| Chiou, Aaron           | 40            |
| Chu, Nicole            | 104           |
| Cintora, Alicia        | 200           |
| Cohen, Itai            | 110, 112, 126 |
| Cortese, Alejandro J.  | 68, 166       |
| Cothard, Nicholas      | 146           |
| Craighead, Harold G.   | 12            |
| Crouse, David          | 152           |
| Cruz Garza, Tanya      | 202           |
| Cui, Weili             | 186           |

### D

|                           |         |
|---------------------------|---------|
| Daly, Brian C.            | 186     |
| Dang, Phillip             | 108     |
| Daniel, Susan             | 44, 204 |
| Daveau, Raphael Sura      | 182     |
| DeBenedetti, William J.I. | 96      |
| Delgado, Robert           | 36      |
| Deyhim, Alex              | 104     |
| Dickens, Andrew           | 134     |
| Dilli, Zeynep             | 70      |
| Dodge, Kenneth            | 168     |
| Dorsey, Kyle              | 112     |
| Duzen, Nilay              | 84      |

### E

|                    |         |
|--------------------|---------|
| Encomendero, Jimy  | 72, 144 |
| Engstrom, James R. | 54, 76  |
| Erickson, David    | 4, 18   |
| Escobedo, Fernando | 102     |
| Esposito, Edward   | 112     |
| Estroff, Lara      | 40      |

*The 2018-2019 CNF Research Accomplishments are online in PDF, at [http://cnf.cornell.edu/publications/research\\_accomplishments](http://cnf.cornell.edu/publications/research_accomplishments)*

**F**

- Farhangdoust, Fatemeh .. ..... 26  
 Fischbach, Claudia ..... 40  
 Flynn, Christopher ..... 20  
 Fuchs, Gregory D.  
 .... 88, 120, 174, 176, 178, 180, 182

**G**

- Giannelis, Emmanuel ..... 60  
 Gillilan, Richard E. .... 20  
 Giloteaux, Ludovic ..... 42  
 Gingerich, Marcus ..... 38  
 Gray, Isaiah. .... 174  
 Gupta, Manish. .... 118

**H**

- Hamed, Ahmed ..... 122  
 Hanrath, Tobias ..... 82  
 Hanson, Maureen R. .... 42  
 Harper, Christine E. .... 22  
 He, Yang ..... 136  
 Henriques, Matthew .. ..... 2  
 Hernandez, Christopher J. .. ..... 22  
 Herzog, Walter ..... 14  
 Hickman, Austin ... ..... 72  
 Hines, Melissa A. ... ..... 96  
 Holladay, Bo ..... 48  
 Howington, Caleb. .... 172  
 Hsu, Jui-Yuan... ..... 62  
 Hu, Zongyang .. ..... 62  
 Huang, Jen-Yu.. ..... 82  
 Huang, Steven He. .... 36  
 Huang, Yuming ..... 86  
 Hwang, James C.M. .... 64

**I**

- Indrajeet ..... 172

**J**

- Jayaraman, Anjana..... 32  
 Jena, Debdeep. .... 72, 74, 108, 144  
 Ji, Xingchen ..... 142  
 Ji, Yanxin ..... 166  
 Jiang, Shengwei ... ..... 192  
 Jiang, Yingchun ..... 196  
 Jung, Minwoo.. ..... 150  
 Jung, Seok-Hyon .. ..... 78

**K**

- Kang, Junhyuk (Andrew) ..... 32  
 Kang, Kaifei ..... 194  
 Kang, Minjee ... ..... 40  
 Khaitan, Rupal. .... 40  
 Khurana, Mohit R. .... 200  
 Kirby, Brian J. .... 32, 124  
 Ku, Jaseung ..... 168  
 Kuan, Johnathan .. ..... 120  
 Kymissis, Ioannis .. ..... 202

**L**

- Lal, Amit ..... 114, 116  
 Lambert, Guillaume .. ..... 2  
 Lammerding, Jan . ..... 24  
 LaValley, Danielle . .... 10, 12  
 Lawlor, Colleen C. .... 54, 76  
 Lee, Hyunjea..... ..... 108  
 Lee, Kevin... ..... 144  
 Lee, Sunwoo..... ..... 68  
 Leifer, Cynthia . .... 50  
 Leonard, Timothy. .... 14  
 Lepak, Lori . .... 34, 154  
 Li, Deyu . .... 100  
 Li, Lei ..... 64  
 Li, Lizhong.. ..... 192  
 Li, Mingxiao ..... 138  
 Li, Ruofan ... ..... 164  
 Li, Tingxin .. ..... 194  
 Li, Wenshen ..... 62  
 Liepe, Matthias ..... 198

**L, continued**

Lin, Qiang... ..136, 138  
 Ling, Jingwei ... ..136  
 Lipson, Michal. ....142  
 Liu, Chengyu ... ..140  
 Liu, Fangchen .. ..30  
 Liu, Qingkun.... ..110, 126  
 Liu, Yebin.... ..168  
 Louge, Michel.. ....94  
 Lu, Junlan... ..36  
 Luo, Jin.. ....104  
 Luo, Rui. ....136

**M**

Ma, Tianyu.. ....126  
 Mak, Kin Fai ....192, 194  
 Manzer, Zachary ... ..44  
 Marohn, John A.... ..52  
 Maroo, Shalabh C. ....118  
 McEntaffer, Randall... ..156  
 McEuen, Paul L.... ..92, 112, 126, 166  
 McEwen, Benjamin.... ..98  
 Miles, Drew ....156  
 Miles, Ronald N. ....128  
 Miller, Joshua .. ..206  
 Miller, Paula ....12  
 Mirbagheri, Golsa. ....152  
 Mokhtare, Amir ....6  
 Molnar, Alyosha C. ....68  
 Munechika, Katie.. ....4

**N**

Nan, Tianxiang ....164  
 Nauriyal, Juniyali. ....190  
 Ndao, Sidy .. ..122  
 Nguyen, Darien ....6  
 Nomoto, Kazuki.... ..74  
 Norris, Samantha L. .. ..166  
 Nowack, Katja C. ... ..184

**O**

O’Neal, Adam .. ....42  
 Ober, Christopher Kemper  
 ....60, 78, 84, 86, 106, 200  
 Oeschger, Taylor... ..4  
 Ozdogan, Mehmet ....128

**P**

Page, Ryan.. ....144  
 Pan, Wenyang.. ....60, 78  
 Parahovnik, Anatoly .. ..130  
 Park, Albert M. ....88  
 Park, Jisung ....66  
 Park, Joon-Suh ....148  
 Parpia, Jeevak M. . ....170  
 Pearson, Tanner.... ..112  
 Peles, Yoav.. ....130  
 Plourde, Britton L.T. .. ..168, 172  
 Plumridge, Alexander ....8  
 Polhemus, Katherine . ....124  
 Pollack, Lois ....8

**R**

Rafson, Jessica ....56  
 Ralph, Daniel... ..164  
 Raut, Sidharth P... ..118  
 Ravi, Adarsh ....114  
 Ravirajan, Abhaiguru ....106  
 Rey, Elizabeth .. ....18  
 Reynolds, Michael F.. ....166  
 Roberts, Melanie F. ....22  
 Roberts, Samantha ....142  
 Rogers, Nathaniel. ....90  
 Rouse, Zachary ....132  
 Roussie, James ....206  
 Russell, Sierra.. ....112  
 Ruyack, Alexander ....116

**S**

|                                    |          |
|------------------------------------|----------|
| Sacks, Gavin .....                 | 56       |
| Sahoo, Shilpa .....                | 94       |
| Sakai, Kazunori .....              | 78       |
| Sawatsky, Andrew .....             | 14       |
| Schaefer, Brian T. ....            | 184      |
| Schiffres, Scott .....             | 196      |
| Schlom, Darrell .....              | 66       |
| Senatore, Michael. ....            | 168      |
| Shahedipour-Sandvik, Fatemeh ..... | 98       |
| Shan, Jie .....                    | 192, 194 |
| Shcherbakov, Maxim . ....          | 150      |
| Shi, Shengjie.....                 | 160      |
| Shire, Douglas . ....              | 38       |
| Shuler, Michael L. ....            | 10, 12   |
| Shvets, Gennady... ..              | 36, 150  |
| Singhal, Jashan .....              | 108      |
| Sohn, Egon . ....                  | 194      |
| Song, Meiting .. ....              | 190      |
| Stacey, Gordon .....               | 146      |
| Stiehl, Gregory M. ....            | 174      |
| Stokol, Tracy.....                 | 50       |
| Suh, Taewon .....                  | 54, 76   |
| Sun, Peter (Hanyu).....            | 52       |
| Sun, Zeming .....                  | 198      |
| Suntivich, Jin.....                | 140      |

**T**

|                                       |     |
|---------------------------------------|-----|
| Tang, Tiffany.....                    | 204 |
| Tapping, Ryan.. .....                 | 162 |
| Thanniyil Sebastian, Abhilash.. ..... | 170 |
| Towfighian, Shahrzad .....            | 128 |
| Tran, Hai Quang ... ..                | 86  |
| Tran, James M.H... ..                 | 76  |

**V**

|                         |    |
|-------------------------|----|
| Velický, Matej .. ..... | 58 |
|-------------------------|----|

**W**

|                          |        |
|--------------------------|--------|
| Wan, Christopher.. ..... | 50     |
| Wang, Michelle D.. ..... | 16     |
| Wang, Wei... .....       | 126    |
| Wang, Yadong.. .....     | 46     |
| Wang, Ying.. .....       | 12     |
| Wanunu, Meni . ....      | 26, 28 |
| Wiesner, Ulrich .....    | 80     |
| Willett, Denis S.....    | 48     |
| Windsor, Aaron .....     | 24     |
| Wong, Patricia . ....    | 38     |
| Wright, John.....        | 108    |
| Wu, Anni .....           | 62     |
| Wu, Mingming . ....      | 30     |

**X**

|                         |                 |
|-------------------------|-----------------|
| Xie, Yanyou. ....       | 176             |
| Xing, Huili Grace .. .. | 62, 72, 74, 108 |
| Xiong, Kuanchen .. ..   | 64              |

**Y**

|                        |     |
|------------------------|-----|
| Yang, Lin .....        | 100 |
| Yan, Shanana... .....  | 104 |
| Ye, Fan ... .....      | 16  |
| Yeh, Chia-Wei... ..... | 46  |
| Yu, Fei.....           | 80  |

**Z**

|                         |     |
|-------------------------|-----|
| Zang, Zexuan... .....   | 108 |
| Zhang, Qi.....          | 80  |
| Zhao, Yang.. .....      | 100 |
| Zhelev, Nikolay .....   | 170 |
| Zheng, Pengyu. ....     | 28  |
| Zhong, Chuan-Jian ..... | 104 |
| Zhu, Lijun ... .....    | 188 |
| Zou, An.. .....         | 118 |
| Zou, Bugao . ....       | 146 |





100  $\mu\text{m}$

